



Optimizing Blast Furnace Hearth Inner State

(OPTIBLAFINS)

A large, abstract graphic of blue and white waves occupies the bottom half of the page, creating a dynamic and modern feel.

EUR 30531 EN

Optimizing Blast Furnace Hearth Inner State (OPTIBLAFINS)

European Commission

Directorate-General for Research and Innovation

Directorate D – Clean Planet

Unit D.3 — Low Emission Future Industries

Contact Andrea Gentili

E-mail rtd-steel-coal@ec.europa.eu

RTD-PUBLICATIONS@ec.europa.eu

European Commission

B-1049 Brussels

Manuscript completed in 2019.

This document has been prepared for the European Commission however it reflects the views only of the authors, and the Commission cannot be held responsible for any use which may be made of the information contained therein.

More information on the European Union is available on the internet (<http://europa.eu>).

Luxembourg: Publications Office of the European Union, 2020

PDF ISBN 978-92-76-27831-3 ISSN 1831-9424 doi:10.2777/037724 KI-NA-30-531-EN-N

© European Union, 2020.

Reuse is authorised provided the source is acknowledged. The reuse policy of European Commission documents is regulated by Decision 2011/833/EU (OJ L 330, 14.12.2011, p. 39).

For any use or reproduction of photos or other material that is not under the EU copyright, permission must be sought directly from the copyright holders.

All pictures, figures and graphs © Tata Steel Nederland Technology B.V., RFSR-CT-2015-00001 OPTIBLAFINS

Research Fund for Coal and Steel

Optimizing Blast Furnace Hearth Inner State

(*OPTIBLAFINS*)

G. Louwerse, J.van der Stel, C. Zeilstra

Tata Steel Nederland Technology B.V.,

Wenckebachstraat 1, NL-1951 JZ Velsen-Noord, The Netherlands.

O. Nechyporuk

ArcelorMittal Maizières Research SA,

Voie Romaine, BP 30320, FR-57283 Maizières-Lès-Metz, France.

R. Soulignac

Center de Recherches Metallurgiques ASBL,

Avenue du Bois Saint Jean 21, B-4000 Liège, Belgium.

R. Lin

Aktien-Gesellschaft der Dillinger Hüttenwerke,

Werkstrasse 1, DE-66763 Dillingen/Saar, Germany.

H. Bartusch, T. Hauck, Y. Kaymak

VDEH-Betriebsforschungsinstitut GmbH,

Sohnstrasse 65, DE-40237 Düsseldorf, Germany.

M. Ölund, D. Sandström

SWERIM AB,

Arontorpsvägen 1, SE-97125 Luleå, Sweden.

M. Henriksson

Luossavaara-Kiirunavaara AB,

Varvsgatan 45, SE-97129 Luleå, Sweden.

J. Mernitz

ArcelorMittal Eisenhüttenstadt GmbH,

Werkstrasse 1, DE-15890 Eisenhüttenstadt, Germany.

C. Feilmayr

voestalpine GmbH,

voest-Alpine-Strasse 3, AT-4020 Linz, Austria.

M. Helle, H. Saxén

ÅBO Akademi University,

Domkyrkotorget 3, FI-20500 ABO, Finland.

T. Lichtenegger, M. Vångö

Johannes Kepler University,

Altenberger Strasse 69, AT-4040 Linz, Austria.

F. Bambauer, S. Wirtz

Ruhr-Universität Bochum,

Universitätsstrasse 150, DE-44780 Bochum, Germany.

Grant Agreement RFSR-CT-2015-00001

1/07/2015 – 31/12/2018

Final Report

Table of contents:

1	FINAL SUMMARY	7
2	SCIENTIFIC AND TECHNICAL DESCRIPTION OF THE RESULTS	12
2.1	OBJECTIVES OF THE PROJECT.....	12
2.2	DESCRIPTION OF ACTIVITIES AND DISCUSSION	12
2.2.1	<i>Work Package 1: Modelling of BF Hearth Processes</i>	12
2.2.1.1	FEM based 3D-Model for thermal stress at hearth wall	12
2.2.1.2	Permeability and Dead Man shape	21
2.2.1.2.1	Introduction.....	21
2.2.1.2.2	Simulation BF hearth	22
2.2.1.2.2.1	Computational Fluid Dynamics (CFD)	22
2.2.1.2.2.2	Discrete Element Method (DEM).....	22
2.2.1.2.2.3	Particle/Fluid Interaction Forces	23
2.2.1.2.3	Model BF development	23
2.2.1.2.3.1	Model Dillingen BF.....	24
2.2.1.2.3.2	Results.....	26
2.2.1.2.3.2.1	Initial Case – Adjustment of parameters.	28
2.2.1.2.3.2.2	Dead Man Dynamics (DMD) indicator < 0	29
2.2.1.2.3.2.3	Dead Man Dynamics (DMD) indicator > 0	30
2.2.1.2.3.3	Results – variation of hot blast	31
2.2.1.2.3.4	Conclusions.....	32
2.2.1.2.4	Model and performance improvements	33
2.2.1.2.4.1	Code adaption.....	33
2.2.1.2.4.1.1	Parallelization via domain decomposition.....	33
2.2.1.2.4.1.2	Periodic boundary conditions for sector models	34
2.2.1.2.5	Model simplifications – time scaling	35
2.2.1.3	Water model studies BF Hearth.....	37
2.2.1.3.1	Research water model TSE.....	37
2.2.1.3.1.1	Basic Engineering	37
2.2.1.3.1.2	CFD set-up water model	38
2.2.1.3.1.3	Results.....	38
2.2.1.3.2	Water model Experimental Blast Furnace (EBF)	41
2.2.1.3.2.1	Experimental blast furnace process conditions	41
2.2.1.3.2.2	Construction and setup of water model.....	45
2.2.1.3.2.3	EBF water model - Implementation.....	49
2.2.1.3.2.4	EBF water model, campaign 1 (uniform inflow) – results.....	50
2.2.1.3.2.5	EBF water model, campaign 2 (non-uniform inflow) – results.....	54
2.2.1.3.2.6	Conclusions - Water model Experimental Blast Furnace (EBF)	55
2.2.1.3.2.7	CFD model of EBF (governing equation)	56
2.2.1.3.2.8	CFD model EBF (geometry and mesh)	57
2.2.1.3.2.9	CFD modelling of physical (water) model	58
2.2.1.3.2.9.1	Eulerian-Lagrangian approach.....	58
2.2.1.3.2.9.2	Streamlines approach	59
2.2.1.3.2.10	The shell temperature measurement calibration	60
2.2.1.3.2.11	Modelling of the drainage of the EBF Hearth	62
2.2.1.3.2.11.1	Case one: reference case	62
2.2.1.3.2.11.2	Case two: Change in the volume fraction of the bed	64
2.2.1.3.2.11.3	Case three: Over pressure	66
2.2.1.3.2.12	Conclusion: CFD Modelling of the EBF hearth	67
2.2.1.4	Simulation of erosion patterns and transient inverse modelling of the lining state	68
2.2.1.4.1	Introduction.....	68
2.2.1.4.2	Asymptotic wear model	68
2.2.1.4.3	Inverse two-dimensional transient model	72
2.2.1.5	Hot metal flow and coke particle movement in BF hearth	83
2.2.1.5.1	Introduction.....	83
2.2.1.5.2	Experimental validation	83
2.2.1.5.3	Numerical instabilities	84
2.2.1.5.4	Simulations results of the experiments	84
2.2.1.5.5	Burden-weight-distribution boundary condition	85
2.2.1.5.6	Small-scale hearth demonstration case, results	86
2.2.1.5.7	Taphole boundary conditions	88
2.2.1.5.8	Demonstration case of full-scale BF hearth	89
2.2.1.5.9	Application to voestalpine's BF5	92
2.2.1.5.10	Heat transfer extension.....	93

2.2.1.5.11	Summary and conclusion	95
2.2.1.5.12	CFD MOHDRAIN 2.0.....	95
2.2.1.6	Validation of the mathematical models	100
2.2.1.6.1	Analysis of BF-A tapping data at voestalpine.....	100
2.2.1.6.1.1	Analysis of BF-A tapping data in the period 2012-2016.....	101
2.2.1.6.1.2	Comparison of tapping data at voestalpine BF-A before and after relining	
	105	
2.2.1.6.2	Analysis of BF-5 data 2010-2015 campaigns.....	105
2.2.1.6.2.1	Data over the entire campaign.....	106
2.2.1.6.2.2	Data comparison of three defined periods.....	109
2.2.1.6.3	Simplified model of liquid levels in BF Hearth and tapping flow rates for CFD validation	
	112	
2.2.1.6.4	CFD MOHDRAIN 2.0 industrial validation.....	116
2.2.1.6.5	Physical model.....	119
2.2.1.6.5.1	General design of the physical model.....	119
2.2.1.6.5.2	Fluids of the physical model.....	120
2.2.1.6.5.3	Preliminary trial using demineralised water.....	121
2.2.1.6.5.4	Conclusion.....	123
2.2.1.7	Fundamentals of behaviour of coke particles in BF Hearth.....	123
2.2.1.7.1	Coke gasification and reactivity.....	123
2.2.1.7.2	Carburization	124
2.2.1.7.3	Interaction between coke and slag.....	124
2.2.2	<i>Work Package 2: BF Hearth Monitoring</i>	125
2.2.2.1	Improved hearth state monitoring data collection.....	125
2.2.2.1.1	Introduction.....	125
2.2.2.1.2	Use of acoustic technique for hearth lining state monitoring.....	125
2.2.2.1.3	Collection of data for monitoring of hearth and design of additional installations	128
2.2.2.1.4	Results.....	129
2.2.2.1.5	Conclusions.....	130
2.2.2.1.6	Use of optical fibres and strain gauge for monitoring of hearth lining state..	131
2.2.2.1.7	Results.....	132
2.2.2.1.8	Relining observations, additional on-line measurements and measurement campaigns	
	133	
2.2.2.2	Data processing and monitoring for existing and new measurements	145
2.2.2.2.1	Modelling of Hearth Echo Excellence technique.....	145
2.2.2.2.2	Conclusion.....	147
2.2.2.2.3	Modelling of crack detection using optical fibre.....	147
2.2.3	<i>Work Package 3: BF Controlling the Dead Man</i>	150
2.2.3.1	Study and collection of solid samples from blast furnace and experimental blast furnace	
	150	
2.2.3.1.1	Exiting solid samples from EBF (campaign 31)	150
2.2.3.1.2	New samples collected from EBF (campaign 32)	151
2.2.3.1.2.1	Collection of solid samples from the hearth of the experimental blast furnace	
	151	
2.2.3.1.2.2	Evaluation of solid samples from physical characterisation	152
2.2.3.1.2.3	Evaluation of solid samples from chemical characterisation.....	157
2.2.3.1.3	Core borings AM Fos	158
2.2.3.2	Flow of slag and hot metal in Experimental BF during tapping	162
2.2.3.2.1	Injection of tracer during operation and before quenching including investigation of the close to wall material for tracer content.....	162
2.2.3.2.2	Flow of slag and hot metal in EBF during tapping	169
2.2.3.3	On-line Model for Dead Man permeability and dynamics	170
2.2.3.4	Dynamic Coke Properties.....	174
2.2.3.4.1	Gasification trials.....	175
2.2.3.4.2	Coke dissolution during its interaction with the molten phases	177
2.2.3.5	Laboratory studies on slag and its properties.....	178
2.2.3.5.1	Chemical analysis and XRD analysis of the slag.....	179
2.2.3.5.1.1	Analysis of the slag samples from EBF campaign 31.....	179
2.2.3.5.1.2	Analysis of the slag samples from EBF campaign 32 and industrial slag	
	181	
2.2.3.5.1.3	The melting behaviour and viscosity of the slag: results from FactSage calculations	
	184	
2.2.3.5.1.4	Laboratory study of the viscosity and wetting behaviour of the slag from EBF and industries	187
2.2.3.5.1.4.1	Viscosity measurement	187
2.2.3.5.1.4.2	Viscosity measurement results and reliability	188
2.2.3.5.1.4.3	Heating microscope study	195
2.2.3.5.1.4.4	Heating microscope study results	196

2.2.3.5.1.5	Multivariate analysis of the data.....	201
2.2.3.6	Properties of coke in the Experimental BF hearth.....	203
2.2.3.6.1	Properties of the coke from the EBF hearth, campaign 31	203
2.2.3.6.2	Properties of the coke from the EBF hearth, campaign 32	205
2.2.3.6.3	The void fraction of the coke bed	208
2.2.3.7	Slag and iron composition vs dead man state.....	210
2.2.3.7.1	Process conditions vs. EBF hearth conditions.....	210
2.2.3.7.2	Dead man versus liquid level.....	214
2.2.4	<i>Work Package 4: Operational data interpretation</i>	222
2.2.4.1	On-line Multiphysics Hearth Monitoring Model for wear and stress and hearth erosion/build-up estimation during a full campaign	222
2.2.4.1.1	On-line Multiphysics model.....	222
2.2.4.1.2	Two-dimensional static hearth model in operation	226
2.2.4.2	Estimation of wear/skull gaps brittle layers, statistical and model-based analysis of operational data.....	236
2.2.4.2.1	Introduction.....	236
2.2.4.2.2	Multipoint thermocouple analysis.....	237
2.2.4.2.3	Statistical analysis of hearth wall temperatures	239
2.2.4.2.4	Balance-based model of liquid levels.....	247
2.2.4.3	Verification and fitting of the on-line CFD model with a monitoring of liquid level indicators ²⁵⁵	
2.2.4.3.1	Liquid level model using strain gauges.....	255
2.2.4.3.1.1	Theory behind the liquid level model.....	257
2.2.4.3.1.2	Model architecture.....	258
2.2.4.3.1.3	Strain gauge measurements.....	259
2.2.4.3.2	Tilting during tapping	263
2.2.4.3.3	Conclusions.....	264
2.2.5	<i>Work Package 5: Management and Reporting</i>	265
2.3	CONCLUSIONS / RECOMMENDATIONS	265
2.4	EXPLOITATION AND IMPACT OF THE RESEARCH RESULTS.....	267
2.5	APPENDIX.....	269
2.5.1	<i>CFD-DEM modelling approach (part 1)</i>	269
2.5.2	<i>Dynamic void fraction model (part 2)</i>	269
2.5.3	<i>Optical Microscope analysis and SEM-EDS analysis</i>	271
2.5.3.1	Optical microscope analysis.....	271
2.5.3.2	SEM-EDS analysis.....	273
2.5.4	<i>SIMCA analysis</i>	292
2.5.4.1	SIMCA	292
2.5.4.2	Terms used in the analysis.....	292
2.5.4.2.1	Principal Component (PC)	292
2.5.4.2.2	Projection to Latent Structures (PLS)	293
2.5.4.2.3	Variable Importance Projection (VIP)	293
2.5.4.3	Variable list used in the SIMCA analysis	293
2.5.4.4	Models.....	294
2.5.4.4.1	Model 1 (M1).....	294
2.5.4.4.2	Model 2 (M2).....	295
2.5.4.4.3	Model 3 (M3).....	296
2.5.4.4.4	Model 4 (M4).....	297
3	LIST OF SYMBOLS, INDICES, ACRONYMS AND ABBREVIATIONS	300
4	REFERENCES	305
5	TABLE OF FIGURES	309
6	TABLE OF TABLES.....	319



1 Final Summary

The RFCS OPTIBLAFINS project aimed to improve the blast furnace hearth life via the following four objectives:

- Modelling of blast furnace hearth processes;
- Blast furnace hearth monitoring;
- Controlling the dead man;
- Operational data interpretation.

To address the above objectives, this research project had five work packages, the results from which are summarized below.

WP1 (FEM, CFD-DEM modelling and validation)

Work package 1 focussed on the investigation and understanding on hearth erosion. The modelling work was mainly done by FEM and CFD-DEM techniques. In the present project, extensive work covering the different methods has been performed, resulting in a better knowledge of their advantages and drawbacks, as well as their current limits of applications. Thanks to the different universities involved, a better understanding could be reached for the BF hearth situation.

All the used models have been validated with plant data and/or measured data.

FEM modelling:

Thermal stress calculations (by FEM) showed gaps between carbon blocks within the refractory of the BF hearth (AMEH BF5). These simulation results were validated with thermography measurements at the shell of the same BF. The relaxed and expanded state of the shell influences the movement of the carbon blocks and the creation of gaps as a result.

Shell strains were calculated and visualised within the FEM model. In addition, the FEM model has been used to study the BF hearth (AGDH BF4) behaviour during stoppages using multi-thermocouples (5 in a row). Thermal conductivity values were determined in WP2.

There was a good agreement between computed and measured temperatures. It is clear, that this FEM model helps to improve the knowledge of the BF hearth thermal state and thermal stresses.

CFD and CFD-DEM modelling:

CFD modelling led to the perception once again, that the flow of freshly molten hot metal strongly affects the wear of the BF refractory in the hearth. The manifestation of such a hot metal flow is the result of a delicate balance between static and dynamic forces acting in the complex three phase system (solids/liquids/gas) within the BF. This flow is mainly influenced (among other factors) by the shape of the lower dead man (DM) boundary and the porosity distribution inside the DM (e.g. porosity near the walls or void space at the lower boundary).

An online model was developed of the "Dead Man Dynamics" (DMD), which shows the current DM state (floating / sitting / transitional) as well as the averaged DM porosity in dependence of operational parameters. This DMD model cannot provide information about the absolute volume of the coke free area below the DM, and the porosity distribution within the DM. Currently, it is difficult for the BF operator to interpret the DMD results for his specific BF with respect to a favourable plant operation strategy ensuring a long hearth operation. For this reason, a simulation model of the blast furnace hearth has been developed to provide details of the void space (filled with liquid metal) below the dead man (DM).

To accomplish this objective, a coupled CFD-DEM approach was chosen, which connects the individual particle movement with the fluid phase. After the code has been successfully developed, improved and reviewed, the simulation tool was finally used to calculate different DM state scenarios of the AGDH BF4. For example, typical wear shapes known from hearth relining (elephant foot wear, local deep holes) or the distinct shape of erosion monitored during relining of the BF, may correlate with the specific flow field existing during the different states of the DM.

Another approach was to implement a coupled CFD-DEM model in the open source software CFDEMcoupling, OpenFoam and LIGGGHTS and validate it with a lab-scale water experiment (using a bed of buoyant particles). Two cases were considered: a floating and a sitting dead man. Model predictions were compared with the measured drainage rates as well as with photographs of the moving floating particle bed. A good agreement was found between predictions and experiments. A dynamic void fraction model was developed which captures the bulk movement of the dead man. The model was applied to an isothermal (diameter 12m) blast furnace. The model was able to simulate several hours of real-time while still accounting for the dynamic dead man with reasonable computational effort. Subsequently, the model was used in a setup corresponding to the voestalpine's BF5 and was found to show good agreement with measured iron flow rate from the plant for a couple of tapping periods.

A multiphase CFD model (MOHDRAIN 2.0) was developed to simulate liquid metal and slag flow in the BF hearth and to describe the tapping process. A sensitivity study was performed to check the most influential parameters (slag viscosity and dead man porosity) during tapping. There was a good validity of the model, when its results were compared with industrial plant data of AM Fos.

Experimental validation:

Water model studies were carried out on small- as well as on full scale. The goal of the small-scale experiment was to understand the fundamentals of natural convection flow through a porous medium near the BF wall. The measurements clearly show different velocity profiles in the mock-up using innovative laser equipment. A boundary layer, close to the wall, was seen with different particle-ball sizes. Such findings could be expected along the BF hearth wall as well. A larger temperature difference develops in the packed bed compared to the no packed bed case. Measurement data was used to optimize the CFD model.

The goal of using the full-scale water model (LKAB's Experimental Blast Furnace EBF) was to determine well-defined porosity, top pressure as well as tapping rate values to be used in the CFD-DEM models. Coke particles were used with the same wetting behaviour as for the real EBF process. The coke bed itself was set up in a way that there were three different porosity zones. Two different tapping rates were used as well as a tracing agent in order to trace the water flow in detail. The distribution of the flow field is independent of the tapping rate for an equal bed distribution. A decrease in bed porosity (with no change in top pressure) increases the time required for the iron level to reach the taphole, but it turns out to be not particularly significant. An increase in top pressure (twice as much in pressure with constant porosity) significantly decreases the time required for the iron level to enter the taphole (up to 40 percent).

WP2 (Monitoring refractory wear and liquid level)

Work package 2 aimed to further develop refractory wear monitoring techniques to achieve a better understanding of the wear process and to enable early detection and prevention of wear.

The Hearth Echo Excellence (HEE) technique was up-scaled to monitor the remaining thickness of the lining and the skull and to detect cracks in the lining. It turns out to be, that several layers of lining materials result in a complex frequency spectrum. Modelling of the Hearth Echo Excellence measurement technique uses an acoustic inversion technique. This technique requires a "field" data-set (measured) and a "synthetic" data-set (model). In this case, the media parameters and geometry of the model must be adjusted until the "field" data set matches the "synthetic" data set. However, the modelling part of the HEE technique was more complicated than expected: the BF hearth wall consists of a multi-layer system, and it requires a highly sophisticated modelling inversion method.

One of the current hearth refractory monitoring techniques, is based on thermocouples installed in the lining. The mutual position of these thermocouples is sometimes quite long and therefore there is no actual information of the lining between these thermocouples. Optical fibres with high-temperature Bragg gratings (FBG's) can monitor the temperature along the whole line of the fibre. The glass fibre sensors used in the BF hearth consist of FBG-arrays each with 20 FBG sensors. The maximum temperature measured by FBG at TSE BF6 is around 70°C. The temperatures are consistent in time, and the device is very robust and reliable. SWERIM developed a numerical simulation model of heat transfer from the liquid metal in the BF hearth out to the surrounding with a simulated crack in the lining. This model can clarify whether it is possible to detect a crack in the lining based on the temperature distribution change in the lining closer to the hearth wall. Three simulations were carried out: no crack in the lining, a crack at the depth of 100 mm and a crack at a depth of 200 mm. The FBG temperature profiles were calculated assuming that the temperature of the crack is the same as for the liquid metal and set to 1450 °C. In the simulation of a 100 mm deep crack, the 5 °C isotherm is about 400 mm from the shell and in the simulation of 200 mm deep crack, the 5°C isotherm is almost at the surface.

The liquid level in the blast furnace is estimated by employing the (electromotive force) EMF measurement technique where the potential difference between for instance the bottom and a position higher up of the blast furnace is determined. Due to insufficient correlation with liquid levels, the use of standard EMF-sensors was limited. By applying a constant voltage between points above and below the liquid level, a change in current can be measured thereby reflecting changes in electrical resistance. These new EMF sensor types are connected with the refractory by making an electrical contact on the existing stainless-steel thermocouple housing, while existing EMF sensors are attached to the BF shell. This resulted in a robust signal without deviating too much. Despite these better EMF signals, the liquid level was still not easy to determine.

During the BF relining work at AGDH BF4 and AMEH BF5A, the real states of the hearth wall (HM-infiltration/ wear/skull/salamander/brittle layers) were investigated, and the remaining wall refractory could be measured and sampled. The observed/measured residual wall thickness is always less than what the numerical models estimates. The rough inner surface of all these blocks

indicated that they had not been in direct contact to the hot metal and they were just the cold parts behind brittle zones. Core drillings samples were taken for physical and chemical tests. For example, heat conductivity, thermal expansion coefficient, and elasticity modulus were measured. Chemical analyses of selected samples are also performed. New hearth concepts at the BFs of AGDH and AMEH include additional on-line measurements, for example, of cooling water, flow rate and temperature:

- The chemical analysis of the carbon block samples from AMEH BF5A and the brittle layer were compared. Higher ZnO concentrations observed on the samples under tuyere 19 support the idea that excessive wear is mainly due to brittle layer progress as a result of Zn accumulation. Na₂O concentration is also higher at the same location. The ash content and Fe₂O₃ concentrations did not deviate much.
- The thermal conductivity (at the hearth wall in AGDH BF4) was measured to be approximately 22 W/(m·K) according to the supplier. The carbon blocks at the hearth wall in AMEH BF5A have a thermal conductivity of approximately 17 W/(m·K). After the campaign, the thermal conductivity of the collected samples, as well as the chemical compositions and physical properties like bulk density and volume of open pores were measured. Thermal conductivity varied between 14 and 23 W/(m·K) and between 19 and 23 W/(m·K) for AGDH BF4 and AMEH BF5A respectively. It is unknown whether these differences are an anisotropy- and/or inhomogeneities effect. Thermal conductivity values were used in the FEM analysis in WP1.
- Small cylindrical samples (AGDH BF4) were cut out for the cold crush test, which yields crush strengths and elasticity modulus (around 40 MPa and 930 MPa respectively). The thermal expansion of the carbon blocks is an essential physical property which governs the internal stress build-up and is used in the modelling work. Therefore, softening and creep tests were performed. In the softening test, a sample was heated to 1700 °C under a small constant load of 0.2 MPa. The maximum thermal expansion coefficient (0.4%) was reached around 1200 °C.

WP3 (Dead man characteristics)

The knowledge of chemical reactions and coke particle movement in the BF hearth has been scattered between the OPTIBLAFINS partners. Therefore, it was decided to undertake a literature survey collecting any further available knowledge. The literature review ("Fundamentals of behaviour of coke particles in BF hearth") was divided into three parts: coke gasification and reactivity, carburization and coke ash and the interaction between coke and slag.

Coke bed samples have been extracted after a couple of campaigns from the Experimental Blast Furnace (EBF) in Luleå. Those samples were extracted in several parts of the hearth with different elevations and angular positions in order to characterise the impact of tuyeres and tapholes on the materials. Main conclusions are that higher contents of fines and magnetic fractions which contribute to higher bulk densities. More aggregates of slag, metal and coke are found in the lower part of the hearth (close to the bottom) and a solidified shell is created at the circumference of the EBF.

Copper was injected through one tuyere and was used as a tracker to determine the flow of the liquid during tapping. The copper distribution indicates that the developed method to estimate the coke bed porosity is reasonable; under each tuyere the resistance to the flow seems to be higher compared to the central region of the hearth.

Two models to estimate the dead man porosity were proposed based on a force balance and on a mass-balance analysis while tapping. Both models give unrealistic results if their relative assumptions are not respected. The DMD (Dead Man Dynamics) model runs both models and decides which one is the best solution for voidage estimations according to sitting or floating dead man assumptions at a given time. These yield information about the reasons of possible tapping / drainage problems in the operation of the hearth, which is useful for the operators in helping them to decide about measures, e.g. increasing central coke charging / central coke quality, to recover the dead man permeability.

A study of coke degradation showed that the gasification degree is the main parameter of coke degradation. The gasification is a direct function of heating time and temperature (there is almost no gasification below 900 °C, while the gasification increases above 950 °C).

Degraded coke samples have been divided into slag and hot metal in order to assess their interactions. At high temperature, slag is very viscous but fragile while cooling. It acts like a protecting barrier of coke particles preventing further degradation. On the other hand, hot metal is easily deposited on coke samples and tends to diffuse inside the particles.

Slag from four different blast furnaces was analyzed. Viscosity and melting temperature were estimated numerically and experimentally and then related to the chemical composition of the samples. The experiments show that viscosity can be described in two domains according to temperature: the glass domain and the melted domain separated by a glass-transition

temperature. Shear rate also has an impact on BF slags: in this case an increase of the mechanical loading led to a decrease of the viscosity of the sample which means that studied BF slags are rheo-fluidifiant. Chemical composition has an impact on both melting temperature and viscosity. For instance, the more CaO content the higher the glass-transition temperature. Globally, models proposed in the literature and FactSage calculations tend to overestimate the viscosity levels but were able to discretize the chemical influence of major and some minor elements. Some minor elements, such as TiO₂, may have a large influence on viscosity. It is therefore not advised to use a quadrant system of SiO₂ / Al₂O₃ / CaO / MgO only to model the viscosity.

Wetting behaviour has also been studied and is strongly correlated to slag basicity. However, there hasn't been a clear evidence of a correlation with Al₂O₃ or MgO content. A statistical analysis was performed to assess the general influence of the four variables Al₂O₃, MgO, CaO and ash content in coke. The major conclusion is that a higher ash content in coke improves the slag wetting behaviour on coke.

Coke bed porosity was determined based on the sampling from the EBF. It appears that porosity is not homogeneous in the hearth. In the first layer (closer to tuyeres), it varies from 0.31 to 0.66 and no pattern was discovered. In the second layer (closer to the bottom), it varies from 0.12 to 0.49. It is important to notice that liquid flows mainly occur in this section of the hearth. The geographical analysis showed that the coke bed beneath the tuyeres seems to be less porous and therefore more resistant to fluid flow. The central part of the coke bed had a higher porosity.

A numerical simulation of the tapping process of the TSE BF7 was performed. A multi-level liquid level model was developed assuming several horizontal pools of liquids in the hearth which are inter-connected. Corrections on both slag and iron levels are done after a mass balance check subsequent to each tapping. In summary, the model has provided further insight into the dynamics of the hearth liquids in the TSE BF7, and shed light on possible reasons for the different patterns of drainage observed for the tapholes in a large multi-taphole BF.

WP4 (Interpretation of operational data for estimation of wear and liquid levels)

Several computational models have been developed for analysing the state of the blast furnace hearth based on existing and novel measurements at the boundaries, but many models have only been illustrated on short (and selected) periods and applications to data from full campaigns are scarce in the literature. Furthermore, different models are often used in isolation and their results are seldom combined. WP4 addresses this problem by applying new models and techniques developed by the partners in earlier work or in other OPTIBLAFINS WPs to gain a deeper understanding of the conditions in the hearth during the campaigns of several European blast furnaces.

The multiphysics thermal stress model was applied in practice on process data to visualize results and to warn operators about incidents (skulls, gap, brittle layers and serious stress patterns) in the hearth lining of the blast furnaces at AMEH and AGDH. The model also helps the operators by making prognoses of hearth lining thermocouple and strain-gauge readings for different inner hearth conditions, which supports the hearth diagnosis process. Signals from multi-point thermocouples were demonstrated to be useful for detecting metal intrusion into the lining, the occurrence of brittle layers and gaps in the lining, or rapid progress of erosion. To further support the analysis, several methods for filtering, normalizing or discarding temperature measurements were developed and applied. By these measures, the quality of the thermocouple signals used by the models is enhanced, yielding more accurate estimates of the conditions in the hearth and its lining. The significance of the measurements is interpreted by a module for plausibility analysis. To be able to efficiently present and analyse the time evolution of lining temperatures, grid interpolation by Delaunay triangulation was applied to yield a continuous map of the non-uniformly distributed signals from the lining. Visualization and correlation analysis of results provide an efficient means of following the occurrence/recurrence and motion of hot or cold patterns, which are associated with changes in the hot metal flow and dead man state in the hearth. These results nicely complement the short-term analysis provided by the inverse transient heat conduction model developed in WP1.

A detailed analysis of hearth erosion and build-up skull formation/melting of TSE BF7 since the campaign start in 2006 until the end of the OPTIBLAFINS project was undertaken using a model developed by ÅBO. As noted in the analysis carried out by BFI on other furnaces, the measurements from some lining thermocouples can be very misleading. A set of thermocouples in the TSE BF7 lining was omitted due to erratic behaviour that occurred after about eight years of operation, and the analysis was based on measurements that were considered relatively reliable. It should be noted that due to redundancy in the model's analysis, single erroneous thermocouple readings are not detrimental for the results. The model revealed interesting stages in the progress of erosion, with a particularly large change in 2008 that in WP3 was hypothesized to be connected to a deterioration of the coke strength. The overall findings were an astonishingly uniform lining wear that led to an elephant-foot shaped wear profile in 2013. Even though the erosion slowly

progressed until the end of the project, it is interesting to note that the actions taken by TSE stabilized the hearth state and very little further wear of the sidewalls occurred. A force balance for the dead man using the hearth profile reconstructed by the wear model revealed that it is fairly unlikely that the dead man would have floated during the present campaign of BF7. This is due to the shallow hearth design, the moderate progress of erosion, and the high injection rate of pulverized coal, which increases the average density of the burden in the lumpy zone (which raises the downward-acting force on the dead man). To gain a better understanding of the liquid levels in a multiple-taphole blast furnace (such as BF7) under different draining conditions, an off-line model of a hearth with alternating tapping through two tapholes was developed following the main assumptions made in the development of the on-line counterpart in WP3. The off-line model was applied to analyse the effect of different factors on the drainage, drawing conclusions about patterns observed in the operation of BF7. Based on the findings it is suggested that the reason why two alternate taphole may show fundamentally different outflow patterns is that the permeability of the coke bed in front of the tapholes differs, which affects the declivity of the slag-gas interface at the end of the taps. The underlying reason for this may be asymmetry at the tuyeres/raceways (non-uniform supply of blast and/or pulverized coal), and this should be studied in more detail in the future.

A strain-gauge model developed at CRM has been reprogrammed and refined to more systematically treat the strain signals obtained from the gauges by proper initialization, calibration and by separation of the results into estimates of the iron and slag levels. The results of the model based on a generatrix in the vertical direction demonstrate that the new model provides more realistic liquid levels with respect to their offsets from the taphole level. The points where the levels start increasing and decreasing are also logical and reflect the outflow orders and rates of the hearth liquids. The reconstructed liquid levels in the AM Fos BF also show general agreement with the results of the on-line liquid level model in WP3 for the TSE BF7. A liquid surface tilting model has been developed based on signals from multiple strain-gauge sets in the peripheral direction (horizontal generatrix) of the wall to estimate the liquid levels at different angles. Vertical strain-gauge sets have been installed at -60°, -30°, 0°, +30° and +60° angles from the southern taphole of the AM Fos BF.

WP5 (Management and reporting)

The OPTIBLAFINS project has shown the potential for utilisation of several-, improved, measurement techniques. These instrumentations, in combination with innovative CFD-DEM, 2D/3D on-line hearth wear modelling, dead man characteristics and operational data from several different blast furnaces have led to a more solid foundation for decision-making in the BF operation and a series of recommendations to improve the hearth life of a blast furnace.

The application (tools and methods) contribute to a stable and more efficient blast furnace process and an improved hearth life as a result. At the same time, they enable many possibilities for further research: new methods in monitoring the hearth wear, CFD-DEM improvements in the new models and coupling of these new tools and methods will provide new process knowledge and industrial benefits.

2 Scientific and Technical Description of the Results

2.1 Objectives of the Project

Improving the blast furnace hearth life was the major objective for this project. That means, the main focus will be on process stability, productivity, material and energy efficiency. Longer periods between intermediate hearth repairs, preventing serious incidents like metal break and reducing hearth wear will help to achieve that main goal.

Four sub-objectives were defined:

- Modelling of BF Hearth processes: Existing BF hearth designs were modelled in order to monitor the actual status of the BF hearth. Innovative CFD-DEM models were developed to improve the knowledge of dead man influence on hot metal flow. Extra attention was given on transient inverse modelling of the refractory state. Actual plant data and water models were used to verify the different models.
- BF hearth monitoring: New hearth monitoring techniques (like Fibre Bragg Gratings and Hearth Echo Excellence) have been introduced. The measurements have been verified with actual excavation and chemical analysis.
- Controlling the dead man: Dead man characteristics were investigated using Experimental Blast Furnace (EBF) data. The work was included by analysing the dynamic coke properties. The on-line Dead MAN Dynamics (DMD) model was improved by introducing accurate voidage data.
- Operational data interpretation: Operational temperature data was used to develop a 2D hearth wear model. Multipoint thermocouple data was used to determine brittle layer formations. An improved liquid level estimation was established using strain gauge data.

2.2 Description of activities and discussion

2.2.1 Work Package 1: Modelling of BF Hearth Processes

2.2.1.1 FEM based 3D-Model for thermal stress at hearth wall

A multiphysics model was developed to simulate the coupling of temperature, stress/strain, displacement, and refractory thermal expansion. The 2D and 3D FEM models which have been developed in the Hearth Efficiency [54] and Sustaintap [55] projects were merged and upgraded to consider the thermal resistance of the gaps between refractory blocks in a 3D model. A special formulation, which was described in the conference papers [58] and [59], has been adopted to compute the stresses in the assembly of refractory blocks.

The design of the hearth linings of AMEH BF5A and AGDH BF4 are shown in Figure 1 and Figure 2, respectively. The basic material properties which are necessary for the thermo-mechanical model are listed in Table 1 and Table 2. The material layout for both furnace hearths is kept the same after the relining. However, the spray cooling system at AMEH BF5A has been replaced with a channel cooling system.

Optimizing Blast Furnace Hearth Inner State (OPTIBLAFFINS)

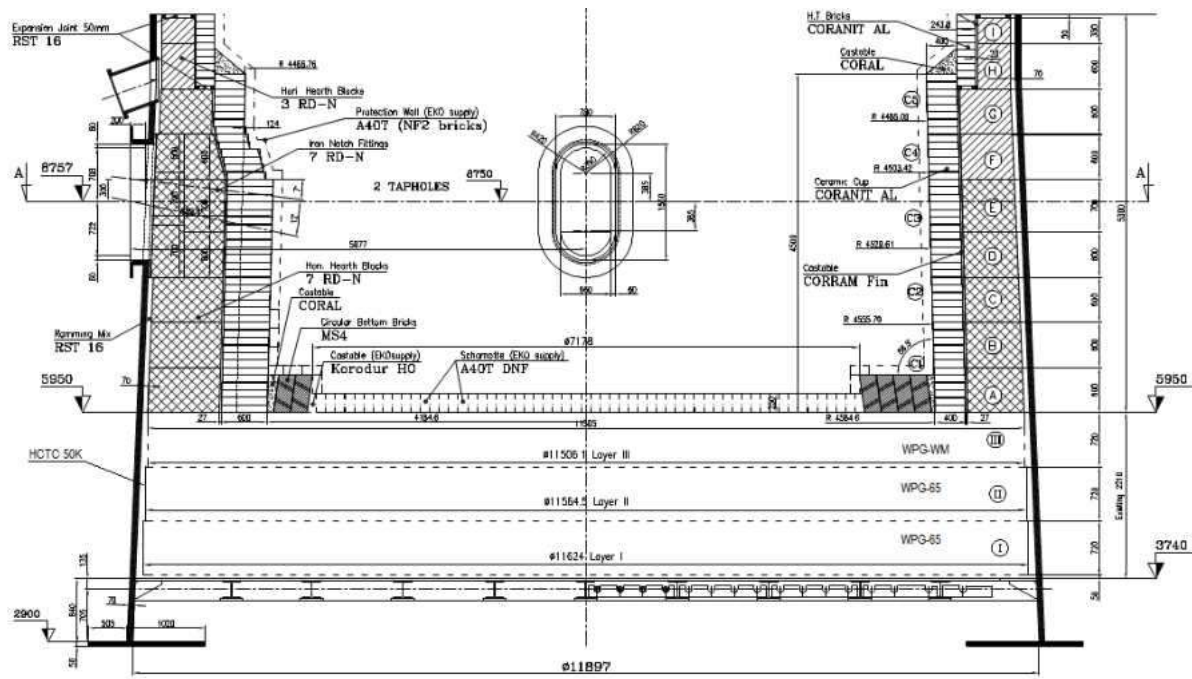


Figure 1: Design of AMEH BF5A before the relining 2016.

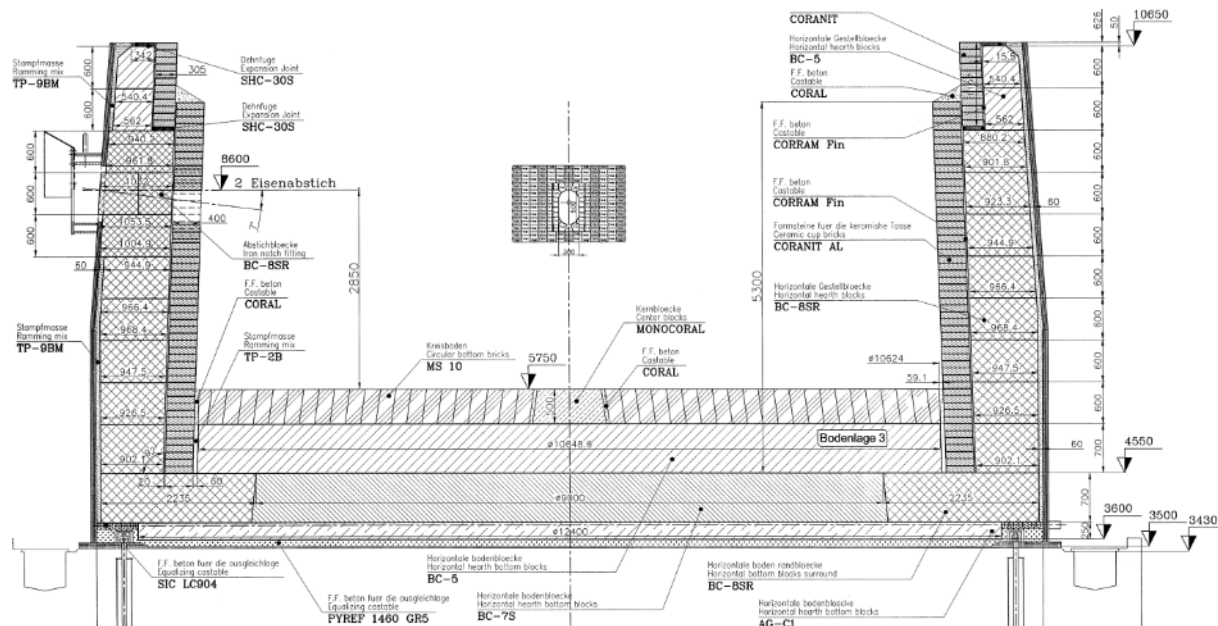


Figure 2: Design of AGDH BF4 before the relining 2016.

Table 1: Material properties of hearth lining at AMEH BF5A (supplier data sheets).

		REFRACTORY					CASTABLES					
		7RD-N	CORANIT-AL	MS4	WPG-WM	WPG-65	BRICKS	RST16	CORRAM Fin	CORAL	HCTC 50K	STEEL SHELL
density	g/cm ³	1.7	3.2	2.5	1.59	1.53	1.75	1.49	2.85	3.35		7.86
Thermal conductivity	W/(m·K)	17	2.8	2.2	9	7	1.5	16	3.5 3.8	3.8 4.0	25 20	50
Thermal expansion	x10 ⁻⁶ 1/K	2.6	5.3	6.4	3	3.5	5	23				12
Strength (comp.)	MPa	55	150	120	42	32	50	10	25 60	40 150	10	420
Strength (rupture)	MPa		12		9	8				8		420
Elasticity Modulus*	GPa	15	10	5	5	5	12	1	1	1	1	200
Poisson's Ratio*	-	0.3	0.3	0.3	0.3	0.3	0.3	0.3	0.3	0.3	0.3	0.33

* assumed values

Table 2: Material Properties of hearth lining at AGDH BF4 (used in [55]).

		Elasticity Modulus† GPa	Poisson's Ratio† -	Thermal Expansion Coefficient *10-6 (1/K)	Density kg/m3	Heat Conductivity W/(m·K)
	Steel Shell	200	0.33	12	7860	50
Castable	PYREF	1	0	10	2300	1.8
	CORAL	1	0	8.1	2100	1.9
	CORRAM Fin	1	0	9.0	2100	2.1
Ramming Mix	TP-2B	1	0	3.1	2800	2.3
	TP-9BM	1	0	3.0	2900	2.4
Ceramic Cup	CORANIT	10	0.28	5.5	3400	2.7
	CORANIT AL	10	0.28	7.7	3200	2.6
Carbon Blocks	BC-5	10	0.30	7.0	1570	14.5
	BC-7S	10	0.30	3.4	1620	14
	BC-8RS	10	0.30	3.6	1560	11
	AG-C1	10	0.30	8.0	2800	1.3
Bottom Blocks	MONOCOR AL	10	0.28	7.8	3350	3.9
	MS-10	10	0.28	8.2	2400	1.7

† assumed values

The temperature field and the wear state were computed basically using the 3D model developed in the project Sustaintap [55]. This model has been further developed (e.g. thermal resistance of interfaces included, transient case studies performed, etc.). The solid mechanics physics were added to the model, in order to compute the thermal stresses in the refractory lining and steel shell. A special modelling technique has been adopted for modelling the non-monolithic structure the refractory linings. This technique was initially developed in the Hearth Efficiency [54] project. It has been extended to 3D geometry. Further details of this modelling technique can be found in the conference papers [58] and [59].

The main idea of this approach is that the assembly of the refractory blocks can only sustain compressive stress but cannot sustain any tensile stresses. That means under thermo-mechanical loadings, local gaps can form between the blocks. Therefore, "no-tension criteria" are applied in hoop and vertical directions for the carbon blocks at the hearth wall. For the hoop direction, it is necessary to transform the stress tensor between Cartesian and cylindrical coordinates systems. Additionally, these gaps between blocks will resist the heat flux. One way of implementing this heat

resistance in the numerical model is to use thin thermal resistive layers. Another way is to reduce the thermal conductivity of the block assembly in perpendicular directions to plane of the gaps (that means to use an anisotropic heat conduction model). Both approaches were adopted and implemented at different parts of the model. That means the heat conduction in the hoop direction is reduced which introduces an anisotropy and thin thermal resistive layers defined between the carbon ring layers which physically reduces the vertical heat flux.

The steel hearth shell is modelled using the shell physics for the mechanical response. Shell elements are computationally much more efficient and accurate than solid elements for modelling thin structures. It is important to minimize the computational effort since the new model is planned to be applied for on-line hearth supervision. The current state of the model computes the thermo-mechanical stresses at the hearth lining wall of AMEH BF5A and AGDH BF4. Some results are shown for AMEH BF5A to illustrate model capabilities. The residual wall thickness and temperature distributions are quite non-uniform. Therefore, the resulting steel shell displacement (Figure 3) and shell stresses (stress component in vertical direction as shown in Figure 4) are non-uniform as well. Commonly used rotationally symmetric models reported in the literature are quite inaccurate in that sense. The steel shell displacement is mostly radial and locally may go up to 7.5 mm as in Figure 3. The shell vertical stress component in Figure 4 is non-uniform. However, it has a different pattern than that of the displacement field.

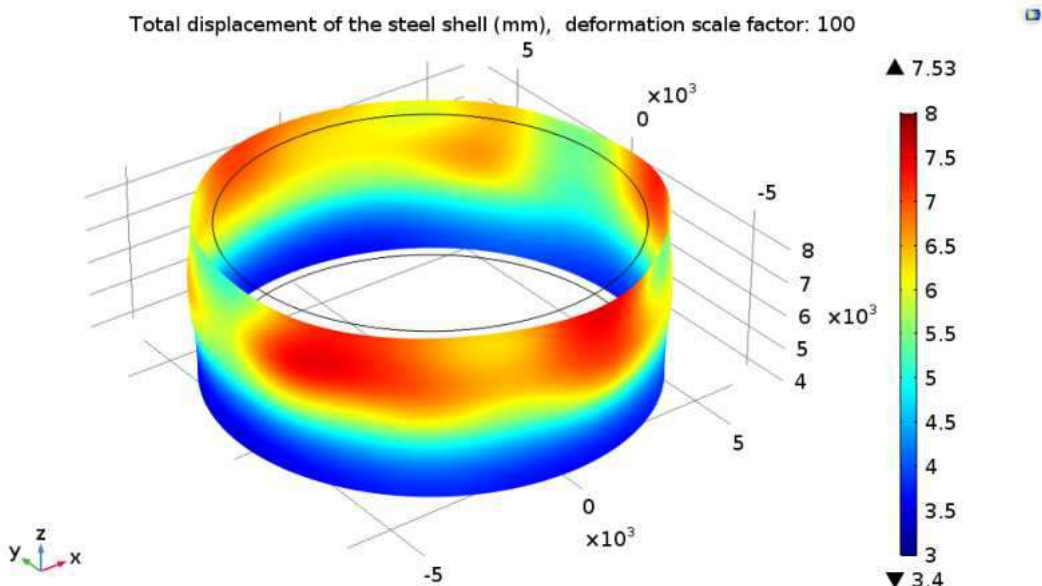


Figure 3: Total displacement at steel shell of AMEH BF5A.

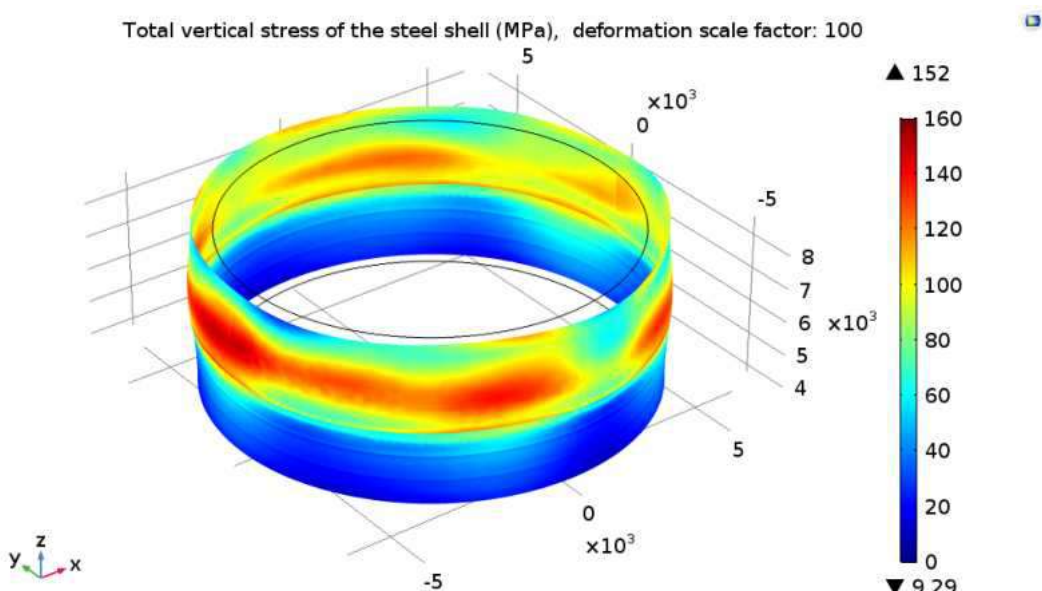


Figure 4: Vertical stress at steel shell of AMEH BF5A.

Optimizing Blast Furnace Hearth Inner State (OPTIBLAFFINS)

The influence of the “no tension concept”, which allows only compression in the assembly of carbon blocks, can be better seen in Figure 5 and Figure 6. The vertical component of the stress tensor is shown in Figure 5 and the hoop (phi) component is shown in Figure 6 through a cut line in the radial direction at level $z=7000$ mm under the tuyere 7 of AMEH BF5A. The compressive stresses on the hot side of the lining are compensated by the tensile stresses of the steel shell (the green point at upper-right corner in the figures). The outer parts of carbon blocks ($r > \text{ca. } 5 \text{ m}$) do not possess any tensile response due to “no tension concept”. That means the structural character of the non-monolithic lining wall is consistently modelled by this concept.

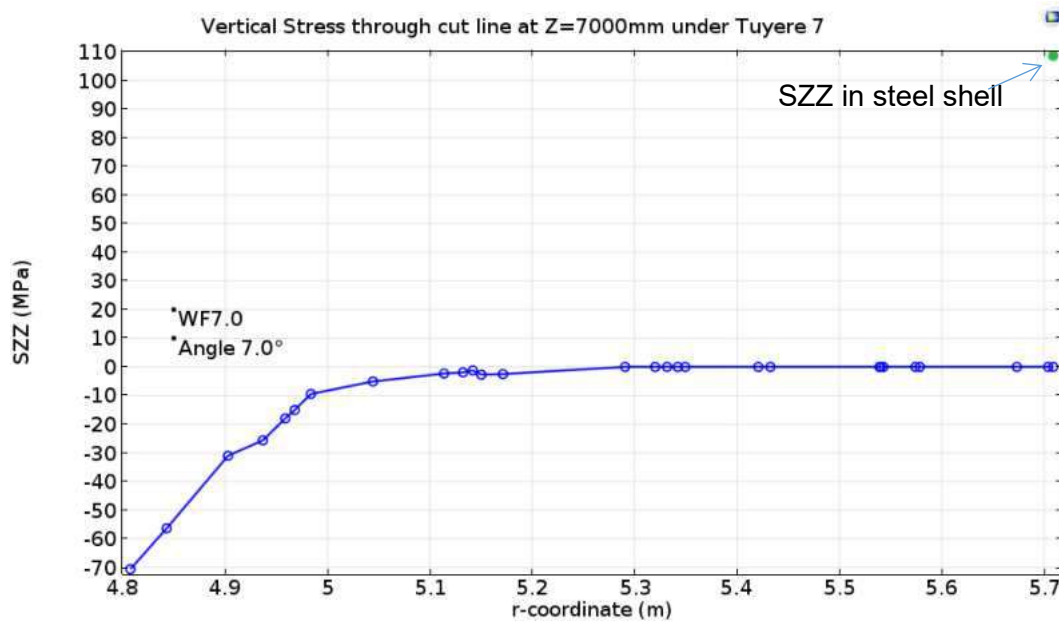


Figure 5: Vertical stress through a cut line ($z=7 \text{ m}$ under Tuyere 7) for AMEH BF5A.

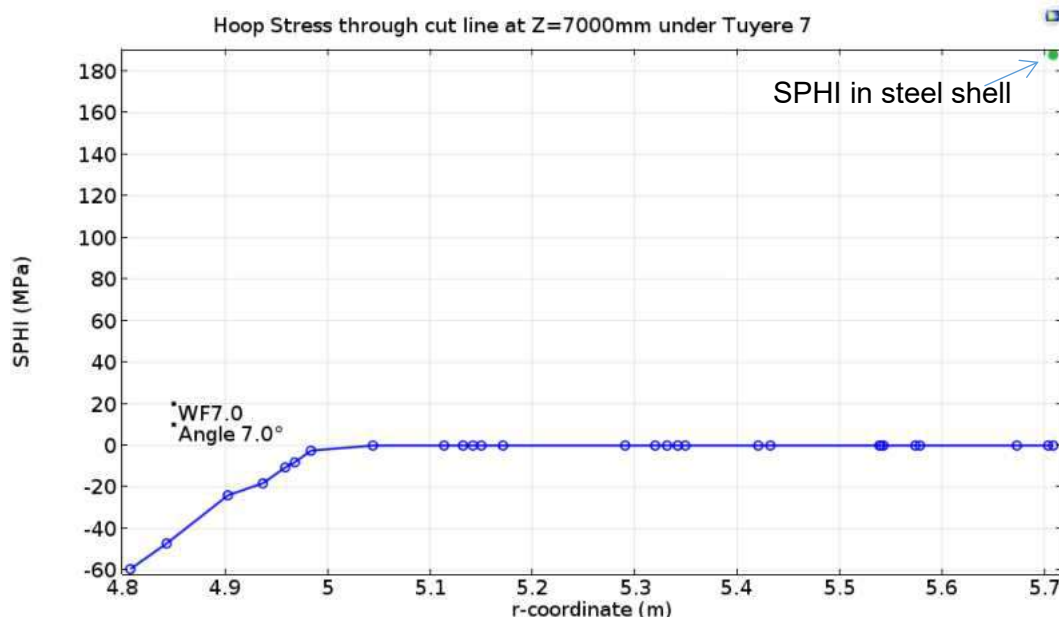


Figure 6: Hoop stress through a cut line ($z=7 \text{ m}$ under Tuyere 7) for AMEH BF5A.

The FEM model can be also used to compute the gap size. The computed vertical and horizontal gaps at the hearth of AMEH BF5A have been shown in Figure 7 (upper 3D plots show the horizontal and vertical gap distribution, lower 1d plots shows the same for a radial cutline at level 7 m under tuyere 7). The hot sides of the carbon blocks are under compression which prevents the gap formation and hot metal seepage. However, on the cold side of the blocks, the model estimates circumferential and vertical gap formations. These gaps possibly allow gas flow by which alkali and zinc might be transported contributing to the brittle layer formation in the hearth lining.

Optimizing Blast Furnace Hearth Inner State (OPTIBLAFFINS)

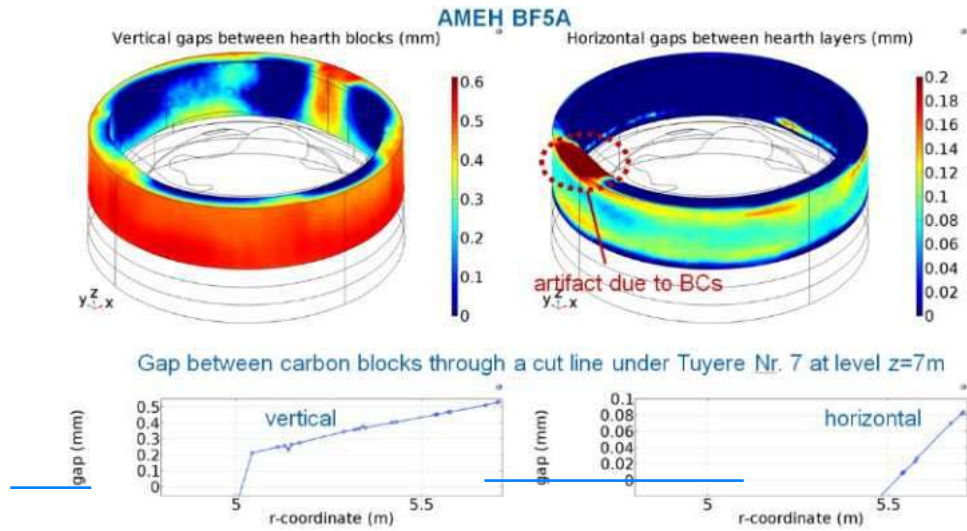


Figure 7: Gap formation between the carbon blocks at AMEH BF5A hearth wall.

Transient simulations of the shell spray cooling at AMEH BF5A hearth have been carried out to investigate the hearth thermo-mechanical state. The heating of the hearth shell has been measured by thermography measurements (from 09.12.2015) and results are given in section 3.2.1.4. This phenomenon is simulated by a transient model to investigate the thermal state and thermal stresses at the hearth wall. The shell spray cooling shut-down (in practice cooling cannot be shut-down more than 1 hour in any case) is implemented in the model by using a time dependent heat transfer coefficient which covers initial drying of wet shell surface and later the convective air cooling. The computed shell temperature is in good agreement with the temperatures from the thermography (Figure 8). The evolution of the thermal stress at the hearth shell and the gap between the two neighboring carbon blocks (in the same hearth layer) are shown in Figure 9. The hoop stress gradually reduces as the steel shell heats-up and expands. This relaxed and expanded state of the shell allows carbon blocks to move outwards and build-up of more gaps. Therefore, shut-down of the hearth cooling system is not a good practice regarding to hearth lining health.

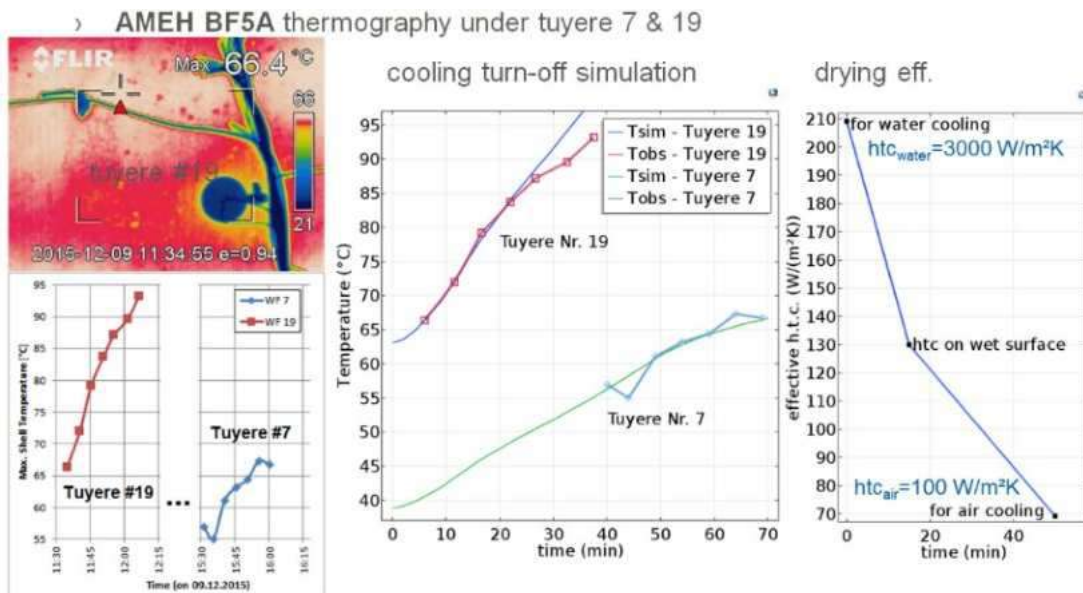


Figure 8: AMEH BF5A hearth cooling shut-down during a stoppage – model vs thermography measurements. Note that drying of the hearth shell is empirically modelled by time-varying heat transfer coefficient.

- AMEH BF5A: hoop stress at shell and gap at tuyere 7 & level Z=7m if the cooling is shut-down for some time

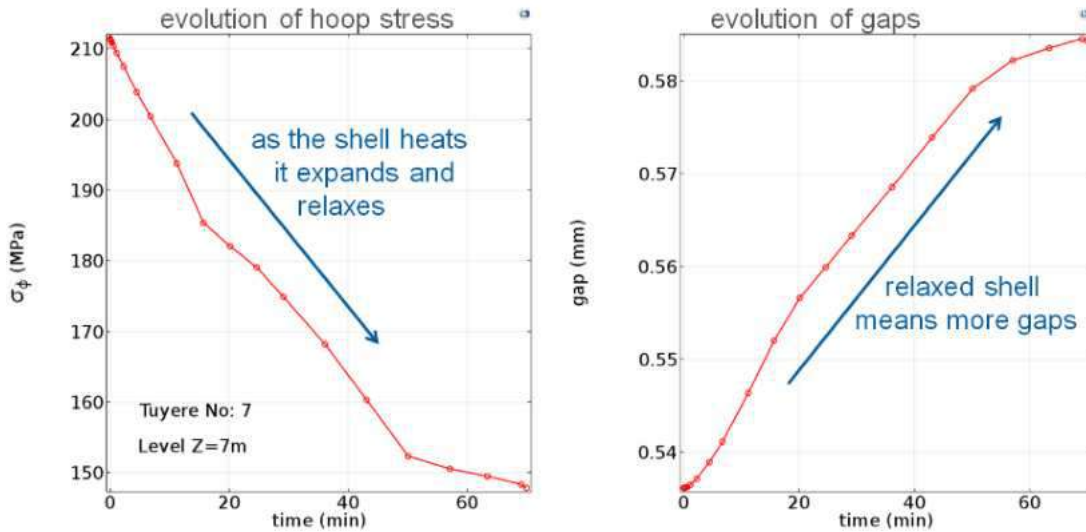


Figure 9: Computed stress at hearth shell and gaps at cold side of carbon blocks at AMEH BF5A hearth when the cooling shut-down during a stoppage.

Case studies are performed for investigating the liquid level, temperature and strain-gauge relations as next step. The hot liquid metal and slag levels are defined relative to the TH level. This extra liquid pressure introduces additional deformation of the hearth steel shell. The main contribution to the steel shell strains comes from the steel shell temperature (the thermal expansion). The steel shell temperature is related to wear (hot spots corresponds to high wear locations). The temperature contours and vertical and hoop strain plots along the upper edge of the steel shell in Figure 10 supports this idea (warmer regions have more strain in absolute value).

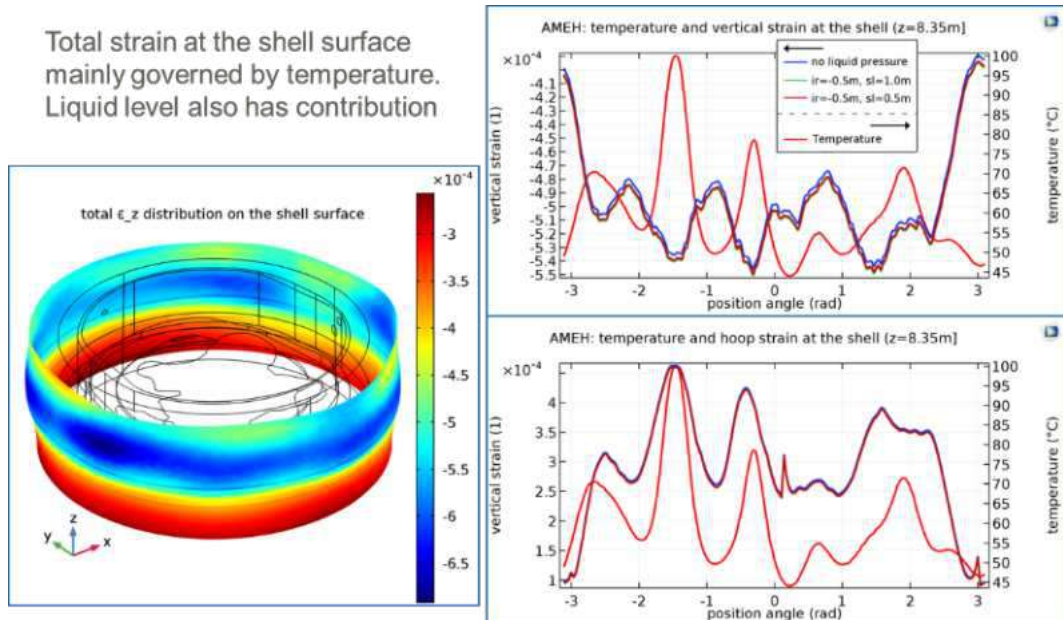


Figure 10: Liquid level, temperature and total strain comparison at steel shell of AMEH BF5A.

Besides the thermal expansion, the liquid hot metal pressure has also a small contribution to the shell strain. The portion of the strain (i.e., Δ strain = "strain without liquid pressure" – "strain with liquid pressure") due to pure liquid pressure for two different slag levels are compared in Figure 11. The vertical and hoop Δ strain variations along the upper edge of the steel shell are shown on the left side in Figure 11. The vertical strain is increased almost uniformly but hoop strain does not have such a trend. The reason for this can be better understood if the contour plots on the right side in Figure 11 is looked. The vertical strain gauges should be placed about TH elevation to have a better liquid level signal on the contrary, the horizontal strain gauges should be placed hearth bottom level or deeper to get a better liquid level signal according to these model results.

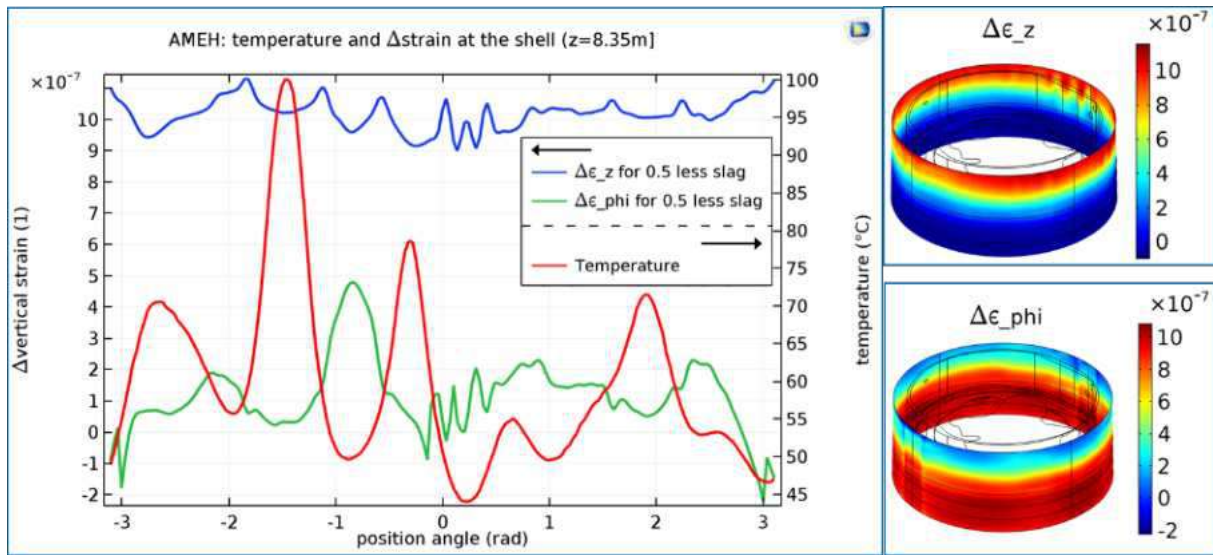


Figure 11: Liquid level, temperature and strain-difference comparison at steel shell of AMEH BF5A.

The hearth of AGDH BF4 is equipped with many thermocouples along 12 vertical sections at its wall and half of these sections contain also thermocouples at its bottom for the wear control. Typical TC placement in a vertical section and at hearth bottom is shown in Figure 12. The wear model estimates the wear profile such that the model with this wear profile optimally reproduces the daily average temperature readings. A comparison of measured and computed temperatures is given in Table 3.

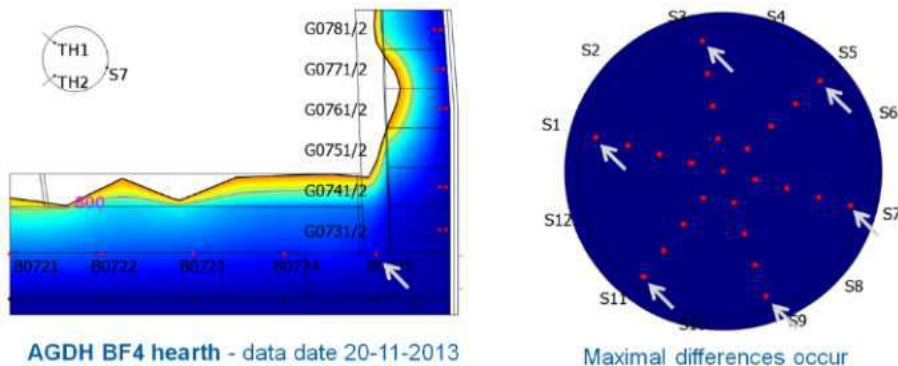


Figure 12: Thermocouple placements at Dillinger BF4 hearth at a typical vertical section and hearth bottom. The computed and measured temperatures differ systematically at the bottom corner (Table 3).

Whereas for most temperatures simulation and measurement are consistent, at the bottom corner positions the computed temperatures are systematically much higher than the measured temperatures. These thermocouples are placed directly under the ceramic cup. The ceramic cup is built-up with relatively small bricks which have, therefore, many vertical and circumferential discontinuities (due to brick wall structure). This constructional structure introduces also a thermal anisotropy (which have not been implemented in the model for those results). This might explain the discrepancy between the model and measurements at these locations. This thermal anisotropy has been implemented to upgrade the wear model.

Table 3: The computed and measured temperatures at Dillinger BF4 hearth differ systematically at the bottom corner (marked in red).

S01	Sim	TC	ΔT	S02	Sim	TC	ΔT	S03	Sim	TC	ΔT	S04	Sim	TC	ΔT	S05	Sim	TC	ΔT	S06	Sim	TC	ΔT
B0121	337.2	334.6	-2.6	G0231	64.3	75.2	10.9	B0322	294.9	297.4	2.4	G0431	70.1	77.0	6.8	B0522	306.7	303.1	-3.6	G0631	66.4	74.4	8.0
B0122	320.1	316.0	-4.1	G0232	54.5	60.4	5.8	B0323	306.9	310.5	3.6	G0432	57.9	60.0	2.1	B0523	285.4	285.4	0.0	G0632	55.7	74.9	19.1
B0123	293.3	295.6	2.2	G0241	106.8	105.6	-1.2	B0324	264.4	264.3	-0.1	G0441	115.9	115.1	-0.8	B0524	244.6	246.8	2.2	G0641	112.3	111.4	-1.0
B0124	233.3	231.3	-2.0	G0242	80.9	79.0	-1.9	B0325	159.5	134.0	-25.5	G0442	85.2	86.0	0.9	B0525	155.9	128.1	-27.9	G0642	84.3	79.5	-4.8
B0125	149.5	124.3	-25.6	G0251	215.1	205.1	-10.0	G0331	62.9	77.1	14.1	G0451	213.3	203.0	-10.2	G0531	62.2	72.1	9.9	G0651	191.6	187.0	-4.7
G0131	62.2	70.0	7.8	G0252	143.1	151.9	8.8	G0332	53.7	62.2	8.6	G0452	143.2	148.0	4.8	G0532	53.2	58.5	5.3	G0652	129.1	128.5	-0.6
G0132	53.4	57.0	3.7	G0261	281.4	282.8	1.3	G0341	101.7	108.1	6.3	G0461	294.3	303.7	9.3	G0541	94.4	108.0	13.6	G0661	244.1	248.6	4.5
G0141	100.9	100.2	-0.7	G0262	183.2	189.4	6.1	G0342	76.0	81.8	5.8	G0462	194.7	205.1	10.5	G0542	72.2	80.6	8.4	G0662	161.4	163.3	1.9
G0142	76.9	74.5	-2.5	G0271	372.9	364.9	-7.9	G0361	249.6	243.0	-6.6	G0471	341.1	341.5	0.4	G0551	171.6	163.3	-8.3	G0671	285.7	277.9	-7.8
G0151	147.5	151.7	4.2	G0272	239.9	254.1	14.3	G0362	164.4	167.7	3.4	G0472	222.8	222.4	-0.4	G0552	119.8	104.1	-15.7	G0672	187.4	194.4	6.9
G0152	104.7	104.2	-0.5	G0281	303.4	299.1	-4.3	G0381	248.2	240.7	-7.6	G0481	257.1	246.6	-10.4	G0561	229.1	237.0	7.9	G0681	218.5	216.0	-2.4
				G0282	197.0	199.7	2.8	G0382	159.9	175.6	15.7	G0482	169.1	184.1	15.0	G0562	153.6	157.6	4.1	G0682	146.3	152.2	5.9
															G0571	265.1	263.9	-1.2					
															G0572	174.2	174.8	0.6					
															G0581	204.8	204.6	-0.3					
															G0582	138.0	137.9	-0.1					
S01	Sim	TC	ΔT	S02	Sim	TC	ΔT	S03	Sim	TC	ΔT	S04	Sim	TC	ΔT	S05	Sim	TC	ΔT	S06	Sim	TC	ΔT
B0721	337.2	334.4	-2.8	G0831	63.1	69.1	6.0	B0922	319.7	316.6	-3.1	G1031	66.1	78.4	12.3	B1122	321.2	324.1	2.9	G1231	62.8	74.2	11.3
B0722	303.8	307.0	3.2	G0832	53.8	59.8	6.0	B0923	300.8	297.6	-3.2	G1032	55.1	63.8	8.7	B1123	313.3	307.1	-6.3	G1232	53.5	62.1	8.5
B0723	273.4	279.2	5.7	G0841	100.9	98.3	-2.6	B0924	247.8	257.9	10.1	G1041	122.1	115.7	-6.4	B1124	255.2	265.9	10.6	G1241	103.7	97.2	-6.5
B0724	225.4	218.3	-7.2	G0842	76.8	76.2	-0.7	B0925	155.1	126.5	-28.7	G1042	87.9	85.3	-2.6	B1125	166.4	135.4	-31.0	G1242	78.4	75.6	-2.8
B0725	150.1	117.1	-33.1	G0851	141.5	138.4	-3.1	G0931	63.2	71.6	8.4	G1061	283.1	280.4	-2.7	G1131	65.4	77.6	12.2	G1251	142.2	139.9	-2.3
G0731	63.0	74.4	11.5	G0852	100.7	97.5	-3.2	G0932	53.9	59.9	6.0	G1062	185.0	192.9	7.8	G1132	55.1	63.9	8.8	G1252	101.0	103.1	2.1
G0732	53.9	61.6	7.7	G0861	146.0	148.2	2.2	G0941	107.6	115.1	7.5	G1081	206.8	199.5	-7.3	G1141	102.5	111.5	9.0				
G0741	106.6	104.8	-1.8	G0862	103.0	107.0	4.0	G0942	81.0	90.0	9.0	G1082	136.0	147.1	11.1	G1142	76.9	88.1	11.2				
G0742	77.8	77.0	-0.7	G0871	163.7	164.0	0.3	G0951	184.0	172.1	-11.9					G1151	191.9	180.5	-11.3				
G0761	261.5	260.6	-0.8	G0872	113.7	113.0	-0.6	G0952	126.1	121.4	-4.7					G1152	128.7	116.2	-12.5				
G0762	172.6	175.8	3.3	G0881	152.2	150.6	-1.6	G0961	179.2	179.9	0.7					G1161	312.6	322.3	9.7				
G0771	267.1	267.7	0.5	G0882	106.5	104.1	-2.5	G0962	122.9	127.8	4.9					G1162	208.2	214.5	6.3				
G0772	175.7	181.7	6.0					G0971	226.1	219.3	-6.9					G1171	327.3	327.6	0.3				
G0781	188.1	188.1	0.1					G0972	151.3	161.1	9.8					G1172	220.1	220.0	-0.1				
G0782	129.2	130.6	1.3					G0981	211.8	204.1	-7.7					G1181	247.9	242.8	-5.1				
								G0982	140.7	147.5	6.8					G1182	164.7	180.5	15.7				

The FEM model has been used to study the thermocouple and model behaviors during stoppages. Several transient analyses are carried out to investigate the hearth thermal state and thermal stresses (as well as built-up of gaps between carbon blocks) during the blast furnace stoppages. In general, the thermocouples show temperature drops during stoppages. This is significant if the stoppage is longer and the thermocouple is placed deep. The hearth of AGDH BF4 is also equipped with several deep multi-thermocouples (5xTCs) besides several double thermocouples. These temperature drops are thought to be due to cooling of the hot metal pool in the hearth. This idea has been tested by carrying out a transient model study in which a time dependent pre-set hot side temperature is adopted whose cooling rate (i.e., the cooling rate of the hot metal pool in hearth) can be approximately estimated by the following calculation:

$$\begin{aligned} \text{hearth inner volume from wear model: } V &= 290 \text{ m}^3 \\ \text{assuming all pores filled with iron: } m &= \rho \cdot \varepsilon \cdot V = 6700 \times 0.35 \times 290 = 680t \\ \text{total cooling power from wear model: } P &= 2.2 \text{ MW} \\ \text{cooling rate from } \Delta T / (1 \text{ hour}) &= P/(m \cdot C_p) = \text{ca } 15^\circ\text{C per 1 hour.} \end{aligned}$$

The computed and measured temperature evolutions at this position (G0673 which is a deepest thermocouple of 5xTCs) are shown in Figure 13. A similar good fit can be also seen in Figure 14 for the computed and measured temperature evolutions at other wall double thermocouples (hot side thermocouples at section 2). They match relatively well even if a simple pre-set hot metal temperature assumption (as given above) is made. This assumption is very coarse since it does not consider any reduced-pressure operation at the beginning and end of the stoppage as well as any thermal inhomogeneity and stratification! Only at the lower parts (i.e. G0231 in Figure 14 and B0121 at bottom center in Figure 15) no evident temperature drop exists in contrast to the model estimates. Clearly, the uniform pre-set hot metal temperature on the hot face of the hearth refractory is too simple to reflect complex convection, thermal stratification and possibly solidification phenomena.

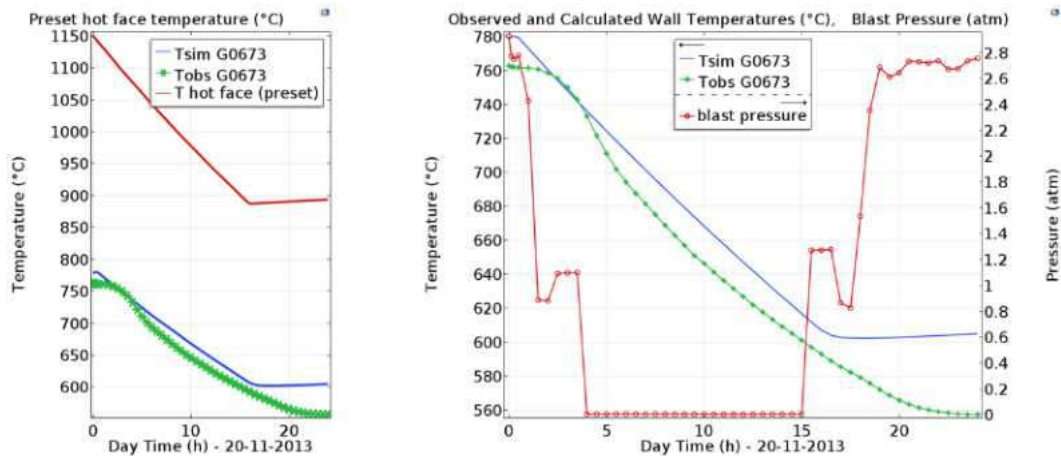


Figure 13: AGDH BF4 stoppage simulation – thermocouple reading (deepest of MTC at section 6) vs transient model computation. Note that the model uses a time varying uniform hot metal temperature on hot face of the hearth wall.

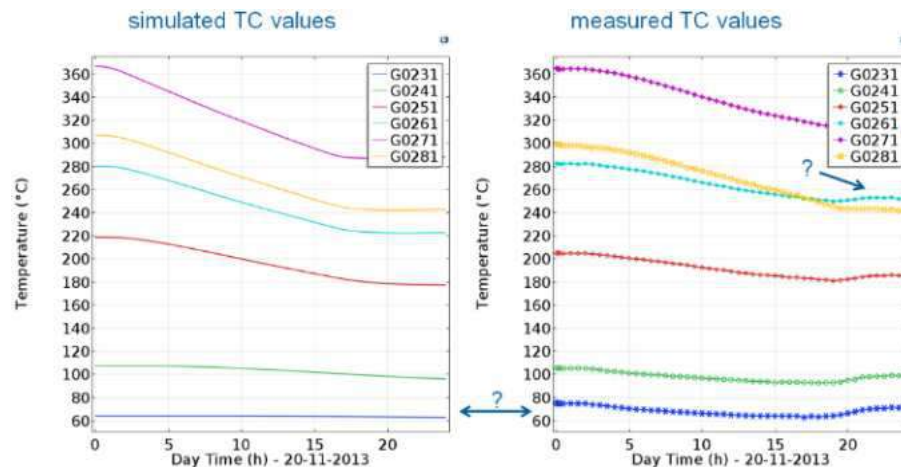


Figure 14: AGDH BF4 stoppage simulation – wall thermocouple readings at section 2 vs transient model computation.

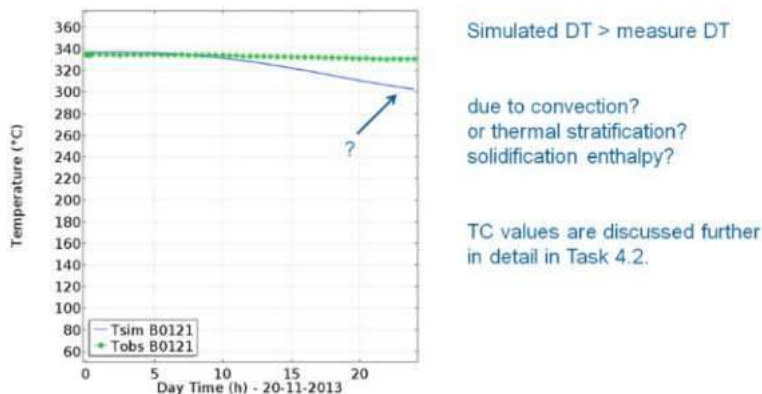


Figure 15: AGDH BF4 stoppage simulation –bottom center thermocouple reading vs transient model computation (DT: temperature drop during the stoppage).

2.2.1.2 Permeability and Dead Man shape

2.2.1.2.1 Introduction

Previous work, specifically CFD modelling within the RFCS project Sustaintap [55] led to the perception that the flow of freshly molten hot metal strongly affects the wear of the BF refractory in the hearth. The manifestation of such a flow field is the result of the delicate balance between static and dynamic forces acting in the complex three phase system (solids/liquids/gas) within the BF. Its characteristics are mainly influenced (among other factors) by the shape of the lower Dead Man boundary and the porosity distribution inside the DM (e.g. porosity near the walls or void space at the lower boundary). BFI has developed an on-line model for the “Dead Man Dynamics” (DMD) which shows the current DM state (floating / sitting / transitional) as well as the averaged

DM porosity in dependence of operational parameters. This model cannot provide information about the absolute volume of the coke free area below the DM, the lower boundary shape or the porosity distribution within the DM. This is why it is currently difficult for the BF operator to interpret the DMD results for his specific BF with respect to a favourable plant operation strategy ensuring a long hearth operation.

A simulation model of the blast furnace hearth will be developed to provide details of the shape of the void below the DM, the spatial porosity distribution within the DM and the velocity fields associated with both regions. Therefore, the movement of individual particles (burden, coke) and the movement/interaction of/with the liquids (slag, hot metal) and the gas phase (hot blast) inside the blast furnace hearth must be considered. In order to accomplish this objective, a coupled CFD-DEM approach is chosen, which connects the individual particle movement to the surrounding fluid phases.

2.2.1.2.2 Simulation BF hearth

Since, at least at present, a full-featured numerical simulation of an actual blast furnace is not yet technically feasible, thoroughly simplified but manageable approaches are sought. In order to describe the mechanical interaction of the ore and coke particles among each other, with their surroundings and the participating fluids, an in-house DEM-Code, which describes the motion of the discretely represented material, is coupled with the CFD Software ANSYS FLUENT (Version 17.2), which solves the governing transport equations of the continuous fluid phases by using the VOF method. The data transfer during the transient calculation is implemented with a two-way-coupling, which is described in detail in [62]. Due to the large number of particles, the assumption of spherical shape and a moderate coarse-graining [63] with adjusted rolling friction is necessary for an appropriate representation of the solid material. Moreover, the fluid flow within the voids of the packed bed cannot be fully resolved, since the determination of local velocity fields around individual particles is computationally not affordable. For this reason, the influence of the moving packed bed on the fluid flow is handled by updating cell averaged void fractions (porosity) for each flow time step from the local material arrangement in the DEM solution.

2.2.1.2.2.1 Computational Fluid Dynamics (CFD)

For the calculation of the fluid flow field, the Volume of Fluid (VOF) method is used, where a single set of momentum equations is solved for two or more immiscible fluid phases. The interface tracking between these phases is accomplished by solution of an additional continuity equation. The resulting velocity field is shared among all phases and employed to determine the particle-fluid interaction forces. The respective continuity (Eq. (1)) and momentum (Eq. (2)) equations are:

$$\frac{\partial(\varepsilon_f \rho_f)}{\partial t} + \nabla(\varepsilon_f \rho_f \vec{u}) = 0 \quad (1)$$

$$\frac{\partial(\varepsilon_f \rho_f \vec{u})}{\partial t} + \nabla(\varepsilon_f \rho_f \vec{u} \vec{u}) = -\varepsilon_F \nabla p + \nabla(\varepsilon_f \bar{\tau}) + \varepsilon_f \rho_f \vec{g} + \vec{f}_{int} \quad (2)$$

Herein \vec{u} , ρ_f and p are the (phase joint) fluid velocity, density and pressure, respectively. ε_F is the local porosity (spatially averaged from the particles contained within a CFD-cell) and $\bar{\tau}$ the fluid viscous stress tensor. The equations are directly dependent on the volume fraction of all phases through the material properties appearing in the transport equation. The fluid density and other fluid properties Γ , e.g. the viscosity μ_f , are calculated as volume fraction weighted values of the fluid phases. The volumetric particle/fluid interaction force is calculated as $\vec{f}_{int} = \bar{\beta}_i (\vec{u}_F - \vec{v}_i)$, averaged across the volume and added as a source term in the momentum equation. \vec{v}_i is the fluid cell averaged particle velocity and $\bar{\beta}_i$ the fluid cell averaged drag coefficient. Both values are calculated within the DEM and are transferred as space (across the control volume) and time averaged (over the so-called coupling interval) values. This is due to the DEM time step, typically being smaller than the CFD step size.

2.2.1.2.2.2 Discrete Element Method (DEM)

The description of the individual particle movement is obtained from integration of Newton's (Eq. (3)) and Euler's (Eq. (4)) equation of motion.

$$m_i \cdot \frac{d^2 \vec{x}_i}{dt^2} = \sum_{j=1}^N \vec{F}_{ij}^c + \vec{F}_i^{pf} + m_i \vec{g} \quad (3)$$

$$\theta_i \cdot \frac{d^2 \vec{\varphi}_i}{dt^2} = \sum_{j=1}^N \vec{M}_{ij} + \vec{M}_i^r = \sum_{j=1}^N \vec{r}_i \times \vec{F}_{ij}^c + \vec{M}_i^r \quad (4)$$

where m_i and θ_i are the mass and the moment of inertia, $d^2\vec{x}_i/dt^2$ and $d^2\vec{\phi}_i/dt^2$ denote the particle and angular acceleration of the individual particle i . The external forces \vec{F}_{ij}^c and external moments \vec{M}_{ij} result from the contact between the interacting particles i and j . \vec{F}_i^{pf} denotes the particle-fluid interaction force and $m_i \vec{g}$ the gravitational force. In the modeling approach used, the soft-sphere concept is applied to obtain the contact forces. The contact force parameters are given in Table 4. The particles can reduce their size due to prescribed conversion or melting rates. Further details on the models and assumptions may be found in [64].

2.2.1.2.2.3 Particle/Fluid Interaction Forces

The predominant particle/fluid-interaction forces considered can be summed up as $\vec{F}_i^{pf} = \vec{F}_i^d + \vec{F}_i^{\nabla p} + \vec{F}_i^b$, where \vec{F}_i^d is the drag force, $\vec{F}_i^{\nabla p}$ the pressure gradient force and \vec{F}_i^b the buoyancy force. The drag force and the pressure gradient force can be written as $\vec{F}_i^d + \vec{F}_i^{\nabla p} = \beta_i V_i (\vec{u}_F - \vec{v}_i) / (\varepsilon_F (1 - \varepsilon_F))$. For the calculation of the drag coefficient, several approaches are available. Due to the successful use in the past and its suitability in order to describe multiphase systems [65], the approach after Di Felice [66] is chosen in this work. The buoyancy force exerted by the fluid displaced by particle i , depends on a phase averaged fluid density ρ_F , thus is computed as $\vec{F}_i^b = \rho_F \vec{g} V_i$.

2.2.1.2.3 Model BF development

Within the project, a multi-phase CFD-DEM implementation at RUB-LEAT was progressively developed to meet the requirements of general BF conditions considering a four-phase system consisting of uniform coke/ore particles, liquid iron/slag and hot blast. Figure 16 summarizes the main development stages.

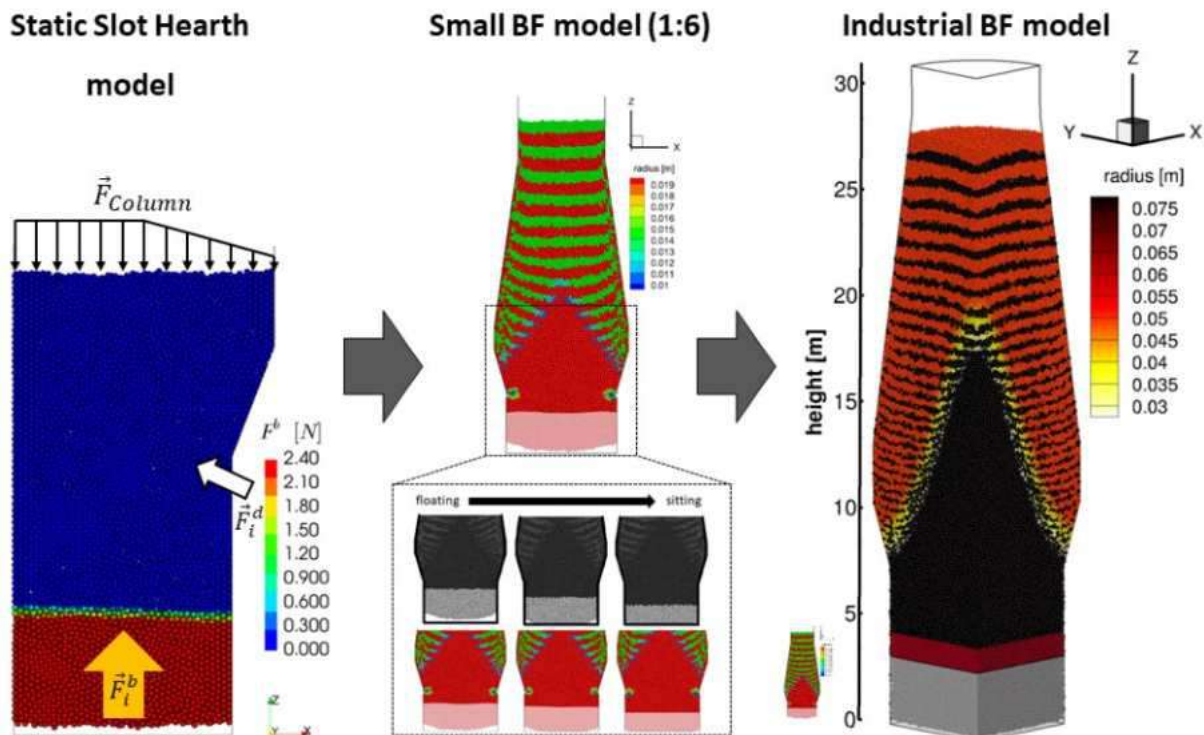


Figure 16: Stages of Model development.

In the beginning of the project, first static hearth simulations evaluating the sensitivity of the main processes, such as the buoyancy force induced by the hearth liquids, the influences of the weight of the burden column and the drag force caused by the hot blast occurring in the blast furnace hearth, were investigated. The first results presented show that the simulation approach chosen is applicable in the context of blast furnace simulations by reproducing the predominant effects. Nevertheless, with this first approach the particle movement inside the hearth due to the coke consumption by dissolution in hot metal was not considered. Previous simulations, for instance the results presented by Zhou et al. [67], showed that the coke consumption in the raceway has a substantial influence on the particle arrangement inside the Dead Man region. Therefore, the approach was extended to a small BF model and reviewed by comparing the results obtained with existing quasi-two-dimensional models presented in literature [67-69]. After the successful evaluation and comparison of the results, a transfer to a scaled blast furnace model of BF4 in Dillingen has been accomplished to review issues related with the portability to larger systems. The

investigation [65,69,70] showed that quasi-two-dimensional slot models, as used for model development, provide an easy way to reduce the size of the computational domain, and the total number of particles, which need to be represented and thus to minimize the simulation time required. But these studies, in particular [69], also showed that slot models cannot accurately describe essential flow features in a cylindrical geometry. Especially when connected with passing gas and liquid flow, the radial increase of available space and the strongly local fashion of gas inflow through individual raceways/tuyeres at the periphery, impose boundary conditions which cannot be reasonably reproduced in a slot model. As a remedy, the model was extended to a three-dimensional model [65], allowing to investigate the actual spatial distribution of the multiphase flow within a circumferential section of the BF hearth. At the same time, if symmetry allows a restriction to a smaller section, this approach allows the inclusion of considerably more particles and fluid cells in a simulation, which directly leads to a better mechanical representation of the bulk material and a higher resolution of flow fields. Therefore, the model was extended from the quasi-two-dimensional approach to a three-dimensional model, in order to reflect important spatial effects, which cannot be captured with 2D models. As such, the movement of the bulk material while passing the space between the individual tuyeres and the related effects on the porosity and especially the fluid flow in the lower part of the furnace were of major interest. With this extension, different liquid (slag/iron) volumes in the BF hearth were investigated. Different dead man states, as experienced in actual blast furnaces, from sitting to floating could be readily observed. Moreover, several aspects of the simulation-tool were improved as discussed in the following. The performed work and the steps taken were important prerequisites to develop the capabilities required for simulations incorporating actual operational data.

After the code has been successfully developed, improved and reviewed, the simulation tool was finally used to calculate different scenarios of three BF states identified by the BFI's DMD-model (all states are realistic, thoroughly checked and have been monitored in 2017 at Dillinger BF4).

Specifically, the simulations provide details of shape and volume below the DM, the porosity distribution within the DM and the velocity fields associated with both phases. The scenarios chosen comprises: a static, fully sitting DM, a DM in transitional state between sitting and floating (no vertical force acting on the hearth bottom) and a fully floating DM. For this purpose, operational plant data from Dillingen BF4 (e.g. burdening, hot blast, production) and the operational states, as identified by DMD, were used as input parameters for the CFD-DEM model. The transitional state was used to adjust the unknown parameters in the model such, that no net force of the DMD solids acts on hearth bottom while, at the same time, no large connected void exists below the DM. The two other scenarios will then, with the same "tunable constants", complement the information obtained from DMD: When the DMD value is low (as in the first scenario), how is the spatial distribution of the porosity in the coke bed and which liquid flow field can be expected? When the DMD value is high (as in the third scenario), how large is the volume of the coke free void and what are the parameters it mainly depends on?

2.2.1.2.3.1 Model Dillingen BF

An actual blast furnace contains an extremely large number of particles and covers a large spatial volume. Even the simulation of the hearth, as addressed in this work, represents about a quarter of the total BF volume and thus is at the borderline of current DEM-CFD capabilities. Unfortunately, the vertical force profile, as induced from the burden, the drag of the counter flowing gas in the shaft and the structure of the cohesive zone, are decisive for a correct evaluation of the particle movement in the BF hearth. For this reason, several simplifications were required to obtain usable results with reasonable computational effort. A first and obvious measure is to apply symmetry conditions and to restrict the size of the computational domain to a quarter (90°) section of the actual domain. To reproduce the particle behaviour, as it may be observed in the three-dimensional space, periodic boundary conditions are utilized at the boundaries of the cyclically repeated partial domains [70]. Figure 17 depicts the setup and summarizes the boundary conditions. The height of the domain considered is 31 m with a hearth diameter of 11.2 m. In the left image, the representation of the solid phase, physically different zones requiring specific internal boundary conditions are indicated.

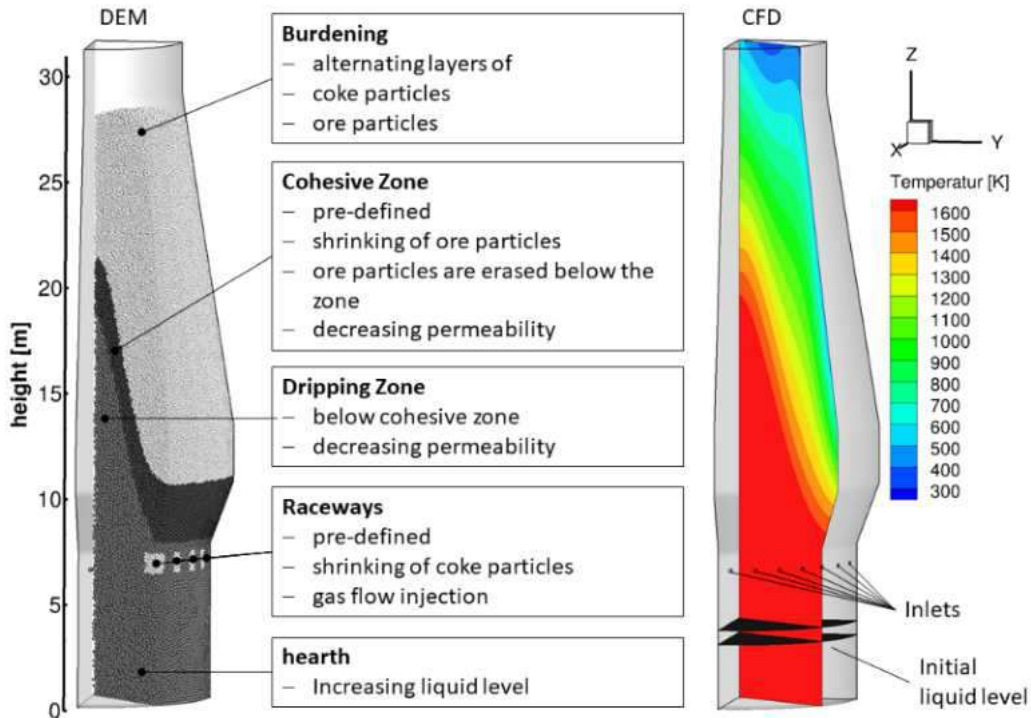


Figure 17: Simulation setup with the main boundary conditions and the static temperature profile of the gas phase.

At the furnace throat, the burden material is charged in alternating, mono-sized coke and ore layers (Table 4). The density of the ore particles is corrected during the descend according to their reduction degree based on plant data [71]. The cohesive zone (CZ), where the iron bearing material starts to soften and becomes finally liquid is considered as a predefined zone, using input data (shape and position) as provided by the ZAP model [72] of the actual plant [73]. The melting process of the ore particles is approximated by a linear reduction of the particle size in dependence on the position in the cohesive zone. When the particles reach the lower bound of the cohesive zone, they are assumed to be completely molten and are erased. Moreover, it is assumed that the hot liquids are still present, partially occupying the voids of the particle column. This leads consequently to locally lower porosities and, thereby, to a decreasing permeability for the counter flowing gas approaching the lower bound of the cohesive zone [65]. Below the CZ the liquid hold up in the dripping zone is considered by a reduced porosity following the findings from excavations of a blast furnace of the Mannesmann-Röhrenwerke [74]. Herein an averaged iron volume of 4.5 % in the voids of the packed bed could be observed. These findings are adopted using a correction factor of the cell porosity in the model. At the tuyere level, in front of the gas inlets spherically shaped raceway zones extending approximately 1 m into the BF are defined. The coke particles within this region continuously shrink with a pre-defined rate, which is estimated from operational data (coke consumption), until they reach a final diameter. When this threshold diameter is reached, the particles are deleted from the simulation. This coke volume removal induces the required burden flow. Inlets, where the hot blast is injected, are defined next to the coke consumption zones. To obtain the correct gas velocities without simulating the actual thermochemical processes, a stationary temperature distribution based on measurements and plant experience is defined to adjust the hot gas properties (density) and to ensure realistic gas velocities (Figure 17). The produced hot metal and slag are considered as two immiscible phases, accumulating in the hearth of the furnace. Table 4 summarizes the global boundary conditions which are identical for the plant simulations.

Table 4: General Boundary Conditions (BC).

Boundary Conditions DEM	Coke	Ore	Boundary Conditions CFD	Gas	HM/Slag
Diameter (representative) [m]	0.16	0.1	Density [kg/m ³]	f (T)	6800/3000
Average Diameter [m]	0.05	0.018	Viscosity [kg/m s]	$1.79 \cdot 10^{-5}$	0.006/0.435
Particle Density [kg/m ³]	800	f (T)	Number of tuyeres	7	
Coefficient of restitution	0.18	0.18	Gas mass flow [kg/s]	3.28	
Static friction coeff.	0.58	0.65	Initial liquid level [m]		2.7/3.15
Rolling friction coeff.	0.02	0.02			
Young's modulus [Pa]	$1 \cdot 10^7$	$1 \cdot 10^7$			
Poisson ratio	0.2	0.2			
Number of particles	550,000		Number of cells	300,000	
Time step [s]	$1 \cdot 10^{-4}$		Time step [s]	$1 \cdot 10^{-2}$	

Each BF simulation is starting with a layer arrangement obtained from a steady state simulation. This was required to fill the shaft with burden and the hearth with an initial level of hot liquid. In this study the time interval between two tapping cycles (approximately 25 min) is investigated, which means that any tapping related processes are not considered.

2.2.1.2.3.2 Results

As mentioned earlier the Dead Man Dynamics indicator (short DMD) developed by BFI in Task 3.3 was utilized to identify different operational states and thus the point in time from which operational plant data (Dillingen BF4, e.g. burdening, hot blast, production rates) was used to define the boundary conditions for the simulations. With the combination of a force balance approach (also known as Dead Man Criterion) [55] and a mass balance approach the DMD is a measure supposed to indicate the position and permeability of the dead man in case of a sitting and floating condition.

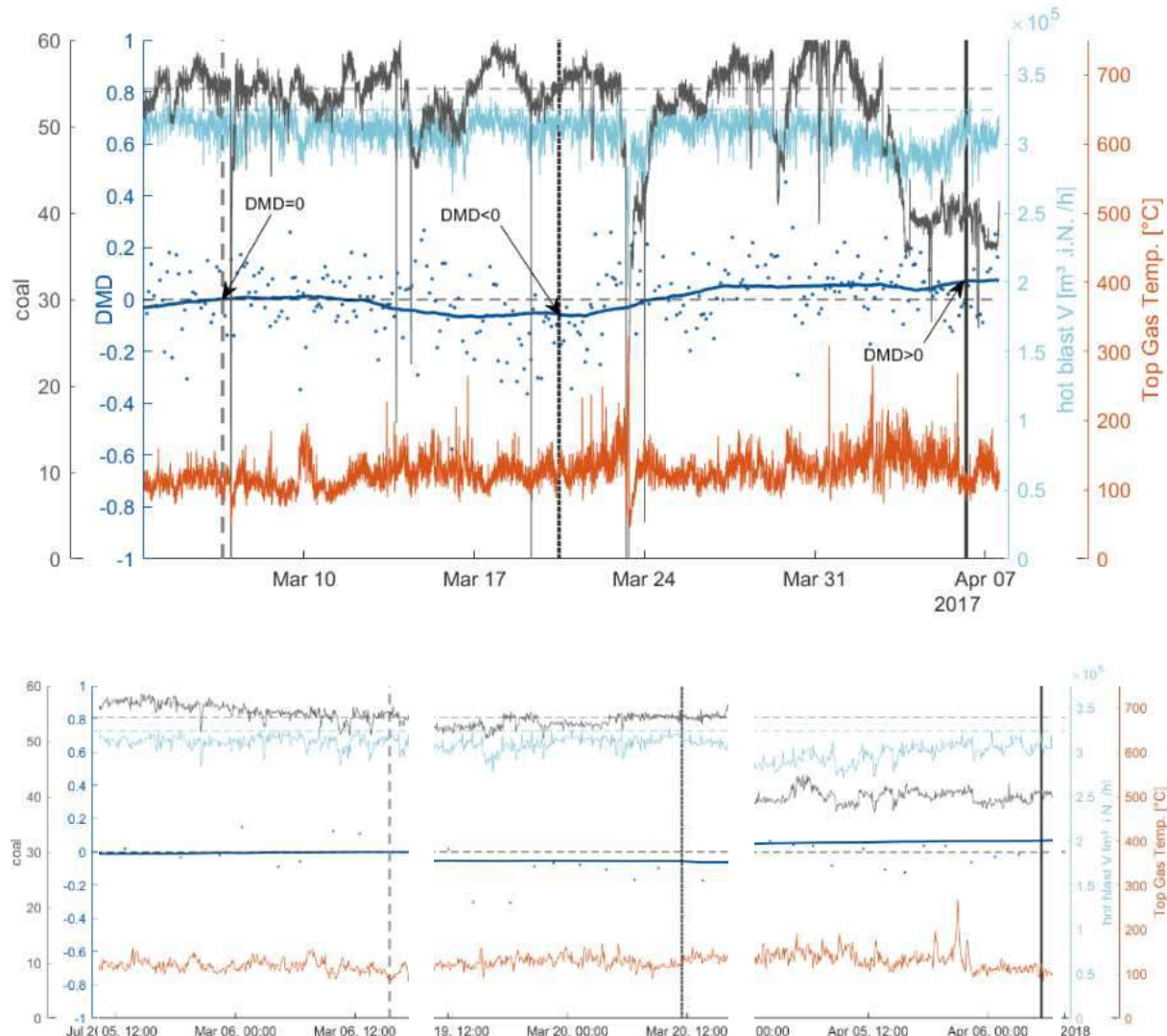


Figure 18: DMD Value for the considered time interval chosen for the calibration scenario (upper figure: overview, lower figure: 24h detail).

The upper diagram in Figure 18 exemplarily shows the results of the DMD-tool for the period from the beginning of March until the beginning of April 2017. Besides the DMD-Value (central blue line), the injected coal rate, the hot blast volume and the top gas temperature are shown. A data period was chosen, where subsequently a situation with $DMD=0$ (vertical grey dashed line) is followed by a period with $DMD<0$ (black dotted line) and $DMD>0$ (black solid line). A DMD-Value higher than zero indicates a floating DM, a value lower than zero a sitting DM, while a DMD value close to zero indicates the herein called transitional state, where the state between sitting and floating is reached. The lower diagram in Figure 18 shows close-ups of 24 hours of data before the three selected states of $DMD=0$, $DMD<0$, $DMD>0$.

Attention was given to find a period where all three states occurred within a short time interval to minimise additional influences on the BF operational state e.g. from changes in the material fed or from change of basic operational strategies. For identification of such a period BFI analysed minute-averaged operational data and tapping data of BF4 from four months in 2017. Supported by experts from Dillinger the best suitable data period (Figure 18) was selected. Furthermore, for the $DMD=0$ scenario, attention was paid to find a situation where $DMD=0$ and in parallel main operational parameters like hot blast and coal rates are within usual limits regarded as "good and normal" during operation. The additionally shown top gas temperature data was used to exclude periods with poorly working furnace since disturbances in the smooth and uniform material descent are usually visible by increased top gas temperatures.

A $DMD=0$ value (grey dashed line, left third, lower part, Figure 18) was observed on March 6th. During the 24 hours before, no operational incident is visible in the detailed data. Blast volume and coal rate are at values indicating good operation (defined as 80% percentile, marked with horizontal dashed lines in same colours as the data). Top gas temperature is constantly low at

Optimizing Blast Furnace Hearth Inner State (OPTIBLAFINS)

~100°C. As shown in the figure the tap end on March 06 15:30 was chosen for calibration. To avoid any tap related flow only the intercast period is considered. The DEM-CFD model correctly reflects this state when at the end of this time interval no burden column pressure acts on the base of the Blast Furnace hearth.

Subsequently the two other simulation scenarios for DMD<0 and DMD>0 were calculated complementing the information obtained from the DMD. The spatial distribution of the porosity in the coke bed and the coke free void were investigated. Table 5 summarizes the boundary conditions for the cases for DMD<0 and DMD>0. The operational situation for scenario I is comparable to the calibration scenario with DMD=0. During the 24 hours before the chosen March 20th, tap end at 11:30 (middle, lower part, Figure 18) operation is stable and coal and blast rate are normal. For scenario II a situation with a low coal rate and therefore higher coke/ore ratio was chosen. This enables to evaluate with the CFD-DEM model how the different composition of the burden column influences the DM state. During the 24 hours before the selected tap end at April 6th, 5:25h (right third, lower part, Figure 18) a single occurrence of slightly higher top gas temperatures is monitored but after the temperature spike >200°C the BF run stable for several hours. Table 5 summarizes the boundary conditions for the cases for DMD<0 and DMD>0.

Table 5: Specific boundary conditions for DMD < 0 and DMD > 0.

	scenario I (DMD < 0)	scenario II (DMD > 0)
Hot blast [m ³ /h]	314.000	309.000
Coke consumption [kg/kg hot metal]	0,3	0,3
coke/ore [t/t]	0,188	0,216
Initial iron volume [m ³]	24,4	24,4
Initial slag volume [m ³]	2,86	2,86
Hot metal production [t/min]	5,05	4,91
Slag production [t/min]	1,24	1,24
Time interval [min]	25	25
Temporal scaling factor [-]	20	20

Additionally, to supply the data needed for model setup of the three scenarios, Dillinger provided three calculations of the ZAP model to define cohesive zone position information. Also, an in-house burdening model developed by Dillinger in an earlier project was recommissioned and executed with charging data of the three selected time intervals to deliver information about position and material of the layer structure in the burden column.

2.2.1.2.3.2.1 Initial Case – Adjustment of parameters.

The initial case was used to define tuneable (free or actually unknown) parameters such as the friction coefficients and some other parameters. Figure 19 shows the results of a calibration case, where a dead man in transition was expected. On the left hand the burden column coloured by the particle diameter is depicted. The red and grey shade indicate the liquid hot metal and slag level respectively. The top diagram shows the temporal evolution of the burden column pressure acting on the base plate of the Blast Furnace. Herein only the normal pressure of the solid material is considered; any pressure induced by the liquids is neglected, since this value is used as an indicator for the dead man state. The more the value approaches zero, the more likely the dead man partially floats or completely floats.

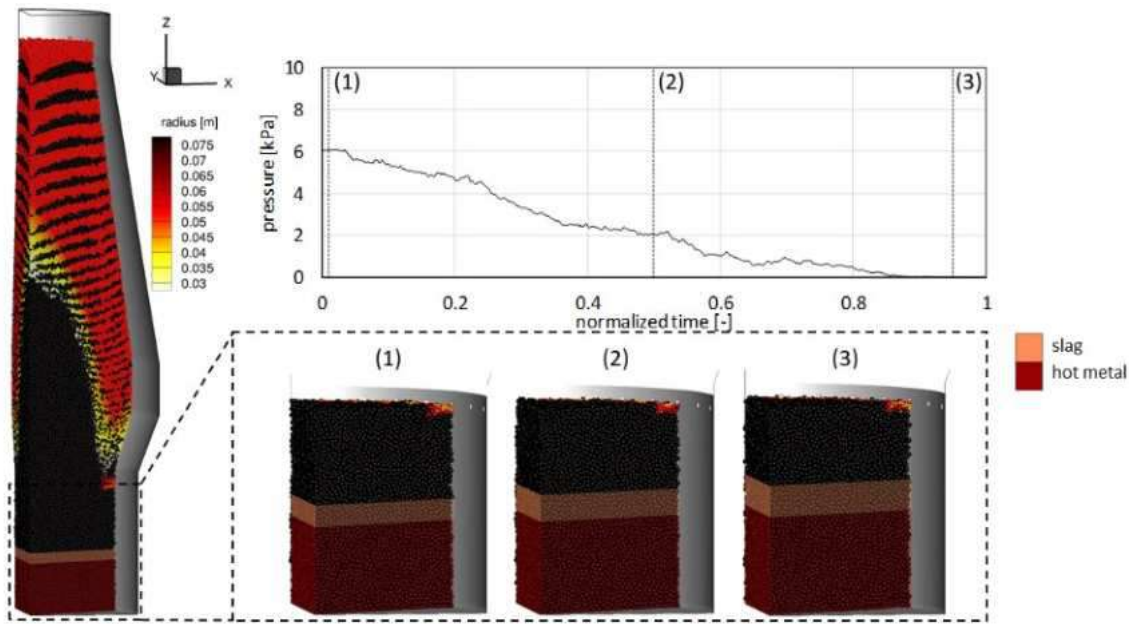


Figure 19: Results of the calibration case to three different times in (1) the beginning, (2) the middle, (3) the end of the intercast period.

In the lower row, snapshots of the particle arrangement at the three marked points of the section below the tuyere level are shown. It can be observed that the liquid level rises due to the hot metal production, which consequently results in higher buoyancy forces supporting the burden column. This vice versa leads to a decreasing load of the “sitting” burden column acting on the hearth bottom until a transitional state is reached, where the load approaches zero and the packing structure of the coke, especially at the periphery, becomes looser. For the case shown the parameters were adjusted and kept constant for the two other cases calculated afterwards.

2.2.1.2.3.2.2 Dead Man Dynamics (DMD) indicator < 0

Figure 20 summarizes the results for the case for DMD<0. On the left hand, the initial condition of the burden column coloured by the particle diameter is depicted. The characteristic layer structure of ore (orange) and coke layers (black) can be observed. The shape of the pre-defined cohesive zone approximates an inverse W shape. The red and orange shades indicate the hot metal and the slag level, respectively. Additionally, to be able to judge the particle arrangement in the lower part of the hearth, snapshots of the particle arrangement at the three marked points of the section below the tuyere level are shown. It can be observed that the liquid levels rise due to the hot metal and slag production, which consequently results in higher buoyancy forces supporting the burden column. This vice versa leads to a reduced pressure at the centre and the periphery of the hearth bottom (diagram Figure 20). In the present case, the supporting forces are not enough for a floating situation.

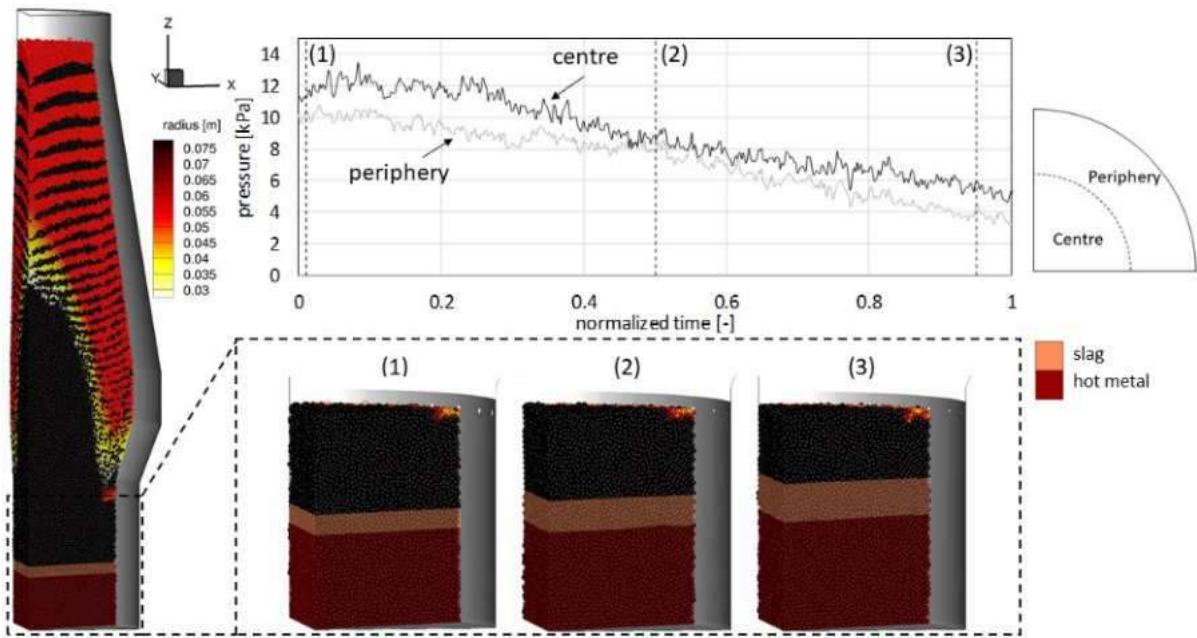


Figure 20: Results of the $DMD < 0$ case at three different times in (1) the beginning, (2) the middle, (3) the end of the intercast period.

2.2.1.2.3.2.3 Dead Man Dynamics (DMD) indicator > 0

Figure 21 shows analogously to the previous figure the results of the case with a high DMD-value. The layering structure of the burden is very similar to the previous case, although the coke/ore ratio as stated in Table 5 is higher. Shape and position of the pre-defined cohesive zone is slightly different; the top protrudes a bit higher in the shaft of the BF and the middle section is thinner.

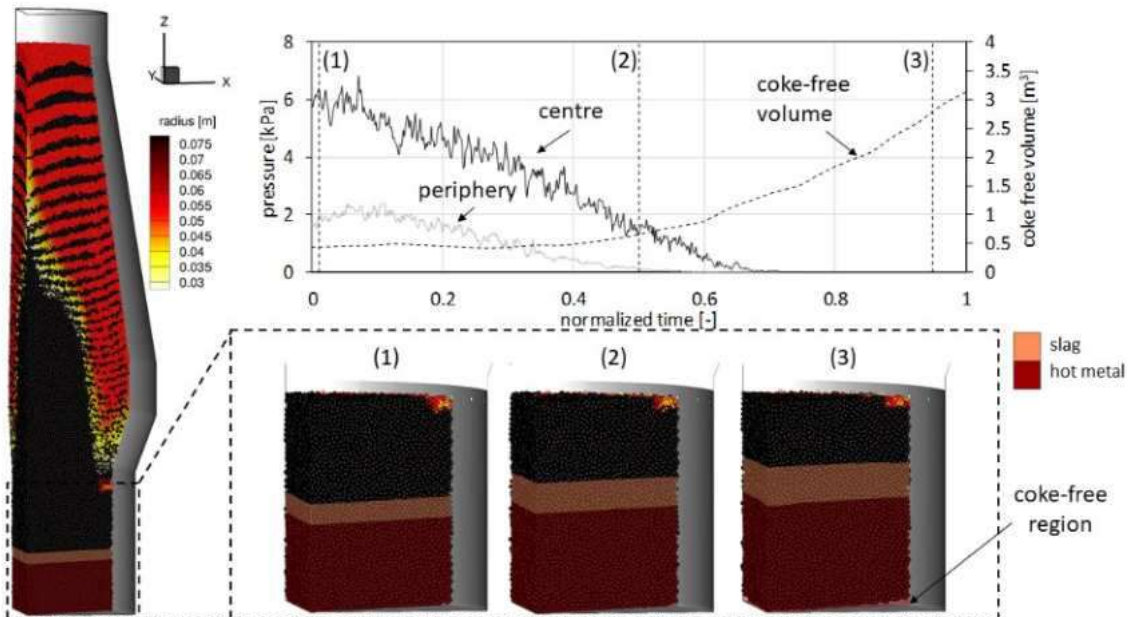


Figure 21: Results of the $DMD > 0$ case at three different times in (1) the beginning, (2) the middle, (3) the end of the intercast period.

The burden pressure at the hearth bottom is shown in the top diagram of the figure. Herein an inner and an outer zone are distinguished, corresponding to the centre and periphery of the hearth bottom. Just like in the first scenario the supporting buoyancy forces increase with the rising liquid levels and the load at the bottom decreases. In contrast to the previous scenario, after half of the time considered, the pressure reaches a value of zero, indicating that the bulk material actually starts to float in the immersed liquids. Specifically, it can be observed that the pressure in the outer zone first approaches zero, leading to the conclusion that the particle bed starts to float in the periphery followed by the centre. Complemental to the burden pressure, the evolution of the coke free region is depicted in the diagram; at the end of this period, the volume of the coke free

region continuously increases. The last snapshot in the lower row shows the shape of the coke free region, as it results from the force balances resolved in the model. Main reason for the floating behaviour is, besides the higher coke/ore ratio (which leads to a lighter burden column) a different gas flow pattern due to the different burden structure. Figure 22 shows a more detailed look of the hearth in the end of the intercast interval. The interface of the volume below the coke bed is highlighted with an iso-surface. It can be seen, that the shape of the coke-free region is characterized by a larger void at the periphery compared to the centre.

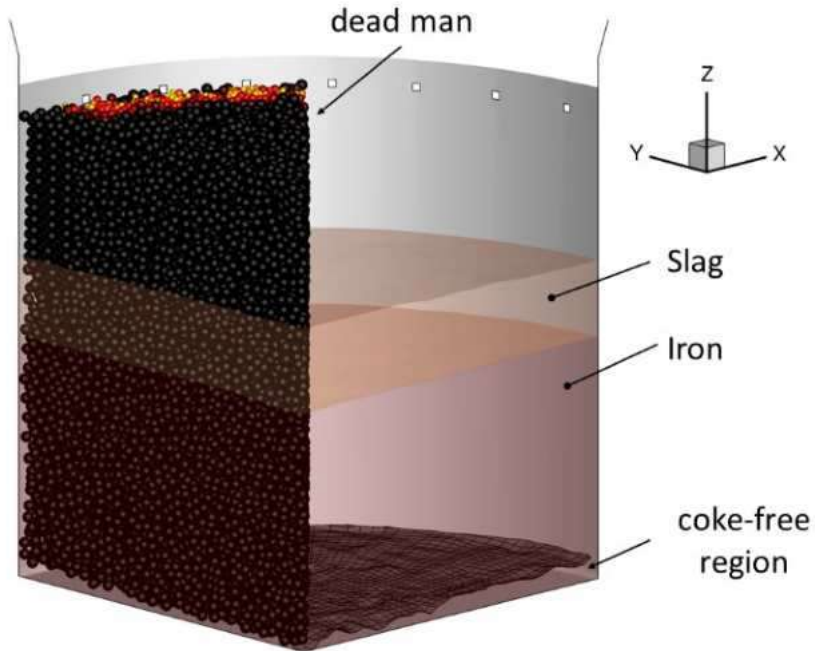


Figure 22: Detail of the hearth in the end of the intercast period for DMD > 0

2.2.1.2.3.3 Results – variation of hot blast

In a further study, the influence of different hot blast volumes on the particle movement in the hearth, assuming constant hot metal and slag volume, was investigated. Three different flow rates were set for each individual tuyere inlet, starting with 80 % (100 % corresponding to the initial condition of the previously described simulation) and finally 110 % of the initial hot blast flow. The results obtained show that the drag forces caused by the hot blast affect the arrangement of the particles located in the hearth (Figure 23). With the increasing hot blast and therewith increasing supporting forces the coke free space increases. In contrast to scaled physical models and respective simulations, a drastic change in the shape of the immersed particles boundary, as characterized by the larger void at the periphery compared to the center, cannot be observed in this model.

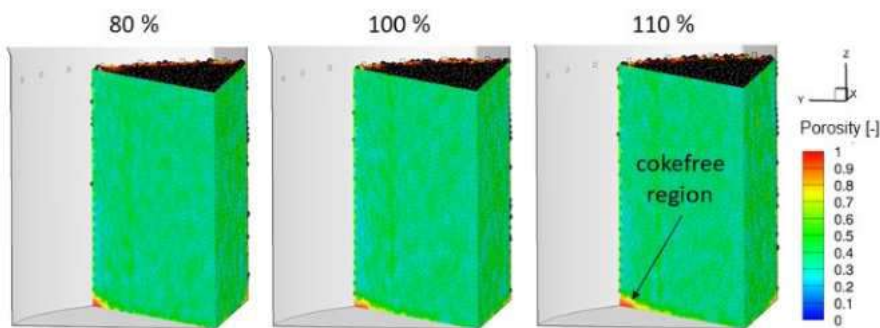


Figure 23: Particle arrangement in dependency of the hot blast volume.

In Figure 24 (left) the dead man region identified as the stagnant particle bed in the hearth is depicted. The particles are colored by their normal pressure, which is defined as

$$p_i^n = \frac{\sum |\vec{F}_i^n|}{A_i} \quad (5)$$

with the normal Force \vec{F}_i^n and the corresponding surface A_i of a considered particle or wall i. On the right-hand side, the averaged pressure acting on the hearth walls and the averaged particle pressure at the tuyere level are shown for the different scenarios. It can be noticed that with an increasing hot blast volume the forces at the walls decrease because of the larger lifting forces induced. Moreover, these simulations can be used to provide boundary conditions for even more detailed models, for example those in Task 1.5. More specifically, the pressure profile in the burden column at any level can be extracted. In this context, the top diagram shows the averaged particle pressure at the tuyere level. Herein also, a noticeable effect of the different blast volumes especially in the centre of the BF can be observed.

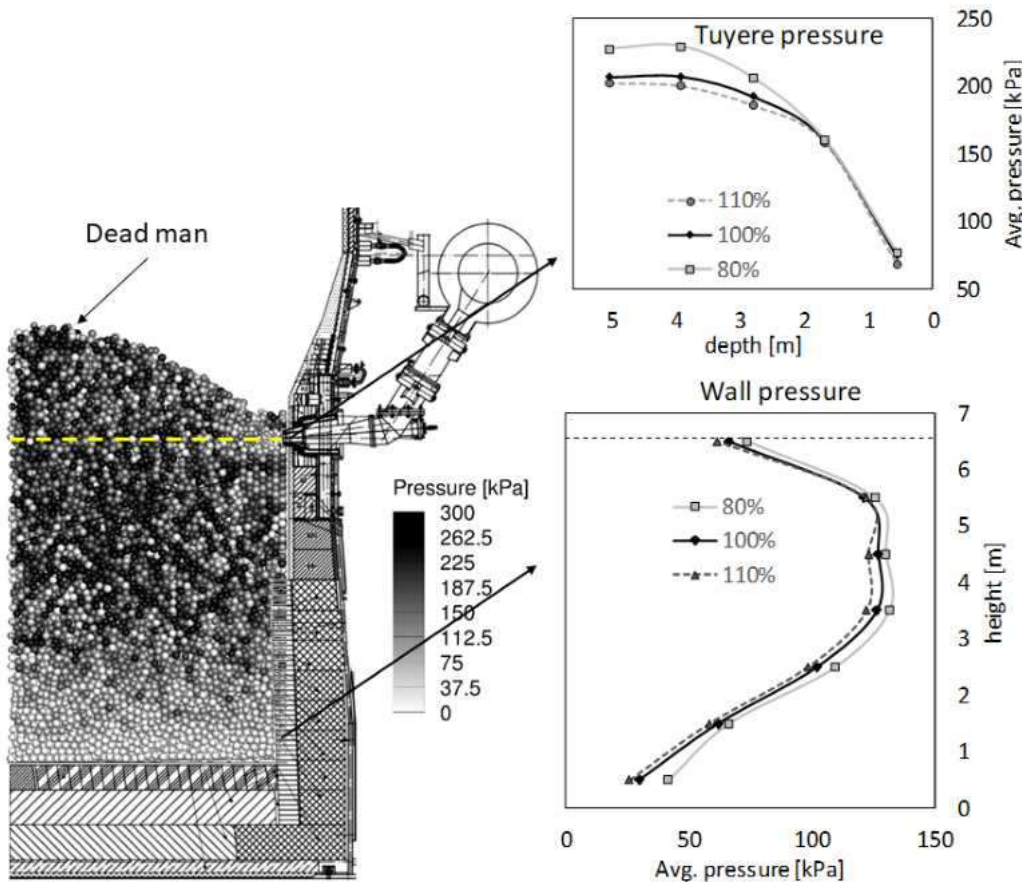


Figure 24: Snapshot of the particle normal pressure for the DM (left), averaged particle pressure at tuyere (upper right) and Normal wall pressure for different hot blast volumes.

2.2.1.2.3.4 Conclusions

The developed simulation tool allows to obtain a multitude of additional information from defined scenarios (DMD-tool) by altering the operational conditions (e.g. burdening, location/form of cohesive zone, hot blast volume etc.). These include the internal structure and the associated processes in the BF-hearth, which are hardly accessible by other means.

2.2.1.2.4 Model and performance improvements

Further improvements related to the simulation technique (specifically for the BF application) achieved during the project are briefly summarized in the following paragraphs.

2.2.1.2.4.1 Code adaption

The technical system investigated here contains an extremely large number of particles and covers a very large spatial volume. Even the hearth, representing about one quarter of the total BF volume, is at the borderline of DEM/CFD applicability as far as computational resources or computing time are concerned. Unfortunately, the influence of the horizontal force profile, as induced from the burden, the counter flowing gas in the shaft and the structure of the cohesive zone, are decisive for the state of the DM, whether sitting or floating at a force dependent height. In case of a floating DM, the shape of the interface between bulk material and hot metal is also influenced by the position, shape and extension of the tuyeres and raceways. Anyway, several approximations and simplifications may be taken to obtain usable results. Besides an increase of particle size in the mechanical model only (while retaining the actual size distribution and other properties), the so called "coarse graining", may improve the situation to a certain extent. If the "mechanical" particles become too large, the computed solid flow field will be deviate from the actual flow field in the BF. Another means to reduce the computational effort is the exploitation of existing or artificially created/assumed symmetry conditions to reduce the volume of the overall computational domain. Cyclic boundary conditions and a special treatment of the inherent singularity on the BF axis allow to reduce the problem to a much smaller volume, e.g. considering only a subset or even only one tuyere and its direct neighborhood. Additional parallelization by domain decomposition, thus assigning individual processors (while still exploiting thread-based parallelism on each of them) to different subdomains of the computational domain considered, provides a further reduction of the computing time needed. Notice, that this decomposition must still allow an efficient coupling with the CFD part of the solution, typically realized by one, or if required several instances of the CFD code used. The communication among these individual processes and the necessary data synchronization pose a complex situation, which, if the code is not implemented in the correct way, may easily exceed the advantage achieved by parallelization.

2.2.1.2.4.1.1 Parallelization via domain decomposition

Figure 25 shows a typical horizontal subdivision of the simulation domain to spread the computational work to different processes, in this particular case to five processes (P0-P4). The particle color represents the subdomain, where each of the particles is located. As the particles in the BF are descending, they are continuously leaving and entering the different subdomains. This information of particles crossing the process borders must be updated and transferred between the neighbor processes in a synchronized fashion. This is the challenging aspect of parallelization, since each process must wait until the necessary information is provided by their neighbor processes to start the next iteration.

During the last working period, this data transfer was optimized and changed from so called blocking, synchronous MPI (Message Passing Interface) communication to non-blocking asynchronous communication. Especially when a larger number of processes is involved, this can reduce the communication overhead considerably. For detailed information and further explanation just check reference [76]. For the current implementation and the BF-System considered, this measure resulted in an overall speed up of about 50 %.

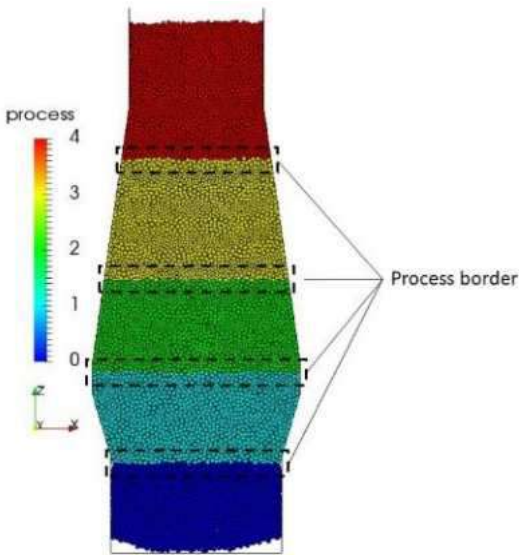


Figure 25: Parallelisation by domain decomposition.

2.2.1.2.4.1.2 Periodic boundary conditions for sector models

The exploitation of the 90° symmetry inherent to the cylindrical BF is visualized in Figure 27. In order to reproduce the particle behaviour as it actually occurs in full 3D simulations, so called periodic boundary conditions (PBC) are utilized at the boundaries of cyclically repeated partial domains. Particles leaving the domain through one of the two, logically adjacent periodic planes are entering the domain through the other plane. Particles located in the periodic boundary like the green particle in Figure 26, temporarily exist on both sides. Both particles are then fully considered in force calculation. Special care and additional measures must be taken at the tip on the axis of the domain.

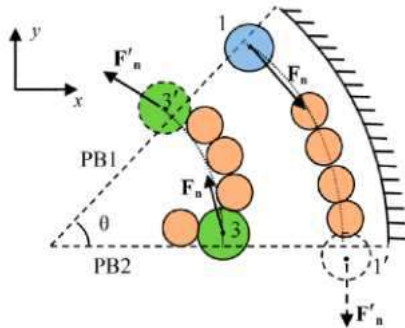


Figure 26: Treatment of particles at periodic boundaries [8]

In Figure 27 the results of a DEM simulation of a quarter section (90° Section) with PBC of the 3D model is illustrated. On the left side, the particles are coloured by their radius, it can be observed, that the particle arrangement is similar compared to the results with the fully 3D model. On the right-hand side, the particles are restricted in the visualization to the lower part to show the operating principle. Those particles, which are intersecting the periodic boundary planes, are coloured in blue and exist on both sides (like the green particle in Figure 26). This ensures comparable conditions for the particles inside the partial domain compared to the fully 3D situation.

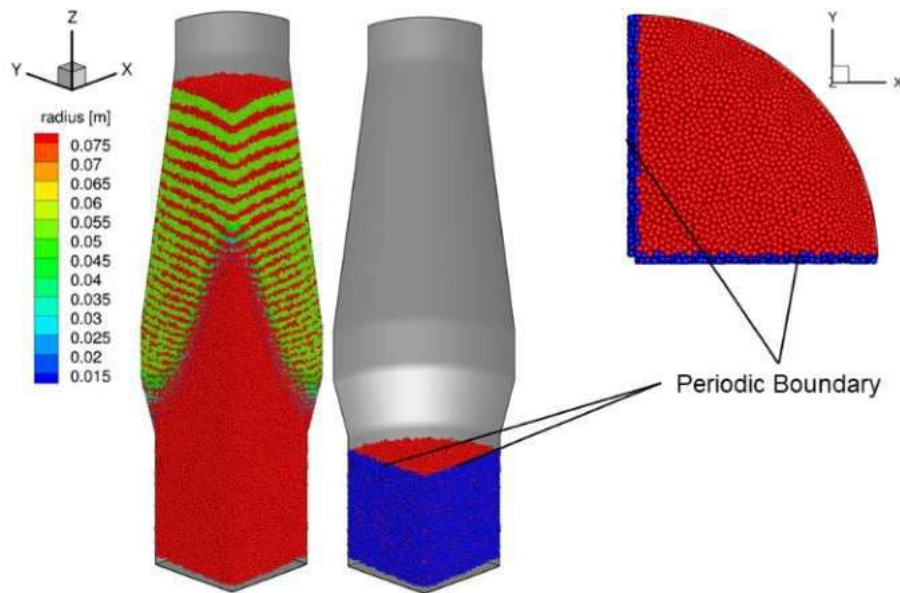


Figure 27: Periodic Boundary Conditions for 90° model.

2.2.1.2.5 Model simplifications – time scaling

The previous investigations showed that the coke consumption in the raceway has a substantial influence on the particle movement inside the BF hearth. For this reason, steady state scenarios without any particle consumption cannot approximate the particle movement. Nevertheless, with the available DEM-CFD tools and the approximation level required, a simulation of the technically relevant timescales (> 2 h) is currently out of reach. Under these circumstances time scaling and size scaling are common and necessary means, already discussed in several publications [67],[76] and [77].

With the modeling approach used, the overall “production rate” of the model BF is controlled by the coke consumption rate predefined in the fixed raceway zones. Artificially increasing this parameter reduces the required total simulation time, since it accelerates the burden flow and thus reduces the overall solid residence time. Until steady state of the flow (and all processes involved) is achieved, the numerical integration of the underlying equation must be performed for at least one residence time, in practice even more. Therefore, this artificial acceleration must be used with caution and its drawbacks should be checked. A simple experiment was performed in order to estimate the quantitative influence and the validity of the time scaling used. The chosen simulation setup is equivalent to the slot model presented in the midterm report.

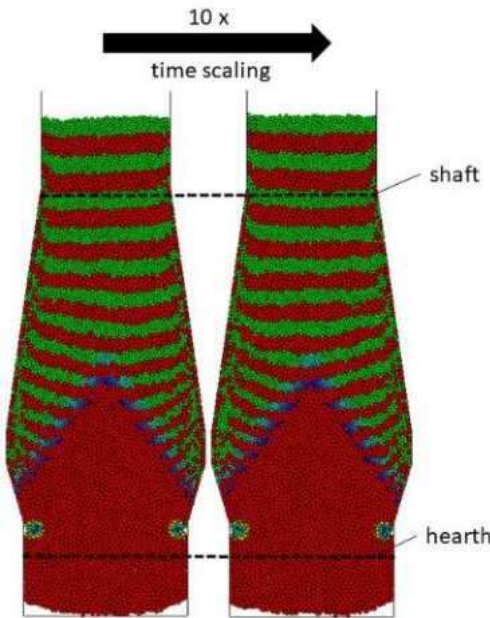


Figure 28: Comparison between 10 times accelerated systems with the original simulation.

For comparison, an initial simulation with a given coke consumption rate was accelerated by choosing a tenfold larger conversion rate in the raceway zones. The resulting particle arrangement (colored by particle radius) of the two scenarios is compared in Figure 28. There are no obvious differences visible. The layering inside the model BF is very similar and the shape as well as the volume of the coke free region are almost identical.

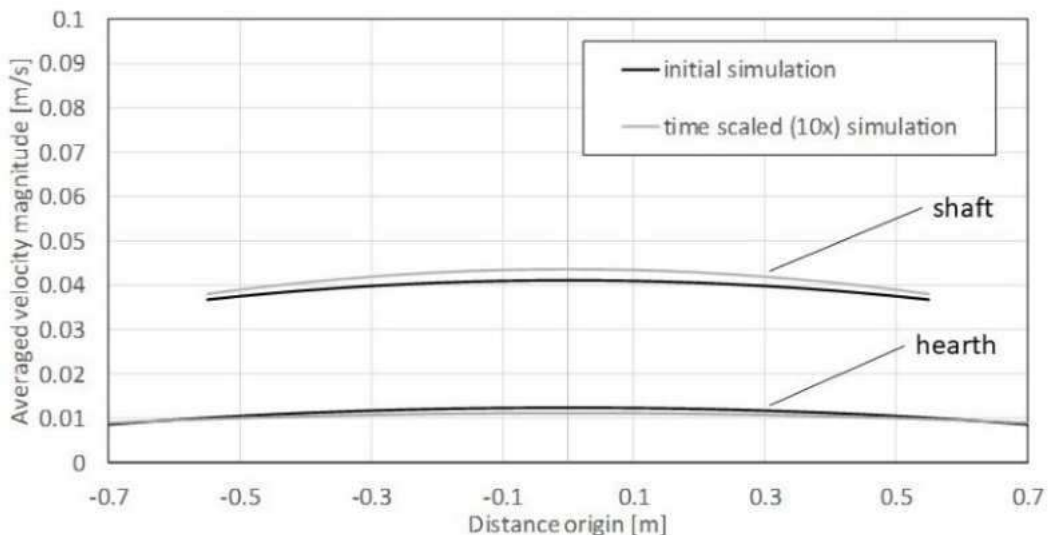


Figure 29: Comparison between averaged particle velocities at shaft and hearth position for the initial and scaled system.

To quantify these findings, the averaged particle velocities across the two marked planes (dotted lines in Figure 28 one in the shaft section and one in the hearth section) are compared in Figure 29. Herein the black line represents the initial and the grey line the time scaled simulation (velocities scaled back and thus multiplied with 1/10 to obtain comparable graphs). For both sections considered only small differences can be observed. The largest deviation between the two simulations occurs in the center of the system (shaft 6%; hearth 9%). Summarizing, the numerical experiment showed, that the assumption of larger consumption rates results in only marginal deviations from the physical situation pursued and thus is justifiable.

2.2.1.3 Water model studies BF Hearth

2.2.1.3.1 Research water model TSE

2.2.1.3.1.1 Basic Engineering

Numerical models are used to gain insight in the flow field and temperature gradients in the blast furnace. These models can be made very complex with a lot of variable parameters, which takes a lot of undesirable computational work. It is not possible to make a model of the whole blast furnace hearth, which includes all particles. Therefore, simplifications are necessary for the smaller scales to improve the whole process. To justify these simplifications, a good understanding of the process is necessary. The goal of this experiment is to understand the fundamentals of a natural convection flow through a porous medium near the BF wall.

This experiment can not be carried out with liquid iron. Instead, a simple and thus controllable experimental set-up will be used with water. Since the dynamic viscosity of both liquids are of comparable magnitude, a translation from the experimental water model to the numerical liquid iron model can be made. The results of this research will be compared with a numerical water model of the set-up.

The velocity measurements will be performed with a Particle Image Velocimetry (PIV) system. A schematic overview of the PIV system can be found in Figure 30.

A Bernoulli PIV 200-15 system from Litron Lasers will be used to illuminate a vertical plane within the main chamber. The PIV system uses two pulsed, Q-switched laser resonators to build up energy and give a pulse of a few nanoseconds. The Nd: YAG laser produces an infra-red light at 1064 nm which is converted to visible 532 nm (green) laser light by a harmonic generation assembly. With use of a light guide arm, the laser beam can be placed at a designated position. The most important output properties of the laser are a maximum repetition rate of 15 Hz and a beam diameter of 6.35 mm.

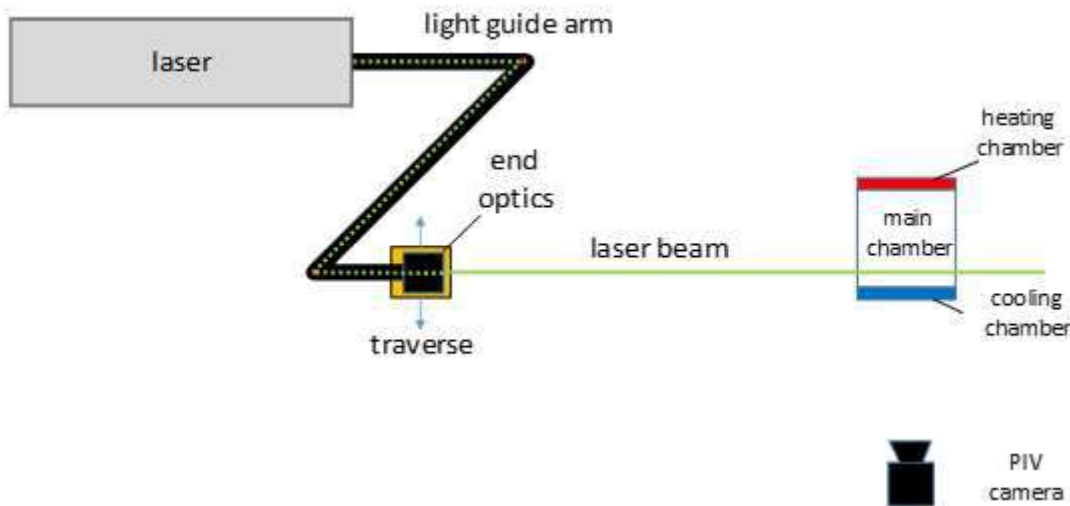


Figure 30: Schematic overview of Particle Image Velocimetry (PIV) set-up.

To generate a flow, a temperature difference between the front wall and the rear wall of the main chamber will be created. In this way, a circular natural convection will occur, where near both walls the flow will go up or down.

Water of constant temperature is pumped through the cooling chamber. This makes sure that the front wall is colder than the main chamber. There will be some heat losses due to conduction to the tubes and the walls in the cooling chamber. These effects should be constant, to ensure a constant wall temperature over time. At the rear, a heating plate is placed just behind the wall. This plate is connected to a controlled power supply. Again, there will be heat losses to the environment, but the effective heat to the system will

reach a constant value. The whole system will reach a steady state after some time, so all of the time derivatives are constant. This contains flow velocities and heat transfer.

To check the wall temperatures, four thermocouples are placed against the wall. Two at each side at 30 mm from the bottom and at 30 mm from the top. The temperature is also measured in the middle of the set-up. A bar with five thermocouples is placed in the middle of the set-up, which measures the temperature at different heights: 10, 75, 155, 230 and 305 mm from the bottom. All temperatures should be at a constant level to make sure the system has reached a steady state. This property is necessary for a good comparison between different experiments.

2.2.1.3.1.2 CFD set-up water model

Although the water model looks simple, the set up in the simulation was rather complex. In order to approximate the heat exchange as well as possible, all parts (bath, walls and cooling) needed to be taken into account. The simulation therefore contains 5 domains (Figure 31) cold water (cooling domain), warm water (measuring domain), a heating element, Perspex walls on the outside and glass walls internally. The white points indicate the schematic thermocouple positions with their names. Positions of the thermocouples are about the same as in the experiment (30 mm from the top and bottom, 0.0001 mm from the wall). Later on, it became clear that the thermocouples in the experiment are placed towards the back of the box and not in the middle. Evaluation of these values showed that there is little difference (temperature, 2nd digit behind the comma) across the depth of the box, so the thermocouples from the simulation are in the middle of the box. The temperature from the centre thermocouples in the experiment were taken from the centre line in the simulation.

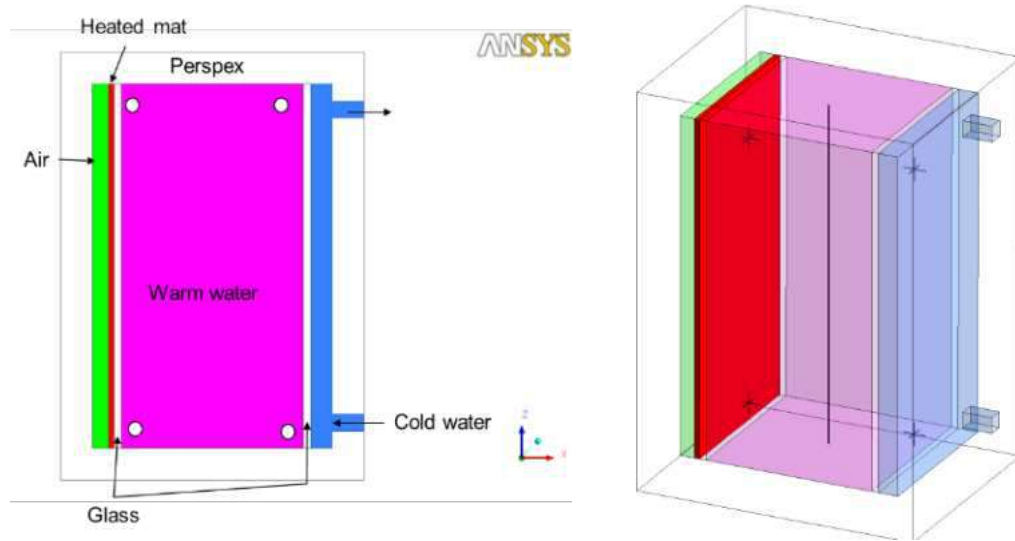


Figure 31: CFD set-up of the water model with the different domains.

The warm water domain is modelled as open as well as with a porous bed. The porous bed is modelled with Ergun and the values are taken from the experiment, depending on the particle size (porosity between 0.31 and 0.36). The particles size also comes from the experiment (9,12,16 and 20 mm). As Ergun is used, the particles of the bed do not participate in the heat conductivity. Material properties can be found in Table 6.

Table 6: Material properties in water model.

	Density (kg/m ³)	Specific heat (J/kg K)	Heat conductivity (W/mK)	Dynamic viscosity (Pa s)	Expansion coefficient (1/K)
Glass	3100	500	0.8		
Perspex	1200	1500	1.9		
Copper	8933	385	401		
Water	997	4182	0.61	8.80E-4	2.57E-4
Air	1185	1004	0.026	1.83E-5	3.36E-3

2.2.1.3.1.3 Results

The "Adaptive PIV" method is an automatic and adaptive method for calculating velocity vectors based on the masked images. The method will iteratively adjust the size and shape of individual Interrogation Areas (IA) in order to adapt to local seeding and ow gradients. The grid step size (distance between two IA's) is set to 32x32 pixels when hydrogel balls are used in the experiment and 64X64 pixels for experiments without balls since less accuracy is necessary here.

One of the results is shown in Figure 32. For each area of 32x32 pixels, one velocity vector is made. A laminar flow and a steady state are assumed, so each of these images should have about the same result.

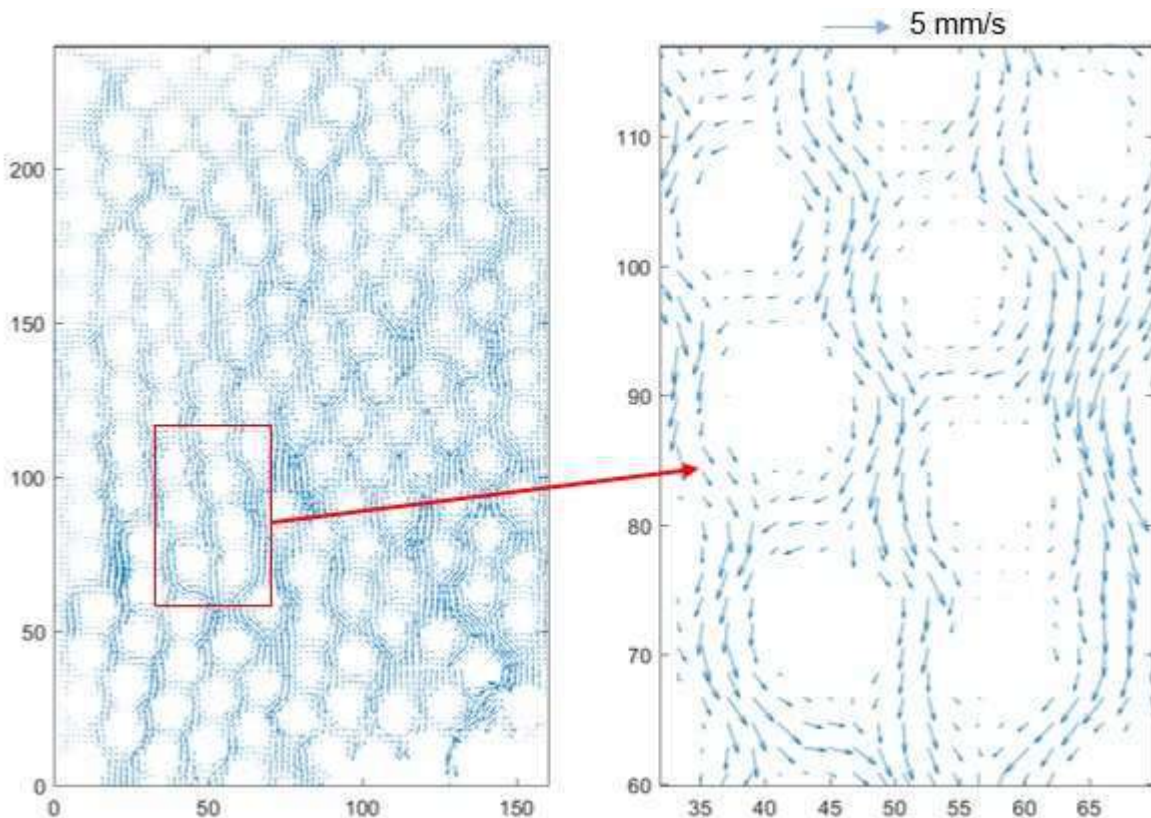


Figure 32: Total vector velocity field (left), enlarged image (right) indicating the size of the interrogation areas compared to the flow structure.

CFD analysis shows remarkable good comparison with measurement. The velocity profile of the vertical centre plane of the model is shown in Figure 33.

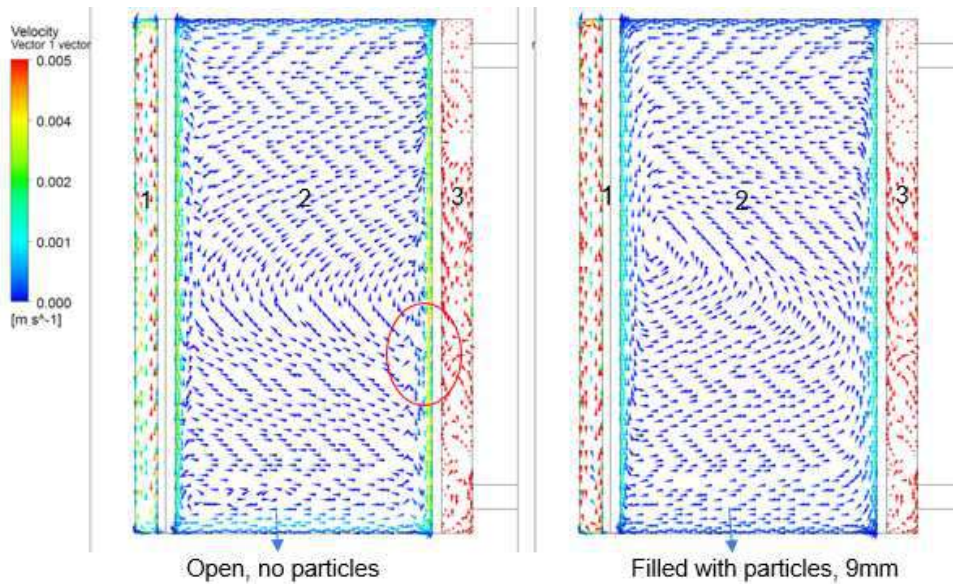


Figure 33: Velocities in the mid plane for no particles and 9mm particles (1= air, 2= warm water and 3= cold water).

In Figure 34, three consecutive image processing steps are shown. In the left image, the bright regions show the seeded flow and the dark regions show the water-soaked water balls where no particles are present. Clearly, all fluid regions are reached using the water marbles while the illumination passes the image from left to right. Also, some shadow streaks and bright lines are visible. These are from imperfections in the illumination, partial reflections to the water marble edges and the thermos-couple wiring. Water marble edge reflections are likely to be stronger when the light sheet passes the marbles at the sides than when they pass through the centre. Since the flow is moving relatively slowly (in the order of 1 to 10 mm/s), the time delay between consecutive images is set to 0.1 sec. and 100 images are recorded.

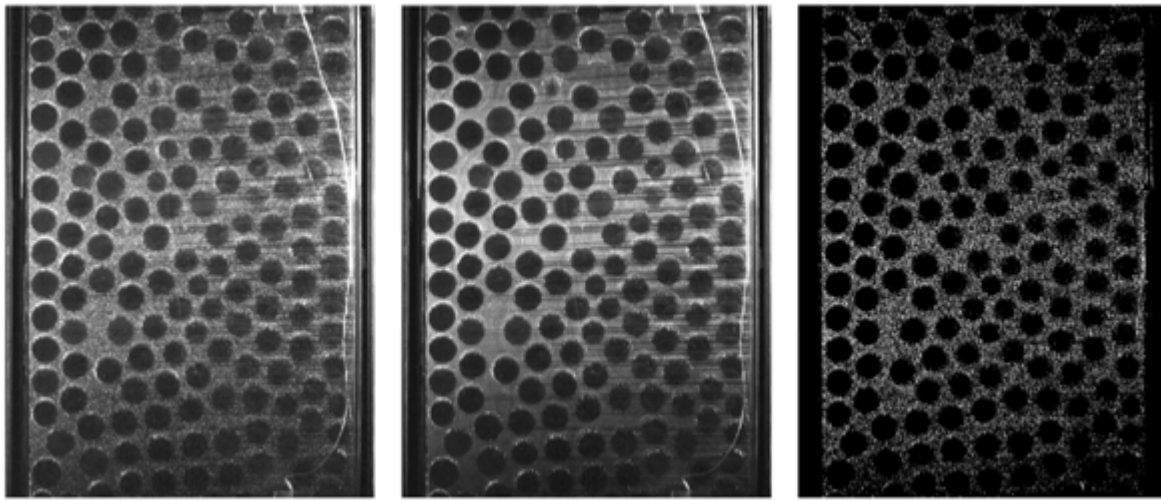


Figure 34: Pictures illustrating three stages of the PIV image processing. The left picture shows the original images, the middle picture shows the average of all 100 recorded images of a single measurement and the right image shows the result after subtracting the average image from the original image.

The full chain of velocity data processing steps results in an 'average velocity' profile shown in Figure 35. The development of the average velocity found from the velocity fields is shown at 0.5 mm steps up to 8 mm wall distance and 1.0 mm steps beyond 8 mm covering a total distance of 20 mm.

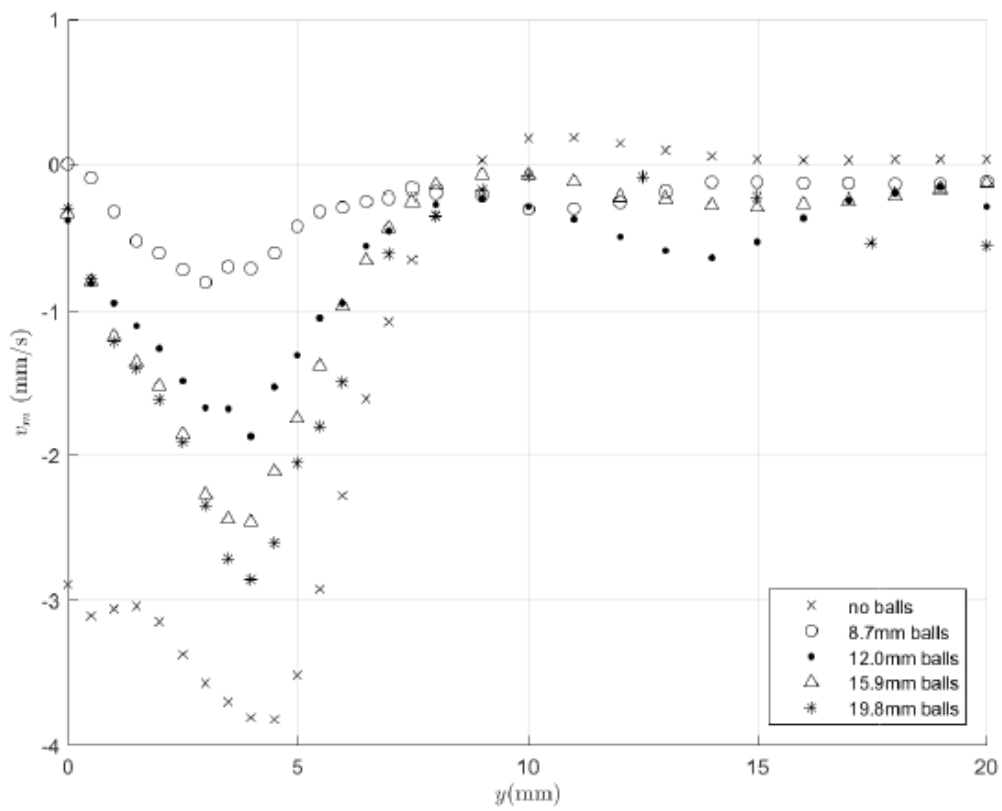


Figure 35: Average velocity as function of distance from wall for different ball sizes.

The measurements clearly show the development of the boundary layer close to the wall. It should be noted that the light sheet thickness is estimated to be around 1 mm so velocities within a plane of 1 mm will be integrated for a single measurement. However, the laser sheet displacement accuracy is within 0.03 mm, so apparently sufficient for clearly resolving the development of the boundary layer.

The temperature profiles measured in the centre of the main box show the stratification that has gradually developed over time. The measurements at the wall also shown some development over time.

Apparently, close to the wall a larger temperature difference develops in the packed bed case than in the no packed bed case. It seems that the vertical transport of heat inside the main chamber is blocked, which is the natural route for the convective flow.

The (CFD) velocities close to the cold wall of the warm domain is shown in Figure 36.

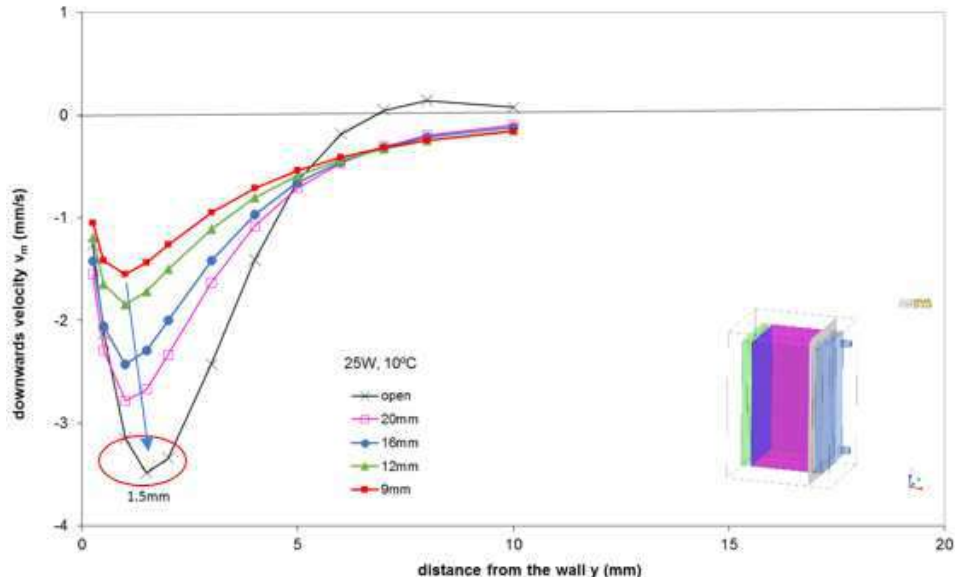


Figure 36: Calculated average velocities as function of distance from wall with different ball sizes.

Comparing the simulation with the experiments (Figure 35 and Figure 36), it can be seen that the maximum velocity is nearly the same. And in both experiments and simulation the peak velocity shifts away from the wall as the porous bed is removed (blue arrow). Yet the maximum velocity peak in the simulations is closer to the wall than in the experiment (maximum peak simulations about 1mm, in the experiment 4mm). In the experiment, the true velocities are calculated using the local porosity, yet in the simulations the porosity is uniform, and this could cause the difference. The velocity in the case of the small particles of 9 mm is relatively high in the simulation compared to the experiment, although it is unclear whether this is because of an incorrect value in the experiment or the simulation. Yet the trend seems more congruent in the simulation than in the experiment. It is known that the velocity measurement becomes more difficult as the particle size decreases. The increased velocity in the simulation is congruent with the low temperatures that are found with the cold bottom thermocouple. The velocity in the simulation of the open domain and the experiment also differ. As the porous bed is not present in this situation other factors must have an influence, such as the heat exchange with the environment, material properties, turbulence or an instable flow, numerical modelling or measurement errors.

2.2.1.3.2 Water model Experimental Blast Furnace (EBF)

2.2.1.3.2.1 Experimental blast furnace process conditions

Before starting the construction of the water model in full scale from the LKAB's Experimental BF (EBF), the EBF tapping procedure was evaluated in detail, in order to set up the model requirements. To reproduce the liquid flow from the process in the water model the achievement of dynamic similarity was of priority.

Due to a lack of measurements of volume flow rates when tapping the EBF of hot metal (HM), experiences from operation, related measurements and prior CFD model results were used to characterize the tapping of the EBF. The diameter of the hearth is 1500 mm and the height is 1252 mm. Above this level, the three tuyeres are entering the furnace creating the raceway regions. For creating the taphole, a drill with a diameter of 32 mm is used, making an ideal taphole diameter. During ordinary operating conditions the production rate is 1.5 ton/h of HM and 375 kg/h of slag, and the operating pressure is 1 bar over pressure (top gas pressure). For a certain period of LKAB's EBF campaign 32 (conducted in Q4 2016) the tapping time was in the range of 3.5-14.5 minutes. When sorting out the extremes a mean tapping rate of 4.5 minutes was found. The main factor to create the difference in tapping time, given the same operating conditions, is expected to be the condition of the taphole. An optimal taphole, holding up a diameter of 32 mm throughout the furnace, i.e. no taphole clay reducing the flow, is expected to give the fastest tapping times. Further, from observations, the tapping rate seems constant during the tapping sequence.

To achieve dynamic similarity between the real process and the water model, the volume flow rate needs to be identical in the hearth. To meet the specifications for the water model, a basic iterative

computer model was developed in Excel. Further, it is called Excel model. First the real EBF process (including the operating over pressure, presence of slag and HM) was evaluated to validate the model in terms of observed tapping times. The model makes use of the equation for conservation of mass and the Bernoulli's equation, i.e. conservation of energy, together with a coefficient taking the pressure loss in the bed into account. The pressure loss coefficient is determined iteratively by making the calculated tapping time conform to the observed tapping times for an ideal condition as well as results from a transient multiphase CFD model created in Sustaintap [55]. By knowing that the operating pressure affects the volume flow rate linearly, derived from Darcy's law (basic law governing the flow of fluids through porous media), the results could be used for designing parameters in the water model to achieve dynamic similarity between the water model and the real EBF process during a complete tapping sequence.

The bed porosity, the operating pressure and the static pressure from slag and HM are important for the tapping procedure of the EBF. The static pressure that forces the flow is only created above the taphole (at the level where the taphole is in direct contact with the environmental air). In the EBF process the HM and the slag is tapped from the same taphole, meaning that the static pressure from slag will be constant during the tapping of HM, while the static pressure from the HM, also known as the ferrostatic pressure, will decrease during the tapping sequence as the HM level decreases. The bed distribution is of great importance for the flow field of the HM in the hearth, which in turn affects the wear of the lining. To estimate the tapping time however, the mean porosity of the bed gives enough information to calculate the mean pressure drop that the coke bed generates.

Bernoulli's equation is valid for incompressible, non-rotational and in viscous flow. For liquids in general the density variation is small, and they are classified as incompressible. The rotation of the liquid flow in the bed can be neglected due to the absence of movement of the coke bed. All liquids are dealt as viscous, but for liquid flow acting far away from a surface the viscous effects are neglectable. However, in the porous media in the EBF hearth, this is not the case. To overcome this obstacle an adjusted pressure loss coefficient is introduced to the mathematical formulation of the Excel model. Bernoulli's equation states that the energy is conserved in every point along an arbitrary streamline of the flow, such as:

$$p_1 + \frac{\rho v_1^2}{2} + \rho g h_1 = p_2 + \frac{\rho v_2^2}{2} + \rho g h_2 \quad (6)$$

where p is the pressure, ρ is the fluid density, v is the velocity, g is the acceleration due to gravity and h is the height (in the same direction as the gravity force) above the reference plane.

Considering the EBF process where index 1 denotes flow at an arbitrary level in the hearth and index 2 denotes flow at the taphole outlet. At index 1 the velocity can be neglected and at index 2 the pressure is atmospheric and the height above the reference plane can be set to 0. Thus, the velocity can be written as:

$$v_2 = \sqrt{2(p_1/\rho + gh_1)} \quad (7)$$

If considering tapping a hearth with constant inflow the conservation of mass (or conservation of volume assumed that the density is constant for the fluid) states that volume change per time unit is equal the difference between the inflow and the outflow. By denoting the effective hearth area A and the taphole area a the conservation of mass can be written as:

$$\frac{dV}{dt} = A \frac{dh}{dt} = \dot{V}_{in} - a v_2 \quad (8)$$

The effective area, A , is the available area for the HM, i.e. the area occupied by the coke bed is reduced from the total area of the hearth. The filling/sinking velocity in the hearth can be expressed with equation 7 such as:

$$\frac{dh}{dt} = \frac{\dot{V}_{in}}{A} - \frac{a}{A} \sqrt{2(p_1/\rho + gh_1)} \quad (9)$$

The height at time t can be determined by:

$$h(t) = h_{t-1} + \frac{dh}{dt} = h_{t-1} + \frac{\dot{V}_{in}}{A} - \frac{a}{A} \sqrt{2(p_1/\rho + gh_{t-1})}, \quad (10)$$

in which index $t-1$ indicates the previous time step. The accuracy of the estimation increases when decreasing the length of the time steps. The pressure losses caused by the coke bed are only affecting the volume outflow rate. To include the losses a pressure loss coefficient, γ , is introduced, enlarging the effective area, A , affecting the HM level over time as:

$$h(t) = h_{t-1} + \frac{\dot{V}_{in}}{A} - \frac{a}{\gamma A} \sqrt{2(p_1/\rho + gh_{t-1})} \quad (11)$$

In the Sustaintap project [55] a multiphase CFD model, including HM and BF gas was created. The slag phase was not included. By extrapolating the results from the CFD model a tapping time of 202 sec. was calculated. By adjusting the pressure loss coefficient to end up with the very same tapping time for the Excel model the tapping sequences could be compared (Figure 37). The value of the pressure loss coefficient was determined to 4.12. The Excel model shows good agreement to the CFD model, which both agree with observed tapping times for ideal tapping conditions of the EBF; as mentioned the shortest tapping time observed in campaign 32 was 205 sec.

After validating the Excel model to the CFD model, the influence of slag was evaluated. As mentioned, the production rate of slag is 375 kg/h during ordinary operating conditions of the EBF. The slag will contribute to the tapping of HM with a constant pressure during the complete HM tapping sequence. If the pressure loss coefficient calculated earlier can be applied for the slag, the pressure is calculated to ~ 1800 Pa; fastening the tapping sequence with only 1.5 sec (total tapping time of 200.5 sec). The wetting behaviour between the coke pieces in the bed and the slag/HM determines the pressure losses. Even if considering that the pressure losses is zero for the slag in the coke bed, the contributing pressure would be ~ 7200 Pa, the tapping time would only be 7 sec. faster (195 sec). Therefore, the slag was determined to be neglected when setting up the Excel model with water. To be mentioned is that the slag has a great influence at the end of the tapping sequence, allowing the tapping of HM to continue even if the HM level is below the taphole.

To obtain dynamic similarity Reynolds number is frequently used. The dimensionless parameter gives a relation between the inertial and viscous forces acting on a fluid and it is defined as:

$$Re = \frac{UL}{\nu} \quad (12)$$

in which U is the velocity, L is the characteristic length of the geometry and ν is the kinematic viscosity (defined as the ratio between the dynamic viscosity and the density). Due to the 1:1 scale of the EBF hearth and the similarity in the coke bed distribution the characteristic length is the identical for the water model. Further, water is a proper material to use to simulate HM processes due to the similarity in kinematic viscosity.

By using the identical hearth geometry and a proper water temperature the only parameter to design in equation (12) is the velocity. A matched volume outflow would generate an identical velocity in the hearth for the EBF process and the water model, and hence dynamical similarity would be reached. There are some different parameters to design in the water model to obtain identical velocity in the hearth. To construct a water model operating with overpressure was expected to be difficult, generating both high equipment costs and being time consuming. Therefore, the water model was decided to be operated under atmospheric pressure. Darcy's law states that the flow rate through the porous media is depending on a material constant (the permeability which depends on the porous media itself), the kinematic viscosity of the fluid, the operating pressure and the liquid level in the porous media. The operating pressure affects the volume flow rate linearly, meaning that the pressure drop is constant in the bed independent of the operating pressure. This justifies the decision to make the water model be operated in atmospheric pressure.

If the statement above holds, the pressure drop coefficient could be applied for the water model (given that the wetting behaviour of liquid/coke is the same) working in atmospheric conditions. By recalling the combination of Bernoulli's equation and the conservation of mass for atmospheric operating pressure the liquid level in the hearth can be described over time as:

$$h(t) = h_{t-1} + \frac{\dot{V}_{in}}{A} - \frac{a}{\gamma A} \sqrt{2gh_{t-1}}. \quad (13)$$

By having an enlarged taphole diameter of 68 mm the tapping time can be adapted to the EBF process. However, the variations in volume flow rate would be large during the tapping sequence. This is illustrated in Figure 37 where the tapping sequence for a constant diameter (water and atmospheric pressure) is compared to the tapping sequence for the EBF process (HM and over pressure). To achieve the same volume flow rates the taphole diameter can be varied during the sequence. The variations in taphole diameter needed to obtain the same volume flow rate as the tapping sequence for the EBF process (Excel model) is also presented in Figure 37.

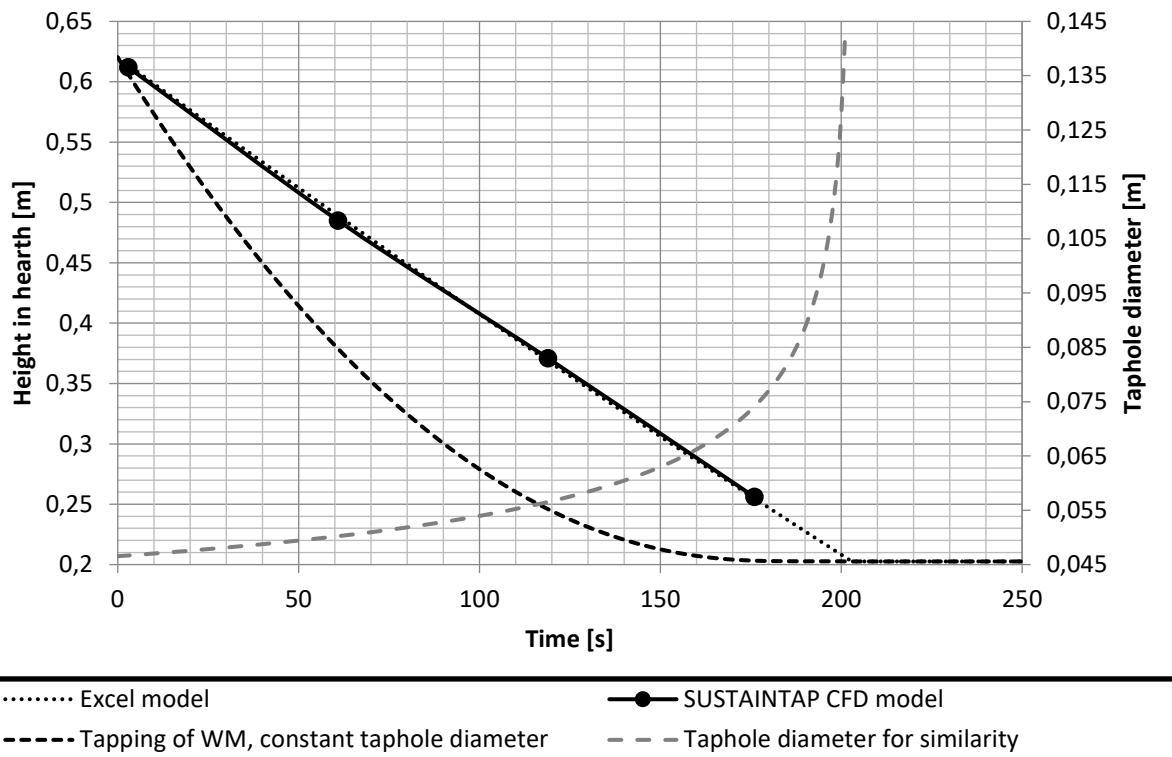


Figure 37: Tapping sequences for the EBF process (Excel model), the SUSTINTAP multiphase CFD model, water model (WM) in atmospheric pressure with constant taphole diameter (68 mm) and variating taphole diameter over time to obtain equal flow rate for the water model as the EBF process.

Changing the taphole diameter over time is possible, e.g. by having an electrical valve continuous fed with data of diameter over time. However, if not exactly the same wetting behaviour between coke/HM and coated coke/water is found the pressure losses in the bed will differ and therefore the flow rates will not be equal and dynamic similarity will not be achieved. From the tapping sequence evaluation, it was stated that the easiest way to control the volume flow rate was to use a pump, forcing the outflow rate to be identical to the EBF process. Then the sinking velocity in the hearth will be identical (given geometrical and coke bed similarity) and by the definition of Reynolds number dynamic similarity will be achieved in the hearth.

From the basic iterative calculations, it has been stated that the volume flow rate during a tapping sequence is not rather constant (it decreases with approximately 10% during the sequence), meaning that a constant flow rate in the water model is a reasonable simplification. By using a pump, the flow rate can be controlled and dynamic similarity in the hearth can be achieved.

The flow field in the hearth is affected by the coke bed distribution. The distribution was evaluated in Task 3.6 and provided requirements for the water model construction. In order to minimize the coke fines contamination of water by enclose the coke particle surface and obtain the same wetting behavior the coke needed some kind of surface treatment. The wetting behavior for HM on coke was therefore evaluated by using the heating microscope. For this purpose, two groups of metal/coke samples were collected from the center of the EBF hearth (EBF campaign 31) and tested by high temperature microscope at 1427 °C (approximates to the tapping temperature of the hot metal from EBF). The results are shown in Figure 38.

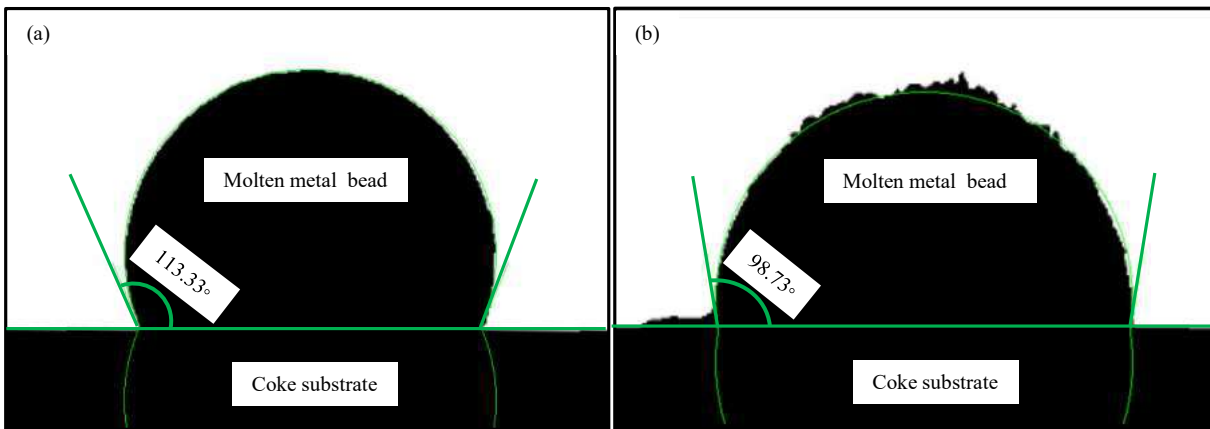


Figure 38: Measured contact angles of the metal beads on coke substrates at 1427 °C: (a) coke and the metal beads collected from the center of the EBF hearth: 2nd core-drilling layer, 10-20 cm sub-sample; (b) coke and the metal beads collected from the center of the EBF hearth: 2nd core-drilling layer, 30-40 cm sub-sample.

To investigate the possibility of using cold-asphalt coated coke in the water model, the wettability of water on cold-asphalt substrate at room temperature was investigated by using the Contact Angle Goniometer. The two measured results are shown in Figure 39. The contact angle of water on asphalt substrate is in average 96.5°, which is comparable to the molten metal on the coke substrate for 30-40 cm sub-sample. This indicates a feasibility to use cold-asphalt coated coke in the water model.

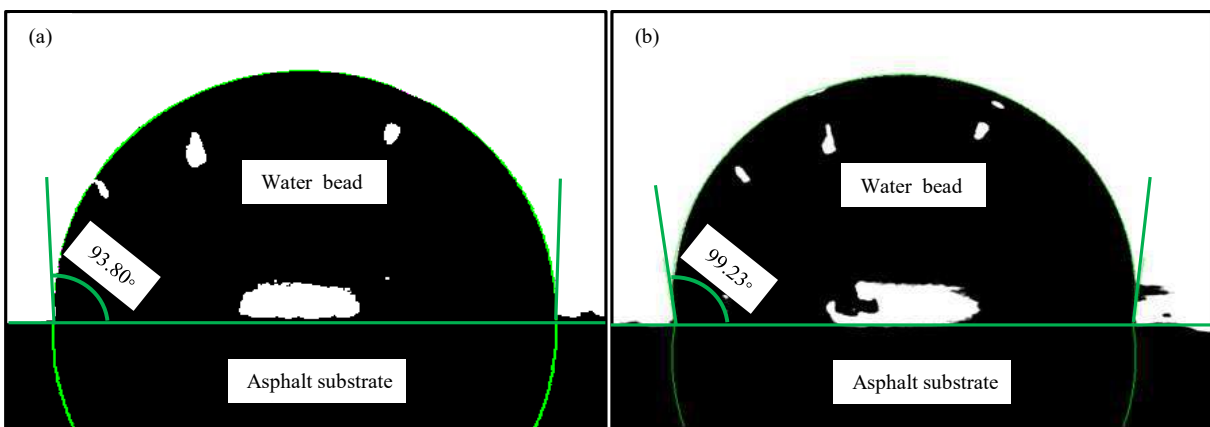


Figure 39: Measured contact angles of the water beads on asphalt substrates at room temperature: (a) the first test; (b) the second test.

Even if the shrinking velocity in the hearth will be similar for the water model and the EBF process by using a pump for flow rate control, similar wetting behavior is desirable; the higher overall similarity, the fewer sources of errors to analyze to explain eventual divergences.

2.2.1.3.2.2 Construction and setup of water model

The requirements served as the foundation when starting the construction work. The hearth was created by lexan sheets supported by stainless steel belts. The pump was placed in direct connection to the taphole; maximum flow rate was 100 dm³/min. A unit to control the pump speed in combination with a rotameter was installed after the pump, which made it possible to control the water outflow rate. Quadratic holes in the bottom plate of the hearth supported the rods holding the conductivity sensors and give the vertical sensor positions. For the evaluated coke bed distribution in the water model; i.e. the EBF case, the symmetric conditions were utilized meaning that the sensors were concentrated to one half of the domain. On each rod, two sensors (three sensors on the rod closest to the taphole) were placed at two different heights above the bottom plate giving the final sensor distribution. Angle of taphole corresponds to the impact angle of the drill. The taphole length, inside the hearth, was correlated to the documented taphole lengths from EBF campaign 32. An additional conductivity sensor was place outside the hearth, just before the pump, to give the residence time distribution (RTD) for a tracer injection.

The inflow to the model is generated by a dripping plate, which is attached to the stands by using shackles. The dripping plate was mainly created by stainless steel but a replaceable lexan sheet provided the final drilling pattern. A regulation system was created to ensure a constant inflow rate to the hearth, despite local variations in the main water supply. To ensure low impact on the flow

conditions in the dripping plate; i.e. prevent variation in flow rate from each hole, the regulation system was placed around the dripping plate at three different locations.

The functionality of the EBF water model stand, dripping box (water inflow during tapping) and pump (water outflow during tapping) was checked before further construction (Figure 40). The drilling pattern for the dripping plate (continuous inflow to the water model hearth), injection points for the tracer, vertical positions of the conductivity sensors on bottom plate of the hearth and the different porosity zones are all illustrated in Figure 41.



Figure 40: EBF water model (left), inflow to dripping box (upper right) and inflow to the model hearth (lower right) from the dripping box. The white box is the pump speed control unit and the grey pipe is the rotameter (left image), the pipes guide the tracer to each injection point (lower right).

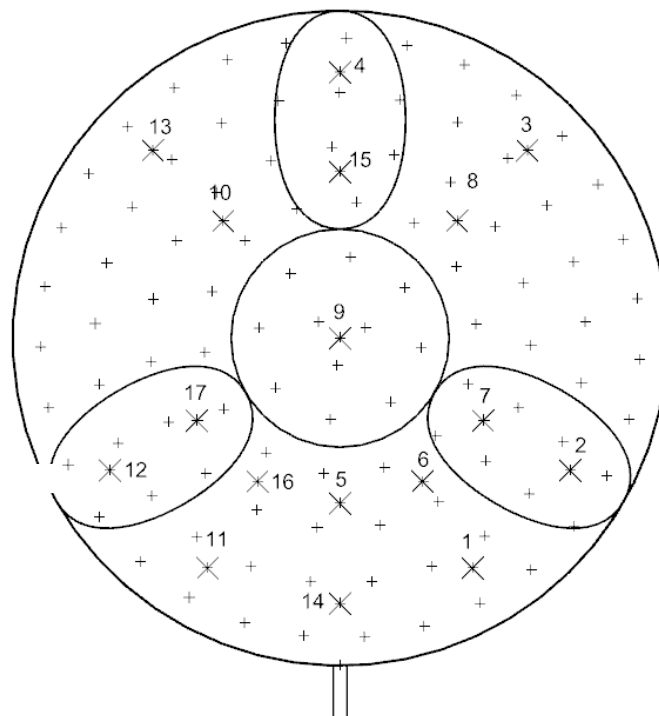


Figure 41: Drilling pattern (small crosses) and tracer injection positions (large crosses) for the dripping plate, seen from above. Taphole location is marked in the lower part of the drawing. Tracer injection positions serve as well as the vertical conductivity sensor positions on the bottom plate of the hearth.

After the functionality check, the conductivity sensors were installed (Figure 43). In total, 21 sensors were installed inside the hearth, the 22nd sensor was placed outside of the hearth in the taphole (just before the pump). The 21 sensors inside the hearth were installed in two layers according to the injection points presented in Figure 41 and Figure 48 (top view). The height of the sensors, measured from the bottom of the hearth, was 20 cm (taphole level) and 40 cm. At injection point 5, the 21st sensor was placed only 10 cm from the hearth bottom. This was done in order to increase the resolution of measurement points close to the taphole. A schematic view of the vertical positions of the sensors is also presented in Figure 48 (side view). After installing the sensors, the function of each sensor and the data sampling software were controlled.

To obtain the same wetting behaviour and hence similar conditions for the real EBF process and the EBF water model, the coke particles were coated with cold asphalt. By mixing 20% white spirit into the asphalt the viscosity was decreased, which facilitated the operation and minimized the consumption. To be able to coat the coke volumes needed to fill up the water model hearth, some equipment had to be built. A metal basket with room for 0.2 m³ coke was created, as well as a metal container to store the cold asphalt. By using a tractor coke was filled into the metal basket. The complete basket was thereafter dipped into the cold asphalt container. After lifting the basket up, it was held stationary for a couple of minutes to remove excess fluid. Then, the coated coke pieces were poured onto tarpaulins. Separation of particles was done in order to favour the drying. After a couple of days, the coke pieces were completely dried. The procedure of coating and drying coke is illustrated in Figure 42.



Figure 42: Coke coating methodology (left) and drying procedure (right).

Results of coke bed distribution from Task 3.2 served as a specification when creating the coke bed for the water model. To be able to create the three different porosities (0.30, 0.39, 0.40) EBF coke was screened and sorted in three different fractions; 10-15 mm (A), 15-25 mm (B) and 25-40 mm (C). By small scale test a methodology was developed to recreate the results from Task 3.2 in the EBF water model. By mixing the different fractions differently and adjusting the mechanically applied pressure the porosity values were variated such as:

- Low porosity for tuyere regions: 1A:0B:1C, compressed by applying an external mechanical pressure.
- High porosity for centre region: 0A:0B:1C, uncompressed; only poured into the container.
- Medium porosity for remaining zones: 0A:1B:1C, compressed by applying an external mechanical pressure.

In Figure 43, the filling procedure is illustrated; the acid-proof baskets used to create the different porous zones were placed in the hearth. Thereafter, coke pieces were placed according to the above specification in the outer zones, while the centre zone was used as the workplace. In front of the sensors the coke pieces were arranged to avoid direct contact between the sensor and the coke in order to avoid failure of the sensors and/or noise in the signal. When the outer zones were filled up to 75-80 cm, the central zone was filled up by the largest coke fraction, no additional pressure was applied. During filling, the weight of each coke fraction was measured to ensure that the requested porosity values were obtained. The resulting porosity for each zone (centre; circular cross section, beneath tuyere; elliptic cross section and remaining regions) is presented in Figure 44. In this figure, the obtained porosity value is compared to the requested values (in brackets) deduced in Task 3.6.



Figure 43: EBF water model hearth before coke bed installation (left) and during fill up (right). The embedding of the sensors in the coke bed is illustrated (right).

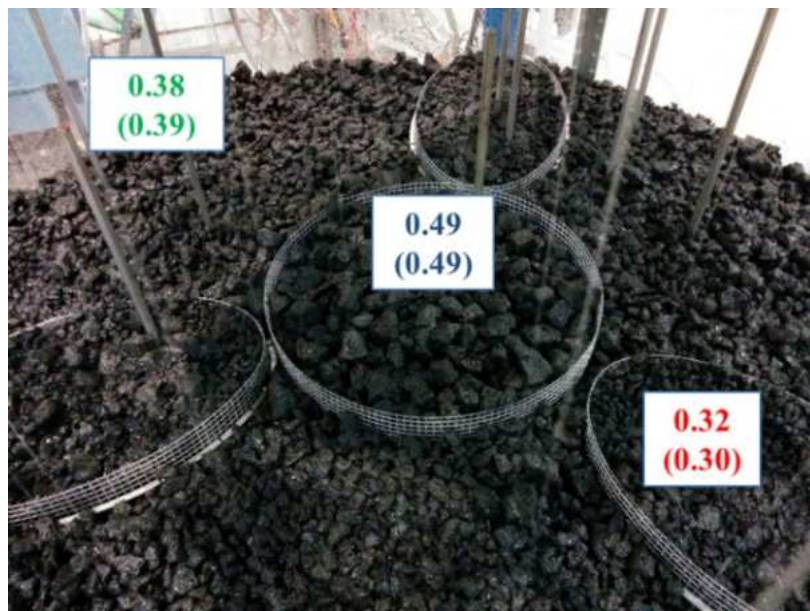


Figure 44: EBF water model hearth including embedded conductivity sensors placed on the square rods, coke bed and acid-proof baskets for zone separation. The obtained porosity is presented and compared to the requested values for each zone (values in brackets).

The finalized EBF water model is illustrated in Figure 45, together with the procedure for injection of tracer. For the final model it was found that one out of 22 conductivity sensors were destroyed or affected in such a way that the signal was corrupted during the coke bed installation. The position of the destroyed sensor is illustrated by the red dashed ring in Figure 48 (side view).



Figure 45: Finalized EBF water model (left) and injection of tracer at the start of one trial (right).

2.2.1.3.2.3 EBF water model - Implementation

To trace the water flow in the model a tracing agent needs to be added. Depending on the quality of the water the electrical conductivity varies. Distilled water has no electrical conductivity while the water going in to the EBF water model had a value of 165-195 $\mu\text{S}/\text{cm}$. Maximum value for the conductivity sensors to detect were 2000 $\mu\text{S}/\text{cm}$, values above this level was reported as 2000, see the flat line for sensor K19 and K9 at the time of 1 minute in Figure 48. The concentration and

amount for each injection was calculated with this limit in mind. By diluting a full hearth (214 dm^3 of water) with 0.1 dm^3 saturated salt solution (26wt% NaCl) the conductivity would be $454 \mu\text{S}/\text{cm}$; i.e. clearly separated from the natural value in the water but still clearly below the upper limit. Campaign 1 corresponded to two different tapping rates; mean tapping rate from EBF campaign 32 (Q4 2016) and a theoretically calculated optimal tapping rate, further called fast EBF tapping rate. The tapping volume was based on the EBF production rate. Which water height to have at tapping start was determined by the mean porosity value of the bed (0.38). Calculations indicated that the flow rate is decreased to a minor extent over time. This is due to the decrease in ferrostatic pressure. However, this pressure is small compared to the working pressure in the furnace (1 bar over pressure for the EBF); the flow rate is calculated to decrease from 51.1 to $45.9 \text{ dm}^3/\text{min}$ and from 93.1 to $84.2 \text{ dm}^3/\text{min}$ for the mean EBF tapping rate respectively the fast EBF tapping rate. Due to the small difference in flow rate over the tapping sequences the flow rate was determined to be constant for the trials, the value was set to the calculated mean flow rate over the tapping sequence. The model conditions are summarized in Table 7.

Table 7: EBF water model operational conditions.

	Mean tapping rate	Fast tapping rate
Outflow rate (dm^3/min)	50	86
Tapping time (s)	264	150
Water height at start (m)	0.52	0.52
Taphole height (m)	0.20	0.20
Inflow rate (dm^3/min)	3.6	3.6

For each tapping rate initially 10 tapping sequences were made; one for each injection point. Even though the hearth was completely drained and then flushed with water after each tapping sequence accumulation of salt solution in the coke bed occurred from time to time. Therefore, the 10 tapping sequences were repeated but in a changed order. This was done in order to reduce the noise, i.e. the sensor response that was due to accumulation of salt solution injected in previous tests.

For each trial (tapping sequence) the hearth was filled by an external water source to a level above 52 cm. Then, the pump started up and the pump speed was adjusted to give the requested flow rate. When the water level reached 52 cm the salt solution was injected through the pipes in the bottom of the dripping box to guide the tracer to each injection point. At the same time the data sampling software was started, and the electrical conductivity was recorded every second. The trial was ended when air reached sensor K22 (the one located outside the hearth in connection to the taphole).

For campaign 2 the inflow from the dripping plate was rearranged from uniform to non-uniform by plugging all the holes over the center region and the tuyere regions (elliptic shapes), see Figure 41. The number of inlets to the hearth was reduced from 100 to 64 meaning that the static pressure in the dripping box had to be increased to obtain the requested inflow of $3.6 \text{ dm}^3/\text{min}$. This was done by adjusting the regulation system, the water height had to be more than doubled to maintain the inflow rate.

Two experimental campaigns were conducted within this project. In campaign 1 the tapping sequence was evaluated for a uniform inflow for two different tapping rates (mean EBF tapping rate and fast EBF tapping rate). In campaign 2 a non-uniform inflow was evaluated for the mean EBF tapping rate.

2.2.1.3.2.4 EBF water model, campaign 1 (uniform inflow) – results

The electrical conductivity over time for each injection point and tapping rate (10 tapping sequences per tapping rate) for sensor K22 is presented in Figure 46. In Figure 47 the residence time for each injection point for both tapping rates is determined from the data in Figure 46 and plotted against the distance to the taphole. The position of the injection points and the sensors are illustrated in Figure 48 (injection points – top view, sensor – side view).

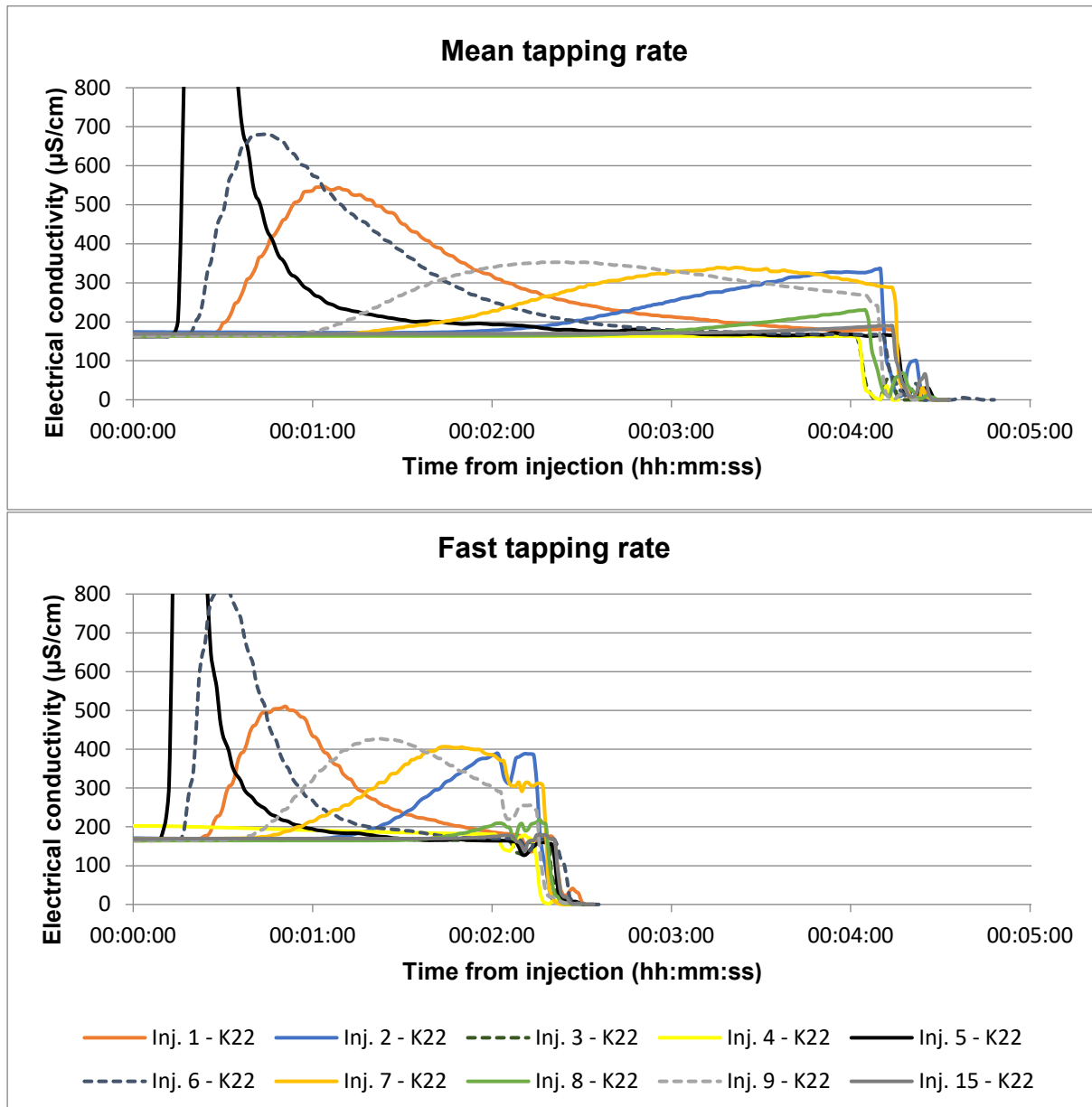


Figure 46: Electrical conductivity at the taphole (K22) for each injection point for mean EBF tapping rate (upper) and fast EBF tapping rate (lower) for uniform inflow.

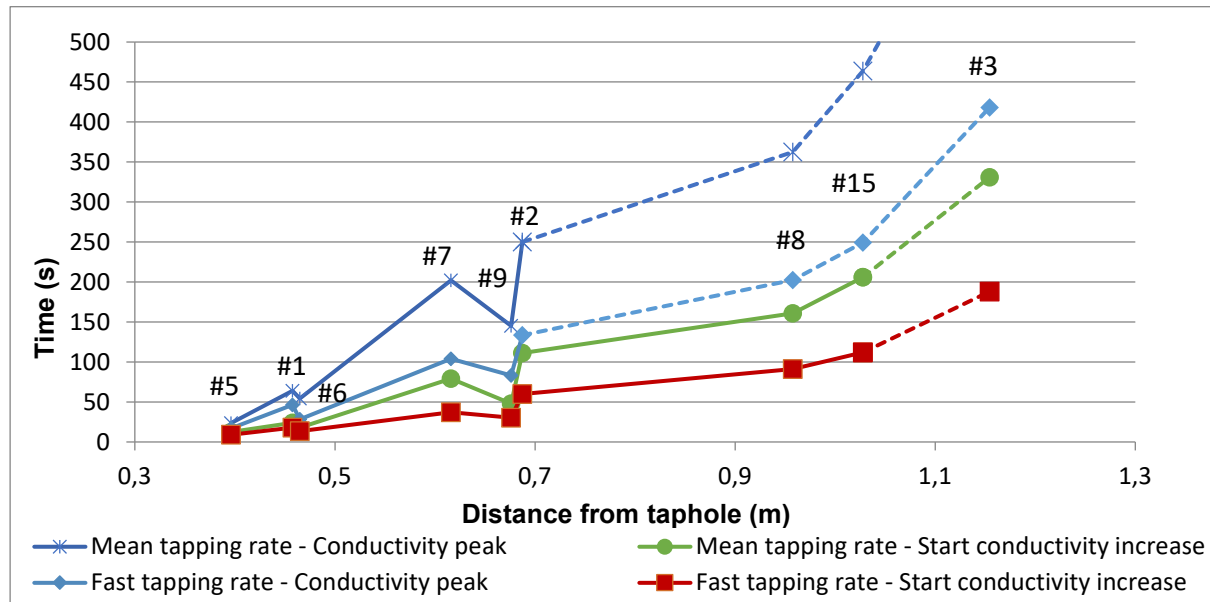


Figure 47: Residence time (either defined by conductivity peak or the start of conductivity increase) for each injection point (#1-#9, #15) for mean and fast EBF tapping rate (uniform inflow). Dashed lines indicate extrapolated values.

As can be seen in Figure 47, both the conductivity peak and the start of conductivity increase are included. Even though the magnitude of the residence time varies, the trend is kept independent of method. The peak is easier to determine but for many of the injection points the peak never occurs during the tapping sequence. By instead looking at the time for the start of the conductivity increase the residence time for more points can be determined. Regardless which method to be used, the residence times for all injection points could not be found in the data. By extrapolating the available data, some further residence times were estimated. For example, when injecting in injection point #3 there was no conductivity increase in K22 during the complete sequence. However, there was a response in K8 after 170 seconds (for mean EBF tapping rate). By adding the residence time for injection point #8 the residence time; defined as start of conductivity increase, could be estimated.

The residence time for injection point #4 could not be found by extrapolating and interpreting the available data. When injecting in #4 no response could be found beside the response in the sensors right below the injection (K4 and K14). If the sensor K10 had been in operation the residence time probably could have been estimated.

The evaluated change in tapping rate does not seem to have any effect on the flow field distribution. In Figure 47 the trend of the residence time is the same when comparing the mean EBF tapping rate and the fast EBF tapping rate, this indicates that the distribution of the flow field is the same and only differs in terms of velocity magnitude.

From the conductivity data path-lines for each tapping rate can be estimated. In Figure 48 the sensor response for the mean tapping rate, injection point #9, is presented. Further, in Figure 48 the sensor response at a certain time (black dashed line) is represented by blue circles (the larger diameter the greater electrical conductivity). From the sensor response an interpreted path-line has been printed out on the side view of the hearth. By following the same procedure for all injection points the complete flow field can be interpreted, for mean EBF tapping rate this interpretation is presented in Figure 49.

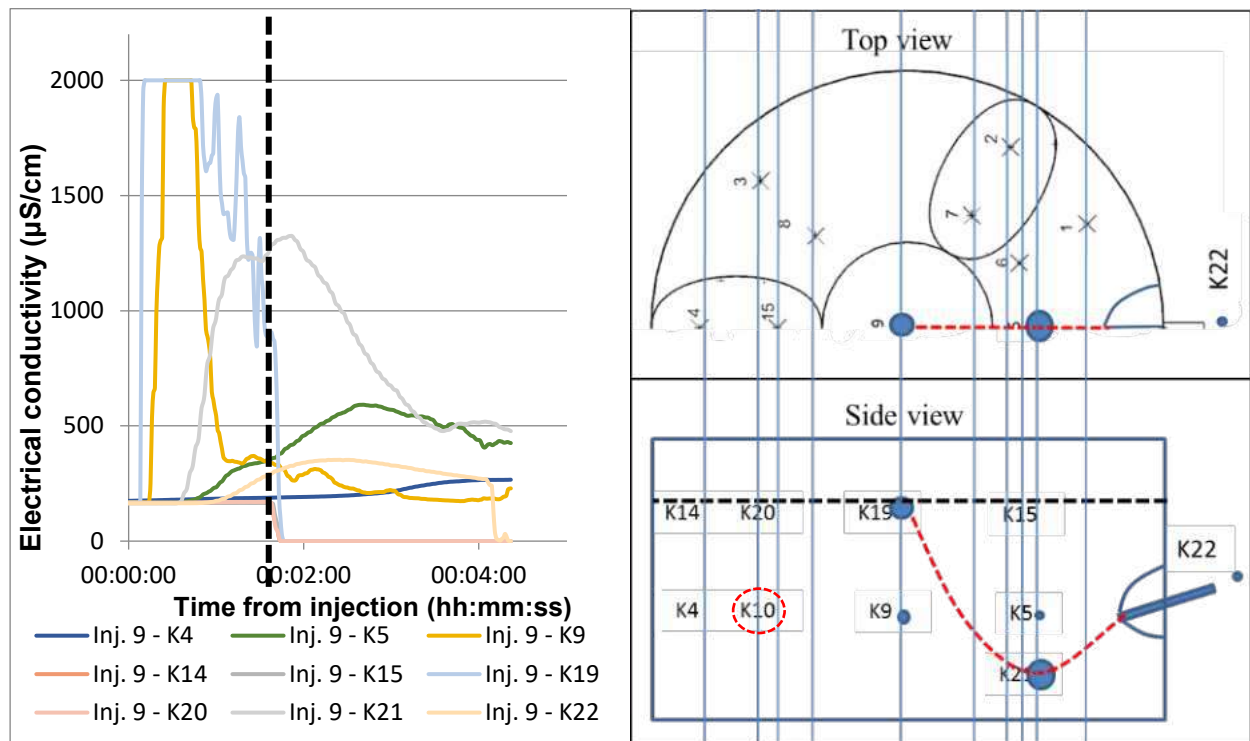


Figure 48: Electrical conductivity over time for mean tapping rate, injection point #9 (left). Sensor response at a certain time (black dashed line) is illustrated by blue circles (top view and side view), together with an estimated path-line (red dashed line).

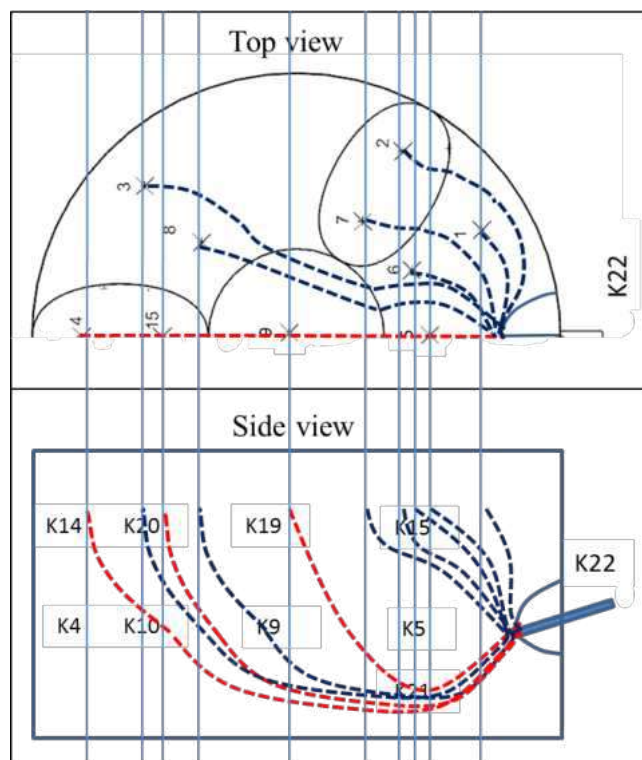


Figure 49: Interpreted flow field for mean EBF tapping rate (uniform inflow). Red dashed lines indicate path-lines located in the centre of the hearth.

The path-lines presented in Figure 49 correspond to the results from the copper injection into the EBF hearth during the EBF campaign 32 (Q4 2016), a comparison is made in Figure 50. In the comparison only path-lines interpreted from related injection points have been used. The Cu-injection was done in tuyere 3 (opposite side as the taphole), and hence only water model injection points in that area are suitable for comparison.

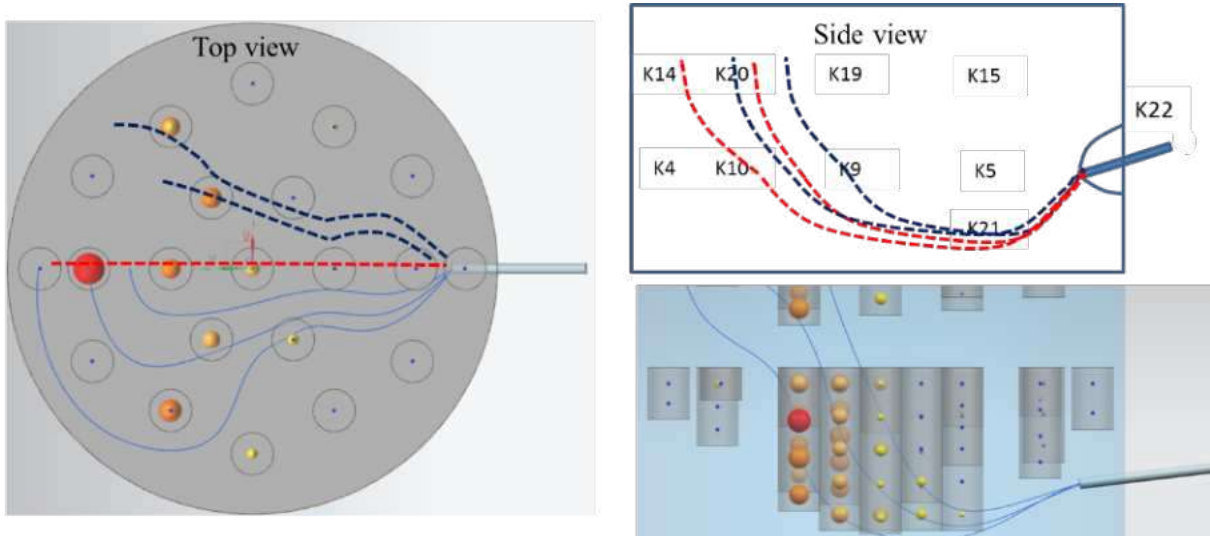


Figure 50: Interpreted path-lines from copper injection trials (solid lines) and related interpreted path-lines from water model trials (dashed lines).

2.2.1.3.2.5 EBF water model, campaign 2 (non-uniform inflow) – results

In Figure 51 the residence time for mean EBF tapping rate for uniform and non-uniform inflow is compared. The sensor response for injection point #9 and #8 are presented in Figure 52 respectively Figure 53, only the sensors giving response are presented in the figures.

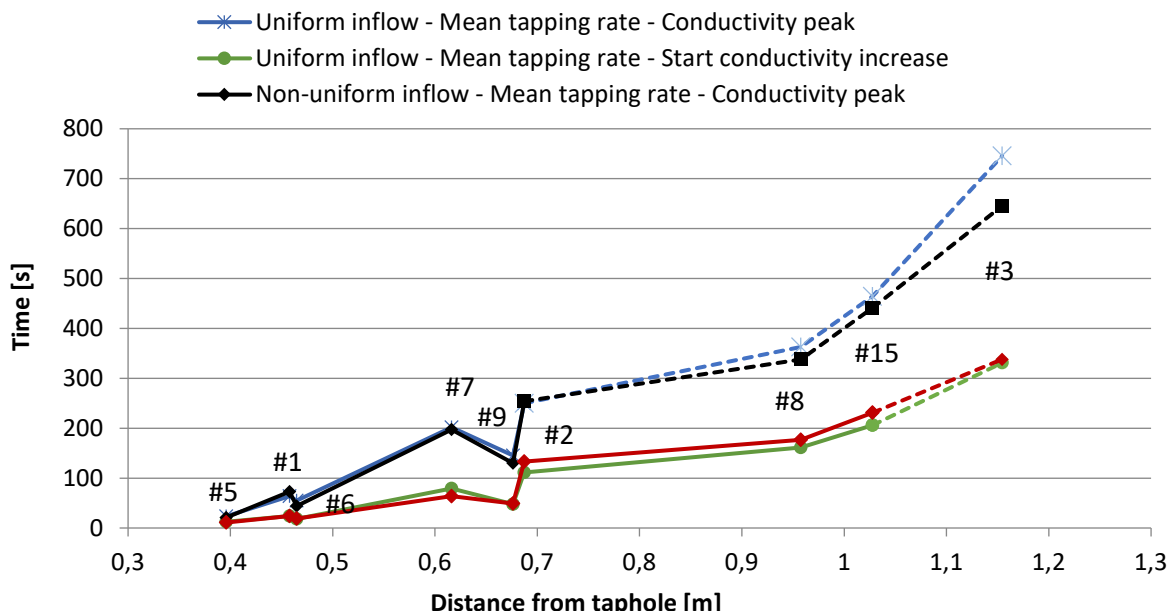


Figure 51: Residence time (either defined by conductivity peak or the start of conductivity increase) for each injection point (#1-#9, #15) for mean EBF tapping rate with uniform and non-uniform inflow. Dashed lines indicate extrapolated values.

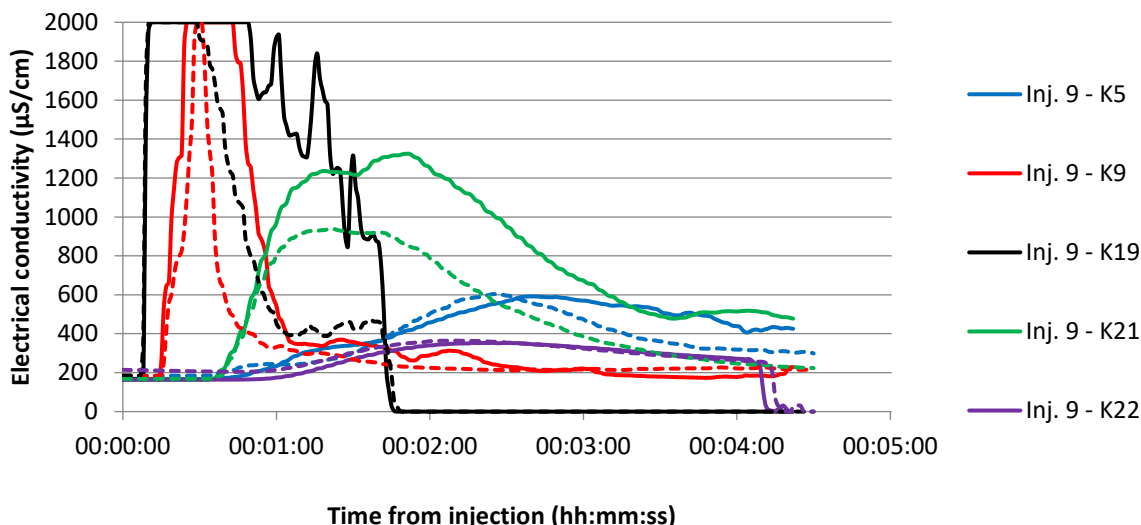


Figure 52: Electrical conductivity over time for EBF mean tapping rate, injection point #9, solid line – uniform inflow, dashed line – non-uniform inflow.

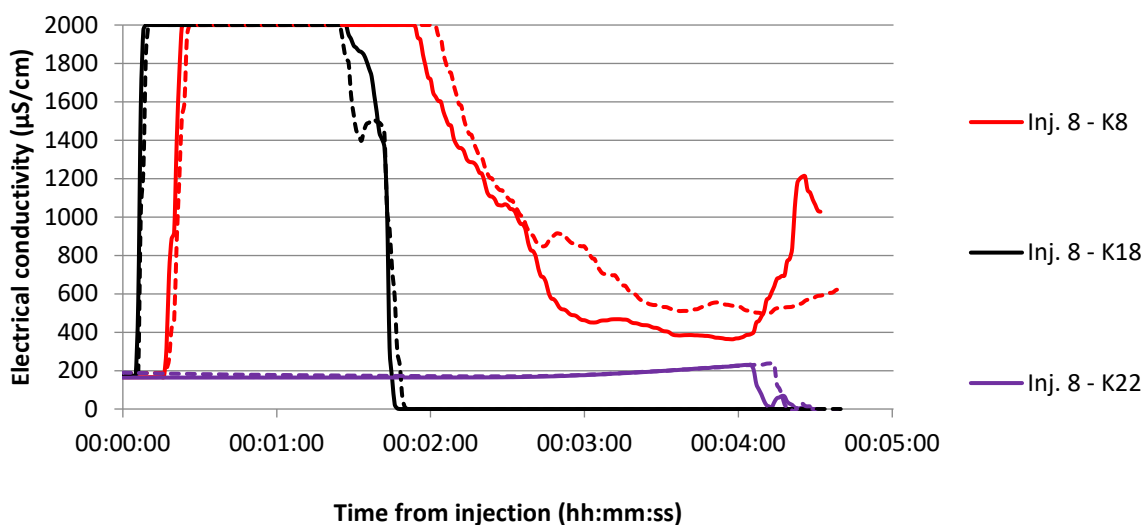


Figure 53: Electrical conductivity over time for EBF mean tapping rate, injection point #8, solid line – uniform inflow, dashed line – non-uniform inflow.

As can be seen when comparing the residence time in Figure 51, the overall differences between uniform and non-uniform flow are small. This indicates that flow field is not affected by the evaluated change in inflow distribution.

When comparing the sensor response in Figure 52 and Figure 53, it can be seen that for injection point #8 the response is almost identical in both time and magnitude. For #9 the response time is corresponding while the magnitude is decreased for non-uniform inflow. This seems to be related to the inflow distribution; above #8 the inflow is remained (slightly higher inflow rate for each hole) while above #9 the inflow is zero. The absence of incoming water at #9 seems to decrease the initial dispersion of the salt solution, which is reasonable since the turbulence on the water surface decreases as well as the downward momentum that is created by incoming water. This explains why the sensor response for K19, K9 and K21 are lower in magnitude; the salt is not dispersed to the same extent initially.

2.2.1.3.2.6 Conclusions - Water model Experimental Blast Furnace (EBF)

A water model corresponding to LKAB's Experimental BF process has been set up within this project (milestone 1.3). Two campaigns have been conducted where the effect of tapping rate and inflow distribution on the liquid flow field have been evaluated. The water model generates reproductive results (two trials was conducted for each injection), which is a presumption for continuous work with the model in potential future projects. The water model results indicate mainly that:

- Interpreted flow field from Cu-injection at EBF campaign 32 (Q4, 2016) and interpreted flow field from the water model corresponds; i.e. the water model set up seems to reproduce the EBF heath conditions to a high extent.

- The distribution of the flow field is constant independent of the tapping rate for an equal bed distribution.
- The flow field is not affected by the evaluated change in inflow distribution.

The water model results provide a rare opportunity for CFD model validation of BF hearth liquid flow, meaning that CFD model results for EBF hearth process validated by the water model results provides information with unusually high creditability.

2.2.1.3.2.7 CFD model of EBF (governing equation)

The blast furnace hearth, as it is known, can be signified as a fully packed bed where it can be described by pressure drop formula using Ergun's equation. The formulation of the pressure drop in a packed bed is described by the following:

$$\frac{\Delta p}{L} = \frac{150\mu}{(\varphi_s d_p)^2} \frac{(1-e)^2}{e^3} + \frac{1.75\rho}{\varphi_s d_p} \frac{1-e}{e^3} u|u| \quad (14)$$

Where, ρ and μ is the fluid density and viscosity, respectively; d_p is the particle diameter, φ_s is the coefficient of the sphericity, e is the void fraction or volume fraction of the bed and u is the fluid velocity.

As the formula suggests, the pressure drop in a packed bed is not only dependent on the thermodynamic properties of the medium i.e. fluid density and viscosity, but also on the characteristics of the bed namely voidage, particle size and its sphericity. The first set of parameters are dependent on the composition of the hot metal and its temperature while the bed characteristics should be adopted based on the excavation of a furnace hearth (here EBF).

Another physical phenomenon in the hearth of any blast furnace is the heat transfer within the fluid medium and the linings of the heart. This conjugate heat transfer behavior of the furnace means that the energy within the fluid medium i.e. hot metal will be transferred into the solid material forming the hearth of the blast furnace i.e. linings. The linings of the furnace hearth are usually formed of number of layers where each layer constructed of specific material with specific sets of thermodynamic properties such as, specific heat and thermal conductivity for solid materials.

Therefore, the formulation of the heat transfer within the blast furnace hearth should be constructed on two parts, convection and conduction. The energy equation within the fluid region, then, can be expressed as:

$$\frac{\partial(\rho E)}{\partial t} + \nabla \cdot (\vec{u}(\rho E + p)) = \nabla \cdot \left(k_{eff} \nabla T - \sum_j h_j J_j + (\tau_{eff} \cdot \vec{u}) \right) + S_h \quad (15)$$

where k_{eff} is the effective conductivity and J_j is the diffusion flux of species j . The first three terms on the right-hand side of this represent energy transfer due to conduction, species diffusion, and viscous dissipation, respectively. The last term, S_h , includes the heat of chemical reaction, and any other volumetric heat sources you have defined. Moreover, E represents the total energy and can be written as:

$$E = h - \frac{p}{\rho} + \frac{v^2}{2} \quad (16)$$

Where h represents enthalpy. Furthermore, the heat transfer within the solid region, the lining, can be formulated as follows:

$$\frac{\partial(ph)}{\partial t} + \nabla \cdot (\vec{u}ph) = \nabla \cdot (k\nabla T) + S_h \quad (17)$$

$$h = \int_{T_{ref}}^T c_p dT$$

with c_p and k are specific heat and thermal conductivity. It should be mentioned that the second term in the left-hand-side represents convective energy transfer due to rotational or translational motion of the solids and will be ignored due to the fact that the linings of a blast furnace hearth are stationary and have no motion.

2.2.1.3.2.8 CFD model EBF (geometry and mesh)

The first step towards any CFD modelling is to construct the geometry and mesh for the domain of the calculation. Moreover, the current study has focused on the modelling of the Experimental Blast Furnace (EBF) of the LKAB located on Luleå, Sweden. Therefore, a newly created CAD model (Figure 54) was build based on the drawing of the blast furnace hearth of the LKAB.

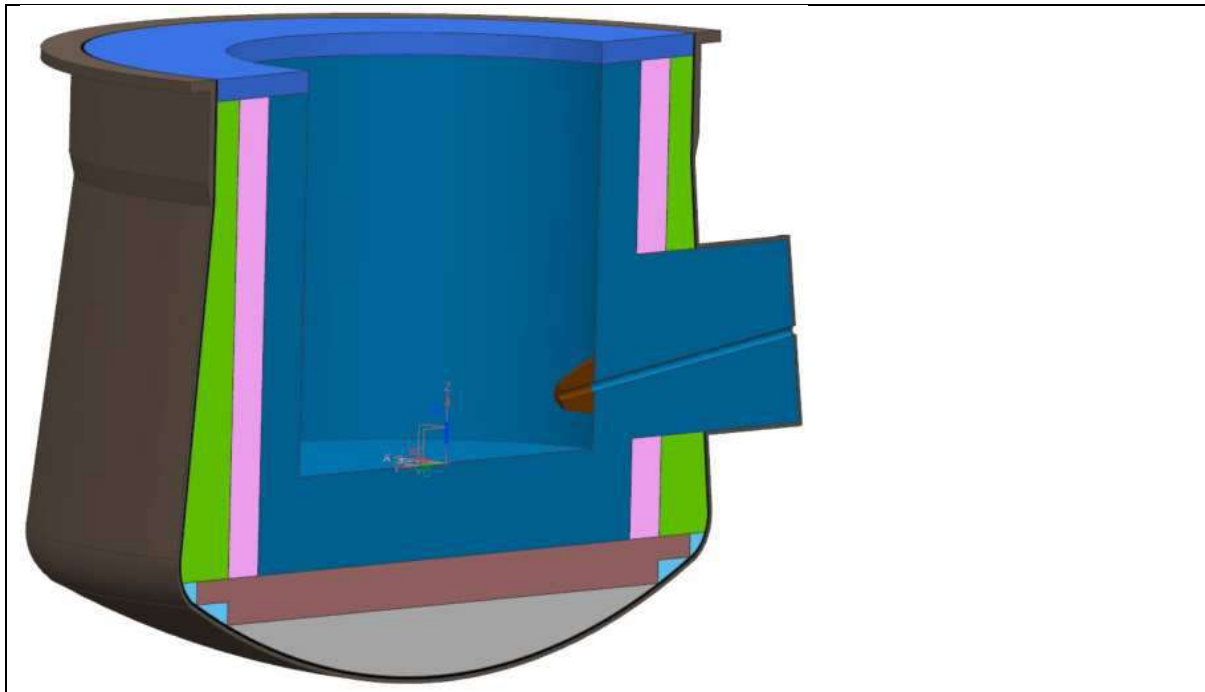


Figure 54: CAD model of the EBF hearth including taphole, taphole mushroom, lining materials and shell.

Figure 55 shows the mesh structure of the EBF hearth. As can be seen in most of the fluid zone (furnace hearth) the mesh is hexahedron while the mesh in the hearth region close to the taphole is a mixture of different types.

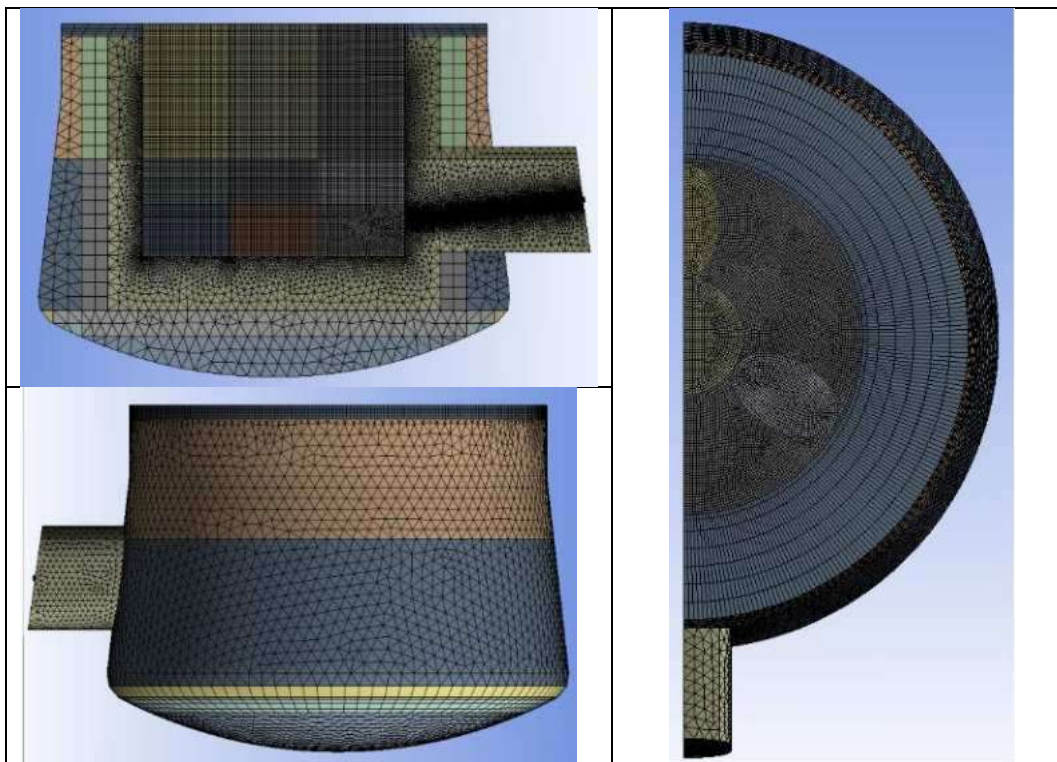


Figure 55: The EBF hearth mesh.

Moreover, it should be mentioned that the mesh showed in the Figure 55 represents the meshing of the whole domain i.e. fluid zone and the solid zone (linings layers). However, in case of the CFD

model of the physical modelling (water model) the solid region was ignored and in case of calibration shell temperature measurement the upper section of fluid zone was ignored Figure 56a shows the domain of calculation for the CFD model of the physical modelling and Figure 56b shows the region which is ignored for the shell temperature measurement.

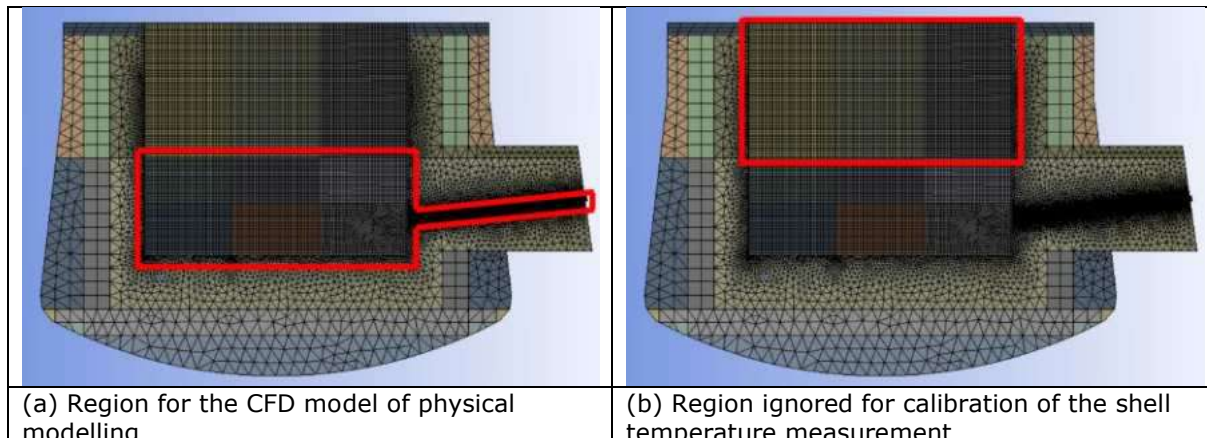


Figure 56: CFD region in BF hearth (a) and ignored region in the CFD EBF model (b).

Furthermore, a comparison between Figure 54 and Figure 55 shows that the thin outer steel shell is not considered in the meshing of the EBF hearth. This is due to the fact, that the think shell model of Ansys FLUENT application has been used to model the heat transfer within the outer thin shell of the EBF hearth. This feature of the Ansys FLUENT package will be explained later in the report.

2.2.1.3.2.9 CFD modelling of physical (water) model

As it is explained above, a one-to-one physical model of the EBF hearth has been built to model the EBF hearth drainage process using room temperature water as a liquid phase. Therefore, the first task in the CFD modelling of the EBF hearth was focused on replicating the water model to calibrate and to verify the response time by comparing the results of the CFD model with tracer injection in the physical modelling. Firstly, as it was shown in Figure 56a, the calculation domain was only limited to the fluid zone (since the physical model was isothermal) and only to the section highlighted in the Figure 56a (with the height of 55 cm).

Two approaches were used to investigate the physical modelling, namely:

- Eulerian-Lagrangian approach
- Streamlines approach

2.2.1.3.2.9.1 Eulerian-Lagrangian approach

There are two main methods to model a multiphase system: Eulerian and Volume-of-Fluid (VOF) where both of these methods are based on the General Conservation Equation. In the first approach (mainly for a two-phase system) a full set of equation is solved for each phase in the system and the system becomes close by defining how existing phases interact with one another. On the other hand, in the VOF model, it is only one set of equation which is solved to calculate the velocity field for the whole system and one extra set of equation is responsible to keep track of interface between phases. As can be seen based on the above short introduction, the VOF method is far more economical in comparison to the Eulerian approach but, of course, it is only possible to use VOF approach where individual velocity field (for each phase in the system) is not of crucial importance and by keep tracking of the interface one can model the whole system.

Generally speaking, VOF is the commonly accepted method to model the two-phase system of gas and liquid (water and air in here) due to the fact that by keep track of the interface of the two-phase when can resolve the velocity field in such systems.

Moreover, as explained previously, addition of tracer has been used in the water model to measure the response time and path-line of individual point of injection. This in a way can be imagined as a particle (tracer) entering a system from a specific point and carried away through the system by means of a carrier phase (water) to the outlet (taphole exit port). It is, of course, natural to assume that the injected particles (tracer) would not have any effect on the carrier phase (water) flow filed.

Modelling of individual particle/parcel in a system can be done through a well-known approach of the Lagrangian method. In this approach position and velocity of each individual particle/parcel is calculated using the Newton second law and force balance. Discrete Particle Method (DPM) is based on Lagrangian method to model the behavior of individual particles/parcels in a system. Since, as explain above, it seemed possible to consider tracer in a water model as individual particles/parcels in the system the current method of DPM was adopted to model the behavior of the tracer which,

thanks to the advancement of numerical methods for computational fluid dynamics, is possible to be coupled with the VOF methods described earlier.

Based on the above reasoning a one-way coupled system of VOF-DPM was the first approached in the modelling of the tracer injection in the water model. Therefore, fixed number of particles from each injection point were injected and while running the simulation the outlet was monitored to identify if and when particles have left the domain. When monitoring plot were showing a pick contour plot of particles were plotted to identify which of the injected particles are leaving the domain. Figure 57a and Figure 57 show the particles injected from injection point 5 and injection point 6 leaving the domain after 75 and 90 seconds respectively.

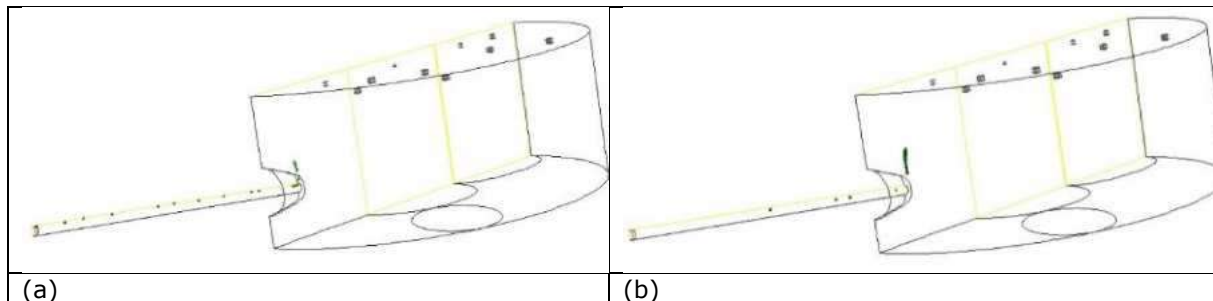


Figure 57: Particles injected from point #5 leaving the domain after 75 sec (a) and from #6 leaving the domain after 90 sec (b).

The same procedure was conducted for all the particles in the domain where Figure 58 shows the particle exit time for all the injection points except injection point 3. This is due to the fact, that the particles injected from injection point 3 did not exit the domain. Moreover, a comparison between the current figure and the water model tracer measurement figure show similar trends. However, as can be seen, in the water model trail tracers injected from injection point 5 and injection point 6 picked below 50 sec after injection while the same points in the simulation exited the domain after 75 sec and 90 sec respectively. Moreover, the same difference can be seen in injection point 1 where in the water model trail the tracer has picked slightly after 50 sec into the injection while particles from the same injection point have exited the domain after 110 sec.

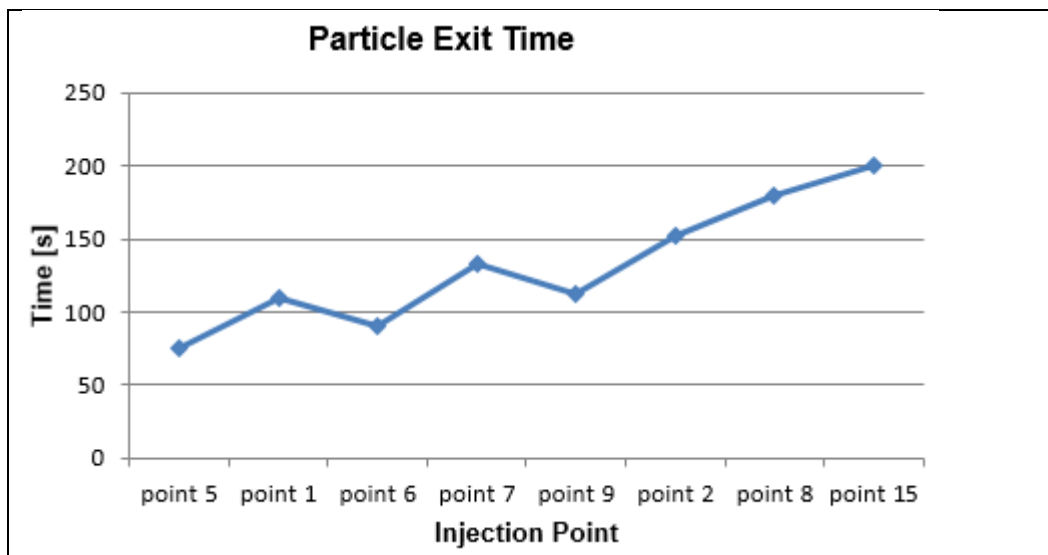


Figure 58: Particles exit time.

Furthermore, the results from water model trial (Figure 47) show that tracers injected from injection point 7, injection point 9 and injection point 2 have picked after 200 sec, 150 sec and 250 sec, respectively. Similar values for the CFD model are 132.5 sec, 112.5 sec and 152.5 sec, respectively.

Therefore, it can be deducted that the CFD model over predict for the injection point 1, injection point 5 and injection point 6 while it under predict for the injection point 2, injection point 7 and injection point 9. It should be noted that since the tracer never picked for injection point 8 and injection point 15 in mean tapping rate it is not possible to compare the actual measured data with the CFD results.

2.2.1.3.2.9.2 Streamlines approach

The next method used to predict the exit time of each injection point was streamline approach. In this case, a two-phase water-air model were solved, and the streamlines were plotted which shows

not only the time it takes for each injection point to exit through the taphole port but also shows the path-line for each injection points. Figure 59 shows the streamline where they are coloured with time each injection point has been in the domain till exiting through the taphole.

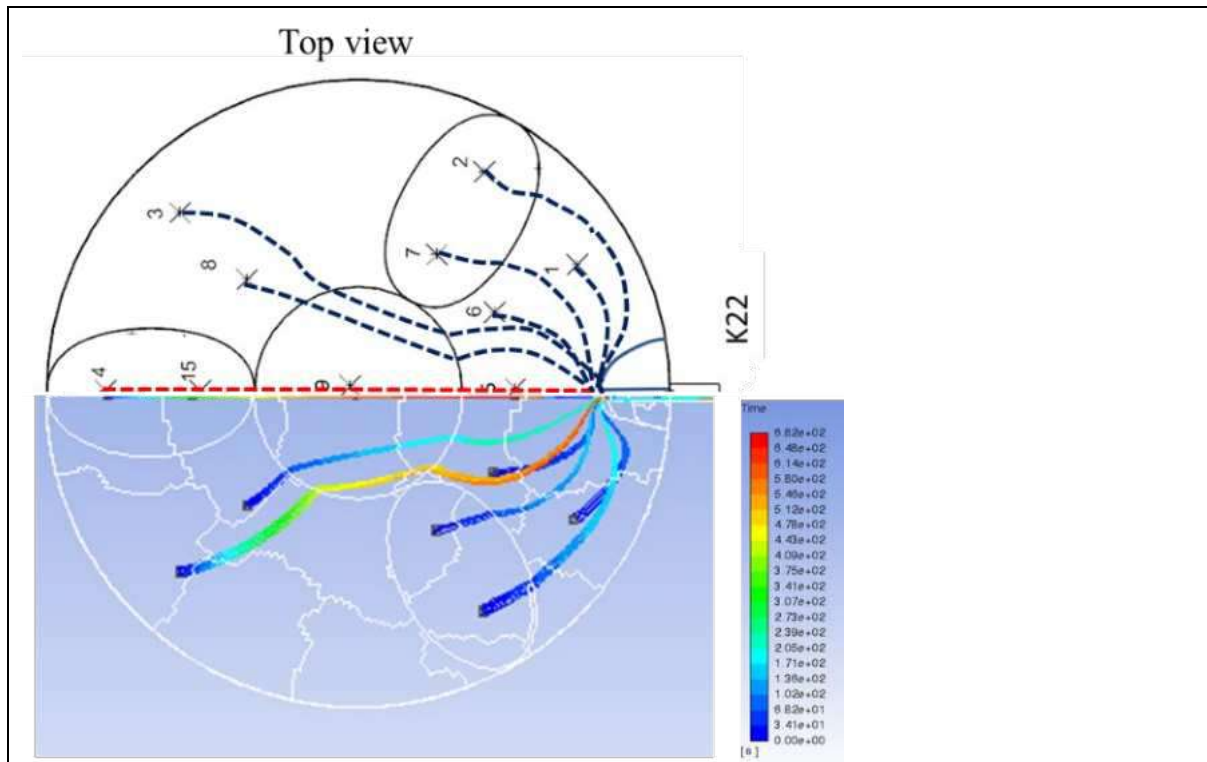


Figure 59; Tracer timing and path-line.

As can be seen, the injection point 5 should be less than or equal to 34 sec while injection point 6 and injection point 1 seems to be between 34 to 68 sec. This suggests that the streamline approach predict the exit time for these three points significantly better than the VOF-DPM model. Moreover, the Figure 59 suggests that it takes more than 170 sec and less than 205 sec to reach the outlet. These values for injection point 2, as figure suggests, seems to be more than 239 sec and less than 270 sec.

Beside the exit time, a comparison between the CFD streamlines and the water model shows a very good agreement. As can be seen in Figure 59 the path-line, for injection point 3, injection point 6 and injection point 7, is almost identical. The same path-line for injection point 1 and injection point 2 seem very similar with minor difference where CFD model suggest the path-line of the injection point 1 bends more towards the wall and less for injection point 2. Moreover, the path-line of injection point 8 in the CFD model seems to initially travels towards the center of the hearth and change its course when reaches the central dead man where the volume fraction magnitude changes while in the water model this path is fairly straight until it exits the central dead man.

Overall, it can be said that the streamline can predict the behavior of the water model better than the VOF-DPM model.

2.2.1.3.2.10 The shell temperature measurement calibration

To model the drainage of the EBF hearth, the first step was to correctly calibrate the temperature profile of the lining layers of the EBF hearth. To this end, some measurement data was needed to be able to calibrate adjust the model parameters in ways to fit the measurements. Hence, an IR-camera and a contact pyrometer were used for sampling data at six occasions over a period of nine days. The 24 measurement points are marked out in the new created CAD-file of the EBF hearth, shown in Figure 60. Mean shell temperature for each point over the sampling time is presented in Table 8.



Figure 60: Marked positions on bottom (lower right) and wall (upper right) indicates locations for shell temperature measurements.

Table 8 suggests that the minimum temperature appears at the bottom end of the vertical face (bend) were the probe number 4 had been installed and the magnitude of the temperature increases in each direction of the probes installation with probe number 6 shows the maximum magnitude of the temperature.

Table 8: Mean temperature in °C for each position on the EBF shell.

Measurement position	1.X	2.X	3.X	4.X
X.1	136.6	110.6	106.6	97.4
X.2	137.0	135.0	125.0	128.3
X.3	111.4	111.9	109.0	116.3
X.4	101.3	101.3	101.4	100.6
X.5	126.3	114.1	124.6	126.7
X.6	167.6	167.6	165.7	174.0



Figure 61 shows the temperature values calculated by CFD modelling against the measurement. As can be seen, the CFD modelling trend is in a good agreement to the measured data and the two sets of data behave very similarly. It should also be mentioned that there is of course some differences between the CFD modelling and the measurement data. The maximum difference between measurement and the CFD modelling is around 20 degree Celsius and appears at point #6. Moreover, the figure shows that the change in the temperature between point #1 and #2 is slightly larger than the same points in the CFD modelling. Also, the figure shows that the temperature values are below the measurement values for all point but point #2. Overall, it can be said that the CFD model results has fitted good into the measurement data for the set of the boundary conditions used in the current set up (and explained in detail above).

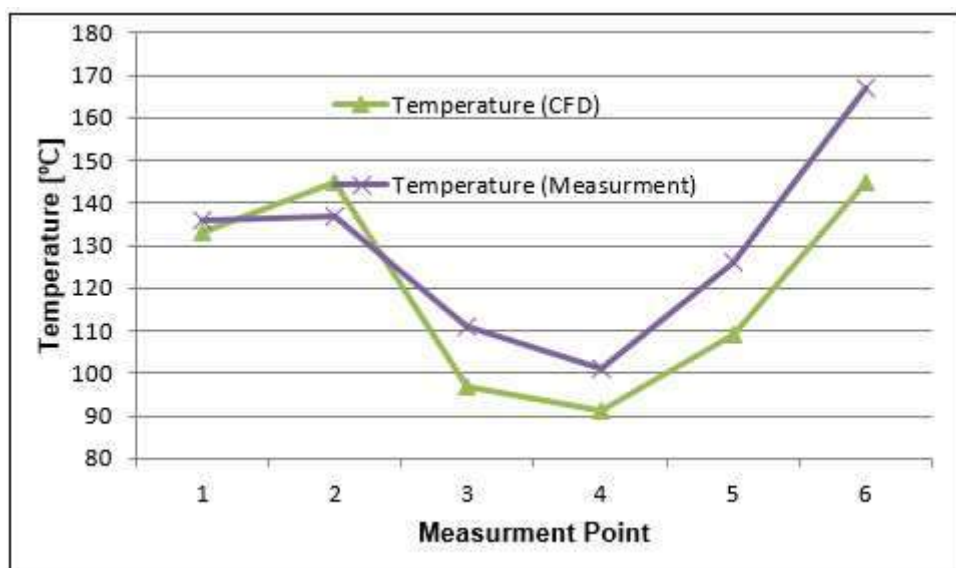
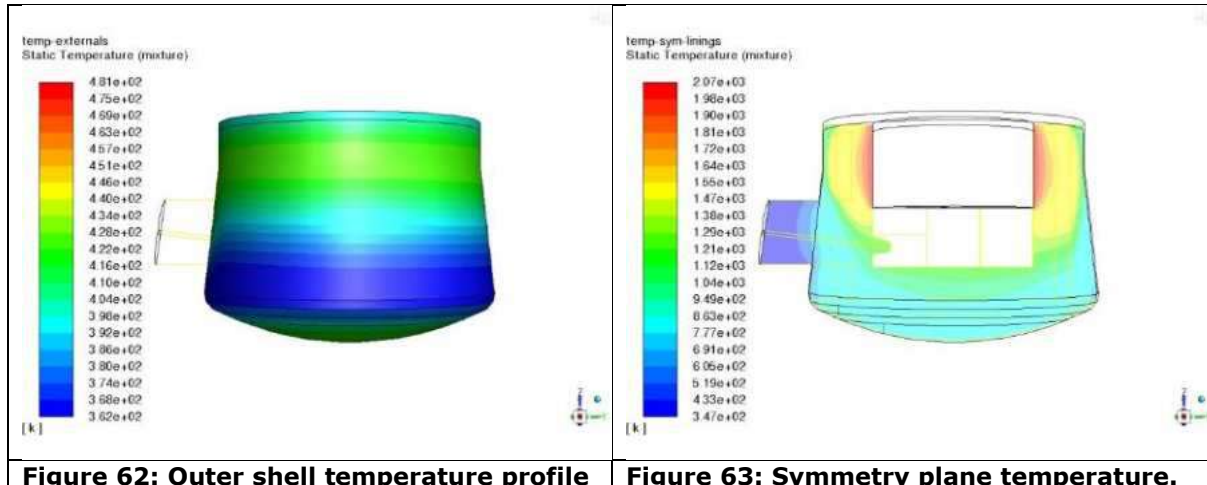


Figure 61: EBF outer shell measurement vs. CFD calculation.

The contour plot of the outer shell and symmetry plane are shown in Figure 62 and Figure 63 where the temperature is shown in Kelvin scale.



After achieving a good agreement between current CFD model and the measurement, the current boundary conditions set up were used for the modelling the drainage of the EBF heath. Moreover, the temperature profile of the current model was interpolated into the new mesh for the drainage modelling.

2.2.1.3.2.11 Modelling of the drainage of the EBF Hearth

After a successful calibration of the EBF hearth temperature profile in the previous step, the boundary conditions for the outer layer of the hearth were adopted into the full domain (Figure 55) for the drainage modelling. Moreover, as the goal in the previous section was to calibrate the CFD model using the measurement data, the calculated temperature profile of the solid zone was saved and interpolated into the current mesh set up. This is done using the "Interpolate Data" feature of the commercial CFD package Ansys FLUENT. Hence, the temperature profile of the previous section was used as the initial condition for the solid zone in the drainage model.

Using the calibrated data, a parametric study was conducted to investigate the effect of change in the voidage of the bed and top pressure on the drainage of the hot metal from the EBF hearth. It should also be mentioned, that the boundary condition at the end of the taphole (outlet) is set to pressure outlet which means the mass flow rate at the outlet will be calculated based on the state of the system.

2.2.1.3.2.11.1 Case one: reference case

This case which is called the reference case is set up using the excavation data regarding the bed volume fraction. Table 9 shows the volume fraction of different regions within the fluid zone of the EBF hearth which is based on the excavated data.

Table 9: Reference case (volume fraction).

Region	Volume fraction
Dead man: region 1 and region 2	0.32
Dead man: central region	0.49
Hearth except dead man regions	0.38

Using the volume fraction values of the bed from Table 9 the pressure-drop based on the Ergun's equation were calculated manually and entered into the model. Moreover, the pressure at the top of the fluid zone (material entry face) was set to 1 bar.

Figure 64 and Figure 65 show the initial condition for temperature and phases in the fluid zone. Figure 65 shows the initial temperature of the fluid zone in Kelvin. Figure 64 shows the phases distribution where the red, green and blue colors represent gas, slag and hot metal, respectively.

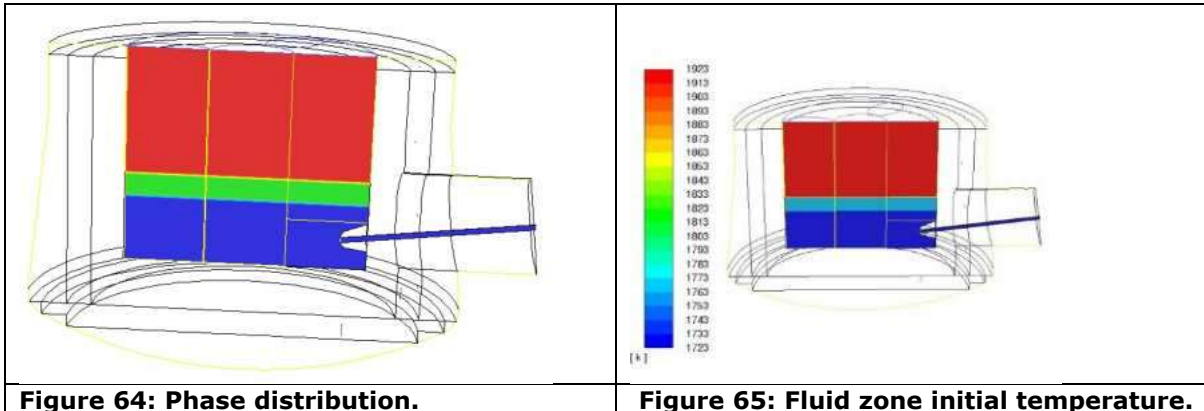


Figure 65 shows that the hot metal phase, slag phase and gas phase initial temperatures are set to 1500 °C, 1550 °C and 1700 °C, respectively. Figure 66 shows the maximum, average and minimum (red, black and green) height of the hot metal interface during the drainage process while Figure 67 shows the volume of hot metal, slag and gas (red, black and green) in the taphole region. As can be seen in Figure 66, the maximum and minimum level changes rapidly (step function) while the average value during the changes of the maximum and minimum level has the curvature form. This is true up to around 90 seconds into the simulation where after that these are more look like a straight line. It should be pointed out, that the minimum level-drop changes from straight line to curvature after 110 sec. Moreover, Figure 67 shows that around the same flow time where the minimum level-drop changes to curvature the volume of the slag material in the taphole region changes from zero to a non-zero value meaning that the slag material has entered the taphole region. Hence, it can be said that it takes more than 110 sec for the hot metal-slag interface to drop to the taphole level.

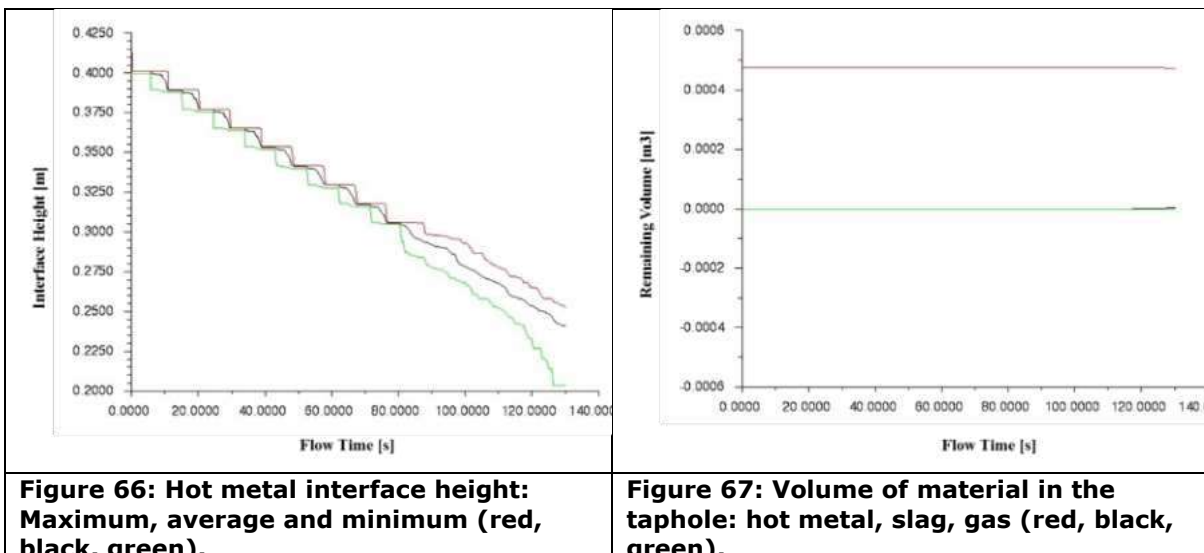
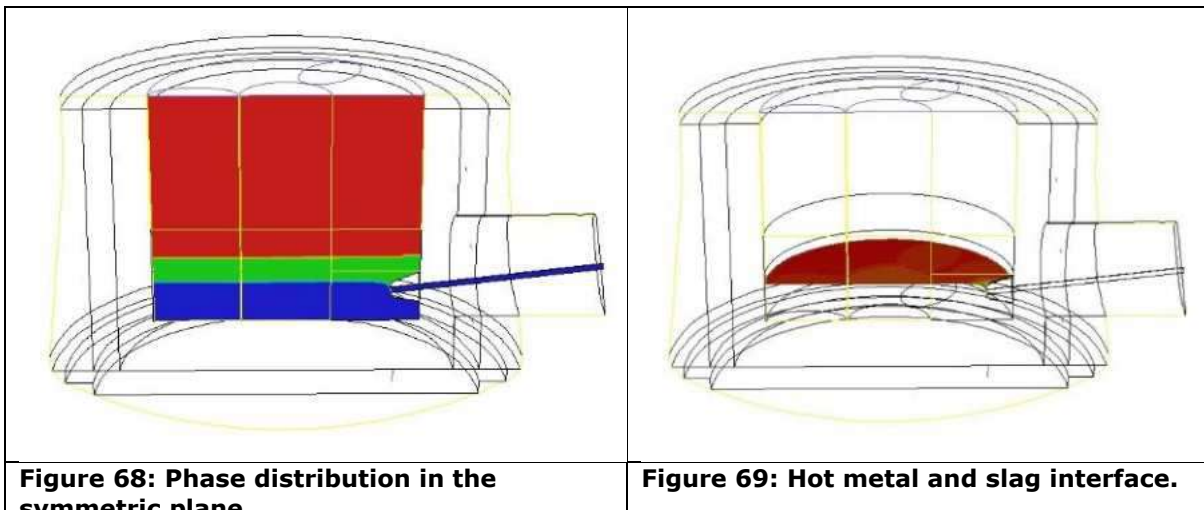


Figure 68 and Figure 69 show the phase distribution and interface level, respectively. As can be seen the slag phase has penetrated into the taphole at the hot metal level.



Furthermore, Figure 70 shows the temperature profile of the hot metal in the symmetric plane in Kelvin. Figure shows that the two corners of the symmetric plane are colored in green which correlate to around 1300 °C, but the right corner has larger green region than the left corner (further from the taphole). Beside these two corners, the figure shows that the magnitude of the temperature at large area of the fluid zone is around 1400 °C and higher.

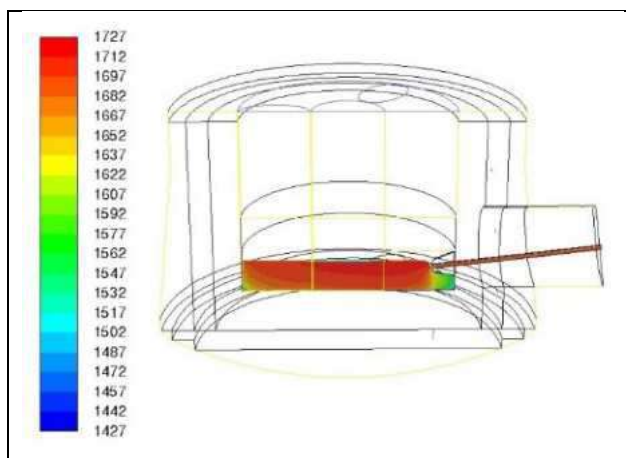


Figure 70: Hot metal temperature profile.

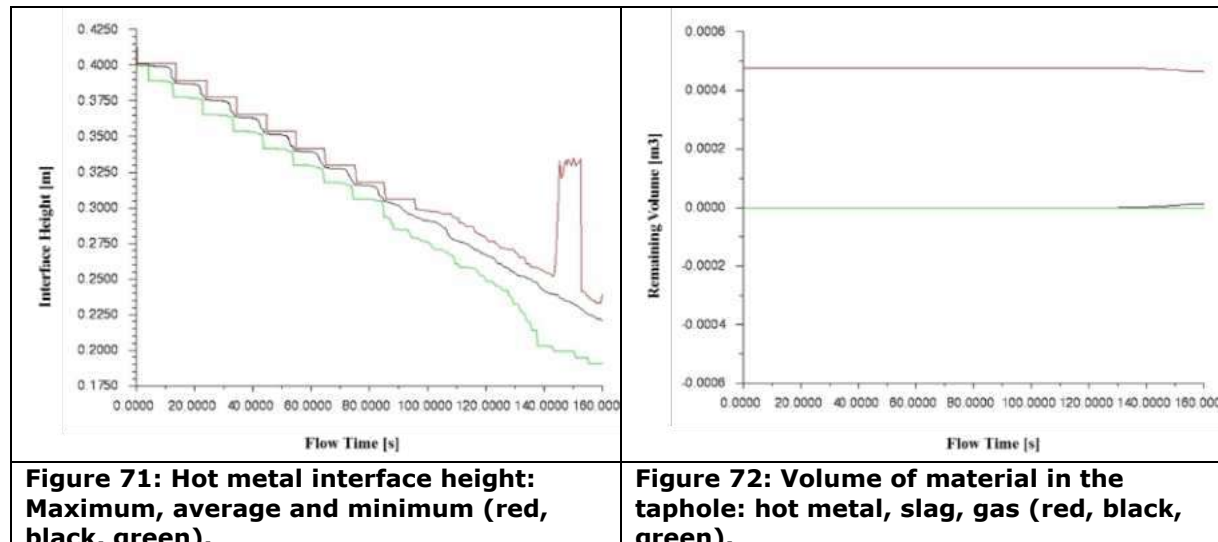
2.2.1.3.2.11.2 Case two: Change in the volume fraction of the bed

In the first parametric study, the volume fraction of the bed has changed in comparison to the reference case. As Table 10 shows, the volume fraction of the bed in all different regions are lower than the reference case.

Table 10: Case two; volume fraction of the bed.

Region	Volume fraction
Dead man: region 1 and region 2	0.2
Dead man: central region	0.4
Hearth except dead man regions	0.3

Similar to Figure 66 and Figure 67 the following figures (Figure 71 and Figure 72) show the hot metal-slag interface and the volume of each phase within the taphole region. the first thing, which can be pointed out comparing Figure 71 with Figure 66, is that the step structure changes to the gradual line decrement in the current case starts slightly later than the reference case.



Moreover, comparing Figure 72 with Figure 67 show that the slag phase enters the taphole region after 130 sec into the simulation which shows a clear difference in slag entering into the taphole region between the current case and the reference case. Figure 71 also shows that between around 140 sec and slightly after 150 sec into the simulation the maximum interface value suddenly picks to more than 32 cm in height. However, due to lack of intermediate files it is not possible to make any conclusive deduction except that since this is happening after slag phase penetrating through the iron phase entering the taphole, it could potentially push back the iron phase and might generate a wave. Figure 73 could, in some way, suggest the previous hypothesis.

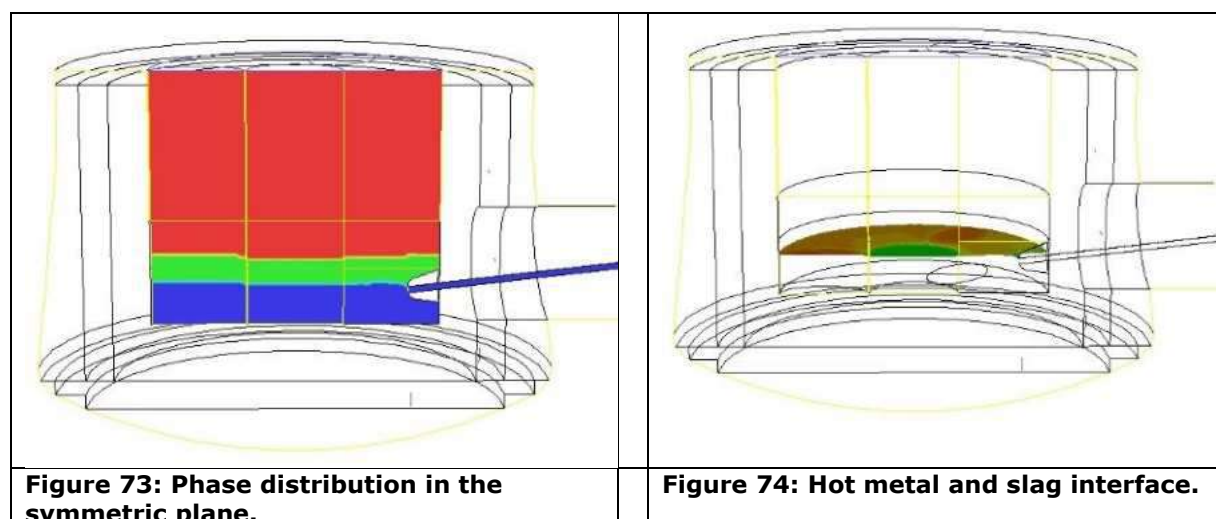


Figure 73 and Figure 74 show the phase distribution in the symmetric plane and hot metal-slag interface, respectively. As can be seen in region close to the taphole in Figure 73 a form of wave behavior can be seen where the interface is not sharp straight line, but a perturbation can be seen in the interface. It should also be mentioned that in comparison to the reference case, the simulation of the current case has been run slightly longer than the reference case where Figure 74 shows that the amount of slag entered the taphole region is larger than the reference case.

Figure 75 shows the temperature profile of the hot metal material at the symmetric plane. It can be seen, that the low temperature regions, similar to the reference case, appear at the two corners of the symmetric plane where green color represent the magnitude of around 1300 °C. A comparison between Figure 70 and Figure 75 shows that the maximum and minimum value of the contour key in the current case is almost 10 degree lower (in both maximum and minimum value) than the reference case. It should be pointed out, that the temperature profiles are very similar between two cases.

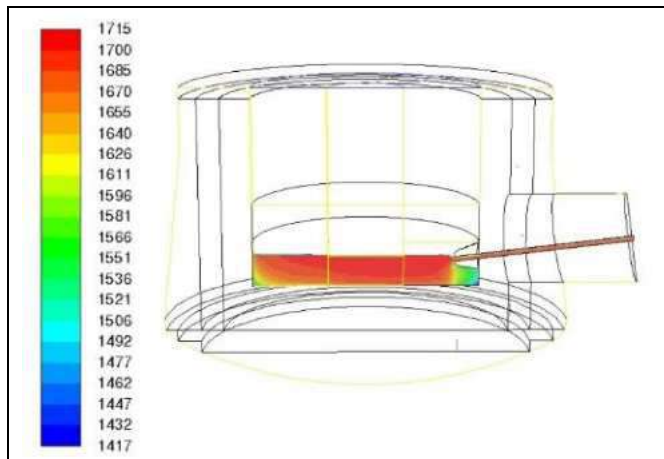


Figure 75: Hot metal temperature profile.

2.2.1.3.2.11.3 Case three: Over pressure

In this case, in comparison to the reference case, the porosities of different regions of the hearth were not changed but the top pressure was set to equal two bars while in the reference case the top pressure was equal to one bar.

Similar to two previous cases, Figure 76 and Figure 77 show the height of the hot metal-slag interface and volume of materials in the taphole, respectively. Firstly, it can be stated that the profile of the interface height for this case is in a way identical to previous cases. Figure 76 also suggest that if the simulation were to continue for a longer period of time, it would have registered similar behavior to the previous case where the maximum height of the interface picked and oscillated at larger magnitude before dropping down again (Figure 71).

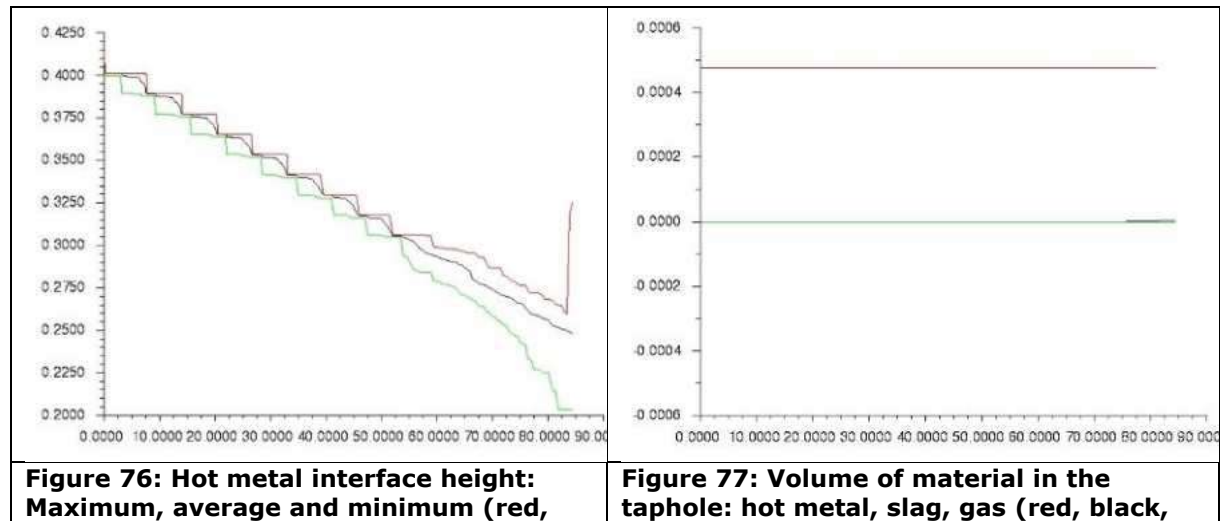


Figure 76: Hot metal interface height: Maximum, average and minimum (red, black, green).

Figure 77: Volume of material in the taphole: hot metal, slag, gas (red, black, green).

Moreover, one significant difference between the current case and the reference case is the moment when the slag phase break through the iron phase and enters the taphole region. In the reference case, it takes up to 130 sec for the slag phase to reach the taphole while this period for the second case is almost like the reference case; by increasing the top pressure, the slag phase penetrates into the taphole region around 80 seconds in the simulation. This is almost forty percent drop in the level drop.

Figure 78 and Figure 79 show phase distribution in the symmetric plane and hot metal-slag interface, respectively.

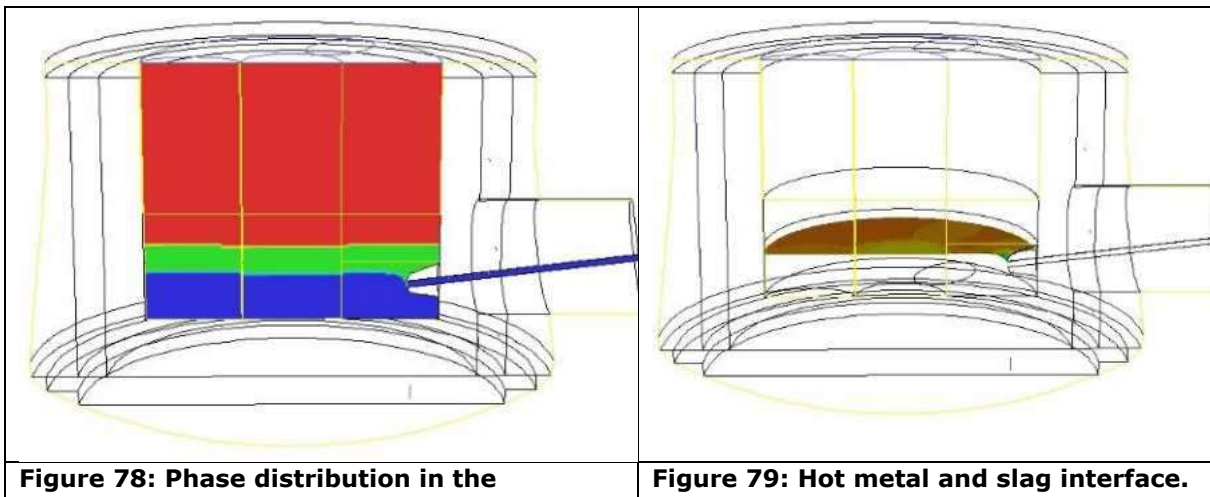
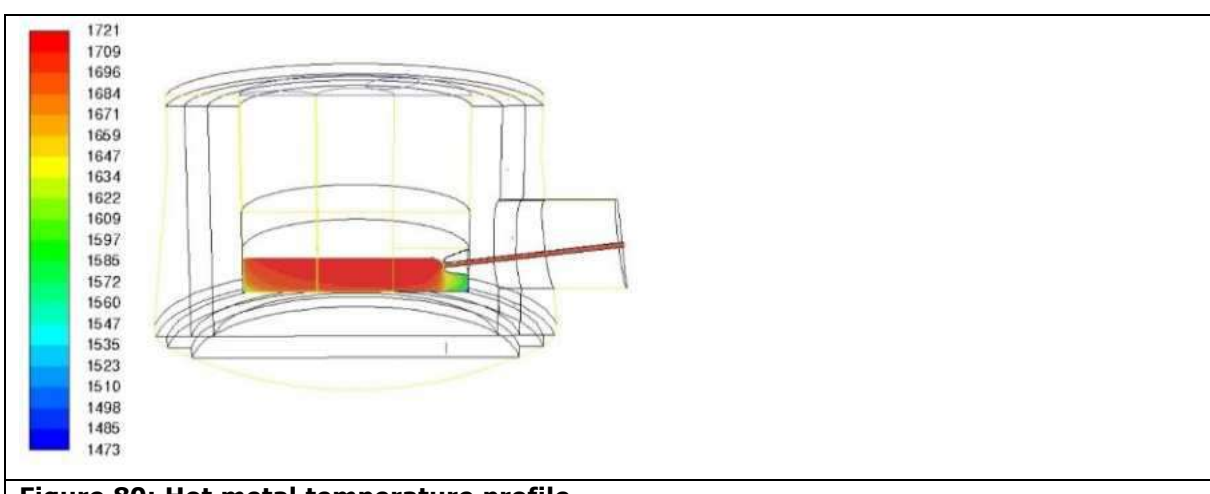


Figure 78 shows that the slag phase is breaking through the hot metal phase to enter the taphole region. Like the previous case, it can be seen that there is a slight fluctuation close to the taphole region while the interface level is rather sharp in the rest.

Figure 80 shows the temperature profile of the hot metal in the symmetric plane. The first thing can be seen from the figure is that the minimum value of the magnitude of the temperature is significantly larger than the other two cases. This is, of course, due to the fact that it has taken significantly less time for the slag phase to reach the taphole, hence the drainage interval is forty percent shorter than the reference case. Moreover, it can also be seen that the area of dark red (largest temperature) is more extended compare to the other two cases.



2.2.1.3.2.12 Conclusion: CFD Modelling of the EBF hearth

In conclusion, it can be said that in the CFD modelling of the physical (water) model, the streamline approach can predict the time and path-line of the injected tracer better than the VOF-DPM approach. Moreover, the VOF-DPM registers the similar profile for exit-time while it over predict for the injection points 1, 5 and 6 and under predict for the injection points 2, 7 and 9. Furthermore, the measurement data of shell temperature were successfully used to calibrate the simulation parameters to calculate the linings temperature profile. This calibrated profile was then used in simulating the drainage of the EBF hearth. The model used to predict the drainage was a three-phase model of hot metal-slag-BF gas. The first case for the parametric study of the drainage of the EBF hearth was used as a reference case. In this case the porosities for different regions were adopted based on the excavation data. Later on, two different cases were set up where in the first one, the volume fraction of the bed decreased while the top pressure was the same as the reference case and in the second parametric study case the volume fraction of different regions were equal to the reference case while the top pressure were twice as much as the reference case. The simulations suggested that a decrease in the volume fraction of the bed increases the time it takes for the hot metal level (hot metal-slag interface) to drop to the taphole level but this increase in the process time is not significant. It should be stated that even though the increase in the process time is not significant, the minimum and maximum values of the temperature in the symmetric plane were lower. Furthermore, an increase in the top pressure significantly decreased the time it took for the hot metal level to drop to the taphole level by forty percent. This was a

drastic change since the hot metal temperature registered larger values for minimum and maximum temperature in comparison to the reference case. This is expected since the time spent is less than the reference case, hence less heat is lost to the linings of the hearth.

2.2.1.4 Simulation of erosion patterns and transient inverse modelling of the lining state

2.2.1.4.1 Introduction

Over the years, many CFD models have been developed and used to simulate the flow of liquid metal in the hearth. Since the iron flow rates affect the heat transfer, which, in turn, affects the lining state, the system is strongly coupled and complex. Therefore, most CFD studies of the BF hearth have been limited to studying the liquid flow only, while the whole system, including the liquid flow and the furnace lining, has only been addressed by a few investigators [80] and [84]. Such efforts have usually been limited to simulating a single steady state, comparing the results with temperatures measured by thermocouples in the wall and bottom lining. Instead of clarifying the hearth state of a specific furnace, it may be meaningful to theoretically study the asymptotic state of the hearth lining under different hearth designs or boundary conditions. A simplified two-dimensional CFD model was developed for this purpose in the project. The task was solved as a forward problem, where the initial hearth design, dead man porosity, and the boundary conditions (e.g., outer wall temperatures, average outflow rate of iron) are given, and the location of the inner profile is iteratively determined by adjusting the interface between the hot metal and lining or skull until the system stabilizes. This model is presented in the next subsection.

Mathematical models estimating the blast furnace hearth erosion state developed in the past have been based on quasi-stationary assumptions, giving a snapshot of the state [78],[81] and [82]. In most cases this is appropriate, since the dynamics are slow, and the assumption considerably reduces the computational burden. However, averaging of thermocouple measurements destroys information that could provide useful knowledge of ongoing changes, e.g., in the liquid flows at the hot face of the lining. In order to use dynamic information, an inverse transient heat conduction model of the lining/skull system was developed and evaluated on data from TSE BF7. The findings can be used to shed light about dynamic changes inside the hearth and to assess the reliability of the thermocouples and the present state of the refractory lining. The model and some of its results are presented in subsection 3.2.1.4.3.

2.2.1.4.2 Asymptotic wear model

A comprehensive CFD model for estimating the asymptotic limits of refractory wear and skull build-up was developed in the project. The model is two-dimensional, stationary and considers flow of only iron. Its domain is the lower part of the hearth, and it considers the liquid flow, the phase transition between liquid and solid and the hearth refractories, but neither turbulence nor chemical reactions is considered. The flow field is solved by stating and solving the mean equations for continuity and momentum

$$\nabla \cdot (\varepsilon \rho \mathbf{u}) = 0 \quad (18)$$

$$\nabla \cdot (\varepsilon \eta \mathbf{u} \mathbf{u}) = \nabla \cdot (\varepsilon \eta \nabla \mathbf{u}) + \varepsilon (\rho g - \nabla p - R) \quad (19)$$

where $\varepsilon, \rho, \eta, u, g$ and p are the dead man porosity, liquid density and viscosity, velocity vector, gravity vector and pressure, respectively. R , the flow resistance of the dead man is expressed by the Ergun equation in vectorial form:

$$R = \frac{\varepsilon}{A} \eta \mathbf{u} + \varepsilon^2 B \rho \mathbf{u} |\mathbf{u}| \quad (20)$$

where A is the permeability of the dead man and B is the inertial term accounting for the kinetic energy of turbulent eddies, which can be generated within the void space when the flow rate is relatively high. The parameters are:

$$A = \frac{d_{\text{coke}}^2 \varepsilon^3}{150 (1-\varepsilon)^2}; \quad B = \frac{1.75}{d_{\text{coke}}} \frac{\varepsilon^3}{(1-\varepsilon)} \quad (21)$$

where d_{coke} is the coke diameter. The energy conservation equation for the liquid phase is

$$\nabla \cdot (u T) - \nabla \cdot \left(\frac{k}{\rho c_p} \nabla T \right) = 0 \quad (22)$$

where T, k and c_p are the temperature, thermal conductivity and specific heat capacity, respectively. The term $\alpha = k/(\rho c_p)$ is often referred to as thermal diffusivity. If the convective term on the left-hand-side of equation (22) is zero, the expression is the Laplace equation of heat

conduction, where the solid phase is treated as a fluid, but where the flow can be suppressed by giving a very small value to the porosity in equation (21), which yields a large momentum sink in equation (20). This treatment reduces the complexity of the model and makes it possible to track the liquid-solid front. The model developed can track interfaces between different phases in a more straightforward and efficient way than in earlier approaches. Here, the 1150 °C isotherm is taken to be the boundary between the iron and the solid phase, expressing the maximum hot metal penetration into the hearth lining. As schematically depicted in Figure 81, an initial guess of the internal hearth profile is given together with other relevant variables (Figure 81a). Based on these equations, the temperature distribution in the hearth is calculated, followed by an updating of the hearth profile (Figure 81b). If the 1150 °C isotherm falls inside the internal profile, the volume of the solid between these two is taken to be eroded, and if it falls within the liquid pool, the volume is taken to be filled with solidified skull. These steps are fully coupled to the CFD solver (ANSYS FLUENT 14.5) by coding a variety of user-defined functions (UDFs). One routine updates the hearth profile by categorizing the computational cells into different groups, including hot metal (i.e., liquid pool), skull and refractory. The liquid-solid interfaces are implicitly recognized during the calculation. The 1150 °C isotherm is repeatedly revised until the profile stabilizes, as shown in the flowsheet in the right part of Figure 81.

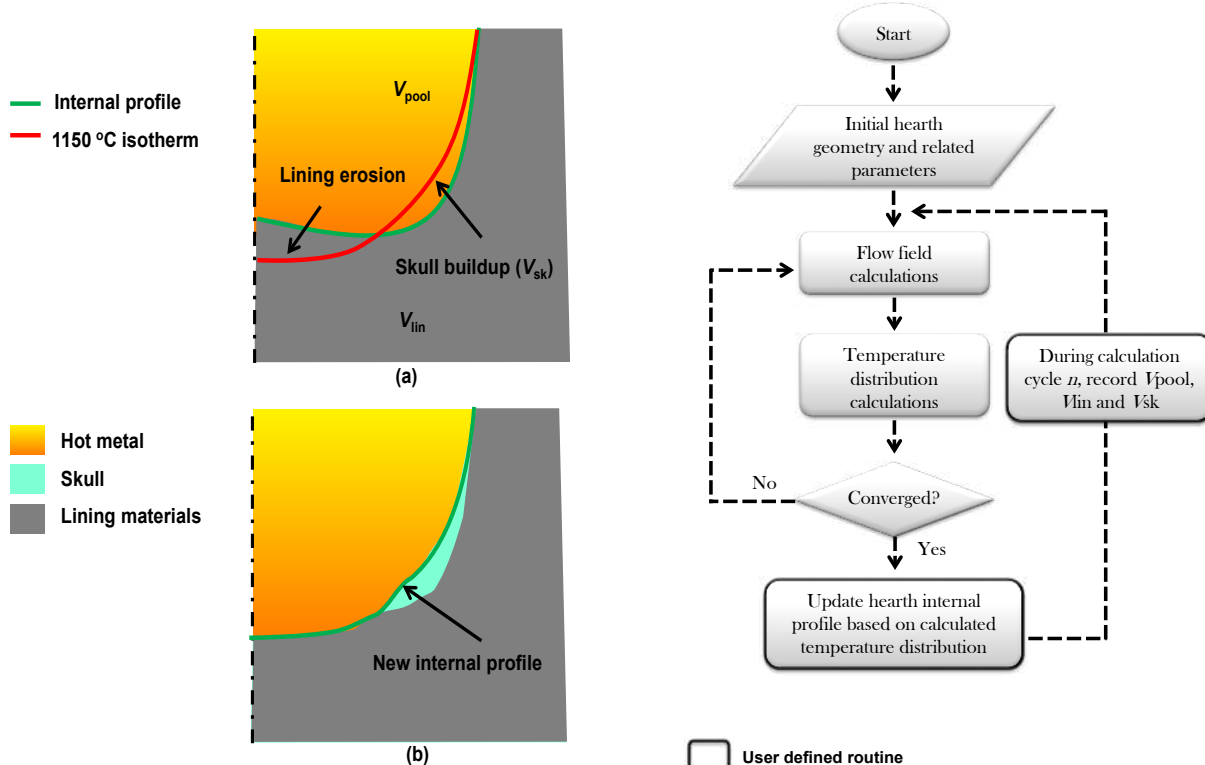


Figure 81: Left: Updating principle of the hot face location in the asymptotic wear model. Right: Flowchart of the iterative calculations.

The model is limited to a two-dimensional treatment to limit the computational burden. Figure 82 illustrates the geometry, which is a simplification of the hearth of a reference one-taphole BF with a working volume of approx. 1000 m³. The hearth is constructed of carbon-based bricks combined with high-quality ceramics in the uppermost layer below the 'A-A' plane in the figure. The hearth sidewall on the taphole side is lined with super-micropore carbon bricks, which have high thermal conductivity and they are ready to extract excessive heat from inside and therefore cools the hot face in the taphole vicinity. The pertinent dimensions and material properties are also shown in Figure 83.

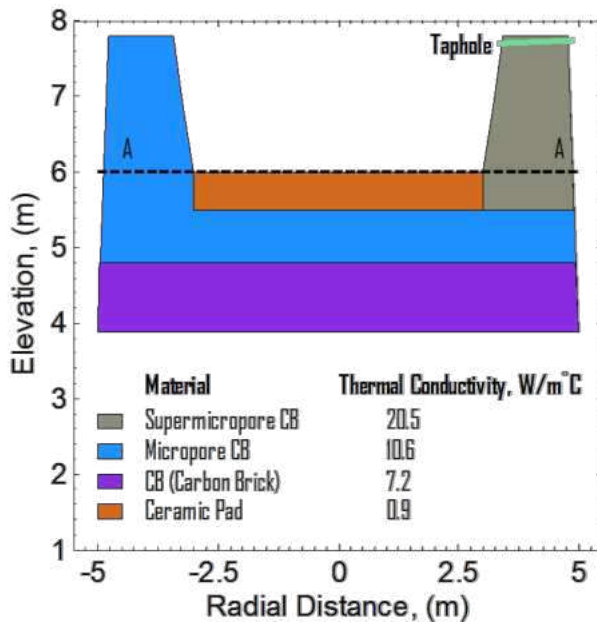


Figure 82: Dimensions of the hearth and pertinent material properties.

With reference to Figure 83, boundary conditions are applied in the following way. For momentum equations, non-slip wall conditions are given to ②–④, except ①, for which a constant inlet velocity of hot metal is provided. A constant pressure is maintained at the taphole. For the energy equation, a constant temperature of hot metal is set along boundary ① and the top surface of ② is assumed to be adiabatic. Owing to lack of reliable information on heat transfer coefficients of the hearth cooling apparatus, constant temperatures are applied to boundaries ③ and ④.

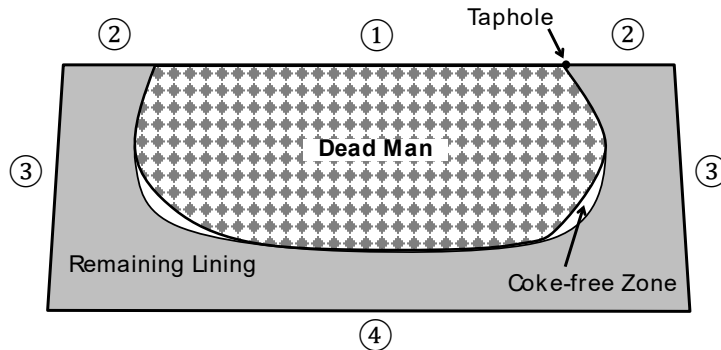


Figure 83: Boundary (referred to by ①–④) conditions applied in the model.

Key thermo-physical properties used are listed in Table 11. The viscosity of hot metal was set to 0.006 Pa·s. It should be noted that an average of the thermal diffusivities of coke and hot metal is used based on the assumed dead man voidage. We assume the dead man to be sitting, so the coke bed extends to the bottom. The computational domain was discretized into 320×420 rectangular control volumes in Cartesian coordinates, and the solution of a case usually required about 40 iterations.

To illustrate the model, three simulations are reported here. In all cases, the dead man porosity was $\varepsilon = 0.3$, the hot metal inlet temperature was 1773 K, and the sidewall and bottom boundary conditions ③ and ④ were set to 423 K, but the hot metal inlet flow rate was changed from 0.1 mm/min in case 1, through 0.15 mm/min in case 2 to 0.2 mm/min in case 3.

Table 11: Key parameters in the model, where the temperature, T , is expressed in °C.

Material	k (W/(m·K))	ρ (kg/m ³)	c_p (J/(kg·K))	$\alpha \times 10^6$ (m ² /s)
Hot metal	–	6800	–	6.2+0.00179($T-1538$)
Ceramic pad (CP)	0.9	2500	1100	–

Carbon brick (CB)	7.2	1570	$486.1 + 1.739T$	-
Micropore CB	10.6	1610	$367.5 + 1.49T$	-
Super-micropore CB	20.5	1820	$357.3 + 4.216T - 0.002T^2$	-
Skull	4	2300	920	-
Coke	-	-	-	1.5

The calculated hearth profile, temperature distribution and hot metal streamlines for case 1 are plotted in the left part of Figure 84. In its upper panel, a general flow pattern of hot metal through a sitting dead man, as indicated by the streamlines, can be seen. The iron that enters close to the taphole gives rise to a flow directly towards the taphole, while from the far-taphole side the liquid flows initially downwards, then quite horizontally and finally upwards to the taphole. This gives a rather uniform flow distribution minimizing the friction losses. The hearth profile clearly exhibits a 'pot-shaped' erosion type that is commonly encountered in practice. The ceramic pad (CP), which serves as the first 'barrier' separating the high-temperature liquid and the bottom part of the micropore carbon bricks (MCB), is severely eroded and has disappeared in the central region. A small portion of MCB in the center is therefore lost. The left and right sidewalls are also consumed below the taphole level, where hot metal flows with a relatively high speed. Skull is formed in the joint between the left sidewall and CP (indicated by ① in Figure 84). These results agree well with operational experience and with the guidelines for BF hearth design. The contours plotted in the lower panel of the figure reveal that while temperature distributes uniformly in the liquid pool, the solid materials locally show higher temperature gradients in regions where the materials have lower heat conductivity, for the remaining CP and skull zones.

The effect of the inlet velocity, which reflects the production rate of the BF, is illustrated in the right part of Figure 84, where the calculated hearth profiles for cases 1-3 are shown. The most striking feature is that the liquid pool grows considerably as the production rate is increased and the CP is practically eroded. It should be noted that the outer boundary temperatures were kept the same for all the cases, which means that the cooling power increased along with the hearth wear.

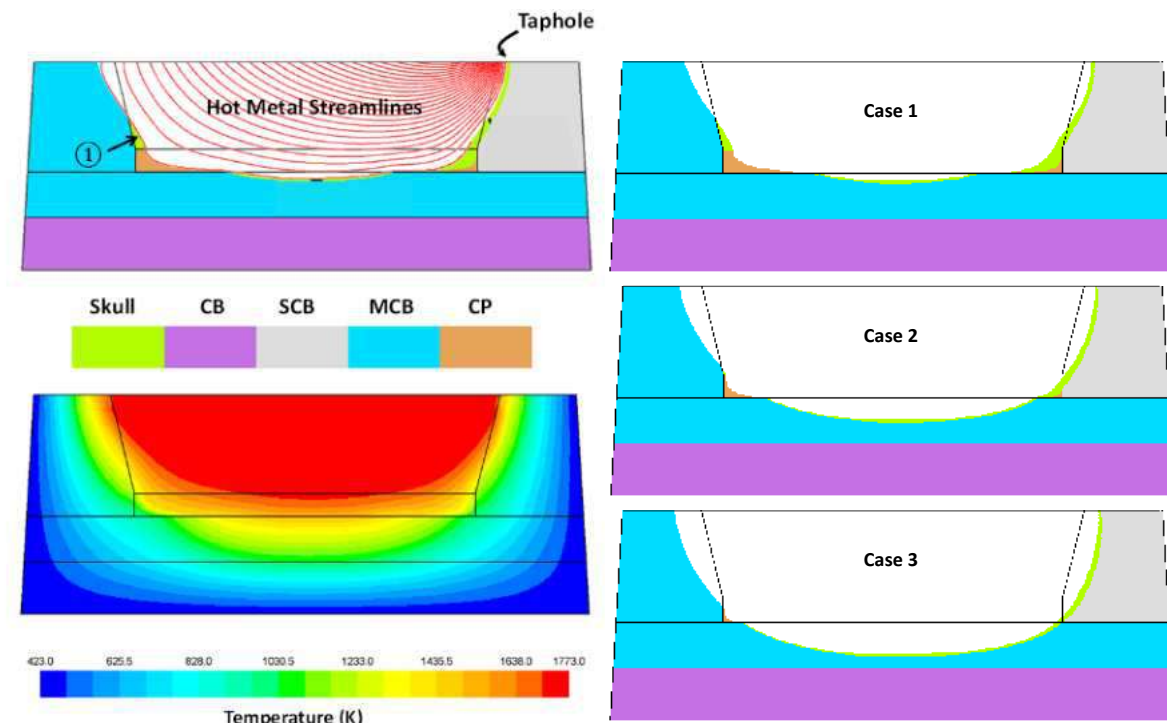


Figure 84: Left: Calculated final hearth profile and temperature distribution for case 1. Right: Comparison of the final hearth profiles for cases 1-3 (Table 11).

The model of asymptotic hearth state has been presented here for only a few cases where the boundary conditions were changed, but the model's use is not limited to such analysis. It can also be applied to study how the hearth design affects the asymptotic wear state of the process. Even though the result of the model, since it is static, cannot be used to follow the hearth state during a furnace campaign, it is useful to know the expected final state, as it in practice has been found that the overall hearth wear in blast furnace often stabilizes after several years of operation [78]. Such

studies of hearth design should naturally be combined with the findings of FEM models of the stress field in the lining.

In future work, the possibilities of extending the model to three dimensions will be explored, which could give a more realistic view of the asymptotic hearth wear.

2.2.1.4.3 Inverse two-dimensional transient model

To explore the feasibility of developing an inverse transient model of the hearth lining based on information from BF7 of TSE and to obtain an overall view of the transient responses of the hearth refractory, thermocouple data for a period of three months was studied. The analysis demonstrated that there are interesting short-term changes in the values, but also that periods and positions with inconsistent behavior occurred, which needed further analysis. An initial analysis of the transients of the hearth sidewall temperatures in conjunction with taphole changes was also undertaken. BF7 has three tapholes, labeled N, Z and W. The top panel of Figure 85 shows sidewall temperatures throughout the three-month period at the same radius (7.21 m) and a vertical level (+4800 mm) which is close to the taphole level, as indicated by the yellow diamond in the small schematic in the right part of the figure. The x axis shows the position on the circumference of the furnace, where the numerals reported refer to tuyere numbers, and labelled arrows indicate the position of the tapholes. The y axis represents time (increasing towards the observer) and the dotted lines next to the axis represent the tapholes in operation, using the same color code as for the arrows. After a taphole has been taken into operation, there is an increasing trend in the closest thermocouple readings, and when it has not been in use for a while the temperatures decrease. The bottom panel of Figure 85 illustrates the dynamics of thermocouples closer to the junction between the sidewall and the hearth bottom. The temperatures at this level are seen to be less affected by taphole changes, which may reflect the slower iron flow in this region.

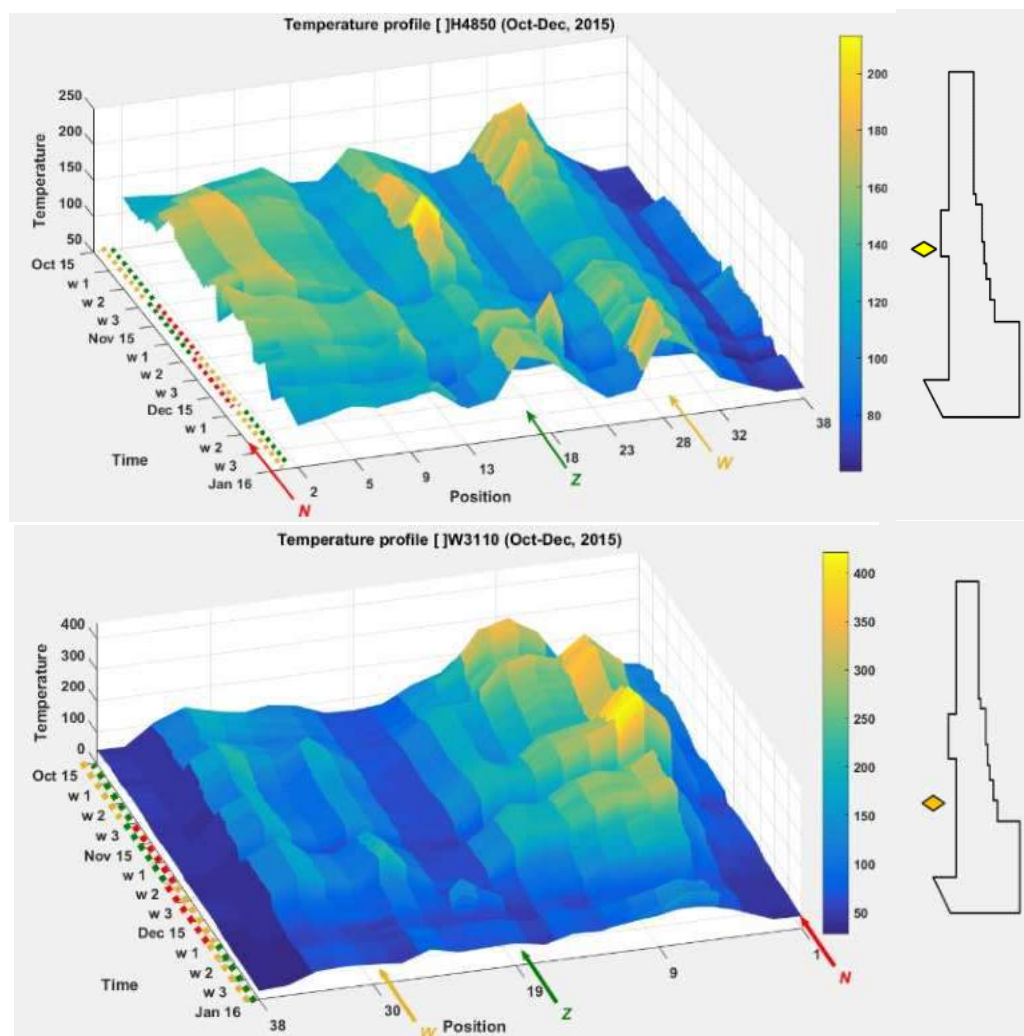


Figure 85: Top: Evolution of thermocouples in the hearth sidewall close to the taphole level. Bottom: Evolution of thermocouples in the hearth sidewall clearly below the taphole level.

Based on these findings, a transient inverse heat conduction model was developed and applied to analyze hearth lining thermocouple dynamics. The model is based on differential equations for the heat conduction in a wall consisting of N layers.

$$\frac{\partial}{\partial x} \left(K_i \frac{\partial T_i(x,t)}{\partial x} \right) = \rho_i c_i \frac{\partial T_i(x,t)}{\partial x} \quad i = 1, \dots, N \text{ for } t > 0 \quad (23)$$

$$\frac{\partial T(x_i,t)}{\partial x} = \frac{\partial T(x_{i+1},t)}{\partial x} \quad i = 1, \dots, N-1 \text{ for } t > 0 \quad (24)$$

$$T(x,t) = T_1(t) \quad x = x_1 \text{ for } t > 0 \quad (25)$$

$$T(x,t) = T_L(t) \quad x = x_L \text{ for } t > 0 \quad (26)$$

$$T(x,0) = T^{\text{init}}(x) \quad x_1 < x < x_L \quad (27)$$

where equation (23) describes the heat conduction in each layer, the boundary conditions are expressed by equation (24) for layer interfaces and by equations (25) and (26) for the first (innermost) and the N^{th} (outermost) layer, respectively. The temperature profile of the wall at $t = 0$ defines the initial condition, equation (27). Thus, the region from the hot face x_1 (in contact with liquid iron) to the cold face x_L (in contact with surrounding air or cooling water) should be considered (Figure 86). However, as it in practice is hard to quantify the conditions at the cold face of the BF hearth wall, the domain studied may be restricted to the region between the hot face of the wall and a thermocouple in the lining close to the cold face. In the present approach, a pair of thermocouples (TC1 and TC2) is used and the computational domain ends at the outer thermocouple (TC2), as depicted in Figure 86b. The layers are characterized by different thermal conductivity, specific heat capacity, density and thickness, and possible build-up material (skull) on the hot face can act as an additional layer.

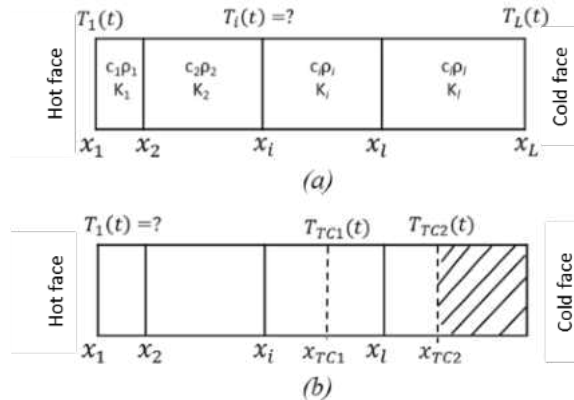


Figure 86: Model definitions: a) direct problem, b) inverse problem.

The inverse problem formulated (Figure 86b) estimates the time evolution of the unknown hot-face temperature, $T_1(t)$, with the temperature at the outer thermocouple (T_{TC2}) as the cold-face boundary condition. As the thermocouple signals are logged at some frequency (e.g., every second), it may be motivated to calculate longer averages of the signals to filter out noise and to save computational effort. Here, we use a "sampling interval", Δt , where averages of the signals over the same interval were taken. To regularize the solution of the inverse problem, the hot-face temperature was reconstructed at considerably fewer points by the following strategy: Given filtered thermocouple information (TC1, TC2) at the time moments $t' - K\Delta t, t' - (K-1)\Delta t, \dots, t' - \Delta t, t'$, where t' is the present time, the hot-face temperature is expressed as a linear interpolation in time between M temperature estimates equally distributed in the time window. These estimates, $z_i = T_1(t' - \frac{K(M-i)}{M-1}\Delta t)$, $i = 1, \dots, M$, are the unknown variables to be solved. Collecting these in a vector of unknowns, \mathbf{z} , the inverse problem is written as:

$$\min_{\mathbf{z}} \sum_{j=1}^{K+1} (T(x_{TC1}, t' - (j-1)\Delta t) - T_{TC1}(t' - (j-1)\Delta t))^2 \quad (28)$$

subject to the model of equations (23-27) with the linearly interpolated hot-face temperatures inserted in equation (25) and using $T_L(t) = T_{TC2}(t)$ in equation (26). The procedure is outlined schematically in Figure 87, where the unknown temperatures (bullets) have to be estimated to provide the closest fit between the observed (upper solid line) and simulated (dashed line) temperature at the inner thermocouple, TC1.

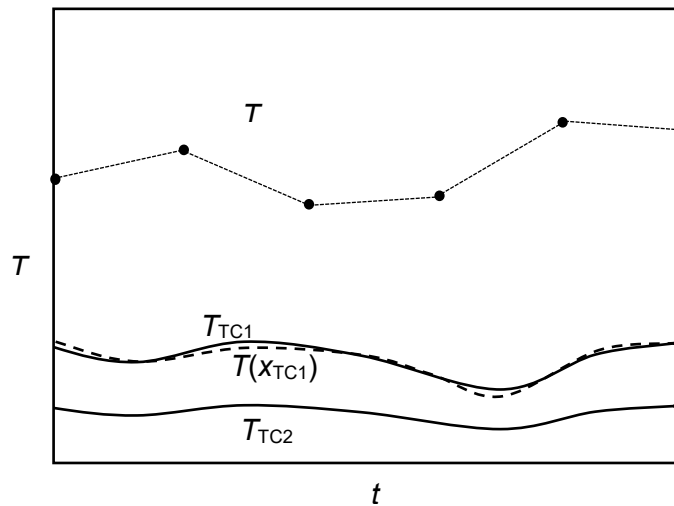


Figure 87: Hot-face temperature (top curve) reconstructed by linear interpolation of $M = 6$ discrete temperatures (dots connected by dotted lines), thermocouple temperatures (solid lines) and temperature at TC1 simulated by the model (dashed line).

The computational steps in the algorithm can be expressed as:

- Set up the computational domain, including the layer material properties and thicknesses, thermocouple locations and, after pre-filtering the thermocouple signals and discretizing them properly in time (time step Δt), also the time window for the study ($K\Delta t$).
- Set the initial temperature distribution of the system (equation (27)).
- Set the cold-face temperature for the period by equating it to T_{TC2} .
- Determine the optimal values of the M unknowns, z , by an optimization routine that tackles the problem of equation (28), which under given boundary conditions solves equations (23-27) of the model.
- Report the solution and repeat from step 2 when new measurement information becomes available.

As the hot-face temperature can be felt at the thermocouples close to the cold face after some time because of the accumulation/depletion of heat in the lining, the most recent time history estimated is inaccurate. Therefore, in the post-processing of the results only the hot-face temperatures estimated in the center of the window are taken as valid values, yielding a sequence of "observations" as the time window is shifted forwards, as illustrated schematically by the red dashed line in Figure 88 for a system with $M = 6$. The algorithm was implemented in Matlab using its "fminunc" function for solving the constrained optimization problem (equation (28)) and "pdepe" for solving the differential equations (equations (23)-(27)).

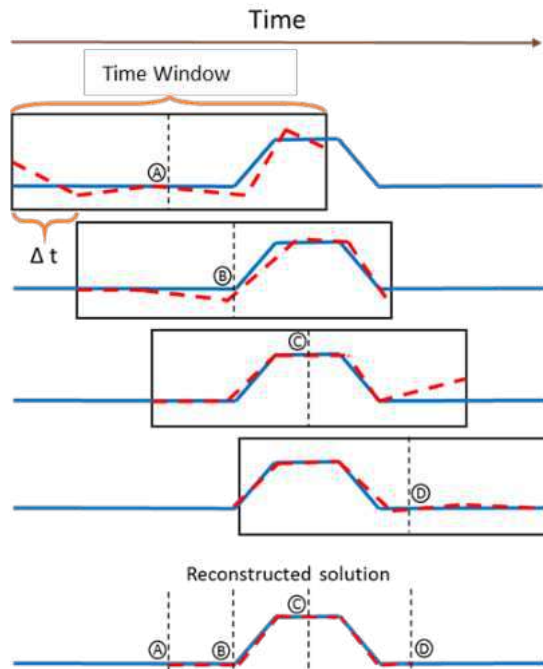


Figure 88: Schematic of the reconstruction of the hot-face temperature history based on a sequence of solutions of the inverse problem for a time window.

Simulated tasks were used to validate the model's performance by first solving the direct problem, imposing different hot-face temperature programs, and then the inverse problem based on the simulated thermocouple signals (TC1). Averages and sampling times of $\Delta t = 5$ min were found to give reasonable results, and a minimum spacing of the thermocouples of 20-30 cm was found necessary [79]

The method is here illustrated on short-term measurements from the TSE BF7 for an 8-day period, studying 15 positions along the hearth sidewall periphery, each representing thermocouple pairs on three vertical levels (L1, L2 and L3 in the left part of Figure 89). A data window of $K = 50$ points (≈ 4 h) was applied in the analysis. To set up proper layer thicknesses of lining and skull, a two-dimensional static wear model [78], also utilized in WP4, was first applied to historical data from the start of the furnace campaign, and its results for the first day of the 8-day period were used. After this, the lining layers thicknesses were assumed not to change, i.e., neither wear nor skulling was considered during the period.

Eleven of the $15 \times 3 = 45$ independent thermocouple pairs showed erratic behavior and gave unreasonable estimates, so their information was discarded. Some of these exhibited considerable fluctuations that were not reflected in the behavior of nearby thermocouples and may be due to electrical disturbances, bad thermal contact of the thermocouple with the lining, bad contact between lining layers, as discussed at the end of this subsection, or brittle lining. The reconstructed temperatures based on thermocouples with less than 20 cm spacing exhibited dramatic excursions, so these were also excluded. In the 34 remaining cases, however, the signals varied gently and within reasonable limits, so these were applied to reconstruct the hot-face conditions using the inverse model. It was found that changes in the hot-face at a local spot were often after some delay observed in neighboring regions, confirming the heating or cooling trend. Here, it should be noted that the thermocouple signals are fully independent, so such agreement in the reconstructed temperatures serves to validate the results. To aggregate the 1D results, cubic interpolation was used to yield a continuous view of the hot face temperature of the hearth, exemplified by the right part of Figure 89.

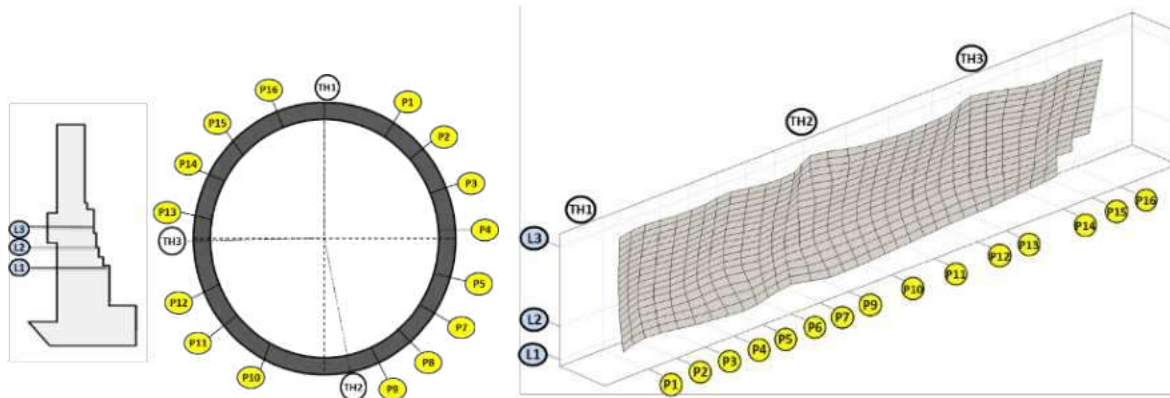


Figure 89: Left: Vertical and horizontal cross-sections of the hearth lining showing the location of the points equipped with thermocouples. Right: Snapshot of surface relief of reconstructed temperatures along the hot face.

A detailed illustration of the time evolution of the hot-face conditions can be made by animating a temperature map in color, snapshots of which are shown in Figure 90. Analysis of the map revealed some interesting findings: in certain regions, hot spots occurred quite regularly, most likely reflecting the dynamics of the hot metal flow in the hearth due to the tapping operation. The occurrence of such spots may reflect an increased hot metal flow in a coke-free zone, enhancing heat transfer to the wall. While the hot spots below the two other tapholes (TH1 and TH2) gradually expanded, the region below taphole TH3 underwent periodic temperature variations up to the 110th hour of the period. This development was found to matches the tap cycle of TH3, showing peak values after tap start, for instance at 59th and 63rd hour. During this period, tapholes TH2 and TH3 operated alternately, which explains the stable conditions in the region close to taphole TH1, which was not taken into use until the 140th hour.

Figure 91, top panel, shows the evolution of the thermocouple pairs (lower curves) on the L1 level below TH3, and the top curve illustrates the reconstructed hot-face temperature. Even though the latter occasionally assumes unreasonably high values (which may be due an incorrect estimate of the lining and skull thicknesses in the inverse model), many interesting observations can be made, when more details are studied. The middle and bottom panels of Figure 91 show the framed regions of the top panel, together with vertical bars indicating the moments when the taphole in question (TH3) has been opened (green) and closed (red). The following conclusions can be made:

- The delay between the “spikes” in the hot-face temperature and TC1 is 2-3 h.
- The hot-face temperature starts increasing 20-50 min after the taphole has been opened.
- The accumulation and depletion of heat in the lining between the two points make the relation between the signals complex.

The thermal cycles at the hot face reconstructed by the model can in the future be used to shed light on the complex flow conditions in the hearth. The findings can also be applied for verifying the results of CFD simulations of alternate tappings, supporting or rejecting different hypotheses of the internal state of the dead man (porosity, floating state). The method thus provides an indirect means of estimating the dead man state.

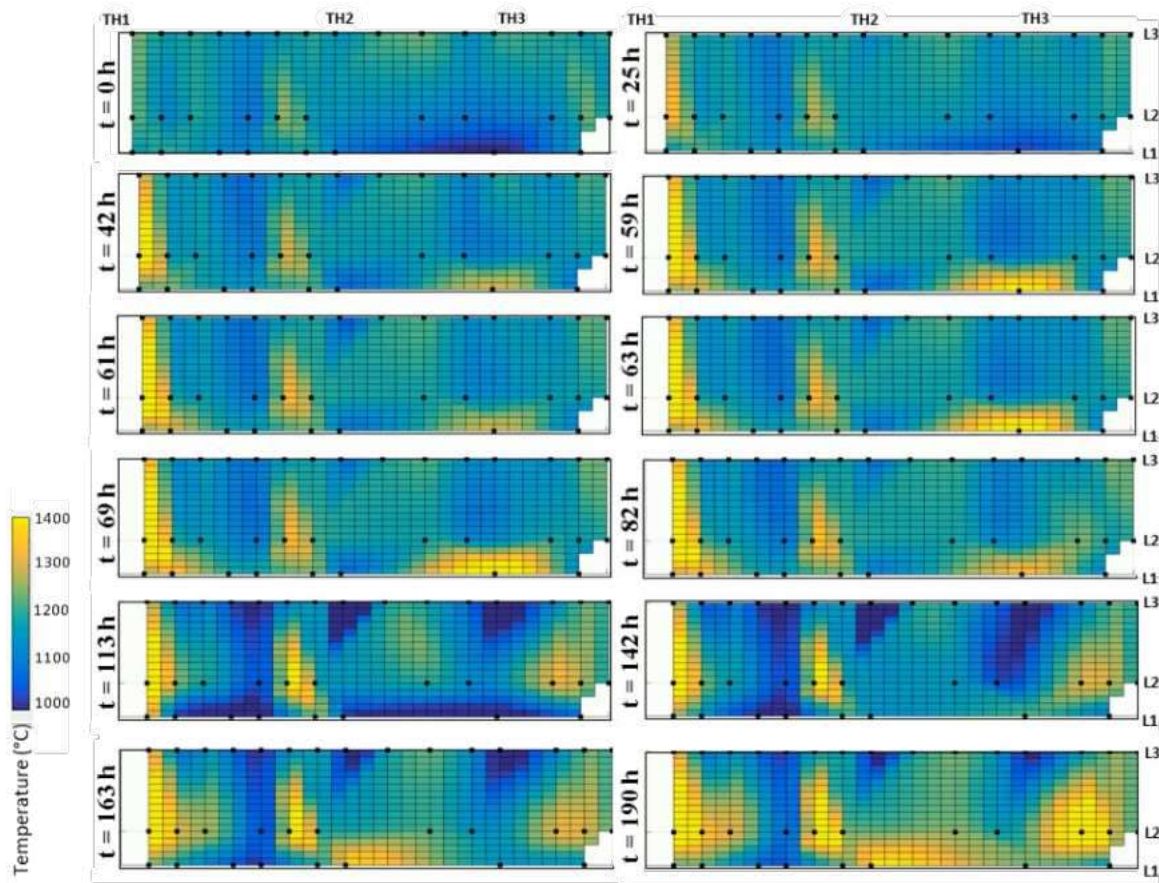


Figure 90: Snapshots of hot-face temperature evolution at different times of the 8-day period studied. The locations of the three tapholes (TH1-3) along the periphery have been indicated above the uppermost panels.

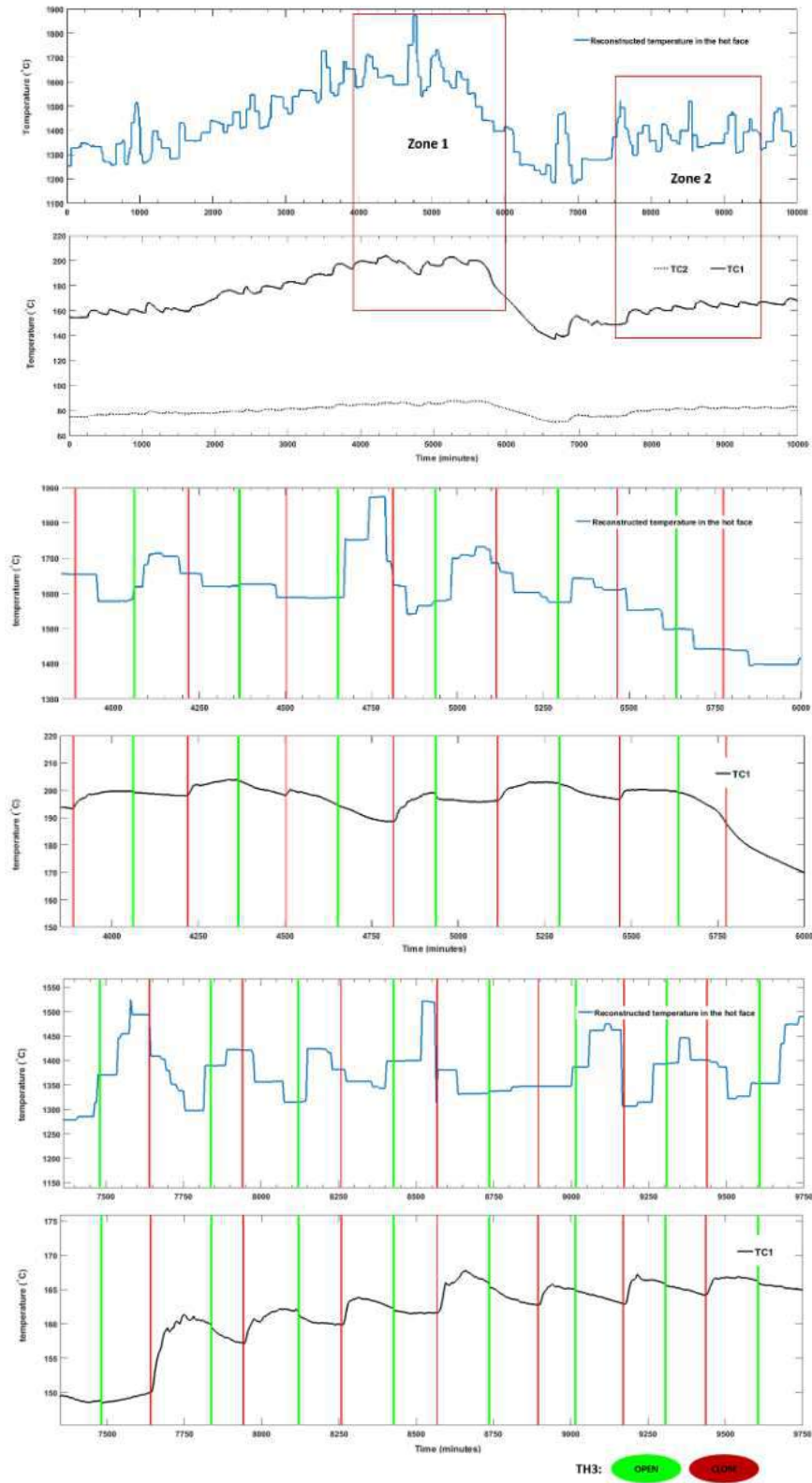


Figure 91: Top panel: Signals for the thermocouple pair on level L1, located 1.7 m below taphole TH3. Middle and bottom panels: more detailed view of the hot-face temperature (blue lines) and TC1 (black lines) for the framed regions in the top panel. Vertical lines indicate opening (green) and closing (red) of TH3.

Below we present a more detailed analysis of the signals from thermocouple pairs in the sidewall lining. Neighboring thermocouples generally followed the same overall trends, as exemplified in Figure 92 by both the long-term (top) and short-term (bottom) behavior of a thermocouple pair close to the north taphole (see small insert to the left), together with the tapped hot metal quantities from the same taphole. During the first week of the period depicted, the north taphole is not operated, so the wall temperatures are lower, but as the taphole is taken into use the

Optimizing Blast Furnace Hearth Inner State (OPTIBLAFFINS)

temperatures increase steadily. As expected, since the heat source is in the hearth, the outer (blue) thermocouple shows a more damped response to changes. Interestingly, the taphole is taken out of operation around January 18, and there is a clear decrease in wall temperatures, followed by a corresponding increase when the taphole is taken back into operation after a few days. Furthermore, the effect of a short stoppage on February 25 is also sensed.

A thermocouple pair located somewhat below the ones shown in the upper panel of the figure was studied with respect to short-term behavior (bottom panel of Figure 92). The signals revealed changes that were expected to be induced by the alternating tappings and the corresponding changes of the hot metal flow in the hearth. Similar patterns as noted above occur in that the outer thermocouple temperature is less noisy and shows somewhat smaller amplitude of the changes. The gray regions in the figure depict the time when the north taphole was operated, and the phase shift of the temperatures was expected to be due to the dynamic action of the wall.

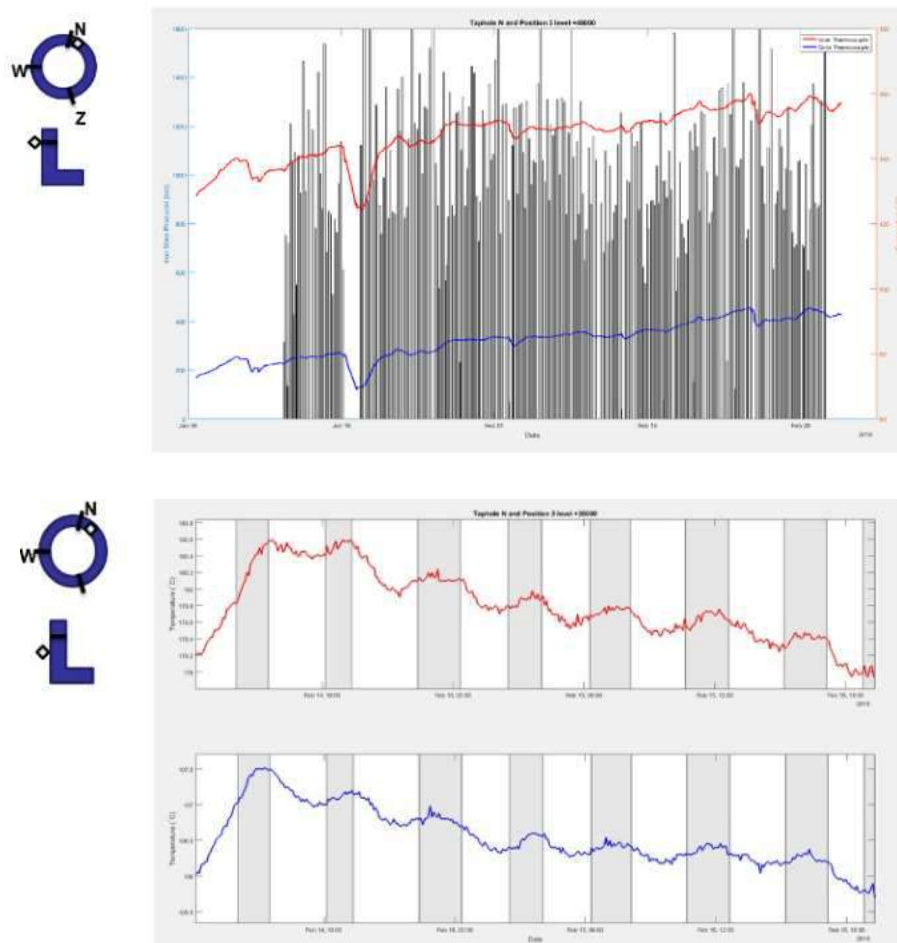


Figure 92: Inner (red) and outer (blue) thermocouple temperatures for a vertical position close to the taphole and a peripheral position slightly east of the north taphole (see small insert). Top: long-term behavior, with bars illustrating the quantities of hot metal tapped from the north taphole. Bottom: short-term behavior, with grey regions illustrating the time when the north taphole was open.

The fact that several of the thermocouple signals showed unexpected behavior called for a deeper analysis, which revealed that for some other locations in the hearth lining, abrupt changes in the thermocouple signals occurred very shortly after the taphole was plugged. A puzzling feature was that these thermocouple pairs showed opposite short-term temperature trends, as exemplified in Figure 93, which depicts the readings for a thermocouple pair located close to the west taphole. Even though the tap durations varied, the response occurred at a practically constant time after the taphole in question was closed. As no thermal effect could have such a response, another explanation had to be found.

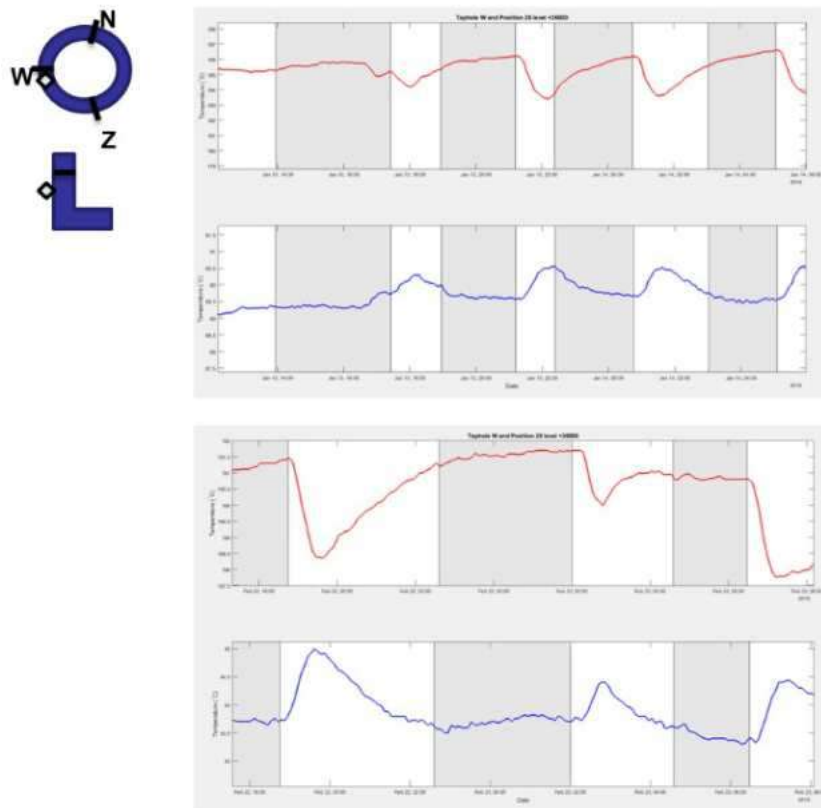


Figure 93: Inner (red) and outer (blue) thermocouple temperatures for a vertical position between the taphole and hearth bottom level and a peripheral position slightly south of the west taphole (see insert), with grey regions illustrating the time the west taphole was open.

The only plausible explanation for such a rapid change would be a factor that physically acts upon the lining system. As no other variable forces act on the lining than those caused by the phases inside the blast furnace, the reason for the variations were hypothesized to be the varying pressure on the wall exerted by the hearth liquids along with changes in the liquid levels. This would also explain the connection between the moments of the main changes and the taphole operation. Analyzing the response in Figure 93, it is seen that the thermocouple readings start changing shortly after the tapping of the nearby taphole has ended, exhibiting a spike about half an hour after tap end. Thus, the thermocouple readings may vary with the local liquid levels in the hearth, showing a rapid change after the taphole has been plugged and the liquid levels increase dramatically as no liquids are extracted.

A possible explanation for the opposite response shown by the inner and outer thermocouple is schematically outlined in Figure 94, which depicts a thermocouple pair mounted in different carbon blocks. At lower liquid levels, i.e., lower forces from the hearth liquids, the thermal contact between the blocks is poor and the thermocouples show a larger temperature difference (as indicated schematically by red lines and dots in the right subpanel). As the hearth liquid levels increase, the force acting on the lining also grows, which improves the thermal contact between the carbon blocks. Thus, more heat flows from the hearth towards the shell, decreasing the inner and increasing the outer thermocouple temperature, eventually leading to the steady-state condition illustrated by blue lines and dots in the right subpanel.

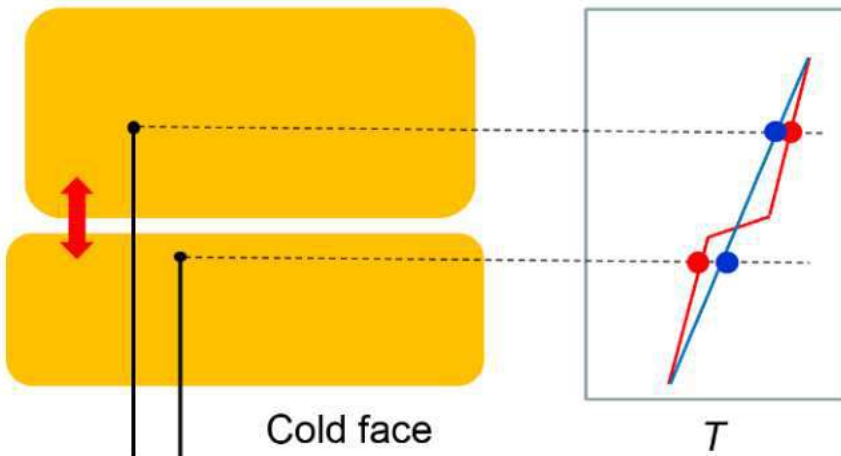


Figure 94: Possible explanation for opposite response shown by thermocouple pairs after a nearby taphole is closed. At lower forces from the hearth liquids, the thermal contact between the blocks is poor and the thermocouples show a larger temperature difference (red lines and dots in right subpanel). As the hearth liquid levels increase, the force acting on the lining increases, causing an improved thermal contact between the blocks and a smaller temperature difference (blue lines and dots).

To study whether the proposed mechanism could be the underlying cause of the observed temperature signals, a simplified system was simulated, where a gap between two blocks was emulated as follows. A system (cf. top of Figure 95) consisting of a 20 cm skull layer ($k_{\text{skull}} = 3 \frac{\text{W}}{\text{m K}}$), and two high-conducting carbon layers (45 cm and 40 cm, $k_{\text{layer},1} = k_{\text{layer},2} = 45 \frac{\text{W}}{\text{m K}}$), the latter two possibly separated by a gap, was simulated with fixed boundary temperatures (1150°C and 40 °C). The gap was described as a 3 cm layer of lining, with a conductivity that can vary between that of the adjacent layer ($k_{\text{layer},1}$) and a lower value ($k_{\text{gap}} = 20 \frac{\text{W}}{\text{m K}}$). Starting from an arbitrary thermal state of the lining, and applying the periodic program indicated in the lower panel of Figure 95, a process is emulated where a gap between two blocks is gradually closed (in $t_1 = 10$ min) and opened again (in $t_2 = 60$ min) followed by a stable period. After the system reached a quasi-stationary state, the simulated temperatures at two points 10 cm from the “gap layer”, but in different carbon blocks (Figure 95), show a behavior as indicated in Figure 96. Even though the temperature levels and time scale of the changes are different from those in the hearth lining of TSE BF7 reported above, the figure shows qualitatively the same behavior as the two temperatures in Figure 93.

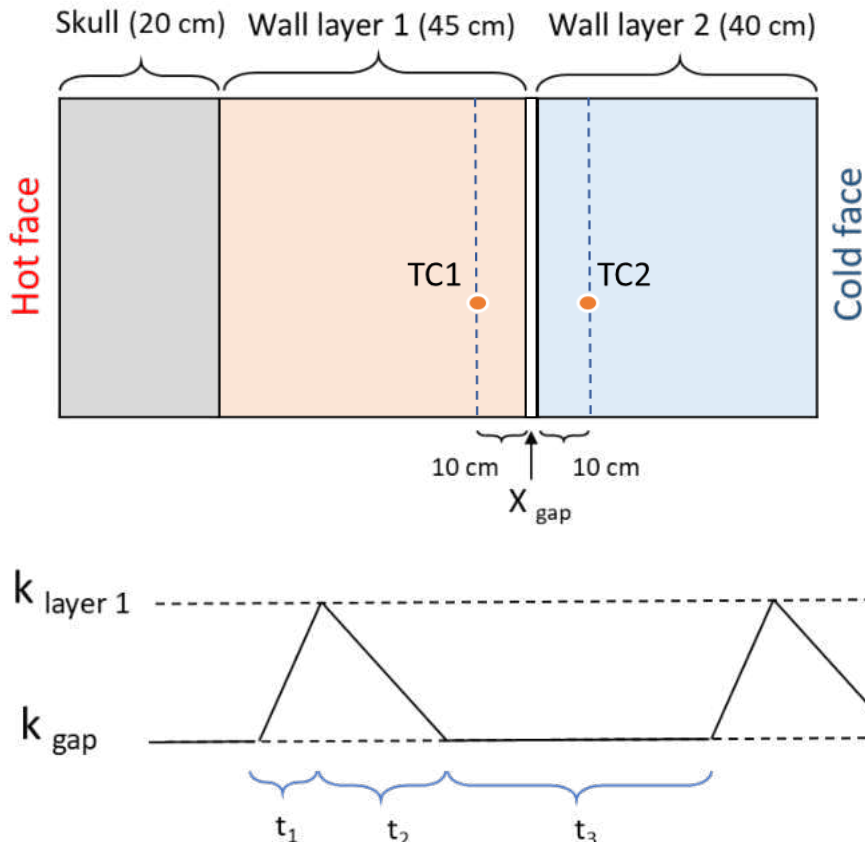


Figure 95: Top: Composite wall setup for testing the hypothesis about a gap between the carbon blocks. Bottom: Gap implemented as a thin layer, the thermal conductivity of which is ramp-wise changed from a low value (k_{gap}) to a high value ($k_{layer,1}$) and back.

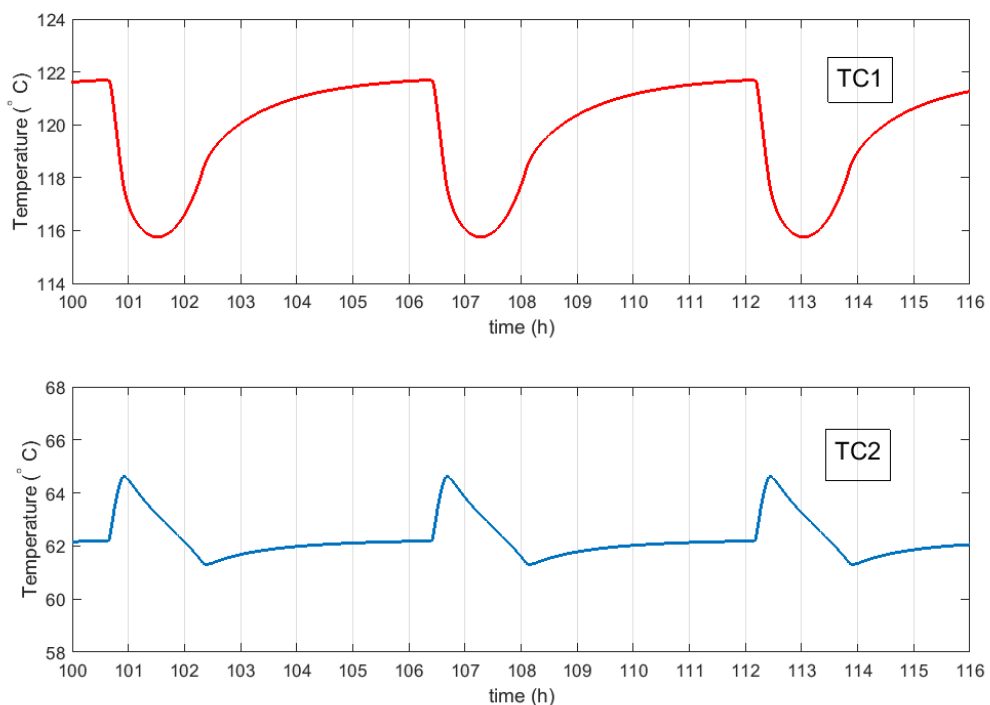


Figure 96: Simulated thermocouple temperatures in the system depicted in the top panel of Figure 95 after repeating the periodic changes in the “gap” conductivity depicted in its lower panel.

In summary, the model-based analysis of short-term changes in the thermocouple signals from the hearth lining have revealed several interesting aspects. For regions where there is good thermal contact between the lining materials, it has been demonstrated that an inverse transient heat conduction model can estimate the hot-face conditions, which can be used to shed more light on

changes in the flow paths of iron in the hearth. Such information can be used in combination with results from a wear model, e.g., to assess whether a coke-free region exists in the BF hearth, and to gain deeper understanding of the complex flow patterns when two tapholes are operated alternately. As indicated in the final analysis of this subsection, it is also possible to use the findings to detect and locate regions with poor thermal contact between the refractory blocks of the hearth lining.

2.2.1.5 Hot metal flow and coke particle movement in BF hearth

2.2.1.5.1 Introduction

This chapter is divided into two parts: part 1, which describes the implemented CFD-DEM model, model validation as well as application to a small-scale blast furnace (BF); and part 2, where a novel approach is presented to model the tapping of full-scale BFs. In the latter, the CFD-DEM model has been utilized to generate realistic porosity distributions, which has been used in another simulation method to approximate the dead man's transient behavior. This enables to simulate several hours of real-time for a full-scale BF hearth, while accounting for the dead man dynamics. Most of the results obtained in part 1 and 2 were published in [1] and [2] respectively.

The BF hearth is a complex area: liquid slag and iron are present along with gas in a packed coke particle bed. To create an accurate CFD model of the hearth, several difficulties must be addressed, such as flow through porous media or conjugate heat transfer [3] and [4]. One can model such a system either with a fully Eulerian approach by treating the particle bed as a porous medium and apply phenomenological models to account for porosity or introduce particles to accurately simulate the discrete phase [5] and [6] (discrete element method DEM).

Since the size of BFs and the resulting huge number of particles are a serious challenge for a DEM-based description, many studies belong to the former, fully Eulerian class and make additional assumptions on the coke bed in general and the dead man in particular. Various CFD models have been used previously to investigate the flow during tapping of the BF [7],[8],[9],[10],[11],[12],[13],[14] and [15]. However, all previous models had a common feature of the dead man being treated as a static porous medium.

The dead man is better described as an inhomogeneous transient as its shape, position and permeability strongly dependent on other BF conditions. In order to better account for its time dependent, inhomogeneous properties, the dead man could be modeled with the DEM where the coke particles are modeled as discrete entities. Previous work with the DEM method has been done in BF research, mainly for investigating raceway- and burden-flows e.g. [16],[17],[18],[19] and [20]. To use the DEM for hearth simulations, the multiple fluids can be described by a volume of fluid (VOF) approach and coupled to the DEM as done for other applications [21],[22] and [23].

In the present work, the problem consists of multiple liquids, gases and solids and a model to simulate this multiphase problem accurately is desired to perform an in-depth study of the BF hearth. Consequently, a CFD-DEM coupled method was implemented that utilizes a VOF method for the multiple fluids. The open source software OpenFOAM, LIGGGHTS and CFDEMcoupling were used to model the fluids, particles and their interactions respectively.

The used modelling part (VOF method) is given in Appendix 3.5.1.

2.2.1.5.2 Experimental validation

Experiments were conducted to validate the implemented model. A rig was set up in which fluids were tapped from a particle-filled tank. The rig was used to measure the mass flow rate as well as to study the dynamic behaviour of the particle bed.

The tank was a transparent box with dimensions 330x150x400 mm. A cylindrical taphole with the diameter $d_{outlet} = 27.5 \text{ mm}$ was located at the bottom of one side. A schematic view of the setup is shown in Figure 97. Because coke particles are buoyant in the BF hearth, wood particles were chosen to be buoyant in water. The particle properties varied between wet and dry, hence the values of a semi-saturated state were used in the simulations.

Two different cases were investigated using the described setup, one sitting- (case A) and one floating-particle bed (case B). The initial water level was set to 300 mm for both cases. For case A, the bed was held down by a grid as shown in Figure 97, while for case B, the grid was removed. In both cases, another grid at the outlet was hindering the particles from flowing out of the tank.

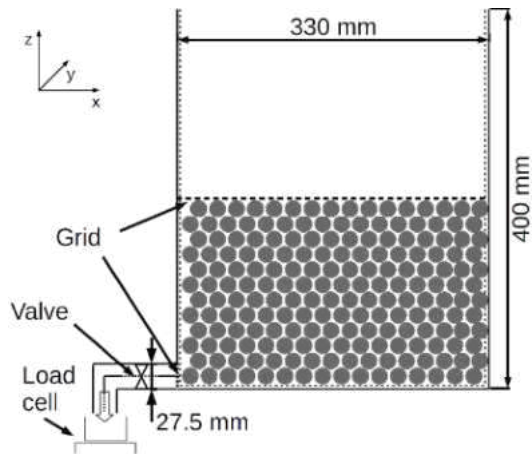


Figure 97: Schematic illustration of the experimental setup, figure from [1].

2.2.1.5.3 Numerical instabilities

Severe stability issues were encountered for the floating bed simulations of lightweight particles. It was reported by Peng et al. [32] that an incorrect calculation of the void fraction causes strong local pressure fluctuations which give rise to this phenomenon. Additional treatment was necessary to simulate the floating particle bed and consequently, we thoroughly evaluated the pressure fluctuations in the simulations using the previously used experimental setup at two probe locations.

It was found in literature that, spatial smoothing approaches by e.g. Pirker et al. [33], Radl et al. [34] and Capecelatro and Desjardins [35], intended to alleviate void fraction fluctuations, which turned out to be insufficient to stabilize our simulations. Hence, a temporal smoothing model was introduced, where high frequency pressure oscillations from the particle force calculations were filtered with a temporal relaxation approach. By doing so the original pressure field was retained for the CFD calculations, while successfully stabilizing the simulations as shown in Figure 98, which shows the evolution of the pressure fluctuations at the two probe locations using various smoothing models. It is evident that in the shown time interval, only the temporal smoothing model succeeded in stabilizing the simulation.

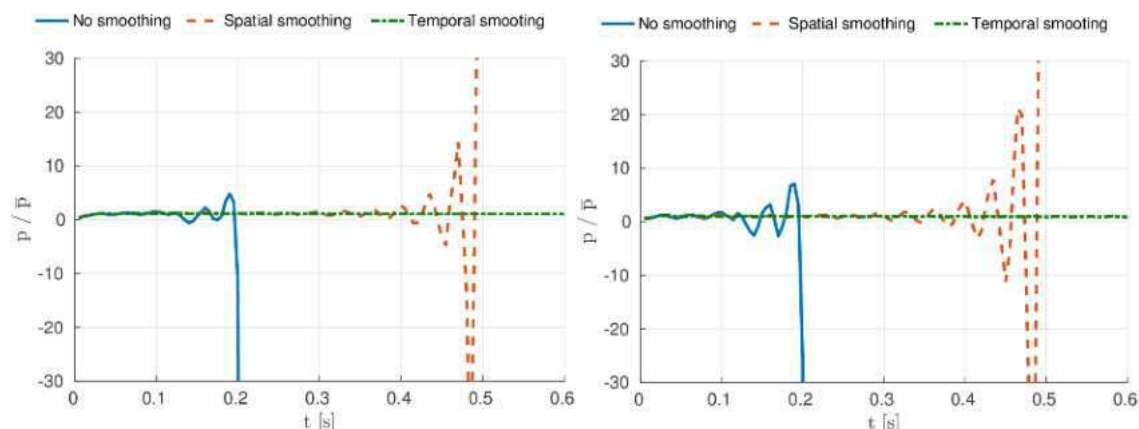


Figure 98: Normalized pressure at probe location 1 (left) and 2 (right) with various smoothing models, figure from [1].

2.2.1.5.4 Simulations results of the experiments

Figure 99 depicts the total mass drained over time from both the experiments and the simulations. The dotted line represents the initial amount of water in the tank. The experimental data is presented by error bars which show the minimum, mean and maximum value of a couple of experimental runs. It can be seen, that the simulations successfully reproduced the drainage pattern observed in the experiments for both cases, with all curves converging towards the expected amount drained.

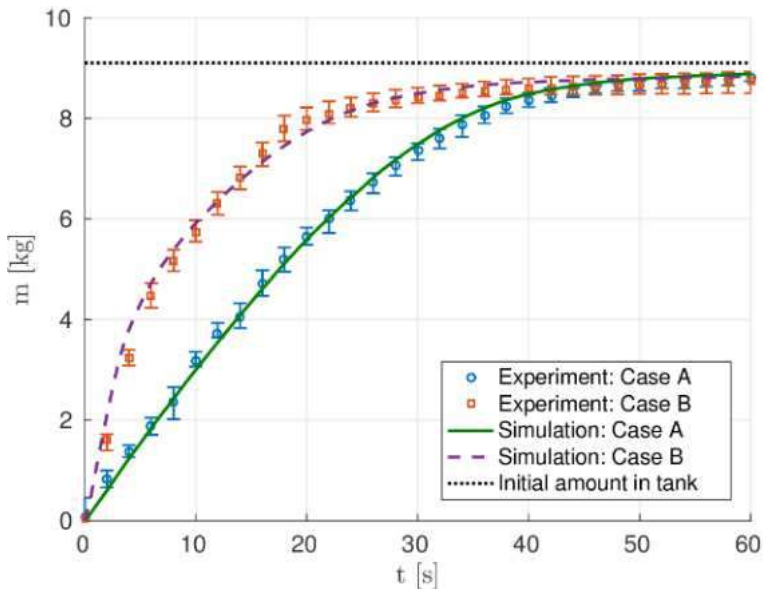


Figure 99:: Total mass tapped over time for the experiments and corresponding simulations, figure from [1].

Figure 100 compares a photograph of the particle structure from the experiment with a snapshot from the simulation. During the bed's descent, particles were dragged to the outlet, which created its distinctive shape.

2.2.1.5 Burden-weight-distribution boundary condition

A detailed simulation of a full BF is very demanding due to the wide range of spatial and temporal scales. For simplicity, only the hearth region has been considered and cut off the remaining parts of the furnace. Consequently, a boundary condition for the burden's weight distribution had to be applied. To do so, it was proposed to establish this boundary condition by employing a set of stress-controlled walls on which forces can be specified. A general pressure distribution can then be approximated as shown in Figure 101.

The proposed boundary condition has been evaluated by comparing simulations with the project partner Ruhr-Universität Bochum (RUB), who had previously performed a CFD-DEM simulation on a scaled slot model of a BF in Dillingen. They investigated the surface pressure experienced by the particles at the top of the hearth and used that data to fit a polynomial with regards to the particle distance to the centre. This polynomial has been approximated by seven stress-controlled walls. Subsequently, the boundary condition has been employed to a simulation of the hearth only. The resulting pressures exerted on the particles at the cut-off location is depicted in Figure 102, where it is compared to the values obtained by RUB. It could be seen that the stress-controlled walls succeeded very well in applying the correct pressures to the particles as obtained by RUB. However, the resulting equilibrium position of the dead man in Figure 103 did not agree with RUB's simulation. It is evident that the surface pressure exerted on the particles does not correctly represent the force required to push down the dead man. This could be ascribed to forces supported by the walls as well as lift forces from the vertical gas flow that are not reflected in the surface pressure. This highlights the difficulty of estimating the burden weight, but improved results could potentially be obtained by scaling the pressure by a certain factor as done by Brännbacka and Saxén [36].

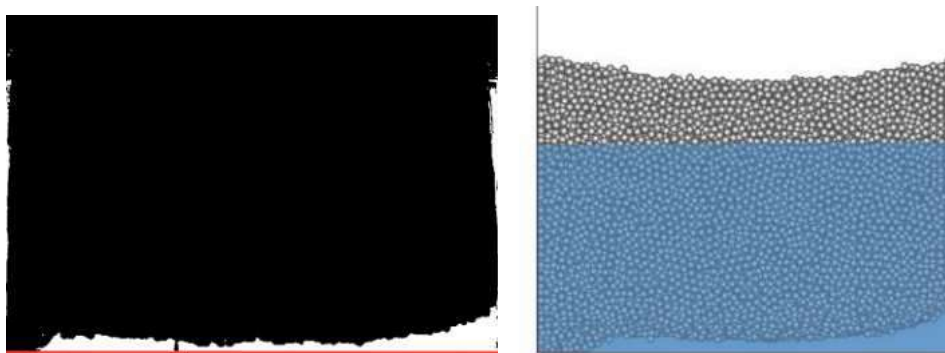


Figure 100: Particle bed structure during drainage for experiment (left) and simulation (right) at $t = 7$ s, figure from [1].

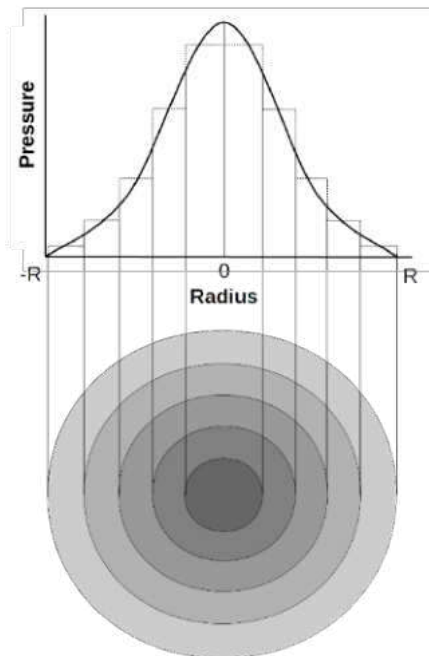


Figure 5
Figure 101:: Burden weight boundary condition, figure from [1].

2.2.1.5.6 Small-scale hearth demonstration case, results

To demonstrate the model, a small-scale BF hearth was set up wherein the tapping of iron and slag was studied. A cylindrical wall was assumed with a radius of 100 mm and a height of 80 mm.

Realistic blast furnace fluid properties were used, taken from Jeong et al. [37]

Table 12), with the initial iron level of 60 mm with a 20 mm thick slag layer. The dead man was composed by approximately 200 000 spherical particles of $d_p = 2.5 \text{ mm}$ and $\rho_p = 1200 \text{ kg/m}^3$.

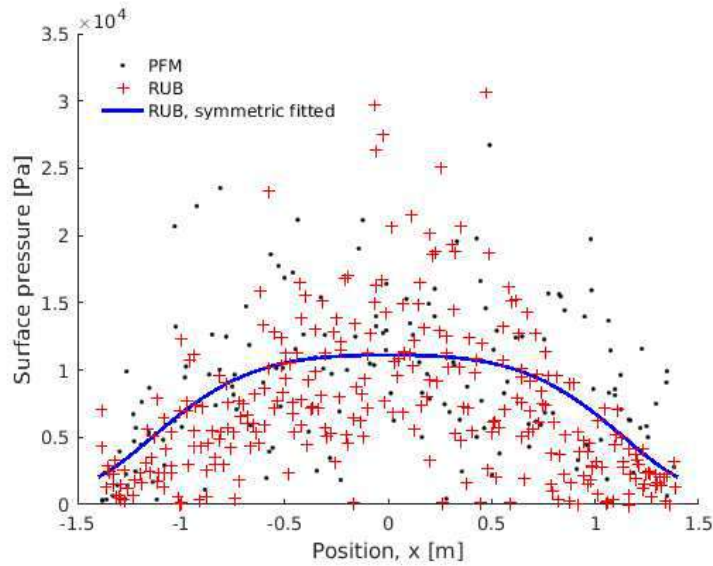


Figure 6
Figure 102: Scatter plot of the particle pressures at the cut-off location, compared with data supplied by RUB.

Initially, the dead man was floating as can be seen in Figure 104 (top-left), where the blue object represents the stress-controlled walls. As tapping began, the fluids were drained, and it could be seen how the dead man descended towards a partially floating state. It was shown how the particles were dragged towards the outlet. Furthermore, the two lower rows depict the velocity fields at a normal and horizontal plane respectively. High fluid velocities in the taphole vicinity were observed as well as significant motion of the fluid beneath the dead man in the coke free zone. Additionally, there was an indication of a circumferential flow which it was presumed to be caused by the higher floating dead man towards the side wall. Furthermore, it was noted how towards the end, the slag interface strongly tilted towards the outlet due to its high viscosity, along with the well-known phenomenon of the iron interface being located below taphole level [4] and [14].

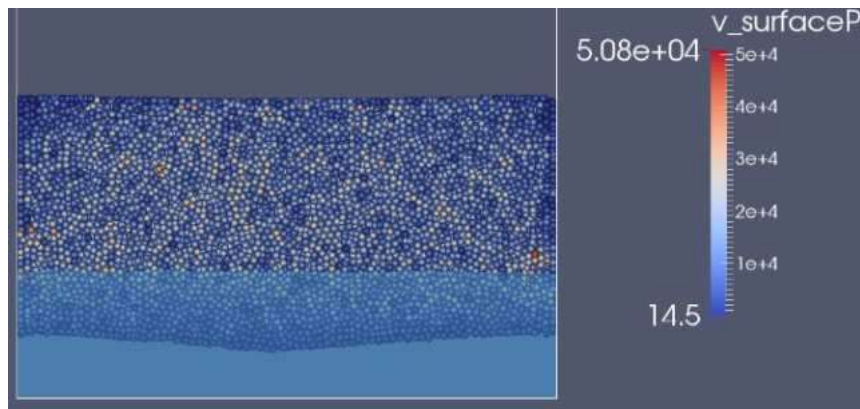


Figure 103: The resulting dead man equilibrium position of the hearth simulation only.

Table 12: Physical fluid properties used in the demonstration case.

	Iron	Slag	Air
$\rho_f(kg/m^3)$	6700	2600	1.5
$\nu_f(m^2/s)$	$1.5 \cdot 10^{-7}$	$1.5 \cdot 10^{-4}$	$1.5 \cdot 10^{-5}$

Figure 105 visualizes the drainage between the dynamic dead man as compared with the dead man being fixed in its initial state. Here we see how the drainage pattern is altered by a higher iron rate and consequently a lower slag one, due to the iron being displaced by the descending dead man. Resultantly, a difference of approximately 10% of the total drained mass was found at the end of the simulation.

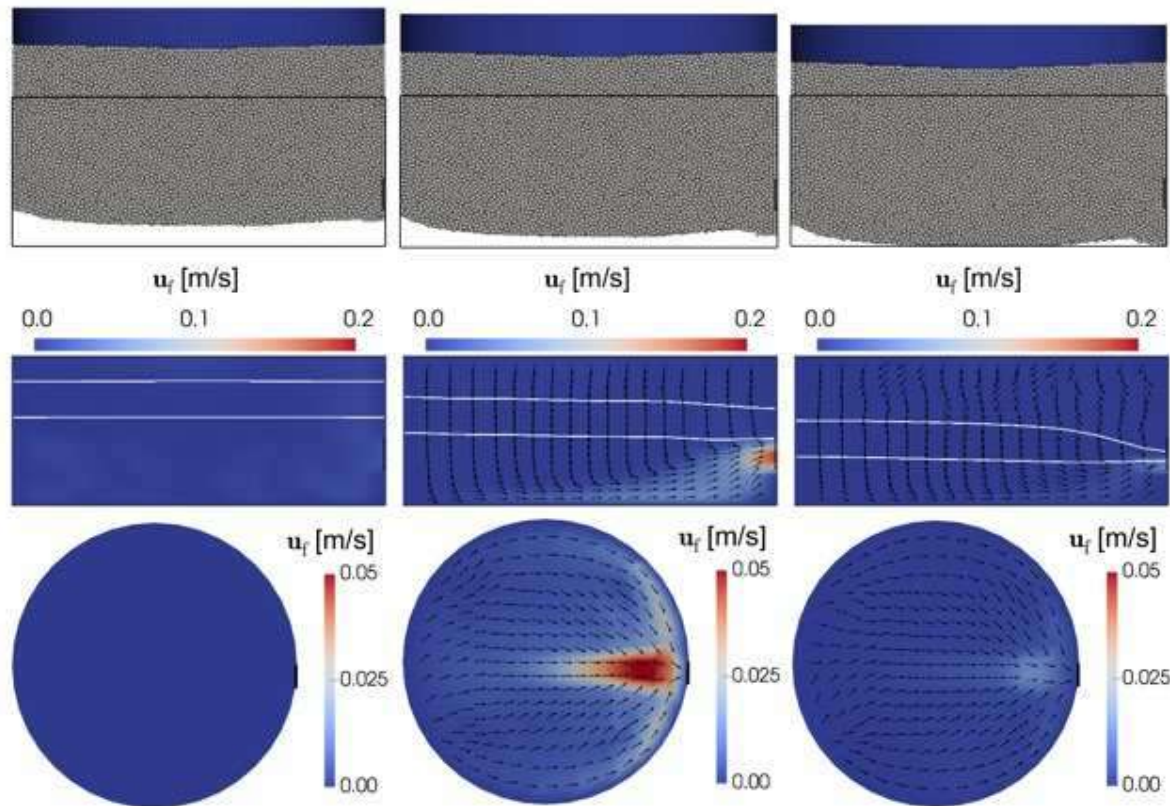


Figure 104: Snapshots of the blast furnace hearth at three different times. The columns represent from left to right $t = 0$ s, $t = 5$ s and $t = 20$ s. The first row shows the dead man and stress-controlled walls while the two lower ones represent the velocity fields at a normal and horizontal plane respectively. The white lines indicate the slag (upper) and iron(lower) interfaces, figure from [1].

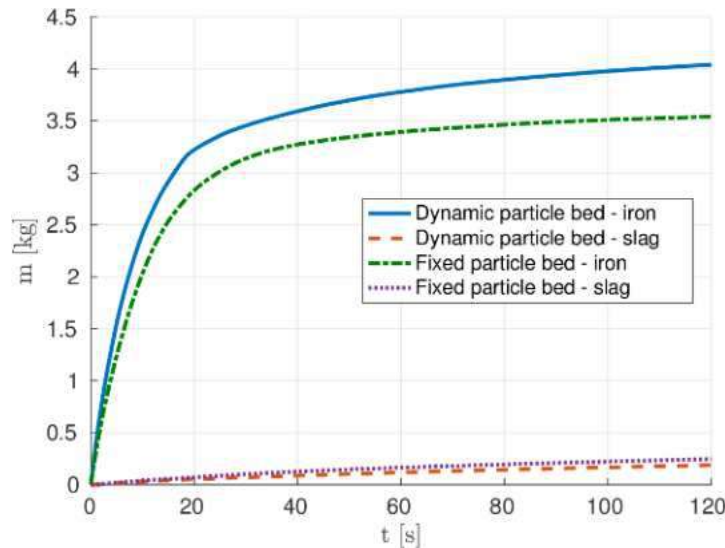


Figure 105: Comparison of the time evolution of the tapped mass for a dynamic dead man and a fixed floating one, figure from [1].

A CFD-DEM coupled model was implemented which was able to simulate the air, iron and slag phases as well as the discrete coke particles. The model was validated against measurements and photographs taken from our performed lab-scale experiments. Subsequently, the model was delivered to the project partners.

Furthermore, the model was demonstrated by employing it to a small-scale BF hearth together with the proposed burden weight boundary condition. Here the drainage was compared with a static floating dead man and highlighted the necessity of taking its movement into account, as it significantly changes the tapping behavior.

While the DEM has several advantages as e.g. automatically giving a dynamic, inhomogeneous description of the dead man, its high computational costs limit its usage in the BF due to huge dimensions along with long process times. To speed up DEM simulations, it is popular to combine several particles into parcels [38],[39],[40] and [41]. However, coupled with CFD it is limited by the mesh resolution. Particularly with the VOF method, a certain fine grid is required to avoid excessive smearing of the fluid interfaces. In part 2 a computational model will be introduced which is intended to enable full scale drainage simulations with a dynamic dead man.

The dynamic void fraction model (part 2) is given in Appendix 3.5.2

2.2.1.5.7 Taphole boundary conditions

According to Nishioka et al. [10], temporal variations of the taphole properties are significant to the drainage rates, where the taphole diameter $d_{t.h.}$ proved to have most impact. While the taphole could be incorporated into the computational domain, also here the computational cost would significantly increase to resolve the flow in it. Hence, it has been chosen to include the taphole effects by imposing time-varying pressure and void fraction boundary conditions at the outlet. An estimated outlet pressure is calculated by $p_{outlet} = p_0 + \Delta p_{t.h.}$, where p_0 is the ambient pressure and $\Delta p_{t.h.}$ the pressure-drop in the taphole. $\Delta p_{t.h.}$ is estimated by the fluid velocity and taphole properties from the Darcy-Weisbach equation [34]:

$$\Delta p_{t.h.} = f_D \frac{u_f^2 \rho_f L_{t.h.}}{2 d_{t.h.}} \quad (29)$$

To account for the taphole expansion, it was modelled to grow linearly as $d_{t.h.} = d_{0,t.h.} + \dot{d}_{t.h.}$, where $d_{0,t.h.}$ refers to the drill diameter and $\dot{d}_{t.h.}$ the erosion rate. Furthermore, f_D is the Darcy friction factor which can be determined from the implicit Colebrook-White equation [35], or as we did for simplicity, approximated by Haaland's [44] explicit correlation.

While the outlet pressure was calculated with a varying taphole size, actual variations of the outlet size had to be considered. Previously, the $\partial_n \epsilon|_{outlet} = 0$ boundary condition has been used with success, which implies that the drainage rate is governed by the effective outlet area $A_{eff} = \epsilon A_{outlet}$ where ϵ is the void fraction in front of the taphole. Consequently, the ϵ has been altered at the outlet boundary as:

$$\epsilon \rightarrow \epsilon \frac{A_{t.h.}}{A_{outlet}} \quad (30)$$

where $A_{t,h}$ is calculated from the specified taphole diameter, and A_{outlet} is the fixed mesh-based outlet area.

To evaluate the dynamic void fraction model, simulations were performed on the previously shown experimental setup (Figure 97). Similarly, both the sitting and floating particle bed were studied and compared the CFD-DEM model's results. Figure 106 depicts the drainage for the sitting and floating particle bed cases for both models. As expected, a perfect agreement could be seen for the sitting particle bed case, which affirms that the drag force was correctly implemented. In the floating particle bed case, a slight deviation was observed, occurring as the particles reached the outlet. This deviation attributes to the zero-particle velocity assumption, which caused an over-estimation of the drag force. Although the deviation was small, it was expected to be less prominent in the BF simulations where the particle velocities are much lower.

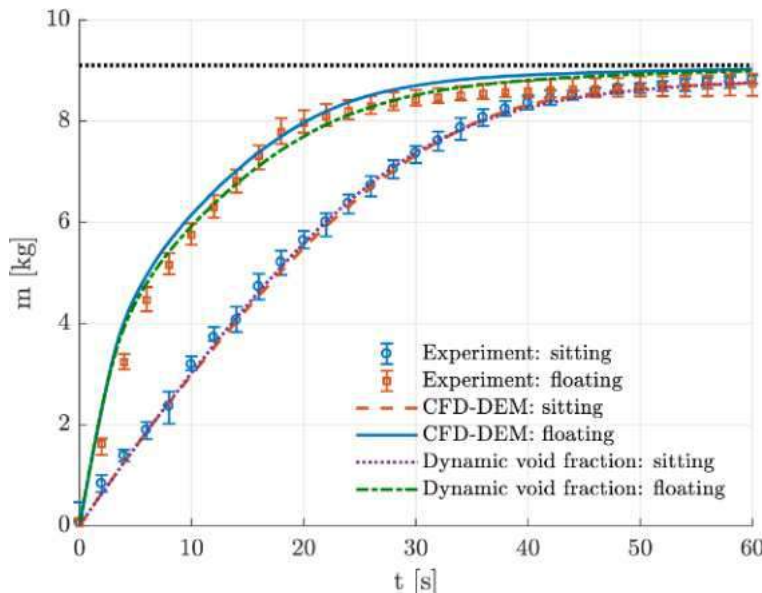


Figure 106: Drained mass over time for the CFD-DEM model and dynamic void fraction model compared with the experiments, where the simulations are visualized by lines and the experiments by symbols, figure from [2].

2.2.1.5.8 Demonstration case of full-scale BF hearth

In this section, the dynamic void fraction model has been used for generating the dead man states. An isothermal BF hearth is assumed to run the long-term simulations faster. Two dead man setups have been studied: a uniform one (mono-size particles with $d_p = 60 \text{ mm}$) and a dense core one with smaller particles in the center ($d_p = 30 \text{ mm}$), to emulate the effect of particle degradation and fragmentation due to poor coke quality and high mechanical stresses.

Similar as in section 3.2.5.1.6, the hearth is modelled as a cylinder, here with the diameter $d_{hearth} = 12 \text{ m}$ and the height $h_{hearth} = 5.8 \text{ m}$. An important advantage of the dynamic void fraction model is that it allows for mesh refinement to obtain a higher resolution of the flow field, whereas the CFD-DEM model is limited by the particle size to obtain a proper average representation of the particles [45],[46] and [47].

The burden weight was approximated by the method presented in section 3.2.1.5.5. Eight short-term simulations were performed with the initial liquid levels ranging between $z_{0,iron} = 1.75 - 3.5 \text{ m}$ and $z_{0,slag} = 2.25 - 4.0 \text{ m}$. A summary of the used CFD and DEM simulation parameters are listed in Table 13 and Table 14.

Table 13: List of simulation parameters for the fluids.

Property	Value
$\Delta_t [s]$	$5 \cdot 10^{-3}$
$\rho_{iron} [kg/m^3]$	7000
$\rho_{slag} [kg/m^3]$	2400
$\rho_{air} [kg/m^3]$	1.0
$v_{iron} [m^2/s]$	$8.7 \cdot 10^{-7}$
$v_{slag} [m^2/s]$	$1.25 \cdot 10^{-4}$
$v_{air} [m^2/s]$	$1.3 \cdot 10^{-5}$
$\sigma_{iron} [N/m]$	1.65
$\sigma_{slag} [N/m]$	0.5

For the long-term simulations with the dynamic void fraction model, a specified initial iron level $z_{0,iron} = 2.5 m$ was used and a slag layer thickness $h_{0,slag} = 1.0 m$, with a constant iron production rate $\dot{m}_{iron} = 150 t/h$ and a slag ratio $\gamma = 300 kg/thm$. The fluid properties remained the same as in the short-term simulations.

Table 14: List of simulation parameters for the particles.

Property	Uniform	Dense core
$\Delta_p [s]$	$2.5 \cdot 10^{-4}$	$1.25 \cdot 10^{-4}$
$\rho_p [kg/m^3]$	1000	1000
$d_p [mm]$	150	75 / 150
$N_p [-]$	$\sim 230\,000$	$\sim 460\,000$
$CG [-]$	2.5	2.5
$\xi [-]$	1.0	1.2 / 1.0
<i>Young's modulus, E [Pa]</i>	$1.0 \cdot 10^8$	$1.0 \cdot 10^8$
<i>Poisson's ratio, ν_p [-]</i>	0.45	0.45
<i>Coefficient of restitution, e [-]</i>	0.3	0.3
<i>Coefficient of friction, μ_p [-]</i>	0.5	0.5

The resulting velocity fields for a fixed floating and sitting dead man (upper row) are presented together with velocities from the dynamic simulation (early on in the simulation to the left, towards the end of the tap on the right) in Figure 107. While quite uniform flow towards the taphole was seen in the sitting dead man case. High fluid velocities were observed in the coke free zone using a floating dead man, which is in good agreement with the isothermal results by Guo et al. [8]. In the dynamic case, the flow field initially looks similar to the floating dead man case, while towards the end of the tap it is altered due to the changed coke free zone.

Furthermore, Figure 108 visualizes the iron and slag flow rates for a fixed floating dead man compared with the dynamic simulation. Here large differences were observed, where the descending dead man seemingly caused an increased iron flow, and consequently a decreased slag one, due to large fluid displacements caused by the moving dead man. This did not only prolong the slag delay, but also extended the tapping duration by ca. 20 min.

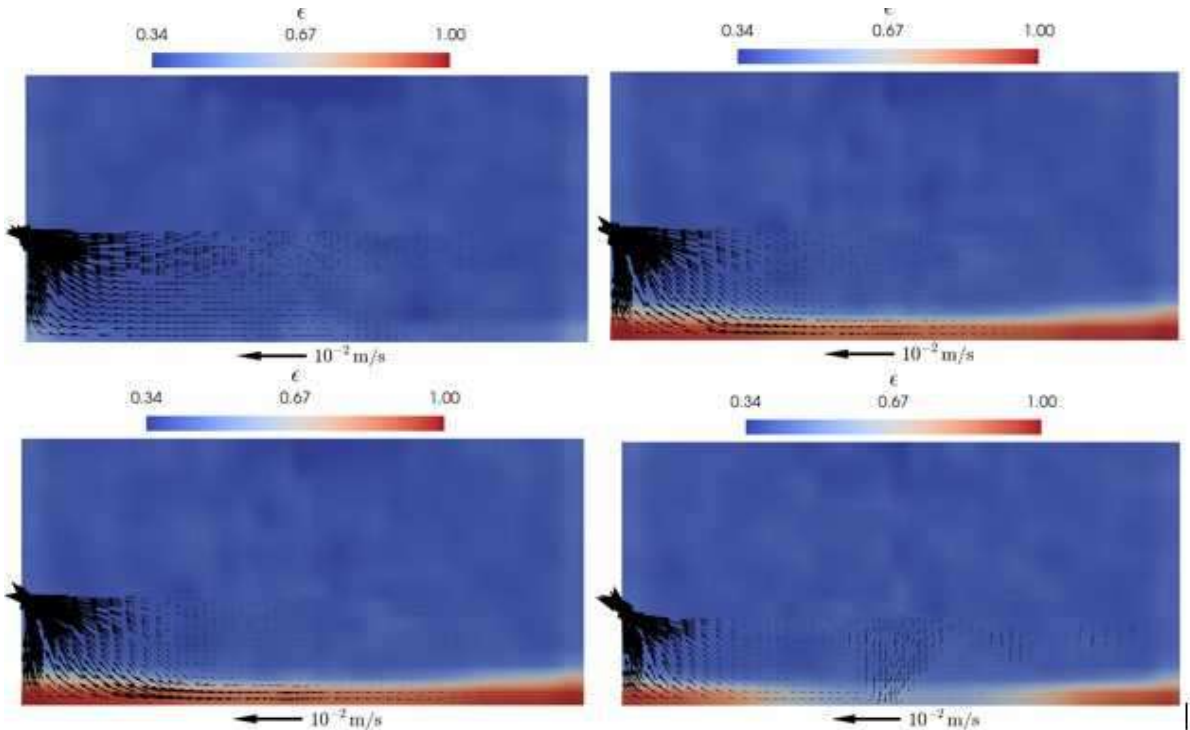


Figure 107: Hot metal velocities for a fixed sitting and floating dead man (upper left and right respectively), as well as with the dynamic void fraction model early and late (lower left and right respectively) during the simulation, figure from [2].

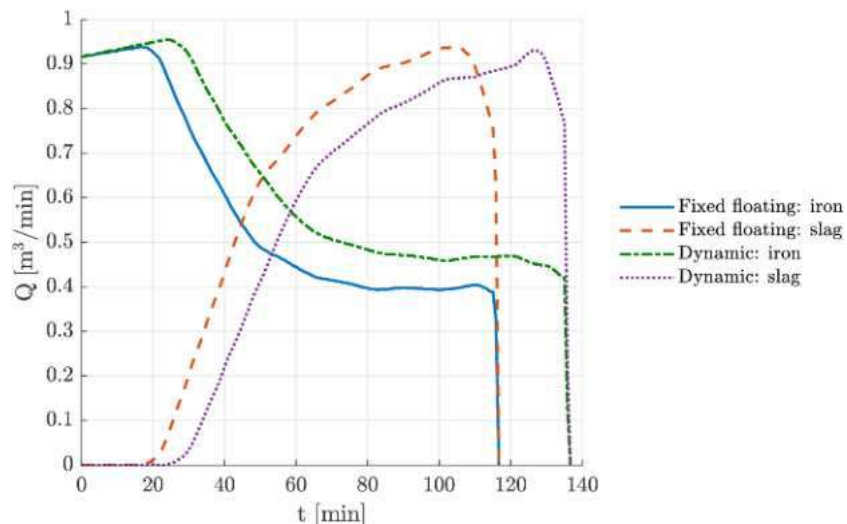


Figure 108: Comparison of volumetric flow rates for a dynamic and a fixed floating dead man, figure from [2].

As previously stated, various morphologies were studied by incorporating a less permeable centre. Mainly, it was to stress the model's ease of introducing large inhomogeneities to the porosity caused by various particle sizes. The horizontal velocity fields for the two dead man formations are shown in Figure 109 at taphole level. Here it can be seen how the smaller particles decreased the permeability, which as expected generates a peripheral flow.

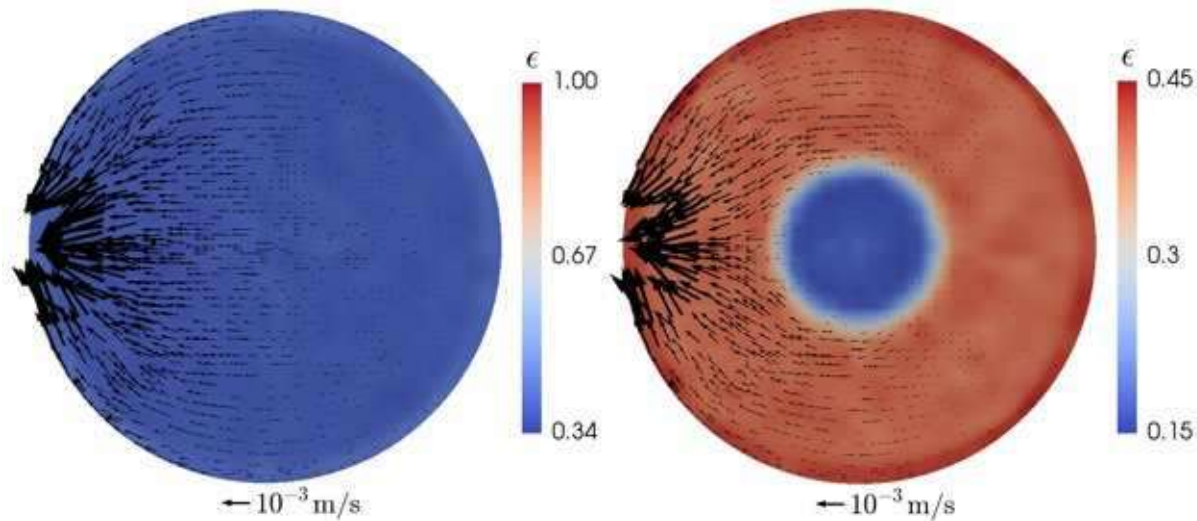


Figure 109: Flow fields on a horizontal plane at taphole level for a uniform and a dense core dead man (left and right respectively). The less permeable center give rise to a peripheral flow pattern, figure from [2].

2.2.1.5.9 Application to voestalpine's BF5

To further strengthen the model's validity, actual operational data from the project partner voestalpine's BF 5 was evaluated. The BF in question is of smaller kind and is chosen to employ the model to this particular one because it is a single taphole BF with significantly longer inter-tapping periods than the larger, multi-taphole ones. The longer inter-tapping periods should cause greater variations of the liquid levels, which makes it suitable for the model.

Similar as in section 3.2.1.5.8, the hearth was modelled as a cylinder with the hearth diameter $d_{hearth} = 8 \text{ m}$ and the height $h_{hearth} = 5 \text{ m}$. The initial iron level was $z_{0,iron} = 2.5 \text{ m}$ with an initial slag thickness of $h_0 = 0.5 \text{ m}$. The gas pressure applied to the top boundary was set to $p_{top} = 1.3 \text{ bar}$. The previously used uniform dead man composed of particles with $d_p = 60 \text{ mm}$ was used, and the remainder of the fluids' properties and simulation parameters were equal to the previous simulation. Parameters used for the taphole boundary conditions were obtained from the supplied operational data as averaged quantities.

Data for measured iron mass flow rate was supplied for several tappings which could be used for comparison. Figure 110 shows the measured iron mass flow rate for two selected tapping periods with similar duration as obtained from our simulations. In both figures for the measured values, an initial sharp increase of iron flow rate is noticed, until reaching a constant level, until it reduces when the slag began to exit the taphole. In the left figure, it is evident that the timing of the slag delay was not perfectly captured, which indicates that the specified initial iron level was too low, while in the right one it is very accurately estimated. However, in both figures the two "plateaus" of flow rates occurring for the pure iron flow, and the mixed iron-slag one was predicted well.

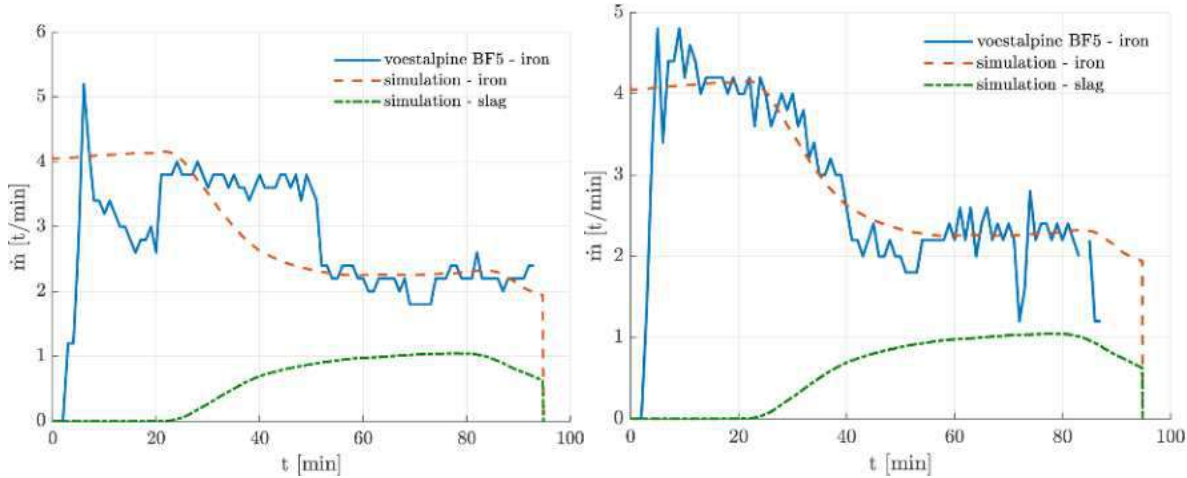


Figure 110: Simulated mass flow rate compared with measured ones from voestalpine's H05. The two figures represent two different tapping periods. In the right figure, we find an overall good agreement while in the left one, the slag delay is poorly captured. However remarkably, we managed to seemingly accurately predict the two drainage rate plateaus of pure iron and iron-slag mixed flows.

While good results were obtained for the selected tapping periods, it should be stated that there were also several ones where bad agreements were reached. Of course, in the actual BF, the input parameters e.g. fill levels and taphole properties are not constant and vary for each tap. To obtain an even better evaluation of the model, several consecutive tapping cycles should have been performed until the system had reached a quasi-steady-state, but due to time limitations and computational effort required, this was not feasible. Additionally, a crucial parameter determining the flow rate is the permeability of the dead man. As arbitrary values were used for particle sizes and burden weight distribution, it is remarkable that such a distinguished agreement was obtained.

2.2.1.5.10 Heat transfer extension

So far, we had only considered modelling of BFs under isothermal conditions, although it was shown by refs. [8] and [48] that natural convection due to temperature variations in the hot metal can significantly alter the flow pattern in the hearth. In order to work towards a more complete model, an extension is proposed wherein the effect of natural convection is incorporated in the simplest manner by the means of the Boussinesq approximation [49].

By assuming small density variations, they only affect the flow through buoyancy. Thus, the governing equations can be solved with a constant reference density and the natural convection modelled with an additional source term in the momentum equation as:

$$F^B = \Delta\rho_f g = -\rho_{f,0}\beta(T_f - T_0)g, \quad (31)$$

where T_f and T_0 are the fluids' temperature and reference temperature respectively. Furthermore β denotes the thermal expansion coefficient.

It is evident that even though there has been chosen for a very simplified model for the natural convection, the fluids' temperature evolution needs to be considered. Continuing in the line with the dynamic void fraction model in an Eulerian framework, transport equations have been introduced for both the fluid T_f and particle T_p temperatures as:

$$\frac{\partial(\epsilon\rho_f T_f)}{\partial t} + \nabla \cdot (\epsilon\rho_f u_f T_f) = \frac{1}{c_{p,f}} [\nabla \cdot (\epsilon\kappa_f^* \nabla T_f) - Q^{pf} + Q^{prod}] \quad (32)$$

$$\frac{\partial(\epsilon_p \rho_p c_{p,p} T_p)}{\partial t} = \nabla \cdot (\epsilon_p \kappa_p^* \nabla T_p) + Q^{pf}, \quad (33)$$

where κ^* denotes the effective heat conductivity, c_p the specific heat capacity and Q^{pf} the inter-phase heat transfer [50]. Furthermore, Q^{prod} denotes the heat source due to produced hot metal and slag, treated similarly as S_p , and is defined as

$$Q_{iron}^{prod} = T_{prod} c_{p,iron} \dot{m}_{iron} \text{ and } Q_{slag}^{prod} = T_{prod} c_{p,slag} \gamma \dot{m}_{iron}.$$

Similar as the other fluid properties, $c_{p,f}$ and κ_f are represented by the phase averaged mixture quantities. Due to the presence of a granular phase, the thermal conductivities are represented by

the effective κ_f^* and κ_p^* , adjusted by the void fraction according to the models of Syamlal & Gidaspow [51] and Zehner & Schlünder [52] respectively.

The fluid-granular heat transfer is governed by the source term Q^{pf} defined as:

$$Q^{pf} = h(T_f - T_p) \quad (34)$$

where h denotes the heat transfer coefficient, calculated with the particle Nusselt number which was estimated from Gunn's [53] correlation.

The heat transfer model was evaluated by applying it to the demonstration case from section 3.2.1.5.8 with the included temperature fields and momentum source. The used thermophysical properties are listed in Table 15. Furthermore, the initial temperatures $T_f = T_p = 1500^\circ\text{C}$ were used throughout the whole domain, with fixed value boundary conditions at the walls of $T_{wall} = 1400^\circ\text{C}$ and an estimated $T_{prod} = 1550^\circ\text{C}$ for the produced hot metal and slag.

Table 15: List of thermophysical properties used.

	Iron	Slag	Coke
$c_p [\text{J}/\text{kgK}]$	825	1840	850
$\kappa_f [\text{W}/\text{mK}]$	33.3	0.864	9.85
$\beta[1/\text{K}]$	$1.37 \cdot 10^{-4}$	0	0

Figure 111 shows the fluid temperature distribution at a cross-section normal to the outlet at an initial stage as well as towards the end of the tap. The hot metal with a high thermal conductivity rapidly cooled down close to the lower wall where a coke free zone was present. Where the dead man was located, it was observed that the iron still cooled down relatively fast compared to the slag. It is clear, that the included fluid-dead man heat transfer slowed down the process as heat had to be removed from the dead man. The slag on the other hand, with its high specific heat capacity and low thermal conductivity, experienced very slow variations of the temperature. However, some strange behaviour of the temperature was seen just above the iron-slag interface. It appears as that the slag temperature in the place where iron was previously present, maintained a similar temperature as the iron.

Also, the effect of the implemented Boussinesq approximation was investigated for natural convection by studying the velocity field at a similar plane which is presented in Figure 112. Initially, the flow looks, as expected, very similar to the isothermal one in Figure 107 whereas towards the end of the tap they differ significantly. It was noticed that almost no flow came towards the taphole from deeper levels of the hearth. Additionally, a recirculation-like behaviour of the hot metal was seen, where relatively high fluid velocities are present in the coke free zone towards the centre, where upwards fluid motion was found. Using the exception of some strange velocities in the corners, the results agree well with the observations by Post et al. [48].

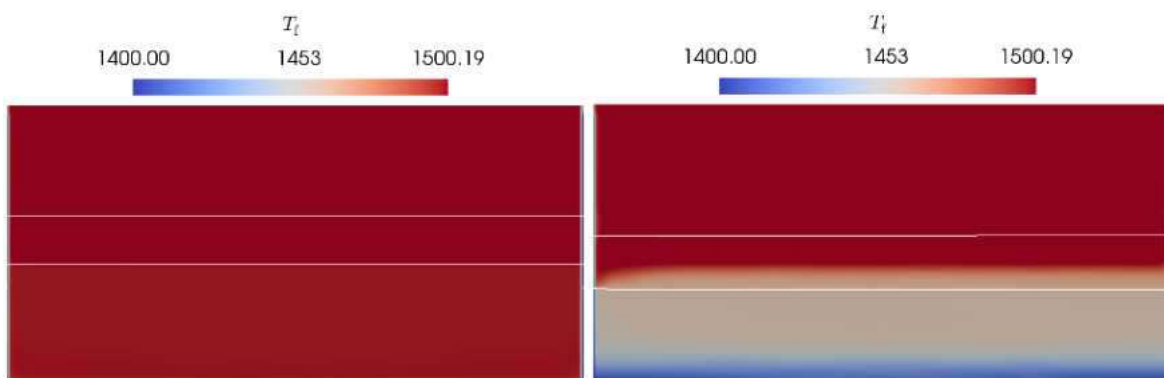


Figure 111: Fluid temperature distribution at a cross-section normal to the outlet (located on the left side) early during the simulation (left) and towards the end (right). The white lines indicate the air-slag (upper) and iron-slag (lower) interfaces. It is seen, that the iron close to the lower wall cooled down rapidly at the coke free zone, which propagated well in the iron with a high thermal conductivity.

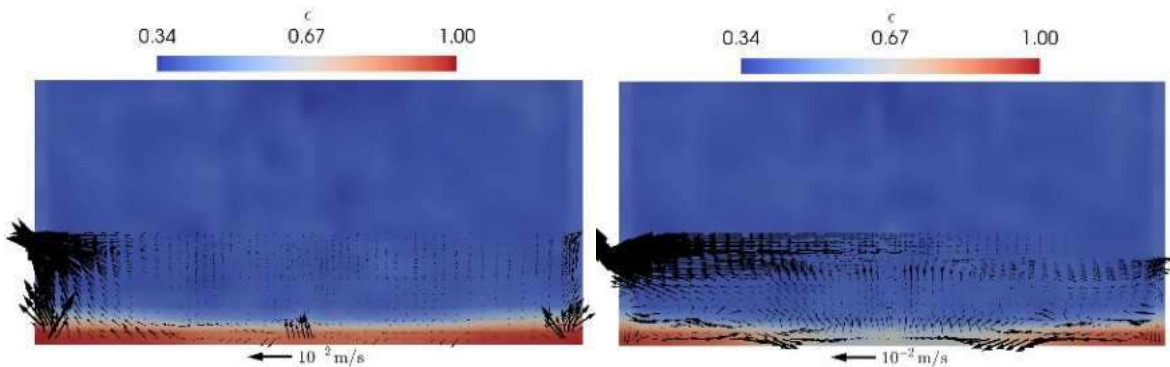


Figure 112: Velocity fields at a cross-section normal to the outlet (located on the left side) early during the simulation (left) and towards the end (right). It is seen, that initially the flow field looks very similar to the non-isothermal one (Figure 107), whereas towards the end of the tap, due to the vertical temperature variation, the flow field changed significantly.

At a first glance, the results look promising as we obtained comparable results as found in literature. However, the model should undergo future validation to ensure that it yields satisfactory results. Especially the Boussinesq approximation is strongly limited to small temperature variations and its validity should be thoroughly analysed. However, we have set up a framework for such studies, which allows for example for modelling of solidification, e.g. by locally altering the void fraction based on a solidification temperature

2.2.1.5.11 Summary and conclusion

A CFD-DEM coupled model was implemented which was able to simulate the air, iron and slag phases as well as the discrete coke particles. The model was validated against measurements and photographs taken from our performed lab-scale experiments. Subsequently, the model was delivered to the project partners.

Furthermore, the model was demonstrated by employing it to a small-scale BF hearth together with the proposed burden weight boundary condition. Here the drainage was compared with a static floating dead man and highlighted the necessity of taking its movement into account, as it significantly changes the tapping behavior.

While the DEM has several advantages as e.g. automatically giving a dynamic, inhomogeneous description of the dead man, its high computational costs limit its usage in the BF due to huge dimensions along with long process times. To speed up DEM simulations, it is popular to combine several particles into parcels [38],[39],[40] and [41]. However, coupled with CFD, it is limited by the mesh resolution. Particularly with the VOF method, a certain fine grid is required to avoid excessive smearing of the fluid interfaces.

The dynamic void fraction model was presented, intended to enable full-scale BF simulations of full tapping periods, while still accounting for the transient dead man behavior. The dynamic void fraction model was demonstrated on a full-scale isothermal example BF with two different dead man configurations: a mono-sized uniform one, and a dense-core one. The dynamic void fraction model enabled us to simulate much longer time scales than the CFD-DEM model, especially in the poly-disperse case where a speed-up was experienced of 5 despite a heavily refined mesh. Additionally, the model was employed to a real BF, namely voestalpine's BF5. Despite several assumptions to the dead man as well as to the liquid levels, good results were obtained, compared to the measured iron flow rate in the plant, suggesting that the model yields reasonable results.

2.2.1.5.12 CFD MOHDRAIN 2.0

The aim of the task was to develop a multiphase CFD model to simulate liquid metal and slag flow in BF hearth and describe effects of tapping as well as impact of tapping practices. The goal of the model was to deliver a real-time estimation of 3D shapes of metal/slag and slag/gas interfaces to operators for a better anticipation of slag arrival and tapping end.

The CFD model to simulate process events such as instantaneous production of liquids and tapping rates was developed. The effect of the coke bed shape and permeability on liquid flow in the hearth was modelled. Multiphase approach to take liquid metal, slag and gas phase into account is another feature of the model.

The CFD model called MOHDRAIN 2.0 was developed employing OpenFOAM. The choice of this package is based on several considerations. Firstly, it is the open source software which provides a researcher with immense flexibility in CFD modelling. Secondly, OpenFOAM has a large user base across most areas of engineering and science where it is reported to be a trusty tool for solving CFD problems. Thirdly, OpenFOAM is continuously enhanced and supported by an established organisation since 2004 which indicates that the software will be maintained in the future. Fourthly,

OpenFOAM users established a wide community which shares the experience of modelling, troubleshooting, and other information. In addition, OpenFOAM is well documented and the training and consulting can be provided on demand.

The CFD problem to be solved within this task is a multiphase flow in porous media. The standard solvers of OpenFOAM [85] cannot handle the multiphase flow in porous media. OpenFOAM was regarded as a framework for developing executables using pre-built or user extended applications. As such, using some pre-requisite knowledge of the underlying method, physics and programming techniques involved, the user can adapt models and create solvers freely [86]. Considering this, the pre-built solvers of OpenFOAM 2.7 called *multiphaseInterFoam* and *porousInterFoam* were used to create a new solver which satisfies the requirements of the model. Thus, *multiphaseInterFoam* is a solver for n incompressible fluids which captures the interfaces and includes surface-tension and contact-angle effects for each phase [85]. While *porousInterFoam* is a solver for 2 incompressible, isothermal immiscible fluids using a VOF (volume of fluid) phase-fraction based interface capturing approach, with explicit handling of porous zones [85]. Thereby, it was necessary to create new solver which combines features of these two. The created solver solves the transport equations for n phases in a porous media using VOF method. The solver allows modelling the gas, slag, and hot metal interactions while draining through the dead man during the tapping.

The following assumptions were taken to build the model:

- Hearth is represented as a 3D fixed geometry domain.
- Hexahedral mesh is applied with the possibility to customise it.
- Homogeneous porosity is assumed for the whole domain with the possibility to have areas of different porosity.
- Inflow of slag and hot metal is simulated as a dilation of phase fields, i.e. there is no inlet for these phases.
- Inflow of gas is done through an inlet situated on the top surface of the domain.
- Phases are considered incompressible, isothermal immiscible fluids.
- Mass and heat exchanges between phases are ignored.

Porous media were implemented in the OpenFOAM v6 *multiphaseInterFoam* solver by adding a source term S_i to Navier-Stokes equation and attenuating the time derivative by a factor as described by the following equation:

$$\frac{\partial}{\partial t}(\varepsilon\rho U_i) + U_j \frac{\partial}{\partial x_j}(\rho U_i) = -\frac{\partial p}{\partial x_i} + \mu \frac{\partial \tau_{ij}}{\partial x_j} + S_i \quad (35)$$

where ε is porosity of the medium, dimensionless.

ρ is density of the phase, kg/m³.

U is velocity of the phase, m/s.

p is pressure of the phase, Pa.

μ is dynamic viscosity, Pa·s.

τ is stress tensor.

S_i is a source term.

The Darcy-Forchheimer equation describes the source term S_i . For a simple homogenous porous medium S_i is written as the following equation:

$$S_i = -\left(\mu D + \frac{1}{2}\rho|U_{jj}|F\right)U_i \quad (36)$$

where D is viscous loss term.

F is inertial loss term.

The viscous loss term D comes from Darcy equation. Having assumed a laminar flow during the hearth drainage, inertial effects become insignificant and thus the term F is removed. Using Kozeny-Carman equation the final equation for the source term S_i becomes the following:

$$S_i = -\mu \frac{180(1-\varepsilon)^2}{d_p^2 \varepsilon^3} U_i \quad (37)$$

where d_p is a particle diameter, m.

Liquid flow in the hearth is a continuous process with intermittent events such as casting (tapping) and hearth filling (inter-cast period). The outflow is modelled by introducing the outlet, while the inflow was implemented in an original way. The management of the liquid inflow is done by means of a so-called phase dilation. The dilation means that the vector containing the volume fraction of each phase in a cell is multiplied by the dilation coefficient K_{phase} . The dilation coefficients for each

phase are calculated via multiplying the flux of the phase by the delta time between simulation steps and dividing by the total volume of each phase as shown in the equation (38).

$$K_{phase} = \frac{Q_{phase} \cdot dt}{V_{phase}} \quad (38)$$

where Q_{phase} is the volumetric flow rate of the phase (hot metal, slag, gas), m^3/s ; V_{phase} is the total volume of the phase at a given moment, m^3 .

The total volume of each phase is calculated by taking the sum of the product of the volume field of the mesh and the phase field.

The phase field is dilated by simply taking the product of the current phase field with the dilation coefficient.

$$phase_{field} = phase_{field} \cdot (1 + K_{phase}) \quad (39)$$

A correction in the pressure equation is required to take into account this direct modification of the volume fields. The first step is to calculate the increase in volume of each phase during the time step and combining them into a total volume increased field `volscalarField`.

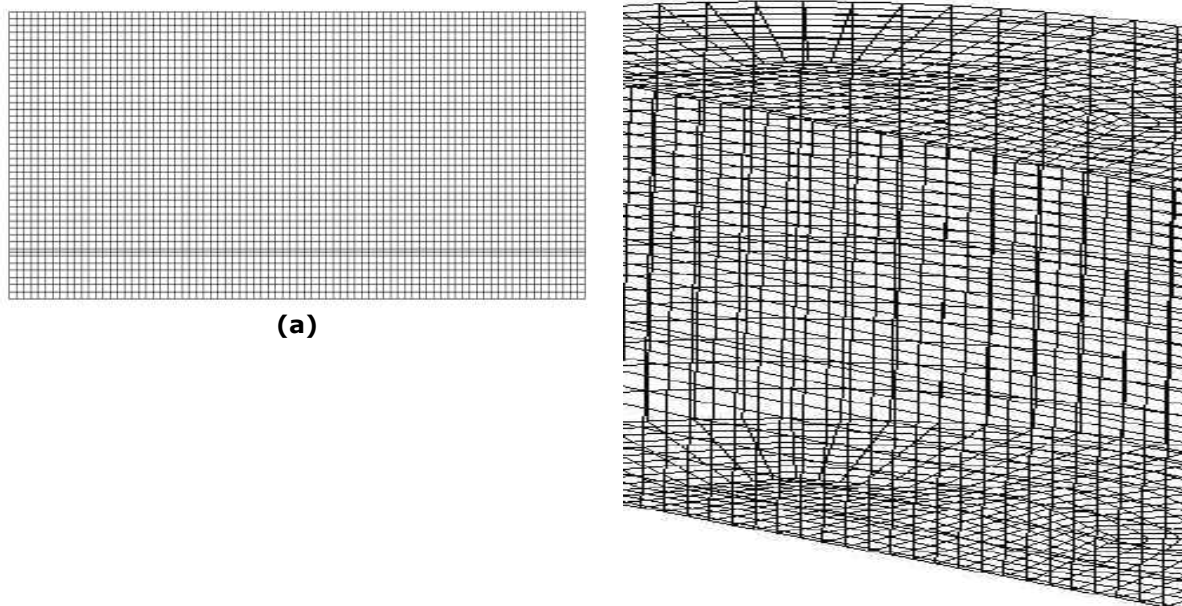
$$\frac{dV_{phase}}{dt} = phase_{field} \cdot K_{phase} \quad (40)$$

This increased total volume also needs to be divided by the case porosity field in order to correctly account for it.

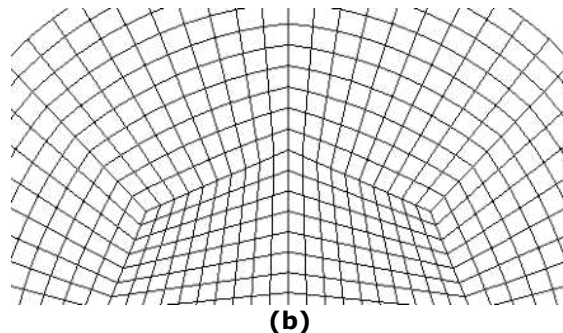
Two domains were used in the model:

- two-dimensional domain for the solver validation, and
- three-dimensional domain representing a real scale simplified hearth of an industrial blast furnace.

The 3D domain covers a 180° sector of the hearth, thus representing a half of the hearth volume. The domain boundaries are set to be the hearth wall, bottom, arbitrary chosen upper surface, and vertical surface of hearth symmetry. The domain is meshed using structured hexahedral elements. The details of the meshing of both domains are given in Figure 113.



Parameter	2D domain	3D domain
Mesh elements	Hexahedral	Hexahedral
Number of mesh elements	3360	19840
Maximum skewness	$6.08595 \cdot 10^{-14}$	0.628925
Mesh non-orthogonality		
Maximum	0	41.1703
Average	0	10.6173



(c)

Figure 113: 2D mesh of validation case (a), 3D mesh of the industrial cases (b), and mesh details (c).

MOHDRAIN 2.0 consists of core and controller (Figure 114). The controller handles the data exchange with core and controls its execution. The controller is built using Python 2.7 and requires Pandas, Numpy, and Matplotlib libraries. The core is realised in OpenFOAM v6. MOHDRAIN 2.0 runs in operational system Ubuntu 18.04 LTS.

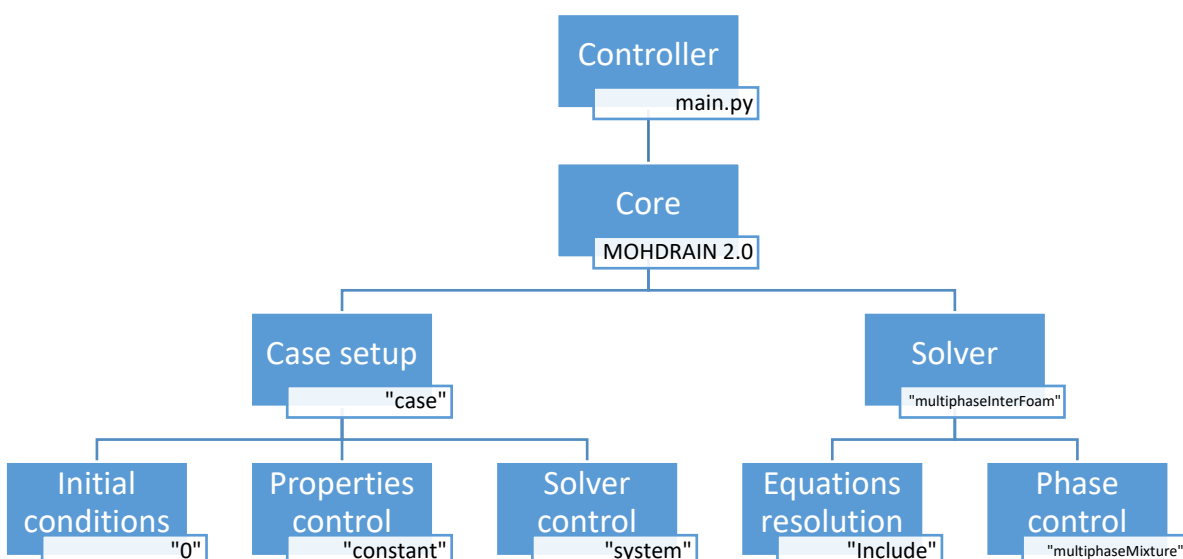


Figure 114: Structure of MOHDRAIN 2.0.

The controller is aimed at creation of cases, their set-up, and execution. Although MOHDRAIN 2.0 handles the casting data off-line presently, yet the controller is built to be flexible to also process the on-line data. In this study, the controller was set to handle the casting data which are fed to MOHDRAIN 2.0 in form of a spreadsheet with historical sequence of casts. A user can define cast numbers to simulate and the first cast to be simulated. Then the controller explores the spreadsheet, finds the corresponding data, creates the first case, and launches execution. The case set-up for every next simulated cast is based on the results of the previous case. The controller thus handles all the data flux starting from the initiation of the model until execution of the last cast in the user defined dataset.

There are two modes of MOHDRAIN simulations, namely:

- casting, i.e. simultaneous production of liquids and their removal, and
- filling, i.e. when the liquids are not being tapped from the hearth and at the same time they are being produced.

The controller decides automatically whether the case corresponds to casting or filling mode based on the spreadsheet data. Technically speaking, the difference between the two modes is in the way the mesh is set up. In OpenFOAM, the file blockMeshDict (situated in the solver control folder "system") describes the mesh parameters. The files p_rgh and U (situated in Initial condition folder "0") contain boundaryField which describes the conditions at of mesh patches. There are two sets of p_rgh and U files corresponding to casting and filling modes. The difference between them is that the boundaryField in filling mode files does not contain the outlet patch thus liquids cannot leave the domain.

The core is responsible for the resolution of the drainage problem. It includes solver and case setup files. The solver resolves equation (35) using the equations (37) – (40) in parallel.

Important feature of the Phase control is implementation of dilation/contraction of phases. The model contains only one Inlet which is set at the upper surface of the domain (opposite to the hearth bottom). Only gas can flow through it. The slag and hot metal are created within the domain via dilation/contraction. In practice, it works in the following manner. The controller sets up the rate of the slag and hot metal production based on the data from the spreadsheet with historical sequence of casts. Every time step, the model updates the phase fields. The ratio of phases within a given cell is calculated based on the amount of liquids produced within this cell. The gas phase serves as a balancing entity which makes the domain always occupied by the phases. The update considers the rate of phase removal from a given cell in case of casting mode as well. The dilation/contraction is implemented in OpenFOAM using the code shown in Figure 115, which is written in updateFlux.h file situated in Equation resolution folder "Include".

```

scalar phiGasIn = flowRateOutlet - phiSlagIn - phiMetalIn;

scalar volMetalTot = gSum(mesh.V().field() * alphaMetal.field());
scalar volSlagTot = gSum(mesh.V().field() * alphaSlag.field());
scalar volGasTot = gSum(mesh.V().field() * alphaGas.field());

scalar dilatMetal = phiMetalIn * dt / volMetalTot;
scalar dilatSlag = phiSlagIn * dt / volSlagTot;
scalar dilatGas = phiGasIn * dt / volGasTot;

ddtVolMetal.field() = alphaMetal.field() * dilatMetal;
ddtVolSlag.field() = alphaSlag.field() * dilatSlag;
ddtVolGas.field() = alphaGas.field() * dilatGas;
ddtVolTot.field() = ddtVolMetal.field() + ddtVolSlag.field() + ddtVolGas.field();

alphaMetal.field() = alphaMetal.field() * (1. + dilatMetal);
alphaSlag.field() = alphaSlag.field() * (1. + dilatSlag);
alphaGas.field() = alphaGas.field() * (1. + dilatGas);
ddtVolTot.field() = ddtVolTot.field() / (dt * eps.field());

```

Figure 115: List of the code handling dilation/contraction of phases in MOHDRAIN 2.0.

Validation of solver was performed in a manual mode, i.e. the case was set up without using of Controller. The solver was validated using the experimental data reported in [87]. The case was set up using the mesh presented in Figure 113a. The properties of phases used in the model are given in Table 16.

Table 16: Properties of phases in validation case.

Property	Units	Distilled water	Air
Density	kg/m ³	1000	1
Kinematic viscosity	m ² /s	1·10 ⁻⁶	1.48·10 ⁻⁵
Surface tension	N/m	0.07	N/A

Figure 116 shows the experimental and modelled drainage. On the left, the images are a validation in which the two-dimensional model was deemed accurate. The coloured phases are the validation results while the black curves are the previous model to be validated. On the right, it is shown that the current simulation produces near identical results.

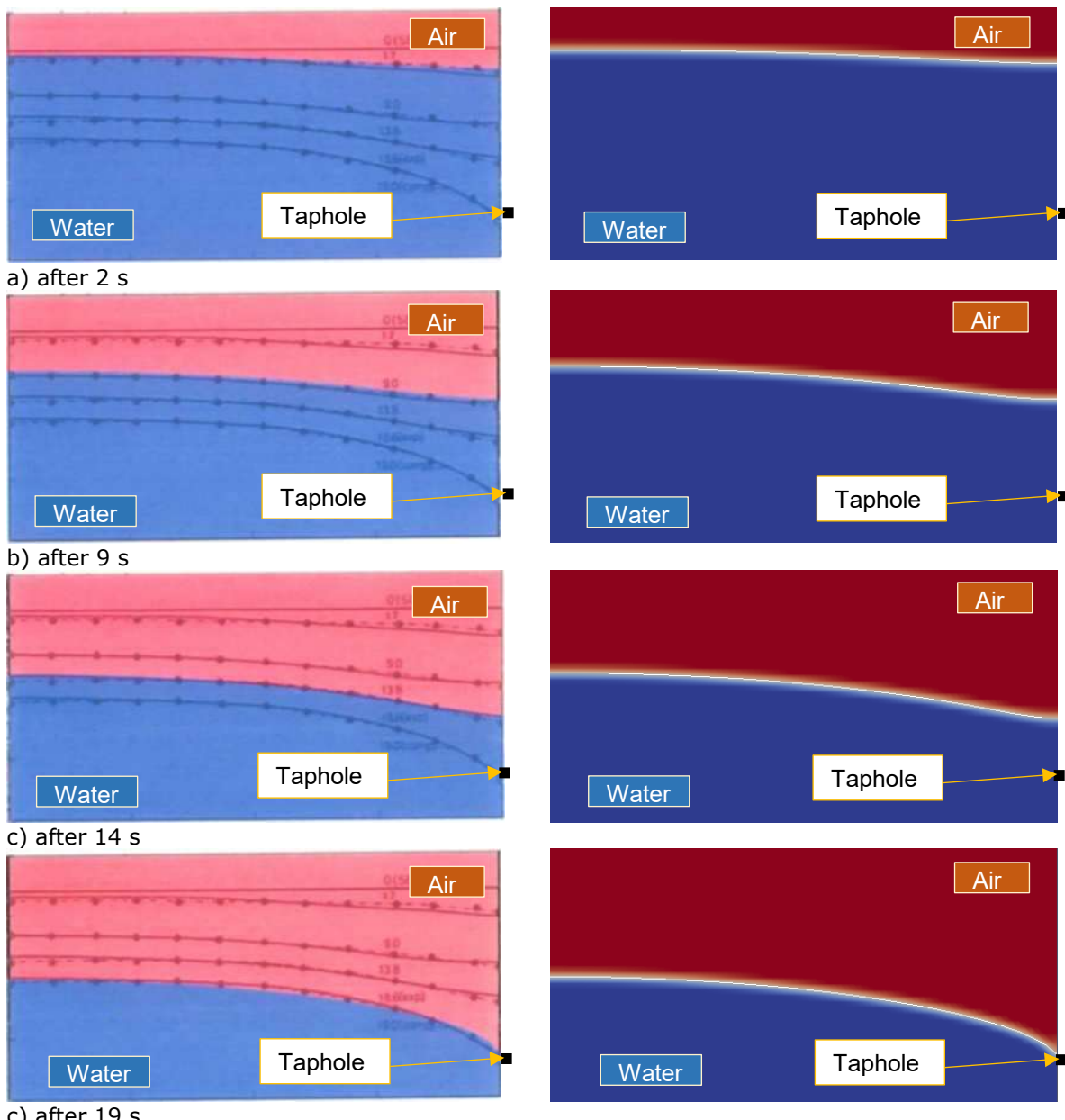


Figure 116: Validation of solver.

The most important feature of the comparison is the advancement and shape of the interface between air and distilled water. Comparing the experimental and simulation results one can reckon that the drainage is done in the same way. It is then possible to conclude that the solver of MOHDRAIN 2.0 is validated.

2.2.1.6 Validation of the mathematical models

2.2.1.6.1 Analysis of BF-A tapping data at voestalpine

For BF-A in Linz two timespans have been analysed in detail:

- December 2012 to December 2016

The primary goal was to check this data for anomalies in blast furnace operation and test correlations of various parameters (coke quality, taphole properties etc.) on blast furnace performance.

- January 2018 to December 2018

During this period a major relining was done at BF-A (June-September 2018), thus we have data right before relining (with already eroded hearth geometry) and data right after relining with brand-new refractories.

2.2.1.6.1.1 Analysis of BF-A tapping data in the period 2012-2016

As can be seen from Table 17, this time period covers more than 20.000 tappings and thus provides enough data to test for correlations.

Table 17: Data coverage and BF-A properties.

Number of tappings (2012-2016 data)	21974
Operating hours	~34000 h
Tapholes	3
Blast furnace volume	3125 m ³

Figure 117 shows the distribution of BF fuel for the covered time span. In fall 2014 the PCI plant at voestalpine was commissioned. Pulverized coal mainly replaced gas, tar and heavy oil and the amount of coke per ton of hot metal was significantly reduced.

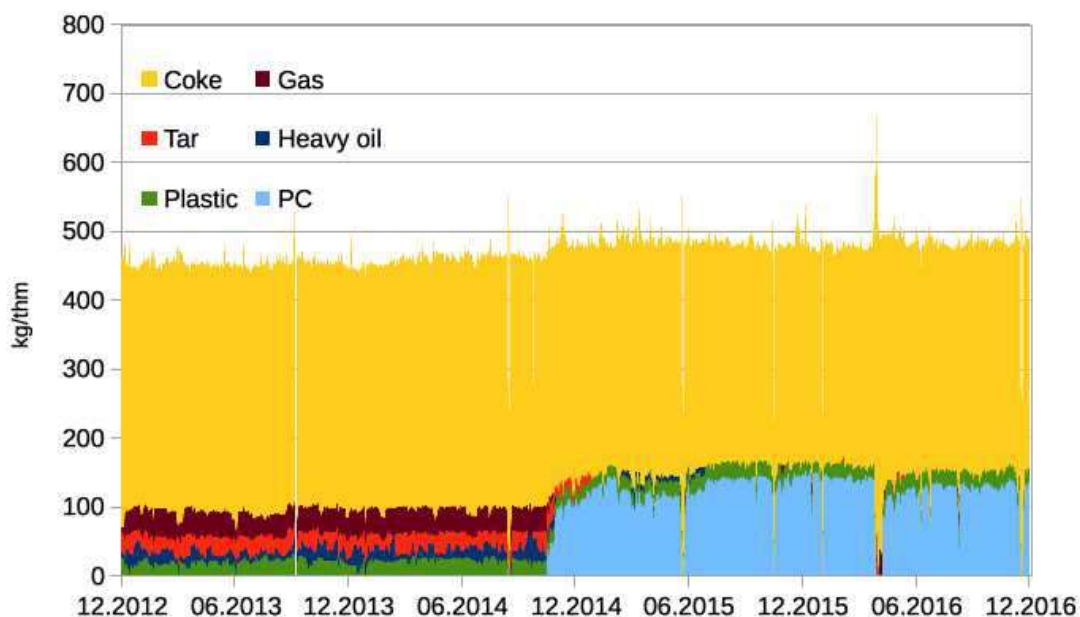


Figure 117: Distribution of coke and tuyere reduction agents (12/2012 until 12/2016).

Table 18 shows averaged values and their standard deviation for some of the major tapping properties.

Table 18: Main properties of tapping data (averages and standard deviations).

	avgd. values +/- std. dev.
Tapping mass	539 +/- 110 t
Tapping speed	355 +/- 35.8 t/h
Tapping duration	90.7 +/- 17.2 min
Average time to slag tapping	10.4 +/- 8.04 min
Pig iron temperature	1481 +/- 24 °C
Intermediate closing of taphole	2945 (13.4%)
Intermediate plugging of taphole	1255 (5.7%)

To check the data for taphole specific features, Table 19 shows the tapping data sorted by taphole. In general, there are no major differences in the tappings of the three different tapholes except the rate of intermediate taphole closings or plugging with taphole mass.

Table 19: Properties of tapping data sorted by taphole.

	Hole 1	Hole 2	Hole 3
Tappings	8796 (40.0 %)	5585 (25.4 %)	7592 (34.6 %)
Tapping speed (t/h)	346 +/- 32.5	362 +/- 36.6	361 +/- 36.4
Tapping duration (min)	91.2 +/- 17.2	89.5 +/- 16.1	91.1 +/- 18.0
Average time to slag tapping (min)	8.45 +/- 6.70	10.08 +/- 7.81	12.75 +/- 8.95
Intermediate closing	633 (7.20 %)	723 (12.9 %)	1592 (21.0 %)
Intermediate plug	403 (4.58 %)	274 (4.91 %)	578 (7.61 %)
Taphole length (mm)	300.5 +/- 13.2	298.8 +/- 14.5	300.4 +/- 14.1
Taphole diameter (mm)	57.4 +/- 3.44	58.0 +/- 3.84	56.5 +/- 3.79
Taphole fill pressure	233.1 +/- 26.7 bar	235.2 +/- 24.4 bar	230.7 +/- 25.0 bar
Taphole fill mass	96.4 +/- 22.3 l	99.7 +/- 24.3 l	100.2 +/- 25.5 l
Taphole fill angle	161.70 +/- 8.73 °	161.65 +/- 9.00 °	161.73 +/- 8.81 °

The data has a very broad distribution and no clear correlation can be stated for a lot of parameters. As an example, Figure 118(a) gives the drainage rate against the tapping duration. One could expect that long tapping durations correlate with low drainage rates, but there is no obvious correlation. Figure 118(b) depicts the expected correlation of the slag to iron ratio for each tapping, but still there is a wide spreading of the data.

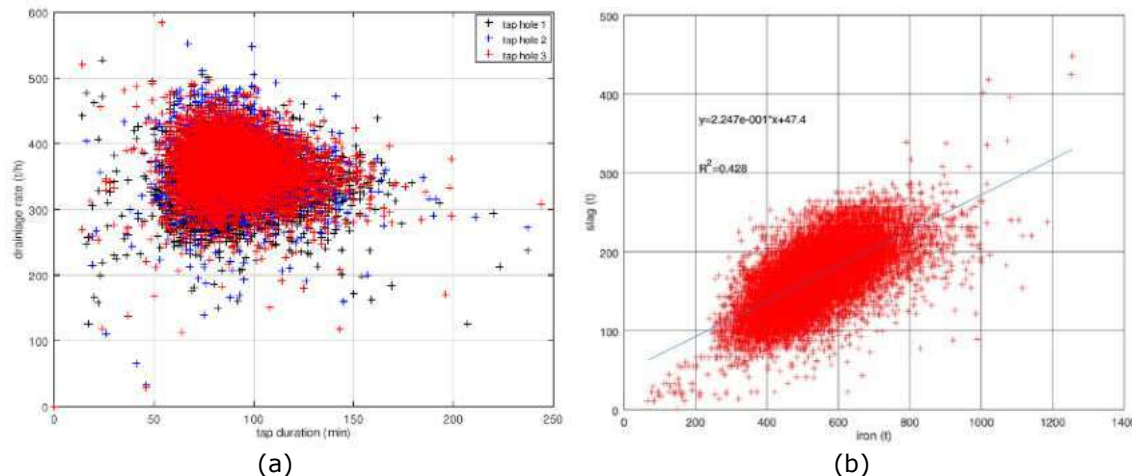


Figure 118: (a) Drainage rate vs tapping duration colored by taphole, (b) tapped slag mass vs. iron mass.

For each day there is an averaged coke size distribution available obtained by sieving (Figure 119(a)). To be able to correlate the influence of the coke size distribution on other operational data by means of statistical values like D_{10} , D_{50} and D_{90} , the particle size distribution was fitted to a Weibull distribution

$$v_2 = 2(p_1/\rho + gh_1) \quad (41)$$

via a least square approach. Figure 119(b) gives the range of cumulative size distributions of these functions and Figure 120 shows the temporal evolution of D_{10} , D_{50} and D_{90} for the analysed period. Figure 121(a) depicts that there is no correlation of the fine and large fractions. On a first guess one could anticipate, that a higher fraction of small particles would lead to a reduced fraction of particles $> 90\text{mm}$. That is obviously not the case. However, there is a weak correlation of the number of small particles $< 10\text{mm}$ with CSR as can be seen in Figure 121(b).

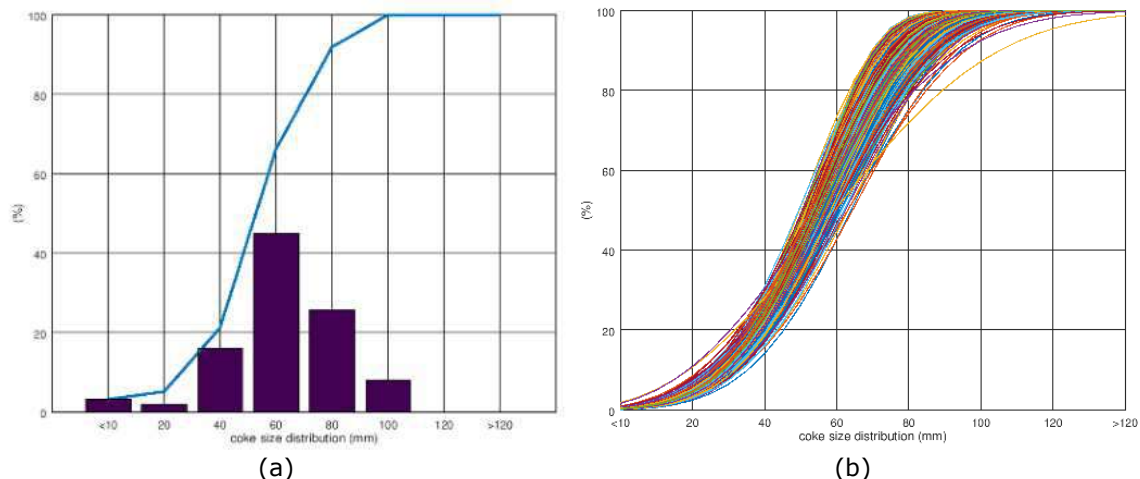


Figure 119: (a) Example of a coke size distribution and its cumulative curve, (b) fitted coke size distributions based on Weibull function.

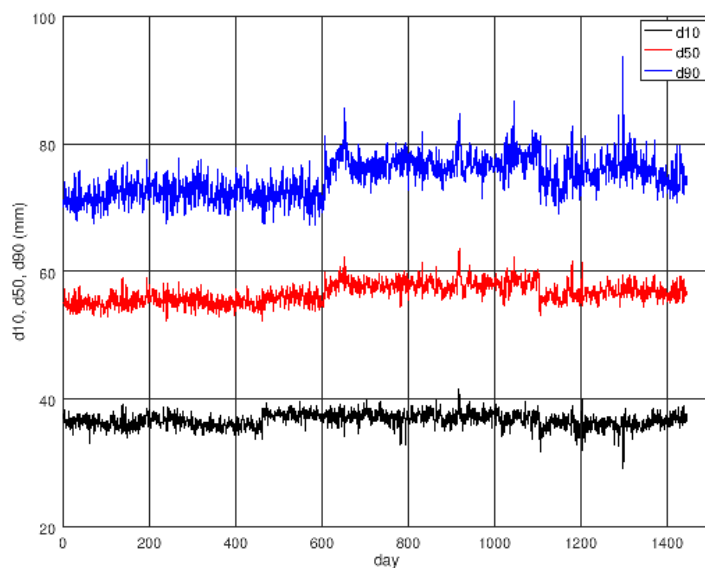


Figure 120: Daily values for D₁₀, D₅₀ and D₉₀ values of the fitted coke size distributions.

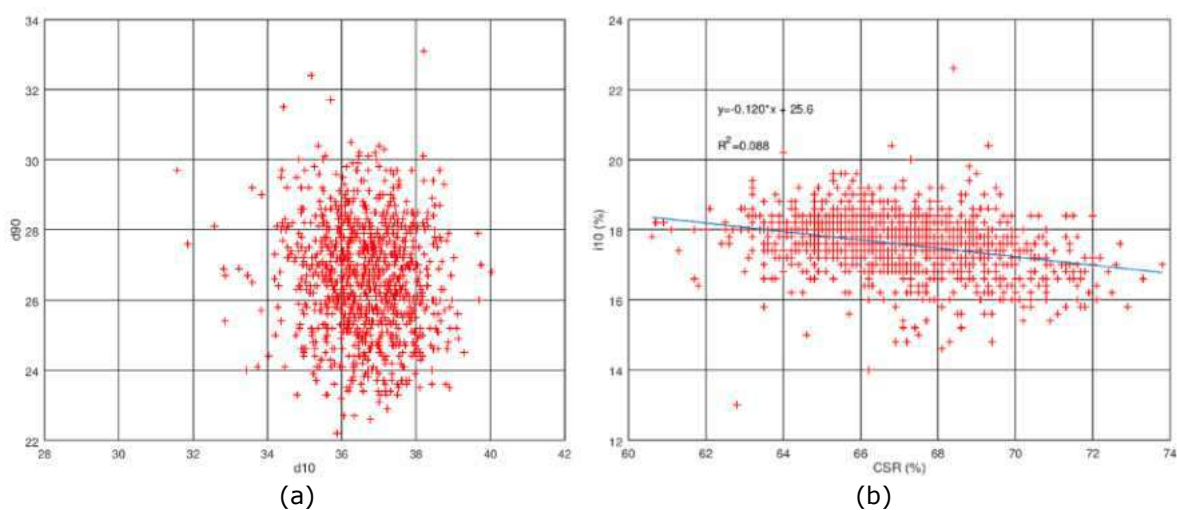


Figure 121: (a) Correlation of d₉₀ and d₁₀, (b) Correlation of I₁₀ and CSR.

In addition to cross-correlation tests of pairs of variables, we also applied multiple linear regression on the data. A multiple linear regression can summarize the most important input variables and their influence on a certain target value and has the form of

$$y = b_1 + b_2 x_1 + b_3 x_2 + \dots + b_n x_n \quad (42)$$

Table 20 gives the results for the melt performance as a function of the seven major input parameters. Together with the coefficients the confidence interval which covers 95% of the data is given.

Table 20: Multiple linear regression result for melt performance.

	Coefficients b	Value	Confidence interval for 95%	
Constant	b_1	-9.73e+000	-1.31e+001	-6.38e+000
Wind flow rate	b_2	4.66e-005	3.32e-005	6.01e-005
Wind O ₂ rate	b_3	3.32e-003	3.28e-003	3.36e-003
Wind pressure	b_4	2.67e+001	2.51e+001	2.82e+001
Wind speed	b_5	7.43e-001	7.28e-001	7.58e-001
Wind Temperature	b_6	8.82e-003	5.18e-003	1.25e-002
Burden pressure drop	b_7	5.16e+000	2.69e+000	7.64e+000
Stockline avg	b_8	-5.18e-001	-7.51e-001	-2.85e-001

The R² value of this model 0.98. This value basically describes how much of the data variance is captured by the model, and a value close to 1 is very good.

Other multiple linear regressions have been tested with the melt performance as the target value y and the major coke parameters as the input variables and another version with the tapping duration as the target value and the taphole properties (drill diameter, taphole length, etc.) as the input parameters, but the obtained R² values were 0.011 and 0.005, respectively, which means that the models are not able to capture the data variance in a sufficient manner. Hence, standard correlation methods between two or multiple variables are very limited in analyzing huge datasets (with lots of noise) from blast furnace plants.

As a third approach, some machine learning strategies have been started, like neural networks to obtain a formalism between operational data and tapping rates. Figure 122 shows an example for a neural network test with one hidden layer containing 10 nodes. One can see that the neural network can follow the general trend but not the variance in iron flow. However, capturing the average flow rates is trivial and does not provide any new insight to the data, hence, as expected also black box models like neural networks have their problems in finding a deterministic formalism between various BF data parameters, mainly because of the large variance in the data.

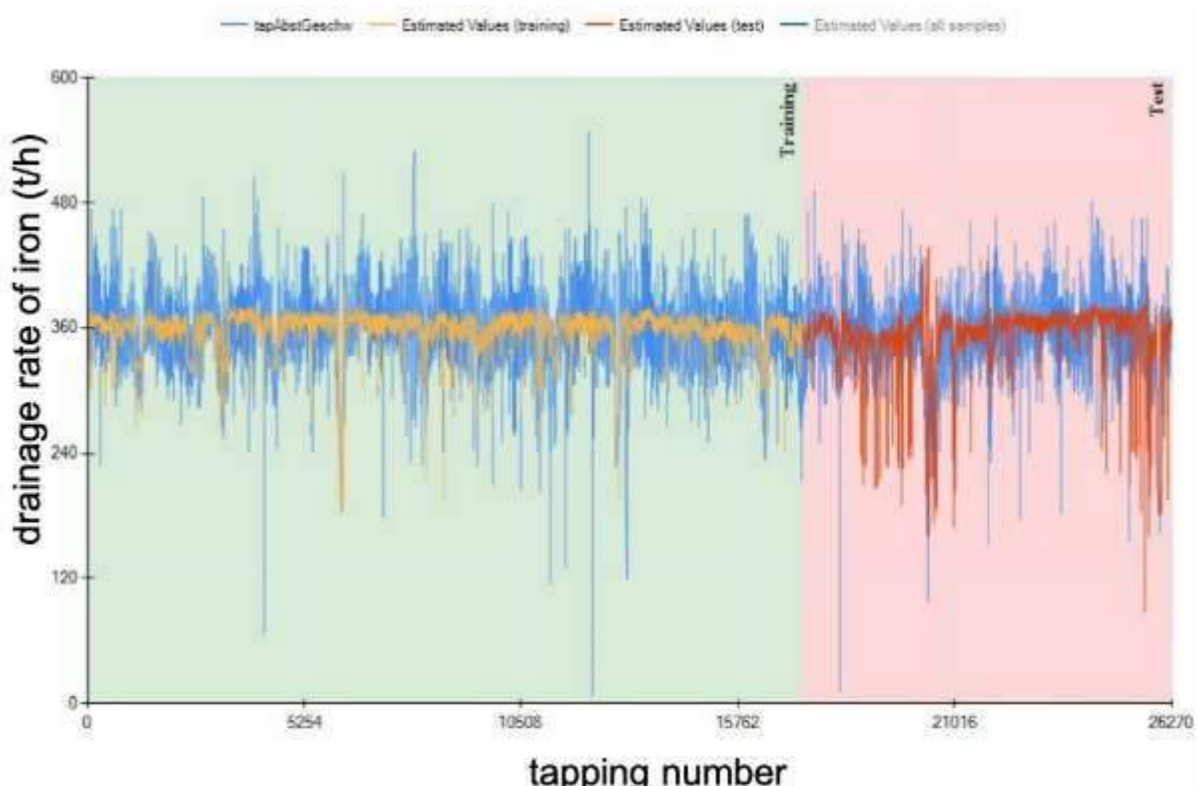


Figure 122: Iron mass flow rate (t/h) over the tapping history (tapping nr.). The blue curve is the original data, the yellow curve is the training data for the neural network, and the red curve is the test data.

2.2.1.6.1.2 Comparison of tapping data at voestalpine BF-A before and after relining

As there was a major relining of BF-A at voestalpine we compared the tapping data over the last few months before the shutdown (January – June 2018) and the first three month after start-up of the new campaign (September – December 2018). Table 21 summarizes the major tapping values. In general, the differences are insignificant. One difference is a shorter slag delay after relining, which could be argued by a higher porosity of the coke bed in the hearth region during the first phase of a new campaign. However, the tapping speed of pig iron did not increase, but the drill diameters are currently smaller than before the shutdown. This would also indicate that the drainage behavior is currently better than before the relining (same tapping speed at lower diameters). Also, the pig iron temperature is slightly higher after relining.

Table 21: BF-A in the period right before and after the 2018 relining.

	before relining	after relining
Nr. of tapping datasets analyzed	2406	1059
Avg. tapped iron	514 +/- 111 t	526 +/- 112 t
Spec. slag	29.5 +/- 4.55 %	30.8 +/- 5.40 %
Tapping speed	347 +/- 33.7 t/h	343 +/- 34.7 t/h
Tapping duration	88.4 +/- 17.6 min	91.4 +/- 18.4 min
Avg. time to slag tapping	13.7 +/- 9.37 min	9.52 +/- 8.51 min
Avg. taphole length	305 +/- 12.6 cm	303 +/- 16.8 cm
Avg. drill diameter	55.0 +/- 3.88 mm	59.7 +/- 4.18 mm
Permeability	5780 +/- 268 (-)	6151 +/- 295 (-)
Pig iron temperature	1480 +/- 19.4 °C	1492 +/- 22.4 °C
Blast flow rate	291685 +/- 6275 Nm3	292305 +/- 6114 Nm3
Wind speed	206 +/- 5.31 m/s	212 +/- 4.71 m/s
O2 specific	227 +/- 6.81 Nm3/t	226 +/- 3.04 Nm3/t
Coke specific	324 +/- 14 kg/thm	335 +/- 12 kg/thm
Tuyere (total) fuels specific	146 +/- 17 kg/thm	125 +/- 15 kg/thm
PC specific	130 +/- 17 kg/thm	104 +/- 25 kg/thm

2.2.1.6.2 Analysis of BF-5 data 2010-2015 campaigns

Beside the analysis of BF-A data a detailed analysis of the BF-5 campaign from 2010 to 2015 was done. During this campaign significant wear of the hearth region was noticed which lead to changes in the overall tapping procedures.

After the blowdown in 2015 it was seen that there was a loss of three bottom layers of carbon bricks in the hearth. Due to wear the hearth volume increased by 75-80 m³ from its original value of 185 m³ up to the tuyere level. Thus, the data of this campaign could give some useful hints if there is a significant influence of hearth wear on the tapping procedure.

Figure 123 shows that the melting rate and specific slag ratio decreased from 320 kg/thm to 220 kg /thm due to operational changes during the campaign. It is therefore not that easy to compare the tapping data over the complete period. The reduction in slag production was caused by a change of burden philosophy. However, three periods labelled '1', '2' and '3' with similar production rates were defined to compare tapping data at the beginning, the middle and the end of the campaign.

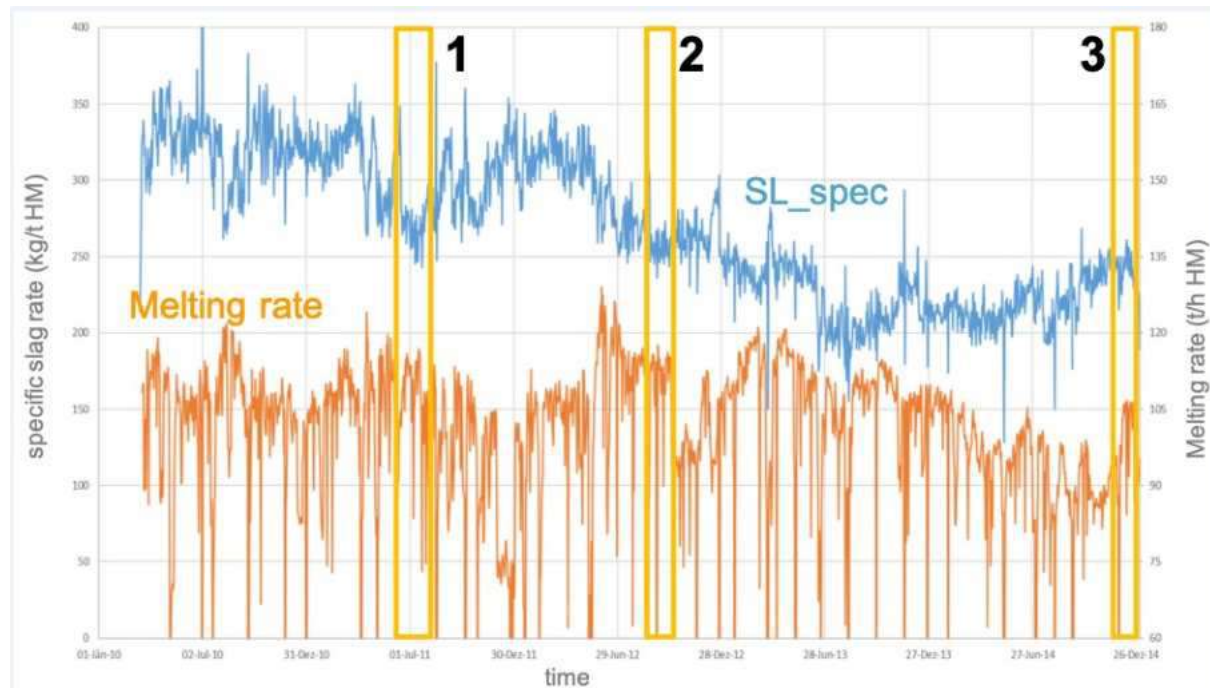


Figure 123: Melting rate and specific slag during the BF-5 campaign from 2010-2015.

2.2.1.6.2.1 Data over the entire campaign

The following figures depict some of the process data over the entire 2010-2015 campaign. Figure 124 shows that the penetration depth of the blast was increased to minimize the effect on wear refractory.

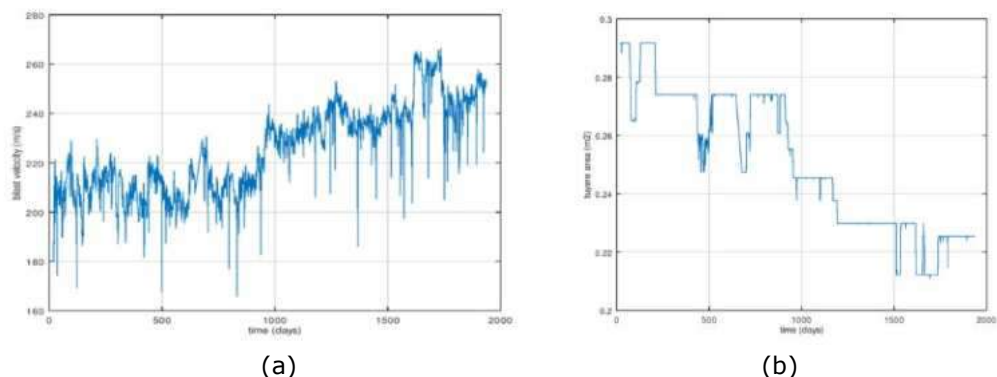


Figure 124: (a) Hot blast velocity and (b) tuyere area during the BF-5 campaign. To minimize the raceway effects on the eroded hearth geometry, the penetration depth was increased.

Due to the increase of hearth volume caused by hearth wear one could argue that the fluctuations in certain process parameters must decrease. As the size of the 'mixing tank' increases, changes in hot metal and slag properties might be reduced for the measurable tapping data. To test this hypothesis, we analyzed the Si content and its standard deviation.

The standard deviation of C, Si and the hot metal temperature correlate with each other as shown in Figure 125. The temperature was quite stable over the entire campaign as depicted in Figure 126. Figure 127 does not give a hint on changes in standard deviation of the Si mass fraction.

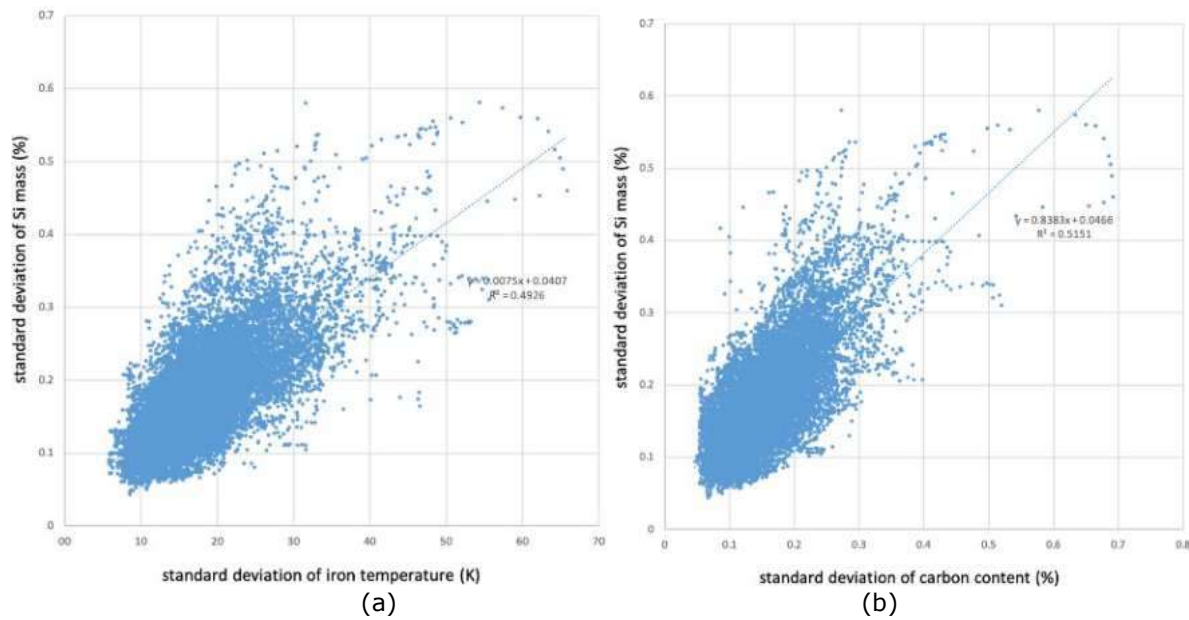


Figure 125: (a) Correlation of the standard deviation of Si %om with the standard deviation of hot metal temperature, (b) standard deviation of carbon content.

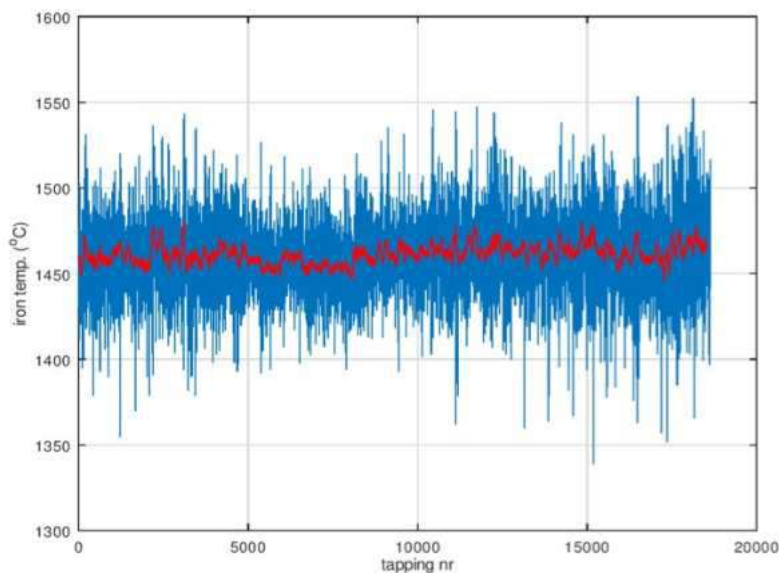


Figure 126: Hot metal temperature over the entire campaign.

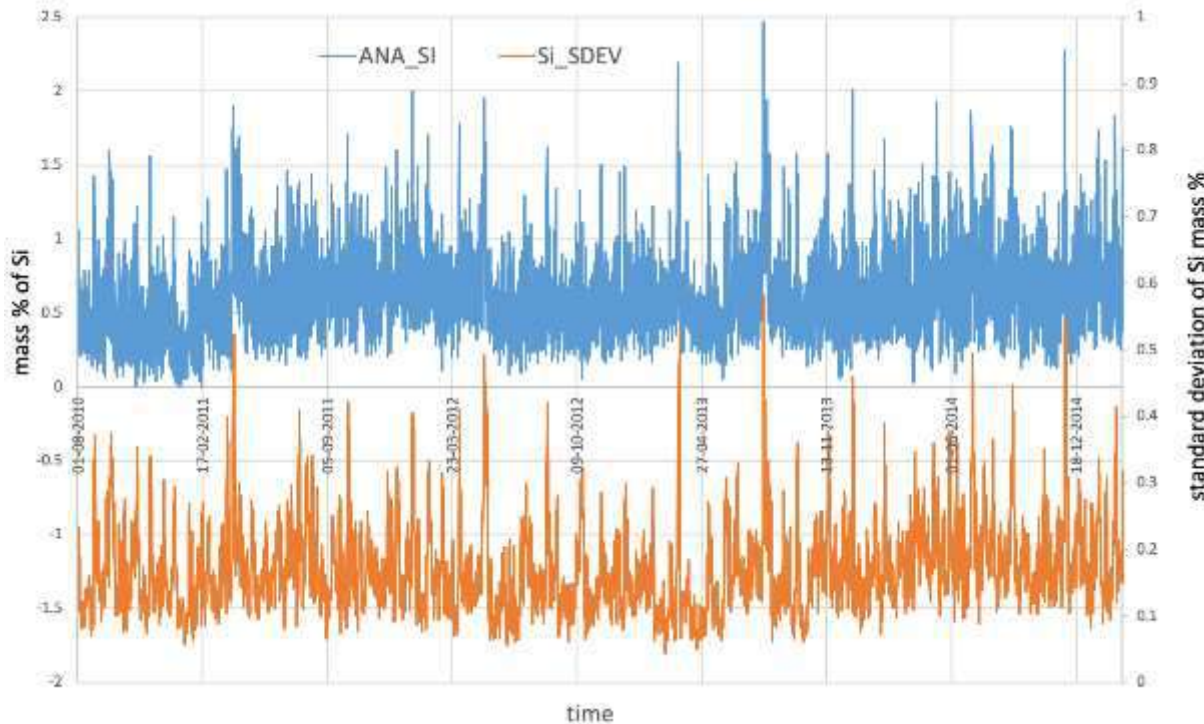


Figure 127: Mass percent of Si (blue) and standard deviation of Si content (orange). No change of the standard deviation if noticeable during the campaign.

The time between taps is subject to decision of the BF crew. The interval time was decreased from about 70 min to 50 min from 2010 to 2015. This has mainly logistical reasons as the tapped hot metal mass would otherwise have exceeded the torpedo limit of 300t. The slag delay remained constant (Figure 128).

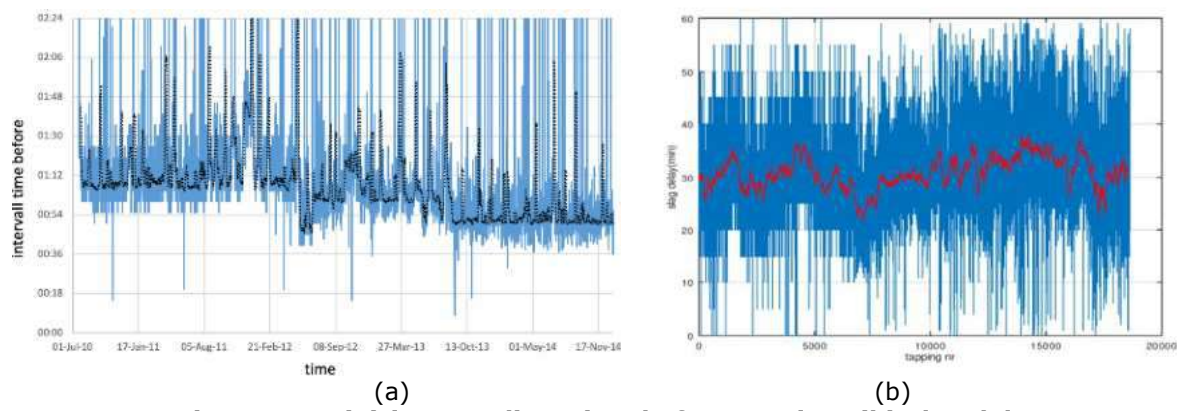


Figure 128: (a) intermediate time before tapping, (b) slag delay.

Also, the drill diameter is an operational decision and as the average drill diameter was decreased during operation time, the tapping duration increased (Figure 129).

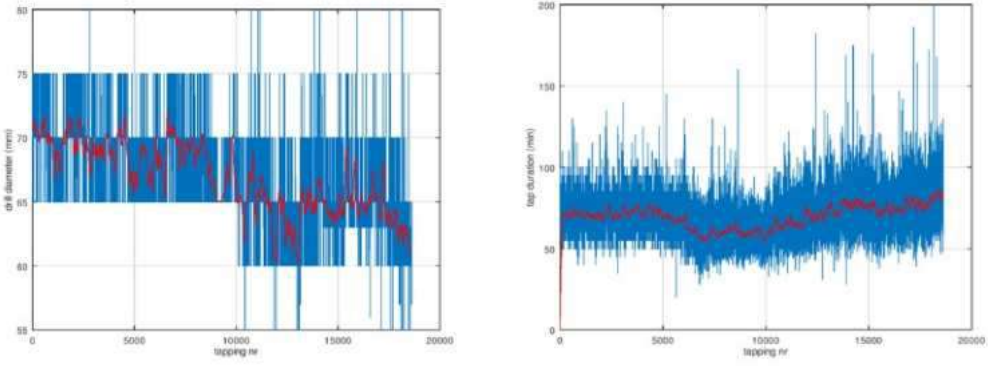


Figure 129: (a) taphole diameter, (b) tap duration.

Due to significant hearth wear it was tried to stabilize the refractory thickness next to the taphole with taphole clay of better quality. Therefore, the taphole length increased in the timespan 2014-2015 and the clay consumption decreased (Figure 130).

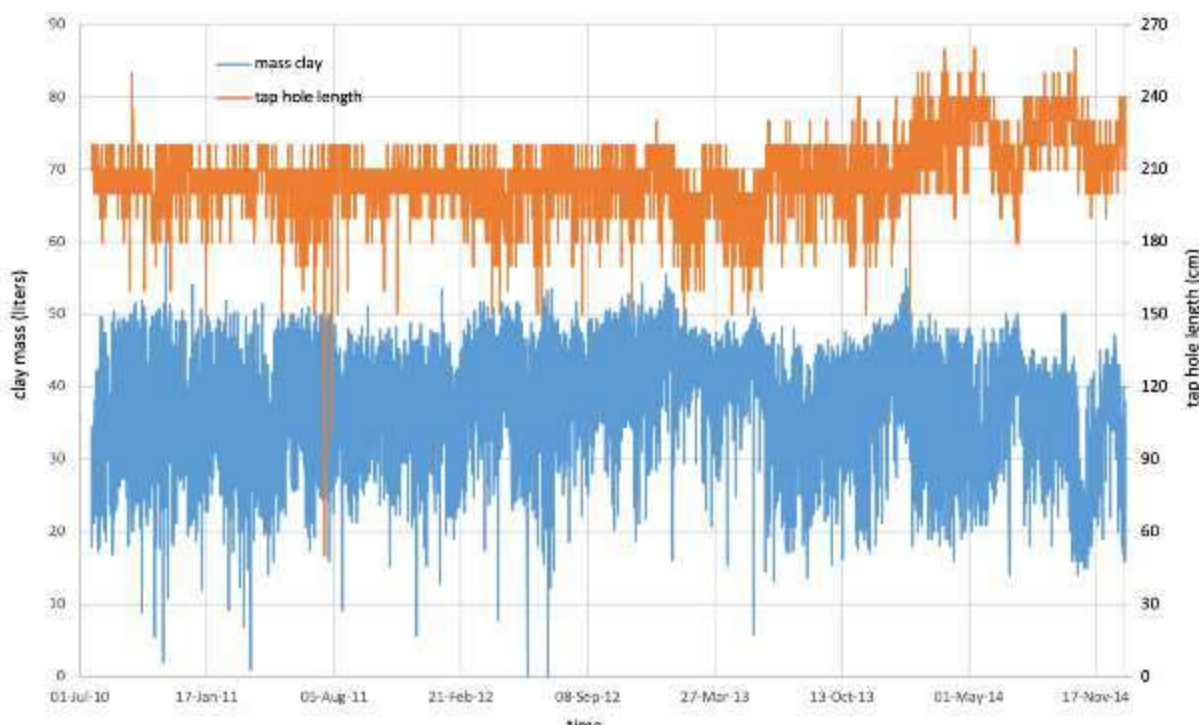


Figure 130: Taphole length (orange) and amount of clay (blue).

2.2.1.6.2.2 Data comparison of three defined periods

As already shown in Figure 123, three periods of similar melting rate and specific slag rate were chosen to compare data at the beginning, middle and final phase of the 2010-2015 campaign.

- Period 1: 10. - 15.7.2011
- Period 2: 22. - 29.9.2012
- Period 3: 15. - 22.12.2014

The following tables give a summary on the process data during these periods. Values with a noticeable deviation during one period have been colored differently for easier reading.

Table 22: Comparison of BF-5 data for the three selected periods, operational data.

	Period 1 (62 tap cycles)				Period 2 (97 tap cycles)				Period 3 (93 tap cycles)			
	min	avg	max	std	min	avg	max	std	min	avg	max	std
Stockline	1.02	1.16	1.42	0.14	1.10	1.20	1.39	0.12	0.82	0.87	0.96	0.05
RAFT	2022	2041	2061	14.0	2059	2067	2074	4.40	2040	2073	2139	33.8
Melting rate	107.8	112.3	114.5	2.60	110.3	114.0	116.2	1.90	101.0	104.4	106.4	1.90
BoshgVol	137.3	140.7	142.1	1.72	139.9	140.7	141.2	414.0	133.7	136.0	137.6	1.53
eta_CO	50.0	50.4	51.1	0.38	49.2	50.1	50.7	0.48	51.0	51.5	52.0	0.39
Permeability	7394	7605	7706	109	7585	7746	7886	115	7026	7210	7377	149
Oil_spec	41.0	42.6	44.0	1.25	46.0	47.0	47.8	0.63	42.9	47.5	57.3	5.65
Gas_spec	43.3	44.4	45.0	0.72	43.4	44.1	45.2	0.63	29.9	34.0	45.2	6.32
Slag_spec	245.1	253.2	277.1	12.1	243.4	254.3	261.1	6.03	230.1	239.4	253.2	6.81
Alk_spec	4.43	4.63	4.84	0.15	3.82	4.25	4.75	0.37	3.18	3.58	3.91	0.26
tHM/m ³	1.80	2.01	2.11	0.10	1.84	2.03	2.15	0.09	1.86	1.95	2.09	0.08
Coke_spec	356.7	358.5	360.4	1.20	366.9	372.9	380.4	5.00	366.6	370.5	377.9	3.70
RA_tuy_spec	84.8	87.0	89.0	1.60	89.9	91.0	91.7	0.70	86.0	87.4	90.2	1.50
RA_spec	441.5	445.5	449.4	2.60	456.8	463.9	472.2	5.30	452.6	458.0	468.1	5.00

Table 23: Comparison of BF-5 data for the three selected periods, chemical properties.

	Period 1 (62 tap cycles)				Period 2 (97 tap cycles)				Period 3 (93 tap cycles)			
	min	avg	max	std	min	avg	max	std	min	avg	max	std
C content iron (%)	3.95	4.24	4.72	0.16	3.95	4.20	4.73	0.12	4.01	4.23	4.84	0.19
Si content iron (%)	0.35	0.79	1.23	0.20	0.22	0.48	0.74	0.12	0.21	0.70	1.22	0.25
Mn content iron (%)	0.30	0.49	0.69	0.08	0.43	0.56	0.72	0.06	0.29	0.43	0.61	0.07
Slag Bas2	0.74	0.88	1.02	0.06	0.81	0.88	0.97	0.03	0.74	0.85	1.00	0.05

Optimizing Blast Furnace Hearth Inner State (OPTIBLAFINS)

Slag alkalinity	1.13	1.84	3.29	0.35	1.12	1.65	2.16	0.18	1.01	1.51	2.42	0.27
-----------------	------	-------------	------	------	------	-------------	------	------	------	-------------	------	------

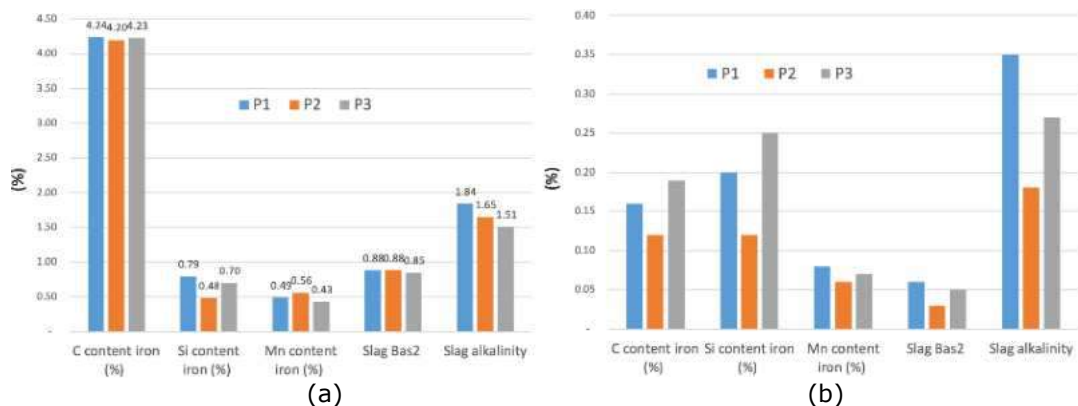


Figure 131: Hot metal analysis for the three selected periods. (a) Average values, (b) standard deviation.

Table 24: Comparison of BF-5 data for the three selected periods, tapping data.

	Period 1 (62 tap cycles)				Period 2 (97 tap cycles)				Period 3 (93 tap cycles)			
	min	avg	max	std	min	avg	max	std	min	avg	max	std
Tapping speed (t/h)	167	210	257	15.6	189	226	297	20.9	137	169	215	15.3
Iron mass (t)	169	250	314	24.2	152	215	267	25.6	151	214	301	28.5
Slag mass (t)	33	64	94	9.7	41	55	66	7.1	32	50	82	9.0
Iron temp. (°C)	1437	1478	1517	18	1421	1453	1481	15	1424	1457	1509	18
Interval before tapping	00:55	1:07	1:30	0:06	0:47	1:00	1:14	0:03	0:38	0:50	1:01	0:01
Tapping duration	45	72	100	10	35	58	91	10	47	74	114	14
Slag tapping duration	10	39	65	9	20	33	68	8	14	39	73	12
Rel.slag tapping time	17%	54%	73%	9%	37%	57%	80%	8%	26%	52%	72%	9%
HM flow (t/h)	167	210	257	16	171	225	297	21	138	176	230	17

Tap.hole length (cm)	180	203	220	10	170	200	220	11	200	218	230	6
Drilling diam. (cm)	65.0	68.6	75.0	2.4	65.0	69.8	75.0	1.2	63.0	66.1	75.0	2.3
Mass clay (liter)	24.9	36.9	49.7	7.3	34.1	42.8	48.7	3.3	20.0	37.9	47.0	3.6

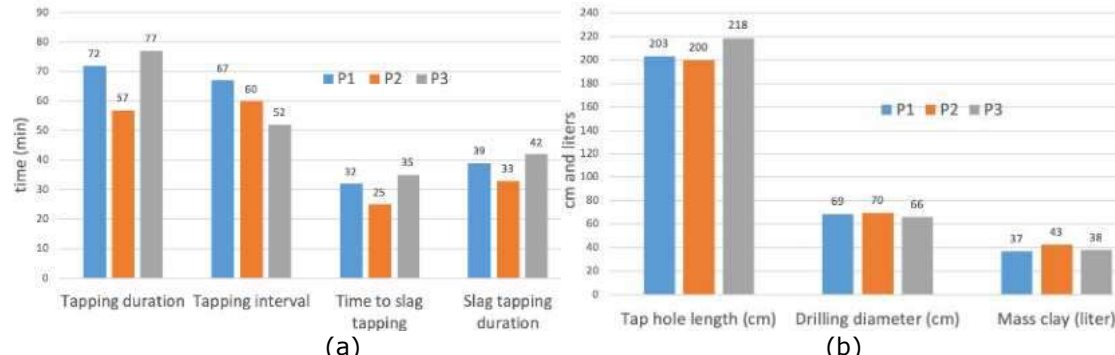


Figure 132: (a) Tapping parameters (values in minutes) and (b) taphole parameters (values in cm and liters).

The analyzed data of BF-A and BF-5 demonstrate the clear interlink of operator decisions and process parameters as depicted in (Figure 133). Our hypothesis that an increased hearth volume affects the mixing behavior and thus the fluctuations of hot metal analysis could not be confirmed. In the available data there is no clear storage or buffer effect of the increased liquid pools visible.

Operator	Process
melting rate	↔ maximum hearth level
drill diameter	↔ hot metal flow
tapping interval	↔ tapping time

Figure 133: Interlink of operator decisions and process parameters.

2.2.1.6.3 Simplified model of liquid levels in BF Hearth and tapping flow rates for CFD validation

Since 2016 the drainage rates of the blast furnaces at voestalpine are stored with an interval of 5 minutes averages in the process control database. This allows a more detailed analysis of the temporal evolution of the tapping of liquid iron and slag. This data can be used for comparison with unsteady CFD simulations as well as a simplified 1D model to estimate the current liquid levels and flow rates. Furthermore, the 1D model can be used to provide unsteady boundary conditions for the highly reduced computational domain of the CFD model.

The drainage model is implemented in a simple state machine which is outlined in Figure 134. From initial fill levels of iron and slag z_{ir} and z_{sl} the basic parameters D_{th} (taphole diameter), and the liquid velocities w_{ir} and w_{sl} are calculated. For the trivial case of a closed taphole (state 0) $w_{ir} = w_{sl} = 0$. After opening the taphole typically solely iron is drained for some time (state 1) until z_{ir} reaches the taphole level z_{th} and slag starts to flow out (state 2).

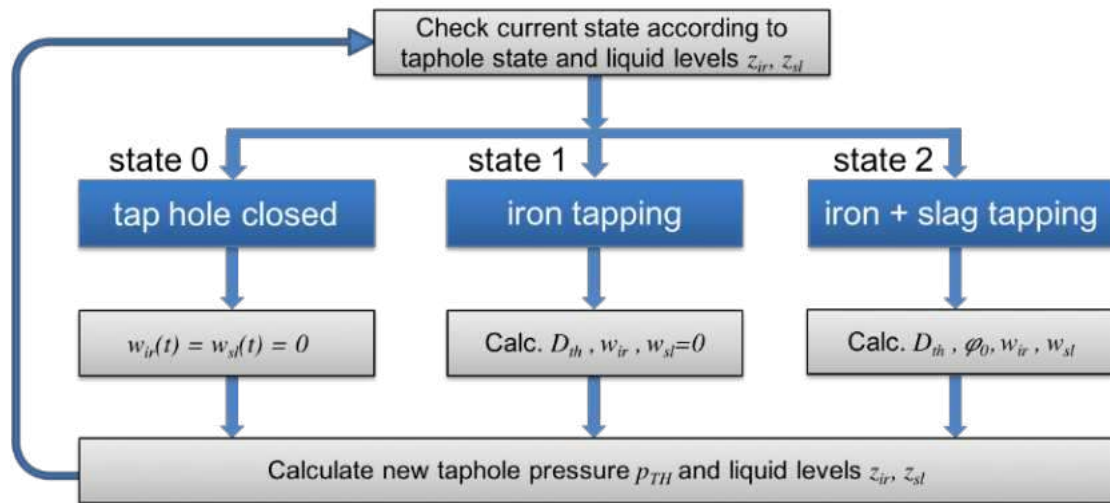


Figure 134: Outline of 1D tapping model via simple state machine.

Figure 135 shows the different states of BF drainage assuming interface deformation as firstly described in [4]. To allow this local deformation close to the taphole, the downward acting pressure inside the BF must be a function of the radius $p_d(r)$. Locally decreasing pressure towards the taphole also leads to decreased downward forces and therefore the buoyancy of the dead man is also a function of radius r .

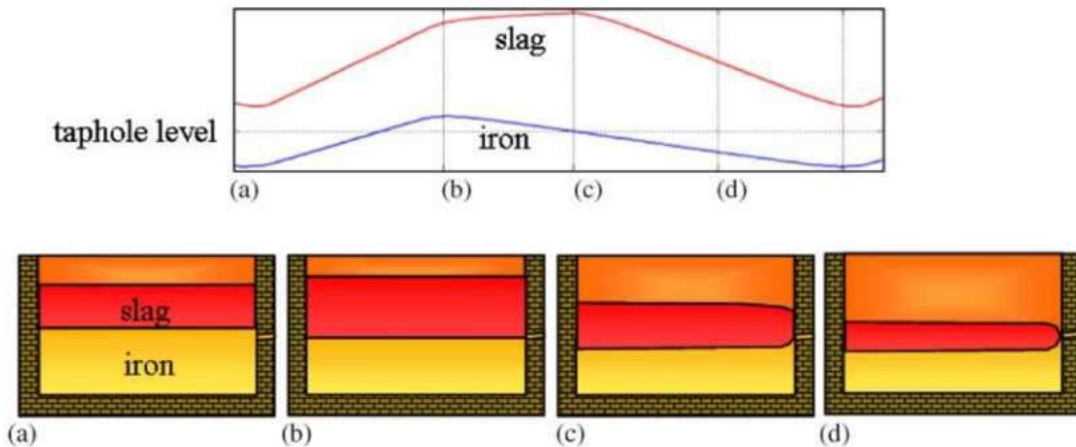


Figure 135: Layer model with interface deformation [88].

Brännkacka and Saxen [36] suggested a simple polynomial approach to account for the local pressure variation towards the outer radius of the BF. The downward pressure on the slag layer is defined by

$$p_d(r) = \begin{cases} p_{dc} & \text{if } r \leq r_0 \\ p_{dc} - a \left(\frac{r-r_0}{R} \right)^n & \text{if } r > r_0 \end{cases} \quad (43)$$

where r_0 is the radius of constant pressure. Figure 136(a) shows the behavior of Eq. (53) for different values of n relative to the hearth diameter R_H and constant pressure level p_{dc} in the center region $r \leq r_0$. Obviously only values $n > 1$ physically make sense.

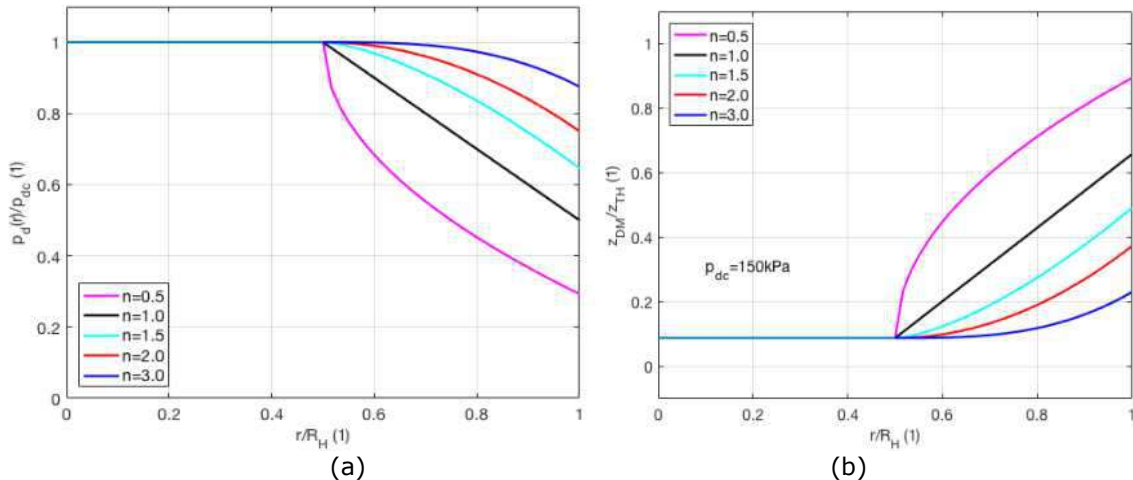


Figure 136: (a) Radial pressure distribution according to eq. (51) for $a = p_{dc}$. (b) Relative radial buoyancy of dead man for $p_{dc} = 150\text{kPa}$ according to eq. (52).

The flotation of the dead man including increased coke free zones towards the outer walls of the BF hearth is calculated by

$$\begin{cases} z_{sl} - \frac{p_d(r)}{\rho_{sl} g (1-\varepsilon)} & \text{if } 0 \leq p_d(r) \leq p_{b,sl,max} \\ z_{ir} + \frac{\rho_{sl}}{\rho_{ir}} (z_{sl} - z_{ir}) - \frac{p_d(r)}{\rho_{ir} g (1-\varepsilon)} & \text{if } p_{b,sl,max} \leq p_d(r) \leq p_{b,ir,max} + p_{b,sl,max} \\ 0 & \text{if } p_d(r) \geq p_{b,ir,max} + p_{b,sl,max}, \end{cases} \quad (44)$$

with the maximum buoyancy forces of slag and iron $p_{b,sl,max} = \rho_{sl} g (1-\varepsilon)(z_{sl} - z_{ir})$ and $p_{b,ir,max} = \rho_{ir} g (1-\varepsilon)z_{ir}$. This leads to the contour of the coke free zone below the dead man as outlined in Figure 136(b) for different radial pressure distributions. Figure 137 shows the lift height of the dead man in the BF center for different liquid levels of iron and pressure levels.

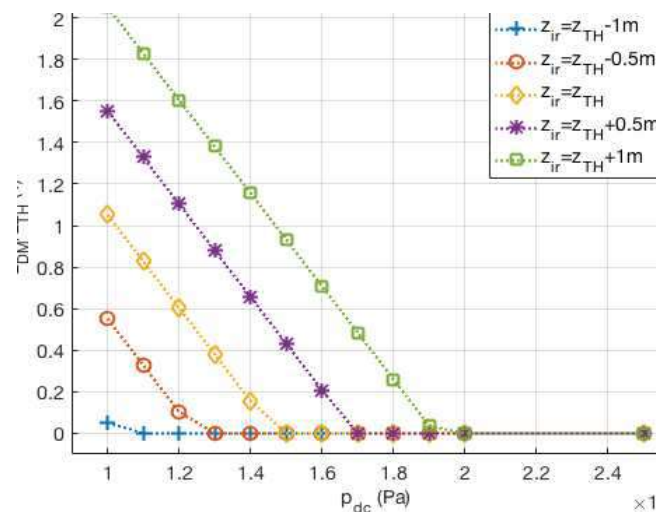


Figure 137: Buoyancy of dead man in BF center for different iron and pressure levels.

To obtain the correct center pressure p_{dc} acting on the slag surface we need to solve the pressure balance of burden load and gas pressure drop:

$$p_{dc} = p_{burden} - (p_{RW} - p_{top}) \quad (45)$$

where the second term denotes the pressure difference from the raceway to the BF head and the burden pressure can be calculated according to:

$$p_{burden} = p_{top} + \rho_{bg}(z_{top} - z_{cz}) + (\rho_c + \rho_{ir}x_{ir} + \rho_{sl}x_{sl})g(z_{cz} - z_{sl}) \quad (46)$$

The force balance is now closed and the local pressure at the entrance of the tap hole p_{th} can be derived by:

$$p_{th} = p_{d,r=R_H} + \rho_{ir} g (z_{ir} - z_{th}) + \rho_{sl} g (z_{sl} - z_{ir}). \quad (47)$$

To implement the change in liquid levels in the model it needs to be coupled with a tap hole flow model to obtain the outflow velocities for iron and slag, w_{ir} and w_{sl} , respectively. A suitable approach for two immiscible fluids is a modified two fluid model as presented in [90]. The finally obtained model can now be solved iteratively. The production rates $\dot{V}_{ir,p}$ and $\dot{V}_{sl,p}$ can either be kept constant or synchronized with available plant data based on hourly or 5 minutes recordings. Figure 138 and Figure 139 give an example for a simulation result for approximately 135 hours of BF operation. The production rates were changed according to hourly data recordings (including a shutdown period of roughly 25 hours). After a stabilizing phase at the beginning of the simulation, the liquid level of iron oscillates around the zero-level (tap hole inlet) and the thickness of the slag layer is between 0.4 and 0.9 m.

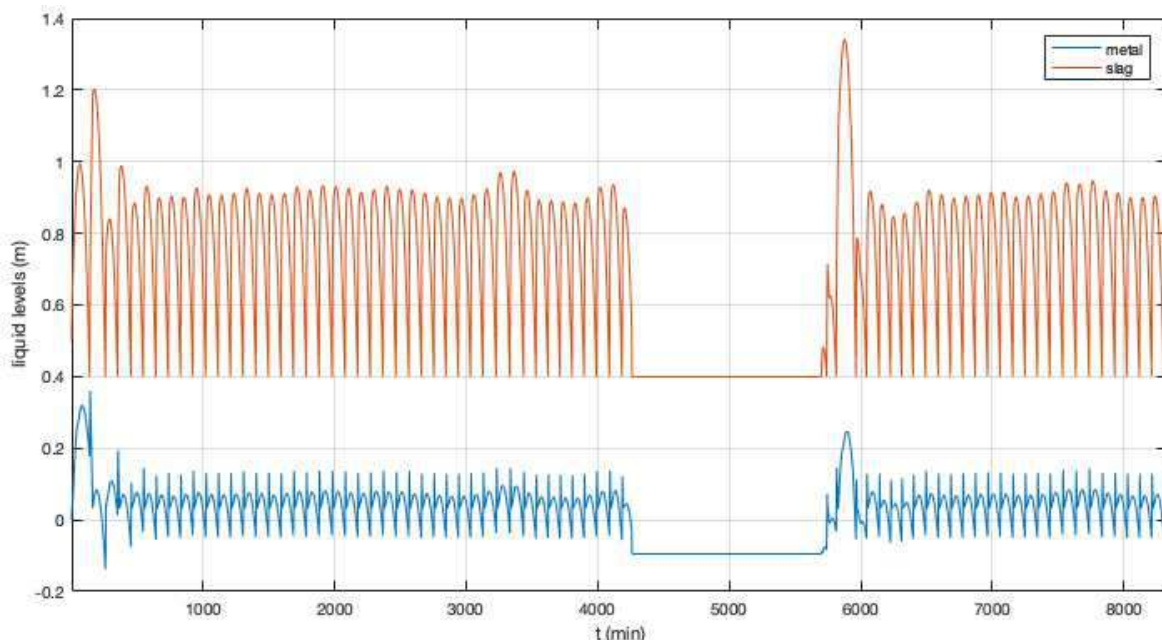


Figure 138: Results of a testcase for the drainage model; calculated liquid levels for a period of 135 hours.

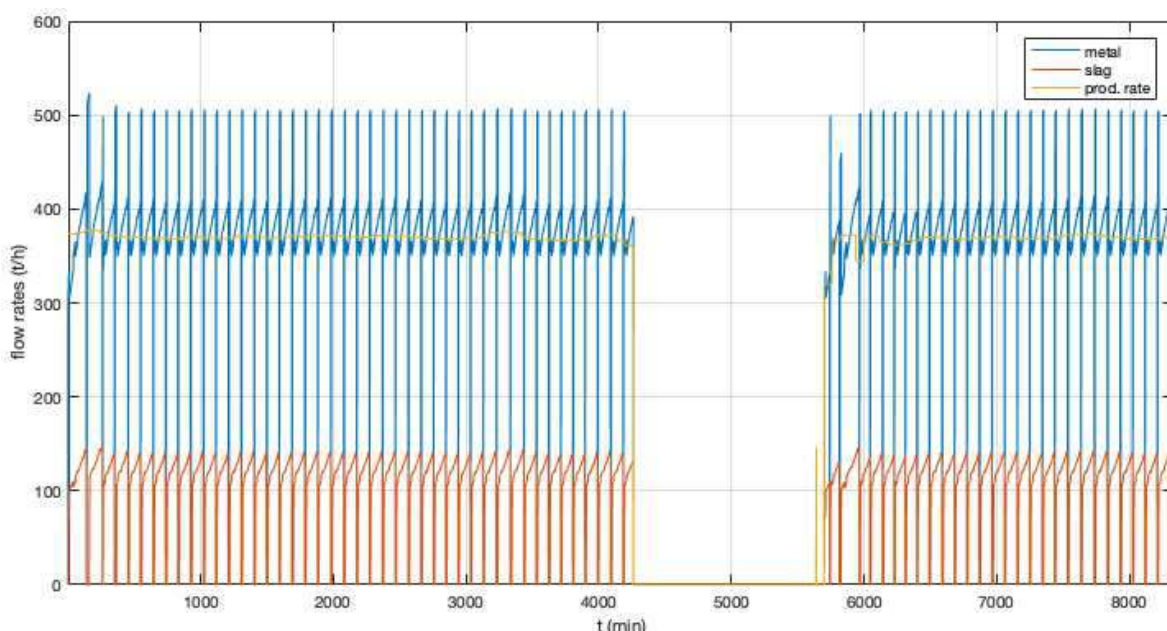


Figure 139: Results of a testcase for the drainage model; calculated drainage rates and the production level of BF-A for a period of 135 hours.

As can be seen from Figure 138 and Figure 139 the model is stable and the liquid levels and flow rates quickly converge to plausible results. Thus, this simplified 1D model is well suited for cross-checking CFD results and providing useful start values and boundary conditions for the CFD drainage model.

2.2.1.6.4 CFD MOHDRAIN 2.0 industrial validation

Validation of MOHDRAIN 2.0 was intended to be done during an industrial campaign on a BF of ArcelorMittal where the MOHDRAIN is already implemented. It was expected that the validation would be based on slag arrival / end of tapping and strain gauge measurements.

The current state of MOHDRAIN 2.0 development allows performing on-line simulations, yet the computing time is rather long and is comparable to a real casting time. Thus, historical data of the industrial blast furnace casting was used to validate the model. A sensitivity study was performed to check the most influential parameters in the drainage performance. The operational principle of MOHDRAIN 2.0 is shown in Figure 140.

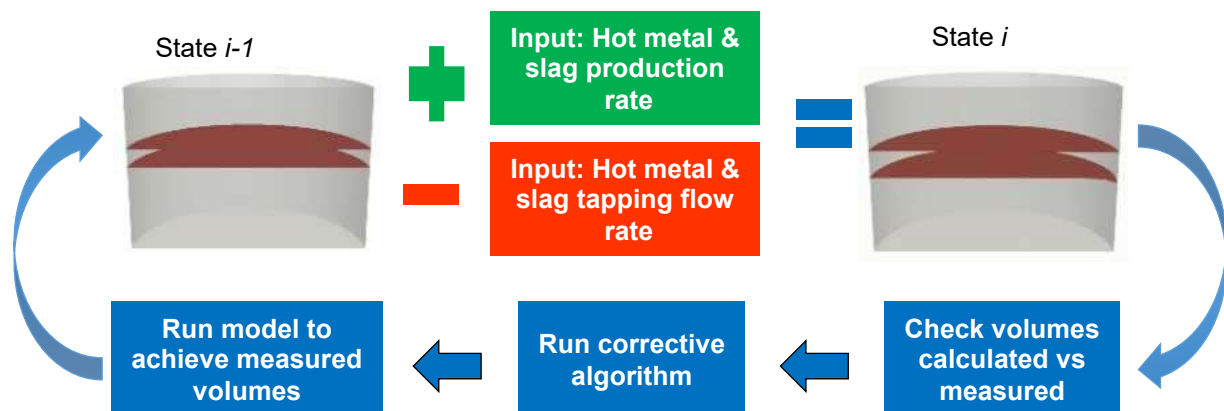


Figure 140: Calculation flow of MOHDRAIN 2.0.

MOHDRAIN 2.0 was planned to operate in the following way. When the cast starts, i.e. tap hole is drilled, the model receives the input data: hot metal and slag production (calculated: coming from an instantaneous mass balance model) and hot metal and slag tapping flow rate (measured). Controller treats the input data to align it in time and units needed for Core (refer to Figure 114). The previous state of the model, i.e. "State i-1" in Figure 140, corresponding to the state at the end of the previous cast is taken as a depart point for the calculation. The model simulates the liquid drainage in the hearth, and the model arrives to "State i" in Figure 140. The calculation time was planned to be minimal owing to applying rather long-time steps in the solver. Whenever the model achieves State i the calculated liquid volumes should be checked with the measurement by Controller. In case if the calculated and measured volumes are not equal, then the Controller would adjust the imbalance and the case would be re-run from the very beginning of the cast to achieve the measured liquid volumes. The whole idea of MOHDRAIN 2.0 is to furnish an operator with a verified by measurement on-line estimation of the liquid levels in 3D domain. It is worthwhile to mention, that the model was built to be easily adjustable. For instance, the porosity of the domain can be set up in a dedicated file which can be fed automatically. The same is applicable to any input parameter. So, implementation of the model to the plant's automation system is rather straightforward.

The current state of MOHDRAIN 2.0 development allows performing the described above process, yet the computing time does not allow a practical application of MOHDRAIN 2.0 on-line at the shop floor. The upscale model MOHDRAIN 2.0 is based on the hearth geometry of one of the ArcelorMittal blast furnaces. The model's domain features the real dimensions of the furnace, i.e. diameter of 9.86 m and height of 6.79 m. For such a domain the computing time for one case representing the whole cast is of order of 2 hours on a single computer fitted with Intel® Xeon® CPU E5-2643 v3 @ 3.40 GHz 3.40 GHz (2 CPUs) and 32 GB RAM. Initially it was planned to increase the timestep of the simulation, but finally it was seen that the maximum achieved timestep was 0.2 s. Beyond this timestep the model is not able to perform the simulation. It means that presently the computing time is in order of the real casting time. This is not favourable for the direct use of MOHDRAIN 2.0 on the shop floor. That is why the sensitivity study and the model validation were performed using the historical data of Fos BF 1 casting.

The historical data on the ArcelorMittal Fos-sur-Mer BF 1 casting was used to perform the sensitivity study and the validation of the model. The details of one of the casts exploited in the study is given in Table 25. This cast was considered a reference case for the sensitivity study.

Table 25: Industrial AM Fos BF1 cast data.

Data	Inter-cast period, (min)	Slag arrival, (min)	Cast duration, (min)	Mass of tapped hot metal, (t)	Mass of tapped slag, (t)	Hot metal production rate, (m ³ /s)	Slag production rate, (m ³ /s)
Industrial cast	21	8	124	631	196	0.006356	0.004398

The purpose of the sensitivity study was to investigate the influence of the input parameters on drainage. Slag viscosity and dead man porosity were considered the main influencing factors on the drainage performance. In addition, the conditions on the taphole were checked. Thus, the taphole erosion was simulated.

Taphole erosion was considered an important element in the drainage description. The technique to measure the taphole diameter enlargement during the tapping has been already tested in SUSTAINTAP project [55]. This technique allows measuring and registering the data in on-line mode, which can be exploited in the model. Such data or rather a given law of the taphole erosion are used in the model.

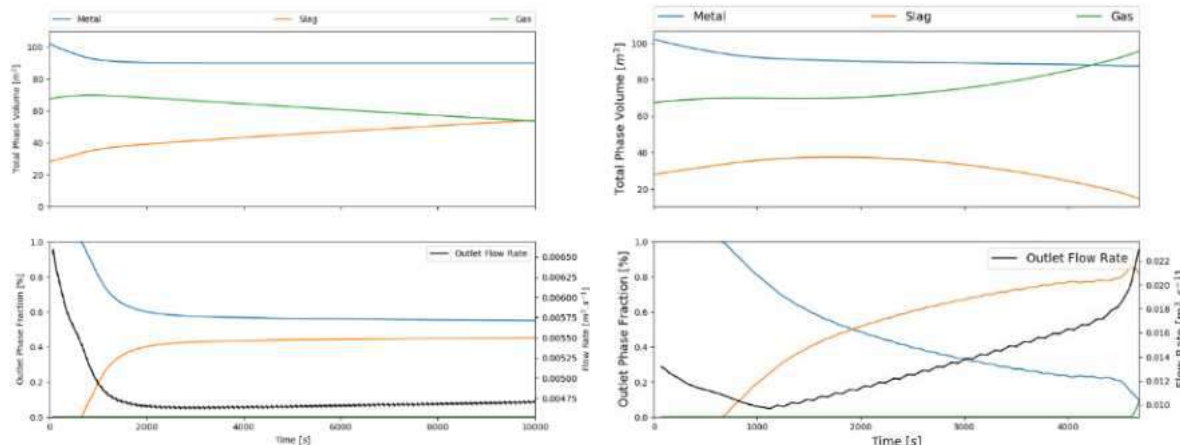
All the cases had the same initial levels of slag and hot metal above the taphole being 1 m and 0.5 m respectively. The drilling bit diameter was of 50 mm in all the cases. The densities of all the phases were kept constant in all the cases being 6700, 2600, and 1 kg/m³ for hot metal, slag, and gas respectively. Hot metal kinematic viscosity was $7.46 \cdot 10^{-7}$ m²/s in all the cases. In all the cases the taphole diameter enlargement during the tapping was enabled.

The details of the cases simulated in the study are given in Table 26.

Table 26: Details of cases run in the sensitivity study.

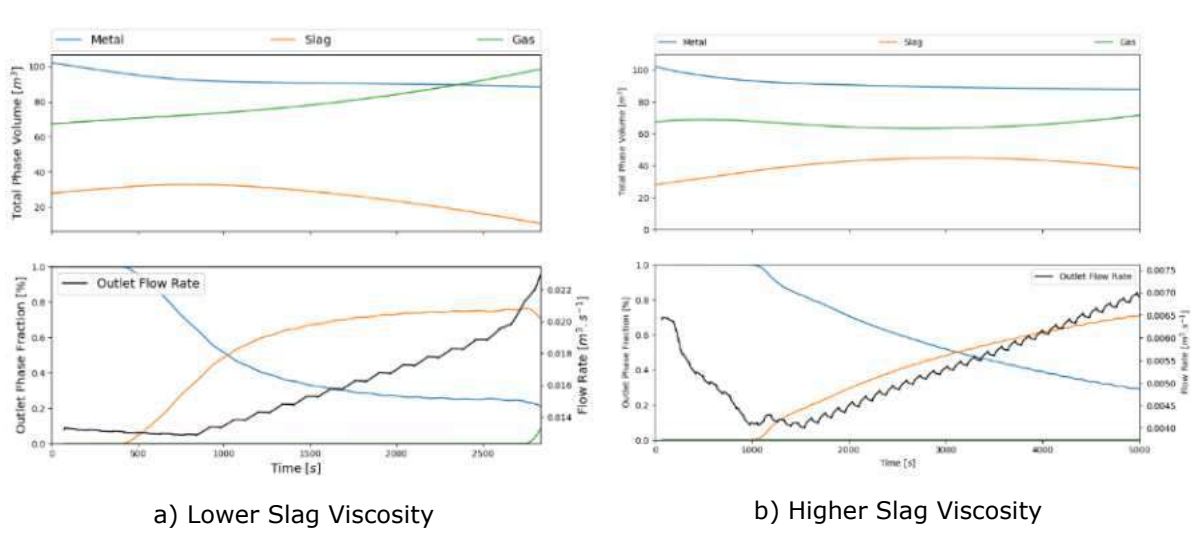
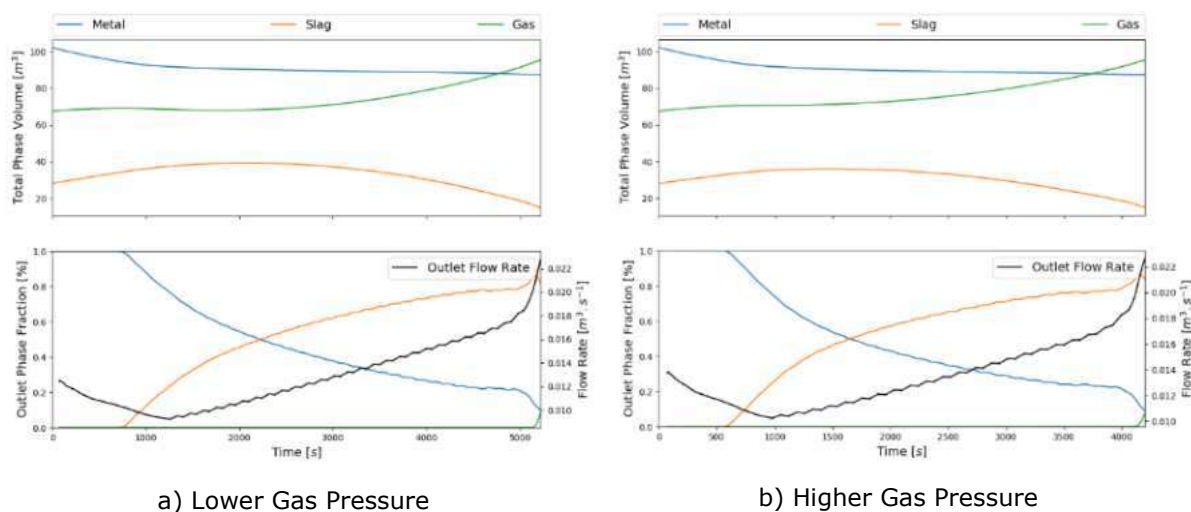
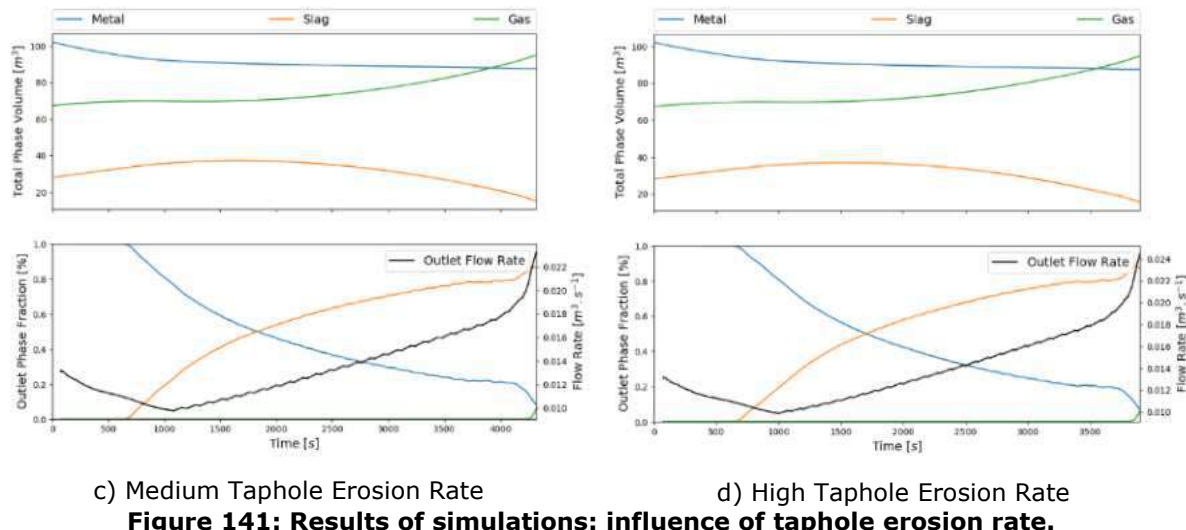
Case	Slag kinematic viscosity (m ² /s)	Porosity	Gas pressure, (bar)	Taphole diameter enlargement (mm/min)
Reference	$1.54 \cdot 10^{-5}$	0.38	3.5	0
Low slag viscosity	$1.54 \cdot 10^{-6}$	0.38	3.5	0
High slag viscosity	$1.54 \cdot 10^{-4}$	0.38	3.5	0
Low dead man porosity	$1.54 \cdot 10^{-5}$	0.37	3.5	0
High dead man porosity	$1.54 \cdot 10^{-5}$	0.39	3.5	0
High gas pressure	$1.54 \cdot 10^{-5}$	0.38	3.8	0
Low gas pressure	$1.54 \cdot 10^{-5}$	0.38	3.2	0
High taphole erosion rate	$1.54 \cdot 10^{-5}$	0.38	3.5	0.60
Medium taphole erosion rate	$1.54 \cdot 10^{-5}$	0.38	3.5	0.50
Low taphole erosion rate	$1.54 \cdot 10^{-5}$	0.38	3.5	0.43

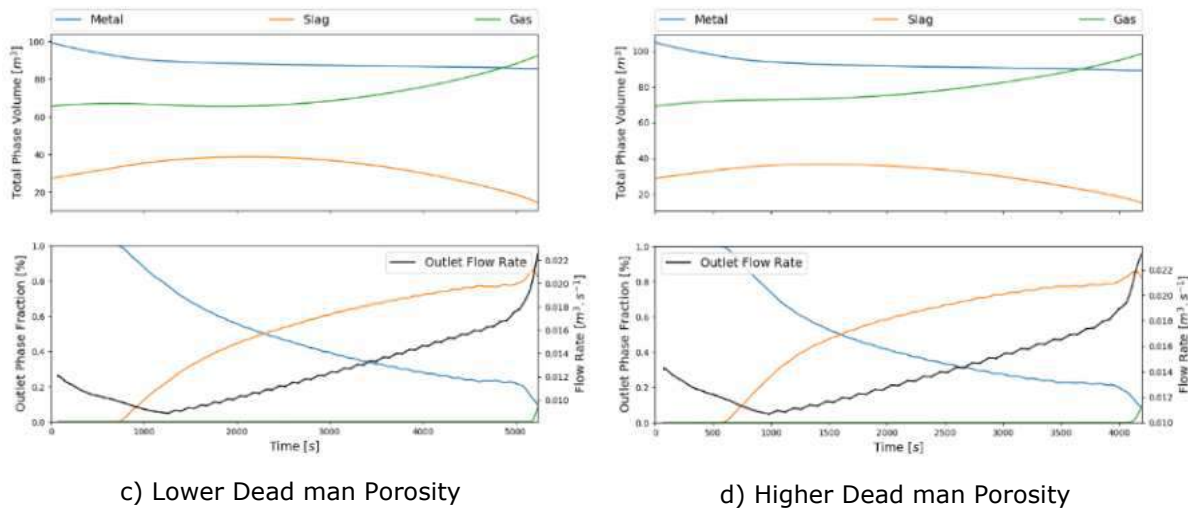
The results of the sensitivity study are given in form of graphs showing the total volume of slag and hot metal in the hearth and distribution of slag, hot metal, and gas volumes at the taphole.



a) Reference

b) Low Taphole Erosion Rate




Figure 143: Results of simulations; influence of slag viscosity and dead man porosity.
Table 27: Results of the sensitivity study.

Case	Slag arrival time (min)	Gas arrival time (min)	Slag volume at the end of the cast (m³)	Hot metal volume at the end of the cast (m³)
Reference	10.0	no event	45.66*	89.98
Low slag viscosity	9.9	47.2	10.91	88.27
High slag viscosity	16.3	no event	36.34*	87.79
Low dead man porosity	17.0	87.3	14.57	85.57
High dead man porosity	13.1	70.0	15.12	89.34
Low gas pressure	16.9	87.2	14.79	87.56
High gas pressure	13.0	60.0	15.07	87.39
Low taphole erosion rate	14.7	78.2	14.89	87.45
Medium taphole erosion rate	14.7	72.0	15.21	87.54
High taphole erosion rate	14.7	65.0	15.43	84.61

* Value obtained at 87.3 min from the start of the cast.

The results of this study show that the model responds adequately to the most critical input data. The model can be further fine-tuned in-order to reproduce the real casts. It was seen that this can be achieved via extensive parametric study of the influence of the most important input data on the drainage behaviour. With this respect, the dead man porosity distribution is considered one of the most influencing factors. It is worthwhile to mention that the model features the possibility to change the taphole diameter during the simulation. It is especially valuable for reproduction of the real casts on-line as there is a technique to measure the taphole diameter enlargement during the casting [55].

2.2.1.6.5 Physical model

2.2.1.6.5.1 General design of the physical model

A physical model is carried out in a cylindrical tank with a porous dead man like made of neoprene beads. The cylindrical tank has been built with a global scale of 1/20 based on TSE BF7 hearth characteristics. It consists in a 700 mm diameter acrylic glass hearth in which are used two rheological fluids to model hot metal and slag.

The global water model is composed of several parts such as tanks, pumps and valves (Figure 144). Preparation tanks can contain close to ten times the effective volume tapped of the process tank, which allows performing several taps successively during the same trial. Then both fluids are decanted and re-introduced in their respective preparation tanks.

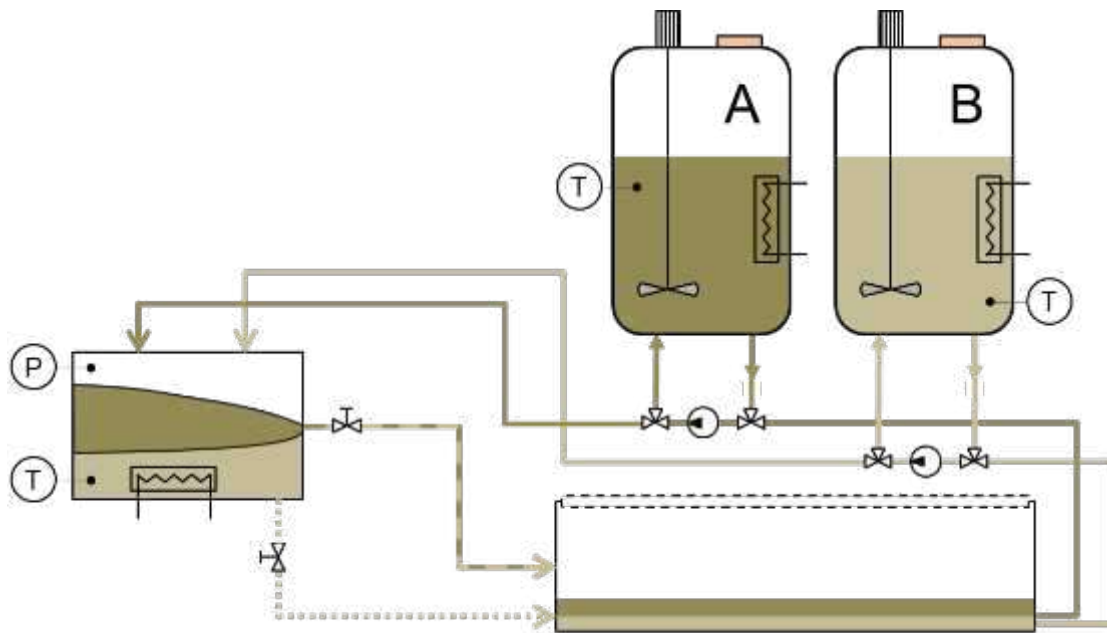


Figure 144: Schema of the "water model" including the process tank (on the left), two preparation tanks (on top) and a decantation bund (on the bottom).

The process tank is equipped with nine theoretical taphole positions (3 angles, 3 heights): before a trial, an angular position is chosen, and three valves are installed at three different heights. The objective there is to observe the impact of the taphole height on the flows inside and outside the hearth during tapping. Later, it will be possible to simulate alternate taps from north to south for instance.

2.2.1.6.5.2 Fluids of the physical model

A major step of the development of the water/physical model has been the choice of both fluids to model slag and hot metal. The important part was to be able to fit both viscosity and density ratios of those fluids close to room temperature (Figure 145).

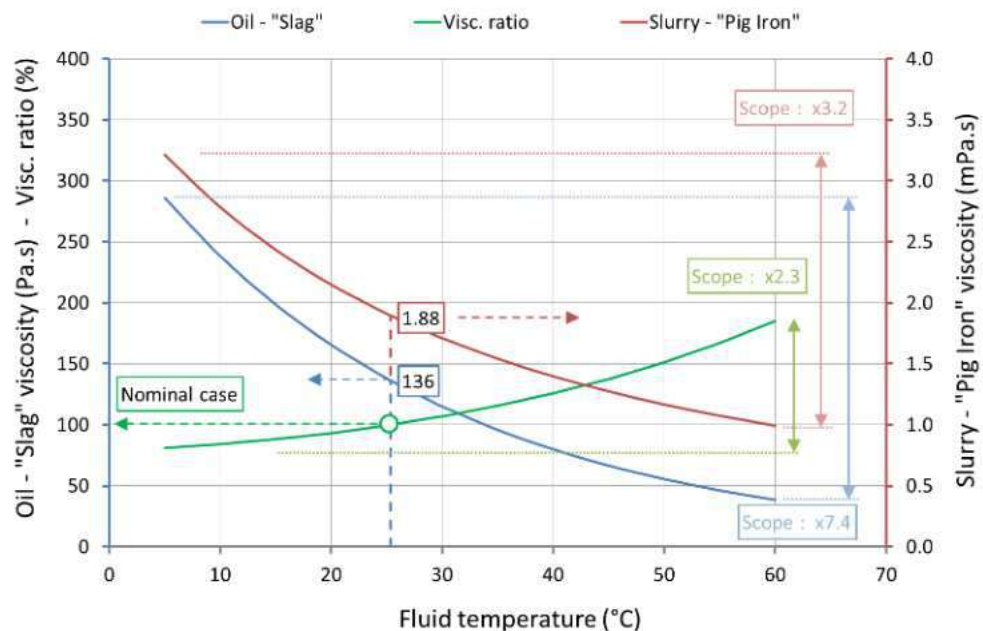


Figure 145: Evolution of oil (blue) and slurry (red) viscosities and viscosity ratio (green) with temperature.

Hot metal has been chosen as a nano-slurry: a water-based liquid charged with nano-particles of zirconia. Commercial oil is used as slag. That type of slurry has cons because it is subject to sedimentation and must be employed in an acidic environment (pH3). To compensate the sedimentation, slow rotating blenders are used in the bottom of the preparation tanks. Moreover, small particles tend to be abrasive while flowing so materials in tubes, pumps and tanks had to be chosen wisely.

A particular care to meniscus shape and flow rates through the taphole has been considered. Many work reports on physical [87] and [92] or mathematical [89] models for tapping, and design philosophy may be different depending on authors. Nouchi assumed that its model should have the same dumping angle during the time of the tapping [92].

Many mathematical tests have been conducted in-order to keep non-dimensional numbers ratios such as Reynolds' at taphole. Unfortunate, those ratios can't be fully retained but flow regimes will be conserved at least. For instance, Reynolds ratio during tapping is estimated to 700.000 in operative conditions but the model can barely reach a value of 10.000, although the flow regime is turbulent.

2.2.1.6.5.3 Preliminary trial using demineralised water

A preliminary trial has been performed using demineralised water inside the process tank. The objective of that trial was to verify that the design of the tank and valves used for the tapping were functional. As such, the process tank was filled to approximately 2/3rd of its capacity and then drained of 50mm (approximately 19L) of water through the taphole. The water level inside the hearth and the water jet at the taphole were both recorded with a CCD camera (Figure 146).

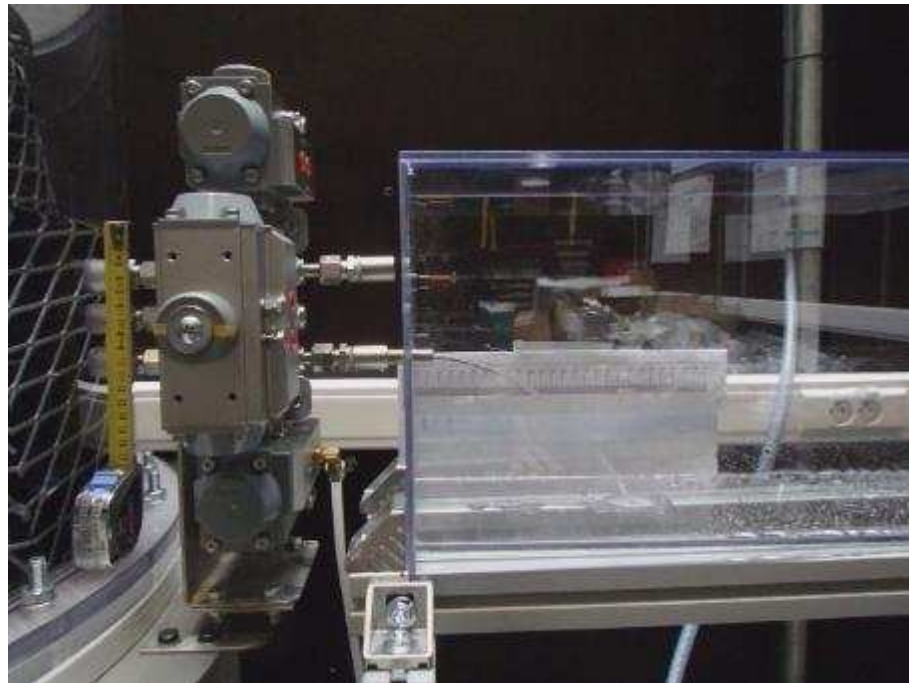


Figure 146: Observations of the water level and water jet at the taphole during tapping of the water model.

An image analysis has been performed with steps of 30s to measure the water level in the hearth and the water jet length. Measurements of the tapped volume of water and the nondimensional jet length are presented at the (Figure 147).

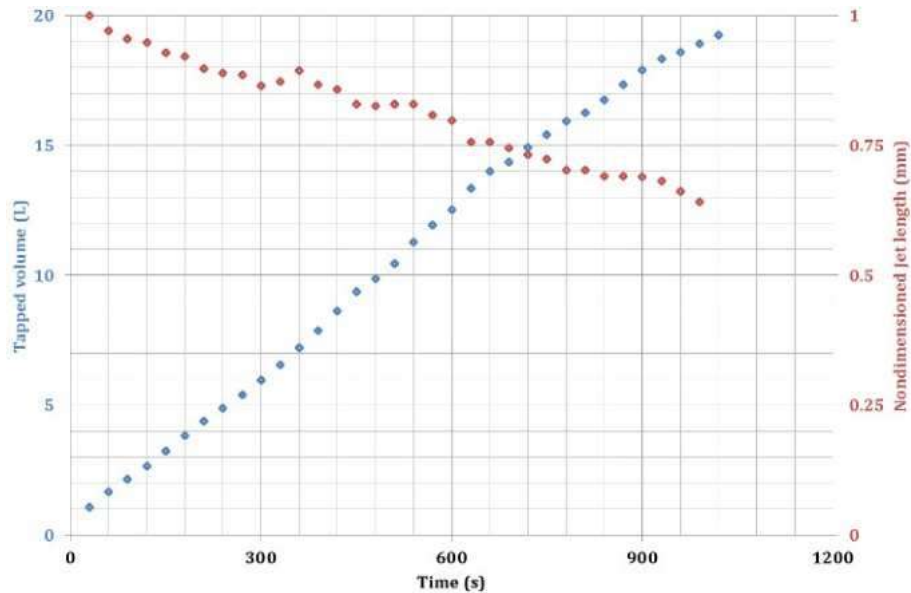


Figure 147: Evolution of the tapped volume of water and the waterjet length during preliminary tapping trial on the water model.

As the pressure decreases inside the hearth due to the tapping of the water, the jet length becomes shorter and shorter. As we expect that the jet length reaches 0 (or close to that depending on viscosity) when the water level is close to the taphole. It can be explained by Bernoulli's equations because the pressure induced by the water level tends to be proportional to the water velocity at the taphole. Then we could expect a quadratic evolution of the jet length because it should be proportional to the water velocity (Figure 148).

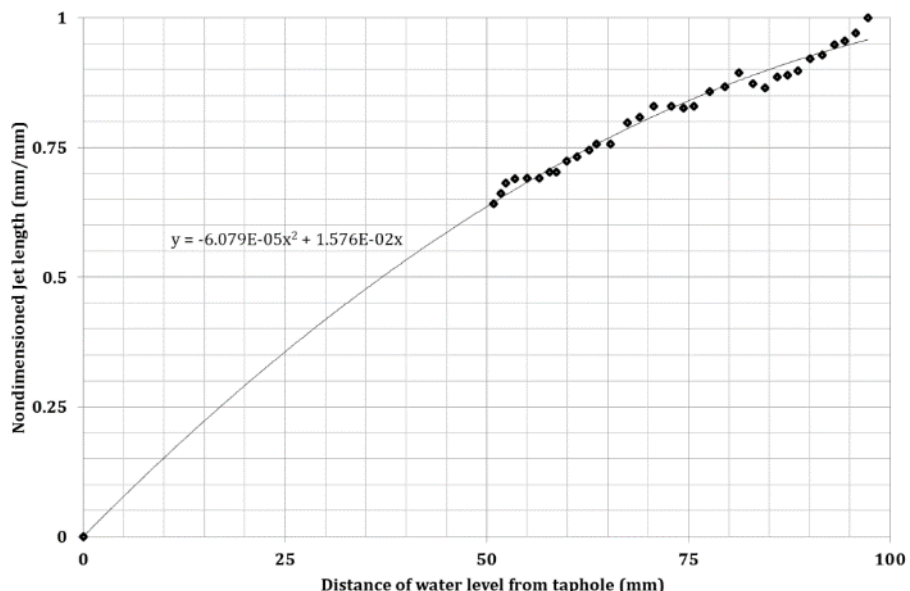


Figure 148: Evolution of the jet length as a function of the distance of the water level from the taphole.

By using a kinematic analysis and Bernoulli's equation, it is then possible to estimate the water velocity at the taphole. However, the former estimates it at the outlet of the taphole, while the latter estimates it at its entrance. It could then be possible to estimate the pressure drop through the taphole using Bernoulli's equations (Figure 149).

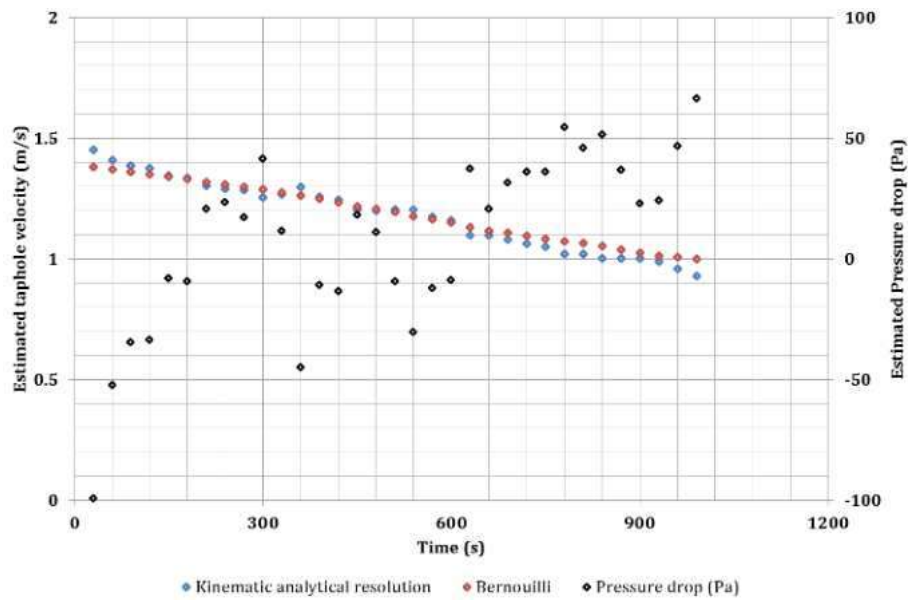


Figure 149: Analytical estimations of water velocity at taphole using a kinematic analysis and Bernoulli's equations, and the estimation of the pressure drop inside the taphole.

Both estimations of the water velocity are close and evolve from 1.4 m.s^{-1} to 1 m.s^{-1} during the trial. The pressure-drop evaluated in this case is really low and sometimes even negative which is not really physically possible. It is too low compared to the precision of the optical measurements.

It is important to note that because of the low velocity and the low viscosity of the water, no dumping angle has been observed. Such a phenomenon is expected, while using oil with the hearth set under pressure.

2.2.1.6.5.4 Conclusion

The initial goal of that task was to develop and build a water model which purpose was to assess the impact of several parameters such as internal pressure, the fluids viscosity and density and the impact of the coke bed on tapping. The design and construction of such a pilot may have been a bit ambitious for a completion during this project. Indeed, we encountered several issues with suppliers because our needs were very specific. The specifications were regularly modified during the construction because of those issues and solutions were often very expensive. At the end of the project, the water model is not fully operational. However, a validation test has been performed with demineralised water to check the process.

2.2.1.7 Fundamentals of behaviour of coke particles in BF Hearth

The knowledge of chemical reactions and coke particle movement in the BF hearth has been widespread between the OPTIBLAFINS partners. Therefore, it was acknowledged to set up a literature survey collecting any available knowledge. A summary of a literature review for the fundamental behaviour of coke particles in the BF hearth is divided into three parts: coke gasification and reactivity, carburization and coke ash and the interaction between coke and slag.

2.2.1.7.1 Coke gasification and reactivity

The reactivity of coke is the result of physical and chemical properties of coke and parent coals as well as conditions during the coke making process. Coke from higher rank coals shows lower reactivity than from lower rank coals. In general, higher rank coals produce coke with coarser mosaic texture than lower rank coals that produce coke with finer mosaic texture which is more reactive. Reactivity of coke is related to the amount of isotropic and anisotropic structure. The isotropic structure is more reactive than the anisotropic structure. Experiments show that the inertinite in the parent coal is the main source for the isotropic structure and that vitrinite is the main source for the anisotropic structure in coke. Defects in a carbon planar network or fissures and edges are more reactive than other coke sites. Increasing porosity leads to higher reactivity of coke. The standardized test for reactivity and hot strength, the NSC test, and conditions in the BF differ. The CO₂ content is 100% in the NSC-test and around 20-30% in the BF at the test temperature. The difference in gas composition affects the reaction mechanisms and disintegration of coke. Iron, calcium and alkali compounds are considered to be the most relevant catalysts to increase the rate of the Boudouard reaction and at low temperatures the coke gasification rate is almost completely controlled by the presence of catalysts. The mineral form of ash seems to influence the reactive properties of coke. The mineral form of ashes between cokes varies more

strongly than the elemental composition of the ash. Catalysts, apart from alkalis, can also be used to improve C consumption in the BF by activating nut coke as a coating by slurry on the surface of nut coke. Tar-rich gas is formed during the carbonization process which can crack and cover the coke surface resulting in a lower reactivity coke.

2.2.1.7.2 Carburization

Carburization of iron in the cohesive zone determines the ease at which liquid hot metal is formed. Carburization of iron is achieved by the direct contact of coke and iron and the transport of carbon atoms through a shallow liquid Fe-C layer on the coke-iron interface. The carburization rate is determined by several parameters as the most important are as follows. Coke ash minerals can accumulate and create a barrier at the interface layer between coke and liquid hot metal that can significantly reduce the carburization rate. An open porous ash layer can facilitate carbon transport by metal penetration through the ash layer. A non-porous layer makes direct contact of metal and carbon difficult. The wettability between coke and liquid hot metal influences the amount surface area that is available for direct contact at the interface. Decreasing wettability reduces the contact area and carburization rate. However, if the wettability is too high, a liquid ash layer can be formed between iron and coke that can also lower the carburization rate. Liquid slag can remove solid coke ash from the coke-iron interface by absorbing the ash and washing it away. Decarburization of liquid hot metal via SiO₂ and possibly Al₂O₃ reduces the carbon content of iron. Iron sulphides in coke ash can reduce to form liquid hot metal droplets saturated with carbon which can travel through the interface when the ash layer is liquid. Sulphur is a surface-active material that can lower the wettability of coke against liquid hot metal and reside at sites needed for carbon transport. The presence of calcium oxide in the ash layer and Sulphur in liquid hot metal can form a calcium sulfide layer which also reduces the carburization rate. The composition of the slag layer can change in time by chemical and physical processes. Ash components are not necessarily mixed together inside the cokes and can be present as inclusions in single or multiple phases. The mixing and melting together of inclusions and fluxes depends on mass transfer and takes time to occur.

2.2.1.7.3 Interaction between coke and slag

Studies include wetting behavior and slag reduction by laboratory and in some cases modeling of different slags and on graphite and/or coke carbon. In one study a graphite substrate and pressed coke powder as well as silicon carbide addition was used together with one type of slag. Both the slag and coke properties were found to influence the wetting behavior and an increase SiO₂ in the slag increased the wetting. This was also seen in another study of the slag wetting characteristics on coke substrate at 1500°C in a horizontal tube furnace and measuring CO/CO₂ generated during reaction was made. Both the slag and the coke properties were found to influence the wetting behavior and increasing SiO₂ in the slag e.g. increased the wetting. Synthetic at 1600 °C pre-melted slag (with B2 1.0, 1.3 and 1.6) was tested on coke, original coke and coke gasified 20%, 40% and 60% weight loss, respectively, was used. The increased basicity leads to decreased wetting, it was also found that the contact angle was decreased over time. Moreover, the wetting increased with gasification degree of coke indicating that higher ash amount should contribute to more wetting. Contrarily, the addition of SiC had the opposite effect.

Studies on MnO containing slag on graphite and three different coke types at temperatures of 1450-1550 °C showed increased reaction rate with increased wetting of the slag on the carbon material. The coke ash reacted with the slag and the wetting angle was increased with time. The basic MnO and acid ashes probably make the slag more fluid.

The reduction of FeO in iron saturated FeO-CaO-Al₂O₃-SiO₂ slag with carbon containing material (graphite, coke, bituminous coal and anthracite coal chars) at 1400-1600°C have been investigated. For the slag reduction by graphite and coke, the slag is partially wetting, and this facilitates the formation of a Fe-C alloy at the slag/carbon interface, providing a secondary source of carbon. Due to the low surface tension between the alloy and the slag, FeO reduction will be facilitated by the dissolved carbon in the alloy.

In general, the contact area between the slag and coke/graphite is about 4 times that of slag and char. Coal chars are poorly wet by the FeO-CaO-Al₂O₃-SiO₂ slags. Metallic Fe formed in the interface between slag and char particle are transferred away from the interface to the external free surface of the slag and can thereby not act as a secondary C source as in the case of reaction between slag and graphite/coke. The overall rates of reduction of iron oxide from slags are faster with graphite and coke than with coal char, despite the fact, that the reactivity's of graphite and coke in CO₂ are significantly lower than coal char.

Slag reduction investigation using two different models indicate importance of contact surface between coke and slag and importance of reaction rate for specific coke in case of small contact surface. The temperature has large impact as well as the reaction rate increases with increasing temperature. The temperature will increase the contact surface due to increased wetting.

2.2.2 Work Package 2: BF Hearth Monitoring

2.2.2.1 Improved hearth state monitoring data collection

2.2.2.1.1 Introduction

The aim of this WP2 is to further develop the lining monitoring techniques to achieve better understanding of the wear process and to enable early detection and prevention of wear. The current hearth monitoring is based on thermocouples installed at regular intervals in the lining. Often the distance between thermocouples reaches several meters over along the hearth circumference, while the wear events are at times known to concentrate at a spot of one meter in diameter. The systems tested in the project are used to deliver more detailed information with higher spatial resolution of the lining temperature and wear.

Optical fibres with high temperature Bragg gratings are capable monitoring the temperature along the whole line of the fibre. The fibres can be arranged as a network thus providing a high-density data set of the hearth temperature. The fibre measurement devices were tested in the SUSTAINTAP [55] project in the experimental blast furnace. In this project, the system has been evaluated in one of the operating industrial BF with harsher conditions in terms of displacements of the lining and the shell, potential liquid iron penetration in the lining joints and water ingresses. In the trial, the readings of the optical system will be compared and correlated with thermocouple data.

Complexity of the hearth structure featuring joints and materials of different wave conductivity is still to be overcome to realize the full potential of non-destructive monitoring systems. The detection of the liquid level variation with ultra-sound measurements [55] was much more difficult than expected. There are some other techniques available (like impact echo) using single receivers. In this project, the capability of the Hearth Echo Excellence (HEE) technique has been up-scaled to monitor the remaining thickness of the lining and the skull and to detect cracks in the lining using multi-receiver techniques. For this optimal signal emitting settings and received data processing routine has been established. It leads to creating a system featuring several transducer-receiver couples continuously monitoring the hearth wear.

2.2.2.1.2 Use of acoustic technique for hearth lining state monitoring

Acoustic measurements have predominantly been carried out by means of the HEE method for determining the hearth refractory thickness. This original method made use of one sensor and one impact device. That method is sensitive to the placement of the sensor on the shell and location of the impact. This may lead to measurement results which are hard to interpret and makes the selection of relevant dominant frequencies difficult.

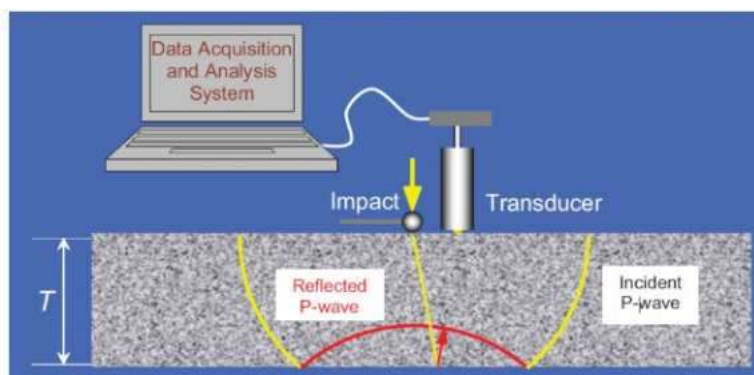


Figure 150: Hearth Echo Excellence, general working principle.

In a solid medium a pressure wave is created by an external impact (Figure 150). The resulting pressure wave is travelling through the medium with a velocity called wave speed C_p . This traveling pressure wave transforms to a standing wave with nodes at both surfaces. Therefore, half the wave length (λ) is equal to the medium thickness (T). The frequency (f) of this standing wave can be measured with the transducer.

The medium thickness than can be calculated from the wave speed and the measured frequency:

$$T = C_p / (2 \times f).$$

Optimizing Blast Furnace Hearth Inner State (OPTIBLAFINS)

Within the project it was proposed to conduct an experiment and increase the number of sensors that register the effect of one impact. This measurement could then be repeated with impacts on different locations. It is expected that in the measurement result of each sensor the dominant frequency associated with the full refractory thickness will be a common factor, making the distinction between "false" reflections and reflections at interfaces more reliably distinct therefore resulting in a more precise thickness measurement.

In general, the blast furnace wall consists of different layers. In this case there are 5 layers (Figure 151). The dimensions of especially the semi-graphite layer may vary per location which is caused by wear. The thickness of the shell, grouting and graphite are consistent for a certain hearth level. The thickness of the ramming, at the time of application a pasty material used to fill the gap between graphite and semi-graphite, is a few centimetres.

The impact echo pressure wave is reflected at each material transition and on larger imperfections, like cracks, within each layer. This results in a complex frequency spectrum.

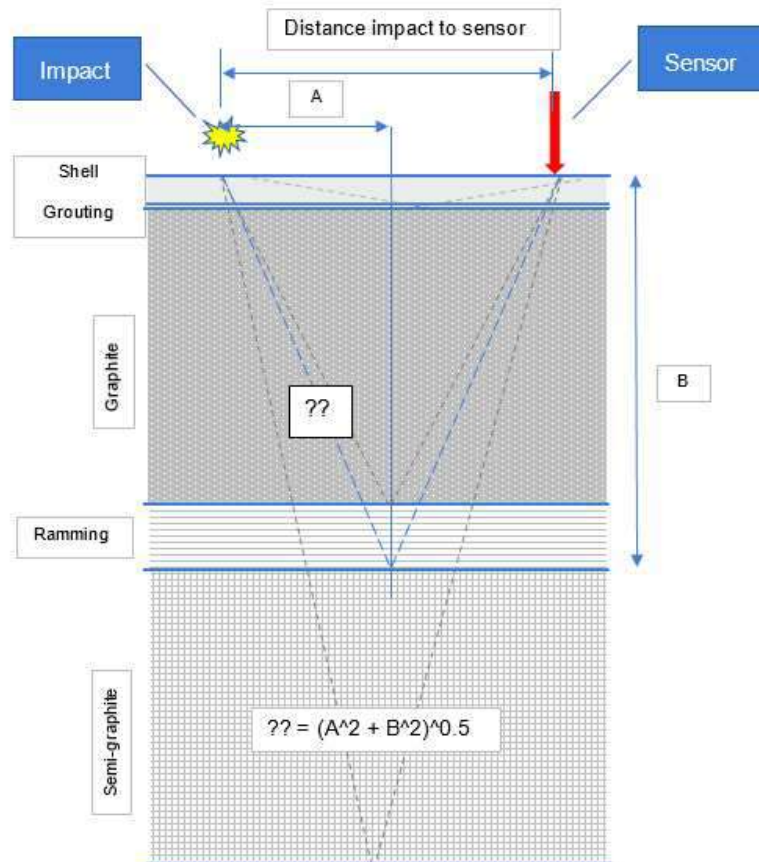


Figure 151: Blast furnace wall in detail.

Six sensors have been placed on a horizontal line on the shell. The shell has been impacted between the third and fourth sensor (Figure 152). An additional sensor has been placed 10 cm below the impact for additional data.

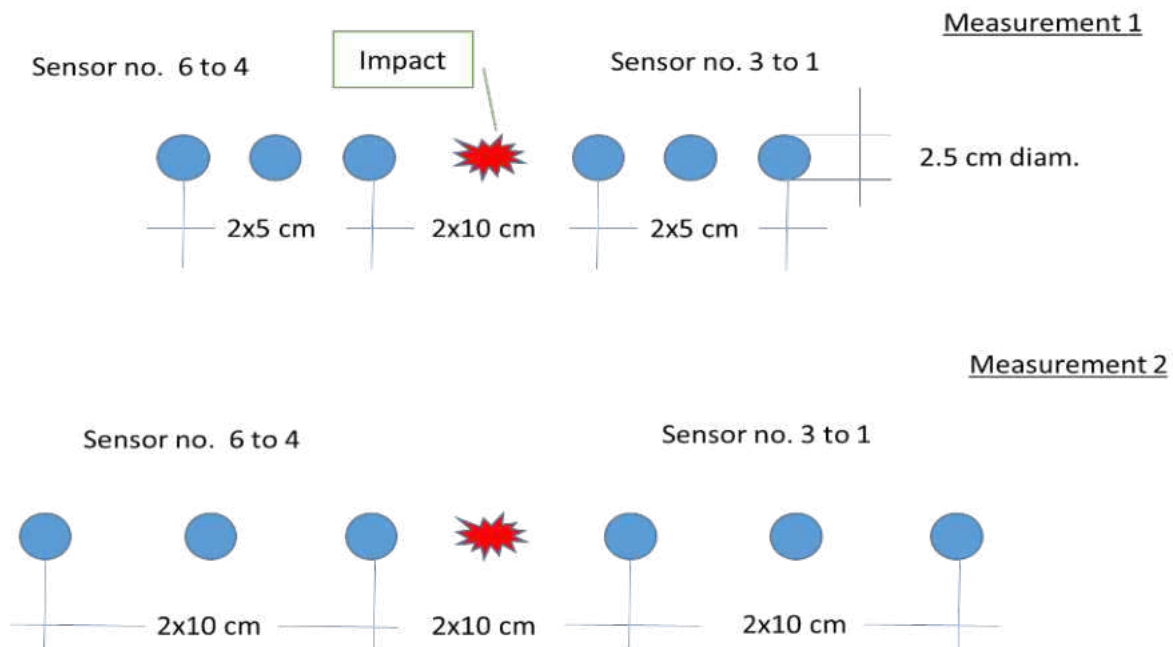


Figure 152: Sensor set up for measurement 1 and 2.

The complication introduced by using multiple sensors originates from the difference in measured frequency for the same material transition. This is due to the difference in traveling distance for different sensors. The further away the sensor is from the impact the larger the distance, the longer the wave length and the lower the corresponding measured frequency will be. In-order to see the effect of the distance on the shift in frequency two series of measurements have been carried out, one with 5 cm centre tot centre of sensor, and one with 10 cm. Due to the size of the hammer, which was used for the impact, the distance between sensor 3 and 4 was for both measurements 20 cm.

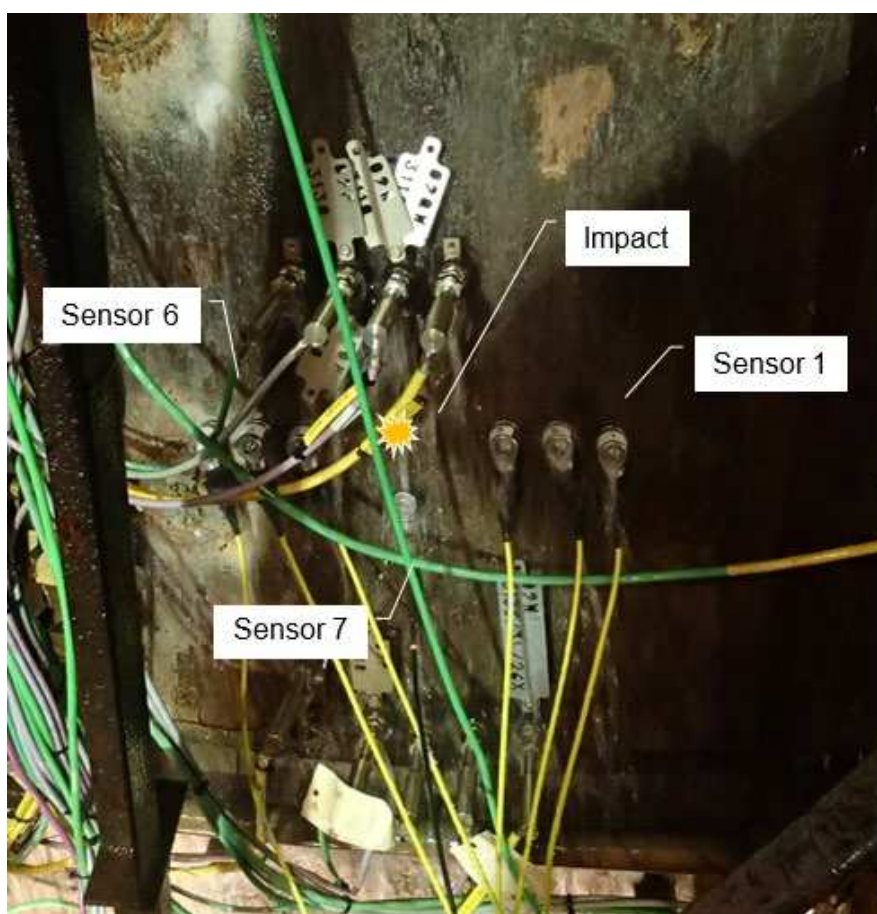


Figure 153: Set up of 7 sensors at tuyere 9, hearth level +3150 TSE BF6.

Figure 153 shows the sensor setup on the blast furnace shell below tuyere 9 at hearth level +3150, for a measurement type 1. This measurement has been carried out 5 times. On the same location, a measurement type 2 has been performed. And the same applies for the locations below tuyere 10, 11, and 12.

These locations have been selected on basis of the established refractory wear, which is based on measured refractory temperatures (Figure 154).

Below tuyere 12 hardly any wear is present, at tuyere 11 wear is apparent and steeply increasing to tuyere 9 where the semi-graphite is gone and only graphite is left.

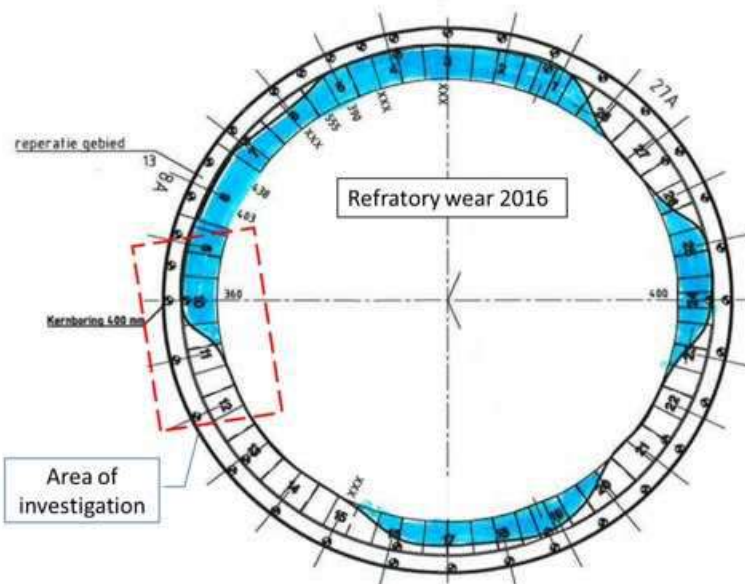


Figure 154: Refractory wear TSE BF6, hearth level +3150, calculation based on temperature measurements.

At the measurement location the sensors have been placed with a tool to ensure the correct distance between the sensors. However, the location for the impact was roughly in the middle of sensors 3 and 4. The individual measurements have been repeated five times per location and the correlation between the frequency spectra is high, showing that the impact does not influence the measurement result significantly.

The sensor data of all seven sensors has been recorded simultaneously. The data acquisition has been setup in that way that recording was triggered by the sensor signal. Sample rate was set at 50 kHz and 16380 samples.

2.2.2.1.3 Collection of data for monitoring of hearth and design of additional installations

In the blast furnace various chemical processes are driven by exchange of electrons. The flow of these electrons can take place via different routes, for instance refractory and shell. Due to internal electrical resistance potential differences are generated. These electrical potentials can be detected at the outside of the blast furnace on the blast furnace shell. By measuring the potential difference between for instance the bottom and a position higher up of the blast furnace an indication of the liquid level might be acquired.

This potential difference is influenced by changes of internal processes, like liquid level.

In the past the success of this shell potential measurement, called the EMF measurement technique, was limited due to insufficient correlation with liquid levels and therefore left room for improvement.

Alternative methods have been developed to improve the correlation between measurement value and liquid level.

These methods rely on change of electrical resistance of the refractory within the blast furnace because of changes in liquid level. The resistance of the refractory changes due to direct contact with the hot metal: the electrical resistance of the hot metal is low causing a short cut, and the temperature of the refractory material changes and with that electrical resistance.

By applying a constant voltage between points above and below the liquid level a change in current can be measured being a measure for the change in electrical resistance.

The conventional EMF sensor type has an electrical connection to the outside of the blast furnace shell. The newly developed EMF sensor types are connected with the refractory by making an electrical contact on the existing stainless-steel thermocouple housing. One EMF refractory sensor

type is still connected to the shell by the steel mounting on the shell, the other EMF sensor type has been insulated from the shell and is therefore only connected to the refractory.

2.2.2.1.4 Results

At the measurement location below tuyere 9 (Figure 154). The remaining wall thickness is 547 mm according to the calculation based on measured temperatures.

For the calculation of the primary dominant frequencies (DF), which correspond with known material transitions, the following data has been used (Table 28).

These DFs are valid for a distance between sensor and impact of 0 mm.

Due to the multi sensor setup the traveling distance of the pressure wave is longer and the DF decreases. Recalculated distance can be found in Table 29 and Table 30.

Table 28: Dimensions per layer and corresponding dominant frequencies for tuyere 9.

	Wave speed [m/s]	Layer thickness [mm]	total thickness [mm]	DF [kHz]
Shell	5800	45	45	64.444
Grouting	1600	2	47	55.502
Graphite	1900	340	387	2.660
Ramming	1460	30	417	2.398
Semi graphite	2600	130	547	1.934

Table 29: Re-calculated dominant frequencies (kHz) per sensor, measurement type 1.

	sensor 1	sensor 2	sensor 3	impact	sensor 4	sensor 5	sensor 6
Distance sensor - impact	-200	-150	-100	0	100	150	200
Thickness							
387	2.363	2.480	2.576	2.660	2.576	2.480	2.363
417	2.162	2.256	2.332	2.398	2.332	2.256	2.162
547	1.817	1.865	1.903	1.934	1.903	1.865	1.817

Table 30: Re-calculated dominant frequencies (kHz) per sensor, measurement type 2.

	sensor 1	sensor 2	sensor 3	impact	sensor 4	sensor 5	sensor 6
Distance sensor - impact	-300	-200	-100	0	100	200	300
Thickness							
387	2.102	2.363	2.576	2.660	2.576	2.363	2.102
417	1.947	2.162	2.332	2.398	2.332	2.162	1.947
547	1.696	1.817	1.903	1.934	1.903	1.817	1.696

In Figure 155 the low frequency part of the spectrum is shown. From this graph, it is clear that the high amplitude is the spectrum occur for similar frequencies and must therefore be related to vibrations. Arrows indicate where the DFs are expected, the numbers represent the sensor numbers and the lightning symbol the DF at the impact location.

No apparent reflections of pressure waves can be detected in the frequency spectra of the transition from graphite to ramming or ramming to semi-graphite.

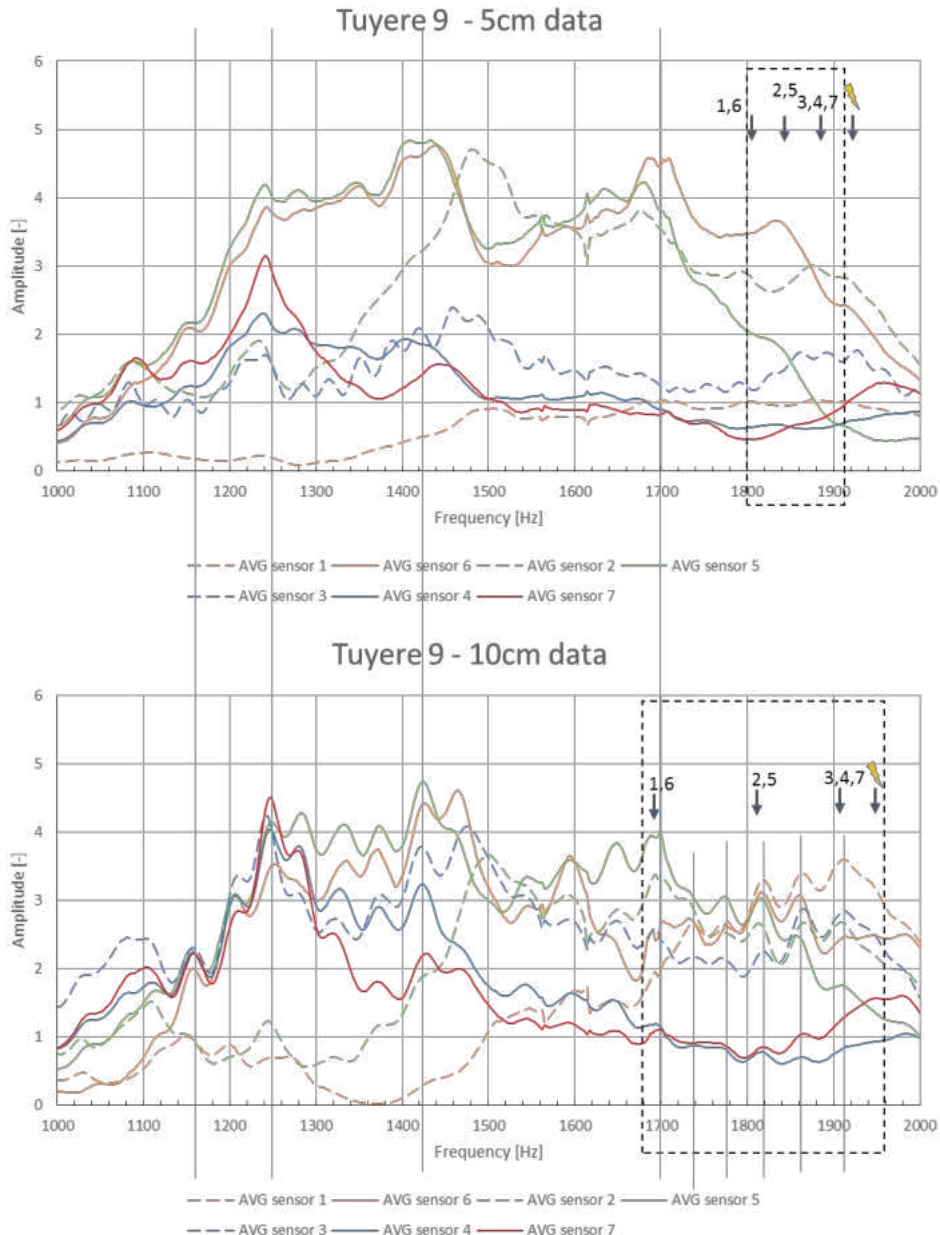


Figure 155: Frequency spectra for type 1 (above) and type 2 (below) measurements at TSE BF6, tuyere 9.

2.2.2.1.5 Conclusions

The analysis using the multi-sensor Hearth Echo Excellence technique showed the following conclusions:

- All measurements showed good correlation of frequency spectra of individual measurements. The quality of the impactor appears to have almost no influence.
- High amplitudes have been found at low frequencies for all locations. In view of the difference in refractory thickness these frequencies cannot be attributed to reflections at final refractory thickness. Seen the fact that this frequency was the same for each sensor it is likely that they have been caused by vibrations also because the signal in the time domain does not resemble the response from the shell and gap.
- The distance between impact and sensor causes a shift in frequency of a DF. In-order to distinguish reflections from vibrations the shift should be noticeable. Not too small with respect to the resolution of the measurement, not too large that correlation between sensors is not possible. Therefore, the spacing between sensors rely on the target depth of the measurement.

2.2.2.1.6 Use of optical fibres and strain gauge for monitoring of hearth lining state

A standard way of temperature measurement in a blast furnace hearth is performed with the use of hundreds of PT100 thermocouples that are installed at regular intervals in the refractory lining. Often the distance between thermocouples reaches several meters along the hearth circumference, while the wear events are at times known to concentrate at a spot with one meter in diameter. Optical fibres with high temperature Bragg gratings can monitor the temperature along the whole line of the fibre. They are insensitive to mechanical vibrations. Their small thermal mass also guarantees fast, sub-second, thermal response. Fibre optic sensors are connected to a read-out system (called interrogator), with a single, non-conducting optical fibre with an outside diameter of 250 microns or less. The fibre itself (around 10 microns) is isolated and protected by a coating, glass cladding, inner cladding and inner core (Figure 156).

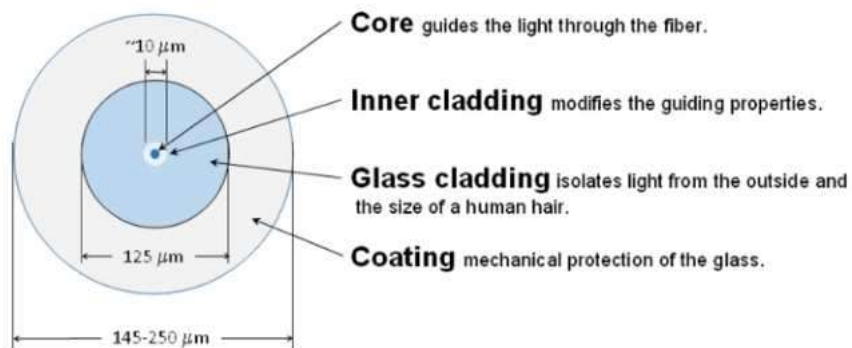


Figure 156: Optical Fibre build-up.

A typical type of a fibre optic sensor for temperature measurements is FBG (Fibre Bragg Grating), in which a periodic refractive index variation is written in the core of the optical fibre, usually UV-light interference. Light modes propagating along the fibre with a wavelength matching the period of the index variation, the so-called Bragg wavelength, will couple to a reverse travelling mode and will be reflected back to the FBG, while remaining, non-matching wavelengths, will pass through the FBG unaffected (Figure 157)

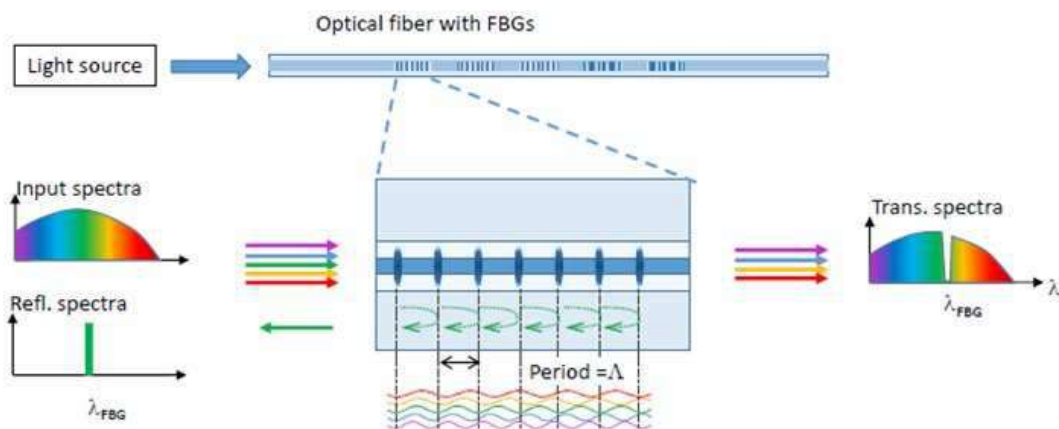


Figure 157: Fibre Bragg Grating (FBG) principle.

The Bragg wavelength is temperature dependent and this property can be used for temperature sensing. The principle is shown in Figure 158 in which a fibre sensor with five separate FBGs is exposed to an external heat source. Each FBG is a separate sensor point distinguished by its position x and its Bragg wavelength λ . The temperatures are calculated from the measured spectral shift for each FBG. By measuring the wavelength spectrum and comparing it with the spectrum taken at a reference temperature, it is possible to calculate the temperature at each sensor point.

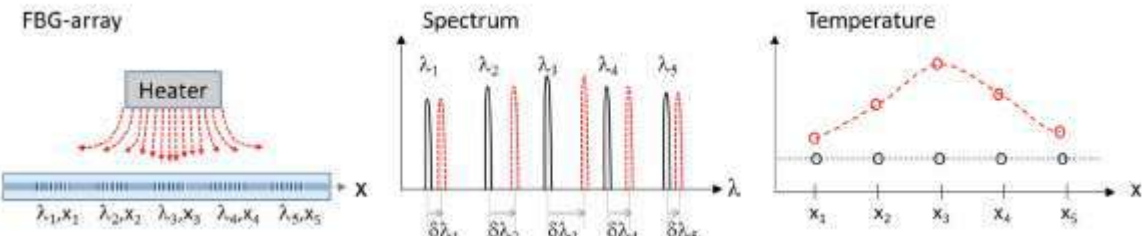


Figure 158: Temperature measurement with FBGs.

The glass fibre sensors to be used in the BF hearth consist of FBG-arrays each with 20 FBG sensors (1st sensor at 5mm from tip) positioned at equal distance, resulting in a total measurement length of 500mm. In total 2 FBG arrays has been assembled in a gas-tight tube and installed near tuyere 13 at +3100 and +3800 level BF6.

2.2.2.1.7 Results

The Fibre Bragg Gratings sensors at +3800 height level (1 meter below taphole) show promising results (Figure 159).

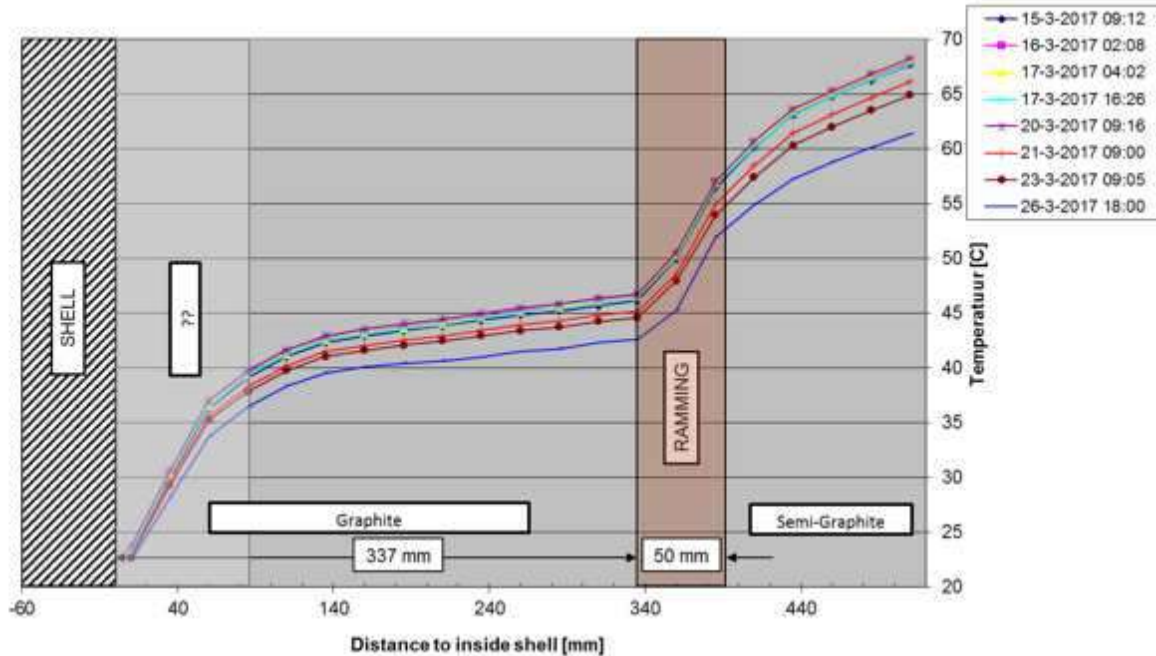


Figure 159: FBG temperature profile +3800 level BF6.

The temperature is changing linear, except for the hearth wall part close to the shell (indicated as ??). This part shows a non-linear behaviour, which could be explained by a temperature dependency of the graphite material. The maximum temperature is, in this case, of around 70 °C, that is far below any critical value. The temperatures are consistent in time and the device was very robust and reliable. Figure 160 shows the comparison with standard thermocouples close to the FBG position.

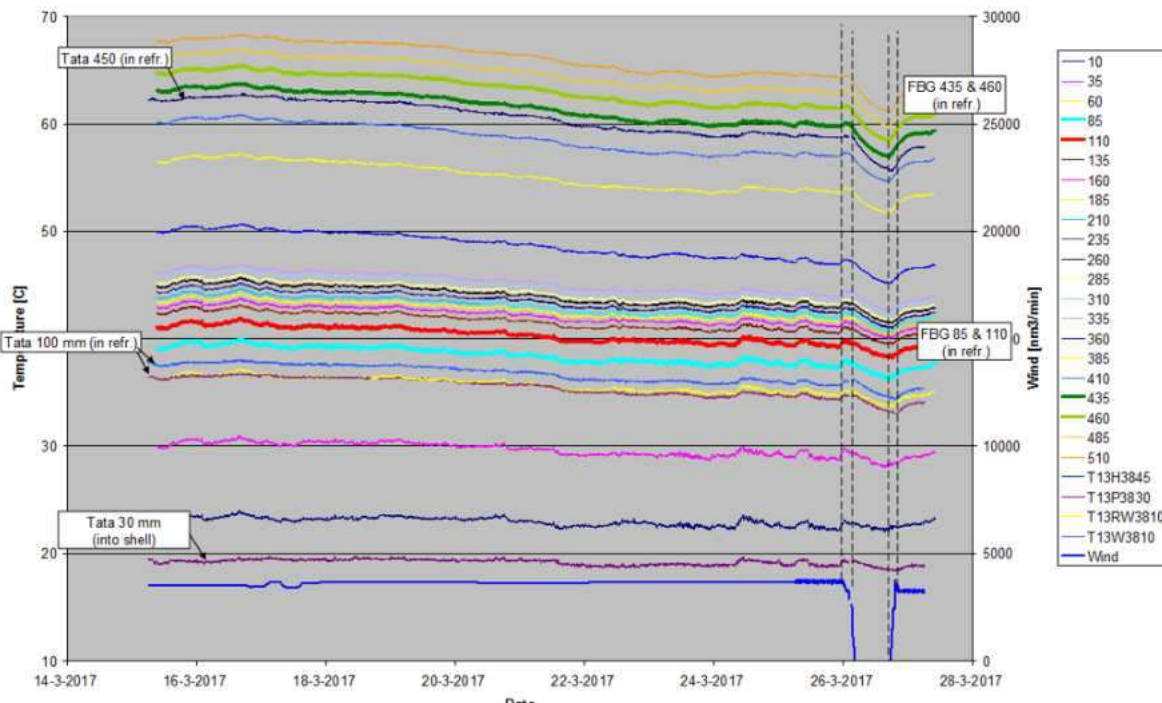


Figure 160: Comparison temperatures of FBG versus standard thermocouples BF6.

Thermocouple as well as FBG temperature data are following the same trend. However, the FBG data is much more detailed, because of the higher dense FBG's.

2.2.2.1.8 Relining observations, additional on-line measurements and measurement campaigns

There were good opportunities to collect samples, locate brittle layers, install new measurement systems and validate the estimations of the on-line monitoring tools since the BF's of AGDH and AMEH were relined during this project. The BF hearth at AGDH BF4 was excavated in July 2016 and at AMEH BF5A was excavated in September 2016. The basic blast furnace data for AMEH BF5A and AGDH BF4 plants can be seen in Table 31 and Table 32, respectively.

Table 31: General data of AMEH BF5A.

Nominal capacity	1650	kt/a
Hearth diameter	9.75	m
Working volume	1767	m ³
Last relining	1997	
Intermediate repair	2005	
Number of tuyeres	26	
Injection capacities	28 / 25	t/h (coal / oil)
Type of charging	PW bell-less top central feed	
Counter pressure	1.5	bar
Number of tapholes	2	at opposite sides
Cooling (bosh/belly/shaft)	Cu/Cu/Fe staves	
Hearth cooling	spray	

Table 32: General data of AGDH BF4.

Constructed	1974	
Enlarged	2003	
Hearth diameter	11.2 (10)	m
Working volume	2358	m ³
Total volume	2960	m ³
Number of tuyeres	30	

Additional multipoint-thermocouples (5x) and cooling water flow rate/temperature measurement systems have been installed besides standard (double) thermocouples at AGDH BF4. AMEH has performed stepped drillings and thermography measurement campaigns at BF5A. The aim of these

Optimizing Blast Furnace Hearth Inner State (OPTIBLAFFINS)

stepped drillings with temperature measurements (at every ca. 3cm progress) at hearth wall is to physically determine the brittle layer locations (Figure 161). The aim of the thermography measurement campaigns (Figure 162) is to measure the temperature evolution (Figure 163) when the hearth cooling is temporarily shut down in order to draw conclusions on the remaining refractory thickness.

Six stepped drillings have been performed at hearth layer C (level ca 7.3m) of AMEH BF5A during 14.01-13.06.2014. The observed temperature evolution through the depth is plotted in Figure 161. In general, a linear temperature increase has been observed. The higher rate of temperature indicates thinner residual refractory thickness. The stepped drillings have been stopped as soon as the brittle layers were encountered to minimize the risks. The results indicate that the wear has been highly progressed under tuyeres 18, 20 and 24 with brittle layer formation.

Several thermography measurement campaigns have been performed (e.g. under tuyere 7 and 19 at hearth layer C) at AMEH on 09.12.2015 as seen in Figure 162. By this way, the evolution of steel shell temperature (Figure 163) is measured when the hearth cooling is shut down. The higher rate of temperature increase is due to higher heat flux which indicates a thinner residual refractory thickness. This thermography measurements further support the findings from the stepped drillings.

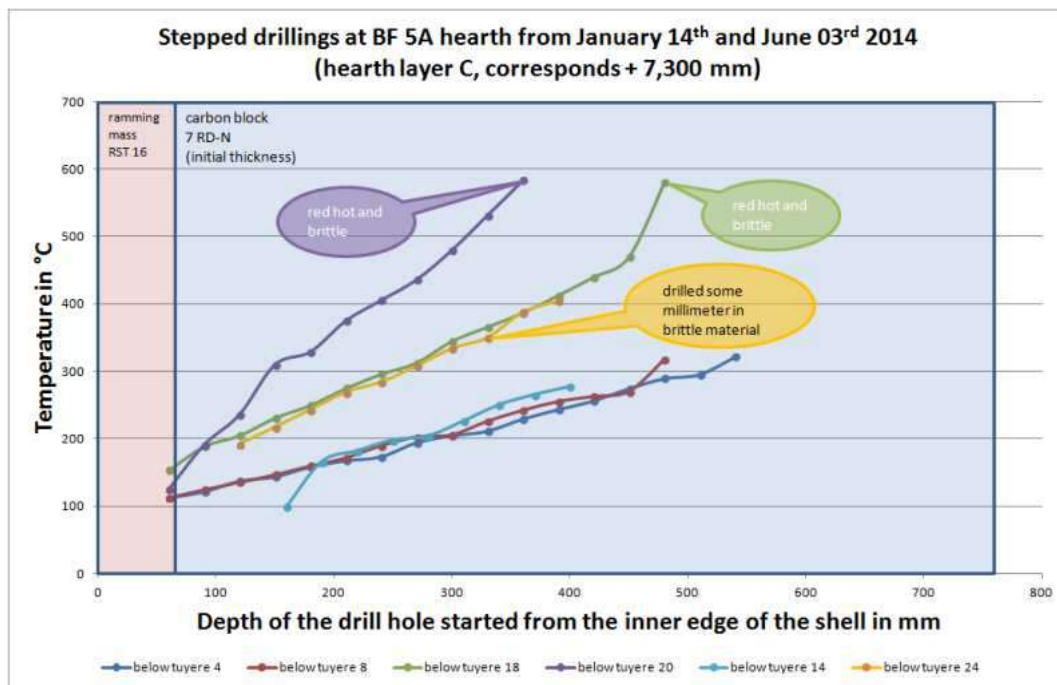


Figure 161: Stepped drillings at AMEH BF5A.

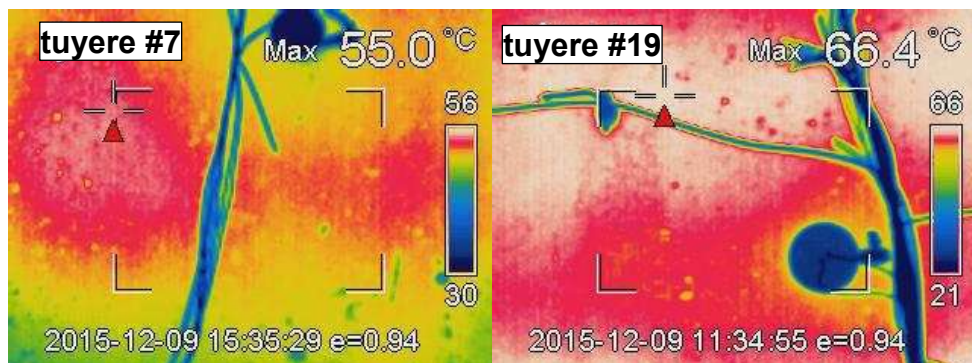


Figure 162: Thermography camera measurements at AMEH BF5A (below tuyere #7 and #19).

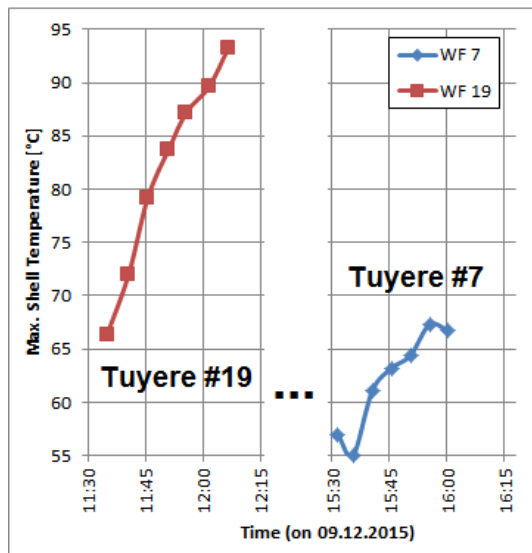


Figure 163: Evolution of hearth shell temperature at AMEH BF5A (below tuyere #7 and #19).

The residual refractory thickness at AMEH BF5A and AGDH BF4 has been carefully measured during their relinings in 2016. A typical residual wall thickness measurement under tuyere 19 hearth layers C, D and E at AMEH BF5A was shown in the photo on the left side of Figure 164. The measurement values are marked on the technical drawing as shown on the right side of Figure 164. The wall thickness measurements can be represented in a contour plot for the unrolled hearth wall and hearth bottom as in Figure 165. For a better understanding of the complete wear topology, the hearth wall and bottom layers are shown together. TH1 region has experienced more wear than that of TH2 region.

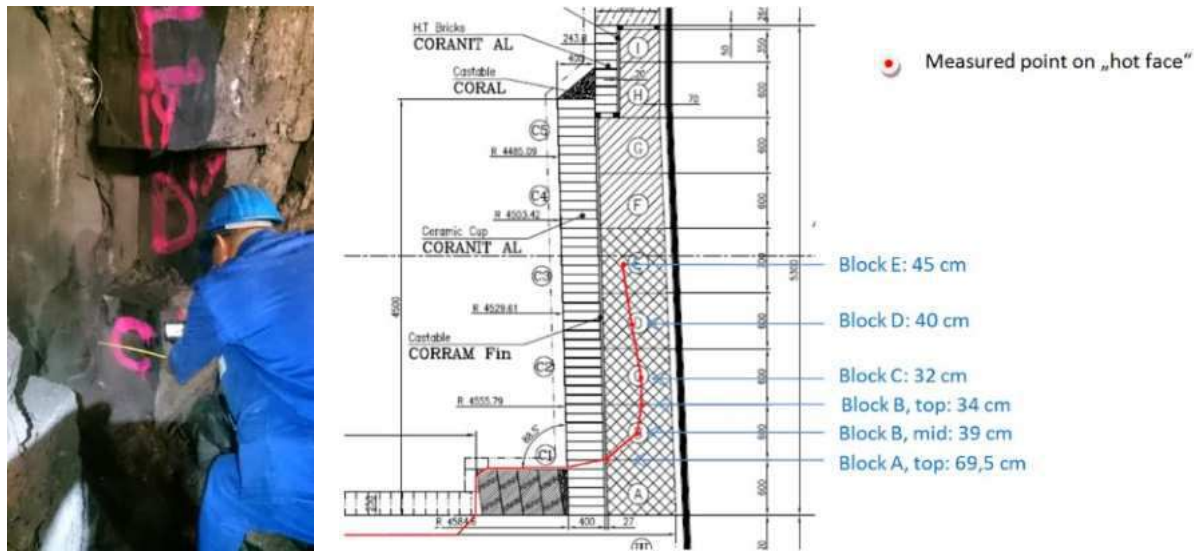
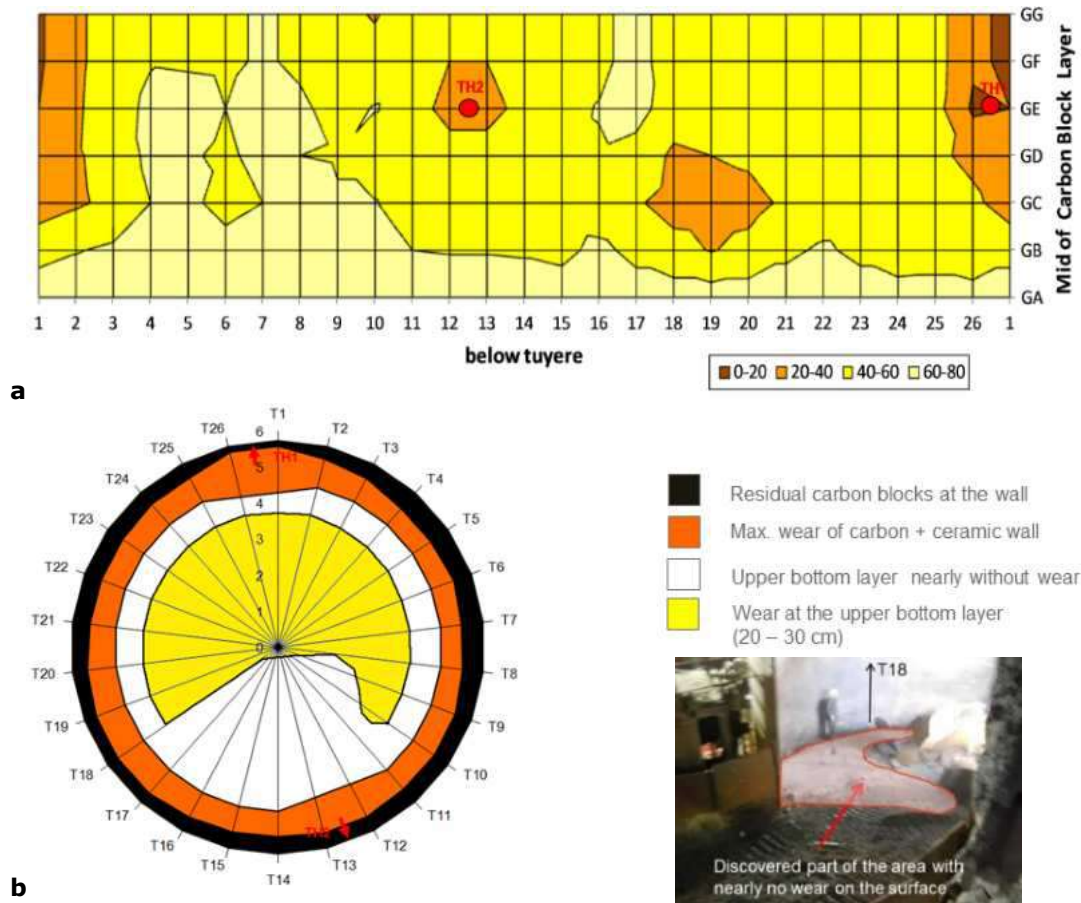


Figure 164: Wall thickness measurement under tuyere 19 during AMEH BF5A relining.



**Figure 165: Results of the wall thickness measurement during relining:
a) the residual wall thickness contours, b) wear at the upper bottom layer.**

The residual refractory thickness at the hearth of AGDH BF4 has been measured in a similar way during its excavation during the relining 2016. The photo on the left side of Figure 166 shows a typical measurement at section 8 of the AGDH BF4. The measured values are also shown as an overlay on the technical drawing on the right side of Figure 166. In Figure 167, the measurements at other sections (2, 4, 6 and 10) are shown for the sake of completeness. Here, the compared model was the existing on-line 2D-HMM (old hearth monitoring model).

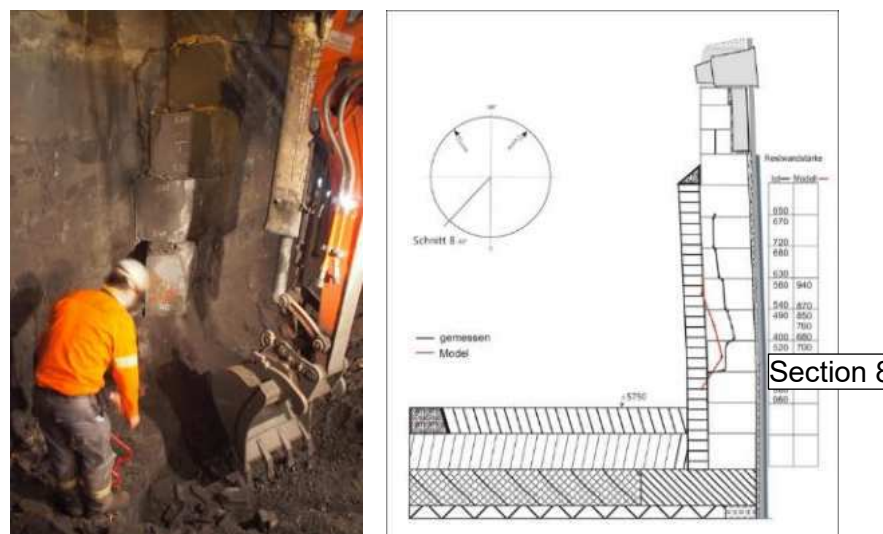


Figure 166: Wall thickness measurement at section 8 during AGDH BF4 relining.

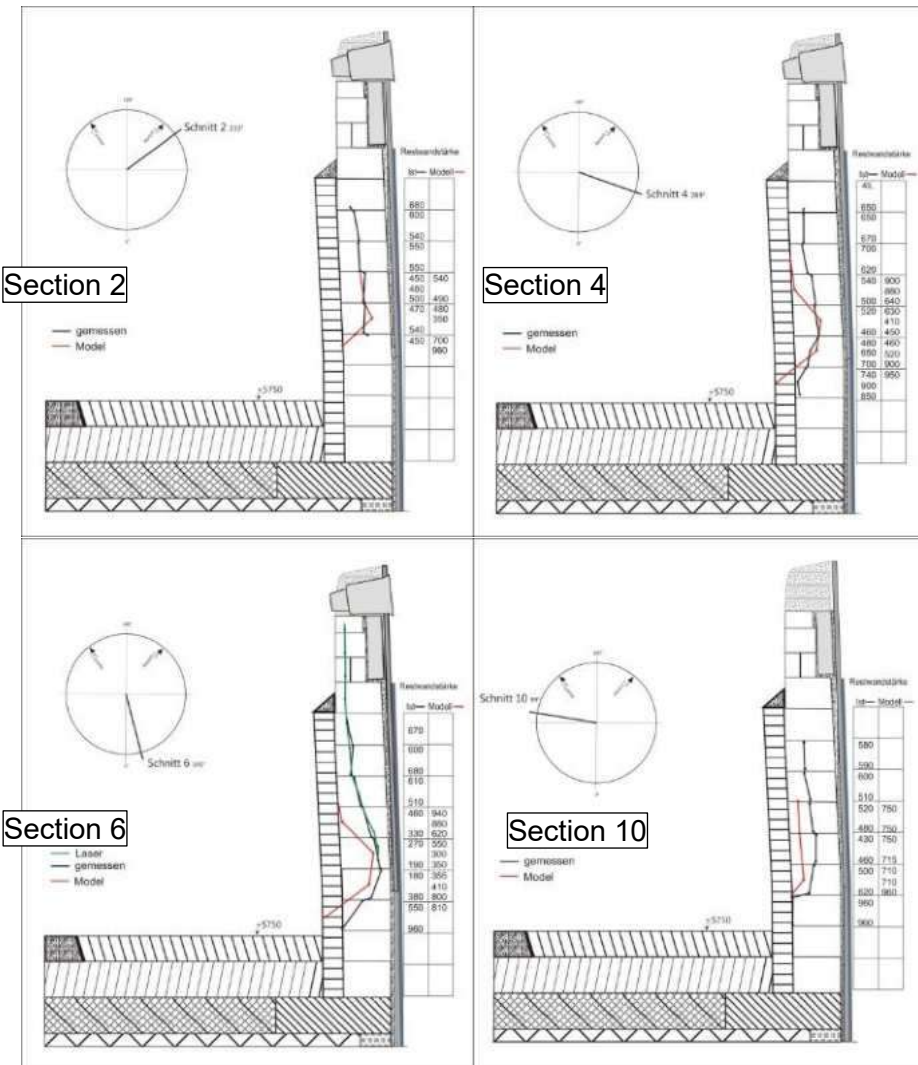


Figure 167: Results of the wall thickness measurement during relining for sections 2, 4, 6 and 10.

During the relining works at AGDH and AMEH, the real states of the hearth wall (HM-infiltration/wear/skull/salamander/brittle layers) were investigated. However, during the hearth excavation it was noticed that mostly the refractory parts beyond brittle layers were already fallen and excavated out with the dead man. These parts could not be retained since they were loose and could not be separated from the bulk coke of the dead man. Thus, just the refractory which remained at the wall could be measured and sampled. Five large carbon blocks from AMEH BF5A and seven large carbon blocks from AGDH BF4 were collected and sampled. The rough inner surface of all these blocks indicated that they had not been in direct contact to the hot metal and they were just the cold parts behind the brittle zone. Approximately 5-6 core drillings samples were taken for the physical tests and chemical tests. For example, the heat conductivity, thermal expansion coefficient, and elasticity modulus are measured (via BFI). The chemical analyses of selected samples are also performed (via plants). New hearth concepts at the BFs of AGDH and AMEH include additional on-line measurements. For example, an improved net of EMF and strain-gauges, cooling water flow rate/temperature, besides standard thermocouples are added.

A lot of data were collected during the last years BF campaigns. All the obtained data have been checked in WP 4 and used for the project purposes whenever it makes sense. The measured residual hearth wall thickness (which generally was just the cold part behind the brittle zone) and the wear model estimations were compared for the AGDH BF4 in Figure 168. Additionally, the positions of the selected seven carbon block samples are marked by purple rectangles in the same Figure 168. The color contours show the model estimated wear profile. The black colored numbers are the measured residual wall thickness and the red colored numbers shows the difference between model estimation and the measured wall thickness. The wear model estimates less wear than the measured wear with different deviations. Two main reasons can be identified for these differences:

Optimizing Blast Furnace Hearth Inner State (OPTIBLAFFINS)

- The measurements do not include the unknown thickness on the hot side of the brittle zones which was fallen off and lost during excavation.
- Due to the existence of the brittle layers, which have an additional thermal resistance, the refractory lining remains relatively cool (this is also remarkable by the on-line thermocouples measurements). This pretends low wear in all model estimations which base on these temperatures, unless the effect can be quantified and considered.

One of the main targets of this project is to improve the wear models to encounter this effect and estimate the brittle layers in WP 4.

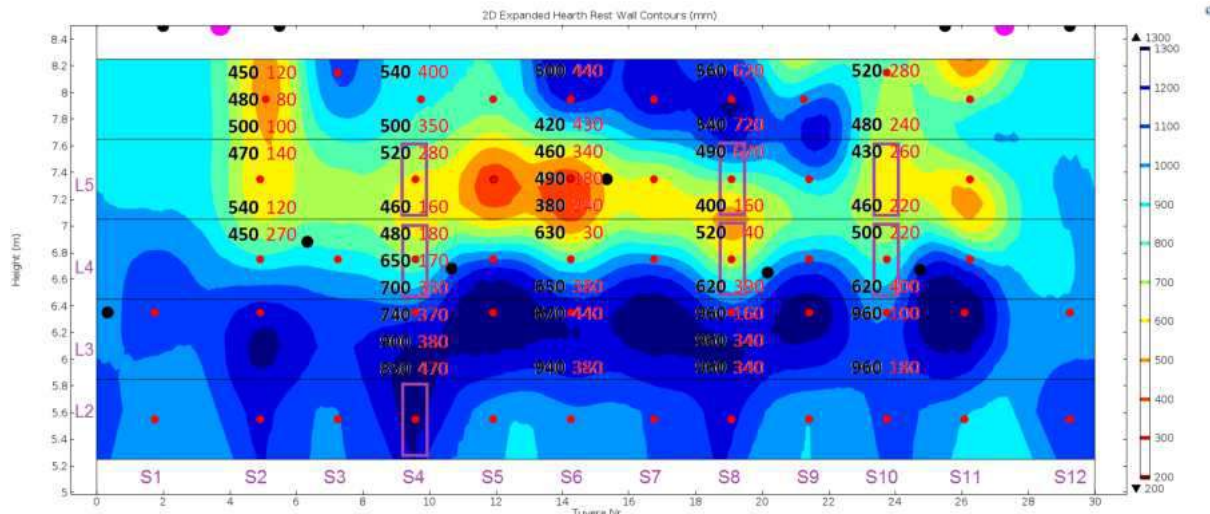


Figure 168: Results of the wall thickness measurements compared with the wear model estimations for the AGDH BF4 (black numbers are measured wall thickness in mm, deviation from model estimation is red numbers in mm). Purple rectangles: sampled carbon blocks. Red dots: TC positions.

The chemical analysis of the carbon block samples from AMEH BF5A are summarized in Table 33 and the brittle layer formation related results of the chemical analysis are compared in Figure 169. Higher ZnO concentrations observed on the samples under tuyere 19 support the idea that the excessive wear is mainly due to brittle layer progress due to Zn accumulation. Na₂O concentration is also higher at the same location (D19-4 hot side). The ash content and Fe₂O₃ concentrations are not deviating that much.

Table 33: Chemical analysis of the carbon block samples from AMEH BF5A.

Parameter	loss of ignition (815°C)	Ash wf.	Analysis of Ash												
			CaO	SiO ₂	Fe ₂ O ₃	MnO	P ₂ O ₅	Al ₂ O ₃	MgO	Cr ₂ O ₃	PbO	TiO ₂	Na ₂ O	K ₂ O	ZnO
unit	wt. %	wt. %	%	%	%	%	%	%	%	%	%	%	%	%	%
C25 cold side corner	82.9	17.1	0.32	73.7	0.98	0.01	0.06	23.8	0.06	0.02	0.01	0.09	0.06	0.24	0.58
E14-4 hot side	79.6	20.4	0.28	78.0	1.3	0.03	0.06	16.4	0.03	0.04	0.02	0.12	0.25	0.82	2.6
D19-4 hot side	75.1	24.9	0.30	59.9	1.4	0.01	0.05	18.2	0.03	0.03	0.10	0.11	0.96	0.42	18.2
E19-4 hot side	77.3	22.7	0.26	73.6	1.2	0.02	0.04	16.4	0.02	0.03	0.04	0.11	0.74	0.79	6.6
Cxx-4 hot side	79.5	20.5	0.23	79.1	1.1	0.01	0.06	16.8	0.05	0.02	0.02	0.11	0.31	1.10	1.0
C25-4 hot side	79.8	20.2	0.41	77.2	1.3	0.01	0.08	18.6	0.07	0.03	0.01	0.11	0.30	0.97	0.71

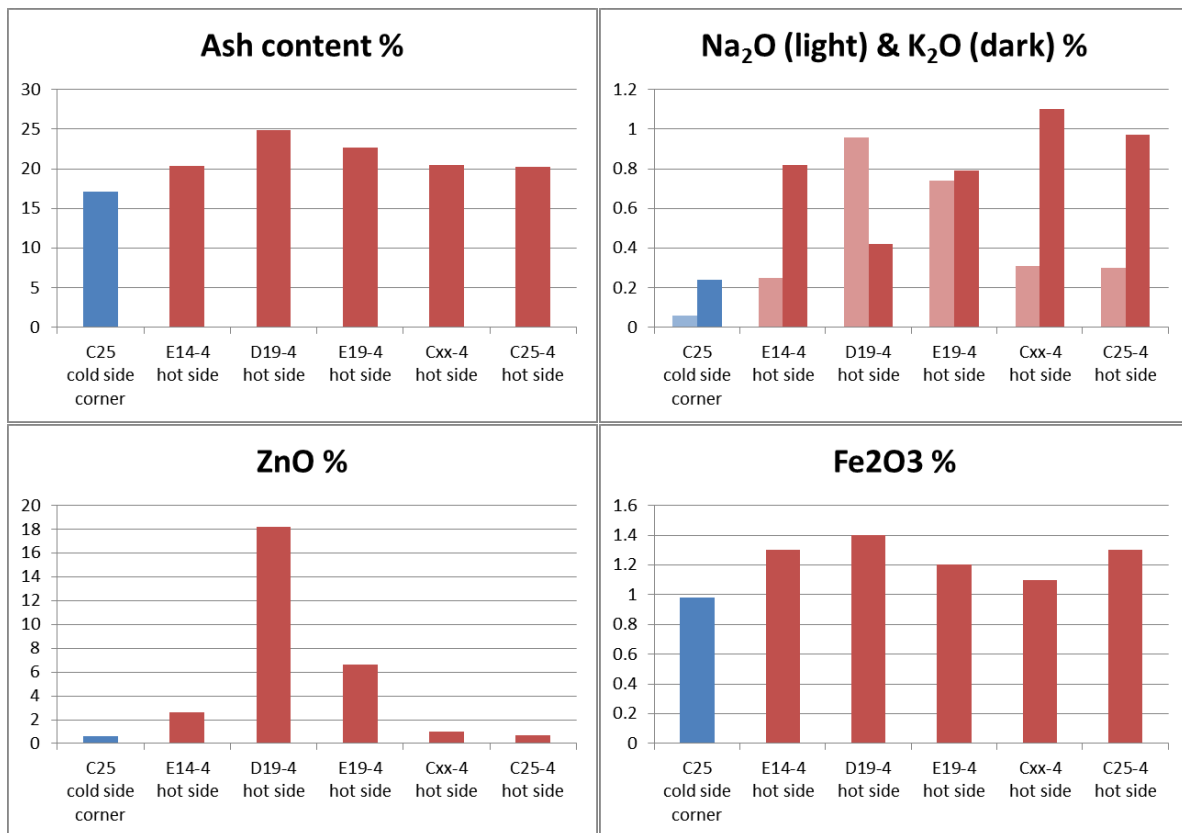


Figure 169: Brittle layer related results of the chemical analysis of the samples from AMEH BF5A.

The selected sample positions can be seen in Figure 170. C25 cold side corner is selected as a reference sample. The corner of the block was lying near the steel shell. It is assumed that aging effects were not significant here. E14-4 hot side sample is taken from the core drilling at carbon block at layer E below tuyere 14. The drilling was done from hot face towards cold face. The hot-end of the drilled sample is colored orange and the cold-end is colored green. The chemical analysis is done for the hot-end.

D19-4 hot side sample is taken from the core drilling at carbon block at layer D below tuyere 19. The drilling again was done from hot face towards cold face. The hot-end of the drilled sample is colored orange and the cold-end is colored green. The chemical analysis is done for the hot-end. E19-4 hot side sample is taken from the core drilling at carbon block at layer E below tuyere 19 and was investigated in similar fashion.

Cxx-4 hot side sample is taken from the core drilling at carbon block at layer C below unknown tuyere (unfortunately the tuyere nr. marking was already erased when it was recovered at excavation dump area). C25-4 hot side sample is taken from the core drilling at carbon block at layer C below tuyere 25. Drilling and investigation for those samples was done similar than for the other samples.

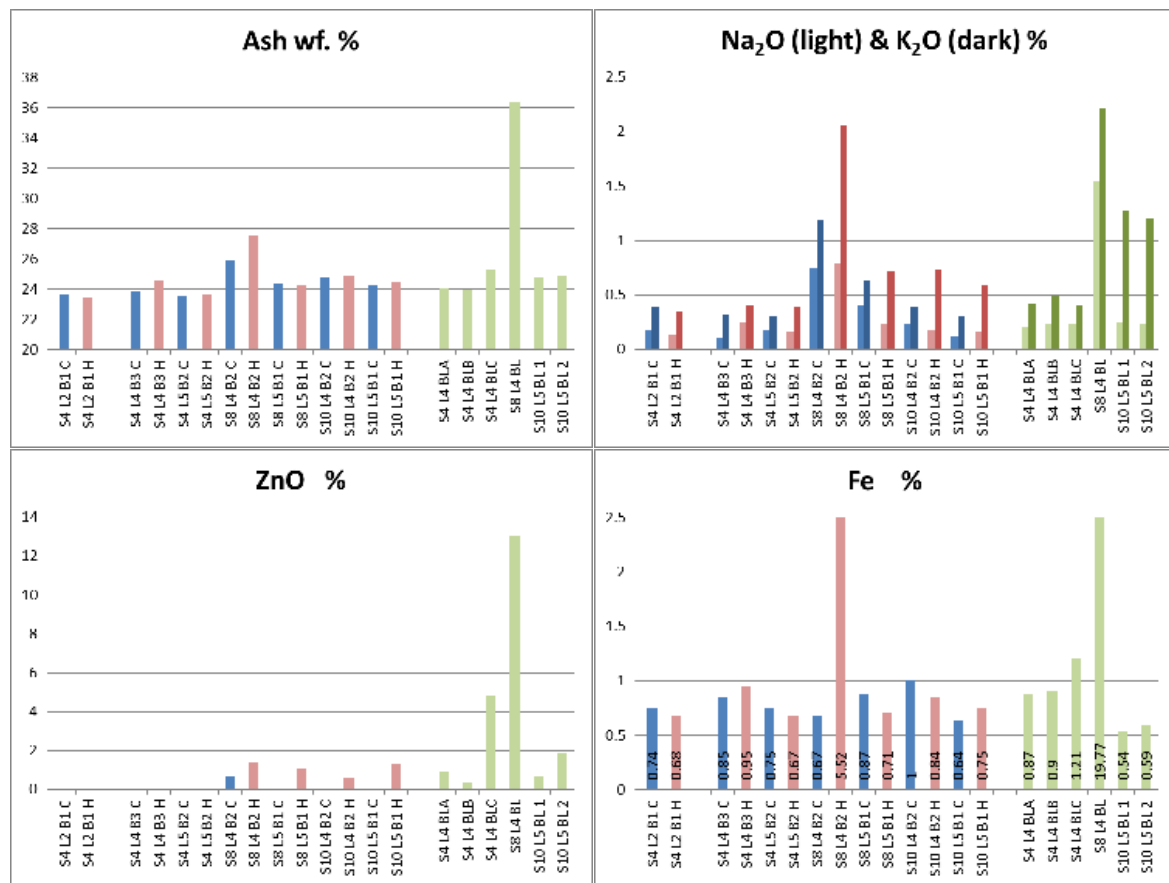


Figure 170: Photo showing some of the AMEH samples for the chemical analysis.

The chemical analysis of the carbon block samples from AGDH BF4 are summarized in Table 34 and the brittle layer formation related results of the chemical analysis are compared in Figure 171. Higher ZnO concentrations observed on several sample positions support the idea that the excessive wear is mainly due to brittle layer progress upon Zn accumulation. Also, a notably increased ash content is observed for the brittle layer sample (S8L4BL). High Fe content is observed only in samples S8L4B2H and S8L4BL.

Table 34: Chemical analysis of the carbon block samples from AGDH BF4.

	H2O hygr.	Ash	S	Fl.B. wf.	Fl.B. waf.	CaO	SiO2	Fe	Mn3O4	P2O5	Al2O3	MgO	Cr2O3	TiO2	Na2O	K2O	ZnO
	wt. %	wt. %	wt. %	wt. %	wt. %	%	%	%	%	%	%	%	%	%	%	%	%
S4 L2 B1 C	0.44	23.66	0.19	0.98	1.29	0.28	81.17	0.74	0.02	0.02	26.45	0.09	0.03	0.15	0.17	0.39	0.01
S4 L2 B1 H	0.13	23.47	0.20	0.70	0.91	0.27	81.66	0.68	0.02	0.02	26.55	0.11	0.03	0.14	0.13	0.35	0.01
S4 L4 B3 C	0.14	23.84	0.19	0.20	0.27	0.27	79.42	0.85	0.01	0.03	27.66	0.12	0.02	0.15	0.10	0.32	0.03
S4 L4 B3 H	0.13	24.57	0.15	0.59	0.78	0.25	73.55	0.95	0.06	0.03	25.32	0.09	0.02	0.14	0.25	0.40	0.06
S4 L5 B2 C	0.17	23.49	0.17	0.13	0.17	0.28	79.82	0.75	0.02	0.03	26.58	0.11	0.03	0.13	0.17	0.30	0.04
S4 L5 B2 H	0.14	23.67	0.15	0.34	0.45	0.28	80.18	0.67	0.01	0.03	26.54	0.10	0.03	0.12	0.16	0.39	0.06
S8 L4 B2 C	0.47	25.90	0.13	0.36	0.49	0.32	75.52	0.67	0.14	0.03	25.34	0.11	0.03	0.14	0.75	1.19	0.67
S8 L4 B2 H	0.44	27.54	0.26	0.73	1.00	0.21	66.72	5.52	1.08	0.05	22.07	0.09	0.02	0.15	0.79	2.06	1.38
S8 L5 B1 C	0.30	24.34	0.18	0.20	0.26	0.27	77.79	0.87	0.02	0.03	25.86	0.12	0.02	0.15	0.40	0.63	0.07
S8 L5 B1 H	0.14	24.25	0.20	0.53	0.70	0.29	76.67	0.71	0.02	0.03	25.50	0.12	0.02	0.16	0.23	0.72	1.03
S10 L4 B2 C	0.41	24.74	0.17	0.06	0.07	0.27	77.35	1.00	0.02	0.03	26.15	0.13	0.03	0.13	0.24	0.39	0.07
S10 L4 B2 H	0.21	24.84	0.21	0.11	0.14	0.25	77.13	0.84	0.01	0.03	26.03	0.11	0.02	0.12	0.17	0.73	0.63
S10 L5 B1 C	0.20	24.20	0.20	0.16	0.21	0.25	79.35	0.64	0.01	0.03	27.17	0.12	0.02	0.13	0.12	0.31	0.05
S10 L5 B1 H	0.17	24.43	0.21	0.33	0.44	0.29	76.50	0.75	0.01	0.03	26.19	0.12	0.02	0.14	0.16	0.59	1.34
S4 L4 BLA	0.15	24.05	0.24	0.37	0.49	0.29	75.67	0.87	0.01	0.03	27.10	0.12	0.02	0.14	0.21	0.42	0.89
S4 L4 BLB	0.18	23.95	0.17	0.37	0.48	0.33	76.22	0.90	0.01	0.04	27.03	0.13	0.03	0.14	0.24	0.49	0.36
S4 L4 BLC	0.12	25.31	0.67	0.35	0.46	0.32	71.00	1.21	0.02	0.03	25.62	0.12	0.02	0.13	0.23	0.41	4.79
S8 L4 BL	0.63	36.35	1.84	3.58	5.63	0.22	42.34	19.77	0.70	0.02	12.76	0.12	0.05	0.09	1.54	2.21	13.08
S10 L5 BL 1	0.20	24.80	0.19	0.25	0.33	0.27	74.25	0.54	0.00	0.03	25.74	0.10	0.02	0.14	0.25	1.27	0.70
S10 L5 BL 2	0.19	24.83	0.26	0.31	0.41	0.23	74.29	0.59	0.00	0.03	25.89	0.12	0.02	0.11	0.23	1.20	1.83

**Figure 171: Brittle layer related results of the chemical analysis of the samples from AGDH BF4.**

The selected sample positions can be seen in Figure 172. The samples have a structured naming convention. S# : indicated the section number, L# : indicates the ring layer number, B# : indicates the core drilling (boring) number. The final suffixes are: C for cold side, H for hot side, BL for brittle layer.



Figure 172: Photo showing some of the AMEH samples for the chemical analysis.

Both BFs (AMEH BF5A and AGDH BF4) have brittle layers on the hot side which defines the wear profile of the hearth lining wall. Some photos showing the damage of the carbon blocks are given in Figure 173. On the left side photo in Figure 173, the embrittlement on the hot face of the AMEH BF5A lining under tuyere 19 is clearly visible. On the right-side photo in Figure 173, there is an interesting damage (crack/embrittlement) along the horizontal contact boundary of blocks at section 10 and layer 5 of AGDH BF4 hearth lining.



Figure 173: Brittle layers in carbon blocks at AMEH BF5A and the crack in AGDH BF4.

One of the most important physical properties of the carbon refractory in the hearth lining is the thermal conductivity. The carbon blocks at hearth wall in AGDH BF4 have a thermal conductivity of approximately 22 W/(m·K) according to the producer / supplier. After the campaign, the thermal conductivity of the collected samples as well as the chemical compositions and physical properties like bulk density and volume of open pores are measured and given in Table 35. The samples and the measurement positions on the samples are shown in Figure 174.

The sample "S4L2 (B5) cold side" is selected to have a reference value since there was no wear and temperature influence on "S4L2 (B5) cold side". Surprisingly, the thermal conductivity on "S4L2 (B5) cold side" is very low as compared to the supplier data. The drill direction of this "S4L2 (B5) cold side" sample was vertical unlike the drill direction on all other blocks. It is unknown

Optimizing Blast Furnace Hearth Inner State (OPTIBLAFFINS)

whether this is an anisotropy effect or inhomogeneity (some blocks may have lower heat conductivity for some reason).

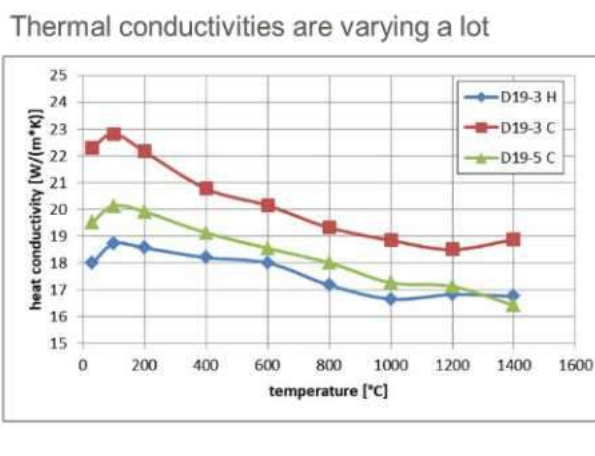
Table 35: Thermal conductivity, chemical composition and some physical properties of the worn carbon block samples from AGDH BF4.

Specimen name	WLF	graphite	corundum Al ₂ O ₃	SiC	willemite Zn ₂ (SiO ₄)	bulk density	open pores	water absorption
	[W/(m·K)]	[wt. %]	[wt. %]	[wt. %]	[wt. %]	[g/cm ³]	[vol. %]	[wt. %]
"S4L2 (B5) cold side"	13.84	86.9	10.2	2.9	-	1.684	14.7	8.70
"S8L4 (B4) cold side"	23.45	86.9	10.2	2.9	-	1.713	17.2	10.02
"S8L4 (B4) hot side"	23.01	87.4	9.9	1.7	1.0	1.941	3.8	1.98



Figure 174: Photo showing some of the AGDH samples for the heat conductivity analysis.

The carbon blocks at hearth wall in AMEH BF5A have a thermal conductivity of approximately 17 W/(m·K) at delivery according to the producer / supplier. After the campaign, the thermal conductivity of the collected samples as well as the chemical compositions and physical properties like bulk density and volume of open pores are measured and given in Figure 175. The thermal conductivity of the refractories can be quite inhomogeneous. The measured values are generally higher than the supplier specification.



chemical analysis

sample	D19-3 H	D19-3 C	D19-5 C
S-Nr.	755/18	756/18	757/18
chemical analyze (wt.-%)			
Fe ₂ O ₃	0.65		
Mn	<0.010		
P ₂ O ₅	<0.020		
SiO ₂	13.1		
TiO ₂	0.06		
Al ₂ O ₃	6.59		
CaO	0.36		
MgO	<0.10		
Cr ₂ O ₃	<0.03		
ZrO ₂	<0.01		
SiC	2.00		
C frei	0.60		
C ges.	77.5		
loss of ignition	79.0		
density (g/cm ³)	1.68	1.66	1.67
open pores (%)	16.8	18.0	17.1

Figure 175: Thermal conductivity, chemical composition and some physical properties of the worn carbon block samples from AMEH BF5A.

Some mechanical tests also have been performed on the sample "S8L4 (B5)" from AGDH BF4. Small cylindrical samples (approximately 40mm in diameter, 40mm in height) are cut out for the cold crush test as shown in upper-left of Figure 176. The stress-strain curves for each sample are given in left side of Figure 176. The small table on the right side of Figure 176 summarizes the data

Optimizing Blast Furnace Hearth Inner State (OPTIBLAFINS)

of the stress-strain curves in terms of elasticity modulus, stress and strain capacities. A remark to the sample 1 and sample 2: the surface where the compression was applied was slightly rougher than the others due to cutting operation. This surface effect may have influenced the stress-strain curve as well. The same kind of tests have been performed on "7 RD-N" carbon block core drilling no: 19D-1 from AMEH BF5A. The measurement results are summarized in Figure 177.

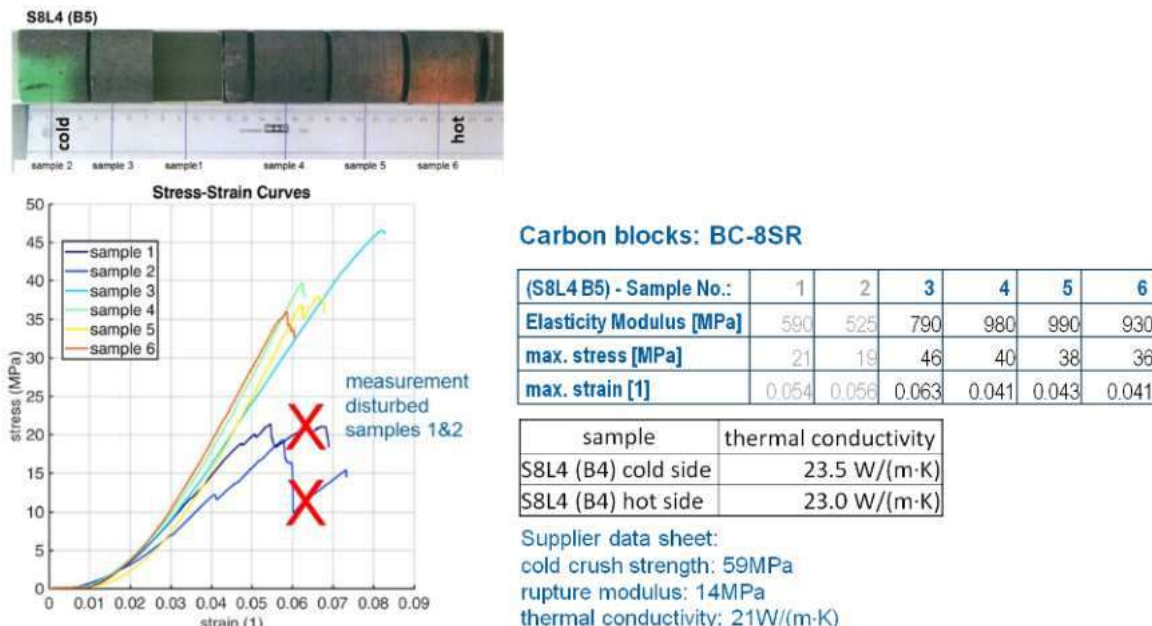


Figure 176: Summary of the cold crush tests of the refractory samples from AGDH BF4.

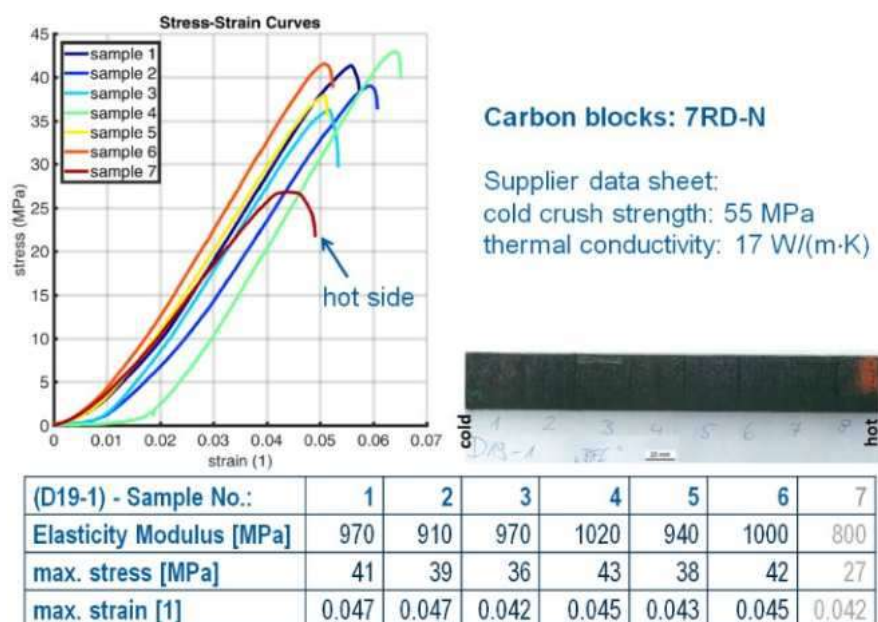


Figure 177: Summary of the cold crush tests of the refractory samples from AMEH BF5A.

The thermal expansion of the carbon blocks is an important physical property which governs the internal stress build-up and thus are needed for thermomechanical modeling. After the furnace start operation, the inner parts of the refractory lining heats up to high temperatures and tries to expand. The outer parts of the refractory lining and the steel shell of the hearth are kept cooled. The FEM model developed in section 3.2.1.1 describes this behavior in detail.

The thermal expansions of the refractory samples are determined by two different tests: thermal softening and creep tests. In thermal softening test, the sample is heated up to ca 1700°C under a very small constant load of 0.2 MPa. The length change of the sample height is recorded. As seen in Figure 178, the material type 7RD-N from AMEH BF5A is tested by this method. The slope of the curve gives the thermal expansion coefficient.

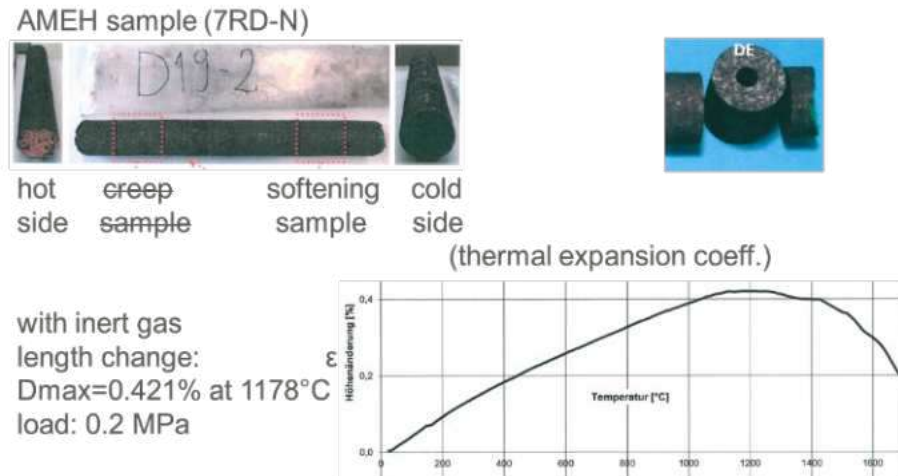


Figure 178: Thermal softening test for AMEH BF5A material 7RD-N.

The creep test is very similar to the softening test. The sample is heated up to 1500°C under a very small constant load of 0.5 MPa. Afterwards, the temperature and load kept constant for 25 hours and time dependent deformations is also recorded. As seen in Figure 179, the thermal expansion coefficient can be obtained from the slope of the heating curve. Additionally, it is verified that the carbon refractory material does not possess significant creep behavior under the investigated conditions. That means, the developed thermal stresses will not significantly relax in time.

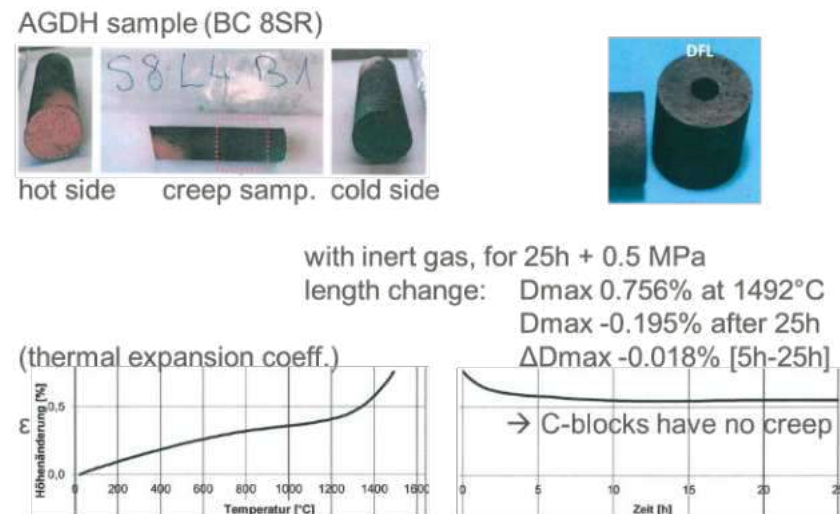


Figure 179: Creep test for AGDH BF4 material BC 8SR.

The observed/measured residual wall thickness is almost always less than what the numerical models estimates (regardless of which numerical model is chosen while simply the measured temperatures are that low). This effect was not obvious from former comparisons of model results with excavations since former models overestimated the heat transfer on the inner side of the refractory what led to an overestimation of the remaining refractory thickness. Most of the hearth lining which located on the hot side in front of the brittle layers has been unintendedly extracted together with the dead man. The most visible evidence of this is the multipoint TC installation at AGDH BF4. The deepest TC (which is even deeper than the observed/measured wear profile) has recorded until the very end (also indicating the brittle layer formation as discussed in section 3.2.4.2). Therefore, it is essential to know the existence of the brittle layers.

2.2.2.2 Data processing and monitoring for existing and new measurements

2.2.2.2.1 Modelling of Hearth Echo Excellence technique

Within this RFCS project, a channel of six sensors is used to record x, t -signals (A-scans) corresponding to lateral positions from the impact zone at the steel shell. These A-scans, corresponding to pre-defined lateral positions on the steel shell, is a so-called "field" data-set.

Optimizing Blast Furnace Hearth Inner State (OPTIBLAFFINS)

Using an acoustic inversion technique is to model the so-called "synthetic" data-set. When the "field" data-set corresponds to the "synthetic" data-set, it is assumed that the model contains the media parameters and geometry of the blast furnace wall. When the "field" data-set and "synthetic" data-set do not match then an iterative process must be designed. In this iterative process the media parameters and geometry of the model must be adjusted until a match occurs. This matching procedure can be done based on fitting the time signals or fitting the frequency spectra.

Dealing with time signals, a matching procedure is needed that exclude the influence of the incident wavefield (the source signature), thus only based on the underlying impulse response of the system. A digital filter process called least-squares matching is used. Kennett (plane wave field response) modeling is used to model the wave response of horizontally multi-layered homogeneous media.

A typical BF hearth lay-out is built up by five different layers: steel shell, mortar joint, graphite, ramming layer and semi-graphite layer. The steel shell layer is surrounded by air and the semi-graphite layer is in contact with hot liquid iron (Figure 180).

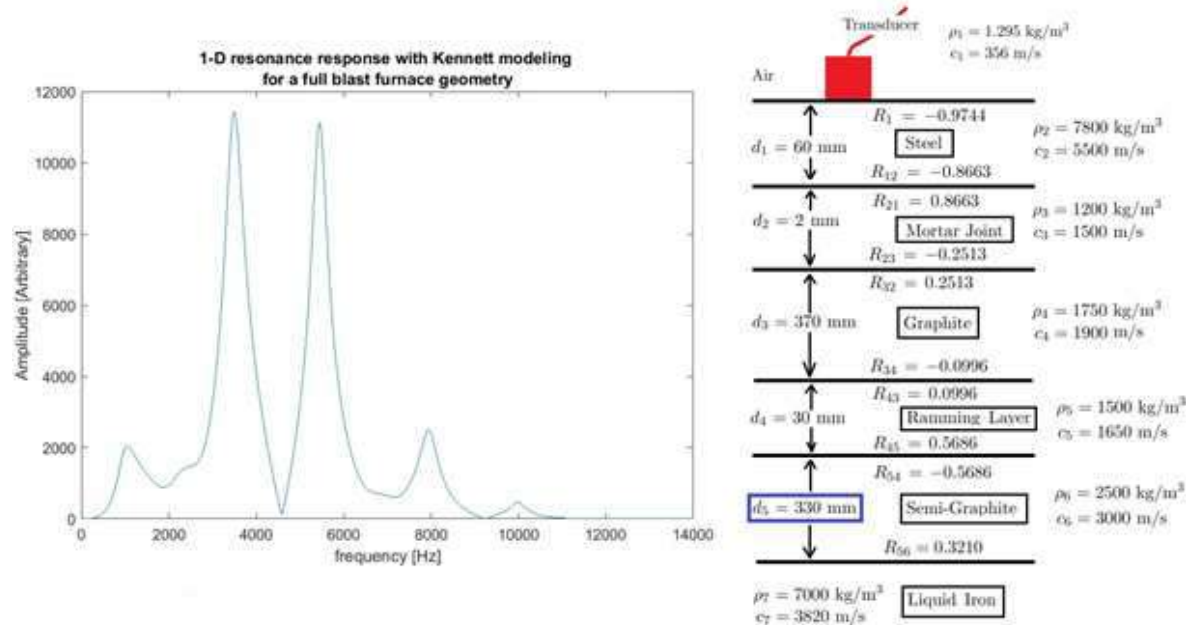


Figure 180: Kenneth modelling response for typical BF geometry.

The iterative inversion process based on the frequency spectra is given in Figure 181. The factor H is a threshold error value showing the efficiency of the HEE.

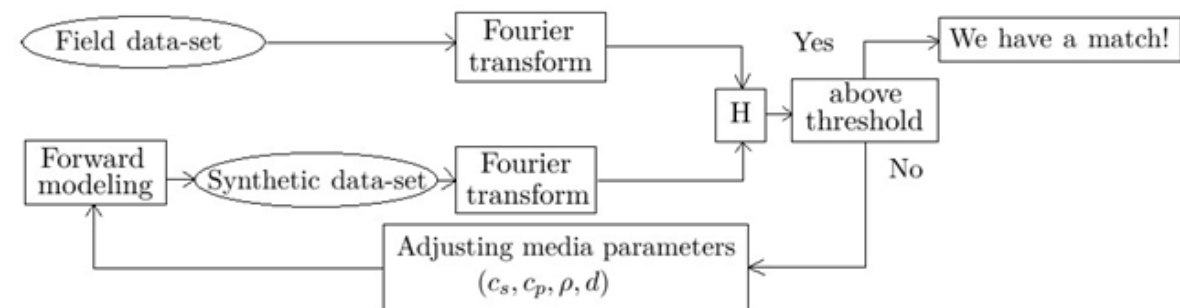


Figure 181: Iterative inversion process based on frequency spectra.

In-order to understand the influence of the material thickness on the reflection response two different setups of the BF wall are considered (Figure 182). The boundary for the steel shell with the outside world is assumed to be a free surface, while the other boundaries are absorbing ones.

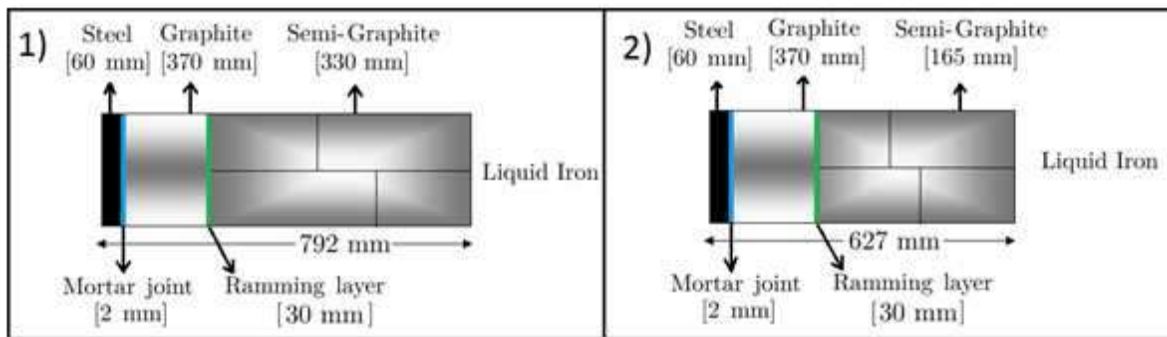


Figure 182: BF setup for modelling analysis using two geometry 1 (left) and geometry 2 (right).

It is assumed that the shear wave velocity (C_s) is 56% of the pressure wave velocity (C_p). The receiver locations in this model are used as a linear array from 0 till 100 cm in steps of 10 cm (10 receiver points in total). The impact zone is located at the zero location. Figure 183 shows the modelled Fourier spectra for geometry 1 (semi graphite layer of 330 mm) and geometry 2 (semi graphite layer of 165 mm) with different off-set locations as well.

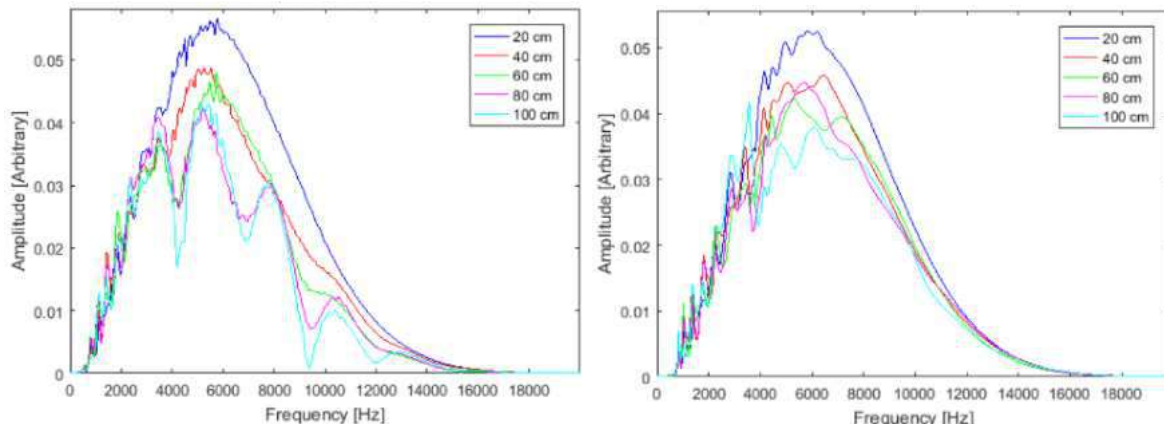


Figure 183: Frequency spectra based on geometry 1 (left) and geometry 2 (right).

It is clear, that the amplitude of the spectrum decreases with increasing offset position. That means a decrease of wave energy. The influence of the thicker semi graphite layer (geometry 1) has a remarkable influence on the amplitude as well, especially for the higher offset positions.

The direct wave is strongly present in the time signals and hiding the other ones. It turns out to be that resonance frequencies rate to be find in the "coda" of the signals, that means the signal without the direct wave component. The remaining signal is not that strong. However, when comparing the actual measured data with the modelled frequency data, a better indication could be given for the residual thickness in the BF wall.

2.2.2.2 Conclusion

The modelling part of the HEE technique is much more complicated than on forehand expected. The standing wave theory turns out to be valid only for simple resonating layers. As the BF hearth wall consists of a multi-layer system, it requires a highly sophisticated Kennett modelling inversion method. In using this inverse method, it became clear that the time and frequency spectra were mainly influenced by the direct surface wave. Time signals without the direct wave ("coda" approach) result in clear coherent resonance lines. However, defining the actual refractory thickness is still challenging.

2.2.2.3 Modelling of crack detection using optical fibre

A computer model of heat transfer from the liquid metal in the hearth of a blast furnace out to the surrounding was done with and without simulated cracks into the lining in order to see if it is possible to detect a crack in the lining outgoing from the temperature distribution change in the lining closer to the outer of the hearth wall (Figure 184).

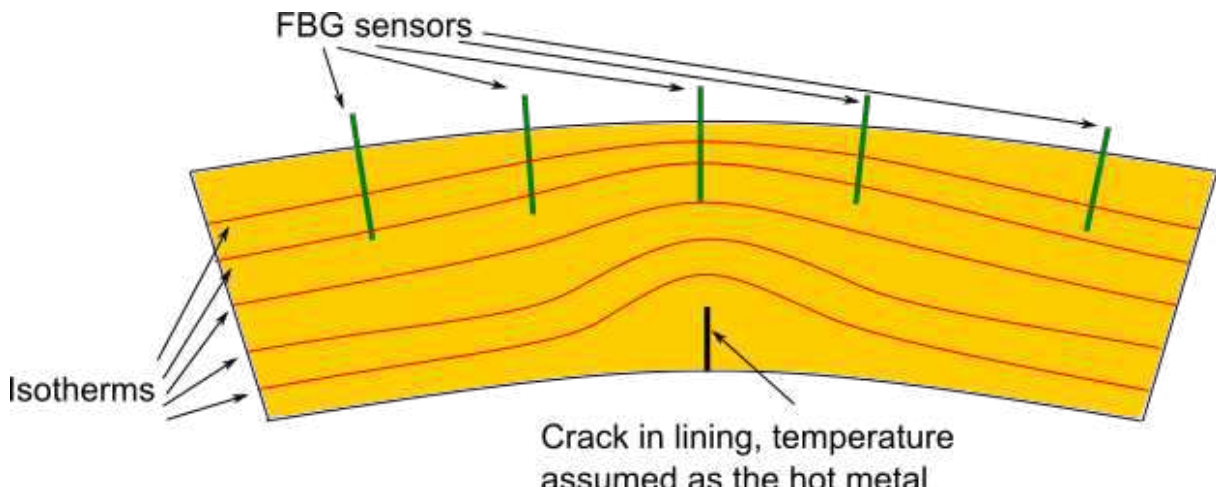


Figure 184: The isotherms in the refractory will be affected by a crack with the same temperature as the hot metal in the blast furnace hearth.

Such measurements would be of great interest to detect refractory damages occurring during production time of the blast furnace. The model did the calculation assuming the same refractory thickness and refractory performance as in the BF6 Tata Steel IJmuiden. The computer model was a finite element method (FEM) method and calculated the temperature distribution through the refractory layers from the liquid metal and out to the shell. Three thermal simulations were done. A first simulation with no crack in the lining, a second with a crack depth of 100 mm and a third with a crack depth of 200 mm. The temperature profile was calculated from the assumption that the temperature of the crack was the same as for the liquid metal and set to 1450 °C. The outer of the simulated hearth surface was set to 25 °C and the heat flow (dQ/dt) in the circular direction was set to zero because of the round shape of the blast furnace hearth (Figure 185). The assumption heat flux is zero implies that the whole refractory lining may be simulated by including a segment of the hole round lining shape. The segment selection although need to be large enough to include the whole segment affected by the changed heat distribution upcoming because of the simulated lining crack.

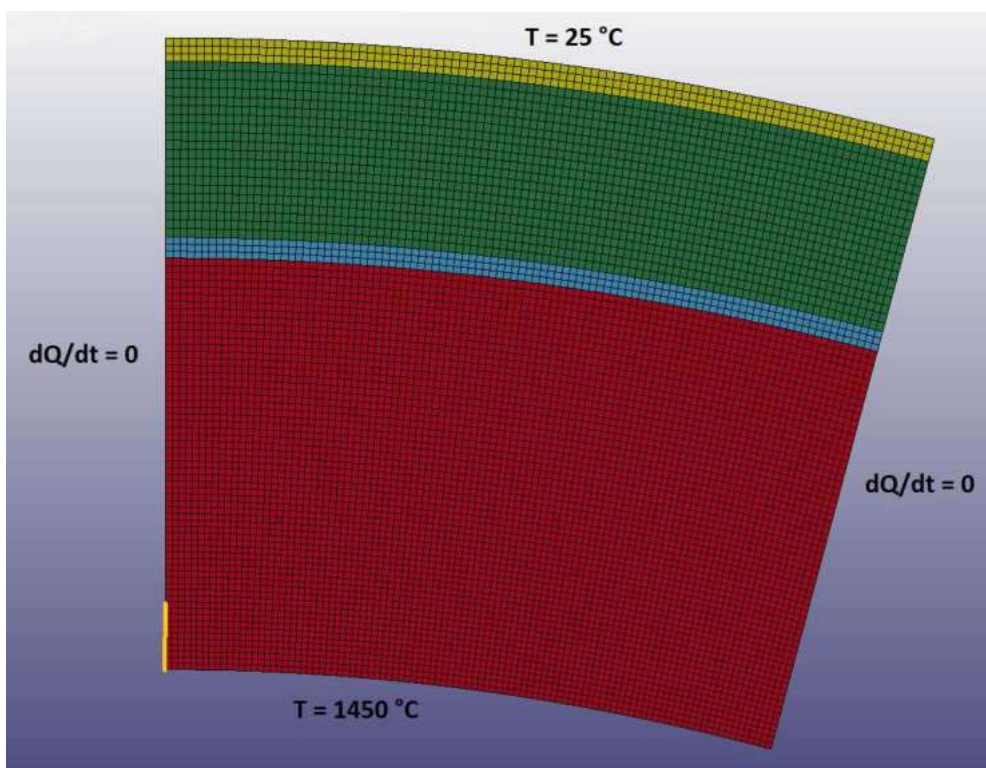


Figure 185: The FEM computer model domain and boundary conditions. The simulated crack is shown orange in the lower left corner.

The solution of the FEM simulation may be represented as a temperature plot where the different temperatures have different colours (Figure 186), where red colour represents the highest temperature and blue colour the lowest temperature. Note the temperature increase in the lower left corner where the simulated crack was located.

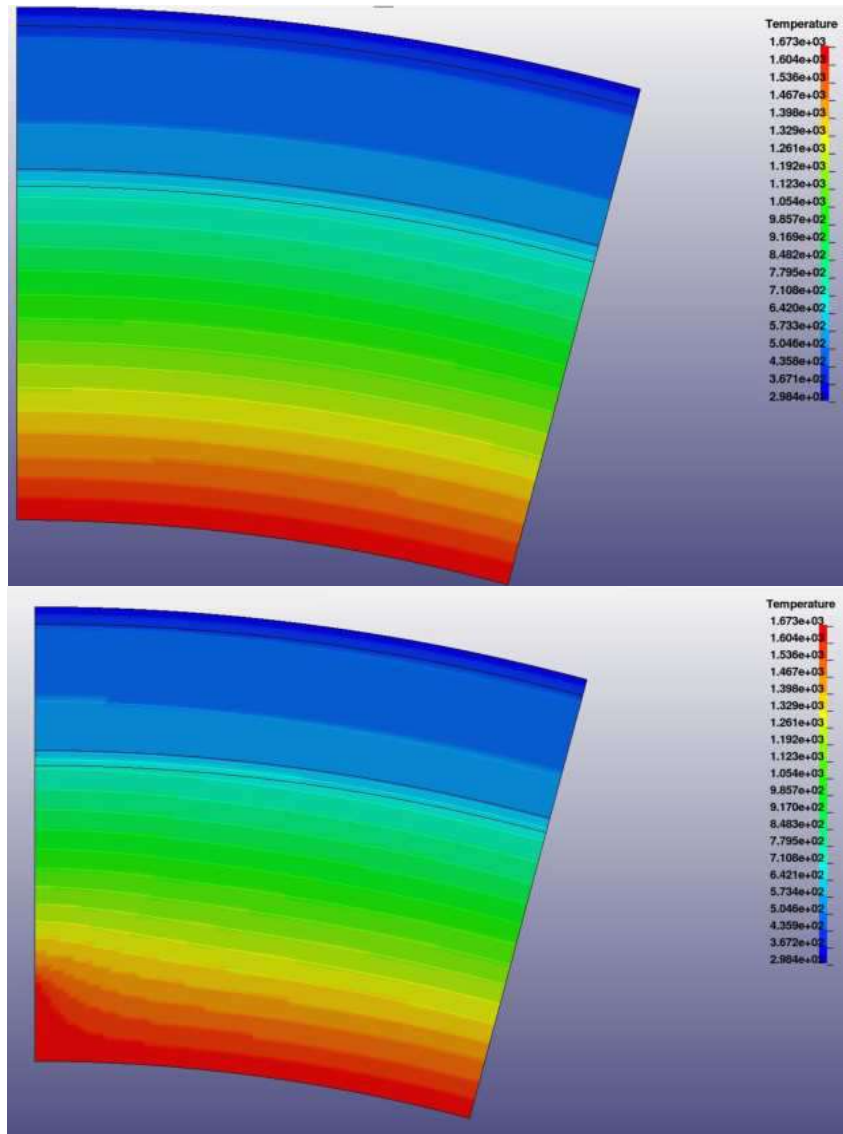


Figure 186: The temperature distribution in the refractory with no crack (top) and 200 mm crack (bottom).

The heat simulation was done for three different cases. From these three simulations two temperature plots representing the difference between simulation of cracked and not cracked refractory was done in-order to investigate the change of heat distribution in the refractory a crack will cause. In Figure 187 the two plots given the temperature differences are shown. The isotherms are presented in steps of five degrees which might be a detectable level of temperature fluctuation using FBG sensors or thermocouples. The simulation also should indicate whether a crack of a certain depth is detectable as far from the hearth inner state as a safe FBG or thermos couple installation might be done in-order to maintain a secure drilling of the refractory.

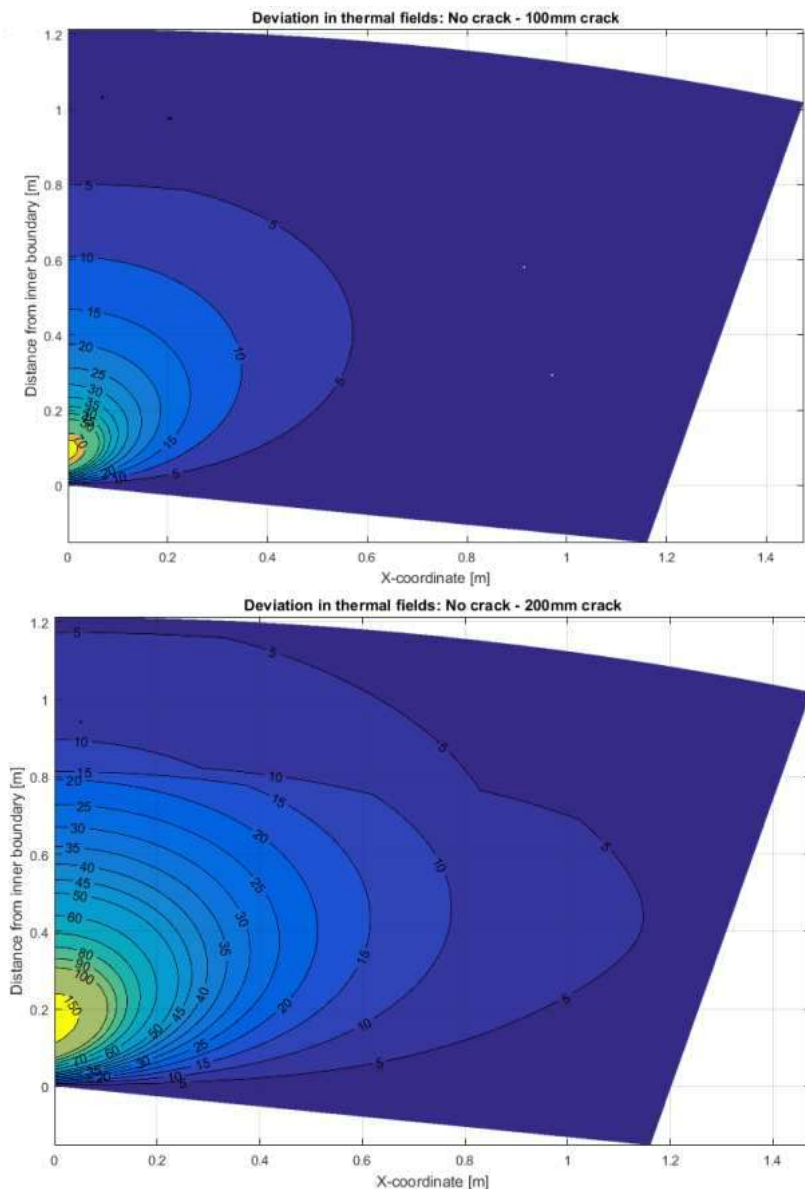


Figure 187: Temperature difference between simulation of 100 mm crack and no crack (top) resp. 200 mm crack and no crack (bottom).

In the simulation of a 100 mm crack the 5 °C isotherm is about 400 mm from the shell and in the simulation of 200 mm crack the 5 °C isotherm is almost at the surface. It indicates, that a FBG sensor installation deeper than 400 mm is required to detect a 100 mm crack in the lining while a crack of 200 mm is detectable just a few cm from the shell surface. Comparing the two simulations the temperature is about 15 °C increased 400 mm from the shell surface for the 200 mm simulation which is three times higher than the 100 mm crack simulation.

As seen in Figure 187 the temperature distribution in the refractory is spread out in circular direction in a way that a distance of around 0.8 meter between FBG temperature measurement fibres installed at a depth of 0.4 m is enough to detect a temperature increase of 5 °C, which creates a crack of 200 mm according to the thermal simulation.

2.2.3 Work Package 3: BF Controlling the Dead Man

2.2.3.1 Study and collection of solid samples from blast furnace and experimental blast furnace

2.2.3.1.1 Exiting solid samples from EBF (campaign 31)

Selected samples were taken from a former core drilling (the core drilling procedure is similar to that shown later for campaign 32) into the hearth of the LKAB's EBF (campaign 31) at two layers. These samples were used for initial studies of coke/slag interaction in the hearth (shown in Task 3.5) and for determining the wetting of hot metal on the coke, the latter of which was used as the reference information for the water model design (shown in Task 1.3). Coke/slag samples were

taken from two layers and at three different levels corresponding to the top and the bottom of the hearth as well as intermediate level. Coke/metal samples were taken from two levels at the second-layer drilling cores and located at centre of EBF hearth. The positions of the collected coke/slag and coke/metal samples are illustrated in Figure 188. At each position, the coke samples were taken from the 5-10 mm fraction, the slag was taken from the > 5 mm fraction and the metal was taken from the 1-2 mm fraction. The slag samples were grinded to obtain a homogeneous composition of the slag. Besides the solid samples from the EBF hearth (campaign 31), 7 tapped slag samples with different chemical compositions from the LKAB EBF campaign 31 were also taken. The coke and slag samples were analysed by X-ray diffraction (XRD) and X-ray fluorescence (XRF) analysis. These results are shown in Task 3.5 and Task 3.6.

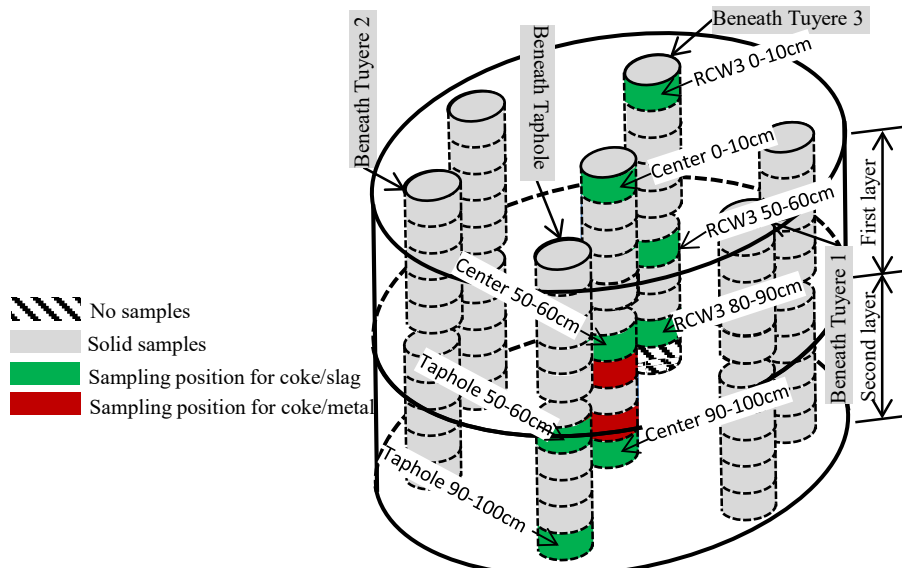


Figure 188: Positions of the selected coke/slag and coke/metal samples from the LKAB EBF hearth, campaign 31 (in the bottom of the hearth beneath Tuyere 3, there was no coke piece, therefore the sub-sample above was used instead).

2.2.3.1.2 New samples collected from EBF (campaign 32)

2.2.3.1.2.1 Collection of solid samples from the hearth of the experimental blast furnace

In the final stage of the LKAB's EBF campaign 32, conducted in Q4 2016, the EBF was quenched to room temperature with nitrogen (N₂). Thereafter the shaft was detached and the materials in the hearth of the EBF were exposed. The solid samples, which later on referred to as core-drilling samples, in the hearth of the EBF was procured by drilling steel tubes (diameter 130 mm and height 500 mm) into the bed of the hearth, as shown in Figure 189.



Figure 189: Procurement of the solid samples by core drilling into the bed of the EBF's hearth.

The core-drilling samples (CDS) were procured from two layers and several different positions (with respect to the positions of tuyeres and taphole) in the hearth of EBF. The core drilling has in general made the distribution of materials in the tube the same as it was in the hearth. In total 28

Optimizing Blast Furnace Hearth Inner State (OPTIBLAFFINS)

core-drilling samples were obtained: 7 from the first layer and 21 from the second layer. The positions (with respect to tuyeres and taphole) of these core-drilling samples as well as their reference numbers are illustrated in Figure 190.

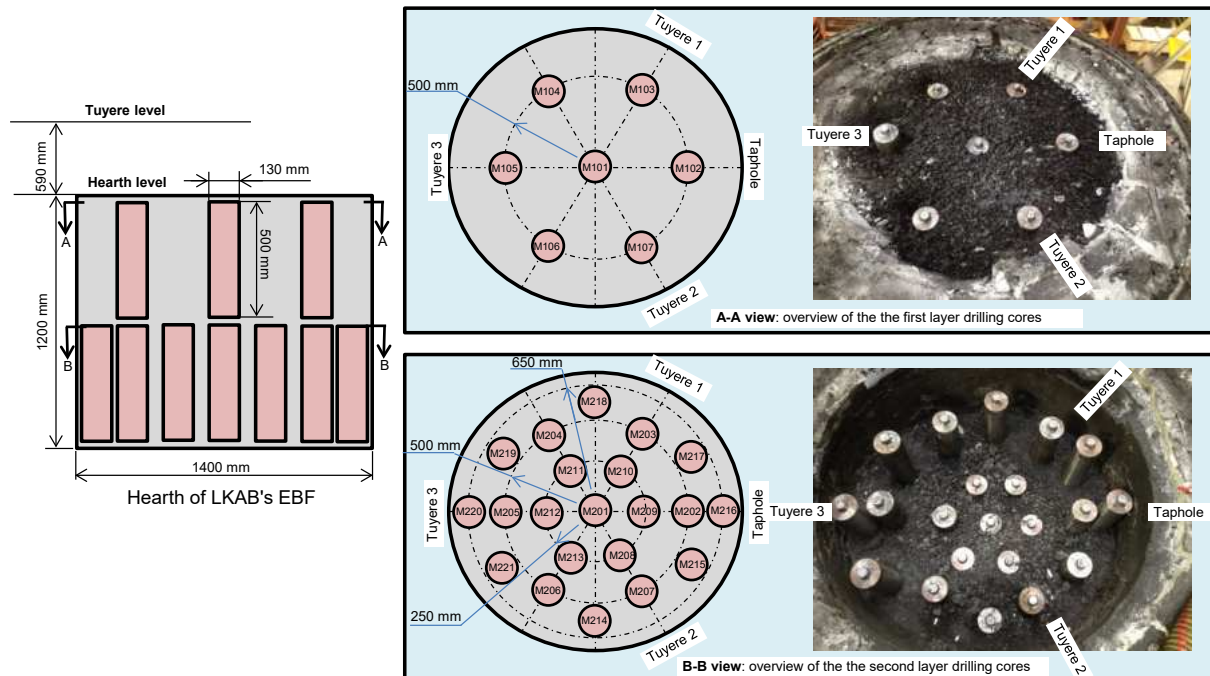


Figure 190: Illustration of the sampling positions (with respect to the 3 tuyeres and taphole) of the core-drilling samples as well as their reference numbers.

From Figure 190 it is also seen that some tubes, especially the tubes from the second-layer core drilling, are protruding above the bed level. This is due to the presence of hard materials, essentially the metals and metal-containing aggregates, which have hindered the core drilling further down into the bed. Therefore, some of the drilling tubes are not fully filled with solid samples. After the drilling tubes from the second core-drilling layer were taken out, several samples were also collected manually. The relative positions (with respect to the depth into the hearth) of the procured core-drilling samples as well as the manual samples are shown in Figure 191.

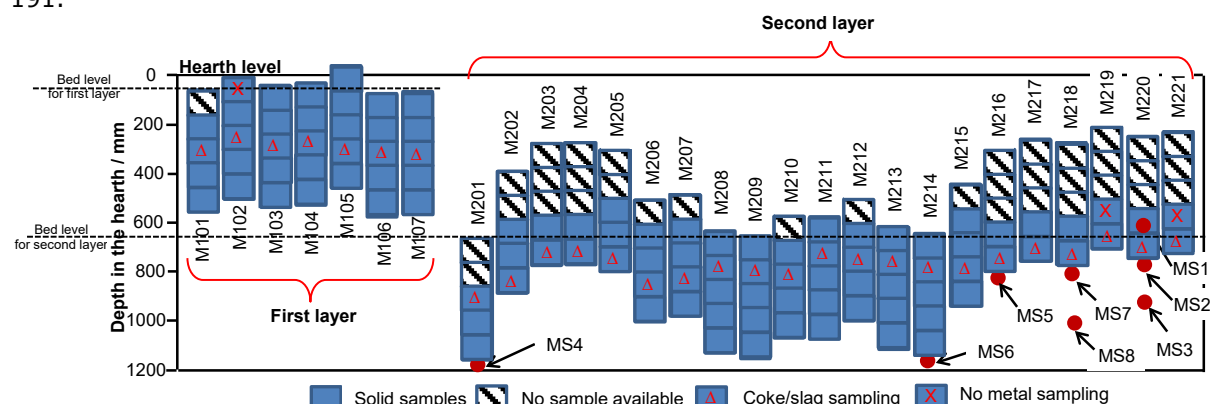


Figure 191: Illustration of the sampling positions (with respect to the depth in the hearth) of the core-drilling samples as well as the manual samples (MS 1-8).

2.2.3.1.2.2 Evaluation of solid samples from physical characterisation

The core drilling samples (as shown in Figure 190) procured from two layers in the hearth of the EBF were firstly physical characterized. Each of the core drilling samples was opened by cutting a window from the side of the core drilling tube; therefore, the appearance of the materials in the tube can be seen and the materials in the tube can be divided into 5 sub-samples (10 cm in length each) and be taken out one by another, as shown in Figure 191 and Figure 192.

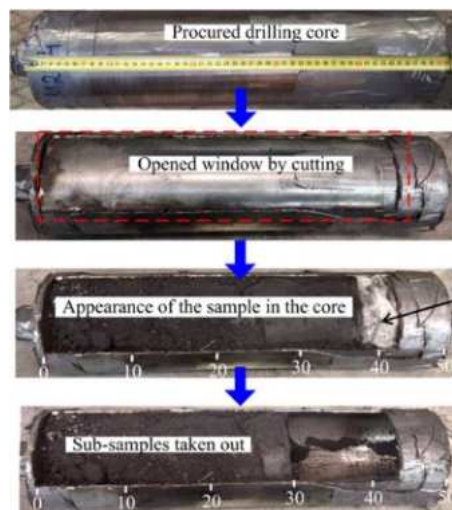


Figure 192: Procedure of the sub-samples from the core drilling tube.

Each sub-sample was screened into > 16mm, 10-16 mm, 5-10 mm, 2.8-5 mm, 1-2.8 mm, 0.5-1 mm and < 0.5 mm fractions. The > 5 mm fractions were manually separated into the magnetic (mainly metal), coke, slag and aggregate; the 1-2.8 mm and 2.8-5 mm fractions were separated into the magnetic and non-magnetic by the magnet. The screened fractions and the separated materials were, each, weighed. The average bulk density of the materials in the CDS as well as the bulk density of the materials in each sub-sample is calculated according to the following equation.

$$\text{Bulk density} = \frac{\text{weight of the sample}}{\text{the volume that the sample occupied in the core drilling tube}} \quad (48)$$

Figure 193 shows the appearance of the materials in the tubes and the relative positions of the drilling cores into the hearth of the EBF. In general, it is seen that: (i) the samples procured from the centre of the hearth (e.g. M101, M201 and M208-M213) are coarser than those from the circumference of the hearth (eg. M214-M221); (ii) the samples procured from the first layer are coarser than those from the second layer and (iii) the samples procured from the positions beneath the three tuyeres contain more fine materials.

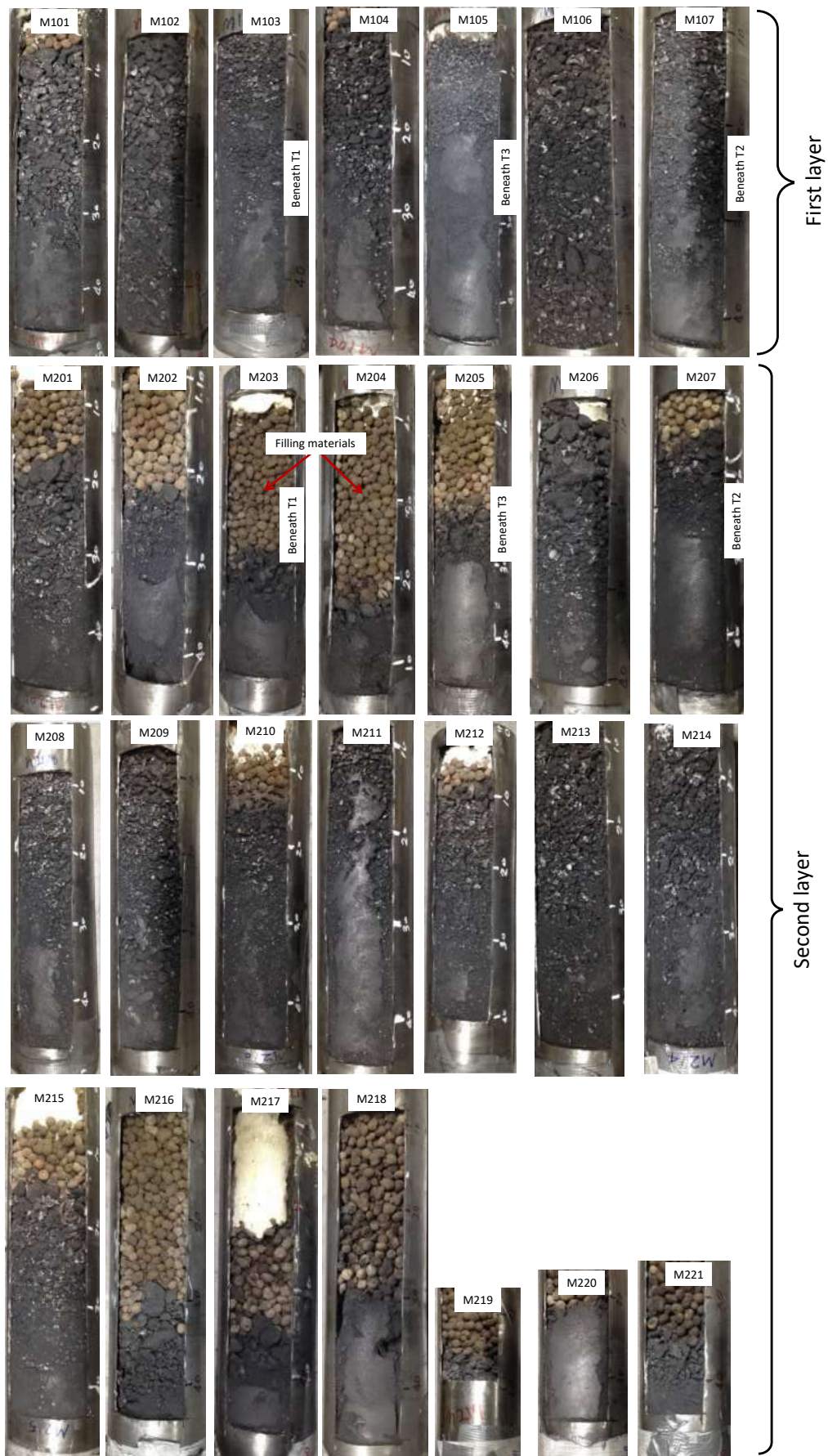


Figure 193: Appearance of the materials in the core drilling tubes.

These results can also be reflected by the particle size distribution of the materials as well as the average bulk densities of the materials in the drilling cores, as shown in Figure 194 and Figure 195. Higher contents of fines fractions and magnetic fractions contribute to higher bulk densities. These findings are consistent with our findings from previous EBF campaigns. Further, it has been found

Optimizing Blast Furnace Hearth Inner State (OPTIBLAFFINS)

that in the second-layer drilling cores (especially at the circumference of EBF hearth), significant amounts of aggregates, which are mixture of slag, metal and coke, were also found. The results from Figure 193, Figure 194 and Figure 195 indicate that there exists a solidified shell at the circumference of the EBF hearth lower part (second core drilling layer).

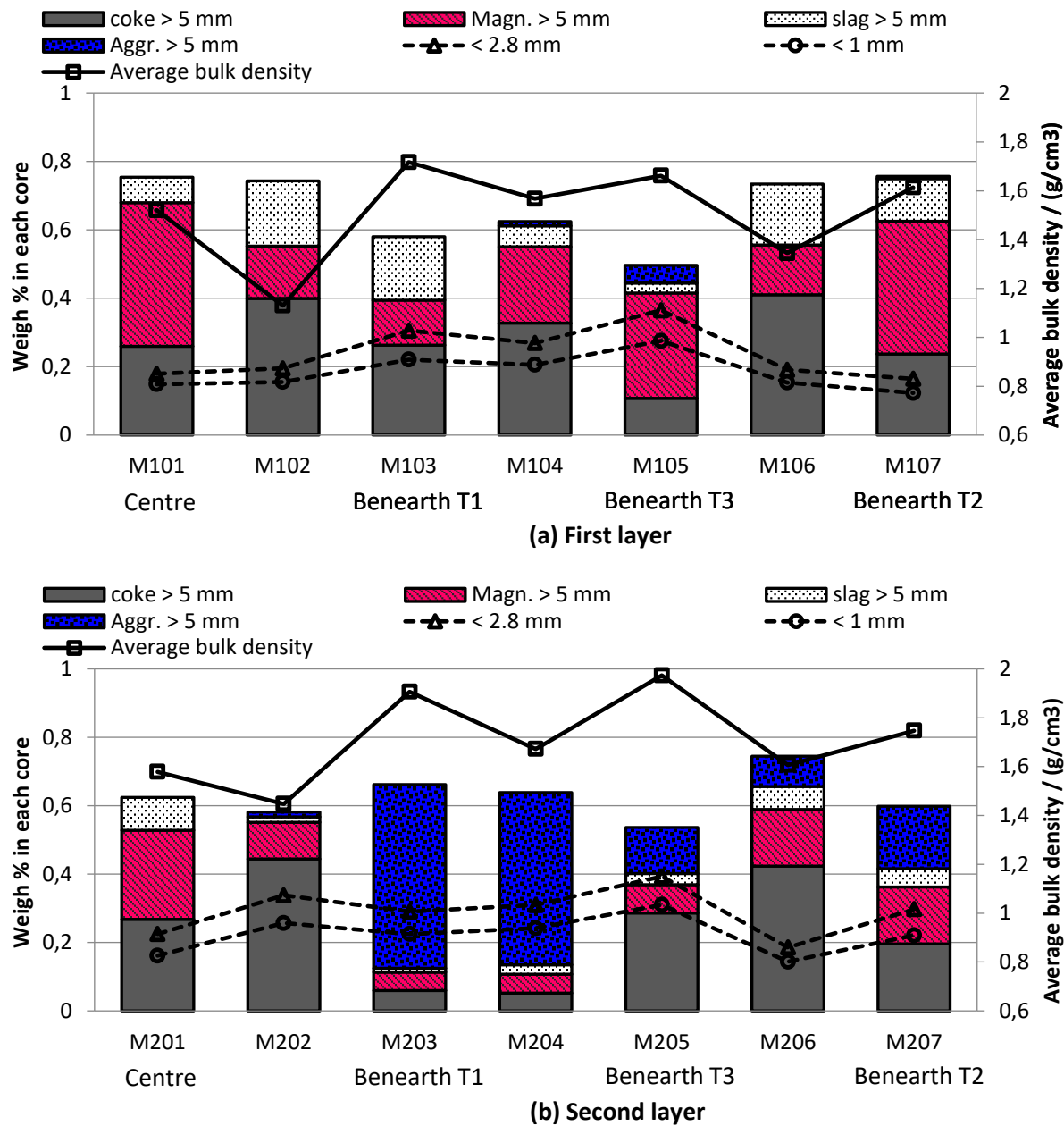


Figure 194: Particle size distribution of (a) first layer drilling cores and (b) second layer drilling cores into the hearth of the EBF as well as the bulk densities of the materials in each drilling cores.

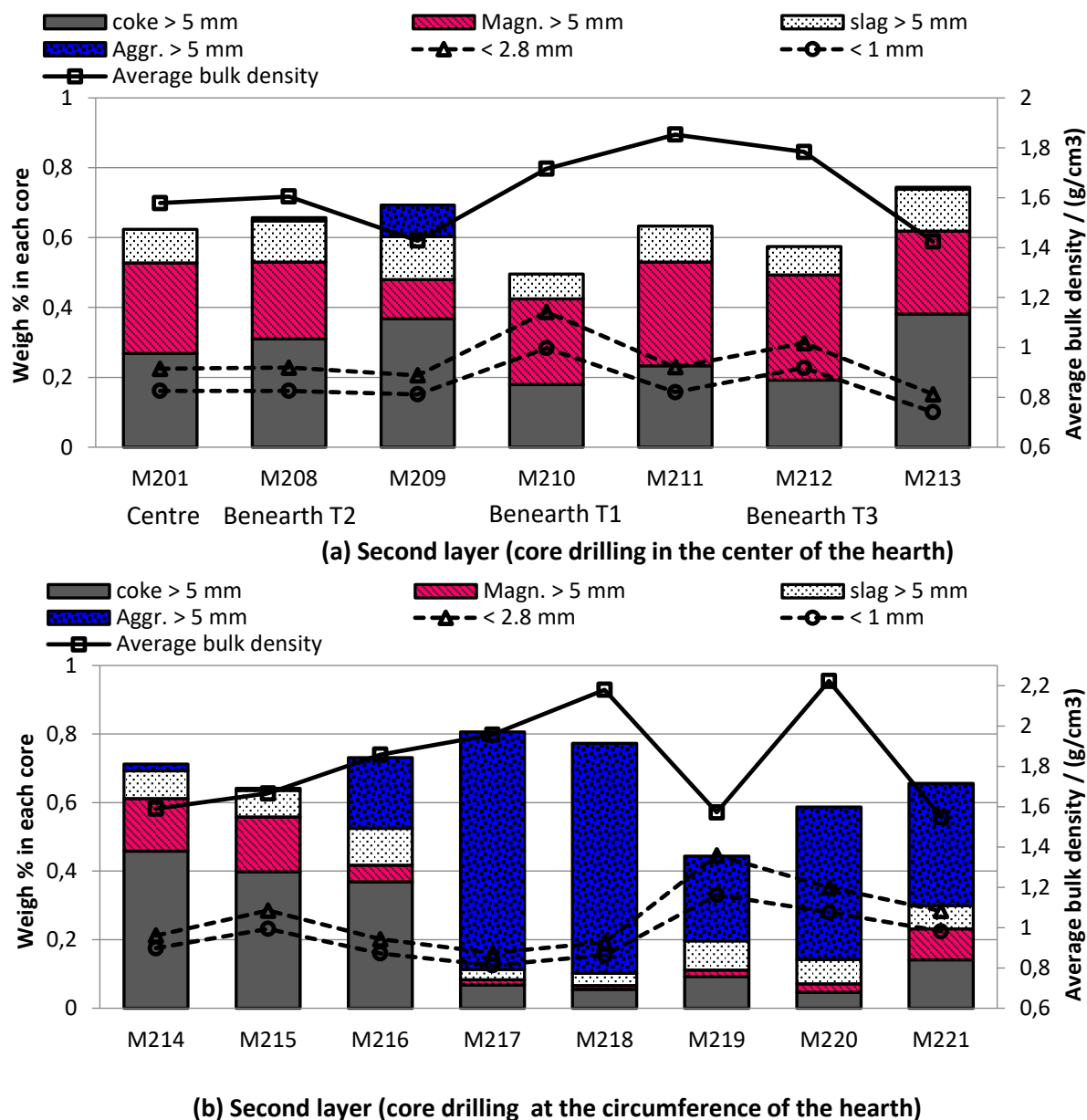


Figure 195: Particle size distribution of the second layer drilling cores procured from (a) the centre of the EBF hearth and (b) from the circumference of the EBF hearth.

Figure 196 shows the distribution of coarse fractions (> 5 mm fractions) of coke, the magnetic, slag and aggregate in each sub-sample of first-layer-drilling cores beneath the three tuyeres (M103, M105 and M107, as shown in Figure 190). It is seen that: (i) aggregates are dominantly in the >16 mm fraction; slag, metal and coke can be found in all the coarse fractions.

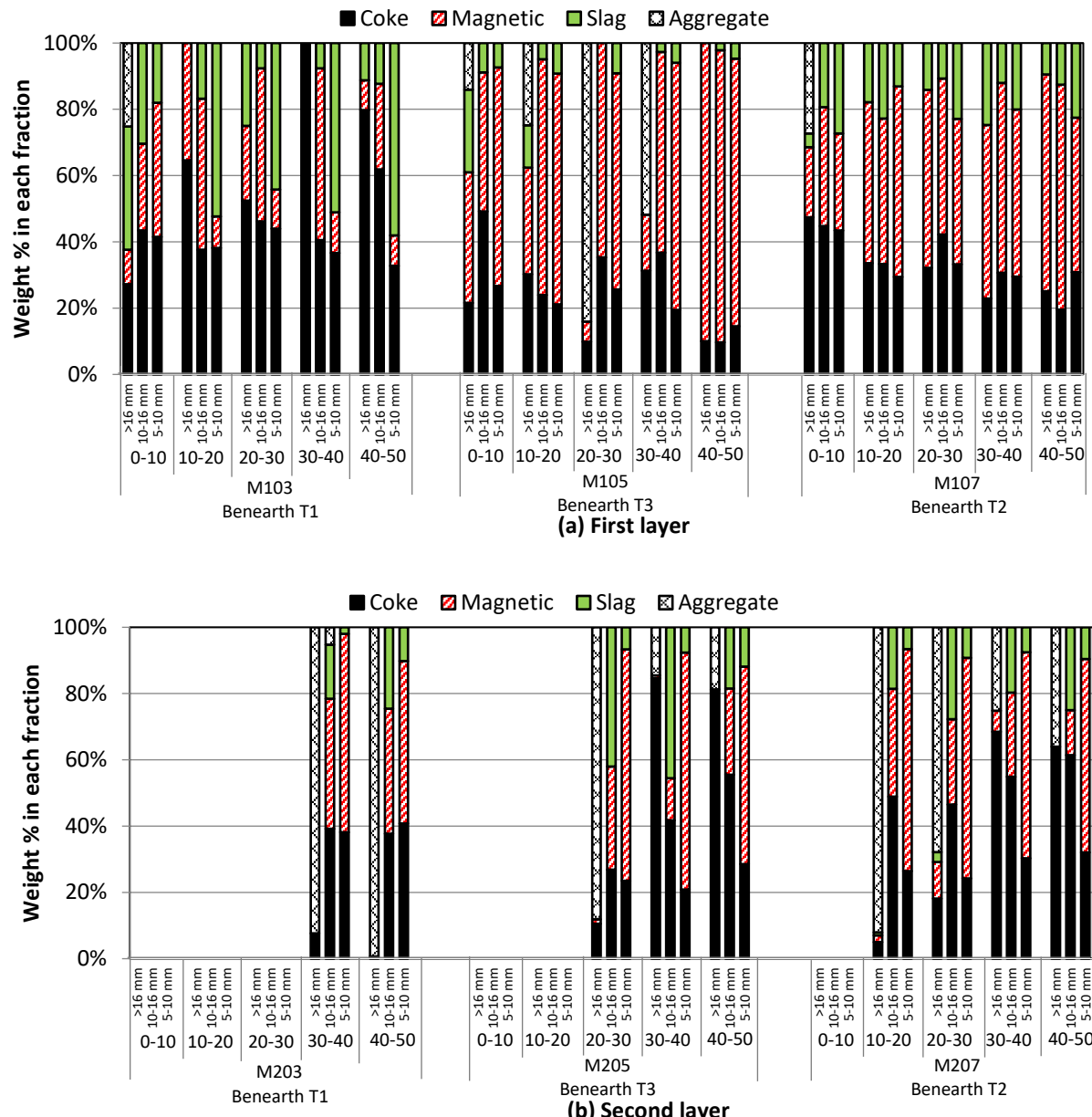


Figure 196: Distribution of the coarse fractions (> 5 mm) of coke, the magnetic, slag and aggregate in each sub-sample beneath the three tuyeres ((a) first layer drilling cores; (b) second layer drilling cores).

2.2.3.1.2.3 Evaluation of solid samples from chemical characterisation

After physical characterization, selected metal samples (in total 101 samples, as shown in Figure 191) in the fraction of mainly 5-10 mm were analysed by XRF with the Cu concentrations in the samples as the main interest. The results are presented in section 3.2.3.2. Selected coke/slag samples (as shown in Figure 191) were also analysed by XRF. Among these coke/slag samples, some of them (as shown in Figure 197) were also selected for the heating microscope study and XRD analysis. These results were shown in Task 3.5 and Task 3.6. Selected samples were analysed by SEM, the results are shown in section 3.2.3.2.

Besides the solid samples from EBF hearth, 13 tapped slag samples from the EBF, one original coke sample from the EBF, two tapped slag samples from TSE (BF6 and BF7) and one slag sample from voestalpine were also selected for XRF analysis and heating microscope study. These results were shown in Task 3.5 and Task 3.6 as well.

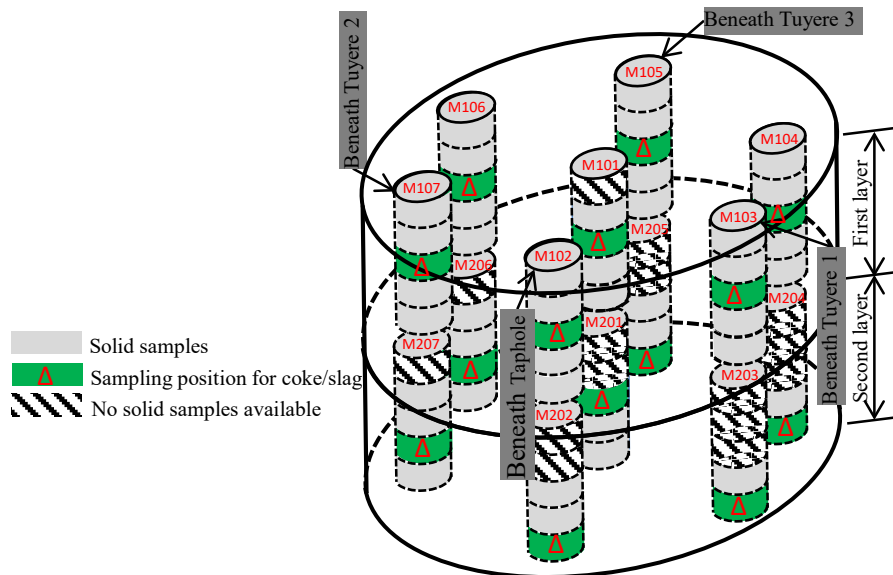


Figure 197: Sampling positions of the coke/slag from the core drilling tubes in the EBF hearth for the heating microscope study (Figure 191 can be referred to for the sampling depth into the EBF hearth).

2.2.3.1.3 Core borings AM Fos

The study was aimed at providing the CFD model developed by AMMR in Task 1.5 with the input data such as the dead man porosity. The sensitivity study done within Task 1.5 by AMMR showed that the dead man porosity plays an important role in the model. Hence a proper determination of this parameter is vital.

AMMR analysed the existing database and the appropriate data were retrieved.

MOHDRAIN 2.0 was developed based on one of the ArcelorMittal Fos-sur-Mer furnaces, so that the study was focused on the core boring done at ArcelorMittal Fos-sur-Mer. In total, 39 core borings were performed at ArcelorMittal Fos-sur-Mer BF 1 and 2 since 1990. These gave a large amount of data on particle size distribution as a function of the radial location of the sample at the tuyere level. This information is related to the former operational parameters of the ArcelorMittal Fos-sur-Mer blast furnaces, which do not exactly correspond to the current ones. Nevertheless, the study showed certain similarities in the former and current operations.

The core borings at ArcelorMittal Fos-sur-Mer were performed by means of two types of the machines: mobile and fixed (Figure 198). The fixed machine was firstly installed at BF 2 and then moved to BF 1. In total, the fixed machine performed 21 core borings (13 at BF 1 and 9 at BF 2) in the period from 1990 to 2002. The complete list of all the core borings performed at both blast furnaces of ArcelorMittal Fos-sur-Mer is given in Table 36.



a) Mobile core boring machine

b) fixed core boring machine

Figure 198: Overview of the core boring machines used at ArcelorMittal Fos-sur-Mer.

Table 36: Core borings performed at ArcelorMittal Fos-sur-Mer BF's 1 and 2.

ArcelorMittal Fos-sur-Mer BF 1				ArcelorMittal Fos-sur-Mer BF 2			
ID	Date of core boring	Tuyere number	Type of machine used	ID	Date of core boring	Tuyere number	Type of machine used
SF101	18/07/1995	23	Fixed	SF20	20/02/1990	20	Fixed
SF102	24/10/1995	23	Fixed	SF21	15/05/1990	20	Fixed
SF103	20/11/1995	23	Fixed	SF22	10/07/1990	20	Fixed
SF104	13/02/1996	23	Fixed	SF23	28/08/1990	20	Fixed
SF105	30/05/1996	23	Fixed	SF24	19/02/1991	20	Fixed
SF106	01/10/1996	23	Fixed	SF25	30/04/1991	20	Fixed
SF107	04/02/1997	23	Fixed	SF26	17/09/1991	20	Fixed
SF108	07/04/1998	23	Fixed	SF27	10/06/1992	20	Fixed
SF109	19/10/1999	23	Fixed	SF28	27/10/1992	20	Fixed
SF110	04/07/2000	23	Fixed	SM12	17/09/1991	6	Mobile
SF111	24/10/2000	23	Fixed	SM24	10/06/1992	12	Mobile
SF112	04/12/2001	23	Fixed	SM49	23/03/1993	9	Mobile
SF113	19/03/2002	23	Fixed	SM50	23/03/1993	10	Mobile
SM25	23/06/1992	9	Mobile	SM55	02/06/1993	6	Mobile
SM53	11/05/1993	11	Mobile	SM92	18/06/1996	8	Mobile
SM68	08/03/1994	7	Mobile	SM93	22/10/1996	9	Mobile
SM70	31/05/1994	8	Mobile	SM115	22/09/1998	7	Mobile
SM168	01/10/2003	7	Mobile	SM131	03/04/2000	9	Mobile
SM209	28/09/2010	9	Mobile	SM169	21/10/2003	11	Mobile
SM210	28/09/2010	7	Mobile				
Total number of borings at BF 1		20	Total number of borings at BF 2			19	
Total number of borings at ArcelorMittal Fos-sur-Mer BF's 1 and 2						39	

Optimizing Blast Furnace Hearth Inner State (OPTIBLAFFINS)

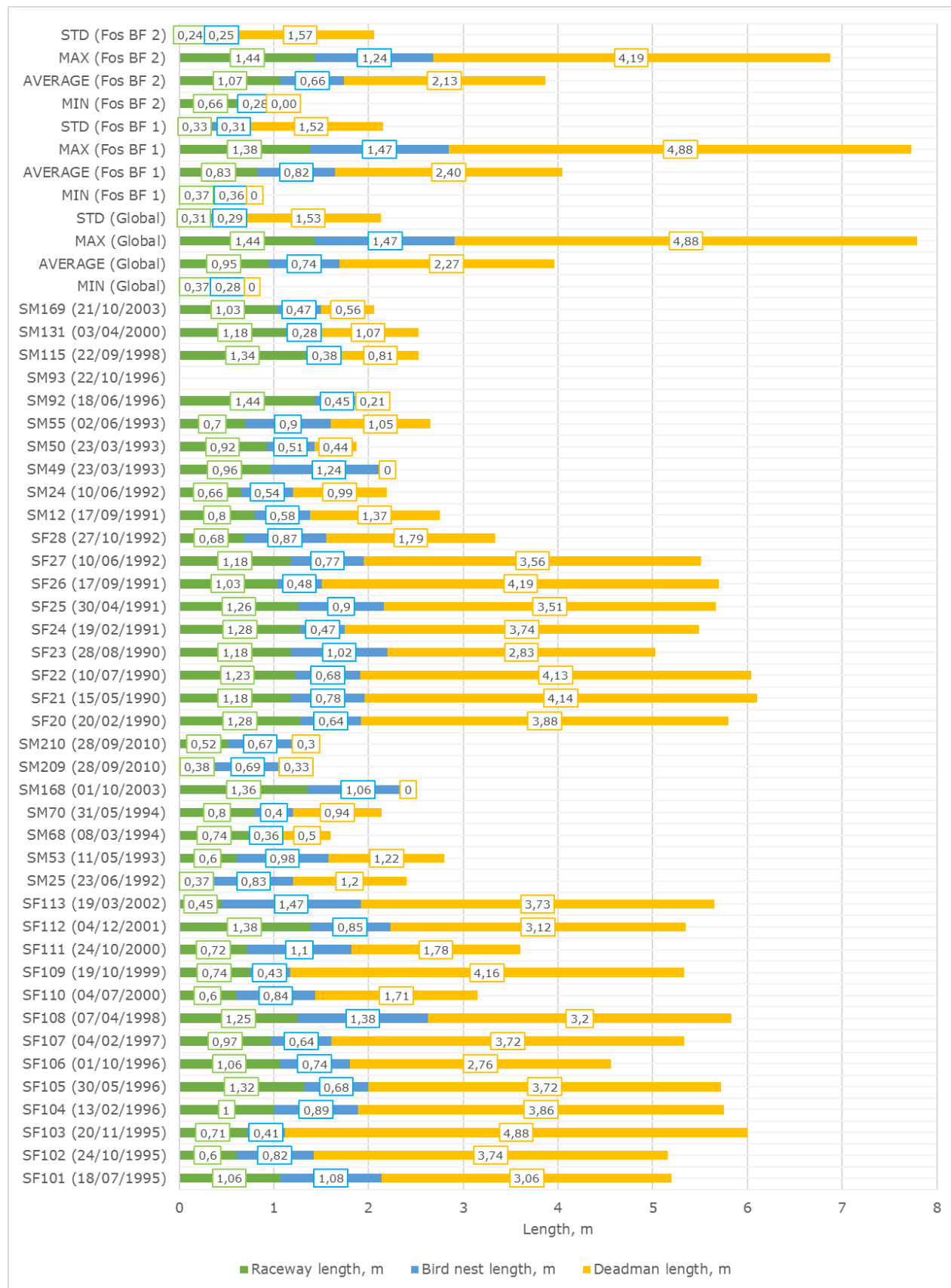


Figure 199: Results of the core borings at ArcelorMittal Fos-sur-Mer; lengths of zones.

Core borings provide different types of data. The data on the particle size distribution within different zones is the most relevant for this study. The data is summarised in Figure 198 and Figure 199. Five zones were observed, namely: raceway, bird's nest, dead man and intermediate and cohesive zones. The last two zones were observed in minority of cases. Their lengths are included in dead man length in Figure 199.

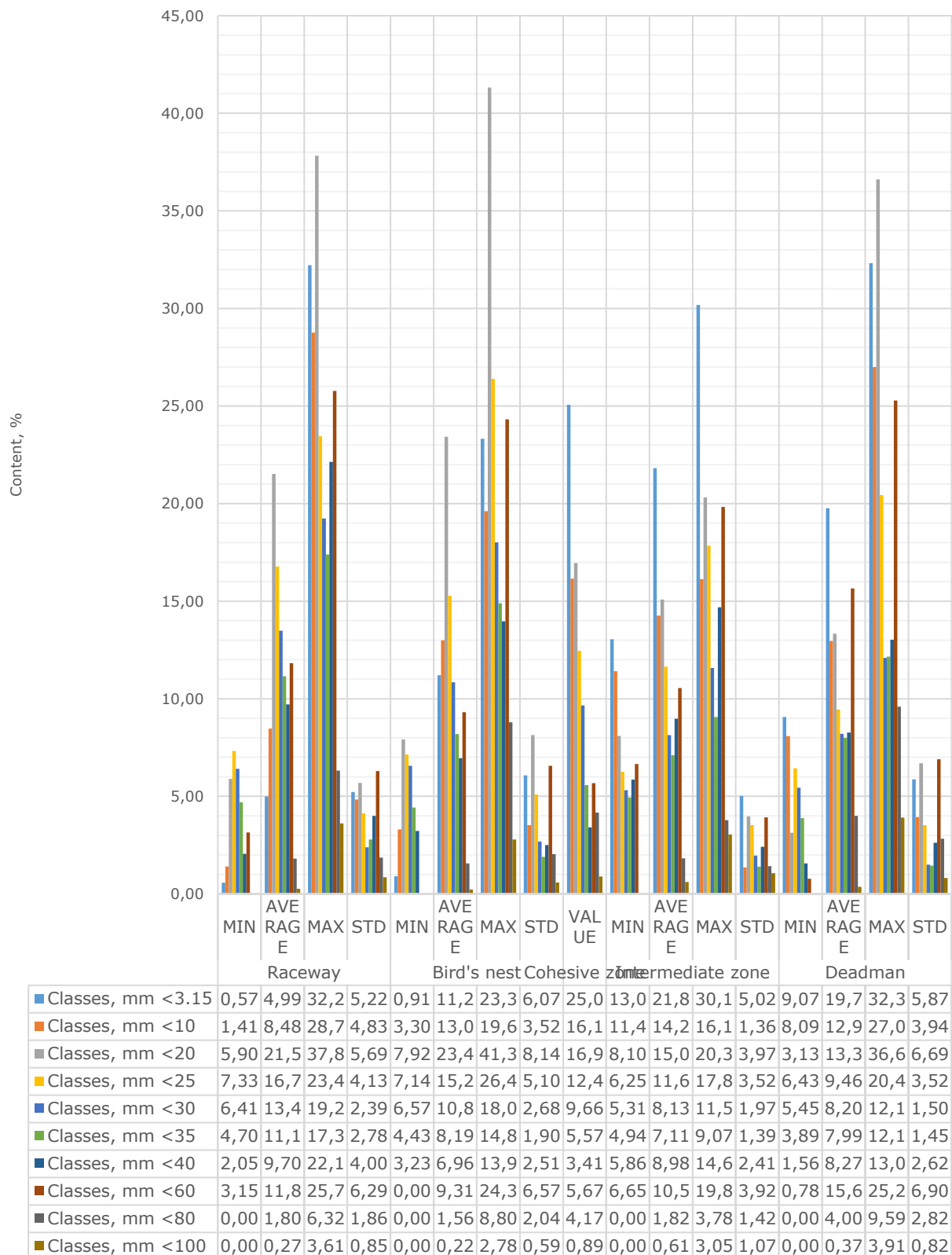


Figure 200: Results of the core borings at ArcelorMittal Fos-sur-Mer: particle size distribution.

The particle size distribution for each core was determined per lot. A lot is a portion of core which was analysed. In total, there were up to 15 lots per core. The whole core can be characterised by the individual lots, as every lot was fully analysed in the same way. Figure 200 shows the distribution of classes per zone. A zone can be composed of several lots thus the overall zone's particle size distribution is expressed in average values. The cohesive zone was observed only once in boring SM68.

Such an analysis of the particle size distribution at the tuyere level gives precious information on the distribution of the zones of different porosity inside the hearth. This distribution can be used in the model developed in Task 1.5 to further increase its precision.

2.2.3.2 Flow of slag and hot metal in Experimental BF during tapping

2.2.3.2.1 Injection of tracer during operation and before quenching including investigation of the close to wall material for tracer content

In the end of LKAB's EBF campaign 32, just before quenching, pulverized copper was injected through the coal injection lance in tuyere 3. Additional moulds for hot metal casting were used to provide the possibility to take out multiple hot metal samples during the last tapping.

The injection device was prepared prior the injection trial by filling the container with copper. Injection of coal had to be interrupted when the copper injection device was mounted to the coal injection lance, as illustrated in Figure 170. The carrier gas flow (N_2) in the lance was however maintained. When the target time was reached the valves to pressurize the device and enable entrance to the coal injection pipe were opened. To ensure that all copper was entering the furnace the device was put to an upright position. After injection the device was removed, and the coal injection was reinstalled and put in operation.



Figure 201: Copper injection device (left) and device mounted onto the coal injection pipe (right).

The target time for copper injection was based on results and analyses from DEMPOLIFE [102] and SUSTAINTAP [55] and was planned to be 20 minutes prior the final tapping. During the injection trial the time was recorded from start of Cu injection to the time slag was exiting the taphole. Advantageous tapping condition made it possible to collect 9 hot metal samples from the last tapping; the moulds were emptied during the tapping and new samples were casted. LKAB's X-ray fluorescence (XRF) instrument, which is installed in connection to the EBF, was used to analyse the samples with respect to chemical composition. In Table 37 the time for each hot metal sample in relation to the injection start is presented together with the copper concentration for the sample. Two samples were of poor quality and analysis in the equipment wasn't possible.

Table 37: Time response from Cu injection in tuyere 3.

Implementation step	Timekeeping (mm:ss)	Cu concentration (wt%)
Cu injection	00:00	-
Taphole open	18:25	-
Hot metal sample 1	18:42	Invalid sample
Hot metal sample 2	18:54	0.044
Hot metal sample 3	19:02	0.054
Hot metal sample 4	19:12	0.056
Hot metal sample 5	19:21	0.057
Hot metal sample 6	19:31	0.062
Hot metal sample 7	19:46	0.061
Hot metal sample 8	20:46	0.086
Hot metal sample 9	20:59	Invalid sample
Slag through taphole	22:56	-

In Figure 202 the new data is compared to Cu concentration data gathered in SUSTAINTAP [55]. Cu is injected in tuyere 3 for all cases. SUSTAINTAP-data covers Cu injection prior quenching as well as injection during operation; injection trials 15- and 30-minutes prior tapping were performed. The target time for injection before quenching was 20 minutes prior the final tapping, but due to the state of the process the taphole had to be opened 7.5 minutes earlier. Therefore, the same target time was preserved for the OPTIBLAFINS trial and the deviation between the

Optimizing Blast Furnace Hearth Inner State (OPTIBLAFFINS)

actual injection time and the target time was significantly decreased in this trial. Collected Cu concentration data shows good agreement to the former samples and increases the credibility for the interpolated curve for expected Cu variation.

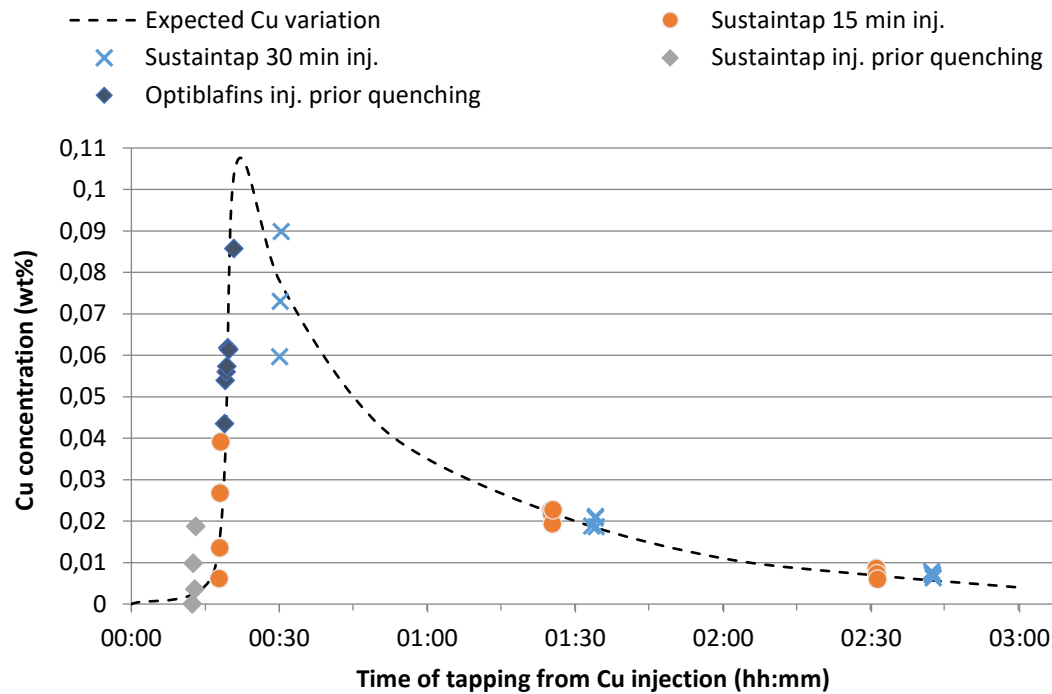


Figure 202: Cu concentration in tapped hot metal.

In SUSTAINTAP [55] copper was mainly found in the second layer; to increase the accuracy of the interpretation of the flow field the resolution of cores in the second layer was increased within this project. Especially of interest and shown by the core positions in Figure 190, was the close to wall regions. The flow of hot metal in the EBF hearth is further evaluated by analysing the core-drilling samples and an interpretation of the hot metal flow field in the EBF hearth was made.

Table 38: Chemical compositions of the metal samples taken from the drilling cores (balanced amount for other elements).

Sample ID	Fe %	C %	Si %	Mn %	S %	Cu ppm	Sample ID	Fe %	C %	Si %	Mn %	S %	Cu ppm
M101-1	92.4	4.48	2.2	0.23	0.107	10	M207-1	89.6	4.81	3.16	0.21	0.019	10
M101-2	92.7	4.08	2.13	0.24	0.248	10	M207-2	90.7	4.53	2.91	0.21	0.010	10
M101-3	92.5	4.64	2.05	0.22	0.011	40	M207-3	90.5	4.54	2.92	0.21	0.007	10
M101-4	92.8	4.14	2.23	0.21	0.016	280	M207-4	90.6	5.00	2.38	0.17	0.077	10
M102-2	93.7	4.71	0.87	0.22	0.070	10	M208-1	92.6	4.45	2.24	0.15	0.013	10
M102-3	93.6	4.7	0.94	0.22	0.050	10	M208-2	92.7	4.20	2.31	0.17	0.002	10
M102-4	93.3	4.37	1.39	0.22	0.205	10	M208-3	92.5	4.46	2.30	0.17	0.007	10
M102-5	93.2	4.53	1.56	0.21	0.046	10	M208-4	92.9	4.21	2.13	0.18	0.004	140
M103-1	94.1	3.12	1.44	0.23	0.301	10	M208-5	92.2	4.60	2.20	0.2	0.008	200
M103-2	92.6	4.86	1.50	0.24	0.023	10	M209-1	92.3	4.87	2.03	0.18	0.027	10
M103-3	91.5	4.77	2.25	0.41	0.032	10	M209-2	92.4	4.60	2.22	0.2	0.009	10
M103-4	91.3	4.84	2.32	0.35	0.011	10	M209-3	92.4	4.72	2.13	0.19	0.010	10
M103-5	93.1	3.9	1.96	0.26	0.004	10	M209-4	92.2	4.30	2.66	0.19	0.026	10
M104-1	93.4	4.72	1.01	0.27	0.017	10	M209-5	92.7	4.09	2.54	0.17	0.019	30
M104-2	93.0	4.92	1.12	0.3	0.025	10	M210-1	92.7	4.35	2.12	0.17	0.005	10
M104-3	93.3	4.48	1.17	0.33	0.043	50	M210-2	92.3	4.47	2.27	0.18	0.011	10
M104-4	92.9	4.24	1.53	0.34	0.155	490	M210-3	92.5	3.90	2.34	0.19	0.002	10
M104-5	92.4	4.46	1.73	0.32	0.109	1100	M210-4	92.6	4.41	2.15	0.2	0.007	10
M105-1	91.6	4.73	2.24	0.17	0.015	4800	M211-1	92.4	4.67	2.04	0.19	0.010	1100

Optimizing Blast Furnace Hearth Inner State (OPTIBLAFINS)

M105-2	91.9	4.49	2.45	0.14	0.022	3100	M211-2	92.6	4.50	2.08	0.17	0.007	1200
M105-3	92.9	3.62	2.25	0.11	0.038	1500	M211-3	92.5	4.49	2.16	0.18	0.010	1400
M105-4	92.7	3.91	1.97	0.17	0.003	980	M211-4	92.8	4.16	2.17	0.18	0.003	1200
M105-5	89.3	7.66	1.93	0.19	0.016	1200	M211-5	92.5	4.65	1.96	0.16	0.019	1100
M106-1	94.8	3.99	0.46	0.2	0.046	10	M212-1	92.4	4.50	2.31	0.15	0.004	1200
M106-2	94.3	4.3	0.63	0.25	0.024	10	M212-2	92.5	4.47	2.19	0.15	0.005	1200
M106-3	94.0	4.71	0.63	0.23	0.021	10	M212-3	92.0	5.21	1.97	0.14	0.013	1100
M106-4	93.4	4.58	1.10	0.23	0.026	1100	M212-4	92.8	4.47	2.02	0.16	0.007	700
M106-5	93.0	4.32	1.59	0.24	0.051	1400	M213-1	92.7	4.75	1.81	0.15	0.006	530
M107-1	92.6	4.61	1.86	0.27	0.042	10	M213-2	92.6	4.50	2.1	0.17	0.004	690
M107-2	92.5	4.8	1.80	0.26	0.058	10	M213-3	92.9	4.36	2.00	0.15	0.003	570
M107-3	92.2	4.99	1.94	0.23	0.034	10	M213-4	92.8	4.37	1.99	0.17	0.012	590
M107-4	92.8	4.55	1.83	0.23	0.022	10	M213-5	92.6	4.62	2.01	0.19	0.013	860
M107-5	92.5	4.72	1.99	0.23	0.052	10	M214-1	92.8	4.40	1.8	0.26	0.023	30
M201-1	90.4	6.52	2.23	0.19	0.032	440	M214-2	92.3	4.42	2.04	0.23	0.022	60
M201-2	92.2	4.68	2.3	0.18	0.023	540	M214-3	93.0	4.38	1.81	0.22	0.016	180
M201-3	92.3	4.68	2.12	0.19	0.03	650	M214-4	92.8	4.54	1.84	0.23	0.024	70
M202-1	90.2	4.63	3.62	0.2	0.055	10	M214-5	91.6	4.61	2.36	0.24	0.017	130
M202-2	90.7	4.25	3.83	0.18	0.018	10	M215-1	93.0	4.51	1.64	0.27	0.046	10
M202-3	90.6	4.66	3.75	0.17	0.056	10	M215-2	92.6	4.53	1.87	0.26	0.036	10
M203-1	90.8	3.33	3.52	0.25	0.100	40	M215-3	92.8	4.32	2.03	0.24	0.027	10
M203-2	93.4	3.87	1.33	0.23	0.002	100	M215-4	91.8	4.46	2.49	0.24	0.026	10
M204-1	92.5	4.53	1.15	0.2	0.021	460	M216-1	93.2	4.50	1.49	0.18	0.023	10
M204-2	93.1	4.99	0.73	0.15	0.074	120	M216-2	91.9	5.09	1.81	0.19	0.050	10
M205-1	92.5	4.47	1.54	0.14	0.009	110	M217-1	92.11	4.21	2.26	0.26	0.023	10
M205-2	93.7	4.56	0.71	0.11	0.081	10	M217-2	92.32	4.11	2.54	0.22	0.027	10
M205-3	92.8	5.68	0.57	0.084	0.112	10	M218-1	93.06	4.51	1.04	0.17	0.061	10
M206-1	92.7	4.90	1.33	0.2	0.061	820	M218-2	93.37	4.24	1.21	0.18	0.035	20
M206-2	92.7	4.72	1.71	0.2	0.011	2000	M219-2	94.11	4.36	0.46	0.08	0.129	10
M206-3	93.0	4.35	1.73	0.2	0.021	1600	M220-1	94.35	4.68	0.2	0.056	0.075	10
M206-4	93.2	4.35	1.67	0.21	0.013	1300	M220-2	94.55	4.46	0.24	0.056	0.128	10
							M221-2	94.21	4.65	0.44	0.076	0.039	10

Sample ID M101-1 indicates 1st available metal samples from the drilling core M101 by counting from the top to the bottom shown in Figure 191.

Table 38 shows the chemical analysis results of the collected metallic samples from the EBF hearth core drilling. Since Cu contents in the metallic samples are of great interest, the Cu contents were shown in Figure 203. It is seen that the highest Cu content was found in the metallic samples from core drilling tube M105, which is located beneath the tuyere 3 (the position where Cu was injected and the opposite side as the taphole). By tracking the Cu contents in the samples, a flow field of the metallic in the EBF hearth can be depicted and shown later in Figure 211 and Figure 212. From Figure 203 it is also seen that the Cu contents in the samples procured from the circumference (close to the wall) of the EBF hearth (M215-M211) are in general quite low. The reason for this could probably due to the formation of a solidified shell (as described earlier in WP 3.1) at the circumference of the EBF hearth lower part and thus the flow of metallic iron was impeded.

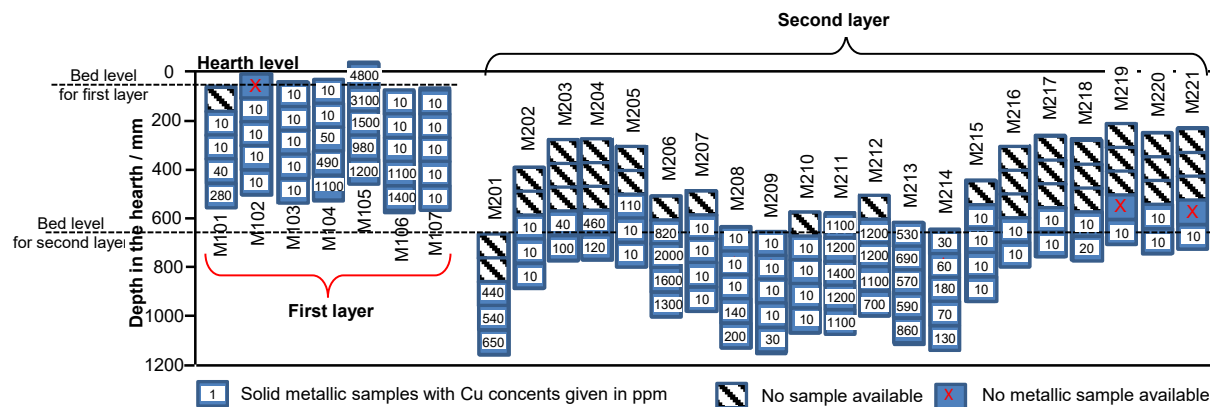


Figure 203: Cu contents (given in ppm) in the metallic samples procured from the EBF hearth.

To further investigate the state of the hearth before quenching, SEM analysis of the manual samples were carried out. As shown in Figure 191, the manual samples were taken from several different points in the furnace. Selected samples were taken for optical microscope and SEM analysis based on their positions (as shown in Figure 204), in order to examine the conditions in different areas. Before the analysis, the samples were prepared by casting in epoxy resin, grinding and polishing. Ethanol was used for final cleaning of the sample surface. The samples did not require graphite coating prior to the analysis.

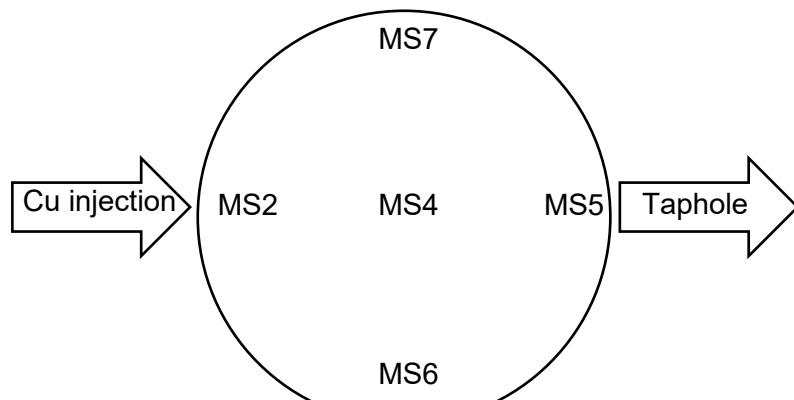


Figure 204: Positions of manual samples selected for SEM analysis.

Figure 205 and Figure 206 show examples of the optical microscope analysis results. All other images from the optical microscope can be found in Appendix 3.5.3. The first phase observed are metallic granules (point 1), with smaller particles of a brass-coloured phase inside (point 2). On the right side of Figure 205 is likely to be an area of coke (point 3). The mottled white/grey areas visually appear to be the slag phase (point 4). There is an additional dark red/brown phase that was observed in several samples (point 5). A smaller area of this phase can be seen in the centre of Figure 205, and a larger area in Figure 206. In some cases, phase 5 also appears to be associated with phase 2.

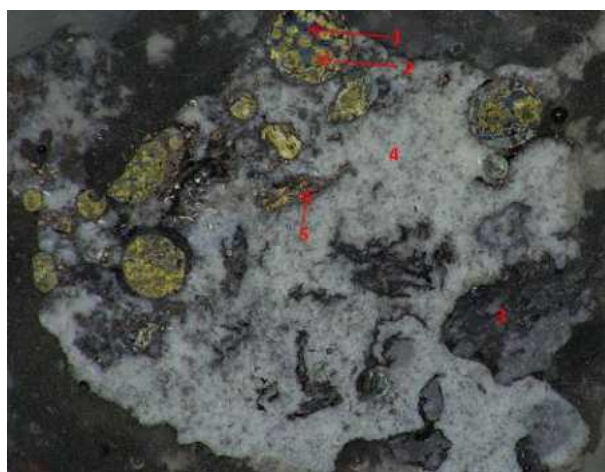


Figure 205: Optical microscope image of sample MS5.

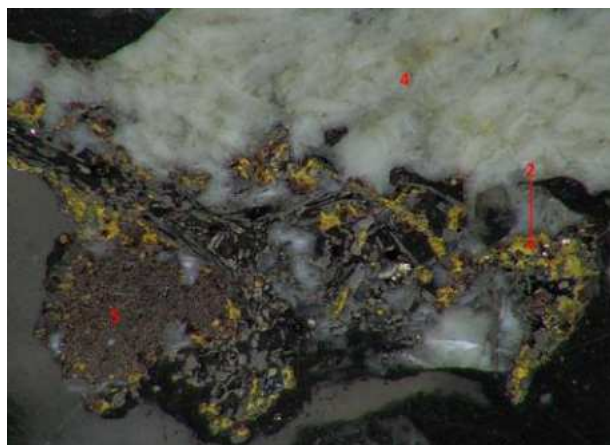


Figure 206: Magnified optical microscope image of sample MS6.

Figure 207, Figure 208 and Figure 209 show example images of the SEM results. All other images and analyses from the SEM can be found in Appendix 3.5.3. For examples of point analysis results (see Table 39). The SEM-EDS analysis showed that the metallic granules (phase 1) is the phase with the highest content of Fe, with some Si, O and C. This confirms that these are granules of hot metal. The brass-coloured phase contains a high concentration of Si and O, but Fe content is significantly lower. In addition, streaks of coke appear to be present in the metal granules. Figure 207 shows an image of these phases from sample MS5.

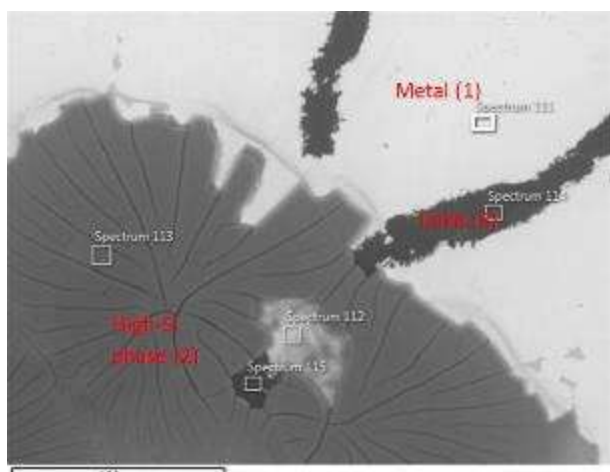


Figure 207: SEM image of sample MS5, Site 2.

The areas designated phase 3 in the previous section, is mostly C and thus most likely coke. The white/grey areas designated phase 4, is a mix of different slag phases, primarily consisting of different proportions of Si, Mg, Al, and Ca oxides. Figure 206 shows an image of these phases from sample MS6. In some cases, significant content of S might indicate the presence of sulphides or sulphates; these are the lightest grey areas.

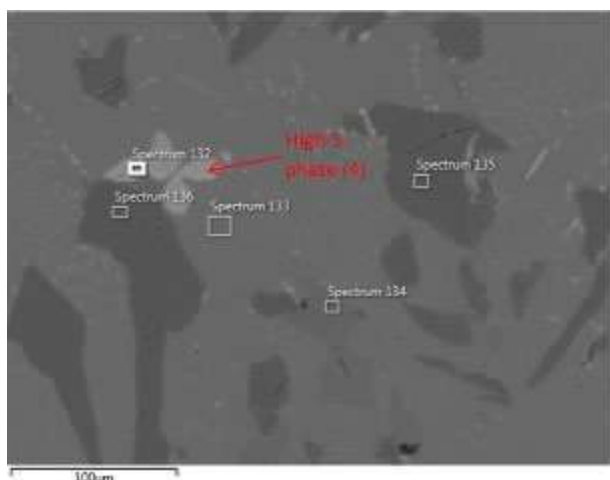


Figure 208: SEM image of sample MS6, Site 2.

The darker areas designated phase 5 is a mix of different slag phases, similar to phase 4, and metallic Fe phases, similar to phase 1. The significant difference is the presence of TiN and other Ti containing phases. Figure 209 shows an example of such an area from sample MS7. The slag phases are dark grey, the metallic phase is white, and the Ti containing phases are lighter gray.

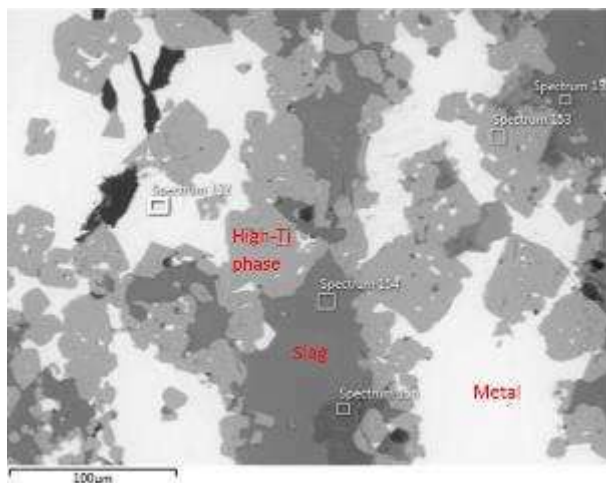


Figure 209: SEM image of sample MS7, Site 3.

Table 39 shows a few simplified (example) analyses of the different phases. Complete analyses for each sample can be found in Appendix 3.5.3.

Table 39: Example SEM-EDS point analysis (wt.%) results.

Element	Metal (1)	High-Si phase (2)	Slag phases (4)	High-Ti phases	
C	47	36	18	19	20
N	-	-	-	-	19
O	10	37	47	47	26
Mg	0.35	-	4.9	15	0.92
Al	-	-	5.3	-	0.65
Si	6.1	19	11	11	2.3
S	-	-	0.43	0.42	0.17
Ca	0.22	-	13	5.1	1.2
Ti	-	-	-	-	24
Fe	37	7.5	-	-	19
					5.2
					5.2

The content of C in almost all analyses, except coke particles, is significantly higher than expected. This has two potential explanations for this phenomenon. The first is that there are trace amounts of epoxy present on the surface, since this is analysed as almost pure C (see Sample MS4, Site 3 in Appendix 3.5.3). The second is that since coke is softer than slag or metal, particles of coke may potentially have contaminated other surfaces during grinding or polishing.

The optical microscope and SEM analysis show that the manual samples are mostly a mixture of metal, slag and coke. No copper was detected in any of the analyses. This may indicate that the aggregates in the EBF hearth were formed before quenching.

To visualize the distribution of copper in the EBF hearth a CAD-model was created, see Figure 210. The positions of the core drills as well as the sub-samples are illustrated in the model, compare to the actual images from the excavation (right hand side in Figure 210). The copper content for each sub-sample is illustrated by a sphere, the larger the sphere the higher Cu-content. The Cu-content is also illustrated by the colour of the sphere; the scale goes from blue (low Cu-content) – yellow – orange – red (high Cu-content).

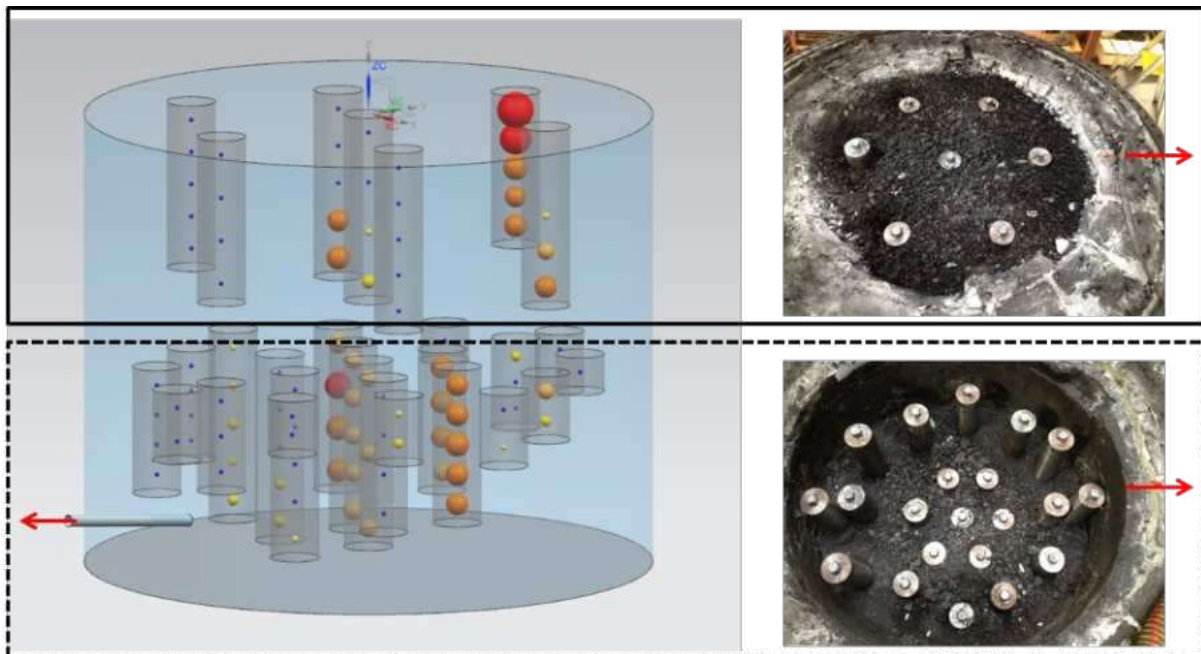


Figure 210: Copper content in each sub-sample illustrated by differentiated spheres (left). Images from the EBF hearth excavation (right) for the first layer (upper right) and the second layer (lower right). The location of the taphole is marked by the red arrow.

As can be seen in the images from the core drilling (Figure 210), only 8 of the 21 tubes in the second layer could be drilled completely into the bed. The resistance was especially high close to the wall on the righthand side of the hearth (seen from the taphole). By combining interpreted 2d-path-lines from a top view and a side view of the CAD-model, Figure 211, the flow field in the EBF hearth at the final tapping of campaign 32 is estimated and illustrated in Figure 212.

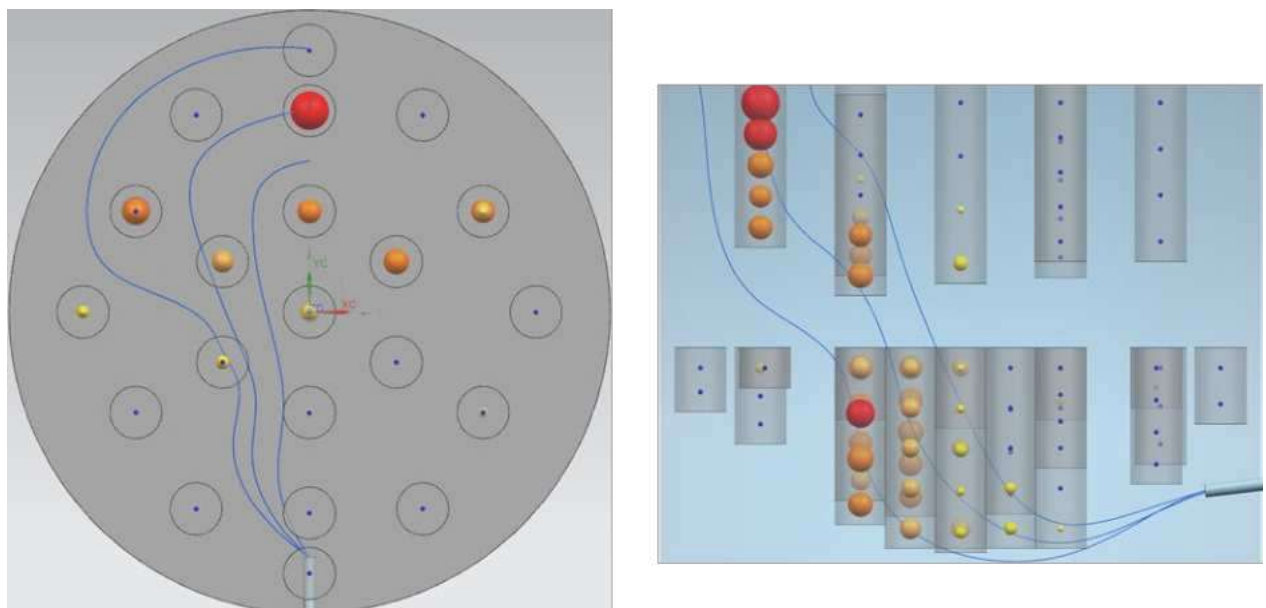


Figure 211: Interpreted 2d-path-lines (top view – left, side view – right) based on the copper content in each sub-sample.

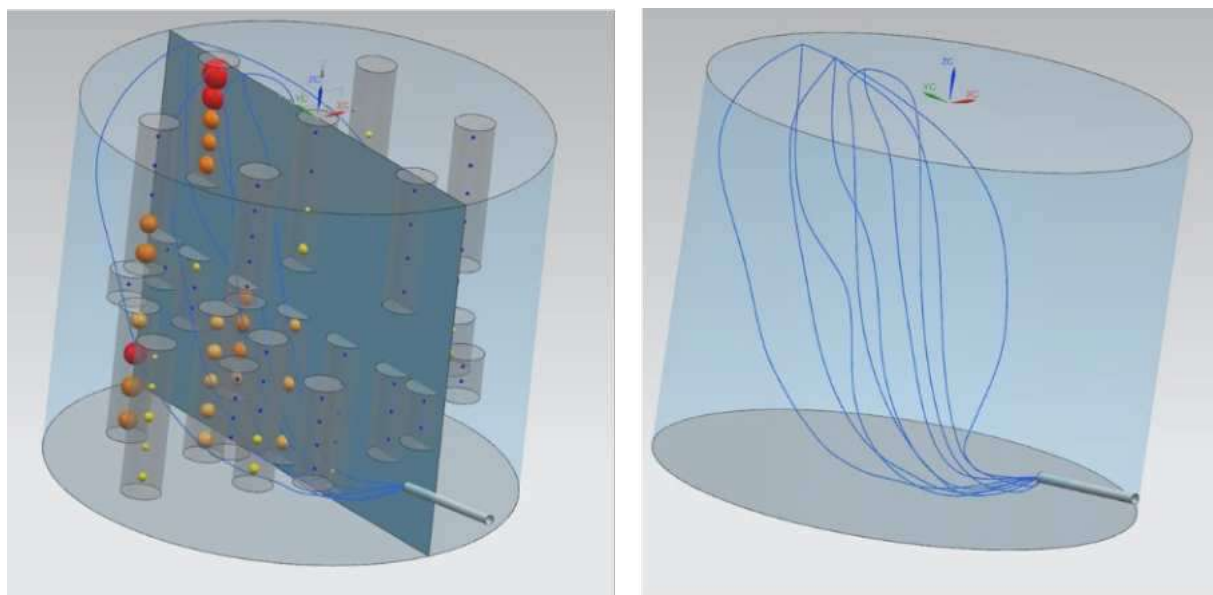


Figure 212 Estimated 3d-path-lines based on the copper content in each sub-sample (left) and the interpreted flow field (right).

The copper distribution indicates that the developed method to estimate void fraction of the coke bed is reasonable; under each tuyere the resistance to the flow seems to be higher compared to the centre region of the hearth. This is of importance because the determined coke bed distribution serves as an input to the EBF hearth water model (Task 1.3: Water model studies BF hearth). Further, the results in Figure 211 and Figure 212 are used to validate the developed EBF water model by comparing the liquid flow field for the real process and for the water model.

2.2.3.2.2 Flow of slag and hot metal in EBF during tapping

The chemistry of slag and hot metal is related to the charged burden materials; a change in the charged burden could lead to a change of the slag and hot metal chemistry. In the end of the EBF campaign 32, the charged MPBO pellets varied from 273.4 kg/charge to 262.1 kg/charge, while the charged coke (82.5 kg/charge) as well as other flux materials were fixed. The change in the pellets/coke ratio could influence the tapped slag amount. However, during the tapping the slag and hot metal were tapped together. Therefore, it is difficult to use the slag amount as a variable.

To determine the delay in changed slag chemistry due to the change of burden, Figure 213 and Figure 214 are plotted by using the collected charging data and tapping data to show the change of the slag and hot metal chemistry with the change of ferrous burden. From Figure 213 and Figure 214 it is seen that when the charged MPBO pellets were decreased from 273.4 kg/charge to 271.8 kg/charge and from 271.8 kg/charge to 264.1 kg/charge, there is no obvious change in slag and hot metal chemical compositions. There were changes in slag and hot metal chemical compositions, as shown in squared areas in Figure 213 and Figure 214. However, such changes were hardly to be related to the change of the ferrous burden, as the changes restored after a while even though the charged pellets continued to decrease. Therefore, by using the available process data it is difficult to estimate the flow of slag and hot metal during tapping. The reason for this could probably be that the change of the charged pellets is of less significance and thus has negligible influence on the slag and hot metal chemistry.

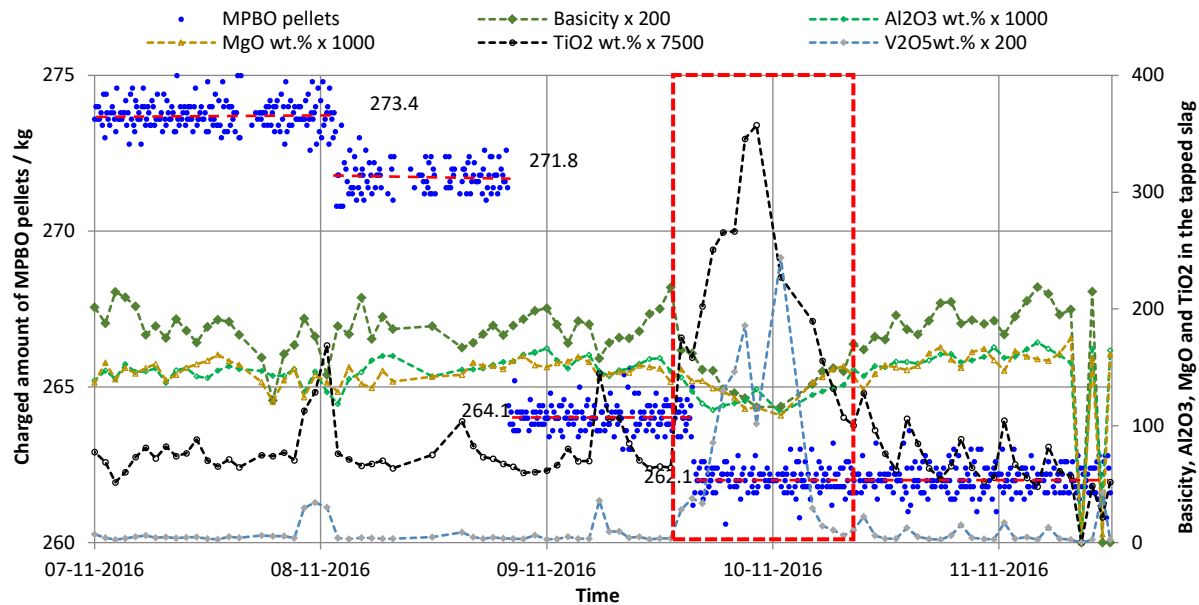


Figure 213: Variations of the slag chemical composition with the charged ferrous MPBO pellets.

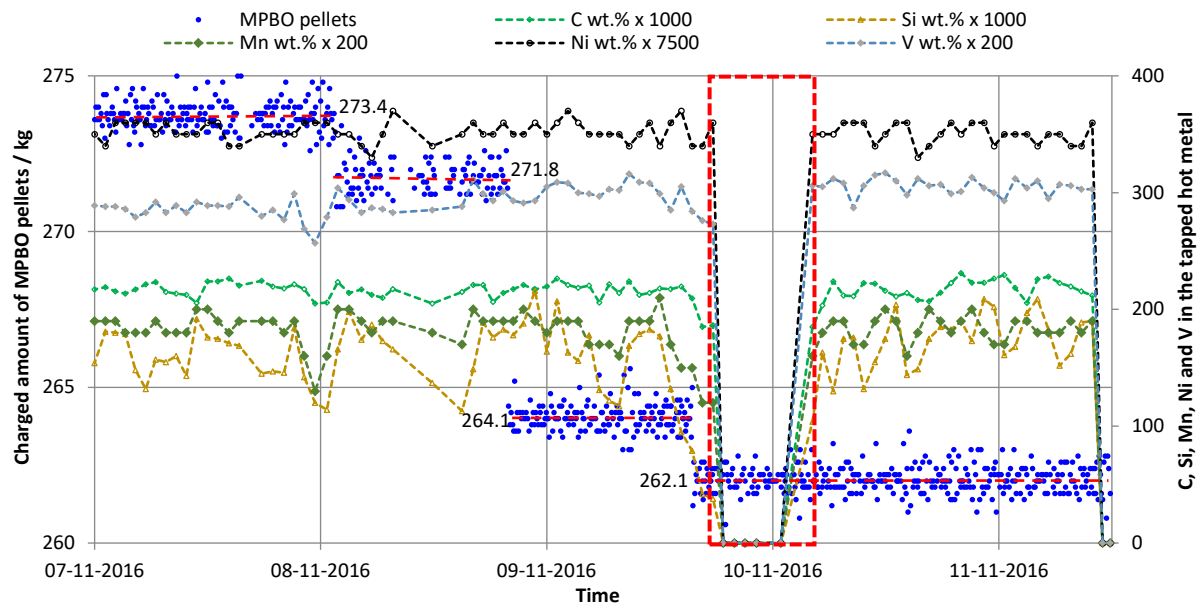


Figure 214: Variations of the hot metal chemical composition with the charged ferrous MPBO pellets.

2.2.3.3 On-line Model for Dead Man permeability and dynamics

In previous RFCS projects, an approach to estimate the dead man position and voidage was introduced [54] and further developed in [55]. On base of a force balance, comparing the buoyancy forces on the dead man at opening and closing of the taphole a formula to estimate the dead man porosity was proposed:

$$\varepsilon_{force\ balance} = \frac{t_{Sl} - t_{tap\ end}}{t_{Sl} + t_{tap\ end} + \frac{m_{HM}}{m_{Sl}} \left(t_{Sl} + t_{tap\ end} - \frac{t_{tap\ end} - end \cdot t_{Sl}}{t_{tap}} \right)} \quad (49)$$

Furthermore Brännbacka et al. [56] developed a model for BF hearth liquid levels in accordance to Nightingale et al. [57] basing on mass-balances considering the produced and tapped hot metal mass over time. They derived a formula for the slag delay during tapping, which can be transferred to calculate the dead man voidage:

$$\varepsilon_{mass\ balance} = \frac{(t_{tap} - t_{Sl\ delay}) \cdot \dot{V}_{prod} \cdot t_{tap\ end}}{t_{tap} \cdot Z_{HM/Sl} \cdot A_{hearth}} \quad (50)$$

Both approaches base on some basic assumptions, needed to eliminate unknown dead man properties and BF hearth parameters which are concluded in Table 40.

Table 40: Comparison of force- and mass-balance sub-model principles and assumption.

	Force-balance sub-model	Mass-balance sub-model
Basic principle	<ul style="list-style-type: none"> Change of buoyancy force during tapping due to change in liquid levels 	<ul style="list-style-type: none"> Balance of produced and tapped Hot Metal vs. hearth volume
Assumed DM state	<ul style="list-style-type: none"> Floating (free movement possible) Homogenous voidage 	<ul style="list-style-type: none"> Sitting (no coke free region) Homogenous voidage
Assumptions for Liquids	<ul style="list-style-type: none"> Hot metal & Slag Flat surfaces No changes in density HM/SL interface at TH level at slag start HM surface at TH level at tap-end 	<ul style="list-style-type: none"> Hot metal casting period only Flat surfaces No changes in density HM/SL interface at TH level at slag start HM surface below TH level at tap-end Constant tapping rates
Other assumptions	<ul style="list-style-type: none"> Constant taphole length and angle 	<ul style="list-style-type: none"> Constant taphole length and angle

Both voidage models suffer from unrealistic results if their basic assumptions are violated. In case of the force-balance based approach, the dead man must be able to move up or downwards. Otherwise if the dead man is statically sitting a part of the weight force of the burden column is not only compensated by the buoyancy force, as assumed in the approach, but also by a supporting force from the hearth's bottom. In this case the model shows too high voidage results. In previous works, these unrealistic high voidage values were used to indicate a sitting dead man. However, this is difficult to rate since the results show strong scattering. Even after averaging values in the range of the voidage ε between 0.35 – 0.40, a large region remains where it is unclear if a good coke quality results in high voidage or if the dead man is at least partly sitting.

In case of the mass-balance approach, the produced and tapped masses of hot metal during a tap cycle are considered. The hot metal density formula can be derived for the height of the hot metal level at tap start and slag start. The tapped hot metal mass exceeding the produced mass during the iron only flow period indicates the volume of hot metal produced during the inter-cast period. Re-arranging this formula and taking into account the hearth diameter give the dead man voidage [57] and [57]. In case of a floating dead man, additionally a coke free volume with voidage $\varepsilon = 1$ exists, which is decreased during the cast due to decreasing liquid level and buoyancy force. If such a coke free volume exists, the mass-balance based approach gives too high voidage values.

Concluding, both approaches result in too high voidage values if their assumptions concerning the dead man state is violated and vice versa. Since the assumptions are opposed, only one of the two sub-models give realistic voidage depending on the real dead man state.

$$\varepsilon = \begin{cases} \varepsilon_{\text{force balance}}; \varepsilon_{\text{mass balance}} > \varepsilon_{\text{force balance}} \\ \varepsilon_{\text{mass balance}}; \varepsilon_{\text{force balance}} > \varepsilon_{\text{mass balance}} \end{cases} \quad (51)$$

From this theory the results of both models must be negatively correlated, and the lower value gives also an indication which models assumption is currently true. The difference of both models therefore indicates the Dead Man Dynamics DMD (statically sitting or dynamically floating):

$$DMD = \varepsilon_{\text{mass balance}} - \varepsilon_{\text{force balance}} \quad (52)$$

At the start of OPTIBLAFINS, AGDH has provided historical data from the year 2011 till mid of 2015 comprising:

- tap-start, slag-start, tap-end times,
- masses of tapped hot metal and slag as well as hot metal production,
- hot metal analysis for estimation of the density,
- temperature readings of selected thermocouples to evaluate the DMD results

For first offline calculations of the dead man voidage and dynamics following the approach described above. The results are shown in Figure 215. Each of the small light and dark blue dots in Figure 215 represent the model results for one tap. For the single taps, the voidage results strongly vary due to the simplifying assumption of the two sub-models and due to measuring inaccuracies. In offline application a centered-moving-average filter can be applied to remove this variance. The

smoothed results for the two sub-models are shown as light blue line (force balance sub-model) and dark blue line (mass-balance sub-model).

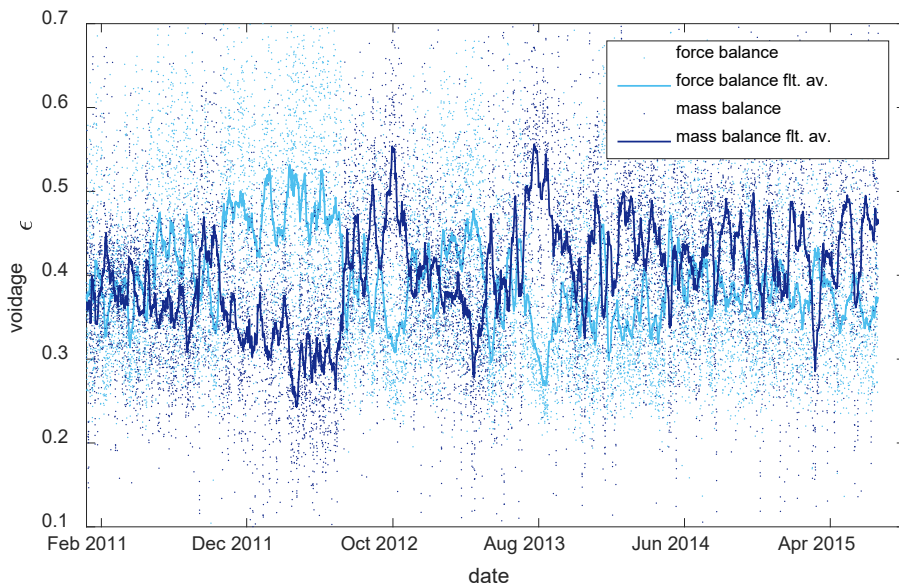


Figure 215: DM voidage calculated by force- and mass-balance sub-models.

Both sub-models deliver voidage results in an expected range. Following the concept of the DMD approach and using the lower value of both sub-models as the realistic voidage, from 2011 to 2015 the dead man voidage at AGDH varied between 0.25 and 0.40 with the mean value around 0.35. These results are consistent with values known from literature. There are periods where the force balance sub-model generates lower results and periods where the mass-balance sub-model gives lower results which indicate changing dead man conditions during the 4-year period with static as well as dynamic periods. As expected from the opposing base sub-model assumption on the dead man position, both sub-model results in Figure 215 show mostly a strong negative correlation, which is presented in detail in Figure 216.

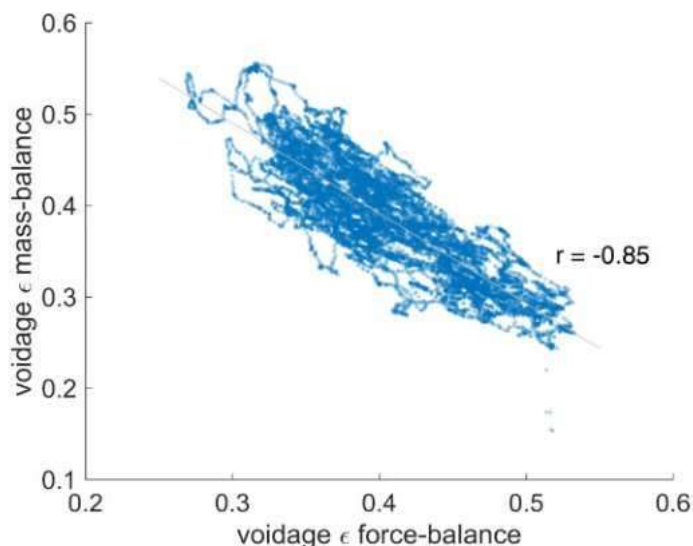


Figure 216: Correlation between force- and mass-balance sub-model results.

The correlation coefficient between both sub-models is $r = -0.85$. This negative correlation gave confirmation that the assumptions used to develop the combined approach as well as the results are realistic.

As next step, the model was implemented on-line on BF4 at Dillinger and on BF5 at AMEH. BFI implemented the model code in MATLAB and installed a compiled model version at the sites. Virtual servers for the on-line model and VPN connections were set up by Dillinger and AMEH. Both industrial partners set up an Oracle-SQL database as data supplier for the models developed by BFI. The database receives data from level 1 and 2 control systems. Continuous operating data like temperatures are stored as minute-averages, tap related data like durations and hot metal properties are stored tap-wise.

A centered-moving-averaging of the single tap results as described in Figure 215 is not possible for the on-line application since the "future" values are unknown. As an averaging based on already

computed values introduces a delay depending on the size of the averaging window, a new kernel-based algorithm for smoothing was developed. This new smoothing kernel weighs new values by considering how good they fit to the past values of the previous taps. Furthermore, newer data points receive a higher weight than older data points.

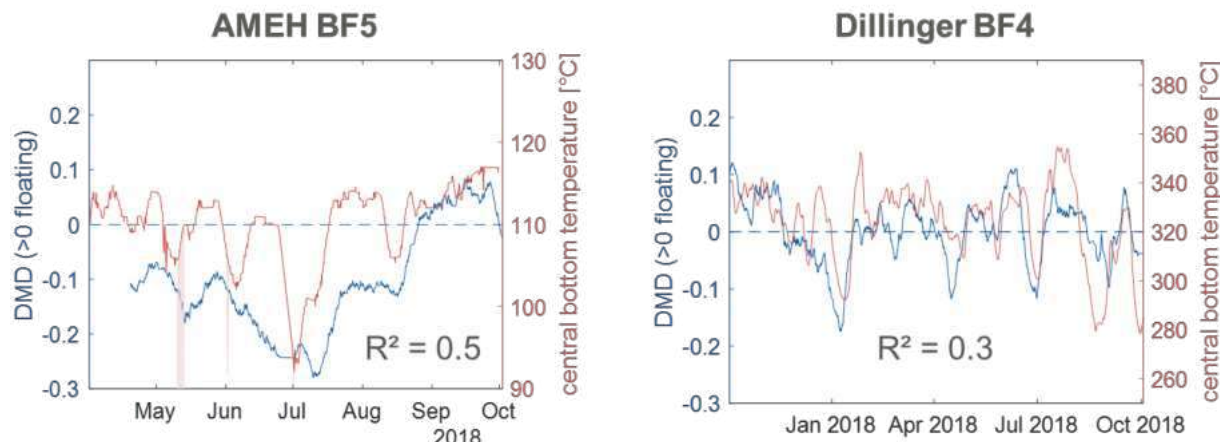


Figure 217: Results of the on-line implementation of DMD at AMEH (left) and Dillinger (right).

The DMD on-line modelling results received for AMEH BF5 and Dillinger BF4 are given in Figure 217.

To evaluate the DMD model results, the data from the central thermocouple in the hearth bottom are used for both BFs. It is assumed that the measured temperature at hearth bottom center is higher for a dynamic dead man than for a static dead man. Of course, besides the dead man state also other effects like salamander build up, hot metal temperature, etc. influence the hearth bottom temperature. That is why, the central bottom temperature is not a reliable dead man state indicator on its own – but it is the best possible measured parameter for model evaluation as it is not used for calculation of the DMD model.

DMD values >0 indicate a dynamic (floating) dead man since dead man is ascending and descending with liquid levels during tap-cycles. DMD values < 0 indicate a static, constantly sitting dead man. For both BFs dynamic and static phases can be observed. For AMEH BF5 the static state seems to dominate whereas Dillinger BF4 shows regular changes between static and dynamic behavior. Strong changes in DMD value are always also accompanied by strong changes of the bottom hearth temperature. Concluding for both on-line implementations the DMD model show a good correlation to the bottom temperatures which confirms the model results.

The MATLAB implementation of the model has its own graphical user interface (GUI) shown in Figure 218 on left side at the server where the model is running. The MATLAB code does not only visualize the modelling results but also stores the computed data in a ".json" file format. For remote access BFI also developed a JavaScript based GUI which reads this data and can show it in a standard browser. That way the DMD results can be visualized on each device (PC or mobile) connected via the sites network to the server. Both GUIs are shown in Figure 218.

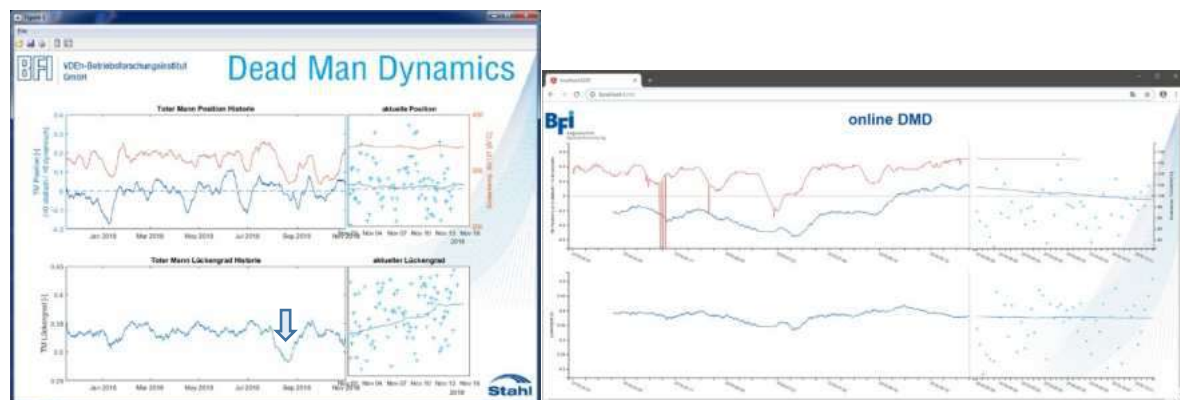


Figure 218: GUI of the MATLAB based model (left) and browser GUI (right).

The GUIs in Figure 218 supply an overview of the calculated dead man voidage of the last half year (lower left of sub-figures) and a detailed view of the voidage model results of the last two weeks (lower right of sub-figures). In the detailed view, not only the filtered results but also the data for

each individual tap are shown (small crosses). The upper sub-figures show the dead man state history (left side of sub-figures) and detailed actual values (right side of sub-figures). For direct evaluation of the reliability of the results together with the DMD values, the central bottom temperature is displayed as red line.

The screenshot of the MATLAB GUI in Figure 218 on the left side also gives an impression of the capability of the dead man voidage model. At the end of August (marked as small blue arrow in Figure 218), a greater mass of fine-grained carbon carrier was accidentally charged to BF4. In the DMD voidage model this resulted in an instant strong decrease of the computed voidage. It took roughly a week after this incident to recover the dead man voidage to a normal level - even though the dead man state was dynamic at the beginning of this event. Concluding, the DMD model provides a realistic contribution for the operators to monitor the dead man voidage. Also, in cases where the reason of a bad dead man state is not that obvious like in the extreme incident above, operators receive a reliable information about the reasons of possible tapping / drainage problems. This helps to decide about tailor made measures, e.g. increasing center coke charging / center coke quality, to recover the dead man. Besides the application of the DMD in this project at AMEH and Dillinger, the model is also installed outside the OPTIBLAFINS project at BF's of Salzgitter Flachstahl. There the model results are used by the Engineers as one source of information to decide about daily BF hearth operation.

To explore further potential to implement the DMD results into daily operational praxis, correlation analysis of the dead man dynamic results with operational BF data was executed. 20 data series suspected to be influenced by the dead man state, including hot blast data, permeability data, reducing agent and burden supply as well as hot metal and slag production and properties were examined. For the correlation analysis, only data from normal operation without BF downtimes was used, outliers were removed, and the data was smoothed by a moving 7-day average (aiming on long term correlations) to adapt it to the comparable slow dynamics of changes in the dead man state. During this overview analyses, a slight correlation between DMD and hot blast Volume and permeability could be found (Figure 219).

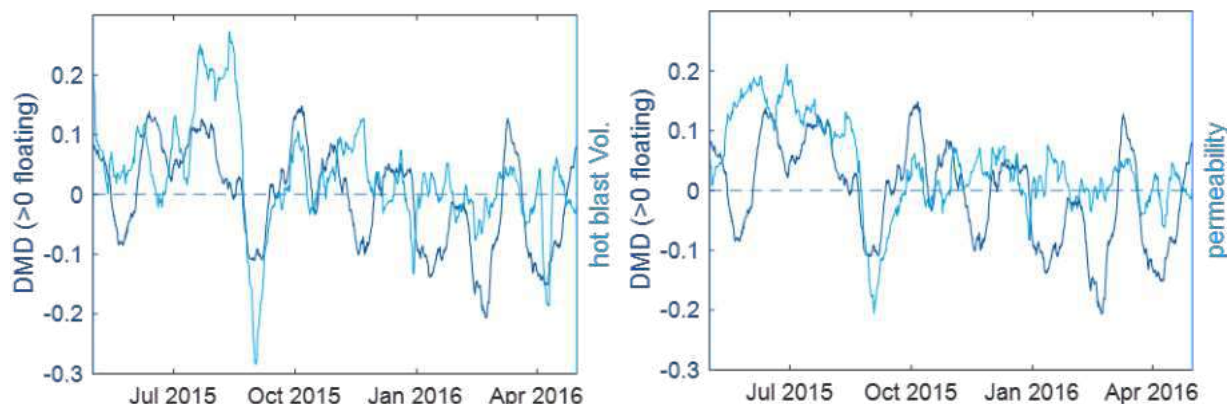


Figure 219: Long time similarities between DMD and weekly averaged hot blast data.

As hot blast volume and pressure loss of the gas during passage through the burden column introduce a vertical, upright oriented force on the dead man, a correlation between hot blast data and DMD in general is plausible. However, it is also clear that the flow conditions above the tuyeres (e.g. cohesive zone state, stack conditions) will mainly dominate blast volume and permeability. Thus, it was expected that just a minor correlation to the hearth state would be found. More detailed correlations and the potential to exploit this relation in operational hearth management will be investigated in a follow up project.

2.2.3.4 Dynamic Coke Properties

In a previous project [104], a test apparatus and procedure were developed in order to determine the evolution of coke size distribution under mechanical, chemical and thermal stresses prevailing in the blast furnace (Figure 220).

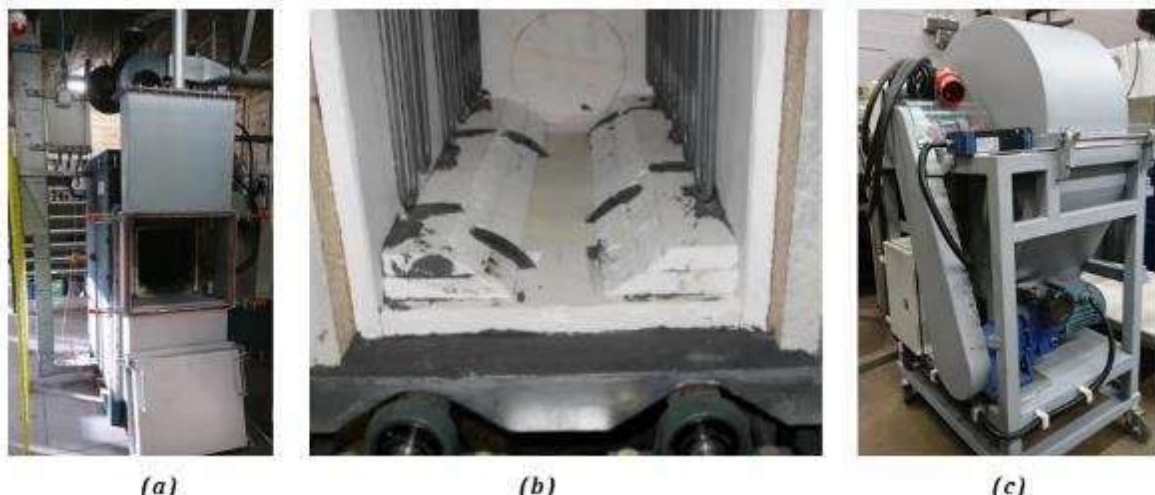


Figure 220: General view (a) and inside (b), without the SiC drum, of the electric furnace and of the mini-Micum drum (c).

The Cokarac facility has been fully revamped during 2017. Several improvements were made in the frame of the “Reverse Metallurgy” (project funded by the Wallonia region) such as a complete redesign of the main aperture of the furnace. Efforts have been made to particularly increase the tightness of the facility. Another important facility used during the Cokarac trials is the mini-Micum drum. Its purpose is to measure the coke degradation by performing several revolutions using the Micum procedure.

2.2.3.4.1 Gasification trials

According to the technical annex of the project, CRM is in charge of performing several tests based on the standard coke characterisation trial described in the previous RFCS DEMPOLIFE project. Test variables that are aimed to be studied are the gasification degree, the heating time and the rotating speeds.

Initially, 21 tests had to be performed: 3 for the reference case and 6 per parameter (Table 41).

Table 41: Initial experimental plan of the coke gasification trials.

Comments	Trial #	Heating phase						Gasification phase						Overheating phase						Cooling phase						
		Temperature		Duration		Flow rate (N2)		Drum rotation		Temperature		Duration		Flow rate (CO2)		Drum rotation		Temperature		Duration		Flow rate (N2)		Drum rotation		
		(°C)	(min)	(Nm³/h)	(rev)	(rev/min)	(min)	(Nm³/h)	(°C)	(min)	(Nm³/h)	(rev)	(rev/min)	(°C)	(min)	(Nm³/h)	(rev)	(rev/min)	(°C)	(min)	(Nm³/h)	(rev)	(rev/min)	(°C)	(min)	
Old ref. case	0	1200	225	0.9	500	2.083333	15	1.5	1200	165	2	500	3.030303	1500	180	0.9	500	2.777778	300	240	1.2	400	1.666667			
Reference case for repeatability	1																									
	2	1200	225	0.9	504	2.1	15	1.5	1200	165	2	495	3	1500	180	0.9	504	2.8	300	240	1.2	408	1.7			
	3																									
	4	1200	225	0.9	504	2.1	15	1.5	1200	90	2	270	3	1500	180	0.9	504	2.8	300	240	1.2	408	1.7			
	5	1200	225	0.9	504	2.1	15	1.5	1200	120	2	360	3	1500	180	0.9	504	2.8	300	240	1.2	408	1.7			
	6	1200	225	0.9	504	2.1	15	1.5	1200	150	2	450	3	1500	180	0.9	504	2.8	300	240	1.2	408	1.7			
	7	1200	225	0.9	504	2.1	15	1.5	1200	180	2	540	3	1500	180	0.9	504	2.8	300	240	1.2	408	1.7			
	8	1200	225	0.9	504	2.1	15	1.5	1200	210	2	630	3	1500	180	0.9	504	2.8	300	240	1.2	408	1.7			
	9	1200	225	0.9	504	2.1	15	1.5	1200	240	2	720	3	1500	180	0.9	504	2.8	300	240	1.2	408	1.7			
Gasification degree	10	1200	225	0.9	504	2.1	15	1.5	1200	165	2	495	3	1500	90	0.9	252	2.8	300	240	1.2	408	1.7			
	11	1200	225	0.9	504	2.1	15	1.5	1200	165	2	495	3	1500	120	0.9	336	2.8	300	240	1.2	408	1.7			
	12	1200	225	0.9	504	2.1	15	1.5	1200	165	2	495	3	1500	150	0.9	420	2.8	300	240	1.2	408	1.7			
	13	1200	225	0.9	504	2.1	15	1.5	1200	165	2	495	3	1500	210	0.9	588	2.8	300	240	1.2	408	1.7			
	14	1200	225	0.9	504	2.1	15	1.5	1200	165	2	495	3	1500	240	0.9	672	2.8	300	240	1.2	408	1.7			
	15	1200	225	0.9	504	2.1	15	1.5	1200	165	2	495	3	1500	270	0.9	756	2.8	300	240	1.2	408	1.7			
Heating time	16	1200	225	0.9	352.8	1.47	15	1.5	1200	165	2	346.5	2.1	1500	180	0.9	352.8	1.96	300	240	1.2	285.6	1.19			
	17	1200	225	0.9	403.2	1.68	15	1.5	1200	165	2	396	2.4	1500	180	0.9	403.2	2.24	300	240	1.2	326.4	1.36			
	18	1200	225	0.9	453.6	1.89	15	1.5	1200	165	2	445.5	2.7	1500	180	0.9	453.6	2.52	300	240	1.2	367.2	1.53			
	19	1200	225	0.9	554.4	2.31	15	1.5	1200	165	2	544.5	3.3	1500	180	0.9	554.4	3.08	300	240	1.2	448.8	1.87			
	20	1200	225	0.9	604.8	2.52	15	1.5	1200	165	2	594	3.6	1500	180	0.9	604.8	3.36	300	240	1.2	489.6	2.04			
	21	1200	225	0.9	655.2	2.73	15	1.5	1200	165	2	643.5	3.9	1500	180	0.9	655.2	3.64	300	240	1.2	530.4	2.21			

During Q1 2018, a first gasification trial was performed (Figure 221), while still encountering some issues:

- Two thermocouples were malfunctioning and were replaced.
- The gas lance at the rear of the furnace has been damaged by the particles. A new lance has been designed and shortened in order to reduce the probability of future failure.
- Refractories were badly damaged supposedly during the trial. Because the heating was tedious during the overheating phase (>1200°C) heat leaks are suspected due to those

refractory failures. The refractory replacement is a huge investment in terms of time and budget because of the complex architecture of the furnace.

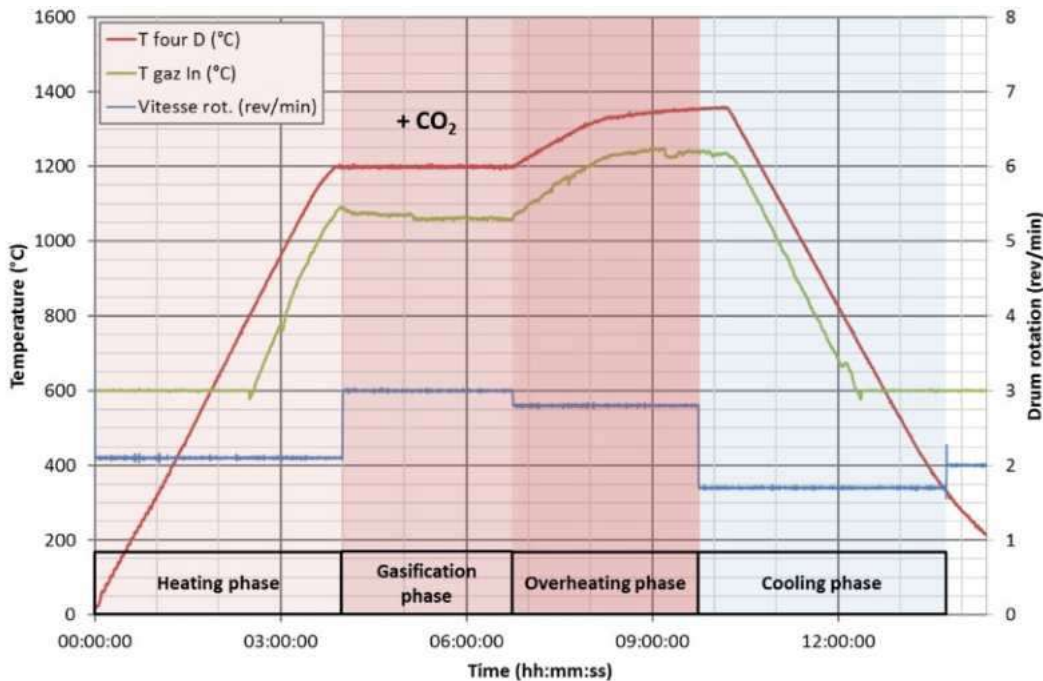


Figure 221: First Cokarac trial (standard).

Due to those several outages during the revamping and after the first trial, it was impossible to perform additional tests in due time. According to past [104], the gasification degree is the parameter with the most important influence on the coke behaviour (Figure 222). Gasification degree is a direct function of heating time.

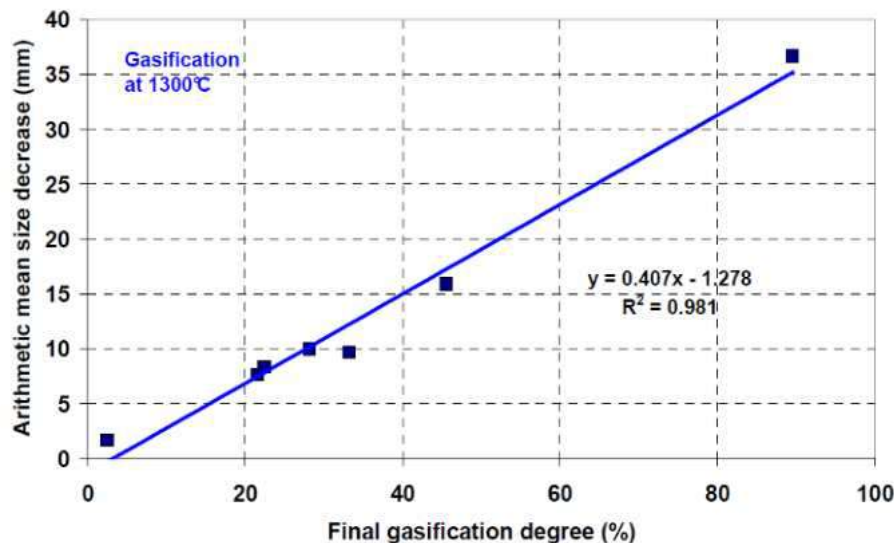


Figure 222: Influence of the gasification degree on the size change in the CRM Cokarac test [104].

However, the impact of the overheating temperature is not as impactful as expected, Figure 223. Even if the gasification rate is increased with a higher oven temperature, the fact that the reaction is very endothermic limits the increase of temperature inside the coke sample.

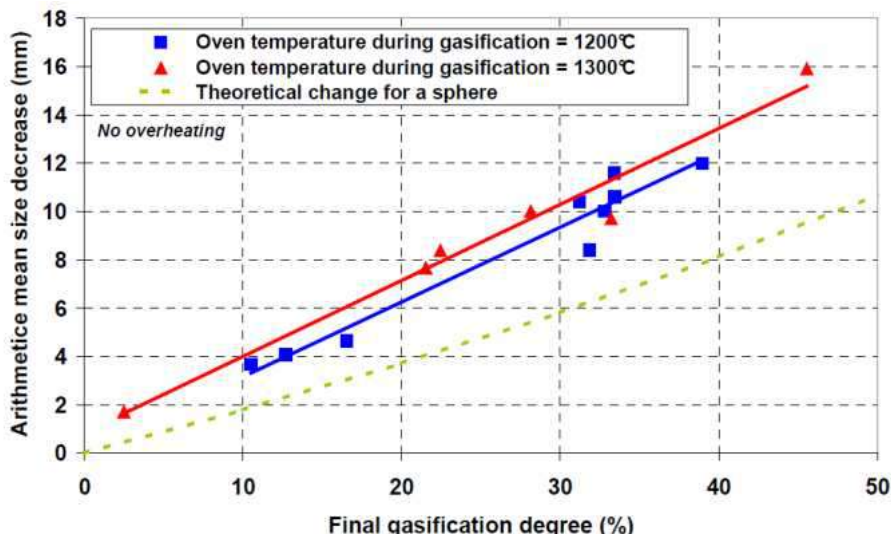


Figure 223: Influence of temperature and gasification degree on the change in size during the CRM Cokarac test [104].

Finally, the time to overheat until 1500°C showed a minor impact on the coke degradation.

2.2.3.4.2 Coke dissolution during its interaction with the molten phases

Once the coke had undergone the gasification procedure, it has been set in contact with slag and hot metal to simulate its degradation in the lower part of the blast furnace. The samples have been rotated in an induction furnace to characterise the effect of the liquid flows on the coke mass loss. The chosen design used for the trials is presented at Figure 224.

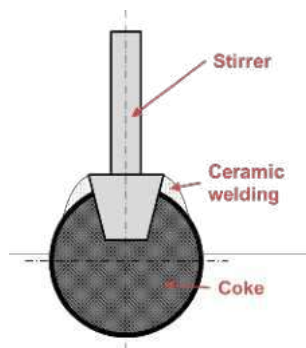


Figure 224: Design of the apparatus used for the dissolution trials.

The design needed to consider several aspects of the trial such as a very high temperature, a chemical degradation due to slag, the floatability of coke inside slag and the ability to retrieve the samples easily after the different dive tests.

The first trial consisted in testing the interaction between coke and hot metal. Three coke samples were put inside the hot metal at approximately 1350°C. Stirrers could handle the trial during a bit more than one minute before melting. An optical measurement of the maximum length of each sample is given at Table 42. No degradation has been fully confirmed but the time before failure was very short and might be not enough to observe any degradation by hot metal by itself. However, those samples presented a slight brown/red coloration in the surface. We suspect that hot metal is either deposited or diffuses into the coke particle.

Table 42: Measured maximum length of each sample before and after dissolution trial in hot metal.

	Length before trial (mm)	Length after trial (mm)
Sample I	76.5	78.9
Sample II	59.1	63.4
Sample III	57.4	56.9

The second trial was performed with a full bath of both hot metal and slag which was heated until 1470°C (hot metal temperature) because the slag was not enough melted to dive anything at a

lower temperature in an open furnace like the this one. In this case we could perform longer tests (close to 2-3 minutes each) because the stirrer wasn't damaged maybe due to the fact that slag was at a highly lower temperature.

In this case, three samples have been dived inside the bath at three different heights, Figure 225. From left to right, samples have been dived at the interface, almost completely inside the hot metal and then only in the slag.



Figure 225: Coke samples used for the second dissolution trial.

The first observation is that the slag is very viscous and tends to agglomerate to the coke samples. During cooling it is becoming very fragile and breaks easily. This way we could investigate the impact of both liquids to the coke sample (Figure 226).



Figure 226: Observation of the coke sample dived into both liquids during the second dissolution trial.

The interface is very clear on this sample and the portion dived into the slag is barely modified. However, observations made during the first trial are confirmed: the hot metal is deposited at the surface of the coke sample and might be diffused inside. An optical measurement of a reference length has been performed on that sample and an increase of that length of more than 5mm has been highlighted.

2.2.3.5 Laboratory studies on slag and its properties

The samples used in this task study include the coke/slag samples from the hearth of the EBF (both campaign 31 and 32), the final tapped slag samples from the EBF (both campaign 31 and 32) and the collected industrial slag samples from Tata Steel and voestalpine. Descriptions of the sampling procedures and positions for the EBF samples can be found in Task 3.1.

2.2.3.5.1 Chemical analysis and XRD analysis of the slag

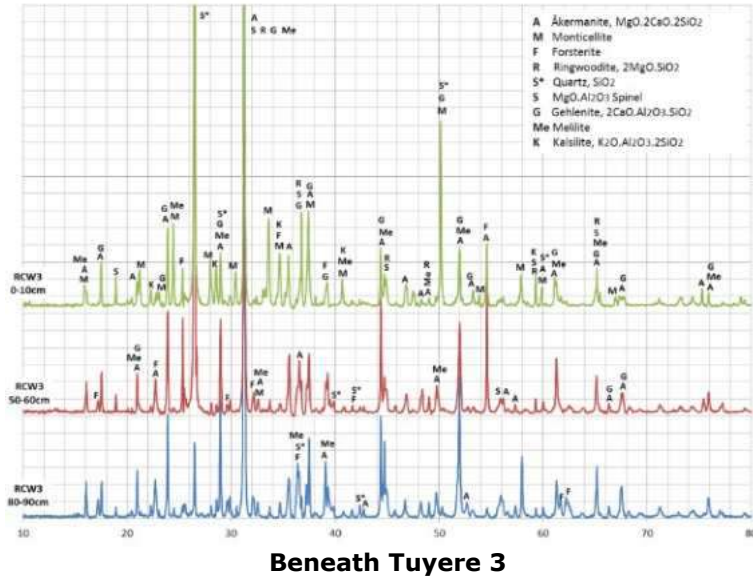
2.2.3.5.1.1 Analysis of the slag samples from EBF campaign 31

The chemical compositions of slag samples procured from the hearth of EBF campaign 31 are shown in Table 43. The positions of these slag samples as well as their coupled coke samples were shown earlier in Figure 188. The four main components of in the slag are CaO, SiO₂, MgO and Al₂O₃. Minor elements in the slag samples such as MnO, alkali, V-oxide and Ti-oxide can be seen as well. The main differences among these samples are given in the last column of Table 43.

Table 43: Chemical compositions of the slag samples procured from the hearth of EBF, campaign 31.

Drilled core	Depth, cm	Fe%	CaO%	SiO ₂ %	MgO%	Al ₂ O ₃ %	Bas. B2	Bas. B4	Remarks
RCW 3	0-10	1.26	31.8	33.2	14.6	19.1	0.96	0.89	Low SiO ₂
	50-60	0.85	30.0	35.2	15.5	18.4	0.85	0.85	High Al ₂ O ₃
	80-90	1.63	29.5	36.3	16.8	15.8	0.81	0.89	High Fe
Centre	0-10	0.33	29.6	35.8	20.9	13.4	0.83	1.03	High MgO
	50-60	0.54	30.1	35.3	18.9	15.2	0.85	0.97	Medium basicity
	90-100	0.80	29.9	37.5	17.6	14.2	0.80	0.92	High SiO ₂
Taphole	50-60	0.68	29.6	36.1	18.3	15.3	0.82	0.93	Medium basicity
	90-100	0.66	25.0	45.0	15.8	13.6	0.56	0.70	High SiO ₂ , low bas.

Figure 227 shows the XRD analysis results of the slag samples presented in Table 43. The key phases present in these slag samples are identified to be åkermanite, monticellite and melilite. Two intense peaks can be seen: the first one at $2\theta = 26.5^\circ$ belongs to quartz and the second intense peak at $2\theta = 31.5^\circ$ belongs to åkermanite. The intensity of silica peak ($2\theta = 26.5^\circ$) decreased towards the bottom of the EBF hearth. The XRD diffraction spectra of the taphole bottom sample show the presence of diopside phase ($5\text{CaO} \cdot 7\text{MgO} \cdot 6\text{Al}_2\text{O}_3 \cdot 5/\text{SiO}_2$).



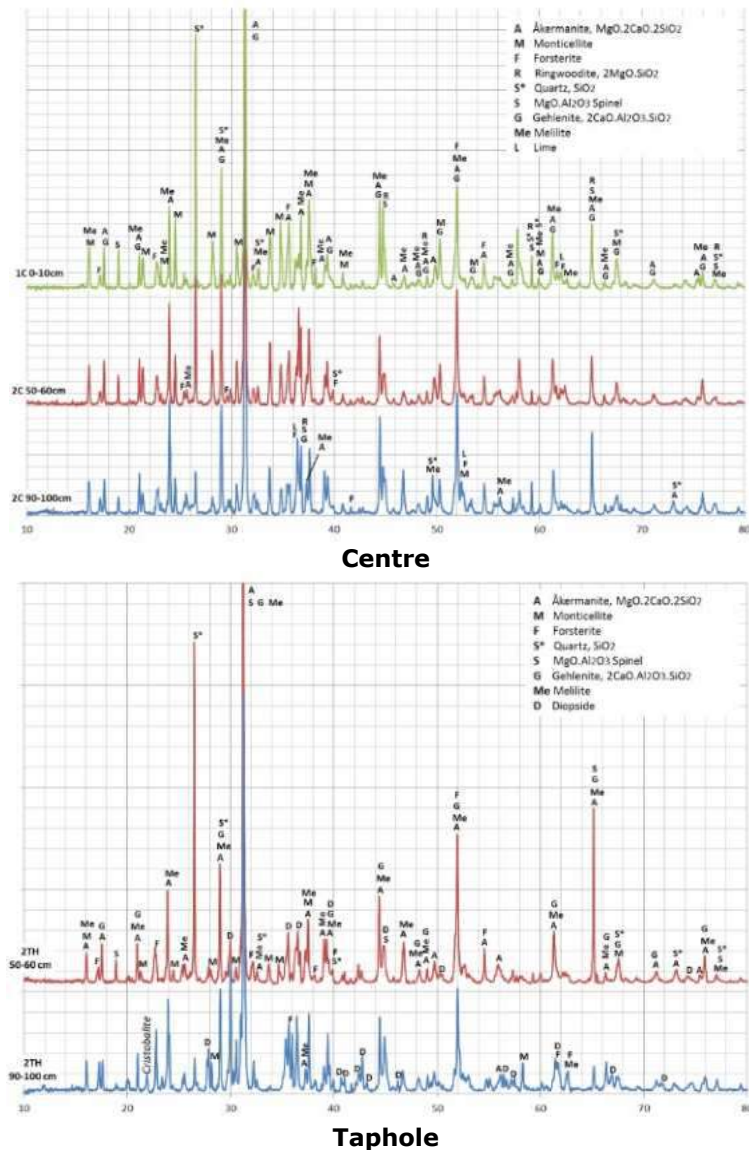


Figure 227: XRD diffraction spectra of slag samples procured from various positions of the EBF hearth, campaign 31.

Besides the samples procured from the hearth of the EBF, 7 samples with different chemical compositions were selected from the final tapped slag. The differences are mainly attributed to the change of the burden materials and/or process parameters during the EBF trial. The differences in chemical compositions will help to understand how the changes of chemical compositions influence the viscosity and wettability of the slag. These slag samples were also analysed by XRD. However, no phases can be identified, as the slag seems to be amorphous, probably, due to the fast quenching of the slag during tapping.

Table 44: Chemical compositions of the final tapped slag samples from EBF, campaign 31.

ID	*Fe %	*CaO %	*SiO ₂ %	*MnO %	*S%	*Al ₂ O ₃ %	*MgO %	Na ₂ O %	K ₂ O %	V ₂ O ₅ %	*TiO ₂ %	B2	Remark
FS1	0.47	31.53	34.51	0.18	1.32	14.53	14.82	0.55	0.67	0.05	1.37	0.91	Ref. average value
FS2	0.53	32.94	30.59	0.08	1.73	18.34	14.81	0.25	0.14	0.02	0.58	1.08	High B2 and high Al ₂ O ₃
FS3	0.45	30.61	31.87	0.17	1.56	19.01	14.73	0.41	0.28	0.04	0.87	0.96	High Al ₂ O ₃
FS4	0.17	36.38	28.62	0.09	1.96	15.29	15.57	0.46	0.46	0.02	0.97	1.27	High B2
FS5	0.61	32.29	32.57	0.11	1.73	15.30	15.97	0.34	0.26	0.02	0.79	0.99	High MnO
FS6	1.66	25.92	40.75	0.74	0.49	12.58	12.67	0.62	0.92	0.58	3.03	0.64	High MnO
FS7	0.87	24.83	42.37	0.34	0.82	14.98	11.15	1.17	1.36	0.21	1.87	0.59	Low B2

2.2.3.5.1.2 Analysis of the slag samples from EBF campaign 32 and industrial slag

After EBF campaign 32, more core drilling samples (slag, coke and metal) were taken. The chemical compositions of the slag samples procured from the hearth of EBF campaign 32 are shown in Table 45.

In the previous EBF campaigns, it was found that alkali (Na_2O and K_2O) were concentrated at certain areas of the EBF hearth, especially the area with lower temperature. To understand the hearth conditions before the quenching of the EBF, the alkali contents in the slag samples were mapped and shown in

Figure 228. It is seen that there is an area (marked with red dot line) around the wall, where the alkali was concentrated. From the visual observation of the core drilling (shown earlier in Figure 190), it was also found that the core drilling was hindered at the same area as that marked in Figure 228. This may indicate that the marked cold area formed before the quenching of the EBF. Similarly, the Fe contents and TiO_2 contents in the slag samples from the second core drilling layer was also mapped, as shown in Figure 229. It can be seen that Fe and TiO_2 were concentrated at approximately the same area as alkali. These results are consistent with the SEM analysis of the manual samples, which were procured from the solidified shell of the EBF hearth.

Table 45: Chemical compositions of the slag samples procured from the hearth of EBF, campaign 32.

ID	*Fe%	*CaO%	*SiO ₂ %	*MnO%	*S%	*Al ₂ O ₃ %	*MgO%	Na ₂ O %	K ₂ O%	V ₂ O ₅ %	*TiO ₂ %	B2
M101	9.64	32.19	24.16	0.05	1.48	11.59	13.11	0.02	0.01	0.10	0.37	1.33
M102	22.89	21.48	21.60	0.12	1.06	8.86	11.22	0.03	0.02	0.25	1.35	0.99
M103	42.95	9.43	11.77	0.37	0.34	4.38	3.44	0.02	0.02	0.98	4.13	0.80
M104	14.55	17.82	20.19	0.15	0.90	20.67	16.45	0.07	0.04	0.38	1.65	0.88
M105	7.58	31.51	21.87	0.05	1.59	17.86	10.09	0.03	0.03	0.59	2.48	1.44
M106	28.06	16.04	20.36	0.21	0.69	6.44	9.86	0.10	0.16	0.47	3.10	0.79
M107	18.89	23.35	20.47	0.19	0.97	12.12	8.37	0.01	0.02	0.65	3.59	1.14
M201	1.29	34.49	27.69	0.03	1.66	16.19	14.53	0.02	0.00	0.02	0.41	1.25
M202	4.53	21.61	45.78	0.07	0.95	13.32	9.24	0.11	0.28	0.09	1.30	0.47
M203	16.20	12.78	15.26	0.18	0.59	6.25	5.52	0.10	0.44	1.63	26.45	0.84
M204	18.61	15.88	18.69	0.19	0.93	10.48	8.88	0.11	0.52	0.63	12.54	0.85
M205	17.12	21.74	25.55	0.16	1.15	9.67	8.74	0.18	0.73	0.39	4.96	0.85
M206	6.90	27.86	29.69	0.06	1.38	12.09	15.23	0.05	0.04	0.11	1.27	0.94
M207	3.69	30.65	28.69	0.05	1.48	16.20	12.96	0.04	0.05	0.14	1.80	1.07
M208	9.64	31.65	24.15	0.05	1.57	14.11	11.33	0.08	0.01	0.08	0.41	1.31
M209	42.27	12.08	13.13	0.16	0.60	5.08	5.07	0.07	0.05	0.27	0.43	0.92
M210	1.11	31.82	31.93	0.04	1.42	15.57	14.19	0.13	0.05	0.05	0.82	1.00
M211	3.75	31.16	27.91	0.61	1.55	14.98	14.85	0.11	0.01	0.04	0.49	1.12
M212	5.07	31.79	27.05	0.04	1.52	15.68	13.15	0.11	0.02	0.05	0.44	1.18
M213	1.08	33.59	29.12	0.03	1.62	14.95	15.44	0.10	0.01	0.03	0.55	1.15
M214	2.45	29.09	30.32	0.06	1.44	13.87	14.87	0.12	0.06	0.35	3.30	0.96
M215	11.23	25.80	27.13	0.10	1.21	12.27	12.23	0.10	0.04	0.26	2.15	0.95
M216	45.69	8.12	12.82	0.21	0.37	3.83	3.76	0.10	0.14	0.43	2.66	0.63
M217	33.64	8.54	12.51	0.23	0.35	3.91	3.95	0.08	0.22	1.13	15.26	0.68
M218	27.09	10.62	13.56	0.24	0.47	4.70	4.76	0.10	0.42	1.29	19.19	0.78
M219	52.61	6.94	7.59	0.15	0.31	2.45	2.39	0.07	0.21	0.55	2.82	0.92
M220	29.19	18.48	19.03	0.12	0.55	8.39	6.62	0.15	0.34	0.43	2.35	0.97
M221	20.11	23.89	24.30	0.13	0.64	11.07	8.31	0.23	0.72	0.30	1.46	0.98

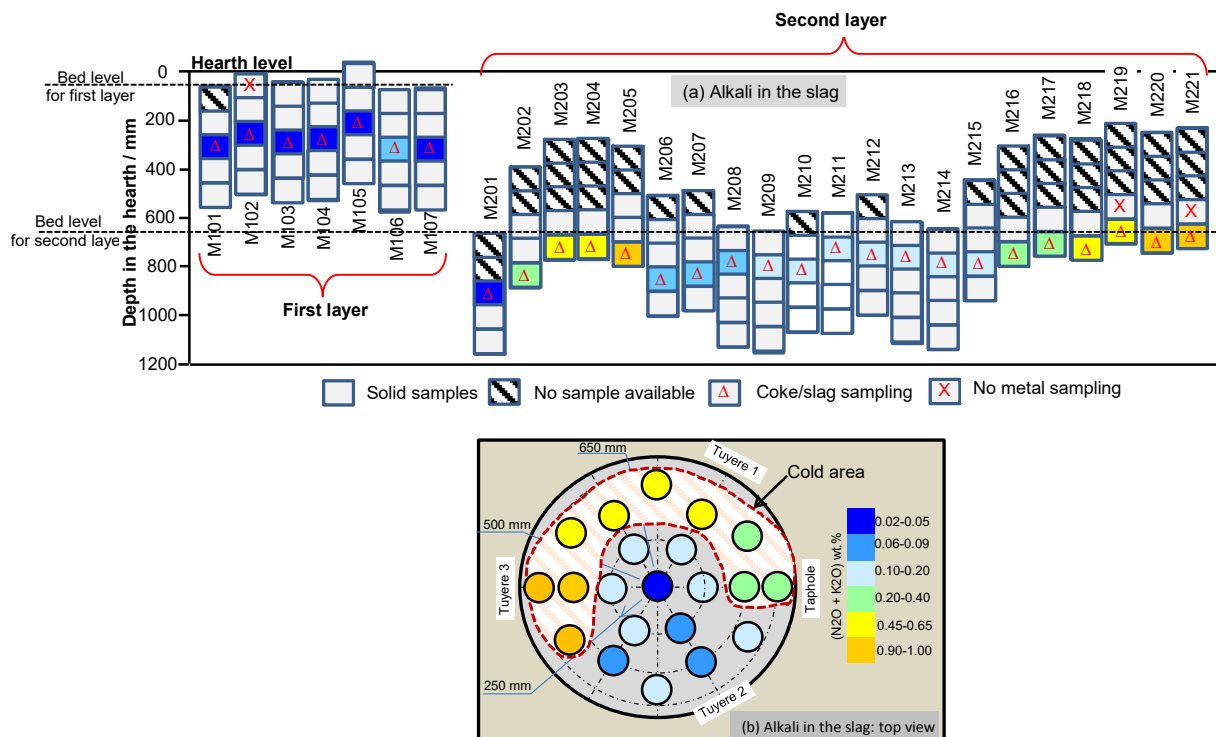


Figure 228: Alkali contents in the slag samples procured from the hearth of the EBF, campaign 32: (a) side view; (b) top view.

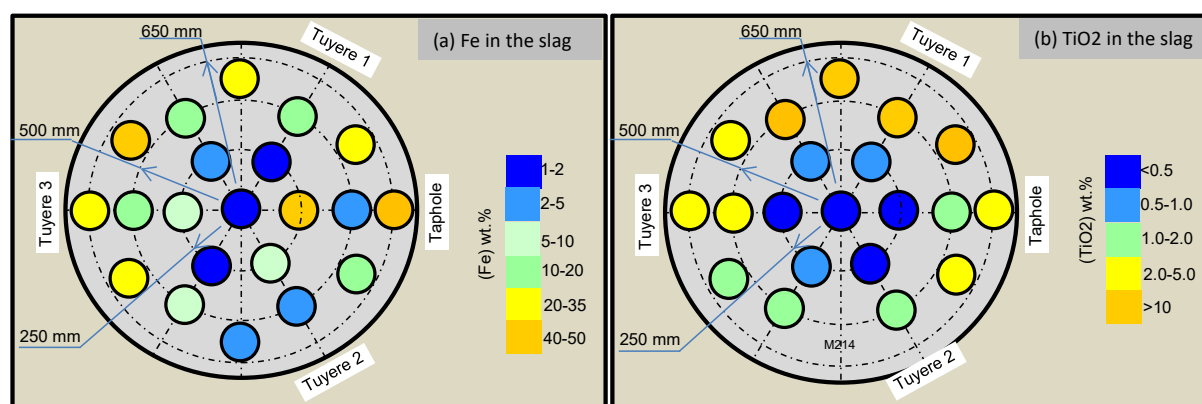


Figure 229: Fe and TiO₂ contents in the slag samples procured from second core drilling layer of the EBF hearth, campaign 32.

Figure 230 and Figure 231 show the XRD analysis results of the selected slag samples from the hearth of the EBF (campaign 32). The dominating phases in the slag samples are minerals of CaO-MgO-SiO₂-Al₂O₃, which are similar as those found in the slag samples from EBF campaign 31 (as shown in Figure 227). However, Ti-containing compounds, Fe and FeO can also be identified in the samples, which have high SiO₂ contents and high Fe contents. In sample M202, a silica (cristobalite) peak was also observed and by referring to the chemical composition of this sample, it is believed that the silica was from the taphole clay, as sample M202 was taken quite close to the taphole.

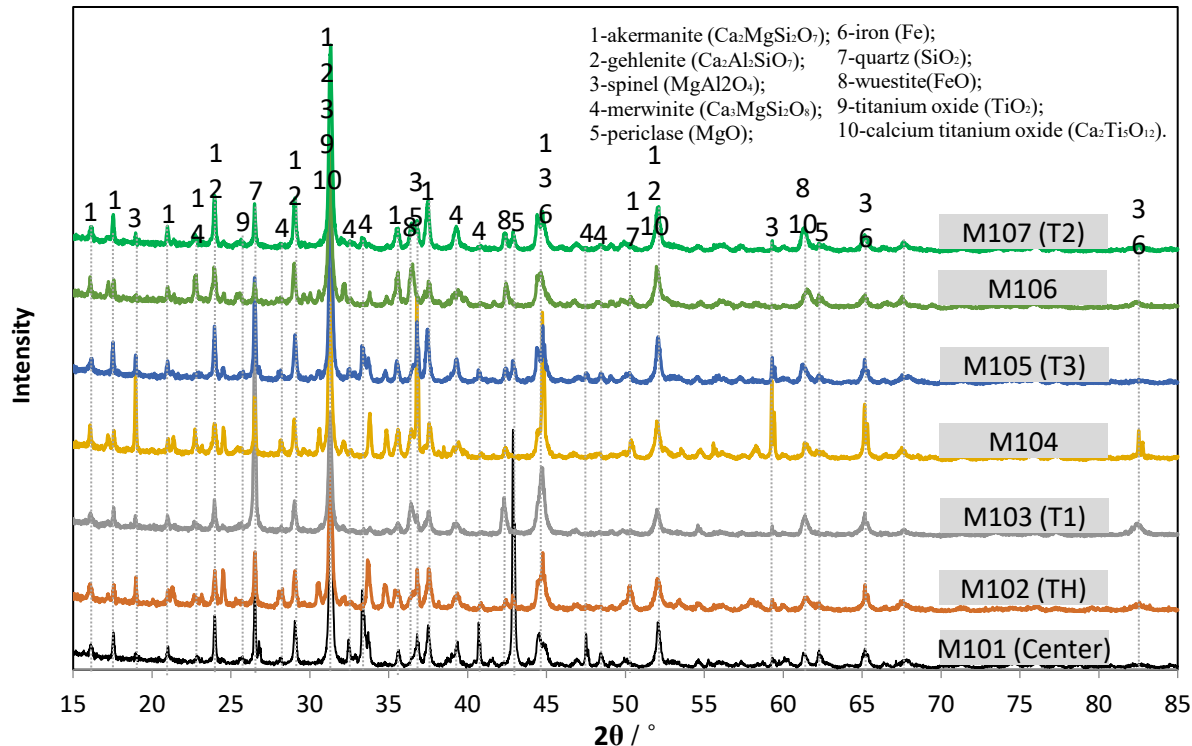


Figure 230: XRD analysis of the selected slag samples procured from first core drilling layer of the EBF hearth, campaign 32.

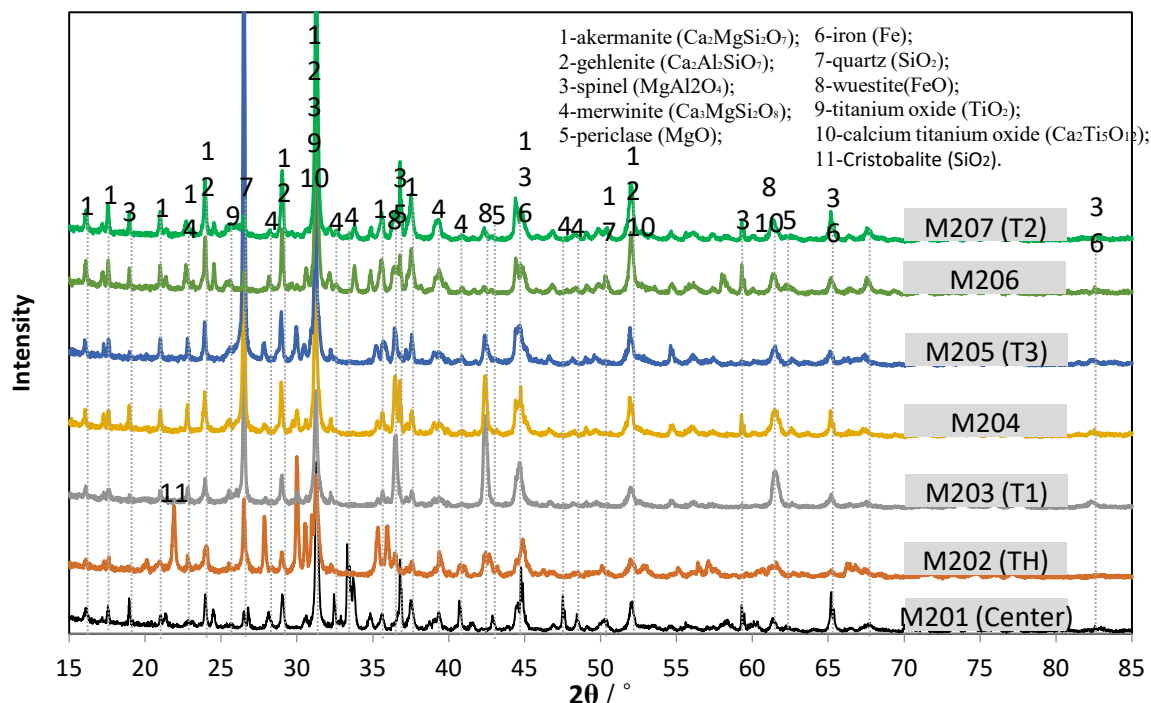


Figure 231: XRD analysis of the selected slag samples procured from second core drilling layer of the EBF hearth, campaign 32.

Besides the samples procured from the hearth of the EBF, 13 slag samples were also selected from the final tapped slag and 3 slag samples were taken from the industrial BF (2 from Tata Steel and 1 from voestalpine). The chemical analysis results for these samples are shown in Table 46. Compared with the slag samples from the hearth of the EBF, the slag samples taken from EBF final tapped slag and industrial BFs have quite low content of Fe and the contents of alkali and TiO_2 have smaller variations. All these slag samples were also analysed by XRD. However, no phases could be identified.

Table 46: Chemical compositions of the selected final tapped slag samples from EBF campaign 32 as well as selected industrial slag samples.

ID		*Fe%	*CaO%	*SiO ₂ %	*MnO%	*S%	*Al ₂ O ₃ %	*MgO%	Na ₂ O%	K ₂ O%	V ₂ O ₅ %	*TiO ₂ %	B2
EBF final tapped slag, campaign 32	#1	2.40	28.10	36.93	0.44	0.79	14.01	13.14	0.56	0.86	0.43	2.33	0.76
	#2	3.57	26.18	38.26	0.56	0.50	13.46	12.16	0.61	1.10	0.65	2.91	0.68
	#3	0.85	27.33	40.76	0.49	0.74	12.80	12.41	0.57	1.05	0.24	2.75	0.67
	#4	2.89	27.75	36.35	0.21	1.23	14.54	14.07	0.61	0.85	0.14	1.34	0.76
	#5	1.61	29.47	35.40	0.15	1.46	14.98	14.45	0.58	0.80	0.05	1.04	0.83
	#6	1.15	30.08	34.91	0.15	1.51	15.47	14.36	0.53	0.76	0.05	1.01	0.86
	#7	0.78	31.63	33.36	0.09	1.63	15.90	15.02	0.40	0.40	0.03	0.75	0.95
	#8	0.83	31.70	32.94	0.08	1.61	16.37	14.99	0.40	0.35	0.03	0.69	0.96
	#9	0.63	30.84	33.46	0.09	1.67	16.18	15.56	0.45	0.38	0.03	0.70	0.92
	#10	1.98	27.65	37.09	0.29	0.92	14.11	14.01	0.58	0.93	0.17	2.25	0.75
	#11	1.73	27.29	38.50	0.38	0.76	13.06	13.63	0.71	1.42	0.30	2.21	0.71
	#12	0.58	25.50	42.23	0.43	0.70	12.19	12.88	0.83	1.95	0.19	2.50	0.60
	#13	1.45	29.37	35.16	0.12	1.28	15.46	15.49	0.39	0.37	0.05	0.87	0.84
TSE BF6	#14	0.34	39.68	33.76	0.30	0.84	14.02	8.84	0.41	0.56	0.02	1.23	1.18
TSE BF7	#15	0.42	36.83	34.92	0.34	0.83	14.87	9.28	0.56	0.61	0.02	1.30	1.05
voestalpine	#16	0.35	33.38	40.88	1.72	0.56	11.51	9.28	0.46	1.22	0.02	0.61	0.82

2.2.3.5.1.3 The melting behaviour and viscosity of the slag: results from FactSage calculations

The melting of the slag is determined by the chemical compositions of the slag; it can be evaluated either by the thermodynamic calculations from software package FactSage 7.2 or by the visual observation under a heating microscope (to be described later). The viscosity of the slag is determined by the chemical compositions and the temperature; while, this can be evaluated either by thermodynamic calculations from software package Factsage 7.2 or by viscosity measurement. The melting of the slag and viscosity of the slag were calculated by using respectively the Equilib module and Viscosity module in FactSage 7.2. The viscosities of the selected slag samples were measured by using a viscometer.

The temperature when the first melt is formed for the slag samples (shown in Table 43) procured from the hearth of EBF campaign 31 are calculated by FactSage and the results are shown in Table 47. For these calculations, only the listed components in Table 43 are included and the iron content was assumed to be either FeO or Fe₂O₃. It is seen that the calculated temperatures vary a few degrees depending on the form of iron oxide considered.

Table 47: Calculated melting temperatures of slag samples from the EBF hearth (campaign 31) assuming either FeO or Fe₂O₃ in parenthesis.

Drilled core	Depth, cm	First melt, °C	50% melt, °C	95% melt, °C
RCW 3	0-10	1249 (1266)	1292 (1295)	1490 (1480)
	50-60	1231 (1244)	1280 (1282)	1465 (1460)
	80-90	1220 (1243)	1253 (1259)	1420 (1400)
Centre	0-10	1241 (1245)	1257 (1257)	1417 (1410)
	50-60	1237 (1245)	1259 (1260)	1447 (1440)
	90-100	1232 (1244)	1250 (1256)	1368 (1360)
Taphole	50-60	1235 (1244)	1256 (1258)	1428 (1420)
	90-100	1231 (1244)	1249 (1253)	1331 (1325)

Table 48 shows the calculated viscosities of the slag samples shown in Table 43 by using FactSage. Obviously, the viscosity of the slag is a function of temperature and the chemical compositions of the slag, especially the main components in the slag (i.e. CaO, SiO₂, MgO and Al₂O₃) [54].

Table 48: Calculated viscosities of the slag samples procured from the hearth of EBF (campaign 31) in the temperature range 1250-1600 °C with FactSage.

Drilled core	Depth, cm	Viscosity (in Pa·s)				
		1250 °C	1300 °C	1400 °C	1500 °C	1600 °C
RCW 3	0-10	2.26	1.52	0.74	0.40	0.23
	50-60	3.08	2.03	0.96	0.50	0.28
	80-90	2.67	1.77	0.85	0.45	0.25
Centre	0-10	1.99	1.35	0.67	0.36	0.21
	50-60	2.19	1.47	0.72	0.39	0.22
	90-100	2.58	1.71	0.82	0.43	0.25
Taphole	50-60	2.42	1.62	0.78	0.42	0.24
	90-100	6.87	4.30	1.86	0.90	0.48

Similarly, the melting temperatures and viscosities of slag samples from the final tapped slag of EBF campaign 31, slag samples from EBF campaign 32 and industrial slag samples were also calculated by FactSage. Due to the availability of more components from the chemical analysis for these samples, the calculations were made by taking into account of 8 key components (marked with *) listed in Table 44 and by assuming FeO in the slag. The calculation results for the melting temperatures and viscosities of these slag samples are shown in Table 49 till Table 53.

The results from the FactSage calculations in the aspects of melting temperature and viscosity are compared with the available experimental data to be presented later.

Table 49: Calculated melting temperatures of final tapped slag samples from the EBF (campaign 31) assuming FeO in the slag.

ID	First melt, °C	50% melt, °C	95% melt, °C
FS1	1312	1317	1430
FS2	1333	1341	1505
FS3	1157	1172	1226
FS4	1301	1364	1498
FS5	1172	1186	1247
FS6	1313	1321	1481
FS7	1292	1296	1339

Table 50: Calculated viscosities of the slag samples taken from the final tapped slag of EBF (campaign 31) in the temperature range 1250-1600 °C with FactSage.

ID	Viscosity (in Pa·s)				
	1250 °C	1300 °C	1400 °C	1500 °C	1600 °C
FS1	3.14	2.02	0.91	0.46	0.39
FS2	3.41	2.15	0.95	0.47	0.39
FS3	4.35	2.69	1.15	0.55	0.46
FS4	1.97	1.30	0.62	0.32	0.27
FS5	2.79	1.80	0.82	0.42	0.35
FS6	4.70	2.97	1.31	0.64	0.54
FS7	10.52	6.26	2.49	1.13	0.92

Table 51: Calculated melting temperatures of the slag samples from EBF (campaign 32) and of the industrial slag samples assuming FeO in the slag.

Sample ID	First melt, °C	50% melt, °C	95 % melt, °C
Slag samples procured from the hearth of EBF, campaign 32	M101	1296	1349
	M102	1234	1245
	M103	N.A.	N.A.
	M104	1263	1290
	M105	1331	1343
	M106	1195	1210
	M107	1241	1248

Optimizing Blast Furnace Hearth Inner State (OPTIBLAFINS)

M201	1340	1353	1526	
M202	1216	1224	1532	
M203	N.A.	N.A.	N.A.	
M204	N.A.	N.A.	N.A.	
M205	N.A.	N.A.	N.A.	
M206	1302	1309	1399	
M207	1326	1336	N.A.	
EBF final tapped slag, campaign 32	#1	1185	1211	1293
	#7	1307	1311	1402
	#12	1144	1172	1253
Industrial slag	Tata BF 6	1357	1357	1391
	Tata BF 7	1327	1328	1377
	voestalpine	1234	1237	1323

Table 52: Calculated viscosities of the slag samples from EBF hearth (campaign 32) and of the industrial slag samples in the temperature range 1300–1600 °C with FactSage.

Sample ID	Viscosity (in Pa·s)				
	1300°C	1400°C	1500°C	1528°C	1600°C
M101	0.41	0.25	0.15	0.13	0.09
M102	1.52	0.11	0.07	0.06	0.05
M103	5.29	0.03	0.02	0.02	0.01
M104	1.77	0.30	0.18	0.15	0.11
M105	2.71	0.40	0.22	0.19	0.13
M106	3.69	0.07	0.05	0.04	0.03
M107	4.17	0.15	0.09	0.08	0.06
M201	0.45	0.66	0.34	0.29	0.19
M202	1.31	2.81	1.26	1.03	0.63
M203	30.41	0.12	0.08	0.07	0.05
M204	13.83	0.14	0.09	0.08	0.06
M205	4.79	0.18	0.11	0.10	0.07
M206	1.38	0.41	0.23	0.20	0.14
M207	1.82	0.64	0.34	0.28	0.19

Table 53: Calculated viscosities of the slag samples from EBF final tapped slag (campaign 32) and of the industrial slag samples in the temperature range 1250–1600 °C with FactSage.

Sample ID	1250°C	1275°C	1300°C	1325°C	1350°C	1400°C	1450°C	1500°C	1528°C	1600°C
#2	3.44	2.75	2.21	1.79	1.47	1.00	0.70	0.51	0.42	0.28
#5	3.51	2.79	2.23	1.81	1.47	1.00	0.70	0.50	0.42	0.27
#9	3.51	2.78	2.22	1.79	1.46	0.99	0.69	0.49	0.41	0.27
#12	6.35	4.99	3.96	3.17	2.56	1.71	1.17	0.82	0.68	0.43
TSE BF6	2.65	2.13	1.72	1.40	1.15	0.79	0.56	0.40	0.34	0.22
TSE BF7	3.42	2.72	2.18	1.76	1.43	0.97	0.68	0.48	0.40	0.26
voestalpine	4.20	3.34	2.68	2.16	1.76	1.19	0.83	0.59	0.49	0.32

2.2.3.5.1.4 Laboratory study of the viscosity and wetting behaviour of the slag from EBF and industries

2.2.3.5.1.4.1 Viscosity measurement

The viscosity measurements performed at CRM were made on a rotational viscometer (Figure 232). The principle is to measure the torque required for rotating a spindle in a fluid and that torque is a function of the viscosity of that fluid. With this device it is fully possible to measure torque in real-time and it gives an easy access to a thermal control unit around the apparatus.



Figure 232: Rheometer used at CRM for viscosity measurements on BF slags.

The viscometer is calibrated by the supplier using reference oils with different known viscosities and is adapted for each range of spindle or crucible diameters.

This equipment allows a heating temperature above 1600°C with viscosity range from several mPa.s to several MPa.s, according to the couple of spindle/crucibles used.

In the case of slags, a procedure had to be established because it was impossible to use alumina based crucible without damaging them and therefore the viscometer. It was then proposed to use molybdenum based crucibles which are chemically neutral to slags. However, they were oxidized at high temperature and could result in the formation of garlands or foams of molybdenum oxides (Figure 233).

To reduce those effects, the procedure consists in adding an additional graphite crucible on top of the molybdenum one in order to focus the oxidation on this one instead. Moreover, we added a flow of nitrogen at a low flowrate in order to reduce the amount of oxygen inside the furnace. It is still possible to observe a flame while heating but the production of molybdenum oxides has been eliminated.

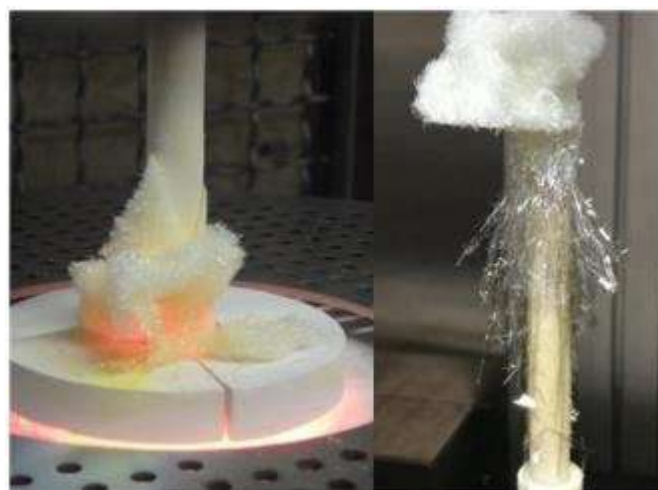


Figure 233: Foams (left) and garlands (right) produced during the early tests of the viscometer using molybdenum crucibles.

2.2.3.5.1.4.2 Viscosity measurement results and reliability

The measurement process and study of various parameters has been performed on the voestalpine slag sample because of its availability. It consisted in a series of trials where temperature, shear rate and time-related effects were tested.

First trial was semi-successful because it was possible to measure non-stabilized viscosities at high temperature and low shear rates. Second and third trials increased the stabilization time for measurements and tested several shear rates at three temperatures (1600, 1550 and 1500 °C), Figure 234. At each temperature threshold, viscosity measurements are performed with a shear rate of 5, 10, 15, 20, 25 s⁻¹ then with a ramp from 5 to 25 s⁻¹.

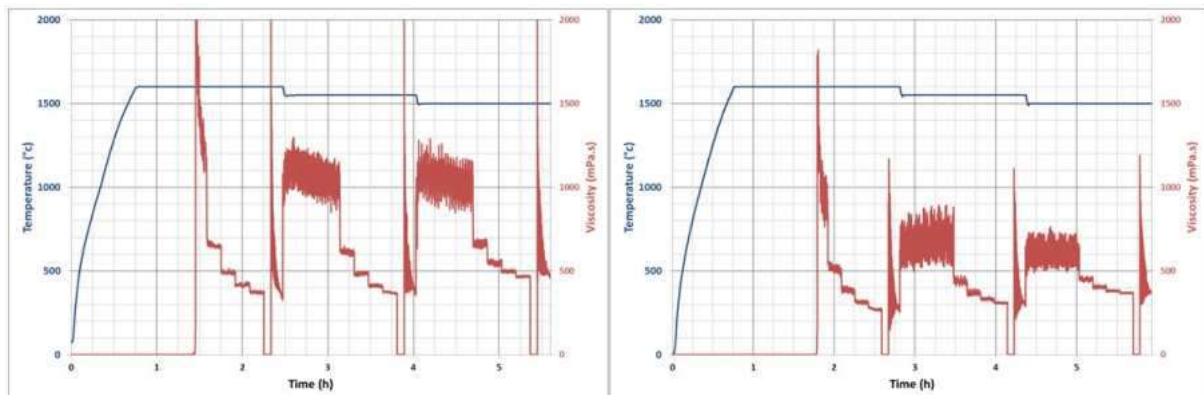


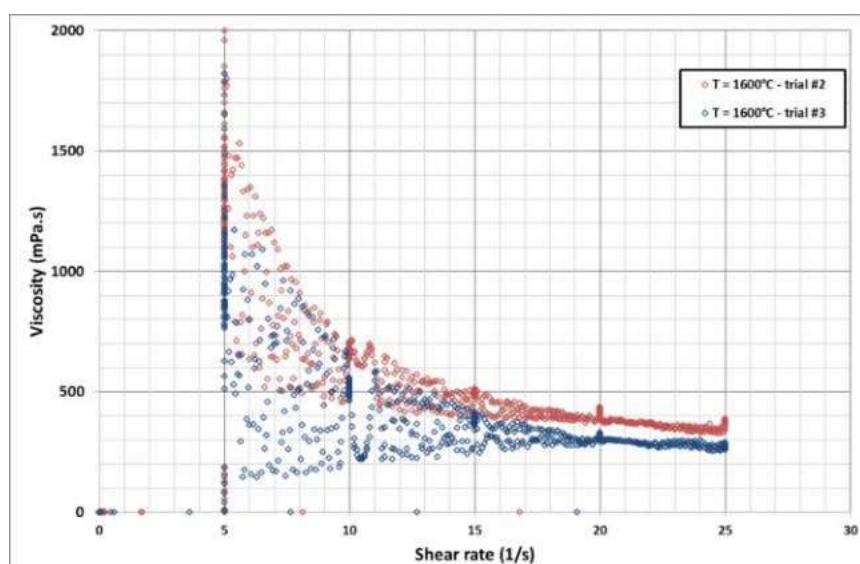
Figure 234: Evolution of viscosity and temperature during 2nd and 3rd viscosity trials.

Viscosity trials are reproducible despite an intrinsic variation due to the operational conditions. Indeed, the composition may not be completely homogeneous. It has been observed a clear difference in coloration inside the crucible, Figure 235.



Figure 235: Cross section of the voestalpine slag sample after cooling.

It is clear, that viscosity increases while temperature is decreasing as stated in literature models and FactSage simulations. However, shear rate also has a huge impact on viscosity measurement (Figure 236).



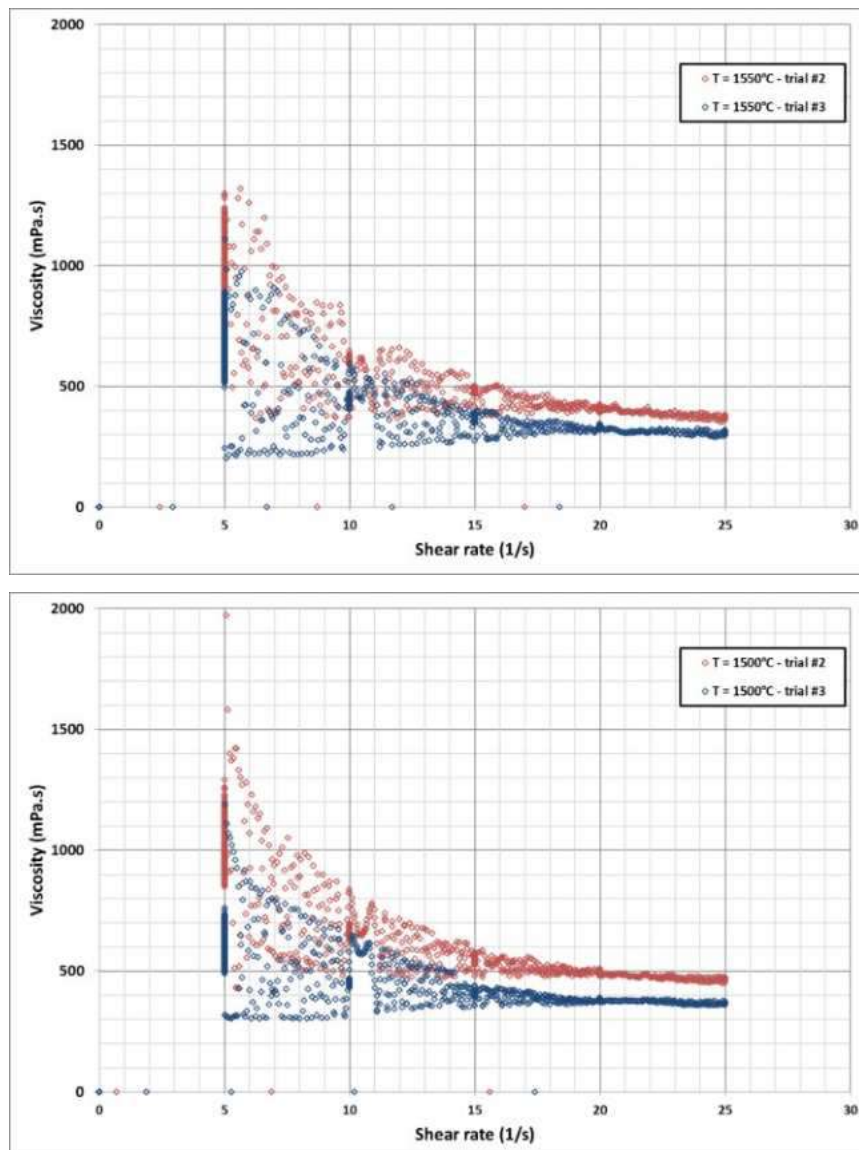


Figure 236: Evolution of viscosity as a function of shear rate at 1600 (top), 1550 (mid) and 1500 (bottom) °C.

Several observations could already be made:

- BF slags are rheo-fluidifiant i.e. viscosity decreases while the shear rate increases; Viscosity on BF slags is a function of three distinct parameters: temperature, chemical composition and mechanical stress.
- Viscosity measurements aren't stable at low shear rate and high temperature. It appears that the spindle used for those tests are not totally adapted to that range of viscosity because the torque is too low to be measured precisely. The solution is else increasing the shear rate, else using another spindle. We decided to keep spindle geometry and increase the shear rate because we plan to investigate lower temperatures where the viscosity should be way higher.

Five other tests were needed to define the final measurement process. Viscosity measurement of the voestalpine slag sample is presented at Figure 237 as an example.

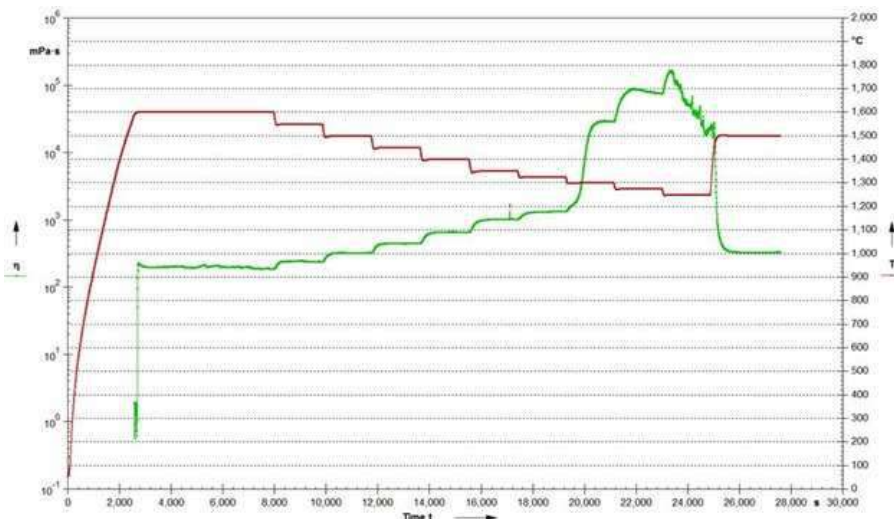


Figure 237: Evolution of viscosity (green) and temperature (red) of the voestalpine BF slag sample under a 20s^{-1} shear rate.

The evolution of the viscosity measurement with temperature is easily observable. Moreover, we could observe the behaviour change close to 1300°C where the slag becomes vitreous.

However, fewer than 1275°C , measurements are no longer reliable because it seems that the else the sample structure breaks during the measurement, else the torque is too high for the device or both.

The viscosity measurement made at the end of the trial at 1500°C is the same as the one made during the trial which means the phase change has no incidence on the behaviour of the sample regarding viscosity.

Viscosity measurements from all industrial slags are presented at Figure 238. The glass transition temperature tends to vary a lot with the chemical composition. For instance, the noted samples "SWERIM 2" and "SWERIM 12" didn't enter the transition at 1250°C yet. Those samples are the ones with the lowest amount of CaO (30 wt%). On the contrary, Tata Steel samples have the biggest amount of CaO (37-40 wt%) and also the highest glass-transition temperature.

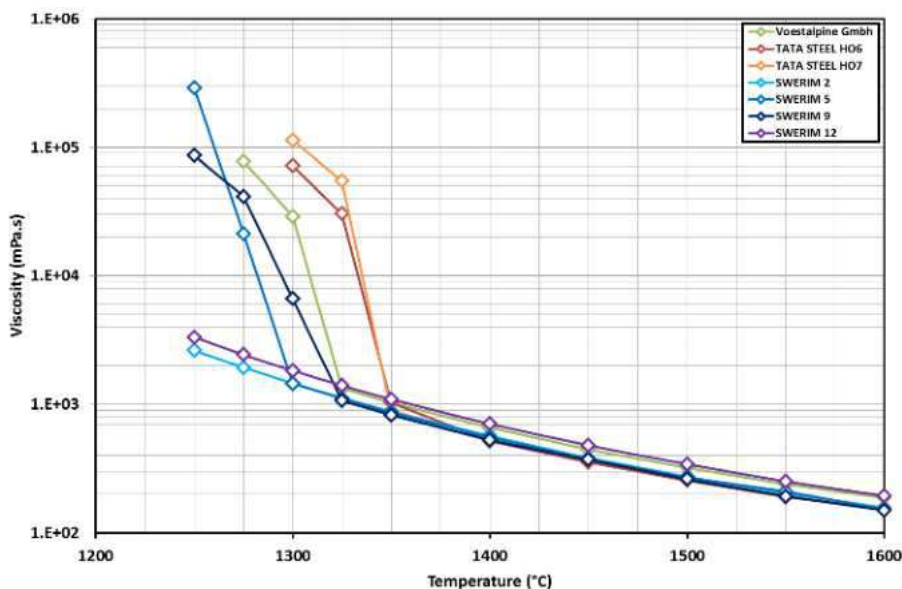


Figure 238: Evolution of viscosity of industrial slags with temperature.

Those blast furnace slags tend to have a very similar behaviour in the melted area. However, their respective levels can be very different (Figure 239).

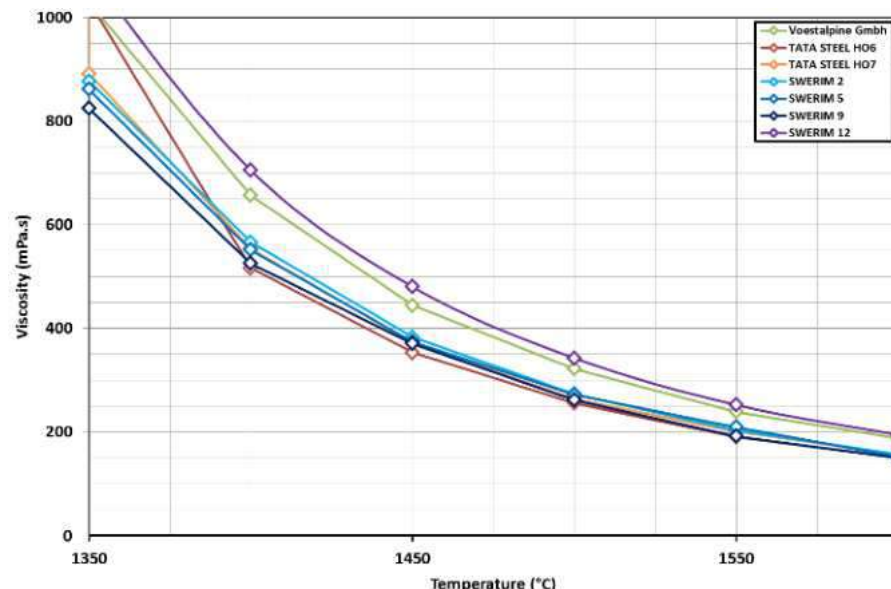
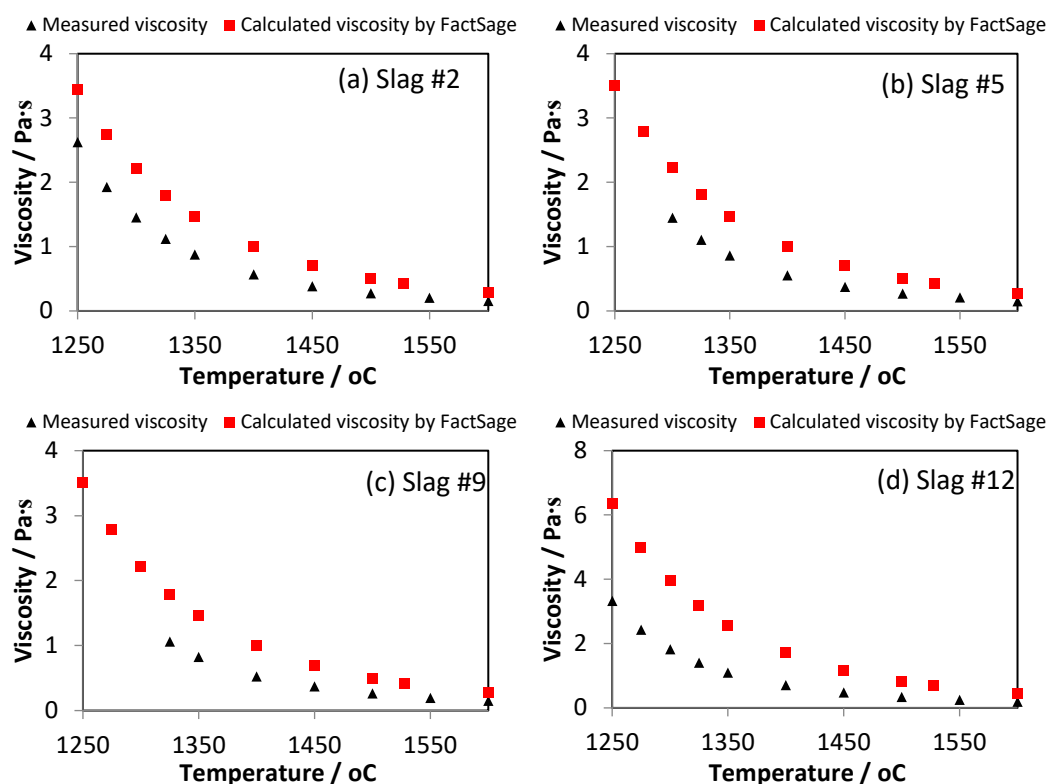


Figure 239: Evolution of viscosity of industrial slags with temperature in the melted zone.

For instance, samples from voestalpine and SWERIM 12 have an increased viscosity close to 20-25% compared to other samples. This could be explained by the lower concentration of alumina in their respective chemical composition.

Figure 240 shows the measured viscosities of the selected slag samples and the measured viscosities are compared with those from the FactSage calculations. It is seen that in general the viscosity of the slag decreases substantially with the temperature. Large deviations are observed between the measured viscosities and the FactSage calculated viscosities. The deviations could be due to the complexity of the slag system and due to that only selected components are included in the FactSage calculations. However, at higher temperatures (>1450 °C) the FactSage calculated viscosities approximate the measured viscosities. This indicates that when the slag is completely melted, FactSage can be used as a tool to estimate the viscosity of the slag and the viscosity data provided in Table 50 till Table 53 are creditable when the temperature of the slag is above 1450 °C.



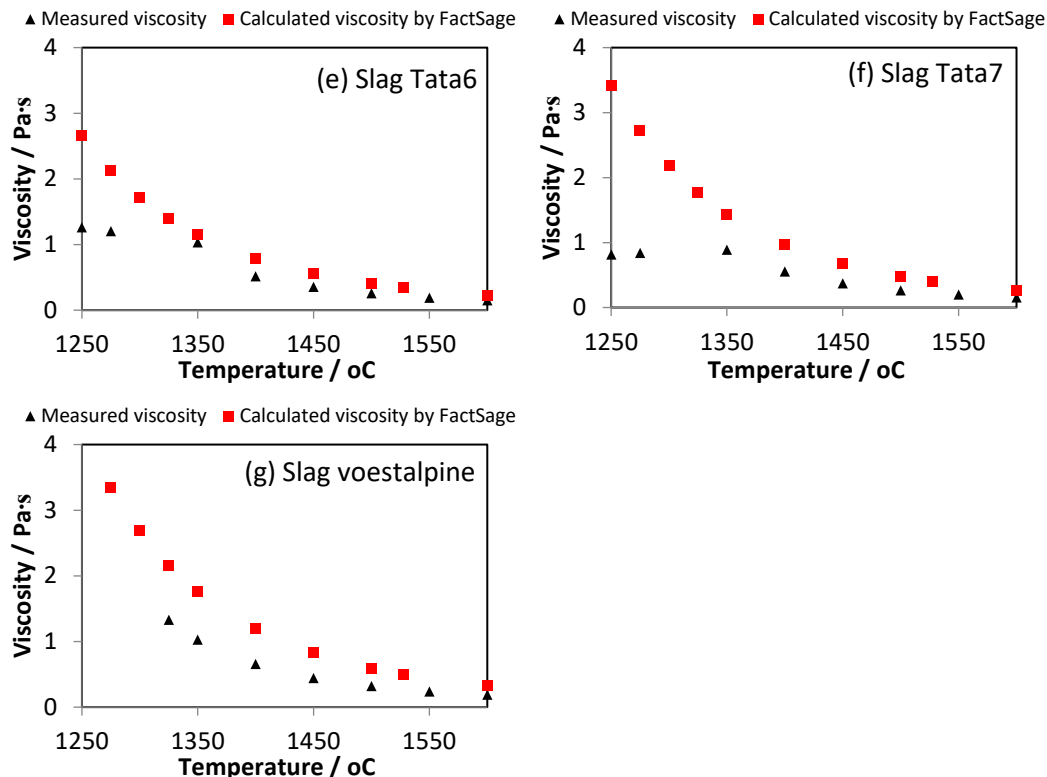


Figure 240: Measured viscosities of the selected slag samples plotted together with the FactSage calculated viscosities in the temperature range 1250-1600 °C, ((a) Slag #2; (b) Slag #5; (c) Slag #9; (d) Slag #12; (e) Tata6 slag; (f) Tata7 slag and (g) voestalpine slag).

It is known that the viscosity of the slag is largely influenced by the four key components $[\text{SiO}_2]$, $[\text{CaO}]$, $[\text{Al}_2\text{O}_3]$ and $[\text{MgO}]$. In the literature, the viscosity of the BF slag at 1500 °C was expressed by an empirical equation [54].

$$V = 0.005 + 0.0262[\text{SiO}_2] + 0.0184[\text{Al}_2\text{O}_3] - 0.0172[\text{CaO}] - 0.0244[\text{MgO}] \quad (53)$$

Where $[\text{SiO}_2]$, $[\text{CaO}]$, $[\text{Al}_2\text{O}_3]$ and $[\text{MgO}]$ are in weight percent and viscosity is in (Pa.s). By using the available data from the experimental measurement, FactSage calculation and empirical equation, a figure can be plotted to compare the viscosities, as shown in Figure 241. It is seen that the viscosities from the FactSage calculations has higher correlation with the measured viscosities than those from the empirical equation. This indicates that the minor components also play a role in the viscosity of the slag.

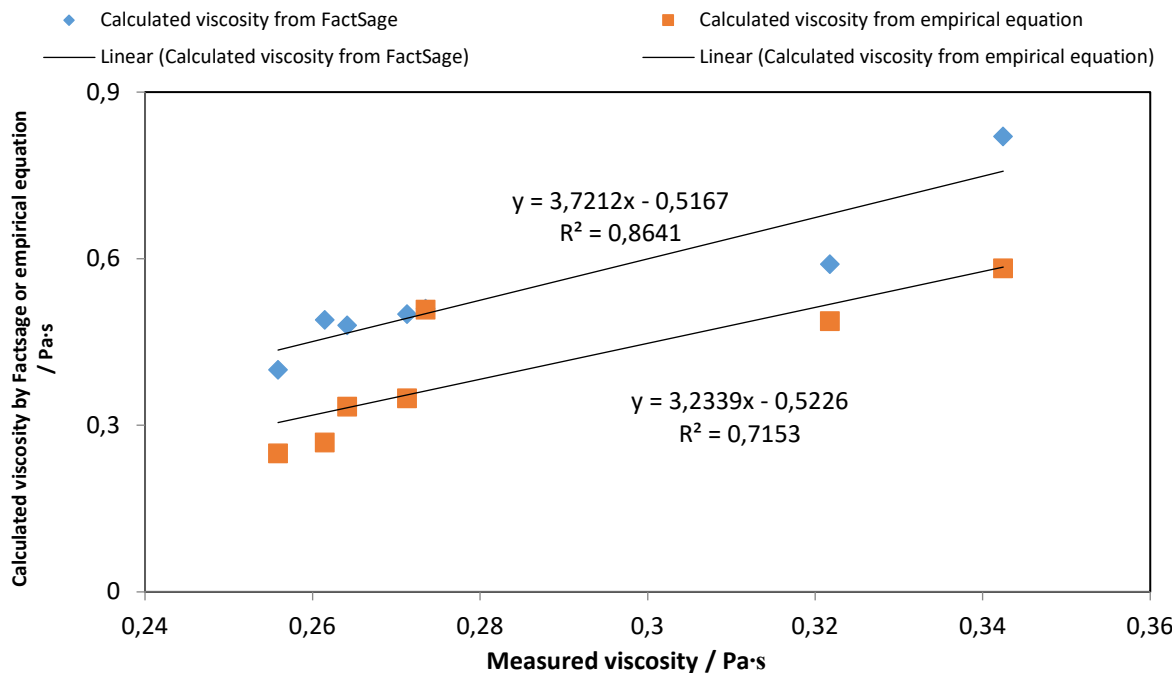


Figure 241 Correlations of the measured viscosities with the calculated viscosities by FactSage and empirical equation at 1500 °C.

The comparison with the most commonly used models of viscosity have been done with four SWERIM samples, described as the most singular ones (Figure 242).

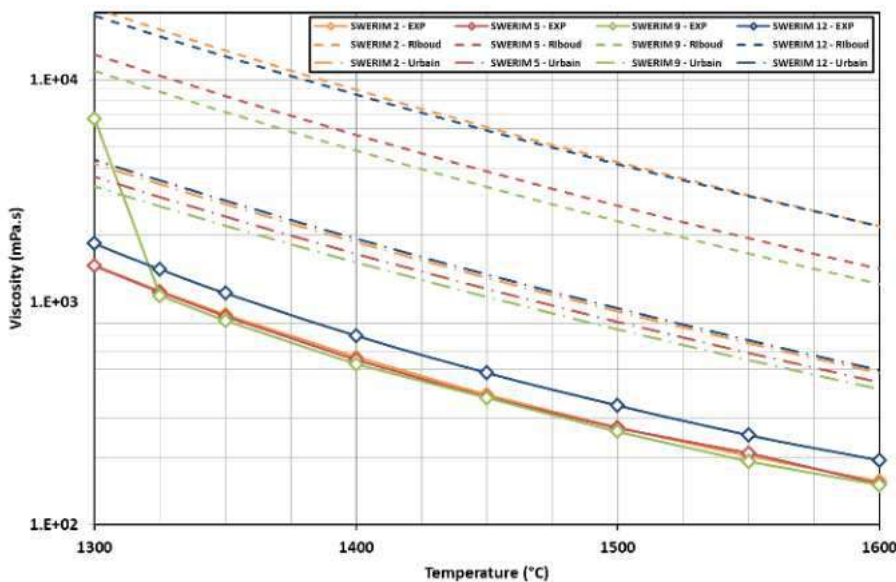
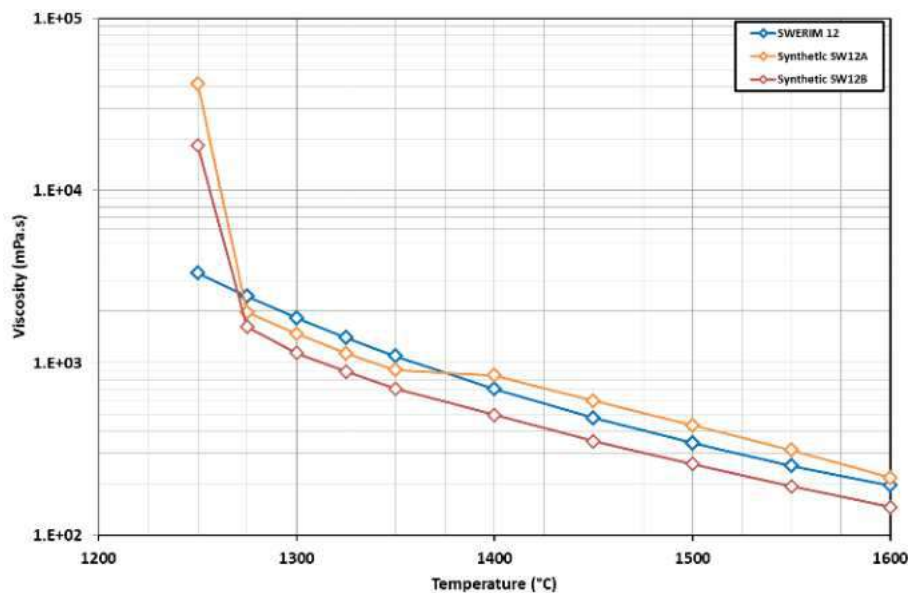
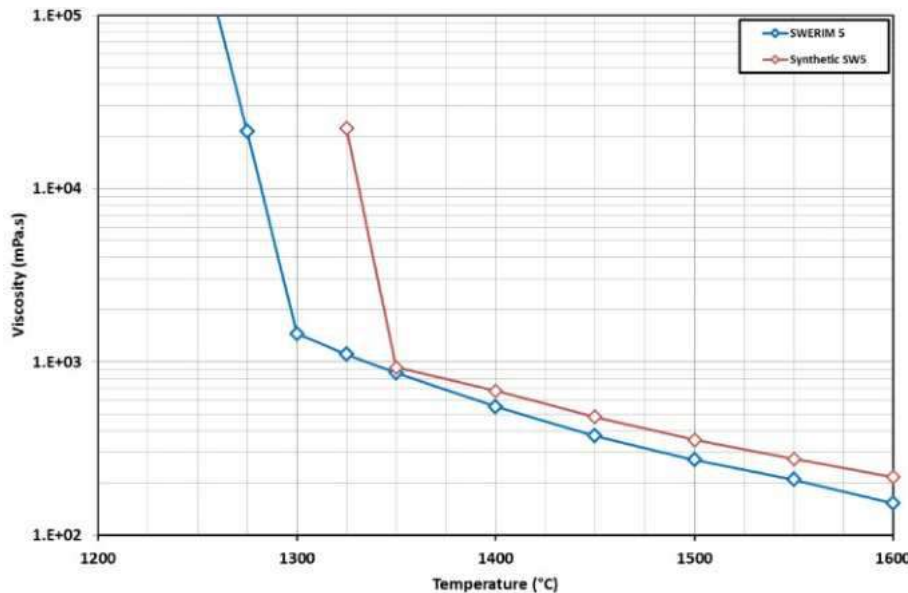


Figure 242: Comparison of experimental viscosities with literature models (Riboud and Urbain) on four SWERIM samples.

As a first observation, it is clear, that models don't predict the same levels of viscosity as the experimental measurements. However, the decrease with temperature is relatively well described. One major issue in this case is the fact that the relative level of viscosity of the sample "SWERIM 2" is not coherent with the model predictions. Indeed, while being close to SWERIM 5 and 9 according to our measurements, both models predict a much higher level of viscosity, close to the sample 12. Nothing amongst the main four elements of the chemical composition can explain such an experimental difference. The major difference between those two samples is the amount of iron, close to 4 wt% in sample 2. Minor elements seem to have a strong impact on viscosity. Some synthetic slags were tested in order to quantify the impact of TiO₂ because it the most dominant minor element (between 1 and 2 wt%). Normalized chemical compositions of those samples are presented at Table 54. Viscosity measurements are presented at Figure 243 and Figure 244.

Table 54: Normalized chemical composition (wt%) of synthetic slag samples and their blast furnace reference samples.

Sample ID	SWERIM 12	Synthetic SW12A	Synthetic SW12B	SWERIM 5	Synthetic SW5
SiO₂	39.63	40.83	39.60	33.78	33.80
CaO	29.36	30.25	29.40	33.50	33.50
Al₂O₃	12.98	13.37	13.00	16.14	16.10
MgO	15.09	15.55	15.10	15.58	15.60
TiO₂	2.94	0.00	2.90	0.99	1.00

**Figure 243: Comparison of viscosity between industrial and slag sample (SWERIM 12) with impact of TiO₂.****Figure 244: Comparison of viscosity between industrial and slag sample (SWERIM 5).**

Evolution of viscosity is clearly different between industrial and synthetic slags even by keeping the five major elements of the chemical composition nearly identical. In each case, the glass-transition phase and the levels of viscosity are completely different. This highlights the fact that all minor elements have a huge role on the viscosity.

If focussing on TiO₂, and then compare the behaviour of both synthetic slags based on the SWERIM 12 sample, then again, they are completely different. It is also the first time a jump in levels is observed in viscosity levels in the melted zone.

In conclusion, the temperature dependency of the slag viscosity is very straightforward and therefore can be described with an Arrhenius law as often proposed in literature. A comprehensive influence of the major chemical elements has been done and suggests that the CaO content should be lowered in order to decrease the glass-transition temperature and then obtain a wider range of melted slag during operational conditions. It has also been highlighted that more Al₂O₃ content tends to decrease the viscosity level.

However, a refined study of the chemical effects on viscosity is still needed because some minor chemical elements with sometimes composition lower than 1% can lead to complete different behaviours on the glass-transition temperature or the viscosity levels. Moreover, considering the relative difficulty to perform precise chemical analysis with a wide range of elements, it is very unlikely that all effects could be described.

A model based on Riboud or Urbain model with a re-estimation of the pre-exponential factor to describe more precisely the viscosity levels is advised. Indeed, both models tend to overestimate the viscosity levels in the melted zone. The estimation of the glass-transition temperature should be done using FactSage.

Impact of shear rate on blast furnace slags could be described as a function of internal pressure on the bath. The higher the blast pressure, the lower the viscosity.

2.2.3.5.1.4.3 Heating microscope study

To investigate the melting and wetting behaviour of the slag on the coke substrate, selected coke/slag couples were investigated by using a heating microscope. The furnace setup used for the experiments is shown in Figure 245.

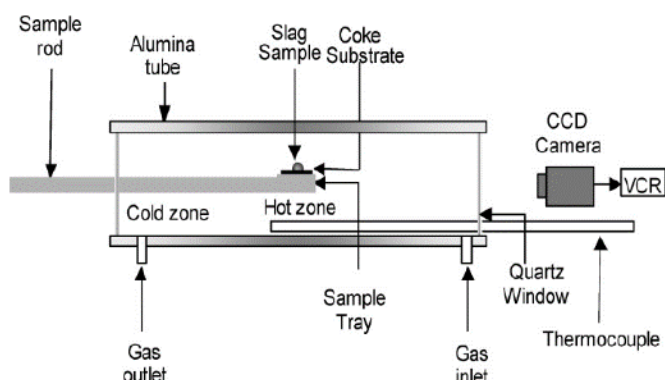


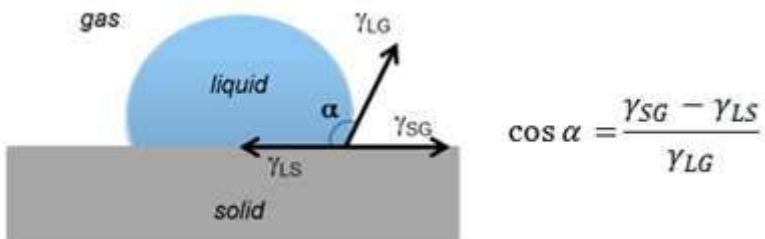
Figure 245: Heating microscope furnace setup [56].

The coke substrates (1-2 mm in thickness) were prepared by cutting the coke pieces using a diamond-cutting wheel and/or by grinding the coke pieces with sand paper. Therefore, the structure and porosity of the coke was kept, to study the interaction with slag. A small slag briquette was added on top of the thin coke substrate and then inserted into the horizontal furnace. The slag was heated and melted until a sessile drop was obtained, as shown in Figure 246.



Figure 246: Principle of the sessile drop test.

The coke/slag interaction is often defined by the wetting behaviour of the liquid slag in contact with the solid coke surface and is measured by the contact angle of the liquid slag on the solid coke surface. The contact angle, α , as shown in Figure 247 is defined by the Young's equation [56],[59], where γ_{SG} , γ_{LS} and γ_{LG} are the interfacial tensions at solid-gas, liquid-solid and liquid-gas interfaces, respectively. The wetting of a liquid on a solid surface is defined as followed in Table 55.

**Figure 247: Definition of the contact angle α .****Table 55: Wetting properties for a liquid according to its contact angle.**

Contact angle α , °	Wettability
$\alpha < 45^\circ$	Very good wetting
$\alpha < 90^\circ$	Good wetting
$\alpha > 90^\circ$	Poor wetting
$\alpha = 180^\circ$	Non-wetting

A CCD camera at the extremity of the furnace is recording images during the experiments; afterwards these images are analysed to determine the contact angle. The contact angle determination is performed using the free software ImageJ with an additional plugin for drop shape analysis for high-accuracy measurement methods of contact angle [105]. The method chosen for this analysis is the LBADSA method, Low Bond Axisymmetric Drop Shape Analysis, which is based on the fitting of the Young-Laplace equation to the image data. This method suits drops that are under the influence of the force of gravity only and stand on a horizontal substrate [95],[105]. By adjusting the coordinates and the height of the drop apex and optimizing the drop detection, the software calculates accurate values of the contact angle ($\pm 3^\circ$), drop volume, drop surface for the liquid-gas surface interface and surface of contact for the liquid-solid interface.

During the experiment, the coke/slag samples were heated up to 1400 °C (or 1528 °C) with a heating rate of 15 °C/min from room temperature to 600 °C and 10 °C/min up to 1400 °C (or 1528 °C), the whole experiment was carried out under inert atmosphere with nitrogen.

2.2.3.5.1.4.4 Heating microscope study results

Melting of the slag under heating microscope

Under heating microscope, the melting of the slag can be visually observed and the temperatures when the slag briquette starts softening and forming sphere can be recorded, as illustrated in Figure 248. From the recorded images, the temperature of the slag for softening and forming sphere can be extracted, as shown in Table 56 and Table 57. By referring to the melting temperatures shown in Table 47, Table 49 and

Table 51, it is seen that the melting temperature intervals from the FactSage calculations are smaller than those from the experimentally recorded data. This is due to the fact that under experimental conditions the slag didn't reach equilibrium at a fast heating rate. When the slag briquette forms a sphere, it is believed that the slag is mostly melted. Therefore, the sphere temperature of the slag from the heating microscope observations can be compared with the melting temperatures of the slag by FactSage. The results are presented in Figure 249. It is seen there exist deviations between the temperatures from the FactSage calculations (50% melt) and from the heating microscope observations. This could probably due to two reasons: (i) chemical reactions between the slag and the coke substrate took place during the heating in the heating microscope and the chemical compositions of the slag changed due to the reactions; (ii) the iron in the slag are both in the form of metallic iron and iron oxide (as shown in the XRD analysis in Figure 230 and Figure 231), which otherwise was only taken as iron oxide in the FactSage calculations.

Optimizing Blast Furnace Hearth Inner State (OPTIBLAFFINS)

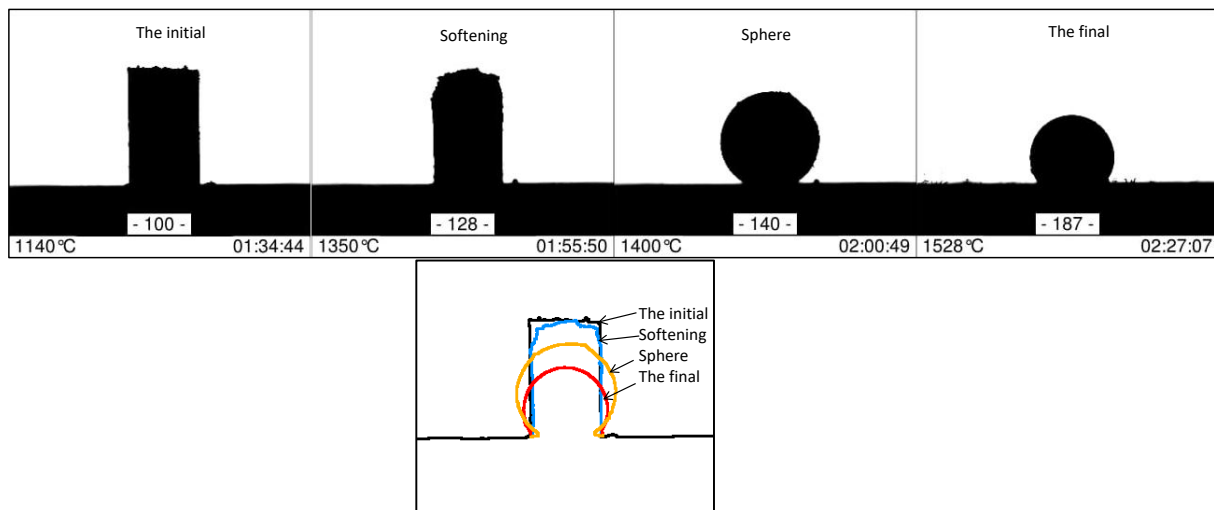


Figure 248: Visual observations of the slag briquettes under heating microscope.

Table 56: Temperatures for softening and sphere of the slag samples from EBF hearth and the final tapped slag (campaign 32) by heating microscope observations.

Sample ID		Softening temperature °C	Sphere temperature °C
RCW 3	0-10	N.A.	N.A.
	50-60	1335	1375
	80-90	1324	1350
Center	0-10	1351-1379	1390
	50-60	1350-1362	1370
	90-100	N.A.	N.A.
Taphole	50-60	1358	1375
	90-100	1256	1279
FS1		N.A.	N.A.
FS2		1330-1343	1360
FS3		1307-1324	1330
FS4		1333-1350	1380
FS5		1326-1337	1360
FS6		1210-1225	1230
FS7		1200-1220	1250

Table 57: Temperatures for softening and sphere of the slag samples from EBF hearth and the final tapped slag (campaign 32) as well as the industrial slag samples by heating microscope observations.

Sample ID	Softening temperature °C	Sphere temperature °C
M101	1396-1405	1450
M102	1370-1380	1410
M103	1470-1490	1520
M104	1364-1366	1410
M105	1392-1407	1440
M106	1322-1335	1407
M107	1357-1368	1410
M201	1378-1383	1400
M202	1253-1265	1340
M203	N.A.	N.A.
M204	1410-1440	N.A.
M205	1470-1550	N.A.
M206	1351-1355	1376
M207	1404-1413	1445
#1	1240-1260	1291
Tata BF6	1370-1399	1420
Tata BF7	1351-1376	1396

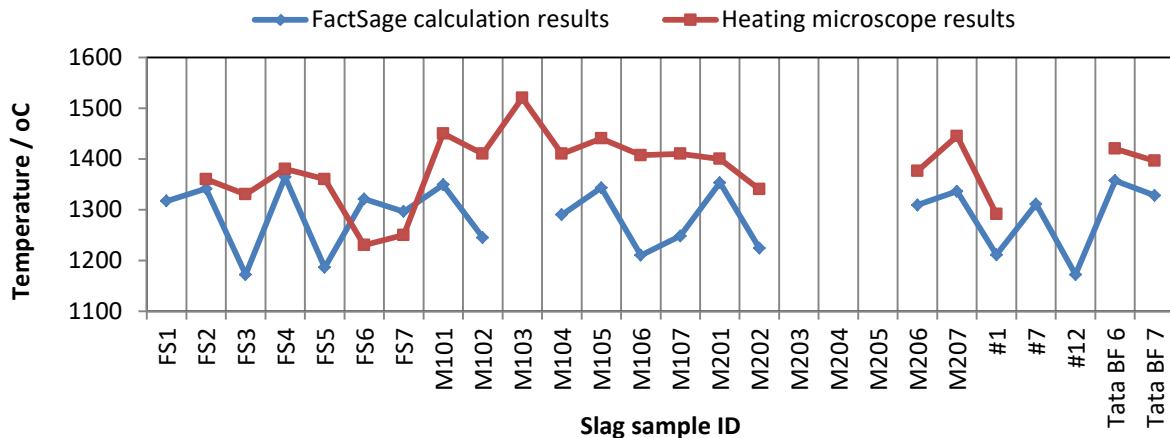


Figure 249: Comparison of the temperatures from the FactSage calculations (50% melt) and from the heating microscope observations (sphere temperature).

Wetting behaviour of the slag on coke substrate

The wetting behaviour of the slag on the coke substrate is dependent on the chemical compositions of the slag and the ash compositions of the coke substrate as well as the temperature. Figure 250 and Figure 251 show the recorded heating microscope images of the final tapped EBF slag and industrial slag on the coke substrate at two different temperatures (around 1500 °C and 1528 °C). In those cases, the coke substrates were all from the same original EBF coke, therefore the compositions of the ash in the coke were all the same. From Figure 250 and Figure 251 it is seen that the selected slag samples perform a poor wetting behaviour on the EBF original coke. This is mainly attributed to the low ash contents in the EBF original coke (to be described later). Further, it is also seen that the contact angles decrease as the temperature increases from 1500 °C to 1528 °C (holding 15 minutes at 1528 °C). The reason from this could be due to the reaction of the coke with the reducible components (e.g. FeO) in the slag, which thus has changed the coke ash compositions at the position where the slag and coke have contact. To find out how the chemical compositions of the slag influence the contact angle of slag, plots in Figure 252 were made to show the correlations between the contact angle and the main components (basicity, Al₂O₃, MgO and Fe) in the slag. In general, it is seen that the contact angle increases with the increase of slag basicity but decrease with the Fe content in the slag. However, in Figure 252, no significant correlations between the contact angle and the content of Al₂O₃ or MgO can be concluded; this is probably due to that the Al₂O₃ and MgO in the investigated slag are in a range of less significance.

Optimizing Blast Furnace Hearth Inner State (OPTIBLAFINS)

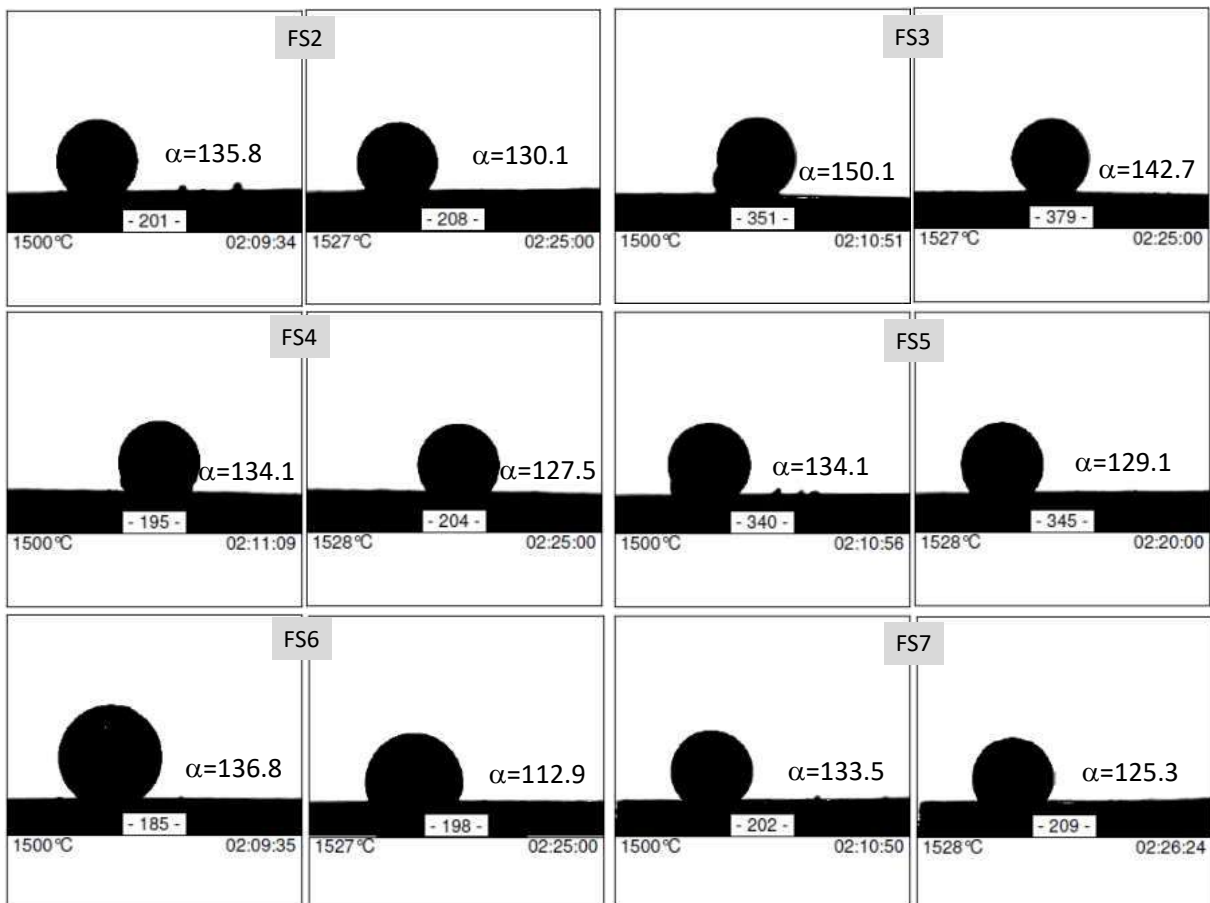


Figure 250: Heating microscope images of the final tapped EBF slag (campaign 31) on the original EBF coke substrate at two different temperatures (1500 and 1528 °C).

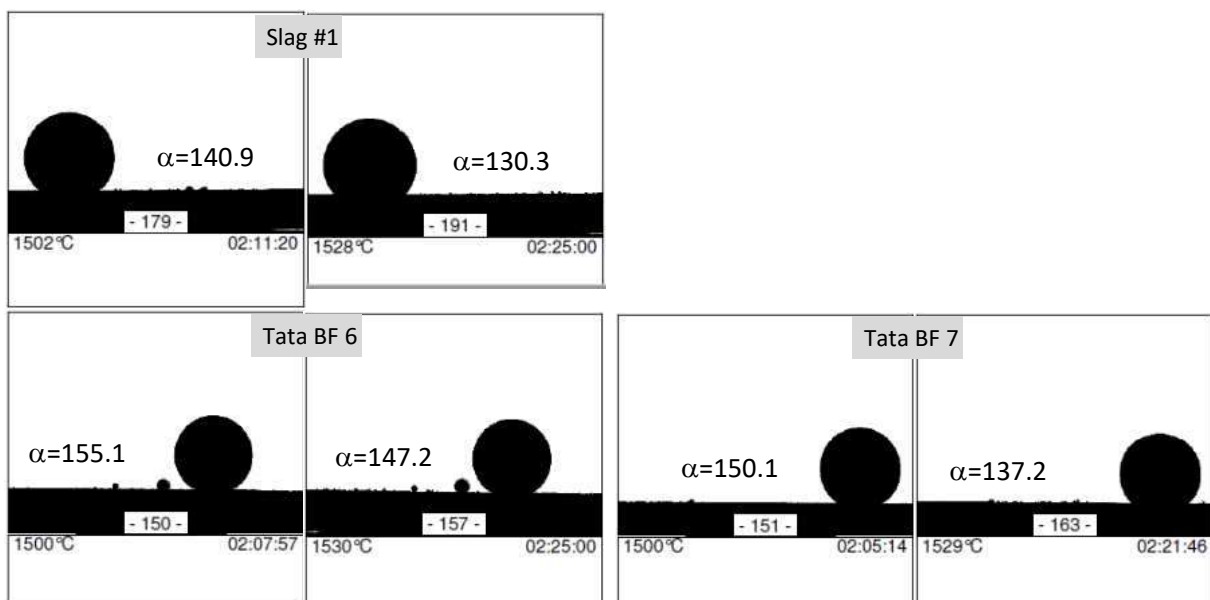


Figure 251: Heating microscope images of the final tapped EBF slag (campaign 32) and industrial BF slag on the original EBF coke substrate at two different temperatures (1500 and 1528 °C).

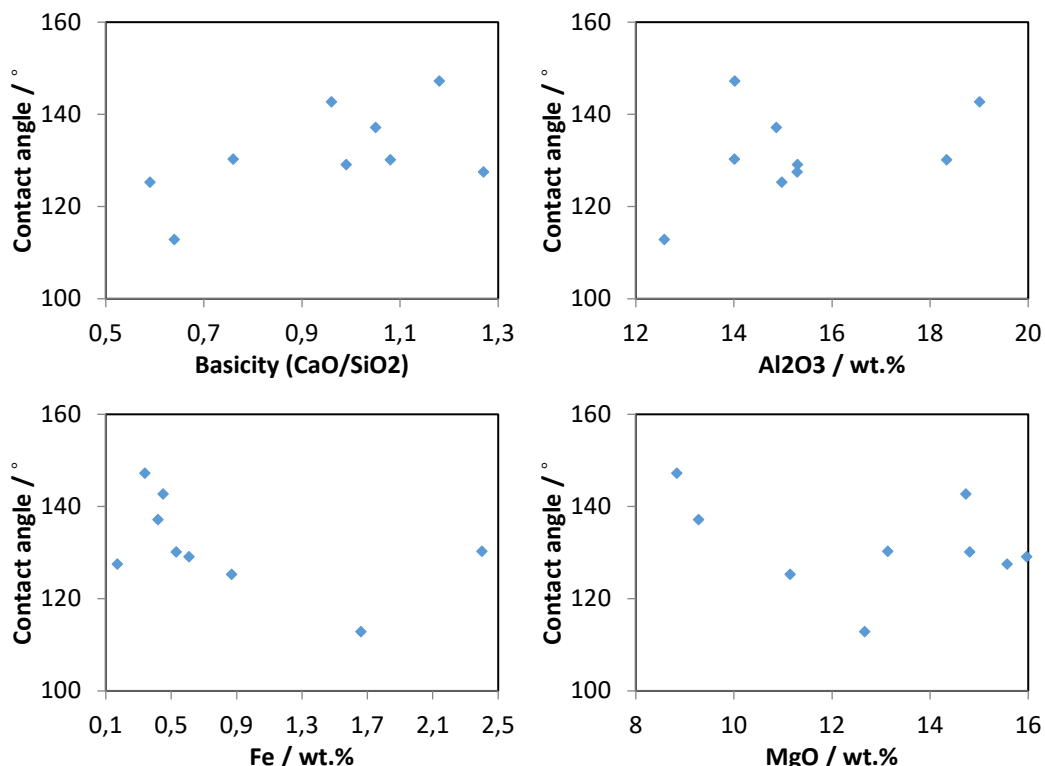


Figure 252: Correlation of the contact angle to the main components (basicity, Al_2O_3 , FeO and MgO) in the slag.

Figure 253 and Figure 254 show the recorded heating microscope images of the EBF hearth slag on their coupled hearth coke substrates. The wetting of the EBF hearth slag on their coupled EBF hearth coke can be summarized in three aspects:

- Several slag samples (such as the sample M203 in Figure 254) cannot be melted even at 1528 °C, therefore these slag samples performed a completely non-wetting behaviour on the coke;
- Several slag samples (such as the sample '2TH 90-100 cm' in Figure 253 and the sample M201 in Figure 254) performed a good wetting behaviour on the coke.
- Most of the slag samples perform a poor wetting behaviour on the coke, which are similar to the wetting behaviour of the final tapped slag and industrial slag on the EBF original coke.

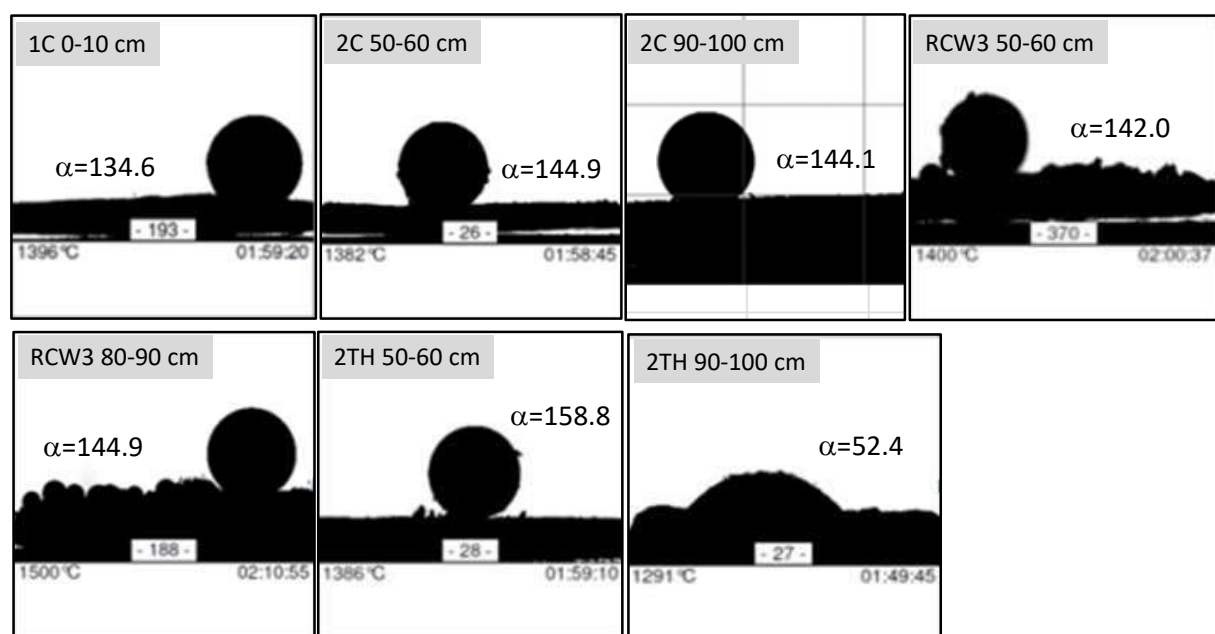


Figure 253: Heating microscope images of the EBF hearth slag (campaign 31) on their coupled hearth coke substrates at around 1400 °C.

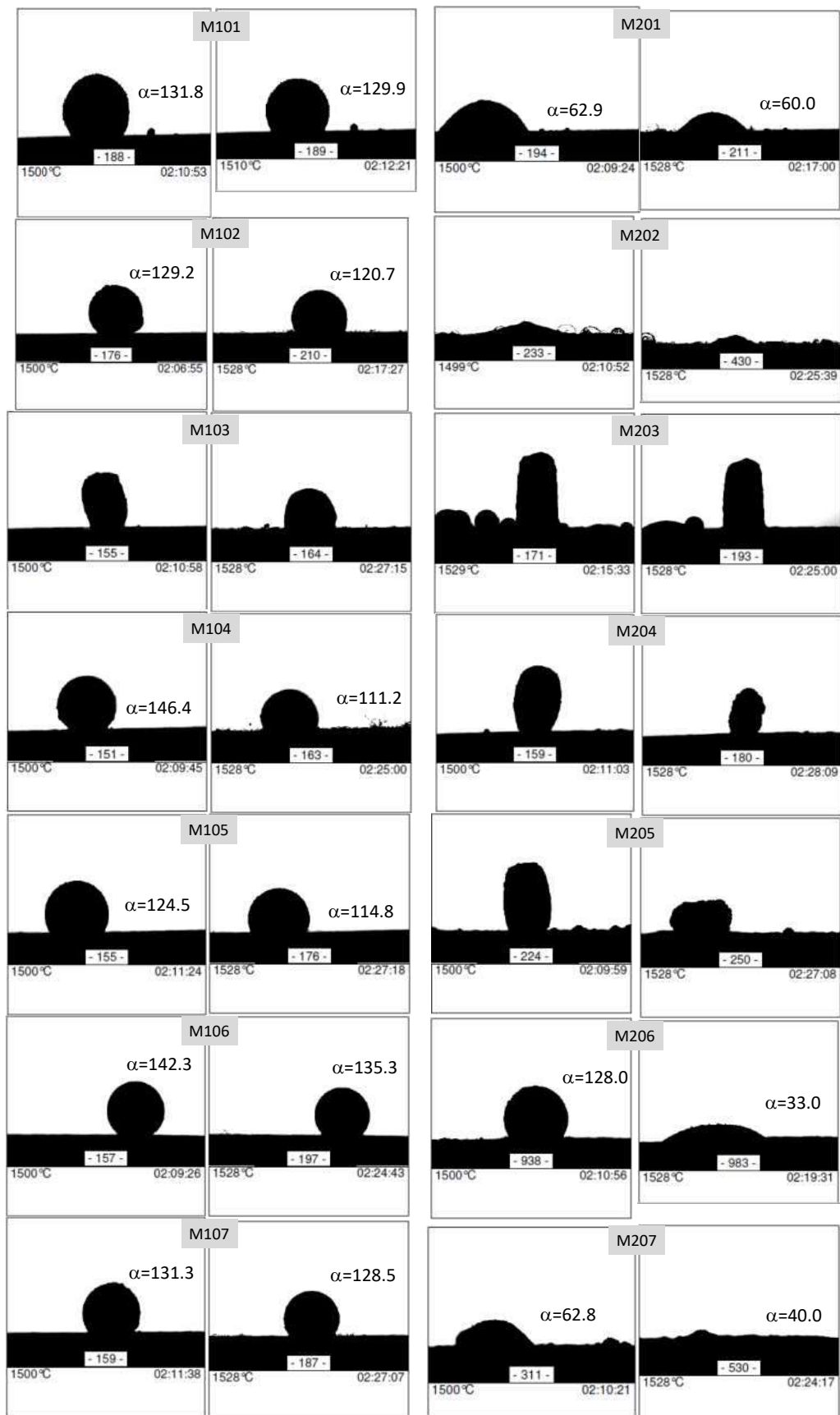


Figure 254: Heating microscope images of the EBF hearth slag (campaign 32) on their coupled hearth coke substrates at two different temperatures (1500 and 1528 °C).

2.2.3.5.1.5 Multivariate analysis of the data

From the chemical analysis, XRD analysis, FactSage calculations and the heating microscope study, a large set of data were obtained in the aspects of chemical compositions, phases, melting temperatures, viscosities, ash contents, etc. To find out the influential factor(s) which determine(s) the wetting behaviour of slag on the coke at the temperature of 1528 °C, SIMCA, a multivariate

analysis tool, is employed to process the available data set. The experimental data and the variables used in the SIMCA analysis are described in the Appendix 3.5.4. In the SIMCA analysis four models were applied by gradually excluding variables of less significance. Finally, it is found that Model 3 and Model 4 yield good results, as shown in Figure 255. It can be seen the predicted data have some small deviations from the experimentally measured data but generally follows the experimental observations (as shown in Figure 256). The final models' coefficients were exported to make regression functions for Model 3 and Model 4 shown as follows.

$$M3(A, B, C, D) = 171.95 - 8.109 \cdot A - 3.531 \cdot B - 0.989 \cdot C - 2.123 \cdot D \quad (54)$$

$$M4(A, B, C) = 182.193 - 10.694 \cdot A - 4.657 \cdot B - 1.304 \cdot C \quad (55)$$

In the above functions A, B, C and D are the weight percentages of Al_2O_3 , MgO , sum ash, CaO , respectively.

The regression function has following boundaries that it's recommended to keep, while the values outside the boundaries might deviate from the regression: CaO : 0.09-9.11; Al_2O_3 (2.49-5.71); MgO (0.09-6.55); sum ash (8.74-34.72) and contact angle (33.0-147.2).

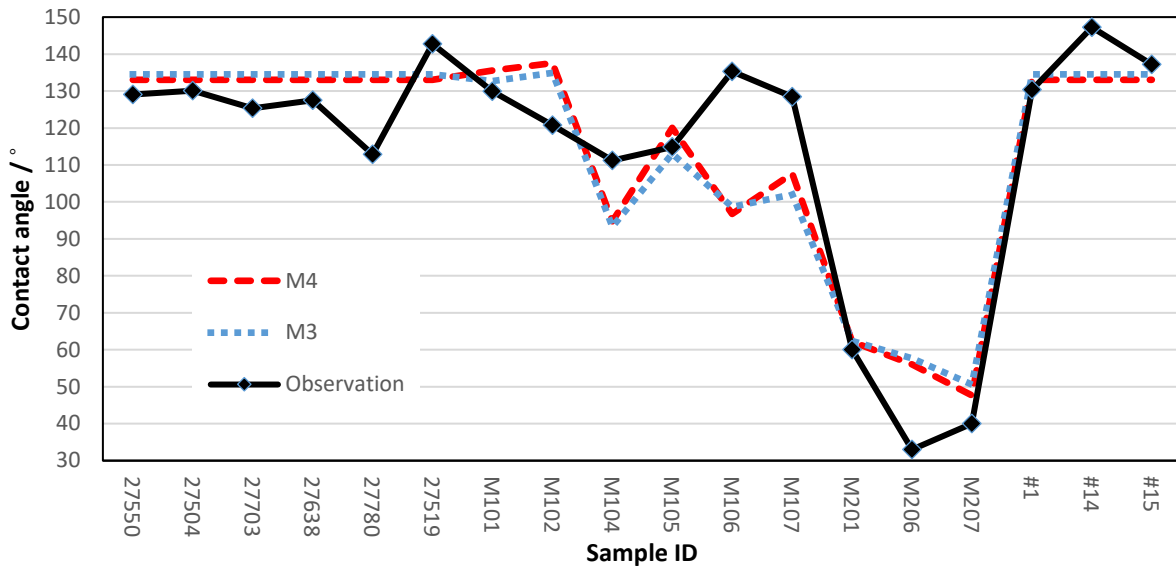


Figure 255: The predicted wetting angles (from Model 3 and Model 4 described in Appendix 3.5.4) and the measured wetting angles for various slag samples on coke.

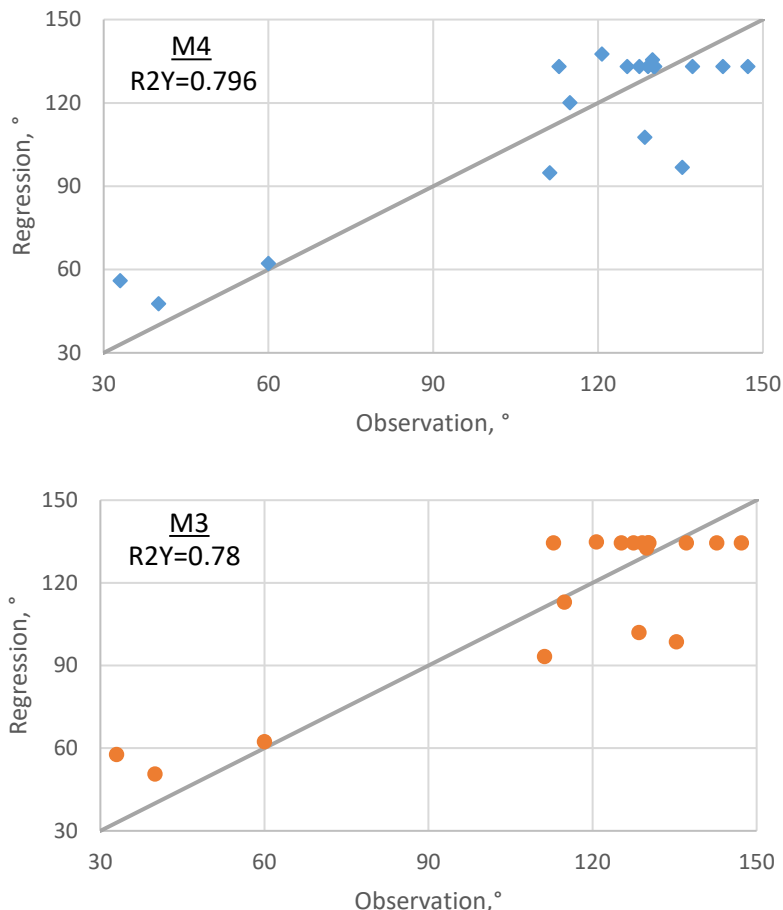


Figure 256: The predicted wetting angles (from Model 3(red) and Model 4(blue) described in Appendix 3.5.4) and the measured wetting angles for various slag samples on coke.

The SIMCA multivariate analysis results show that the variables deciding the wetting of slag on coke at high temperature (1528 °C in this analysis) were the contents Al_2O_3 , MgO , CaO and the sum ash in the coke. In the original coke, the ash content in the coke is 11.8%. This lower ash content makes the slag performing a poor wetting behaviour on the original coke (as shown earlier in Figure 250 and Figure 251). This can be reflected by Figure 255 that in cases that when original coke is used as the substrate, the wetting angles are higher (in the range of 130–150°). Once the coke enters the BF, the ash content in the coke increases due to the partial gasification of carbon in the coke and penetration of slag and metal into the coke, especially in the lower part of the BF, where the molten slag and hot metal is flowing around the coke. The higher ash content in the coke makes the slag performing a good wetting behaviour on the coke. This can be reflected by Figure 255 that in cases that when the coke procured from the EBF hearth is used as the substrate, the wetting angles are lower (as low as 33°).

2.2.3.6 Properties of coke in the Experimental BF hearth

2.2.3.6.1 Properties of the coke from the EBF hearth, campaign 31

Table 58 shows the chemical compositions of the coke ashes for the coke samples taken from EBF hearth (campaign 31). The sample taken in the bottom of the hearth close to the taphole was revealed to be taphole clay due to the high Si-content.

These coke samples were analyzed with XRD. The XRD diffraction spectra of coke beneath tuyere 3, centre and taphole are shown in Figure 257, Figure 258 and Figure 259, respectively. The mineral compounds found in the coke were identified to be mainly carbon (x), iron (▼), spinel as $\text{MgO} \cdot \text{Al}_2\text{O}_3$ (♦) and gehlenite (○). Monticellite (◊) as well as quartz (◊) could be seen in the upper samples in the centre of the hearth in small amounts. It seems that the gehlenite was increasing towards the bottom of the hearth while the iron and carbon peaks were decreasing and even disappear in case of the iron peak.

Table 58: Chemical compositions of coke ashes for the coke samples taken from EBF hearth, campaign 31 (in wt.%).

Drilled core	Depth, cm	Fe	CaO	SiO ₂	Al ₂ O ₃	MgO	Na ₂ O	K ₂ O	S	Others*
RCW 3	0-10	9.93	30.3	16.5	22.8	8.88	1.03	2.79	2.58	2.25
	50-60	21.5	34.1	16.6	9.86	6.95	0.43	1.97	6.21	2.32
	80-90	8.68	36.4	21.1	8.37	8.33	0.52	2.15	6.27	7.95
Center	0-10	7.88	23.1	22.8	18.3	11.6	2.24	6.46	2.33	2.99
	50-60	15.9	24.2	18.0	18.5	7.71	0.88	5.42	5.12	4.21
	90-100	6.69	38.4	23.8	10.2	10.3	0.02	1.66	7.09	1.78
Taphole	50-60	19.1	23.8	17.0	14.4	9.32	0.38	5.63	6.76	2.98
	90-100**	5.53	8.71	66.0	6.14	2.83	0.70	7.14	1.29	1.69

* MnO, P₂O₅, TiO₂, V₂O₅; ** the analysis revealed taphole clay instead of coke.

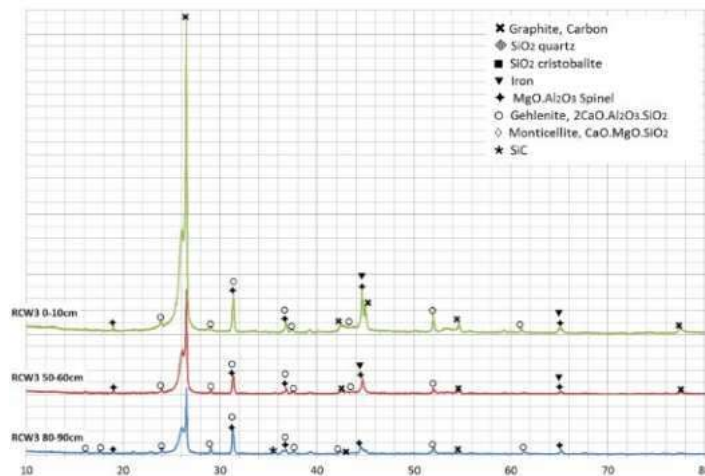


Figure 257: XRD diffraction spectra of the coke beneath tuyere 3 of the EBF, campaign 31.

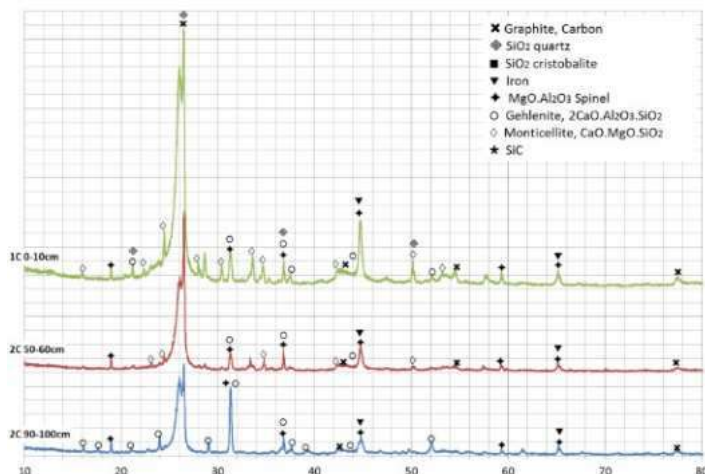


Figure 258: XRD diffraction spectra of the coke in the centre of EBF hearth, campaign 31.

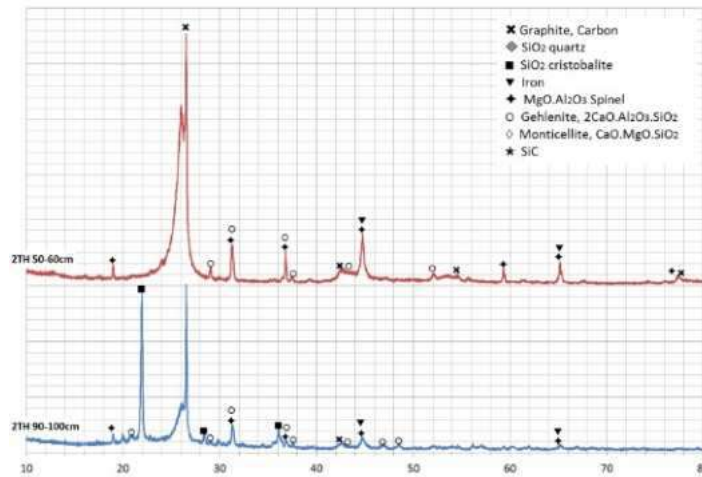


Figure 259: XRD diffraction spectra of the coke close to the taphole.

2.2.3.6.2 Properties of the coke from the EBF hearth, campaign 32

Table 59 shows the chemical compositions of the ash components in the coke samples procured from the EBF hearth (campaign 32). Compared to the EBF original coke (as shown in Table 60), it is seen that the sum amounts of ash from the EBF hearth coke are much higher than that of the EBF original coke. This may indicate that the coke in the EBF hearth has been subjected to severe gasification and chemical/physical interaction with the surrounding molten slag and metal. By using a similar method used earlier in Task 3.5, the alkali contents in the coke samples were mapped and shown in Figure 260. It is seen that the alkalis in the coke are concentrated in an area around the wall of the EBF hearth. This result is consistent to that shown in

Figure 228, which indicates that the alkalis are concentrated in approximately the same area. Figure 261 shows the XRD analysis of the EBF original coke. The dominating phases in the coke are identified to be graphite and carbon; the minerals in the ash in the coke are mainly quartz and mullite. This is consistent to the chemical analysis of the EBF original coke, which shows that the main components are SiO_2 and Al_2O_3 . Figure 262 and Figure 263 show the XRD analysis results of the selected coke. Compared to the EBF original coke, the minerals in the coke procured from the EBF hearth are much different and complex. Firstly, the intensity of the graphite peak becomes higher in the XRD spectra of the EBF hearth coke. This is due to the graphitization of the EBF original coke under high temperature in the EBF. Secondly, the dominating phases of the ash in the coke samples are minerals of $\text{CaO}-\text{MgO}-\text{SiO}_2-\text{Al}_2\text{O}_3$, which are similar to that of the surrounding slag samples. In sample M202, a silica (cristobalite) peak was also observed, this is because the taphole clay was mistaken as the coke during the manual separation.

Table 59: Chemical compositions of the ash components in the coke samples procured from the hearth of EBF hearth, campaign 32.

Sample ID	Fe	CaO	SiO ₂	MnO	S	Al ₂ O ₃	MgO	Na ₂ O	K ₂ O	TiO ₂	Sum
M101	2.49	1.86	0.23	0.06	0.27	3.14	0.36	0.01	0.08	0.26	9.7
M102	1.22	1.50	1.45	0.24	0.34	2.49	1.27	0.05	0.47	0.22	9.6
M103	1.47	7.45	7.27	0.10	0.35	4.43	3.35	0.08	0.13	0.34	25.4
M104	1.08	5.83	6.43	0.08	0.37	3.60	4.29	0.08	0.20	0.23	22.5
M105	1.08	5.55	2.30	0.01	0.40	3.37	1.50	0.02	0.12	0.26	14.9
M106	1.46	4.02	7.21	0.37	0.31	3.85	3.35	0.33	0.80	0.27	22.5
M107	1.30	6.32	2.94	0.04	0.47	4.47	1.01	0.02	0.07	0.25	17.2
M201	1.12	8.76	7.27	0.00	0.58	5.69	4.73	0.05	0.04	0.22	28.6
M202	0.49	0.77	45.91	0.03	0.00	7.31	1.45	0.90	0.69	0.17	57.9
M203	0.79	8.22	12.13	0.10	0.50	5.27	5.15	0.25	0.30	0.52	33.3
M204	1.31	6.60	8.82	0.12	0.46	3.59	3.92	0.14	0.47	0.63	26.4
M205	2.57	6.65	8.83	0.10	0.42	3.68	3.62	0.14	0.26	0.65	27.8
M206	0.86	8.77	11.20	0.01	0.54	4.88	6.55	0.08	0.08	0.41	33.5
M207	0.75	9.11	11.62	0.01	0.52	5.71	6.06	0.14	0.12	0.68	34.8
M208	1.64	9.07	8.97	0.01	0.56	5.95	5.11	0.07	0.02	0.58	32.4

Optimizing Blast Furnace Hearth Inner State (OPTIBLAFFINS)

M209	2.09	7.76	8.47	0.03	0.43	5.31	4.78	0.06	0.03	0.61	30.3
M210	1.00	9.34	11.44	0.01	0.57	5.87	5.91	0.09	0.07	0.40	34.8
M211	0.94	9.12	9.59	0.00	0.58	5.45	6.22	0.07	0.03	0.40	32.5
M212	1.00	9.43	9.54	0.00	0.59	5.12	5.37	0.07	0.04	0.28	31.6
M213	1.62	9.12	9.02	0.00	0.58	5.74	5.82	0.07	0.05	0.40	32.8
M214	0.65	9.53	11.80	0.01	0.65	5.95	6.69	0.09	0.07	0.50	35.9
M215	1.71	7.81	9.97	0.04	0.44	5.01	4.65	0.07	0.08	0.47	30.8
M216	0.62	2.16	31.30	0.04	0.06	7.22	2.33	0.95	0.94	0.26	46.1
M217	1.00	5.61	17.93	0.13	0.30	4.83	4.27	0.36	0.69	0.39	35.8
M218	0.93	7.40	11.06	0.16	0.46	4.29	4.38	0.24	0.39	0.87	30.3
M219	2.55	6.17	8.45	0.14	0.40	3.13	3.20	0.19	0.57	1.36	27.1
M220	2.45	7.13	10.26	0.14	0.40	4.43	4.27	0.26	0.54	0.96	31.7
M221	2.36	5.94	6.08	0.10	0.38	2.27	2.06	0.13	0.81	0.39	21.4

Table 60: Chemical compositions of the ash components in the EBF original coke.

Sample ID	Fe	CaO	SiO ₂	MnO	S	Al ₂ O ₃	MgO	Na ₂ O	K ₂ O	TiO ₂	Sum
EBF original coke	0.36	0.09	7.07	0.04	0.56	3.12	0.09	0.06	0.17	0.17	9.7

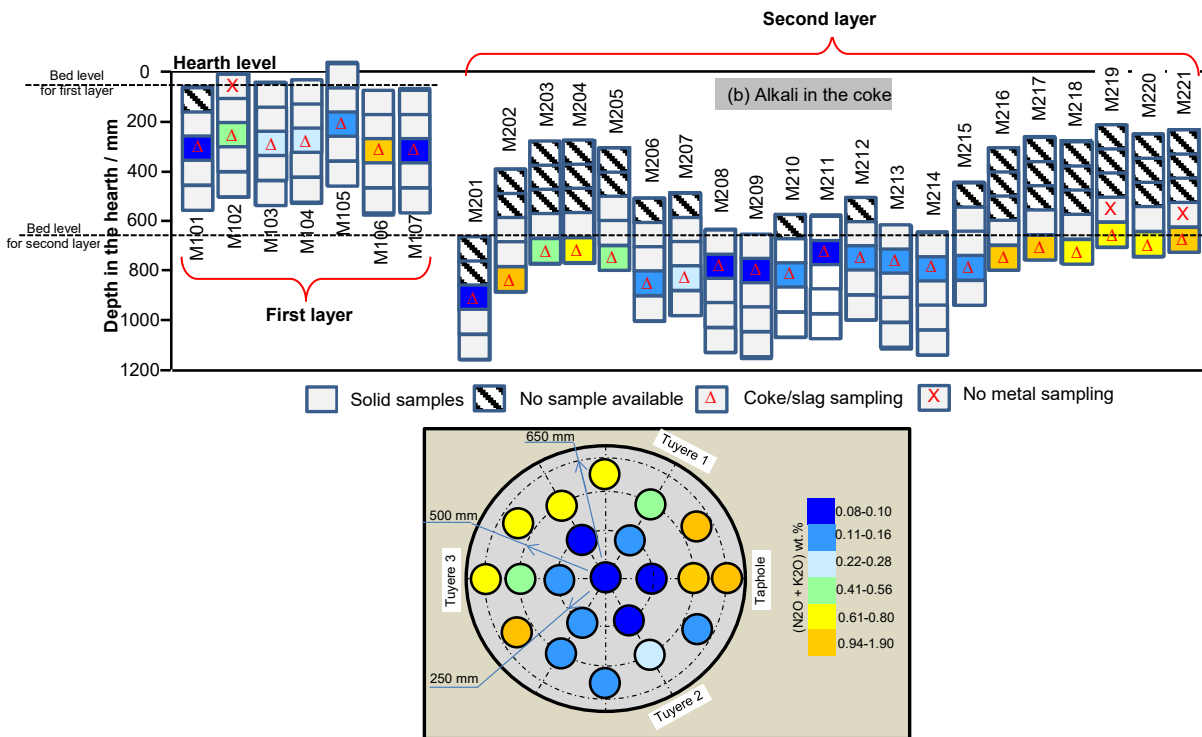


Figure 260: Alkali contents in the coke samples procured from the hearth of the EBF, campaign 32: (a) side view; (b) top view.

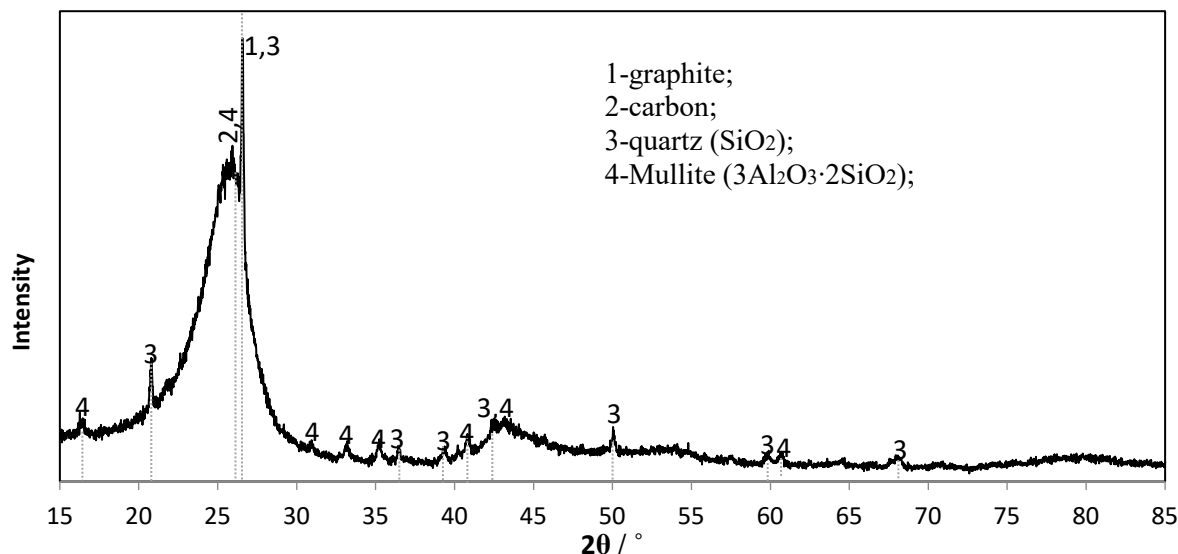


Figure 261: XRD analysis of the EBF original coke.

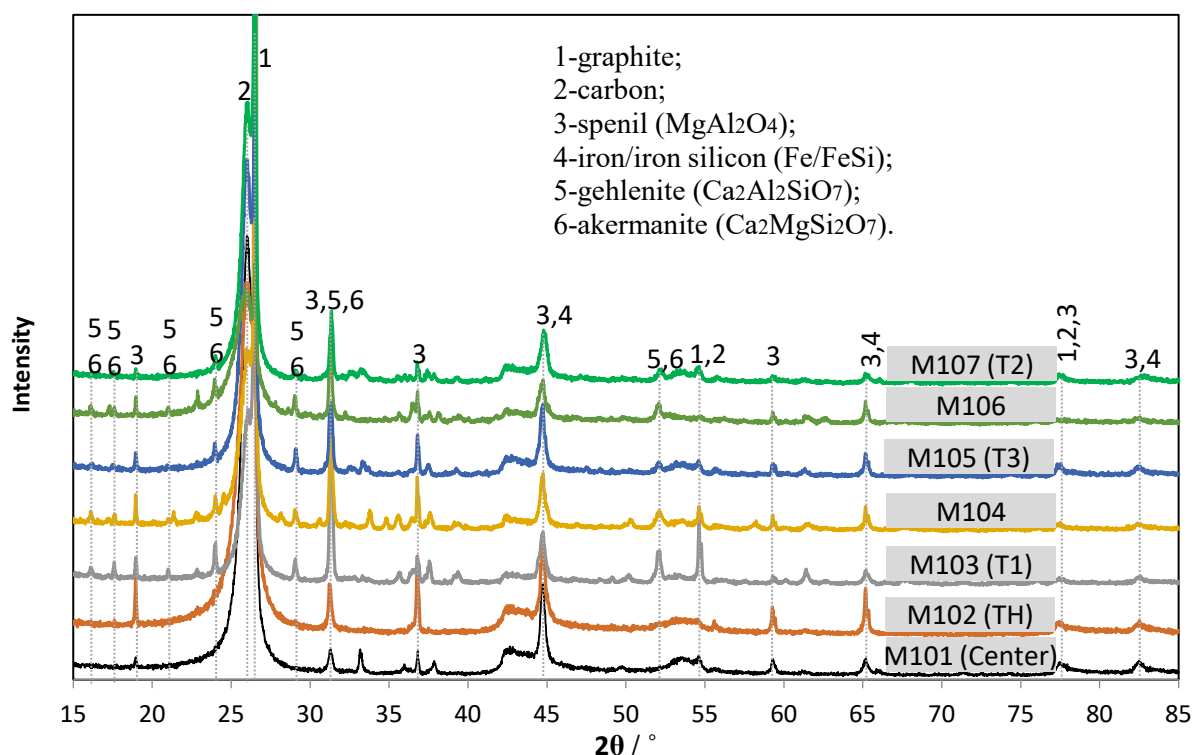


Figure 262: XRD analysis of the selected coke samples procured from first core drilling layer of the EBF hearth, campaign 32.

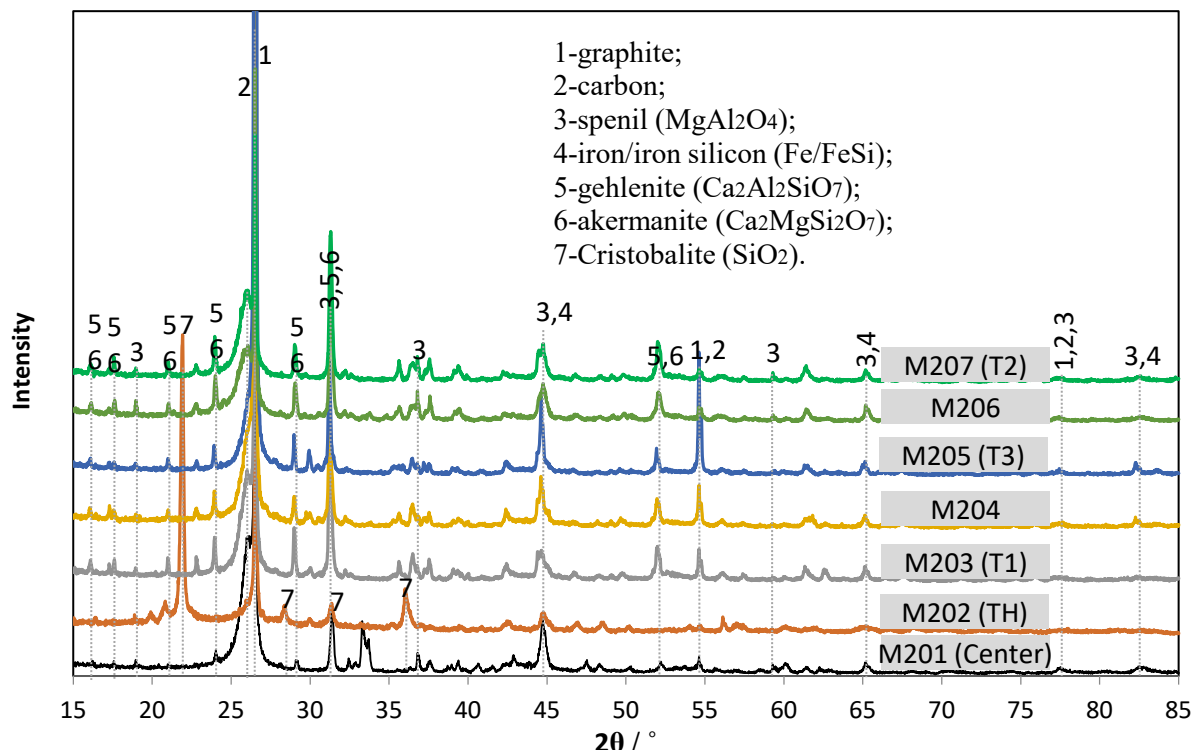


Figure 263: XRD analysis of the selected coke samples procured from second core drilling layer of the EBF hearth, campaign 32.

2.2.3.6.3 The void fraction of the coke bed

From the core drilling samples (shown earlier in Task 3.1) the coke bed porosity distribution was determined. The coke bed porosity is defined as the void divided by the total volume, i.e. an empty steel tube has a porosity value of 1.

The developed methodology will be presented briefly followed by the calculated results. In Figure 264 the cross-section of the center core drill for the first (upper) layer is shown. By looking at Figure 210 it can be seen, that the center tube was drilled completely into the coke bed. However, the tube is not completely filled with hearth material. The upper part, 0-6 cm, is filled with hydrograins (brown beads) and joint foam to fixate the material and ease the sub-sampling. This means that the material in the tube was compressed during the drilling; hence, the total tube volume should be used when calculating the porosity of the core drilling sample. Further, by evaluating all core drilling samples it was found that the proportion of fine grain material was higher in the bottom of each tube. This is reasonable, the vibrations and material movement forced by the drilling will make the smaller grains move downwards. Because of this, i.e. that the coke bed porosity calculated for each sub-sample (0-10 cm, 10-20 cm, 20-30 cm, 30-40 cm and 40-50 cm) is not representative for the bed distribution, the mean value of the complete core drilling samples was used.

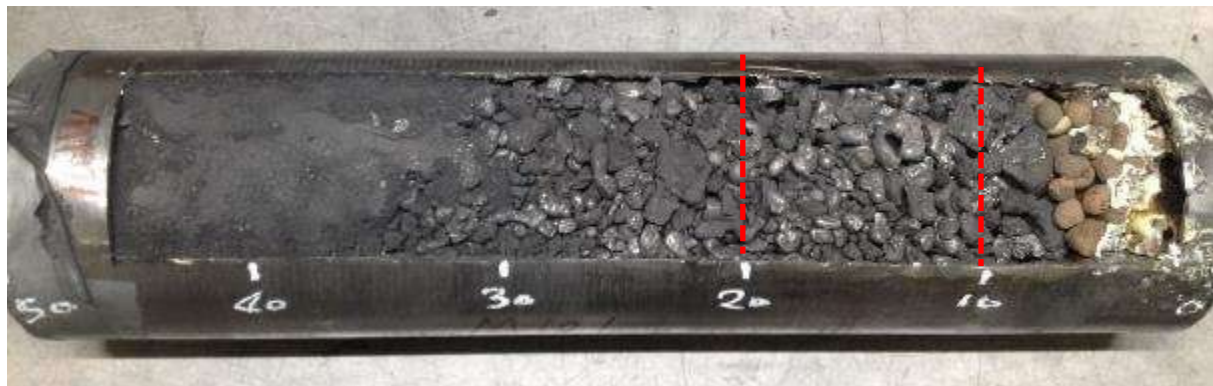


Figure 264: Cross sectional view of the core drilling sample M101 (first layer, center). The top of the sample is indicated by 0 and the lowest part by 50 (cm). The material between the red dashed lines illustrates the sub-sample 2 (10-20 cm).

Optimizing Blast Furnace Hearth Inner State (OPTIBLAFINS)

The categorization of sub-sample 2 (10-20 cm) and 5 (40-50 cm) for the M101 drill core is presented in Table 61 and Table 62, respectively. The categorization procedure is the same for all core drilling samples. The difference in grain size distribution is clear when comparing sub-sample 2 and 5, the fraction of small grains (<5 mm) are neglectable for sub-sample 2, while the same fraction amounts 39% of the total weight for sub-sample 5. By practical reasons only the total weight is measured for the smallest grain sizes. However, the fraction of coke for those grain sizes is of importance to determine the coke bed porosity, especially for the sub-samples in the bottom of the core drilling sample. Therefore, a distribution coefficient is calculated. The coefficient is based on the weight fraction of coke for the grain size of 5-10 mm. For the sub-samples presented in Table 61 and Table 62, the coefficient amounts 0.189 and 0.179, respectively. By averaging the fraction coefficient for all sub-samples and knowing the initial material volume in the steel tube the weight of the coke in the complete core drilling sample can be calculated. By knowing the coke density, the mean porosity for the core drilling sample can be calculated. Determination of the coke density was done in WP1, and it is explained under Task 1.3: Water model studies BF hearth. In the situation where aggregates were present in the sample; this was especially the case for core drills from the second layer, the same distribution coefficient was used to determine the coke weight in the aggregates for the particular sample.

Table 61: Categorization of sub-sample 2 (10-20 cm) from core drilling sample M101.

Size (mm)	Total weight (g)	Magnetic (g)	Coke (g)	Slag (g)	Aggregate (g)
>16	687	160	510	14	0
10-16	452	275	125	51	0
5-10	217	132	41	43	0
2.8-5	31	20			
1-2.8	4	0			
0.5-1	1				
<0.5	5				

Table 62: Categorization of sub-sample 5 (40-50 cm) from core drilling sample M101.

Size (mm)	Total weight (g)	Magnetic (g)	Coke (g)	Slag (g)	Aggregate (g)
>16	214	186	27	0	0
10-16	630	530	74	24	0
5-10	918	548	164	194	0
2.8-5	252	124			
1-2.8	139	74			
0.5-1	71				
<0.5	654				

The coke bed porosity for each core drilling sample from the first layer is presented in Figure 265 (left). No definitive trend regarding the coke bed distribution could be found for the first layer. The calculated porosity values are unevenly spread in the range of 0.31 to 0.66. Regarding fluid flow during tapping the second layer is of more importance; the liquid level in the hearth is mainly occurring in this part of the hearth. For the second layer different porosity zones were determined by averaging the porosity values calculated for single core drilling samples, see Figure 265 (right). Which core drilling samples to count to which zone was partly determined by the magnitude of the calculated porosity value, but also by the results from the copper injection and the associated flow field analysis (Task 3.2). The coke bed distribution for the second layer presented in Figure 265 is coincident with the interpreted flow field from the Cu-injection; the coke bed beneath the tuyeres seems be more resistant to fluid flow. Further, the center part of the hearth seems to be the least resistant to liquid fluid. With some slight simplifications the determined coke bed distribution for the second layer served as the target when building the coke bed of the EBF water model. The procedure of recreating the determined coke bed distribution is presented in Task 1.3: Water model studies BF hearth.

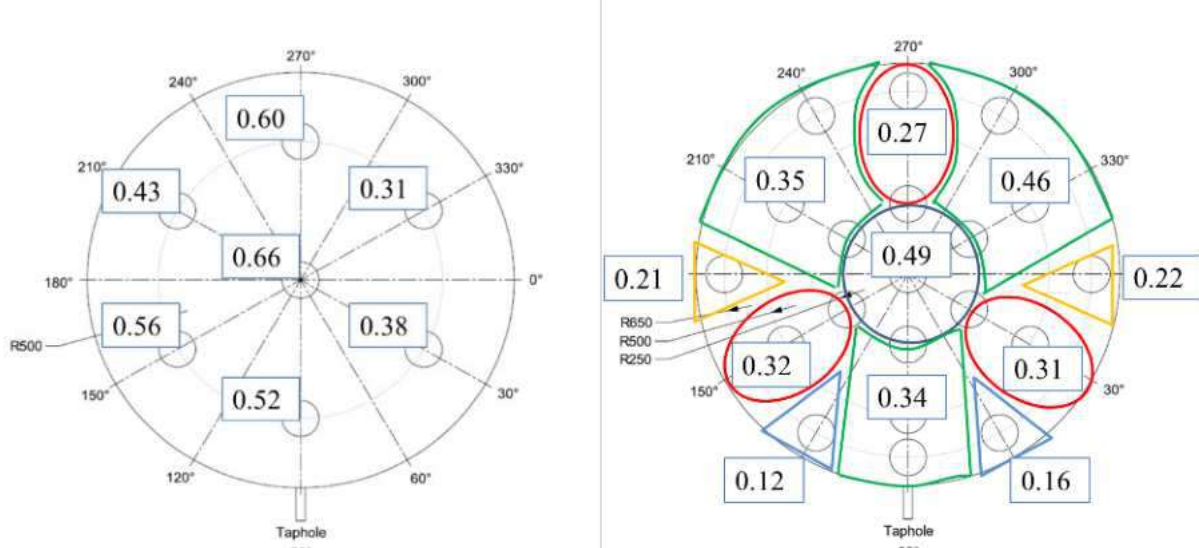


Figure 265: Coke bed porosity distribution for the first layer (left) and the second layer (right).

2.2.3.7 Slag and iron composition vs dead man state

2.2.3.7.1 Process conditions vs. EBF hearth conditions

The process conditions have substantial impact on the hearth conditions. To understand how the change of the process conditions could influence the hearth conditions, process data before the end of the campaign and hearth excavation data from campaign 31 and campaign 32 are collected. Campaign 31 is selected to be compared with the current EBF campaign 32, because it is believed that the process conditions from these two campaigns are quite different. One of the significant characteristics of the campaign 31 was that the three tuyeres were equipped with different lances: Tuyere 1 (T1) was equipped with a coaxial lance, tuyere 2 (T2) with a straight pipe with modified tip and tuyere 3 (T3) with the swirl-tip lance. In the coaxial gaps of the lances in T1 and T3 air was supplied. Comparison of the selected process parameters before the quenching of the two EBF campaigns is shown in Figure 266. It is seen that there are differences in the PCI rate and hot blast pressure during the EBF operation, even though the pressures at the top of the EBF and the cooling effects at the tuyeres were quite similar. Figure 267 and Figure 268 show the slag and iron compositions of selected elements/components as well as the temperature of the tapped slag and hot metal. It is seen that variations of the selected elements/components/ or temperature with time are much larger in campaign 32, while those in campaign 31 are much stable over time.

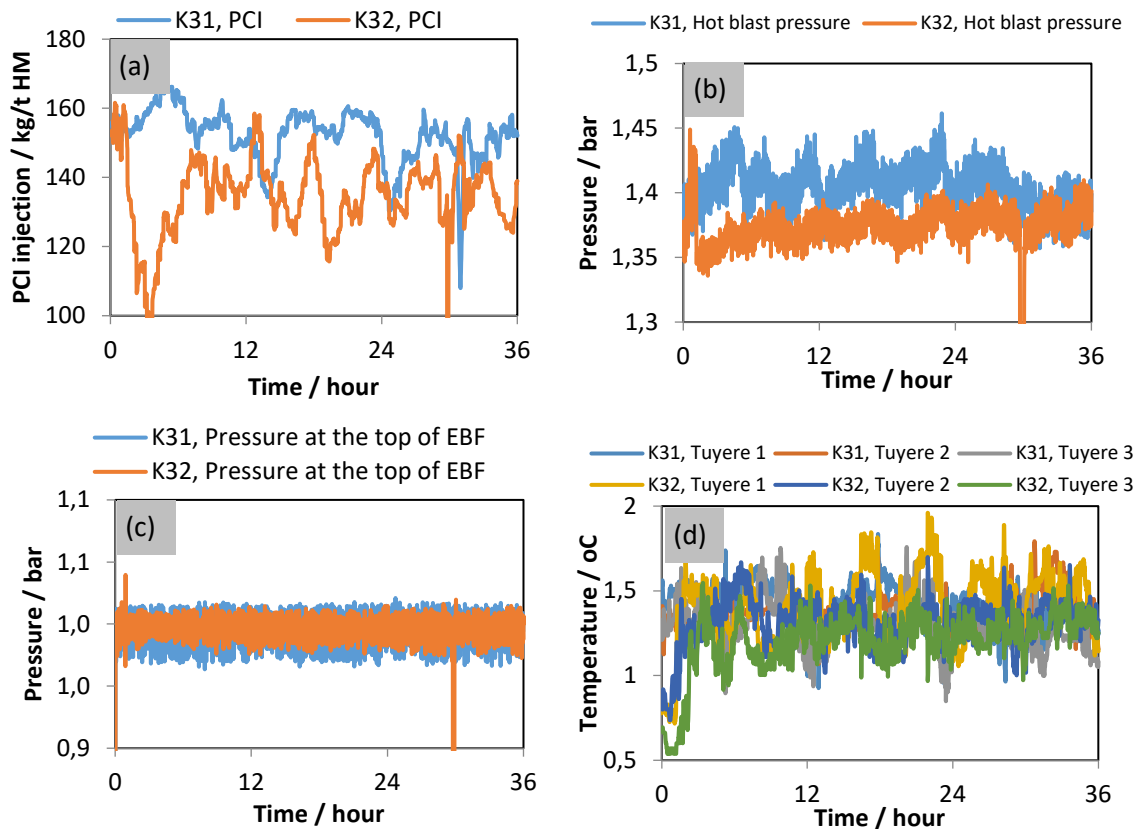


Figure 266: Selected process parameters 36 hours before the end of the EBF campaign 31 (K31) and campaign 32 (K32): (a) PCI rate; (b) hot blast pressure; (c) pressure at the top of EBF and (d) cooling effect at the tuyeres.

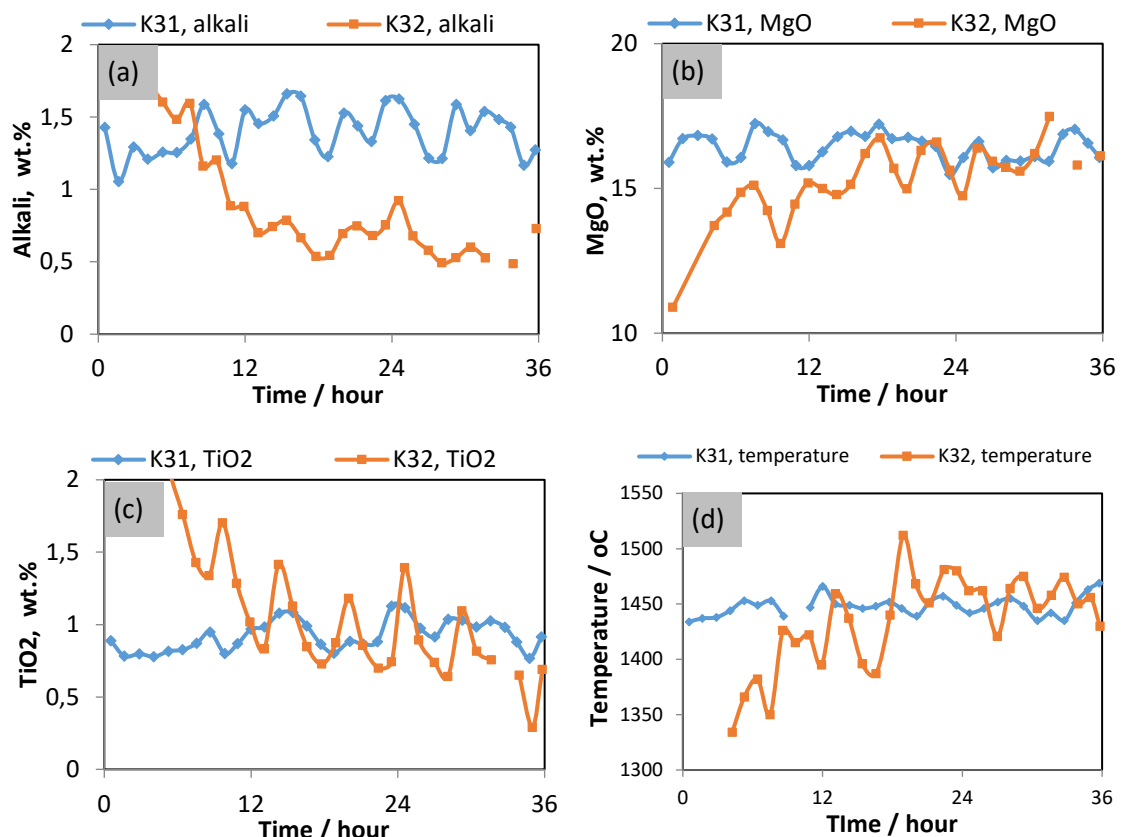


Figure 267: Variations of the selected elements/components in the slag 36 hours before the end of the EBF campaign 31 (K31) and campaign 32 (K32): (a) alkali in the slag; (b) MgO in the slag; (c) TiO₂ in the slag and (d) temperature of the tapped slag/hot metal.

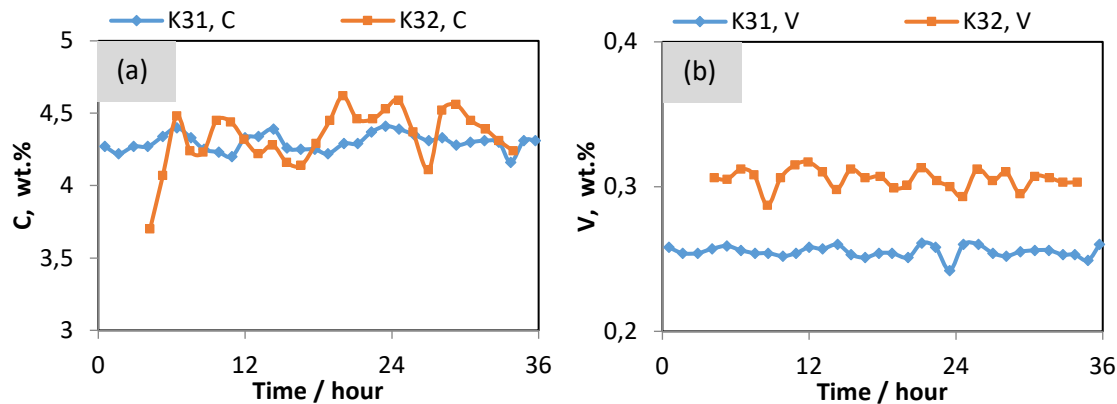


Figure 268: Variations of the selected elements/components in the hot metal 36 hours before the end of the EBF campaign 31 (K31) and campaign 32 (K32): (a) C in the hot metal and (b) V in the hot metal.

During the EBF campaign, the temperatures were measured by the thermocouples inserted into the side refractory wall and bottom refractory wall of the EBF hearth at different levels. Figure 269 shows the positions of the thermocouples in the side refractory wall of the EBF hearth. The logged temperatures by the 6 thermocouples (4 from the side and 2 from the bottom) before the end of the EBF campaigns are shown in Figure 271. It is seen that the logged temperatures from campaign 32 are lower than those from campaign 31. This indicates a colder hearth in campaign 32, especially in the area around the wall of the EBF hearth.

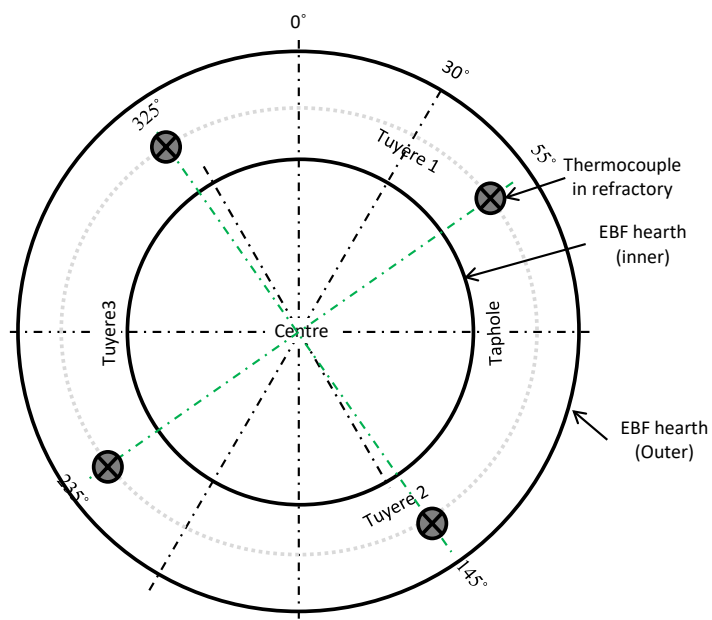


Figure 269: Illustration of the positions of the thermocouples into the refractory of the EBF hearth.

Optimizing Blast Furnace Hearth Inner State (OPTIBLAFINS)

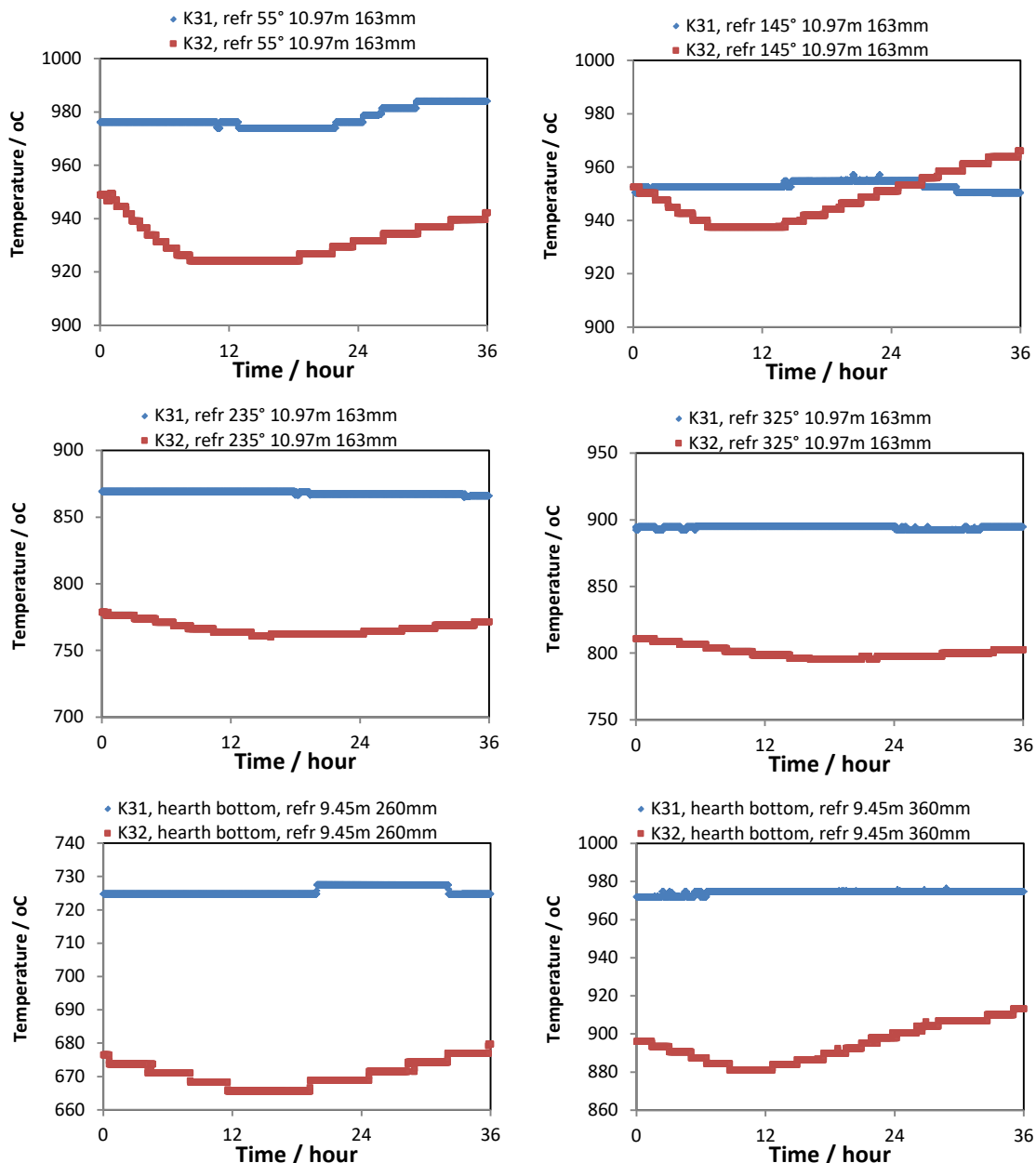


Figure 270: Variations of the measured temperatures into the refractory of the EBF hearth 36 hours before the end of the EBF campaign 31 (K31) and campaign 32 (K32).

Figure 271 shows the positions of the procured solid samples as well as the appearance of the core drilling into the EBF hearth (campaign 31). Compared with the core drilling of EBF campaign 32, it is seen that the drilling tubes in both first core drilling layer and the second one can be fully filled. This clearly indicates a completely different hearth condition.

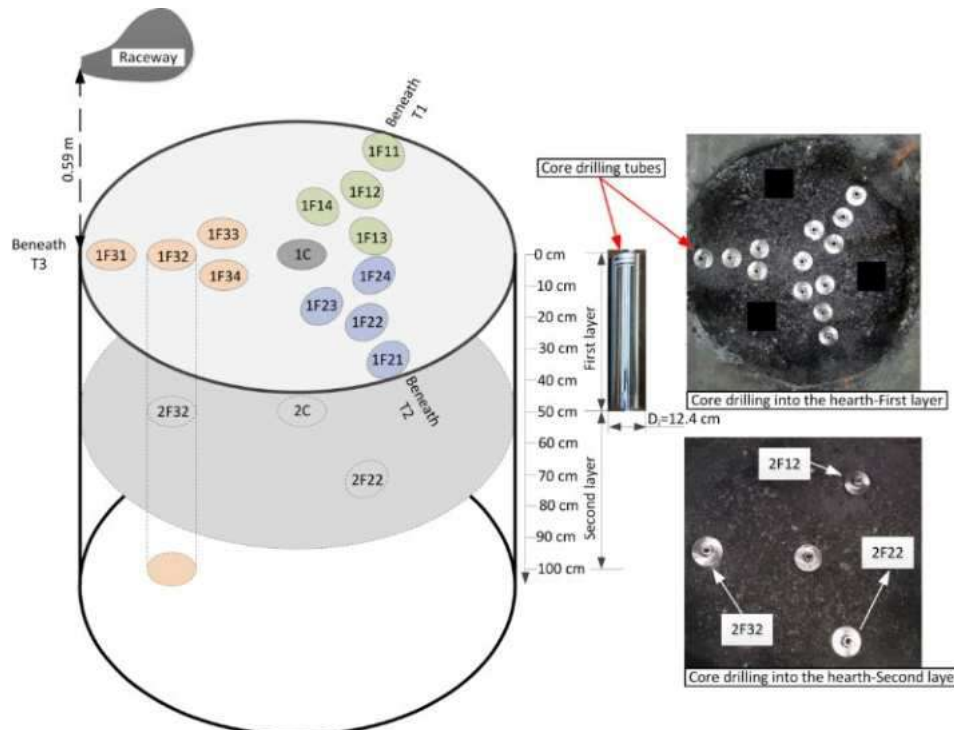


Figure 271: Procurement of core drilling samples into the hearth of the EBF, campaign 31 (T1-T3: tuyeres 1-3)

According to the process data and the data from the hearth excavation, following conclusions can be made:

- Differences in the process conditions have led to differences in hearth conditions.
- There may exist a solidified shell around the wall of the EBF hearth, and this could negatively influence the permeability of the dead man and flow of the hot metal and molten slag. This is reflected by the lower measured temperatures in the refractory of the EBF hearth, by the appearance of the core drilling tube in the EBF hearth (campaign 32) and by the absence of the Cu tracer in the manual samples.

2.2.3.7.2 Dead man versus liquid level

In order to better understand the performance of the hearth and drainage or iron and slag during the campaign, a balance-based on-line model of the liquid levels was developed. Such models have been proposed in the literature, but the way in which the balances are corrected has not been properly described, and most investigators simply seem to reset the signals occasionally. This is clearly not appropriate for an on-line mode, where a systematic treatment of the information is a prerequisite. Furthermore, in large blast furnaces with multiple tapholes, the conditions and liquid levels may vary in the different parts of the hearth. The model that was developed was based on the following main assumptions:

1. The hearth cross-section area (A) and dead man voidage (ε) are known and the dead man sits on the hearth bottom.
2. The hearth is divided into m pools, each representing a share, $s^{(j)} = \frac{A^{(j)}}{A}$, $j = 1, \dots, m$, of the hearth cross-sectional area.
3. The iron and slag flow between adjacent pools are proportional to the pressure difference between them, and to communication factors, φ_{ir} and φ_{sl} , respectively.
4. Estimates of the production rates of iron and slag, $\dot{m}_{ir,in}$ and $\dot{m}_{sl,in}$, are available from material balances.
5. Estimates of the tapping rates of iron and slag, $\dot{m}_{ir,out}$ and $\dot{m}_{sl,out}$, are available from measurements of the outflows.
6. The moment when both phases occur in the taphole sets a condition for the iron level in the tapping pool.
7. The tap ends when the slag surface in the tapping pool declines to the taphole.

The first assumption is introduced to simplify matters and since the analysis presented in subsection 3.2.4.1.2 indicated that the dead man in TSE BF7 is likely to be sitting. The assumption about multiple pools is motivated by the treatment of other investigators [95],[96] and also by observations of the drainage patterns in the furnace studied. Assumption 3, i.e., laminar flow, is

justified by a slow flowrate of liquids far from the draining taphole. Assumptions 4 and 5 are valid since TSE calculates on-line estimates of the hot metal and slag production and tapping rates. The sixth assumption is very central, and it is introduced to prevent drift in the iron level, and assumption 7 is a well-established fact based on fluid mechanics [99].

Figure 272 schematically depicts the system for a hearth with $m = 4$ pools based on the number of tapholes and their locations in BF7 (here just illustrating one of the liquids for clarity), each pool is characterized by its own iron and slag levels.

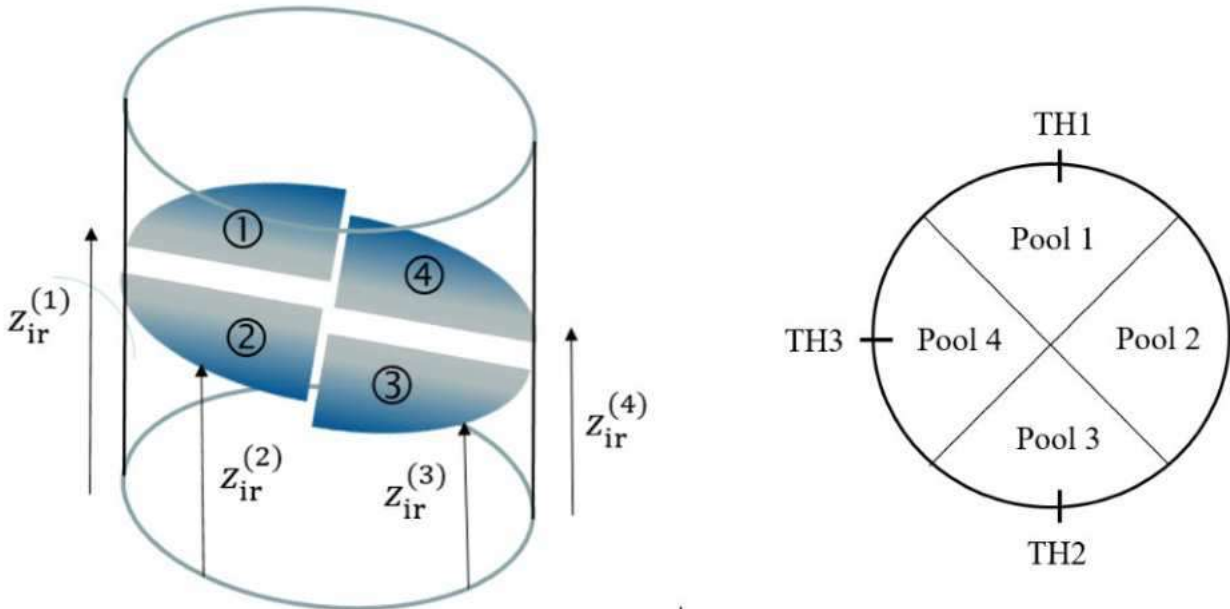


Figure 272: Schematic illustration of the iron levels in a four-pool liquid level model (left) with the three tapholes in the reference furnace indicated (right).

The liquid levels in the pools are expressed by differential equations:

$$\frac{dz_{ir}^{(j)}}{dt} = \frac{s^{(j)}\dot{m}_{ir,in} + \sum_{i \neq j}\dot{m}_{ir}^{(ij)} + \delta_{j,j^*}\dot{m}_{ir,out}}{\rho_{ir}A^{(j)}\varepsilon} \quad (56)$$

$$\frac{dz_{sl}^{(j)}}{dt} = \frac{dz_{ir}^{(j)}}{dt} + \frac{s^{(j)}\dot{m}_{sl,in} + \sum_{i \neq j}\dot{m}_{sl}^{(ij)} + \delta_{j,j^*}\dot{m}_{sl,out}}{\rho_{sl}A^{(j)}\varepsilon} \quad (57)$$

where the first term in the numerator of the right-hand-side expresses the liquid inflow (from above) to the pool, the second is the cross-flow while the third is the outflow if this is the pool that is being tapped (j^*). The Kronecker delta is defined as $\delta_{j,j^*} = 1$ if $j = j^*$, else $\delta_{j,j^*} = 0$, and the cross-flow between the pools is written as

$$\dot{m}_k^{(ij)} = \varphi_k L^{(ij)} \Delta p_k^{(ij)}; \quad k = ir, sl \quad (58)$$

with

$$\Delta p_{ir}^{(ij)} = g [\rho_{sl} (z_{sl}^{(i)} - z_{sl}^{(j)}) + \rho_{ir} (z_{ir}^{(i)} - z_{ir}^{(j)})]; \quad \Delta p_{sl}^{(ij)} = g \rho_{sl} (z_{sl}^{(i)} - z_{sl}^{(j)}) \quad (59)$$

In these equations, ρ_{ir} and ρ_{sl} are the iron and slag densities, g is the gravitational acceleration and $L^{(ij)}$ is the length of the segment between the pools, which is the hearth radius for neighbor pools and zero for non-neighbors. The factors φ_{ir} and φ_{sl} parameterize the communication rates between the pools, making it possible to consider impermeable zones or free channels between the pools. The liquid levels in the pools are obtained by integrating Eqs. (56)-(57) under boundary conditions. A complication is that drift in the levels must be avoided, so we correct the iron level of the draining pool for the last tapping so that it is at the taphole level at the moment when both iron and slag appear, as detailed below. For the slag end level in the draining pool, an estimate based on a flow-out coefficient-like expression [99],[97] and [98] is used. As it is unlikely that the inner end of the taphole wall/clay remains intact as the drill breaks through the lining, we introduce a band around the centerline of the (estimated) inner end of the taphole, $z_{th} \pm \Delta z_{th}$, as indicated by the insert in the right part of Figure 273, and assume that the two-phase outflow starts when the iron levels enters this band. A similar band around the estimated slag-end level is also introduced to consider uncertainty.

The tapped quantity of iron is weighed in torpedoes, so it is, despite occasional errors caused by, e.g., torpedo changes (see below) relatively accurate, while the tapped quantities of slag are much more difficult to measure accurately. The on-line estimates of the produced quantities are also somewhat uncertain. Therefore, the tapped quantities of iron were relied upon, subjecting the estimated iron production rate to correction. The production rate of slag was changed accordingly, after which the remaining balance error was addressed by correcting the slag outflow rate. The procedure for correcting the liquid levels is indicated schematically in Figure 273. The differential equations (56) and (57) are solved from the moment when both liquid phases appear in the taphole during the previous tap to the corresponding point for the present tap. The iron production and slag outflow rates are then adjusted gradually until the levels satisfy the criteria listed below.

For iron, three different cases are considered:

- i. Iron taps first: The slag in the draining pool is located above the taphole band, so the iron level is at the upper limit of the uncertainty band at the moment when slag enters the taphole. The iron inflow is corrected until this condition is met.
- ii. Iron and slag enter the taphole simultaneously: The iron level may fall anywhere within the taphole band at tap start. If the original level satisfies this condition, no correction is undertaken. If the original level is above (below) the band, a correction downwards (upwards) is made until the upper (lower) limit of the band is reached.
- iii. Slag taps first: The iron in the draining pool is located below the taphole band, so the iron level should be at the lower limit of the band at the moment when iron enters the taphole. The iron inflow is gradually corrected until this condition is met, but to account for the lifting effect of the outflowing slag, the taphole band is extended downwards by Δz_{lift} .

For slag, the condition is less complicated: the slag level at the end of the previous tap is required to enter the uncertainty band around the target level, i.e.,

$$|(z_{\text{sl}}^{(j^*)} - z_{\text{th}}^{(j^*)}) - z_{\text{sl,end}}| \leq \Delta z \quad (60)$$

where the target

$$z_{\text{sl,end}} = \omega^{(j^*)} \frac{\dot{m}_{\text{sl,out}}^{(j^*)}}{\rho_{\text{sl}} A^{(j^*)} \varepsilon} \quad (61)$$

is taken to be proportional to the average descent velocity of the slag level in the draining pool. In this declivity expression of the slag surface, there is a model parameter, ω , that controls the final slag end level. The above procedure results in two corrected liquid level evolutions, as indicated schematically by the dashed lines in Figure 273.

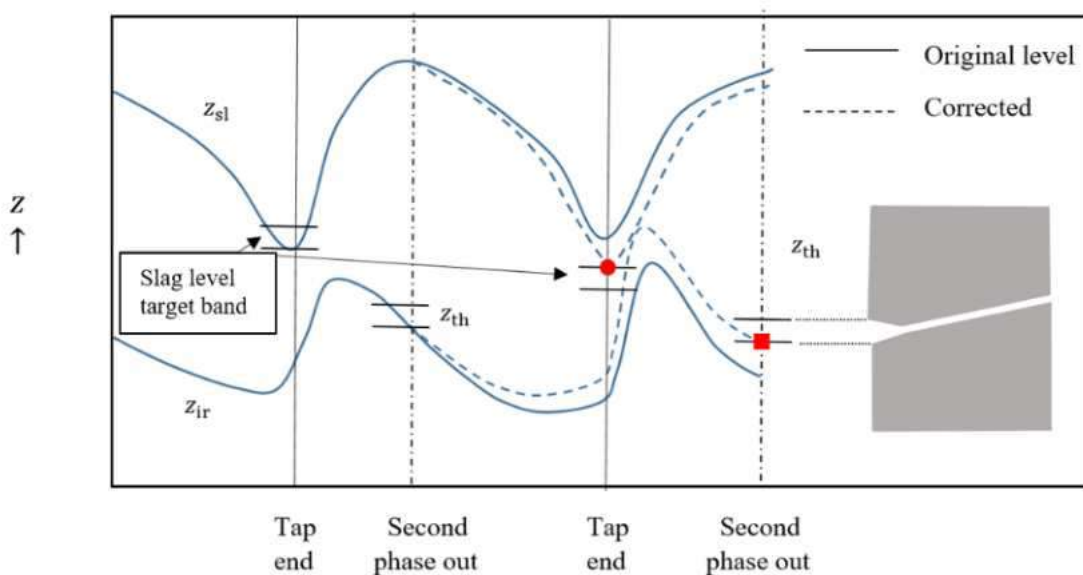


Figure 273: Principles of corrections in the model, with vertical lines denoting important times for the corrections and horizontal lines denoting the bands around the taphole and the estimated slag-end level. The insert in the right part of the figure indicates the idea behind the band of uncertainty around the inner end of the taphole.

In the results to be presented, the hot metal outflow rate was pre-filtered before the signal was fed into the model, as it was found to be occasionally seriously disturbed, and the disturbances obviously occurred in conjunction with torpedo changes. The blue line in Figure 274 illustrates the reported hot metal outflow rates for seven consecutive taps, where large spikes are seen to occur

once or twice per tap. Such sudden changes are clearly too high to be physically feasible. An algorithm was designed to detect and remove unreasonable changes, yielding the signal depicted in red in the figure: for periods without large changes, the original signal was retained so the blue line falls behind the red one. Figure 275 illustrates an example of the estimated production rates (dashed lines) and outflow rates (solid lines) of iron (blue) and slag (red) for a tap, where spikes in the iron outflow at two torpedo changes have been removed.

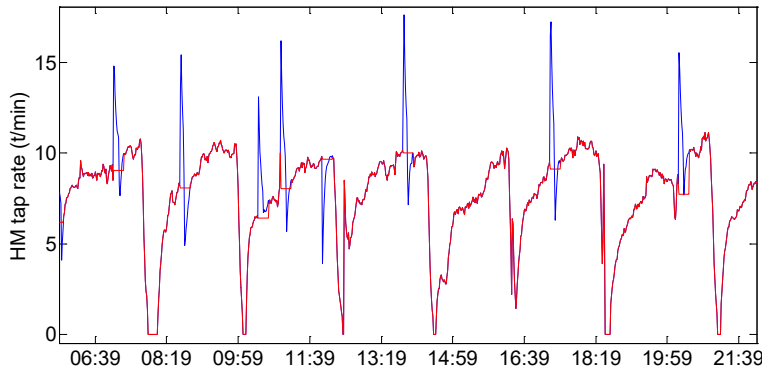


Figure 274: Iron outflow rate in BF7 reported in the data base of TSE (blue lines) and the revised signal after removing spikes at torpedo changes (red lines) for a period of two shifts (the two signals overlap most of the time).

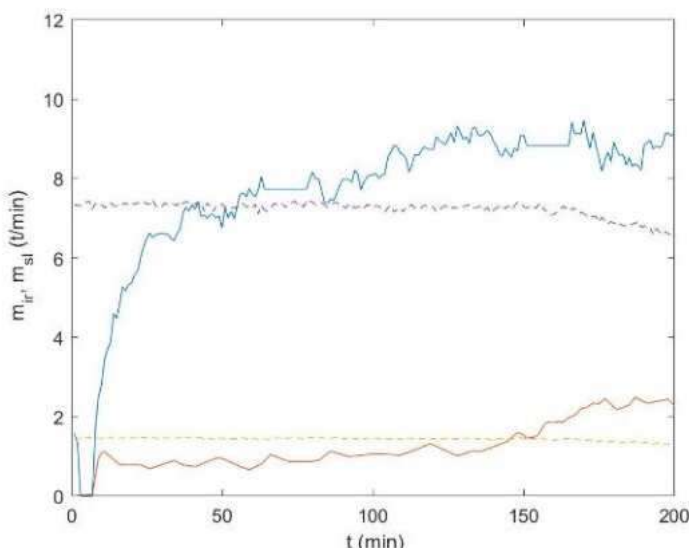


Figure 275: Estimated outflow (solid lines) and inflow (dashed lines) rates of iron (blue) and slag (red) for a tap at TSE BF7. At the end of the period, a decrease in production rate is seen. The periods with constant iron outflow are the result of the correction algorithm.

The model is based one-minute values of the variables retrieved from the TSE data base. A period of three months of data from early 2016 for BF7 was used to study the model, dividing the hearth into four pools representing the three taphole regions and one non-draining region (cf. right panel of Figure 272). The different regions were taken to represent equal shares of the cross section ($s^{(j)} = \frac{1}{4}$ in Eqs. (56)-(57)).

Two examples are presented here where the pool communication factors were set to $\varphi_{ir} = 2.8 \cdot 10^{-4}$ s and $\varphi_{sl} = 1.4 \cdot 10^{-4}$ s, yielding pools showing some level differences, and the slag-end level parameter in Eq. (61) was set to $\omega = 20$ min for all four pools. The period studied has a duration of 2000 minutes and comprises 14 tap cycles, where the two opposite tapholes (TH1 and TH2) are operated. Figure 276a illustrates the liquid levels in Pool 1 (Blue solid line), Pool 2 (black dash-dotted line), Pool 3 (red dashed line) and Pool 4 (magenta dash-dotted line). Due to symmetry of this system, the two dash-dotted lines fall on top of each other, so the black line is not seen in this figure. The end levels for both iron and slag exhibit some drift from one tap to another but stay within reasonable limits due to the corrections. The levels naturally vary most in the pool that is being tapped. A stronger slag outflow for some taps (5, 7 and 13) yields a higher slag-end level. Figure 276b shows how the bands around the taphole and slag-end point vary, where red squares

and circles indicate the places where the iron-slag and slag-gas interfaces of the draining pool are at the end of the period after (possible) correction. The level of the iron band is constant since the taphole lengths stay practically unchanged, but the shifts in the slag-end level bands are considerable. The lower slag-end levels primarily occur in Pool 3 (taps 1, 3, 5,...), where TH2 drains more slag than TH1 in Pool 1. Figure 276c shows the corrections of the mass of produced iron (black bars) and tapped slag (red bars), revealing that the iron balance is satisfied exceptionally well, but that slag corrections are needed for all taps. Two slag taps (3 and 13) require corrections exceeding 50 tons, both in the negative direction, indicating that the reported outflow rate is too large. It is seen that the two major iron corrections occur simultaneously, but in the opposite direction (since the inflows of iron are corrected).

The first example was characterized by relatively small corrections without clear trends. Figure 276d shows results for another 2000-minute period, where the neighbor pools Pool 1 (blue solid lines) and Pool 4 (magenta dash-dotted lines) are tapped. Their drainage patterns show large differences. A lower tapping rate of slag in Pool 1 makes TH1 drain slag to lower levels than TH3 in Pool 4. Some more variation in the inner levels of the tapholes are seen in Figure 276e and the lower slag-end levels for taps 1, 3, 5 and 7 from TH1. As seen in Figure 276f, nearly all iron taps are smaller than expected, leading to a correction that decreases the production rate, while the taps of slag generally show alternating positive and negative corrections. Such non-uniform drainage of slag has been reported by Iida and co-workers [96], who attributed it to drainage from zones of different size separated by a low-permeability region. However, such behavior may also be caused by different coke-bed permeability in front of the two operating tapholes, as discussed below.

To gain more experience about the required corrections and how they are affected by the model parameters, four different periods, each spanning 40 consecutive taps, were studied. Period 1 corresponds to the end of a course of time when the adjacent tapholes TH2 and TH3 operate, Periods 2 and 3 to the initial and final part of a stage of operation of the opposite tapholes, TH1 and TH2, while Period 4 corresponds to the initial part of a course of time when TH2 and TH3 operate. The upper panel set of Figure 277 depicts the corrections that arise when the slag-end level parameter in Eq. (61) was, like in the examples above, set to $\omega = 20$ min for all four pools, with iron corrections depicted above the corresponding slag corrections in the subpanels. The results indicate that the iron and slag corrections are independent. The correction of the iron balance sometimes shows negative terms followed by positive terms, or vice versa, while the slag shows more stochastic corrections. However, for Periods 2 and 4 the two operating tapholes alternately drain more and less slag than the average. Even though different taphole pairs operate at these periods, TH2 is the one draining more slag in both cases. This may indicate that the local conditions in the pools are different. It is also interesting to note by comparing the results for Periods 2 and 3 that the drainage pattern seems to change during the time when these two tapholes are operated, indicating that structural changes of the dead man may appear as the taphole pair has been operated for some time.

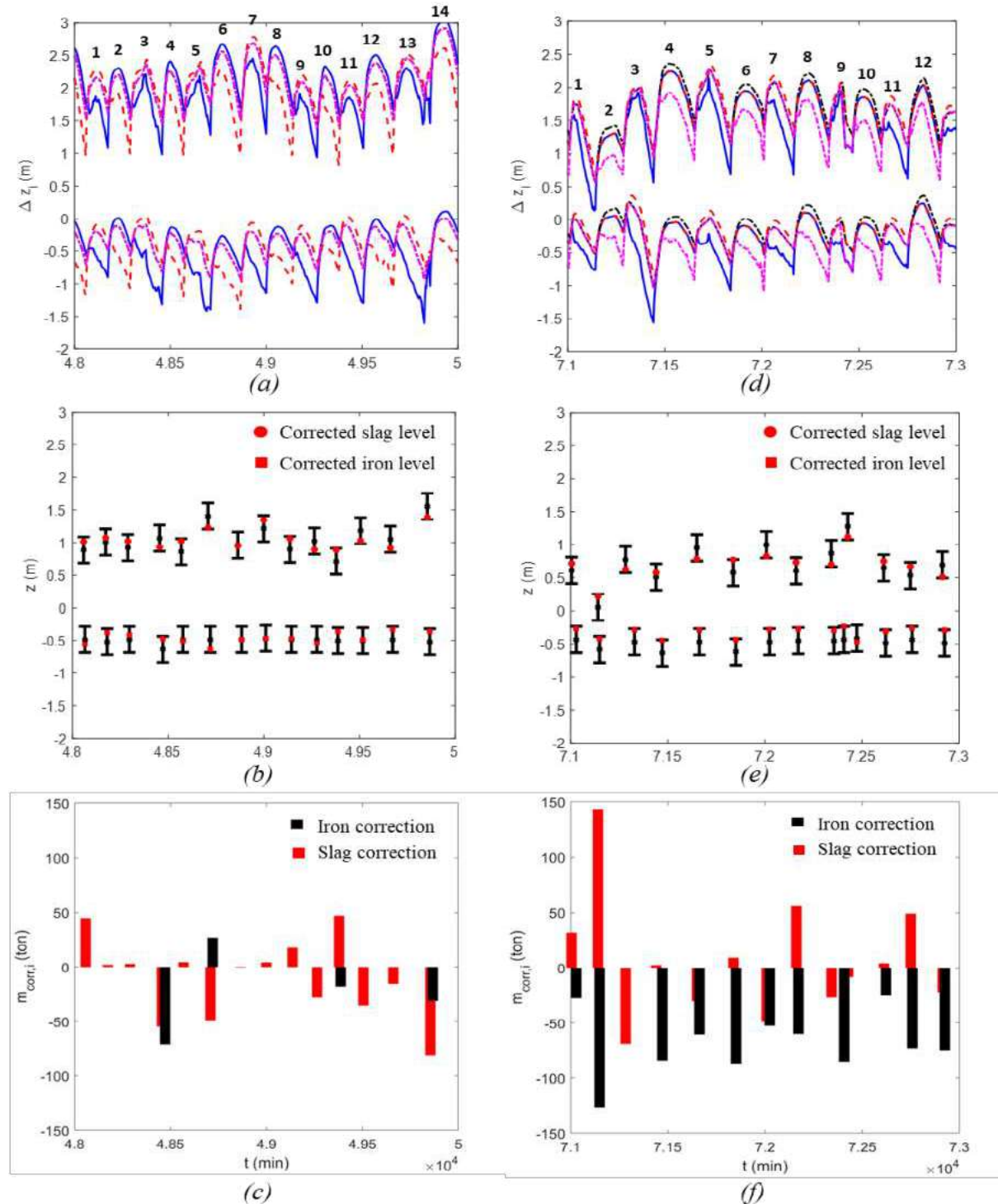


Figure 276: Estimated liquid levels (a and d), location of bands around the (inner end of) the taphole and the nominal slag-end level (b and e) and correction of the mass of produced iron and tapped slag (c and f) for a period where pools 1 (TH1) and 3 (TH2) were operated (left panels, a-c), and for a period where pools 1 (TH1) and 4 (TH3) were operated (right panels, e-f). Pool 1: blue solid line, Pool 2: black dash-dotted line, Pool 3: red dashed line, and Pool 4: magenta dash-dotted line.

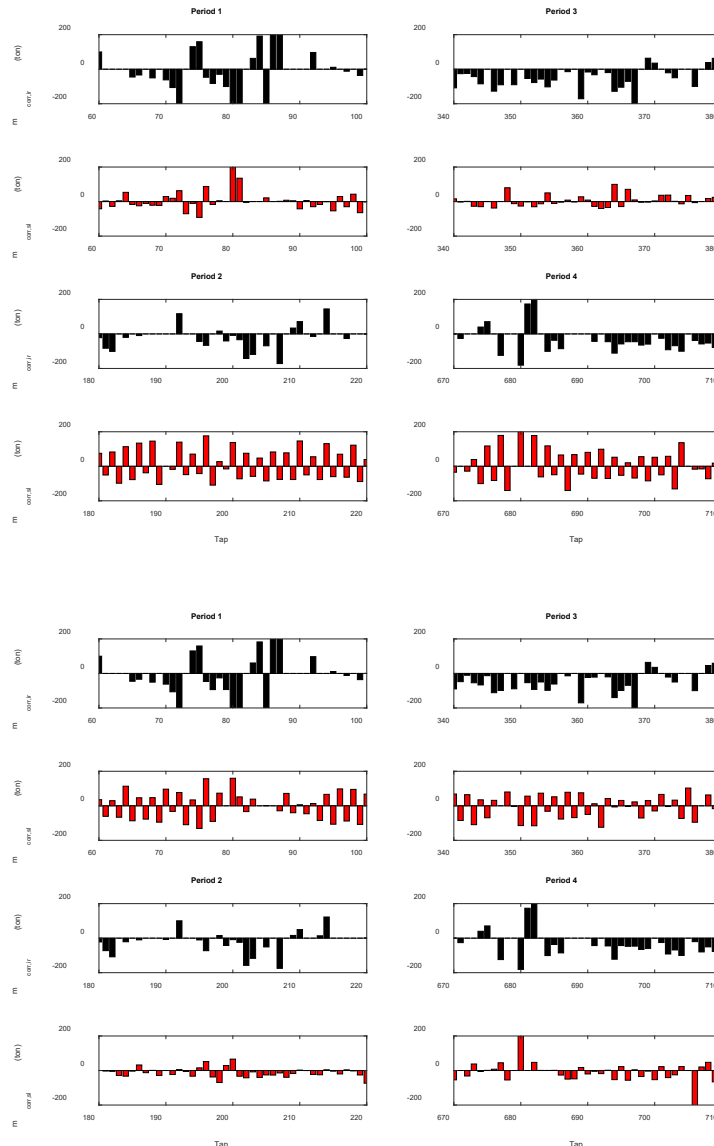


Figure 277: Corrections of the mass of produced iron (black) and tapped slag (red) for four different periods. Top panel set: Slag-end level parameter $\omega^{(j)} = 20 \text{ min}$; $j = 1, \dots, 4$. Bottom panel set: $\omega^{(1)} = \omega^{(4)} = 20 \text{ min}$ and $\omega^{(3)} = 5 \text{ min}$ in Eq. (61).

To test the hypothesis that the slag-end level may explain the differences in the required slag corrections, the parameters in Eq. (61) were changed to $\omega^{(1)} = \omega^{(4)} = 20 \text{ min}$ and $\omega^{(3)} = 5 \text{ min}$. The lower value for Pool 3 (drained by TH2) could reflect a lower coke-bed voidage in front of this taphole or that the dead man contact with the inner end of the taphole is poor, yielding a smaller declivity of the slag-gas interface towards the taphole at the end of the tap. The hypothesis is schematically illustrated in Figure 278. The resulting revised iron and slag corrections for the four periods are depicted in the lower panel set of Figure 277. It is interesting to see, that this parameter change has practically eliminated the alternating corrections in the slag balance for Periods 2 and 4, but now Periods 1 and 2 instead show alternating slag corrections. An explanation of these observations may be as follows: The dead man in front of TH1 (draining from Pool 1) and TH3 (draining from Pool 4) is denser compared to the conditions in Pool 3 in front of TH2 during periods 2 and 4, but not in Periods 1 and 3, where the taphole pairs have been operated a few weeks. One may suggest that the conditions above TH1 and TH3 lead to a low coke-bed permeability in front of the taphole, but along with the operation of these tapholes the permeability gradually improves. Possible reasons for the differences in the bed permeability can be, e.g., differences in operation of the tuyere/raceways above the tapholes, including blast acceptance, pulverized coal injection rate, or partial tuyere clogging of individual tuyeres. An indication of the local conditions can also be obtained by analyzing the results of the wear model. Figure 279 shows the wear/skull state predicted by BFHEM along the three radial cuts through the taphole lines for a day in March 2016, indicating that there is clearly more skull on the wall in the regions of TH1 and TH3, while the skull layer is thin at TH2.

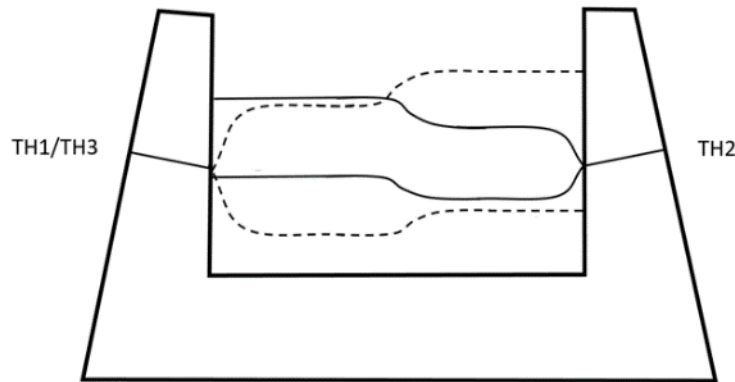


Figure 278: Schematic of the expected end state of liquid levels for the case where the coke-bed permeability in front of one taphole (here TH2) is higher than in front of the others (TH1 and TH3), yielding smaller bending of the iron and slag surfaces.

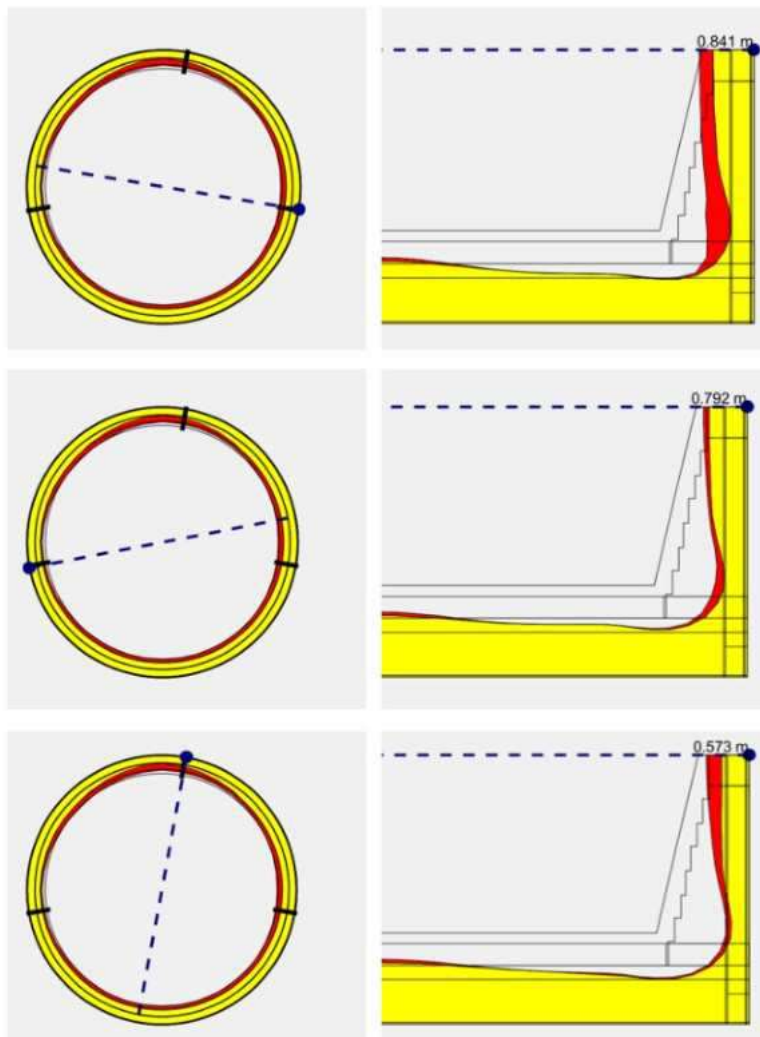


Figure 279: Vertical cross-sections along three radial lines going through the tapholes (top: TH1, middle: TH2, bottom: TH3) for TSE BF7 for a day in March 2016 reconstructed by BFHEM.

In summary, the model has provided further insight into the dynamics of the hearth liquids in the TSE BF7, and, in particular, shed light on possible reasons for the different patterns of drainage observed for the tapholes. Another possible use of the liquid level model is to apply it to tap-end prediction. This option, and more details about the model, are presented in reference [101].

2.2.4 Work Package 4: Operational data interpretation

2.2.4.1 On-line Multiphysics Hearth Monitoring Model for wear and stress and hearth erosion/build-up estimation during a full campaign

2.2.4.1.1 On-line Multiphysics model

The multiphysics model, developed in section 3.2.1.1., for thermal stresses has been connected to the on-line database of the AGDH and AMEH plants. Graphical User Interfaces (GUIs) have been developed for visualization of results and for warning operators about skull/gap/brittle layer/stress in the hearth lining. The model can prognose the expected hearth thermocouple/strain-gauge readings. The model capability to consider influences of different liquid levels are presented in section 3.2.1.1. The remaining campaign life is estimated using the average wear rate and thinnest wall thickness. The statistical tools developed in section 3.4.2.2 have been converted to on-line plausibility algorithms and implemented as a plausibility module for the measurements. BFI has developed and installed the multiphysics hearth monitoring model at AGDH BF4 and AMEH BF5A. AGDH and AMEH have provided the hardware and software as well as the interface to supply the needed BF data and VPN connections between BFI and plants.

The time evolution of the measured temperature and computed values (e.g., plausibilities, wear, skull, etc.) can be evaluated using the GUI shown in Figure 280. This GUI is developed in MATLAB® environment. The vertical section of interest is chosen using the radio buttons and the thermocouple (TC) positions or wear vectors of interest are selected using the checkboxes. These individual selections can be visualized by pressing the corresponding button. The neighbouring small “All” buttons plot all variables at each of 12 sections in a separate plot for a quick overview. All figure windows can be closed by using the “Close All Figures” button. The time evolution of the average wear rate and thinnest wall thickness together with the estimation of remaining campaign life can be seen by clicking the “Plot Relining Estimation (extrapolation)” button.

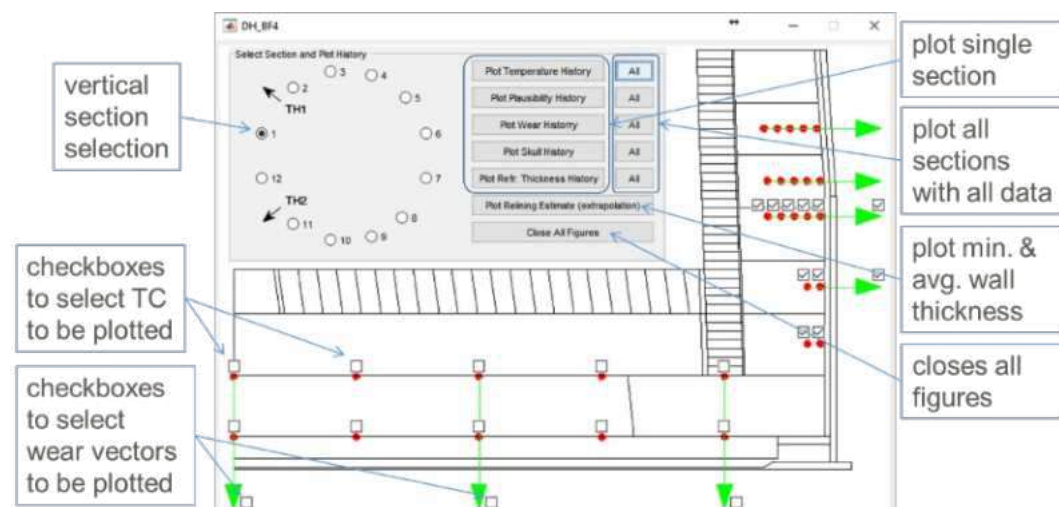


Figure 280: Improved GUI for the time evolution of wear and residual wall thickness.

Several examples of such time evolution plots are shown below in Figure 281. It can be easily seen in the temperature evolution plot that the multipoint thermocouples at section S1 are all failing. The failing TCs are recognized by the plausibility algorithm and their contribution to wear model is reduced. The wear model computed data (e.g., wear vectors, skull, residual wall thickness) are shown for the computed date range (from 01.01.2017 to beginning of Jan. 2017). The estimation of next relining is based on an extrapolation of the wear rates. It simply averages the wear rate of all wear vectors. Then, it assumes that the thinnest part of the wall would erode at this rate in the future to estimate the remaining life time. However, this might be misleading especially when all the TCs along some wear vectors fail and the computed local wear is not reliable at all at this region, so the results must be carefully interpreted.

The wear model results for a selected date can be evaluated using the GUI shown in Figure 282. Many visualization options are available and listed on the left side of the GUI. A copy of the solved COMSOL model file can be saved using the “Save As” option in File menu. This is useful for further thermomechanical analysis of the hearth using the COMSOL Multiphysics®. The date of interest is chosen using the pull-down combo-box and loaded by clicking the “Load” button. The vertical section position as well as the cut-line position can be freely given. The interactive graphics allow

Optimizing Blast Furnace Hearth Inner State (OPTIBLAFINS)

zooming, panning, exporting, etc. Moreover, this GUI can be opened using a web-browser by any device which is connected to the intranet.

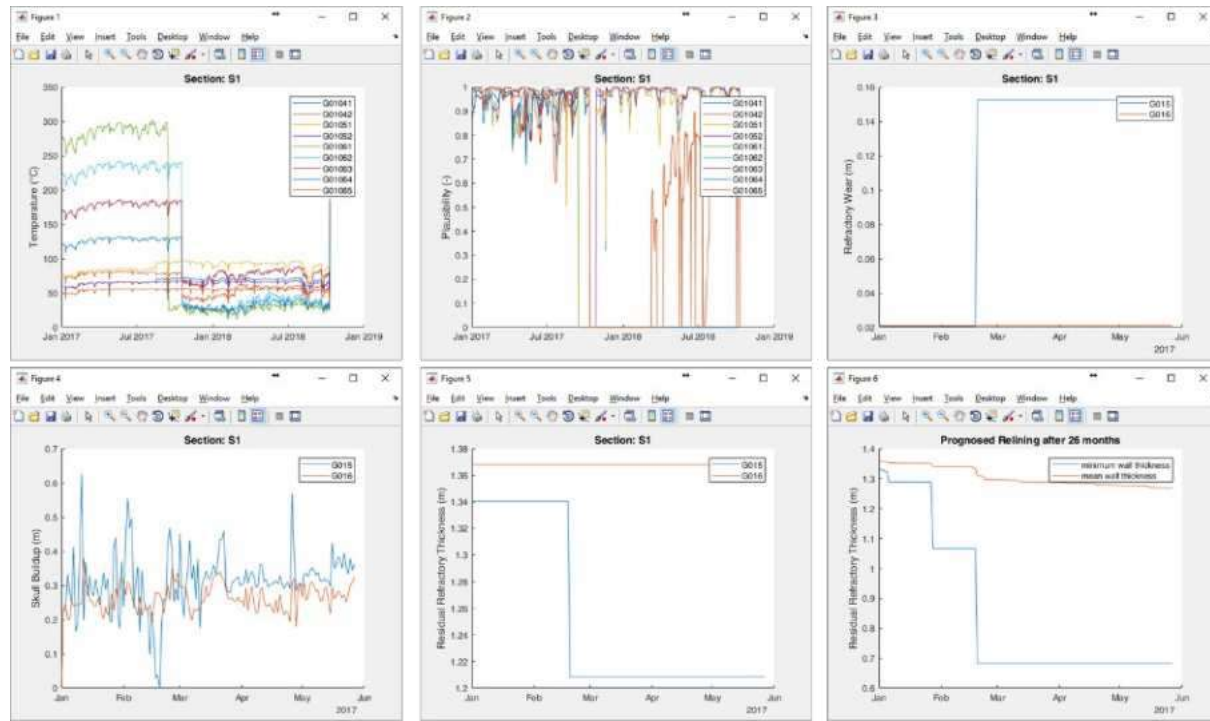


Figure 281: Several examples of time evolution visualizations.

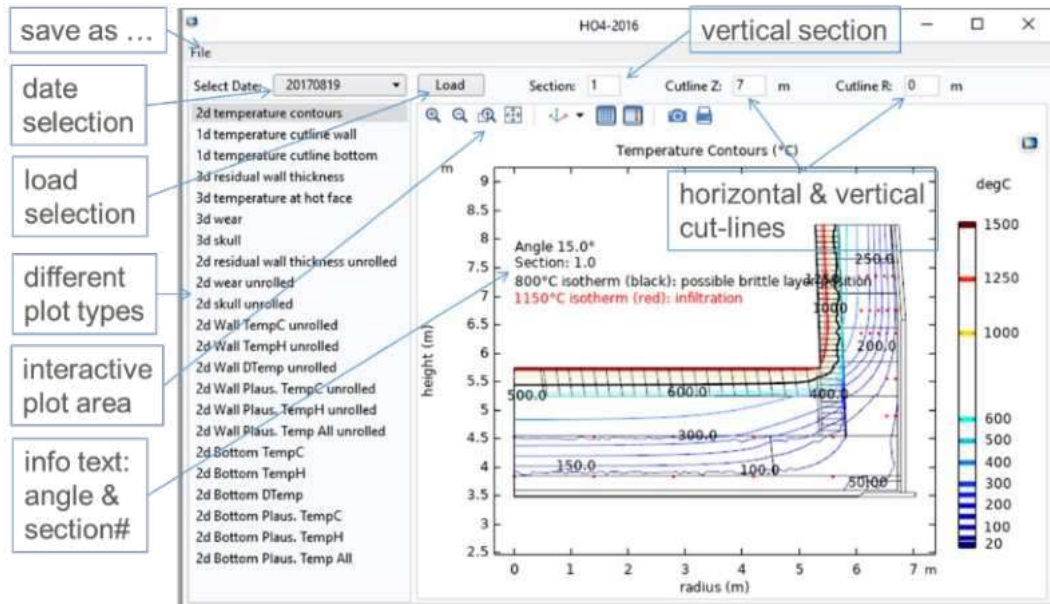


Figure 282: Visualization-GUI for a selected date.

As examples, the temperature contours at the vertical section S1 are shown in Figure 282, and the temperature along a horizontal cut-line at hearth wall and vertical cut-line at hearth bottom are presented in Figure 283. The temperature jumps are the results of the thermal resistance of the gaps between different refractory layers (e.g., ceramic cup and carbon blocks). This may influence the bottom TC measurements since the bottom TCs are exactly placed at the interface between the carbon blocks. The measured temperature can vary depending on its contact to which carbon block. The thermal resistance of these interface layers is calibrated with the TC measurements for the "no wear state" after relining. 3D contour plots shown in Figure 284 at the hearth inner surface allow the operator to identify the critical sections of the hearth. The position of tapholes (THs) are shown as annotation text to orientate.

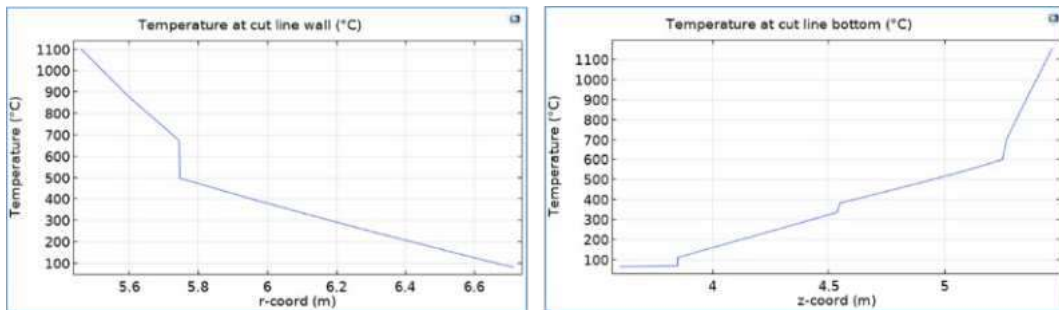


Figure 283: Cut-line visualizations for a selected date.

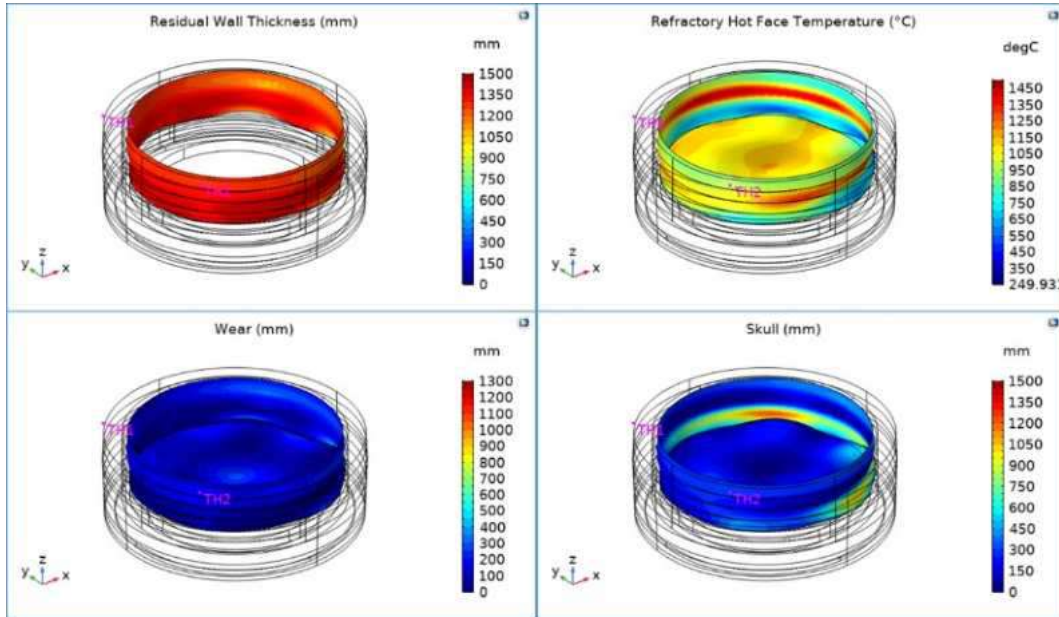


Figure 284: 3D Visualizations for a selected date.

As an alternative to such 3D plots, unrolled 2D contour plots, as exemplified in Figure 285 at the hearth inner surface, allow the operator to identify critical sections of the hearth. The position of tapholes (THs) as well as vertical section names are shown as annotation text to orientate. The black points mark the TC positions on the contour plots.

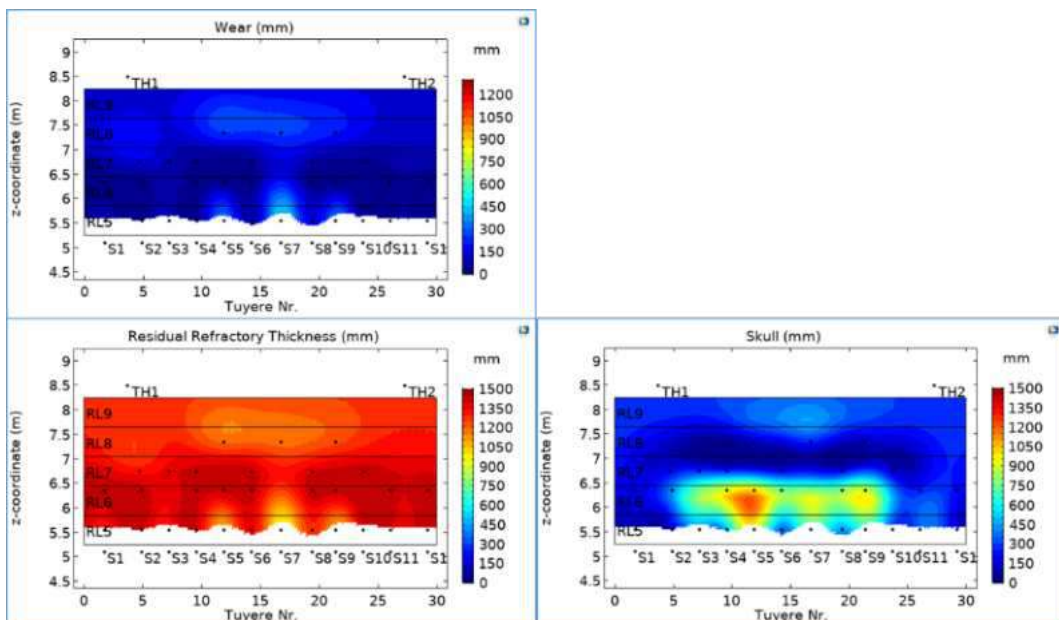


Figure 285: Unrolled 2D visualizations for a selected date.

In addition to the plots of all these computational results, measured temperatures and their plausibilities are also visualized. The temperatures in the hearth wall and bottom are grouped into two categories, as cold side TC with TempC and hot side TC with TempH (Figure 286). The outermost two TCs of multipoint TCs are used for the temperature visualization since their depths

Optimizing Blast Furnace Hearth Inner State (OPTIBLAFFINS)

are compatible with the double TCs. The temperature difference between the TempH and TempC, and the plausibilities are plotted in Figure 287 for the hearth wall. The temperature difference can be negative for some failed TCs. A cut-off value of 0°C is applied to keep the contour range visually nice.

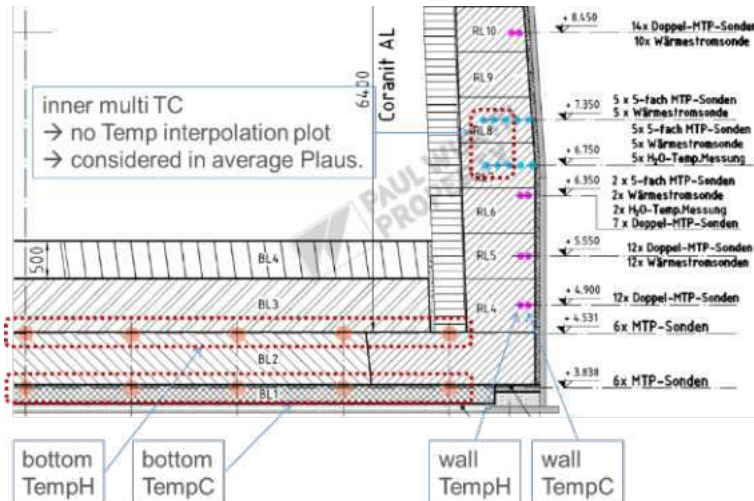


Figure 286: Explanation of visualizations of measured temperatures and plausibilities.

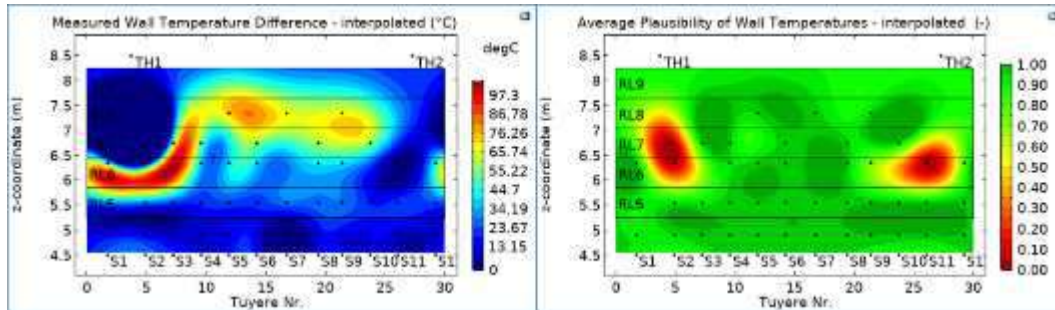


Figure 287: Visualizations of measured temperature differences and average plausibilities at hearth wall.

The interpolated measured temperature plots in Figure 288 and Figure 289 are useful to identify the hot spots, which should correspond to high-wear locations. The measured temperature and computed plausibility values are shown as annotation text next to the TC positions (Remark: The texts overlap here because of small figures. They do not overlap on the PC monitor.)

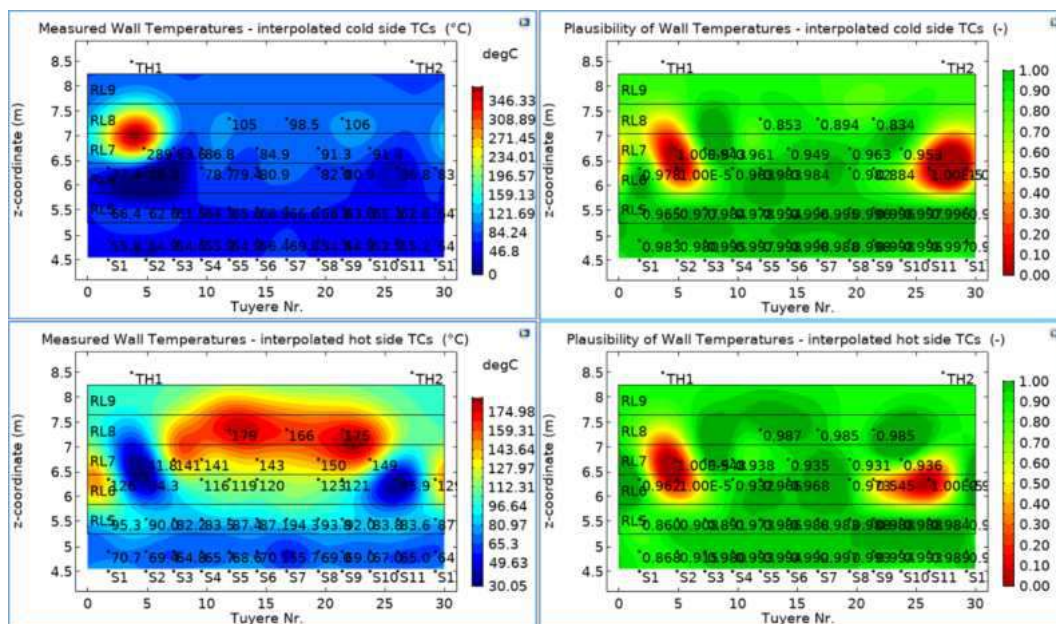


Figure 288: Visualizations of measured temperatures and plausibilities at hearth wall.

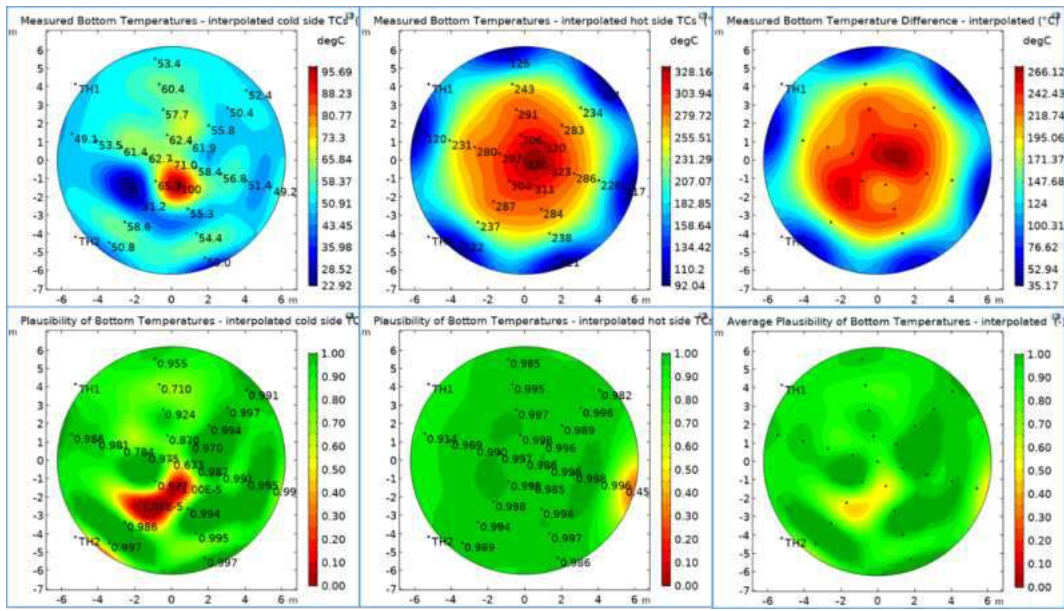


Figure 289: Visualizations of measured temperatures and plausibilities at hearth bottom.

2.2.4.1.2 Two-dimensional static hearth model in operation

A two-dimensional static hearth wear model, BFHEM, developed in earlier research efforts [60] has been adapted to BF7 of TSE, IJmuiden, by including information about the lining materials (geometry and heat conductivity) and from more than 300 thermocouples (locations, measured temperatures). The left part of Figure 290 shows the levels of the thermocouples and their general location in the sidewall, and the outer part of the bottom, while the locations on a specific vertical level (+1650 mm) in the bottom are depicted in the right part of the figure.

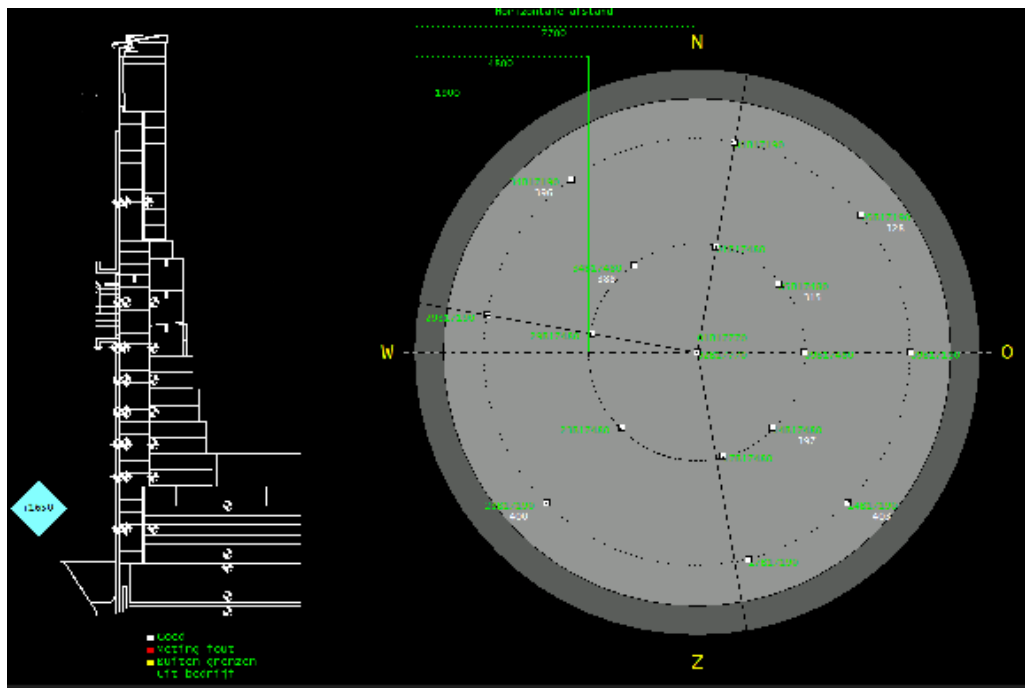


Figure 290: Left: General locations of the TSE BF7 hearth lining thermocouples in the sidewall and (the outer parts of) the bottom. Right: Location of thermocouples in the bottom layer at the height (+1650) indicated by the turquoise diamond in the left part of the figure.

Figure 291 shows the lining refractory material setup tool of the model (top left) and the calculation lines (top right) of a cross section of one half of the hearth. The bottom panels show, as an example, the locations of thermocouples in the sidewall (left) and in the hearth bottom refractory (right) at two vertical locations. All the main refractory materials have been included with thermal properties reported by TSE.

Optimizing Blast Furnace Hearth Inner State (OPTIBLAFFINS)

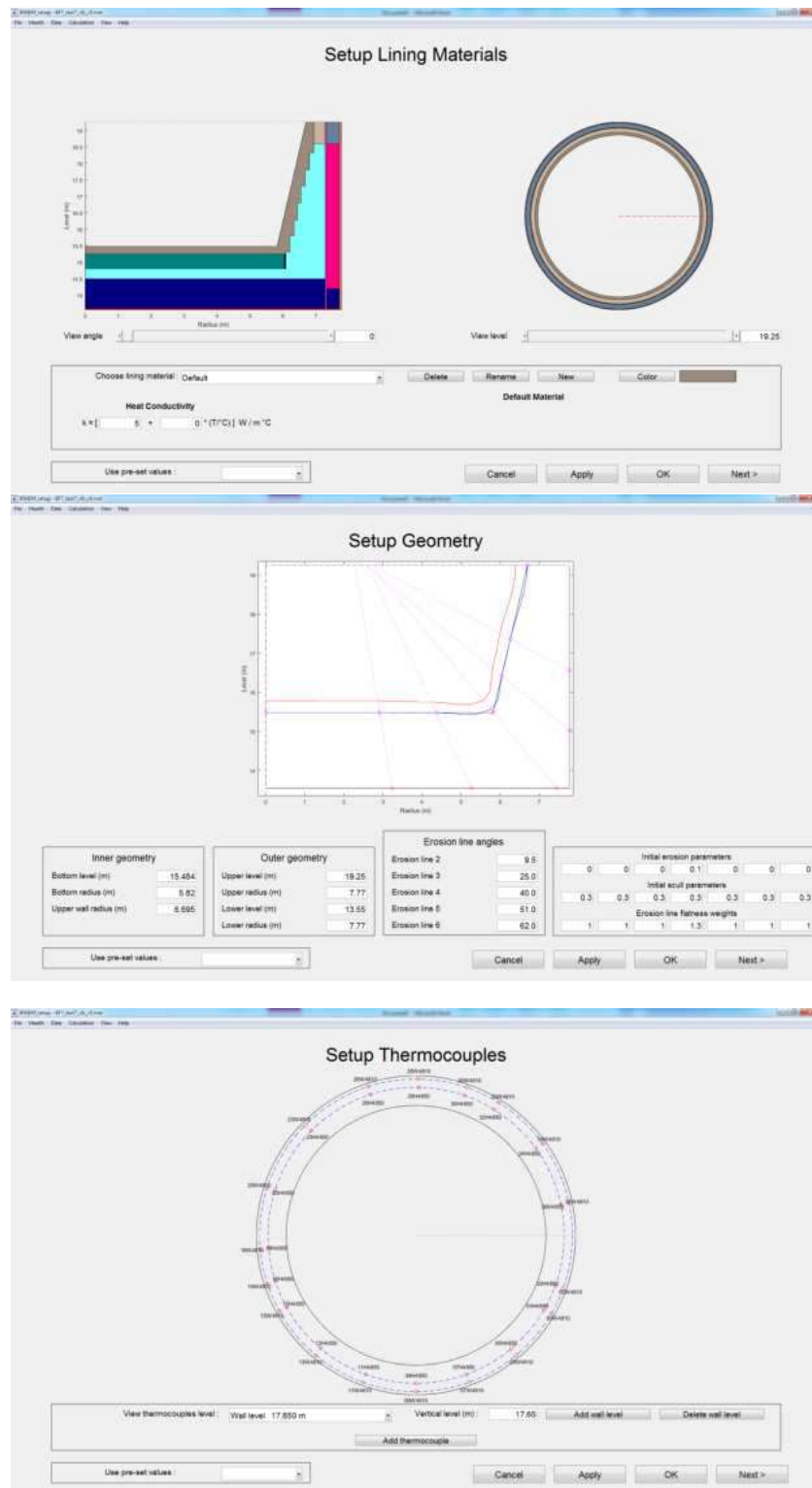


Figure 291: Top: interface of wear model material setup tool. Middle: calculation lines. Bottom: thermocouples positions in the sidewall on one level.

As an example of the results of the model, the conditions for a cross section along one radius and for a specific day are presented: Figure 292 shows the inner profile and isotherms "reconstructed" by the model as well as some thermocouple. By comparing the isotherms with the measurements, a quite good general agreement can be noted. However, there are some points of conflict. One problem is that it seems difficult to accurately estimate realistic temperature of the steel shell considering the given information about the geometric setup. An obvious source of errors is the degree of thermal contact between the shell and the lining material, which may vary in time and location. It is also clear by examining some conflicts in the lining temperature (point values vs. isotherms) in more detail that no perfect solution could ever be obtained without violation of the

conservation equations since nearby thermocouples at some points show large deviations in the readings.

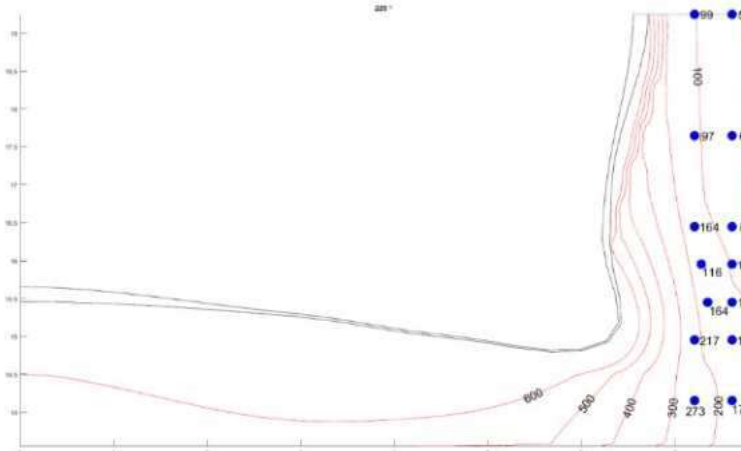


Figure 292: Wear profile and isotherms reconstructed by the model for a specific day. Thermocouple readings (expressed in °C) for the day at two radii have been inserted as labelled blue bullets.

It should also be noted that some thermocouple information has been discarded due to obvious conflicts e.g., with strong variations or periods without true signals. Another main problem encountered was that many thermocouples on the uppermost level in the hearth bottom (level +1650 mm, cf. Figure 292) after showing reasonable behaviour for about 8 years of operation, in early 2015 gradually drifted into unreasonably low levels. Figure 293 illustrates the evolution of four thermocouple temperatures in the hearth bottom lining along the radius ending at tuyere #29: The dashed lines correspond to the uppermost level (+1650 mm) and the solid line to the second-highest level (+900 mm), where thermocouples located at a radius of $r = 2.9$ m are depicted by red and $r = 5.8$ m by blue lines. When the furnace comes about 2950 days into its campaign (in early 2015), the thermocouples at the higher level gradually drift to the level of the outer thermocouple on the lower level (blue solid line) and finally below it, while the thermocouples at the +900 mm level maintain their temperatures. This behaviour is not only limited to the depicted temperatures, but similar trends are shown by other bottom temperatures on these two levels. The reason for the odd behaviour is not clear, but it is obvious that the thermocouples on these upper vertical levels cannot be used for setting the lower boundary conditions of the wear model.

Therefore, the lower boundary conditions were set based on bottom temperatures on the +900 mm and +700 mm levels. As for the sidewall, it was decided to base the analysis on the innermost thermocouples in the lining and the shell thermocouples.

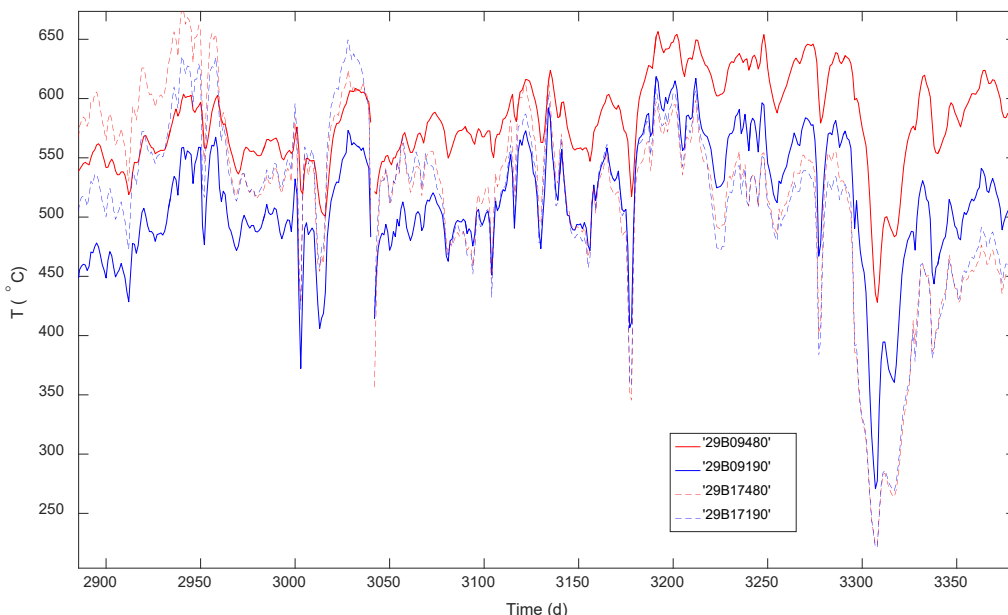


Figure 293: Hearth bottom temperatures on the +1650 mm level (dashed lines) and +900 mm level (solid lines), at two radial points, $r = 2.9$ m (red) and $r = 5.8$ m (blue).

After resolving the above problematic issues, the model was implemented at BF7 of TSE and has been used for analysing the hearth wear and skulling during the ongoing campaign, applying it to daily mean values of the thermocouple signals for all days from campaign start (at the end of 2006). Below, the findings of the model and interpretation of the results are summarized.

Figure 294 shows an excerpt of the model's interface for the results, illustrating a horizontal cross-section of the lining (top left) and vertical (top right) at the starting point of the study, i.e., at campaign start. To computationally initialize the model, a (red) skull layer of (quite) uniform thickness on top of the intact (yellow) lining is applied, including the blow-in lining. The lower graph illustrates the evolution during the campaign until the end of 2016 of the hearth volumes, defined as the volume of the computational domain inside the skull (lower blue curve) and the volume inside the intact lining (upper green curve). The difference between the two curves thus represents the estimated skull-layer volume. In the following, a brief overall interpretation of the furnace state during the campaign is provided.

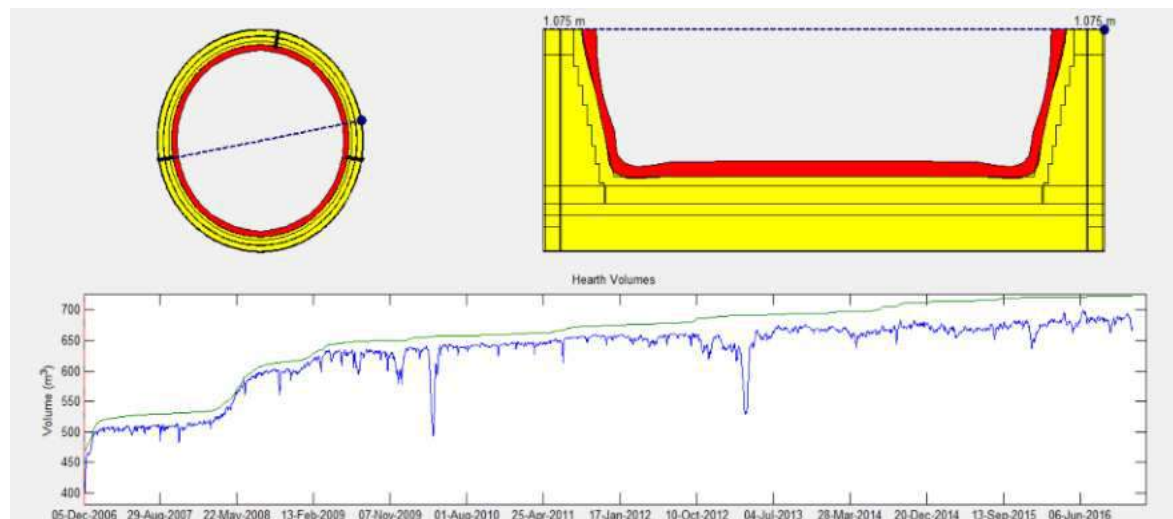


Figure 294: Top: horizontal (left) and vertical (right) cross section of the hearth of TSE BF7 at campaign start. Bottom: evolution of the estimated hearth volume inside the (red) skull (blue curve) and inside the (yellow) intact lining (green curve) to the end of 2016.

After 1.5 months of operation, the blow-in lining has almost fully eroded (Figure 295, top panel). This initial erosion is followed by a rather stable one-year period (middle panel) with some slight erosion (mainly wear of the remaining part of the blow-in lining), but the hearth volume stays almost constant. However, some more wear of the intermediate part of the sidewall is seen along the perpendicular cross-section axis, as depicted by the bottom panel of the figure.

About four months later, the available hearth volume has increased by about 40 m³ and the hearth shows its first signs of an elephant-foot profile, with potential gutters for the hot metal flow at the edges of the hearth. In these regions, substantial parts of the inner lining layer have been eroded. The wear of the sidewall is quite uniform along one cross section (Figure 296, top panel) but quite non-uniform along the perpendicular cross section (bottom panel), with least wear in the sector without a taphole and the strongest wear on the opposite side: Here, half of the second layer of the bottom lining has disappeared.

Eight months later, i.e., 2.5 years into the campaign, similar—but more eroded—profiles characterize the hearth (Figure 297): about half of the uppermost bottom layer has been eroded, while the upper sidewalls are remarkably uniformly worn.

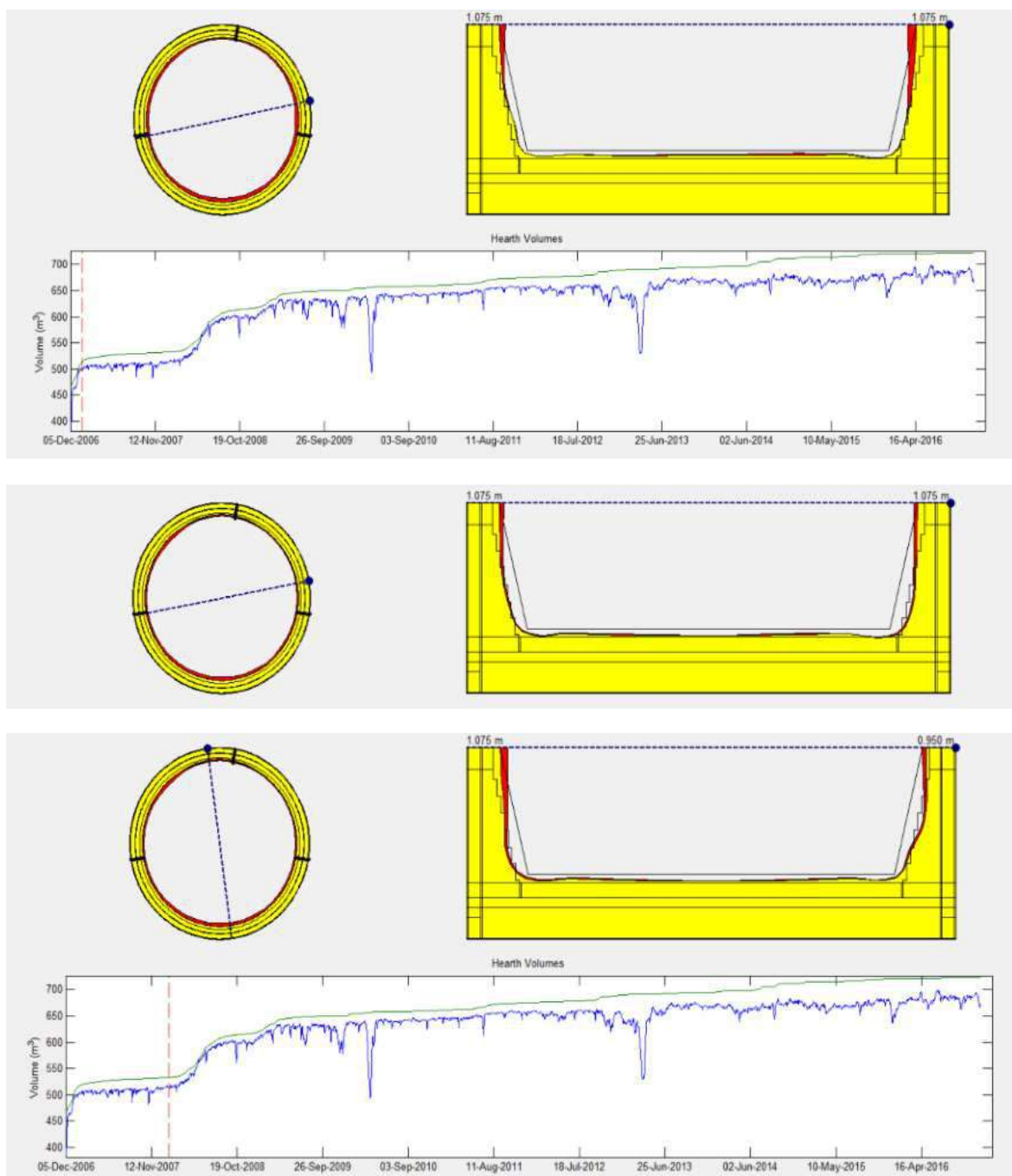


Figure 295: Estimated hearth lining state 1.5 months after blown in (top panel) and one year later (middle and bottom panels) for two different cross sections (cf. dashed lines in top left subgraphs).

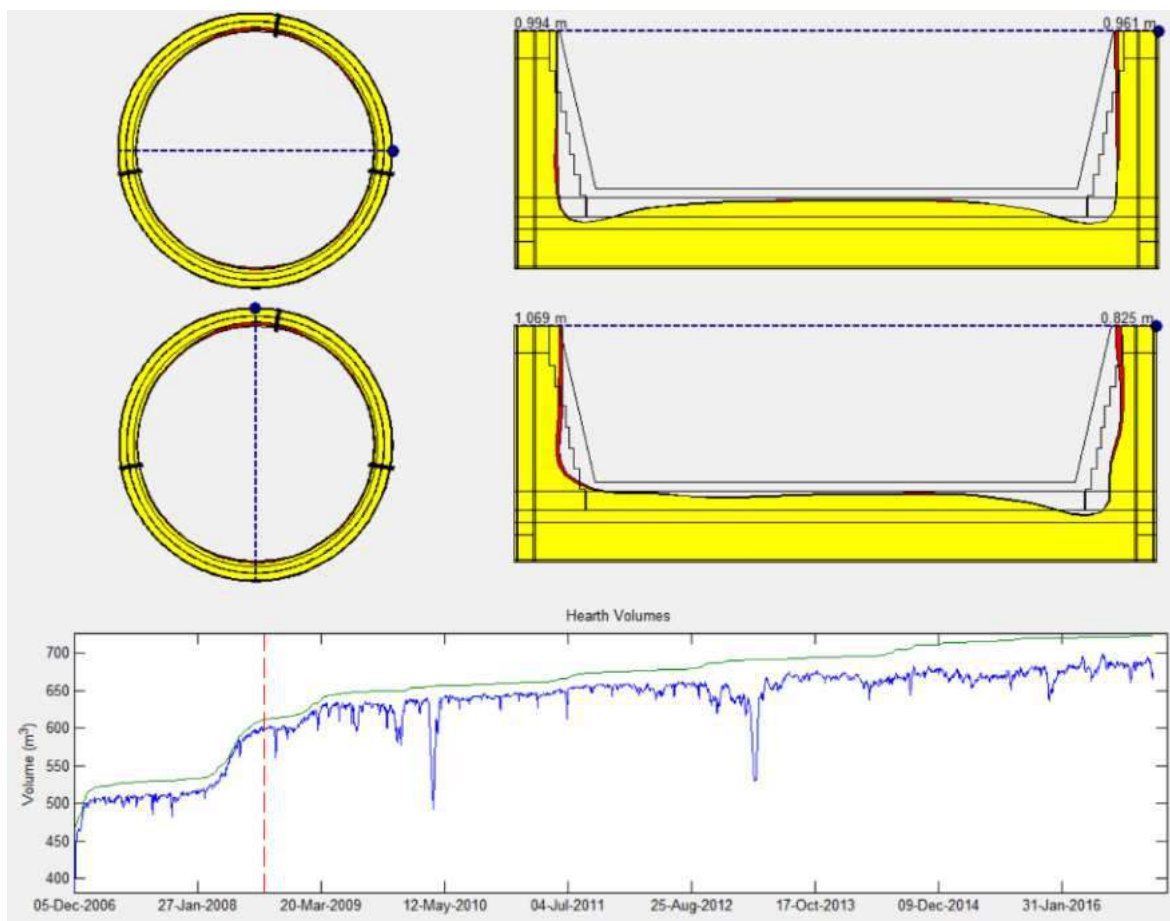


Figure 296: Estimated hearth lining state for two different cross sections 21 months into the campaign.

After this period of quite strong hearth wear, a rather stable state follows, which, in fact, lasts till the end of the period studied. Even though the wear is still slowly progressing, as indicated by the slight upward slope of the green line in the lower panel of the figures, the wall is in general spared from severe wear. Still, seven years into the campaign (Figure 298), a more severe wear pattern is seen to have developed at the lower part of the sidewall, where the inner lining layer has been eroded (except in the hearth sector without a taphole). The uppermost bottom layer is practically gone and parts of the second layer have also been eroded close to the sidewall. The wear pattern is now of elephant-foot type, and since campaign start about 150 m³ of lining has worn (excluding the blow-in lining).

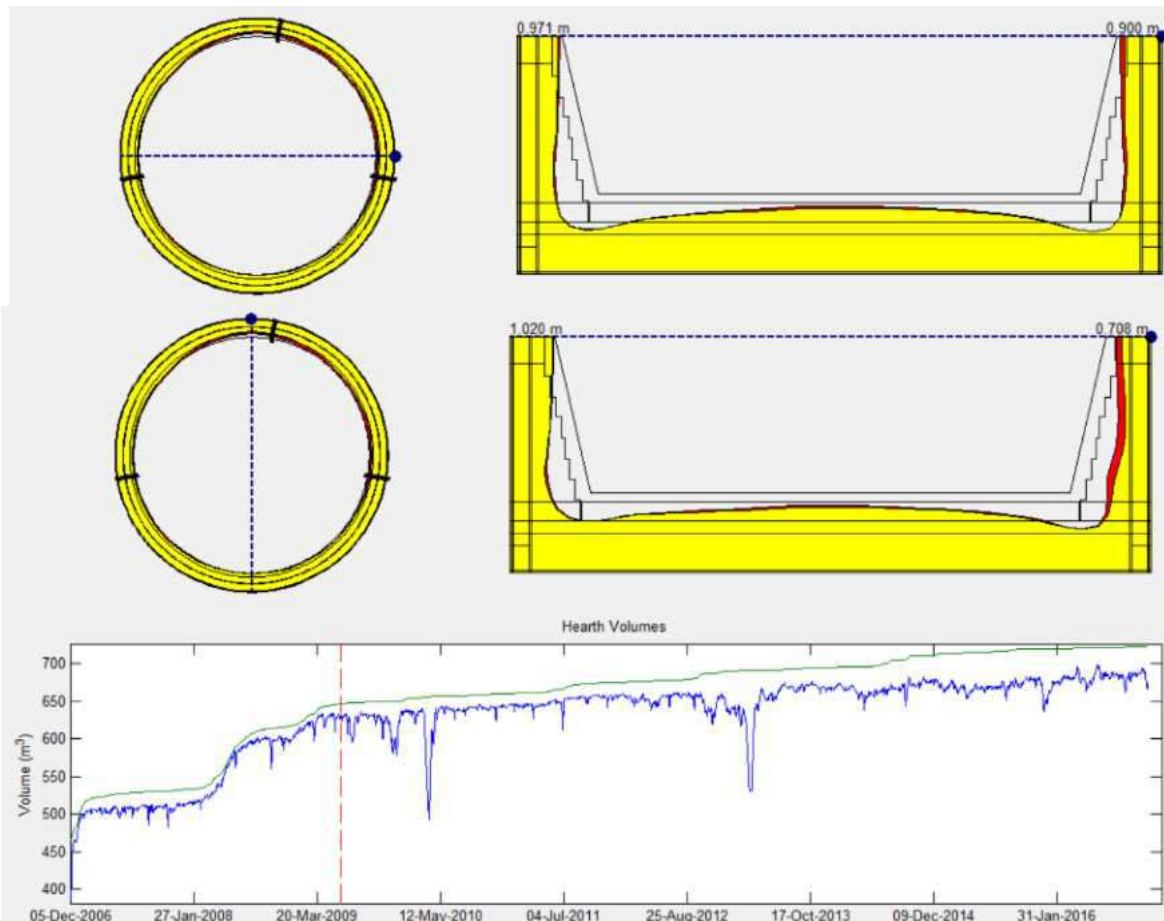


Figure 297: Estimated hearth lining state for two different cross sections 2.5 years into the campaign.

Two cross sections of the estimated hearth state at the end of 2016, ten years into the campaign, are depicted in Figure 299. The uppermost bottom layer is now fully eroded, but a protective skull layer has formed on the most eroded parts of the lining at the lower sidewall, yielding a practically cylindrical inner profile. It should be noted that parts of this protective layer may occasionally melt, as seen about half a year earlier at the point of the spike in the (blue) hearth volume curve, indicated by the red arrow in the lower part of Figure 298.

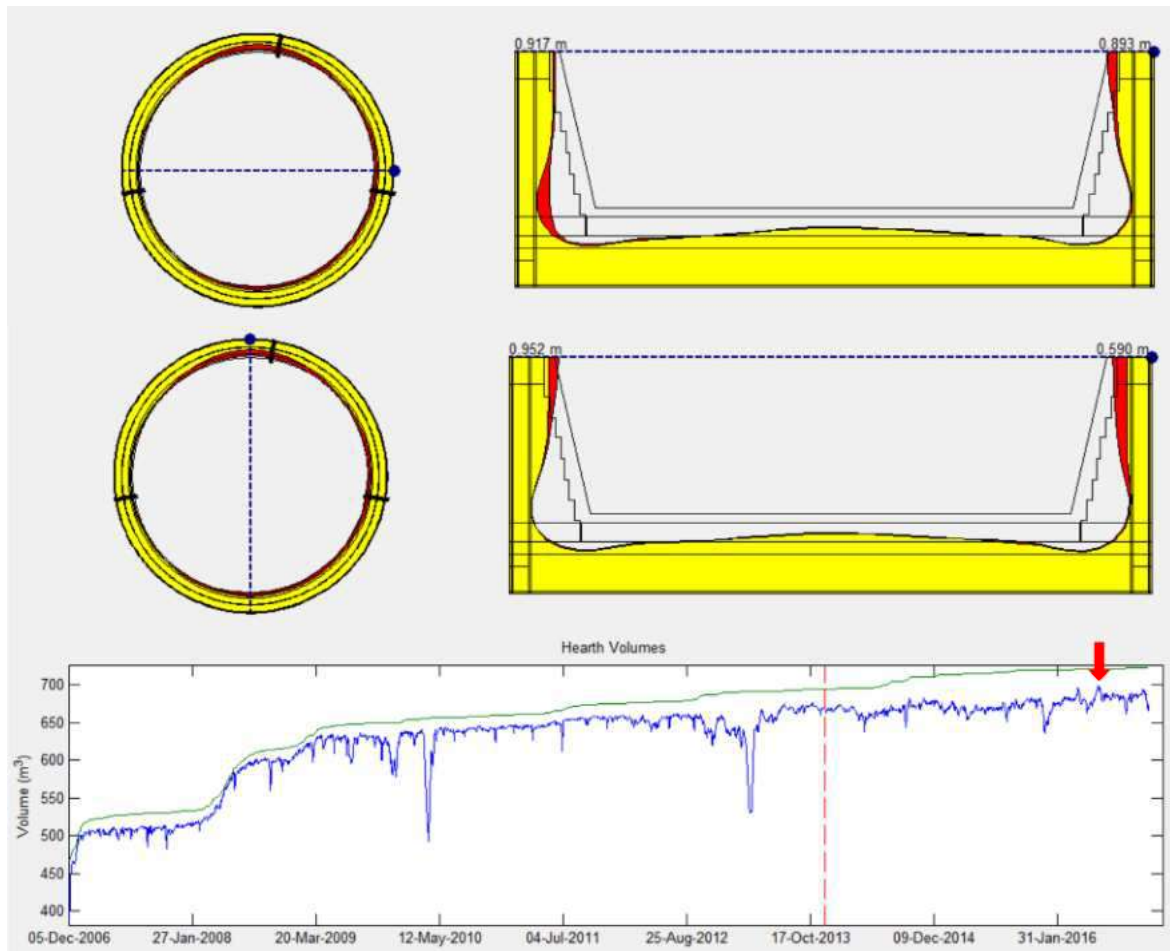
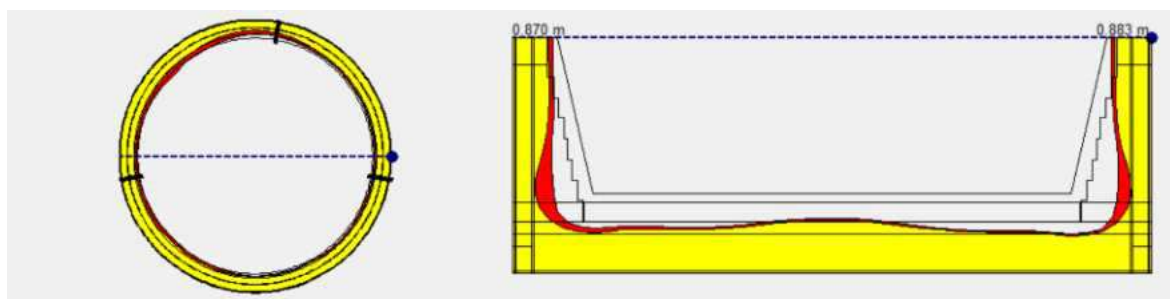


Figure 298: Estimated hearth lining state for two cross sections 7 years after blow in.

The analysis presented above was undertaken in 2017, but at the end of 2018 the most recent data was also included and briefly analysed. The results presented in Figure 300 show that the hearth during the time period 2017-2018 has experienced some more erosion, mainly of the bottom lining between November 2017 and February 2018, but that the total skull-layer volume has increased. As the profiles in the upper part of the figure presented for two cross-sections depict, the hearth bottom erosion has progressed in the intermediate region, and a minor progress is also observed at the sidewall along the S-W diagonal (cf. lower subgraph). The bottom erosion progresses slightly in October 2018, just before the end of the depicted period.

Summarizing the findings, it may be concluded that the hearth state of TSE BF7 has undergone a 1.5-year period (early 2008 - mid 2009) of more substantial erosion, where the hearth volume increased by more than 100 m³ in a year. When the rapid wear occurred, the production rate of the furnace was high, exceeding 10,000 t/day, but after the onset of the global financial crisis in late 2008, the production level has been about 20 % lower. This may have contributed to the decay in the erosion rate experienced during the later years of the campaign. Naturally, measures taken by the company to master the wear also contribute to the results. According to the model's estimates, the sump depth has increased by 80-100 cm from the blow-in state (again excluding blow-in lining), which increases the upward acting buoyancy pressure by 20-30 kPa. Furthermore, the diameter of the hearth inside the intact lining has on the lower sidewall level increased by about 3 m. This may contribute to a partial floating of the dead man at the edge of the hearth as a combined result of a larger sump depth and an increased "shading" effect of the raceways on the downward-acting forces [93],[60]. A brief analysis of this is presented in the next paragraph.



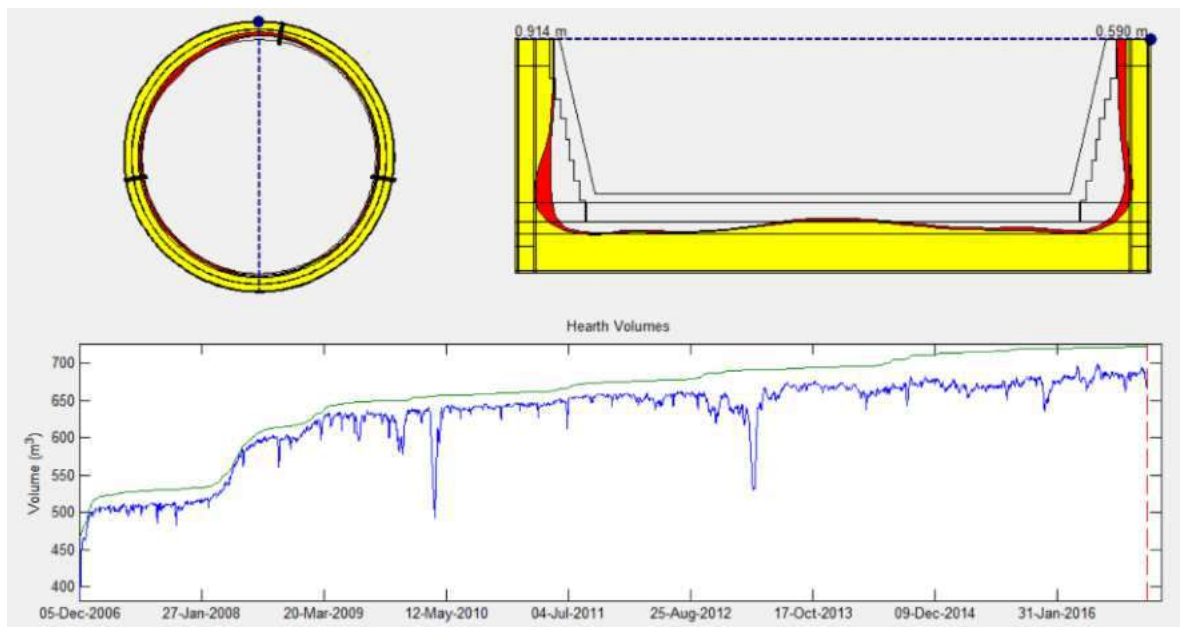


Figure 299: Estimated hearth lining state for two different cross sections at the end of 2016, ten years after blow in.

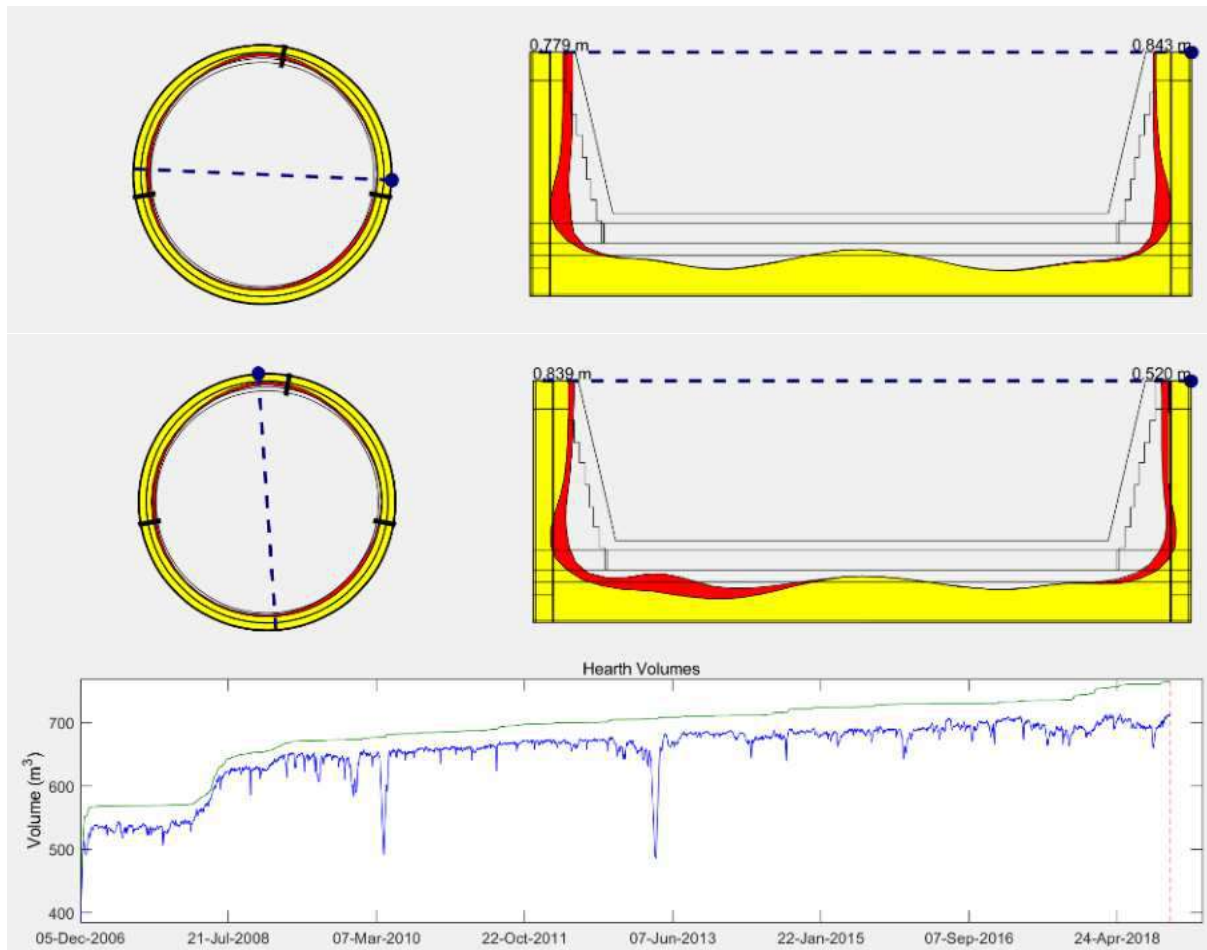


Figure 300: Estimated hearth lining state for two different cross sections at the end of 2018, twelve years after blow in.

The results of the wear model were used in a study of whether the dead man in BF7 possibly would float. To simplify matters, the three-dimensional wear profile reconstructed by BFHEM was approximated to be cylindrical with a depth and radius that corresponded to the average values for each day during the campaign. A force balance for the furnace was stated, considering the main terms indicated in Figure 301, i.e., the weight of the burden in the lumpy zone (L), the weight of coke and effect of iron and slag holdup in the dribbling zone (D), the weight of coke below the slag level, the buoyancy of slag (S) and iron (I), and the effect of wall friction (F) and drag of the gas

(G). The levels of the cohesive zone and liquid surfaces, as well as the holdup of iron and slag were estimated based on furnace geometry and general process knowledge. Daily mean values of the ore-to-coke ratio and the gas pressure drop over the furnace (Figure 302) were used to calculate the bulk density of the burden in the lumpy zone and the drag force of the ascending gas. The effect of wall friction was here neglected.

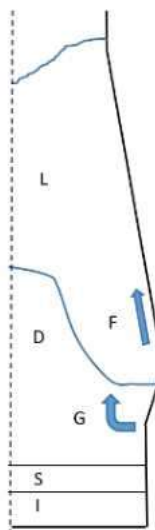


Figure 301: Terms considered in the simplified force balance of the blast furnace for estimating the dead man floating level in TSE BF7.

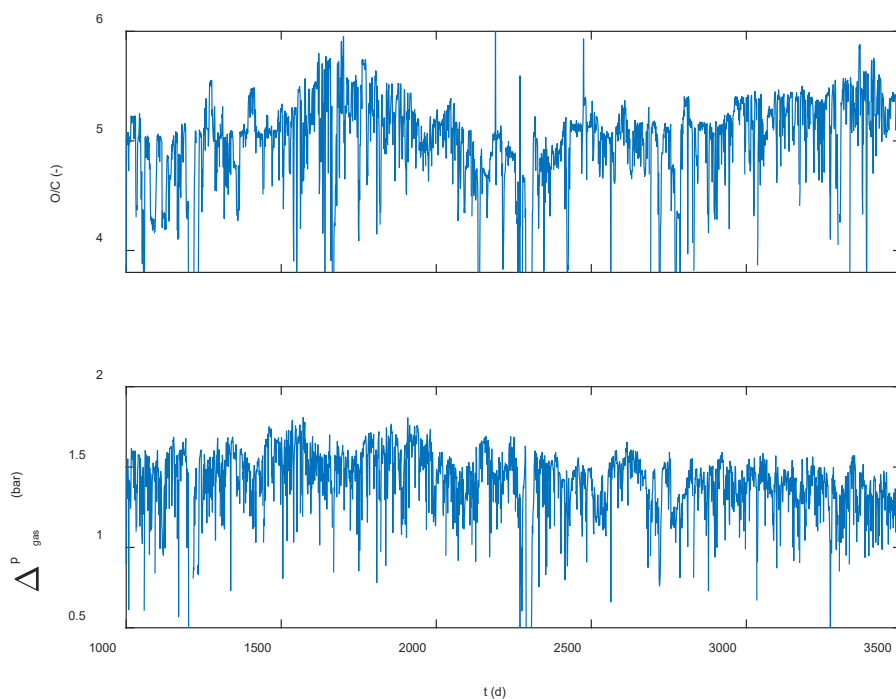


Figure 302: Daily mean values of the ore-to-coke ratio and the gas pressure drop in TSE BF7 for days 1000-3500 of the campaign.

Using a parameterized expression of the radial pressure distribution of the bed introduced in [93], the average dead man position was determined from the force balance, using three different levels of the cohesive zone: 9 m, 12 m and 15 m above the taphole. Figure 303 shows the coke-free volume (i.e., the volume under the dead man) for the same period as that depicted in Figure 302. Since the third case corresponds to a very high cohesive zone level, it may be concluded that the dead man may only occasionally float during the campaign. The reason why the dead man does not float more along with a progressing hearth wear is that the later parts of the campaign are characterized by a high ore-to-coke ratio and a low gas pressure drop over the furnace (Figure 302).

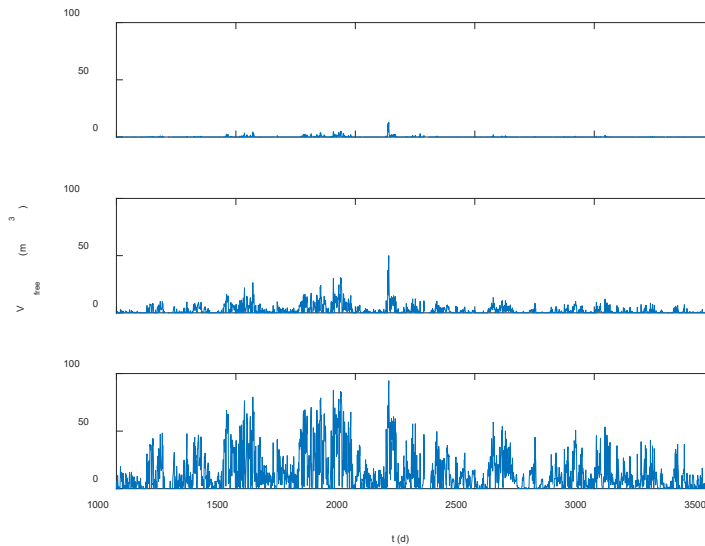


Figure 303: Estimated coke-free volume for TSE BF7 for days 1000-3500 of the campaign for an average cohesive zone level 9 m (top panel), 12 m (middle panel) and 15 m (bottom panel) above the taphole.

In order to illustrate how the model interprets the dead man state, the situation for a day in late 2010 when the dead man was estimated to float most (corresponding to the main spike seen in all subpanels of Figure 303) has been depicted in Figure 304. The figure shows the position of the lower end of the dead man as a function of the (normalized) radial coordinate for the three different cohesive zone levels. It is seen that the floating for the lowest cohesive zone level is limited to a small region at the joint of the bottom and sidewall, while the dead man floats completely, but on different levels, for the other two cases.

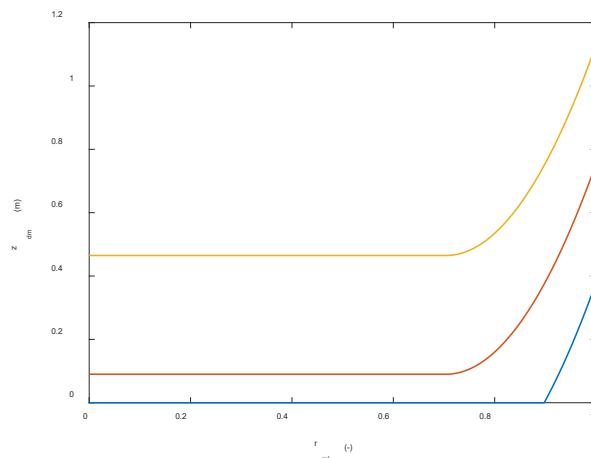


Figure 304: Lower dead man profile on a specific day in late 2010 estimated by the force balance with a cohesive zone level 9 m (blue curve), 12 m (red curve) and 15 m (orange curve) above the taphole. The abscissa expresses the normalized radius of the hearth.

2.2.4.2 Estimation of wear/skull gaps brittle layers, statistical and model-based analysis of operational data

2.2.4.2.1 Introduction

In this subsection, overall operational data from AGDH, AMEH and TSE is analyzed together with the hearth related data. Results from statistical analysis results is used to develop plausibility algorithms to eliminate failing measurements. The multiphysics model developed in section 3.2.1.1 for thermal stresses is used in an extensive parametric study of the wear/skull/gap/brittle layers to determine the characteristic ranges and behaviors of the quantities measured on-line (e.g., thermocouple temperatures or heat fluxes). The results can not only be used to identify wear/skull/gap/brittle layers but also to check the validity and plausibility of the on-line measurements. DMD results from WP3 were used to distinguish time periods with different hearth state and then to provide the dead man properties within the statistical evaluation. Since the most likely state of the dead man in TSE BF7 was found to be sitting (in the analysis of the previous subsection), the study of liquid behavior in the hearth was focused on gaining a better

view of the liquid levels in a multiple-taphole blast furnace under different draining conditions. For this purpose, an off-line model of a hearth with alternating operation of two tapholes was developed. The model is largely based on the same assumptions as the on-line model described in subsection 3.2.3.7, but since the outflow patterns of slag and iron are unknown, they were represented by a parametric expression. This simulation model was applied to analyze the effect of different factors on the drainage, drawing conclusions about patterns observed in the operation of TSE BF7.

2.2.4.2.2 Multipoint thermocouple analysis

The observed/measured residual hearth lining of AGDH BF4 and AMEH BF5A both seemed to exhibit much more wear than the models expected. The main reasons for this were explained with respect to the relining observations in section 3.2.2.1.8. In summary, the thermal resistance of the brittle layers leads to lower thermocouple measurements and thus less wear estimates by the models. Moreover, unfortunately and unintendedly the hearth lining lying on the hot side in front of the brittle layers was removed during hearth excavation. Therefore, the measured residual hearth lining is highly questionable and the real residual wall thickness including brittle layers could not be measured. It is crucial to keep this in mind when interpreting the model estimation in comparison to the observed/measured wear.

A new way to observe brittle layer formation during blast furnace operation is to install and carefully monitor multipoint thermocouples (MP TCs), which can measure the hearth lining temperature at multiple depths of up to more than 500 mm. A drawing of the MP TCs which have been installed at AGDH BF4 during the later stage of the last campaign is shown in Figure 305. These MP TCs were installed at six different positions; the positions of all (double) and multipoint thermocouples are shown in Figure 306. Double TCs are depicted with larger red points and MP TCs are with larger blue points.

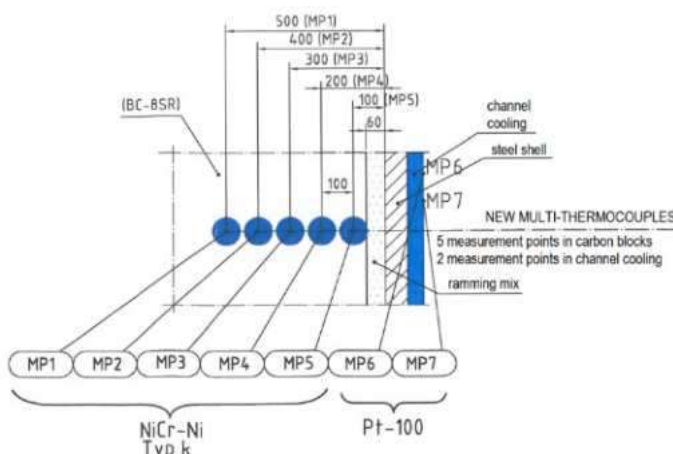


Figure 305: Installation of Multipoint Thermocouples (MPTC) at AGDH BF4.

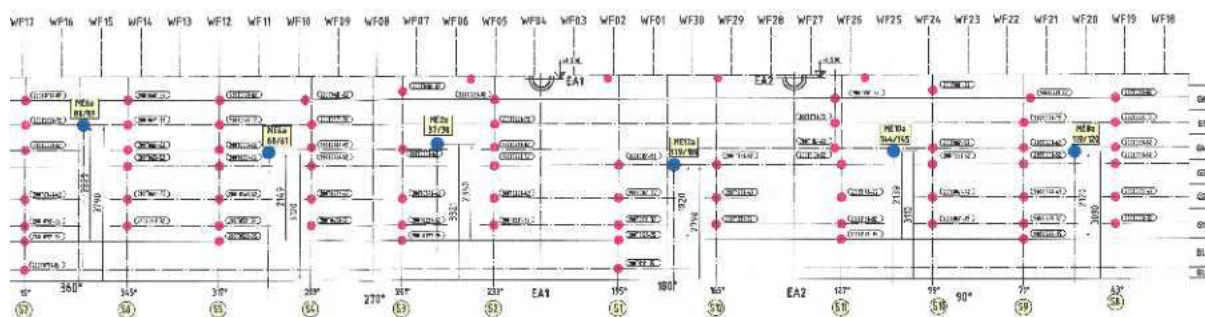
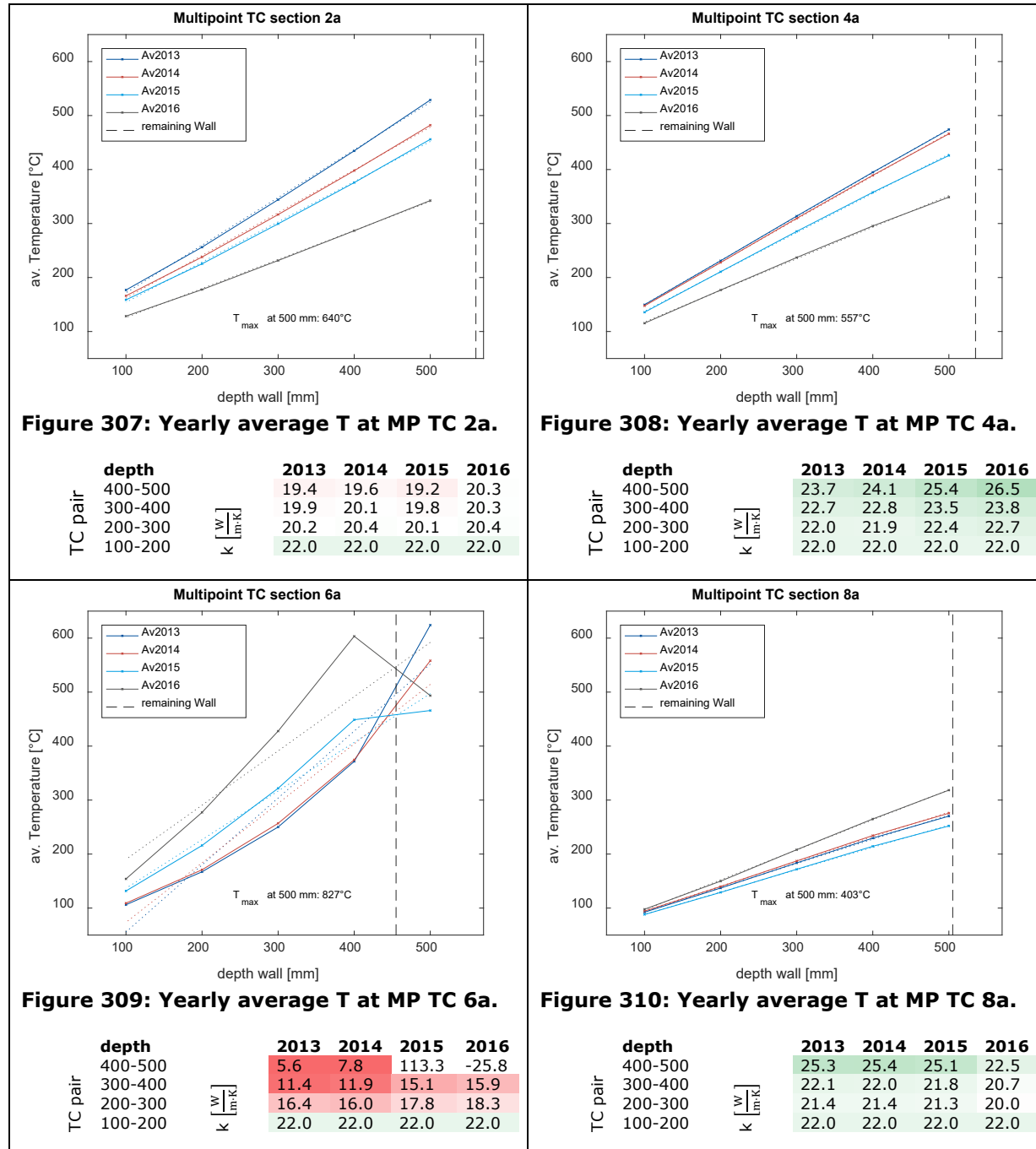
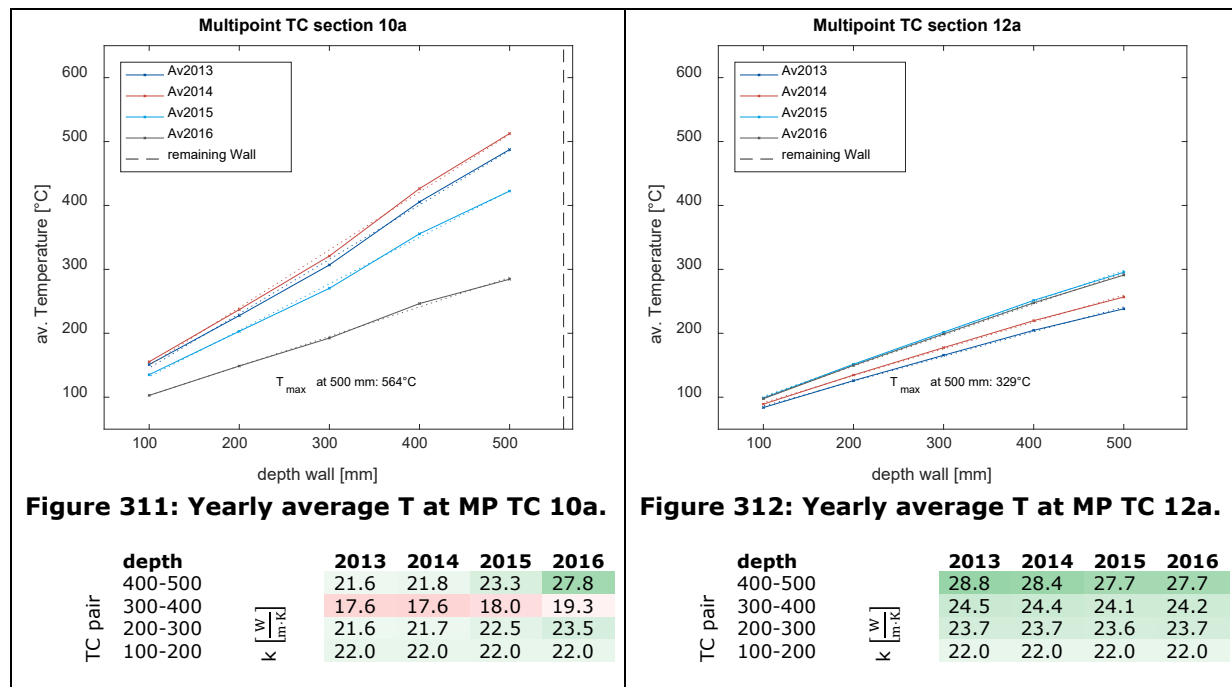


Figure 306: Positions of 6 MPTCs at AGDH BF4.

The MP TCs were installed in the last quarter of 2013 and survived until the campaign end. Approximately three years of data were recorded by these TCs. The data were very useful in-order to estimate the conditions of the hearth refractory lining, such as the brittle layers formation and material aging. Initially the temperature difference between the different depths at each MP TC was evaluated to derive an estimation of the thermal conductivity in between. The yearly average temperatures were calculated and shown in Figure 307 till Figure 312. The x-axis shows the installation depth with reference to the inner surface of the steel shell (Figure 305). It is assumed that the physical refractory properties at the cold side of the wall did not change and that the thermal conductivity given by the supplier ($k = 22 \text{ W}/(\text{m}\cdot\text{K})$) is still valid for at least the first pair of thermocouples, between 100 mm and 200 mm. The thermal conductivity of the remaining pairs

was calculated using the radial heat continuity assumption. The green colors in the tables below the figures indicate higher thermal conductivity and red colors indicate lower thermal conductivities, i.e. progressed brittle layer. The observed/measured wear is only known for the double TC sections but not documented at the position of the MP TCs. So, it is interpolated from the nearest double TC section. This interpolated wear line is shown by the black dashed lines on the right side in each Figure 307 till Figure 312.





For the MP TCs 2a, 4a, 8a and 12a, a nearly linear increase of temperature with the depth can be seen for each of the evaluated years (from 2014 to 2016). In a more detailed view, the values for the deepest thermocouple at Position 4a, 8a and 12a are slightly below the linear behavior which results in calculated thermal conductivity values which are higher than for the original material. This might be interpreted as beginning infiltration of substances with higher thermal conductivity from the hot side as discussed in the literature [60] and [61].

For MP TC 2a, a slight decrease of thermal conductivity is calculated and MP TC 10a shows a decrease in thermal conductivity between the thermocouples at 300 and 400 mm. Clearly different results are received for MP TC 6a, the position where the strongest wear was documented during excavation. Here a thermal conductivity decreasing with depth is calculated. At the inner thermocouple pair 400 – 500 mm for the years 2013 and 2014 a value of approximately 6 – 8 W/(m·K) is calculated. This is a clear sign for the progressed brittle layer. In the years after 2014, the inner thermocouple at 500 mm is obviously disturbed. Nevertheless, it was seemingly not completely damaged and was measuring until the end of the campaign.

The average yearly temperatures and the maximum temperature (shown in each figure as annotation at the bottom) measured at the 500 mm position of each MP TC is incompatible and conflicts with the observed/measured residual hearth lining thickness (given as black dashed line). The thermocouple at the 500 mm position at sections 6a and 8a should have been destroyed by hot metal if the refractory thickness recorded during excavation would have been the actual inner wear line. The maximum temperatures at the other sections (2a, 4a and 10a) should be much higher if the thermocouples were as near as 60 mm to the hot metal. Therefore, it is confirmed that there must have been a further hot part of the refractory in front of the documented part which was lost during excavation without documentation. The documented residual wall thickness after excavation only corresponds to the depth of the brittle layer.

In conclusion, the MP TCs seem to be very useful for determining the brittle layer formations during the blast furnace operation, which is crucial for a correct estimation of hearth wear according to the findings at AGDH and AMEH. Typically, the deepest TC shows an anomaly as soon as the brittle layer formation starts. The relative conductivity at this region first increases due to infiltration (possibly Zn). It follows a dramatic reduction of the apparent thermal conductivity due to the damage/cracks upon brittle layer formation. Therefore, in the new design MP TCs are installed at 12 positions at an increased maximum depth of 700 mm.

2.2.4.2.3 Statistical analysis of hearth wall temperatures

Current state-of-art of hearth refractory wear models is to interpret the continuous measurement of the temperatures by thermocouples as a function of residual refractory and skull thickness. That is, new high temperatures are interpreted as wear whereas the decreasing temperatures are regarded as skull build-up. The time series analysis of thermocouple data at the AGDH BF4 questions this straight approach. Normally, somewhat gradually rising temperatures should be expected from this theory due to advancing refractory wear over the years. At AGDH BF 4 some thermocouples show a conflicting behavior. Their maximum occurs just one year after (2011) the

Optimizing Blast Furnace Hearth Inner State (OPTIBLAFINS)

intermediate repair of the hearth wall refractories (2010) and afterwards generally showing a decreasing behavior (see Figure 313 e.g. G0671). Therefore, it is believed that hearth wall temperatures are affected by a couple of phenomena such as:

- hearth thermal state,
- hearth flow phenomena,
- gaps/brittle layers and
- refractory wear.

All these phenomena are expected to influence the thermocouple readings either locally or globally and on different time scales with different characteristic patterns. Temperature changes due to hearth thermal state should affect all thermocouples and should be related to BF operational parameters like rate of production, blast parameters, coke & coal rate, etc. The flow phenomena should be expected to be related to tapping regime in the short time scale and to (local) dead man permeability and dead man dynamics on longer time scales.

It is the objective of this task to enhance the understanding of these different influences on hearth wall temperature readings, mainly by comparing correlations between thermocouples at different positions on the one hand and correlations of thermocouples with different operational and model-based BF parameters on the other hand. The correlation as a measure to compare thermocouple readings has been chosen due to good experiences from automated correlation, based plausibility checks of thermocouple data prior to wear model calculations and due to observations from long time temperature time series.

Figure 313 shows selected hearth wall thermocouples readings from AGDH BF 4 beginning in January 2010 when an intermediate relining of the hearth walls was carried out. The diagram includes data from five thermocouples located in vertical sections 2, 4, 6, 8 and 11, all at the same height in refractory layer 7 approximately 1 m below the taphole level. The highest dynamics of the measured temperatures are observed at this height almost at all sections. If all temperatures were only influenced by wear and skull build-up, a gradual increasing behavior of the temperatures would be expected after the relining. However, section 6 and section 8 have an opposite trend with high temperature levels shortly after the repair in 2010/11 (indicated by blue arrow ①) and then lower levels in the following time span, e.g. in 2013 (indicated by blue arrow ②). Nevertheless, during the relining in 2016 in these high temperature locations the strongest refractory wear was found.

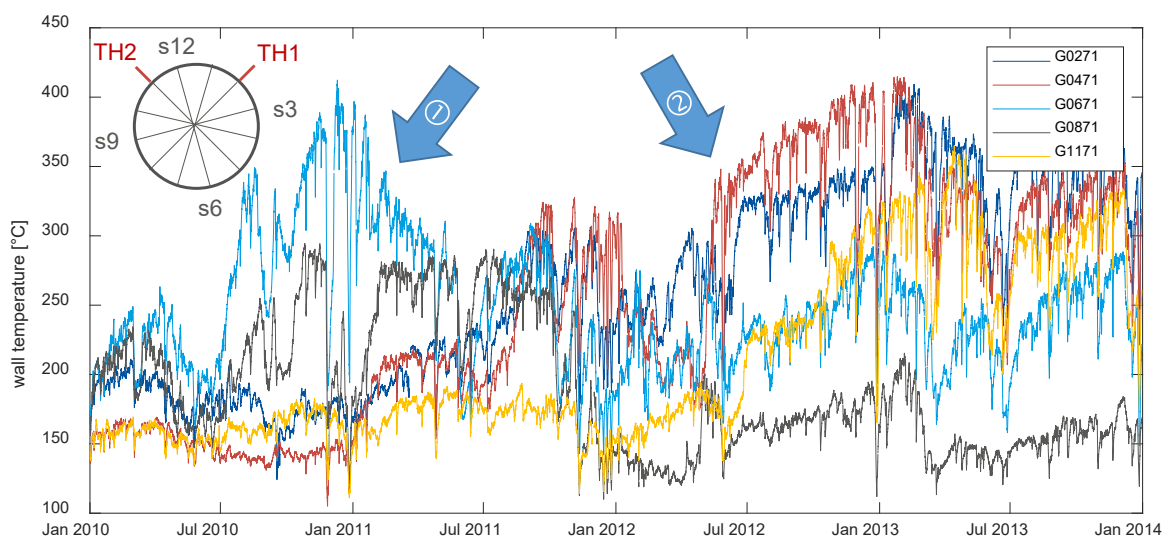


Figure 313: Selected time series of hearth wall thermocouple readings at AGDH BF4.

The temperatures at the opposite section 2 and section 4 of the hearth show completely different behavior with low values during 2011 and high values in 2013. The measurements at sections 6 and 8 as well as 2 and 4 show good correlations of the temperatures in both regions, and with other thermocouples not shown in Figure 313. Therefore, a disturbance or defect of the measurement seems improbable. Obviously, the situation inside the hearth led to stable temperature constellations in this region over more than one year noticeable by high correlations between the thermocouple readings in the affected regions during 2010/11. Later, the situation in the hearth seems to slowly change to another regime which was also stable during a long part of 2013. This leads to a situation that the hot spot monitored at the hearth wall in 2011 (opposite to the tapholes) completely changed position (to the area directly below the tapholes) in 2013 as shown in Figure 314.

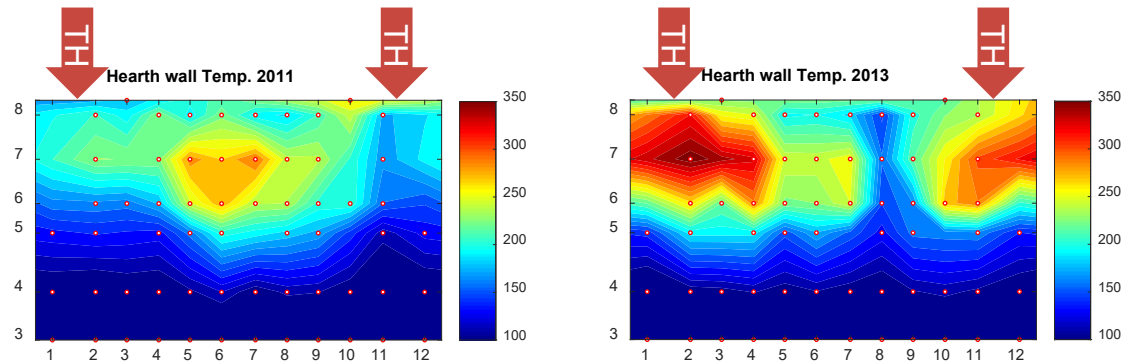


Figure 314: Flat projection of temperatures measured at the hearth wall of AGDH BF 4 in 2011 and 2013.

The objective of the following data analysis is, therefore, to develop methods to visualize and evaluate the correlations between different thermocouples at the BF hearth wall on different time scales to derive information how this behavior might – at least partly – be influenced by other BF operational parameters (i.e. not wear/skull).

Data evaluation and filtering: Prior to the analysis, some careful data plausibility checks and filtering were required in-order to remove outlier data (e.g. defect thermocouples, stoppages, etc.) which would disturb the calculation of correlation coefficients. For example, high but unwanted correlations occur during the stoppages since all temperatures first drop during these periods and slowly increase just after them (Figure 315). This results in high correlations for all measured temperatures without any relation to the measurement position or to wear.

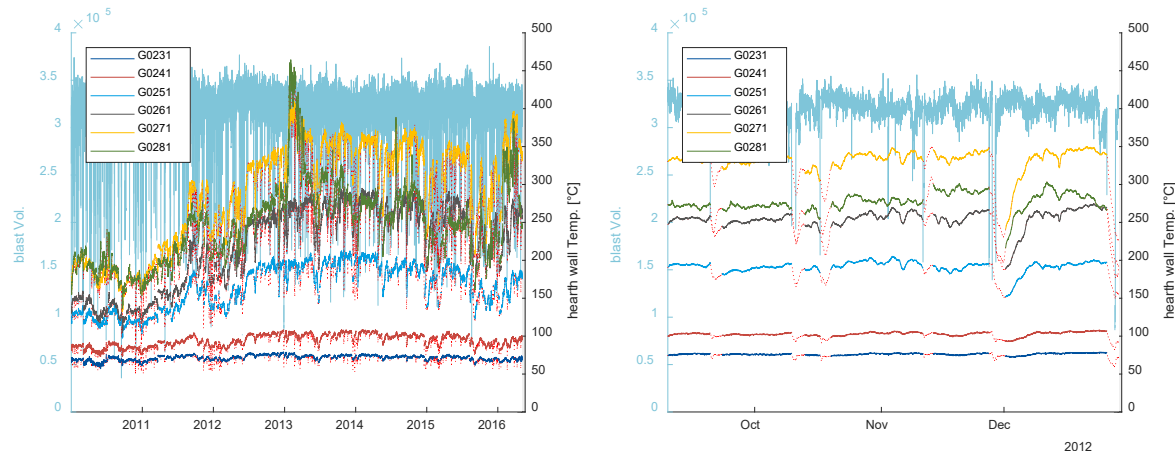


Figure 315: Filtering of effect from stoppages on hearth wall temperatures (left: all campaign, right: zoom to end of 2012).

An analysis of temperature developments during a stoppage revealed that a time span of around 1 h before stoppage (due to operational changes to prepare the stoppage) and 54 h after the stoppage are influencing the temperature readings for most of the short stoppages. Normally after 54 h the hearth wall temperature reaches a similar level as before the stoppage. Based on the data about blast volume (noted in light blue on the left y-axis in Figure 315) all time spans around stoppages have been removed from the data (marked by red-dotted lines in Figure 315). This filtering method has removed the influence of shorter stoppages on the analysis but as also visible in Figure 315 (the long stoppage in Dec 2012) it cannot compensate the effects of the longer stoppages. The automated removal of the effects of such long stoppages would have removed too much data, therefore these stoppages were considered without further filtering.

Furthermore, the data analyses revealed that the temperature measured by thermocouples in the BF hearth wall can be subject to different other conspicuous effects. The two most frequent ones are:

1. Sudden drop of measured temperatures followed by a period of data (with a duration up to 1.5 years) with plausible temperature dynamics (possibly even correlated to other data series) but in total on a lower temperature level, which even might recover after months.
2. Erratic small or short jumps in temperature or sudden appearance of additional data noise.

These disturbances differ from disturbances caused by defected thermocouples which deliver no physical reasonable data any longer. The automated detection of such disturbances in the

thermocouple data provides two benefits. On the one hand, such disturbances provide information about where to search for signs of crack or brittle layer formation in the refractory wall in the recorded data. One the other hand, the removal of such disturbed data is needed to eliminate the influence of corroding thermocouple or thermocouples losing their thermal contact to the refractory.

Data showing the behavior explained in (1. at page 240) is removed by an algorithm implementing a ΔT -based criterion. For this criterion, the first derivation of each thermocouple data series is computed and divided by the floating daily median value of the temperature. Sudden temperature changes weighed by the median which exceed an empirically chosen threshold value of 17 as well as all following data are removed from the analysis. An example case is shown in Figure 316. The diagram at the left side shows the temperatures of three thermocouples on the heights of layer 3-5 in vertical section 1 (solid lines, right y-axis). The value for the ΔT -based criterion is noted as thin dotted lines (left y-axis) in the same colors as the temperature data.

Between July 27 and August 03, the temperature at G0141 suddenly drops around 50° C and afterwards stays on this lower level. The ΔT -based criterion exceeds the threshold marked by the dashed line – the data is considered as implausible.

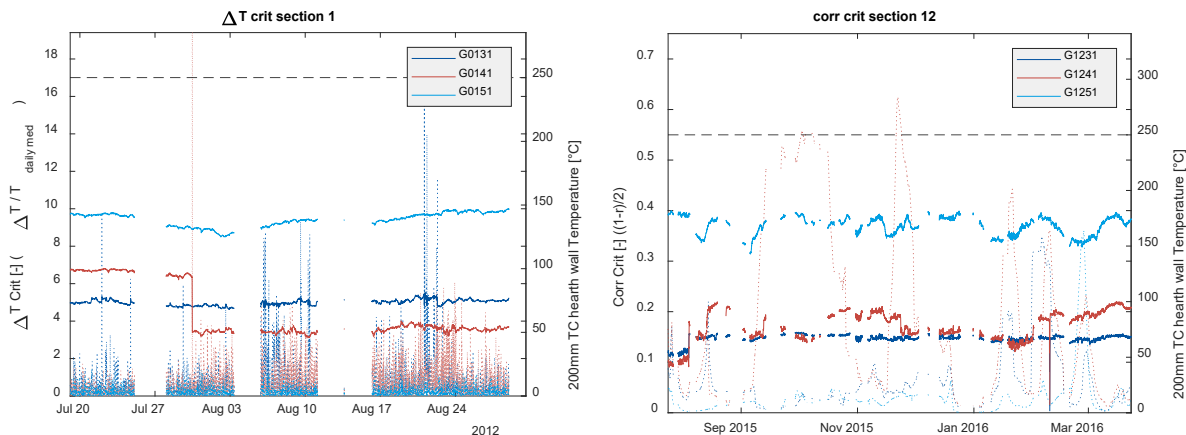


Figure 316: Removal of implausible data (left: by ΔT criterion, right: by correlation criterion).

The right side of Figure 316 shows the application of the correlation criterion, used to remove the data with behavior explained in (2. at page 240) of erratic small jumps / high noise. For this criterion the average value of the correlation coefficient r of the data of a thermocouple with its three nearest neighbors (identified by Delaunay Triangulation, see also Figure 318) in a moving interval of data from 24 h is computed. The value of r in the interval $[-1, 1]$ is transformed into the interval of $[0,1]$. Again, an empirically chosen threshold value (here 0.55) is used to identify and remove disturbed data.

The right side of Figure 316 shows the temperature data from thermocouples at three different heights (layers 3-5) at section 12 as solid lines. Gaps in the lines represent data removed due to stoppages. Thin dotted lines show the correlation criterion value. In Oct. 2015 and Dec. 2015 temperatures from G1241 show several small and short jumps as well as higher noise compared to the other data series. This results in the correlation criterion exceeding two times the threshold value.

These two plausibility criteria have been applied to all data during the analysis. After violation of one criterion all data from the affected thermocouple is removed until the values for both criterions recover a value below 50% of the threshold and total temperature is back in a window of +/- 25% of the last plausible value.

The final step of data preparation is standardization. All data series are transformed to a shape with $\mu=0$ and $\sigma=1$ by subtraction of their mean value and division by their standard deviation. The effect is visualized in Figure 317.

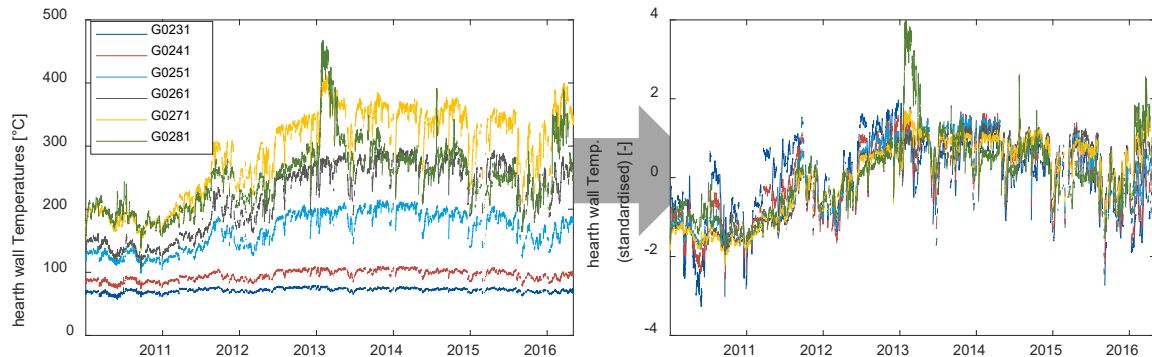


Figure 317: Standardization of thermocouple data (left: before, right: after).

In daily operation hearth wall temperatures are often rated by their absolute values. The high temperatures are considered as dangerous whereas the low temperatures are considered as inconspicuous. With the focus on rest wall thickness of the refractory, this is an approved approach. But with the focus on regions in the hearth showing similar behavior, this is misleading since changes in dynamics of thermocouples data with low temperature level might be missed. Standardization of the data enables comparability of the dynamics of the temperatures without influence of the total temperature level. As an example, in Figure 317 the thermocouples G0231 and G0241 (with lowest temperatures) at the wall near sump level show much higher dynamics in 2011 than in 2014. This is difficult to notice in the left side diagram whereas it is obvious after standardization in the right-side diagram (see Figure 317).

AGDH implemented the IT – infrastructure for the data analysis. A VPN-Connection between BFI and AGDH was arranged and access to a PC, dedicated for the MATLAB based analysis in the AGDH network was guaranteed. Via this PC it is possible to access a SQL database containing most of the operational data from BF4 and BF5 at AGDH. A copy of AMEH-BF5A operational data was send to BFI and implemented to a SQL database hosted at BFI for data analysis. Moreover, AMEH-BF5A hearth geometry and TC-positions were sent to BFI. Basic blast furnace data (geometry, material, measurement and operational data) were made available as well.

BFI started with an offline correlation analysis of the operational bf data with the measured wall temperatures. Currently the data from different data sources (e.g. thermos couples, blast parameters, tapping data, etc.) is synchronized, plausibility checked and filtered if required by BFI, AGDH and AMEH.

Correlation of hearth wall thermocouple data on different time scales: The identification of the regions at the hearth wall which are showing similar temperature behavior requires as first step the identification of the neighbors of each thermocouple. As modern BFs can be equipped with more than 200 thermocouples an automated algorithm for identification of neighbors was developed. A list of all radial positions and heights (e.g., theta and h) of all thermocouples in one radial depth (e.g. 200mm from outer wall) is provided. The continuity of the thermocouple grid in theta direction are considered by adding the sections 11 and 12 at the beginning, sections 1 and 2 at the end of the grid as shown in Figure 318. Afterwards the Delaunay Triangulation is applied to generate a list of triangles connecting all thermocouples positions. This grid as shown in Figure 318 connects all thermocouple positions with its neighbors. So, thermocouples are drawn as red circles and each triangle edge has a '+' in the middle, to which the correlation between the thermocouple pairs is computed. These midpoints are used for interpolation of flat projections of the correlations.

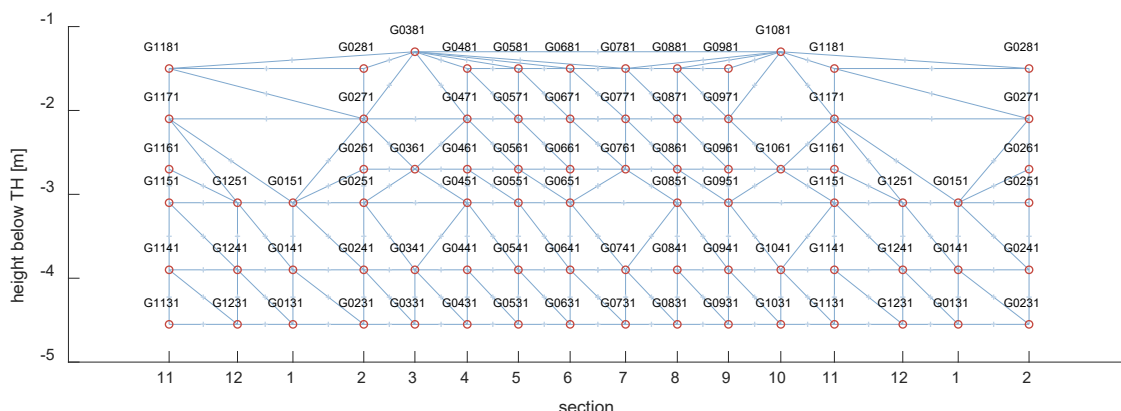


Figure 318: Grid used for interpolation for flat projection of AGDH BF4 hearth wall thermocouple data obtained from Delaunay Triangulation.

Optimizing Blast Furnace Hearth Inner State (OPTIBLAFINS)

As learned from CFD simulations of hearth liquid flow during drainage in the preceding BF hearth RFCS project SUSTAINTAP [55] and suggested by the CFD/DEM applications in WP1, the local dead man conditions (e.g. permeability) play an important role for the preferred flow paths during hearth drainage. Heat transfer from the liquid phase to the refractory wall by flow of hot metal is supposed to influence wall temperatures on short time scales. Therefore, the short time correlations between nearby thermocouples have been analyzed in a first attempt. Correlations of the data in a moving interval of +/- 12 h have been computed and animated. Figure 319 shows as an example a sequence of four images from this animation covering ~ 14 hours in ~4-5 h steps. Black crosses mark data positions between neighboring thermocouples whereas red dots mark the thermocouple positions themselves.

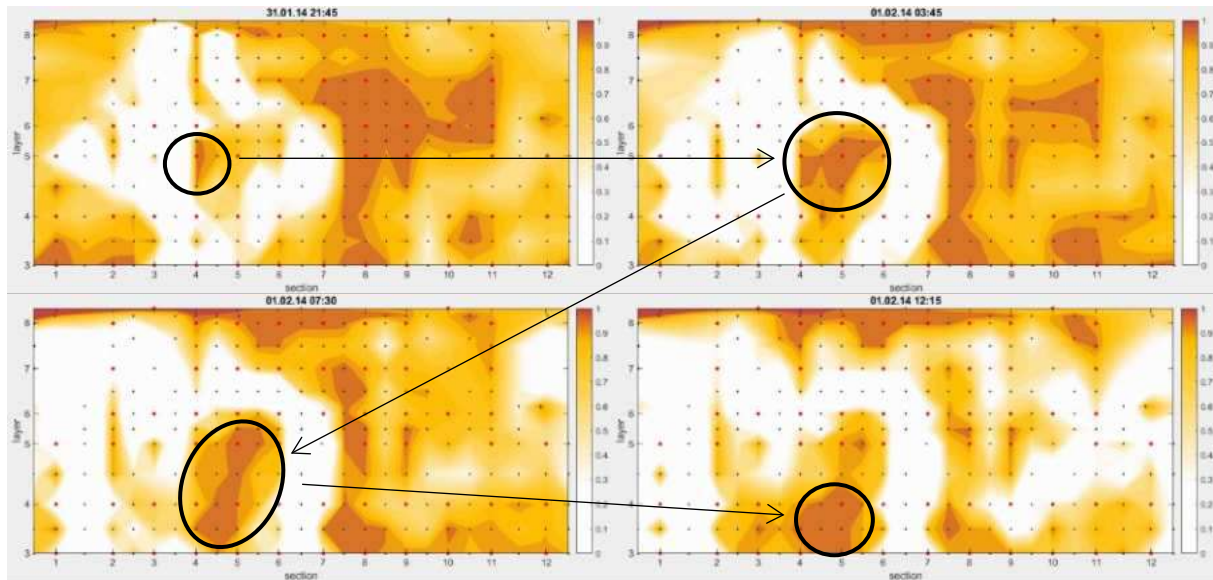


Figure 319: Movement of regions with high correlations.

The sequence shows a region in vertical section 4 with high correlation between two thermocouples which grows also including vertical section 5 and afterwards moves to a lower layer. Such phenomena can often be monitored in the animation of the short time correlation data. For better understanding of the phenomena, the standardized temperatures along two cut lines (through the vertical section 9 and a horizontal hearth layer 4) have been analyzed as shown in Figure 320. Two different groups of thermocouple trends (the large region of high correlations covering sections 4-8 and layers 4-6) can easily be recognized when the time series are plotted.

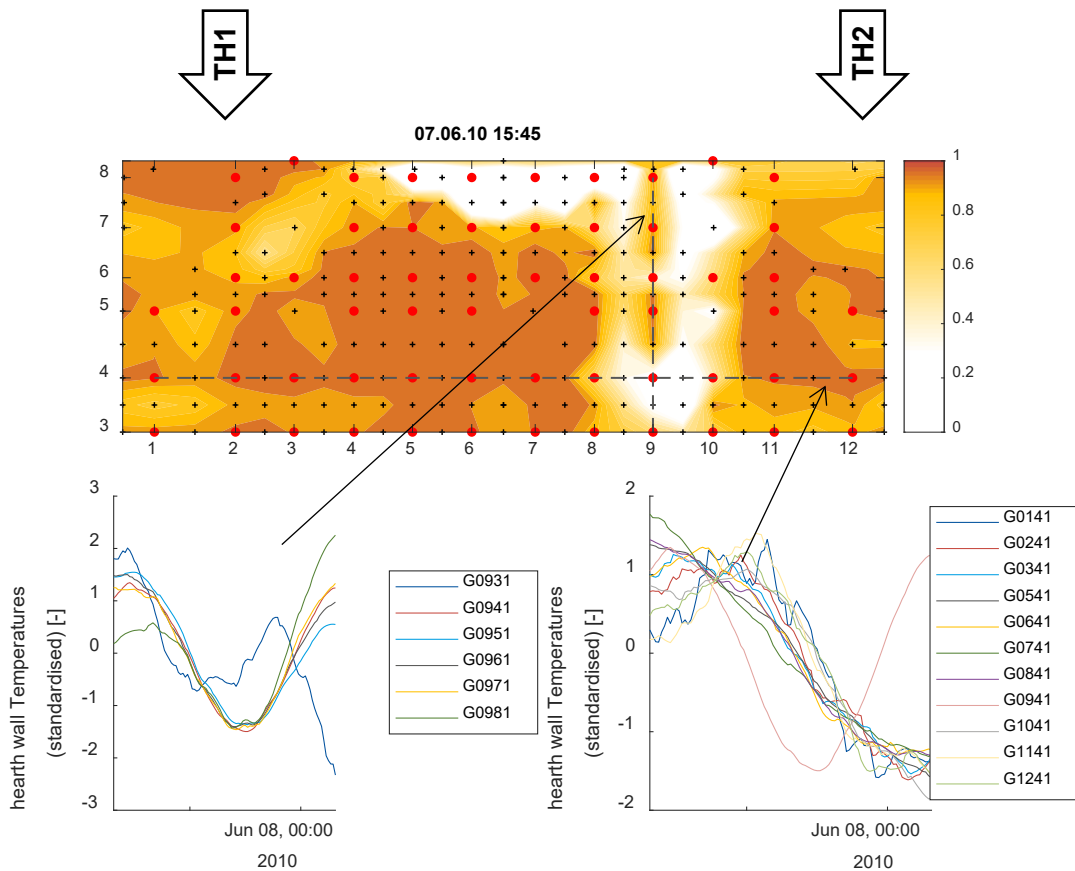


Figure 320: Example for local correlation of hearth wall thermocouple data (upper: flat projection of correlation coefficient r , lower left: temperatures at section 9 – vertical cut, lower right: temperatures at layer 4 – horizontal cut).

The lower right diagram in Figure 320 shows the temperatures along the horizontal line at height of layer 4. All those temperatures start with high values and then slowly decrease to lower temperatures. Only the thermocouple located in section 9 shows a different behavior (first decreasing and then again increasing), virtually separating the region of high correlation (sections 4-8 and layers 4-6) from the area to the right side (section 9-12).

The diagram at the lower left of Figure 320, illustrating the temperatures along section 9, shows a comparable effect. All thermocouples above layer 4 show the same, first decreasing and then increasing, behavior, only the thermocouple nearest to the sump level shows a different evolution. Obviously, the region with high correlation (sections 4-8 and layers 4-6) was influenced by different boundary conditions than the region along the vertical section 9.

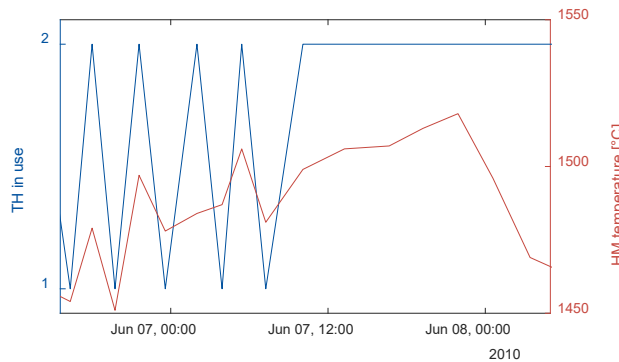


Figure 321: Tapping regime at 07.06.2010.

A possible explanation might be found in the tapping regime during this time span. On 07.06.2010 the tapping was shifted (from a strategy using TH 1 and TH 2 alternately to only tapping at TH 2). Also, the HM temperatures at TH 1 and TH 2 differed: The temperature at TH 2, which is nearer to section 9, was higher (Figure 321). This indicates that the regions drained during tapping of one taphole are different from those covered by the other taphole. Possibly the region of high correlation (sections 4-8 and layers 4-6) was affected by the lower hot metal temperatures near

Optimizing Blast Furnace Hearth Inner State (OPTIBLAFINS)

TH 1. But restrictively, it must also be stated that the following analysis shows that the vertical section 9 showed the tendency to isolated behavior even over longer time spans (Figure 322).

It can be concluded that the short time correlations of wall temperatures seem to be affected by local flow phenomena through the dead man, but a confirmation of this theory requires further detailed analysis of a multitude of the events monitored in the short time correlation animation, which will be provided in a follow up project. The occurrence of regions with high correlations for a moving +/- 12 h time span in the first view seems to be random. But computation of correlations for a whole year as shown for the years 2010 – 2015 in Figure 322 show that some regions have a higher probability of showing uniform temperature behavior than others. For example, from 2010 – 2014 vertical sections 10-12 often show high correlations, whereas vertical section 9 always shows isolated behavior, also vertical sections 4-6 and 1-3 often show high correlations.

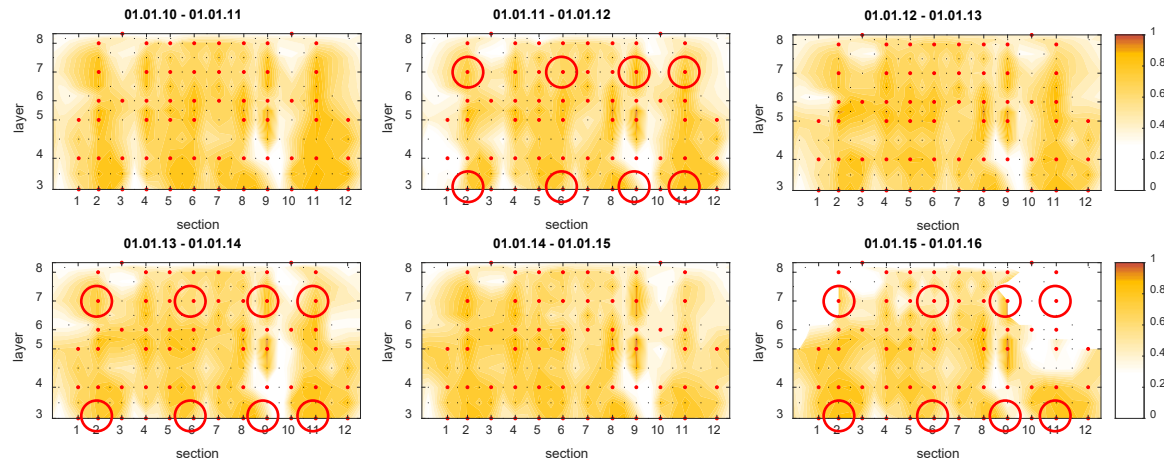


Figure 322: Long term correlation patterns of hearth wall thermocouple data.

To identify influences on those regions, the temperatures measured in 2011, 2013 and 2015 at two different heights, ~1m below tapholes at layer 7 and near sump depth at layer 3 (red circle marks in Figure 322), have been analyzed. These thermocouples were correlated with BF operating parameters influencing hearth thermal state as well as with results from the DMD model from (Task 3.3). The computed correlations coefficients r of the temperatures with the Dead Man Dynamics model DMD, production rate, hot metal temperatures and coal rate are summarized in Figure 323. In addition, blast volume and O₂ content, permeability, raceway adiabatic flame temperature, slag rate, heat loss via cooling water, share of coke, sinter, pellets and lumps in burden have been considered, but they either showed no clear influence or showed the same behavior as production rate (e.g. blast volume and O₂).

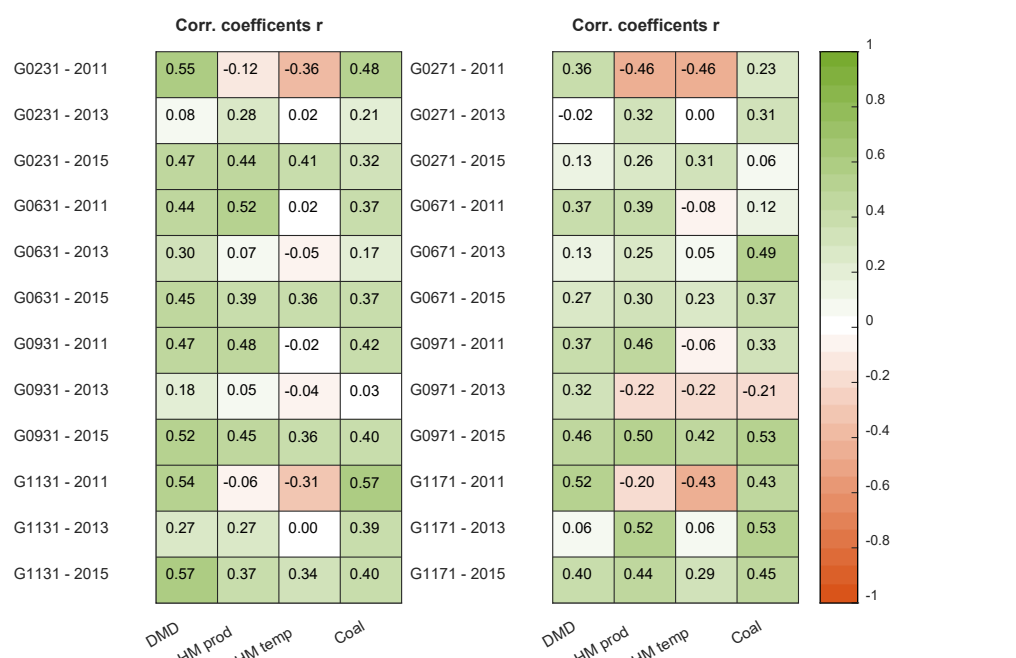


Figure 323: Correlation of hearth wall temperatures with BF operational and data and model results (left: thermocouples at layer 3 – sump level, right: thermocouples at layer 7, ~1m below taphole).

The Dead Man Dynamics model shows the highest positive correlation to the hearth wall temperatures among all analyzed data series. The correlations (Figure 323) near sump level (left table) are systematically higher than the correlations to the thermocouples closer to taphole level (right table).

Also, HM production rate and coal rate show high positive correlations to most thermocouples. However, in this case the correlations to the lower thermocouples (near sump level) were similar than to the higher ones (near taphole level). The hot metal temperature shows no clear influence on the wall temperatures. That means for some thermocouples the correlation is high, for others it is low or even negative.

As a conclusion, this analysis gives a first impression on how hearth wall thermocouple temperatures might be affected by the operational conditions. Clearly dead man state has a strong influence. Also, high production rate often causes higher wall temperatures.

The unclear influence of HM suggests that flow conditions are not stable in the whole hearth region. In fact, some regions seem to be blocked for direct flow influence from time to time. A possible approach for better understanding of the flow conditions are the short time correlations between neighbored thermocouples. In either case the analysis of the hearth wall temperatures clearly revealed, that both, BF hearth liquid flow patterns and BF operation, have a significant influence on the hearth wall temperatures. So, this must not be neglected, when the hearth wall temperatures are used for the estimation of the residual hearth wall thickness.

2.2.4.2.4 Balance-based model of liquid levels

The results of the liquid level model outlined in subsection 3.2.3.7 and the findings of the wear model in subsection 3.2.4.1.2 compared to data related to the operation of the blast furnace hearth revealed that it was necessary to deepen the understanding of drainage of blast furnaces operating with several tapholes. Earlier analysis at ABO had focused mainly on the conditions in the smaller Nordic one-taphole furnaces, where the tapping procedure is different. As the slag delay, i.e., the time elapsed before slag enters the runner after tap start, has proven to be an interesting signal characterizing the liquid levels in one-taphole furnaces [93], an approach was made to describe the liquid levels in a BF hearth with two tapholes operating alternately by an off-line simulation model. A complication in such larger furnaces is that the period during which both tapholes are plugged simultaneously is usually very short, and the iron-slag interface may not have the time to ascend above the level of the other taphole. The situation close to the end of tapping the "right" taphole is depicted schematically in the left panel of Figure 324. Therefore, there may be tappings where slag enters first, followed by iron after some time, which could be termed taps with negative slag delays. Furthermore, as the furnace hearth diameter is considerable, it is unlikely that the liquid (particularly slag) levels are the same at the tapping and non-tapping side of the hearth. This motivates an approach where the hearth is divided into several pools [95], [96]. The model is based on simplifying assumptions, in much following those presented in [93], but with some modifications to accommodate for the two pools (right panel of Figure 324) and a special treatment of the conditions in front of the tapholes.

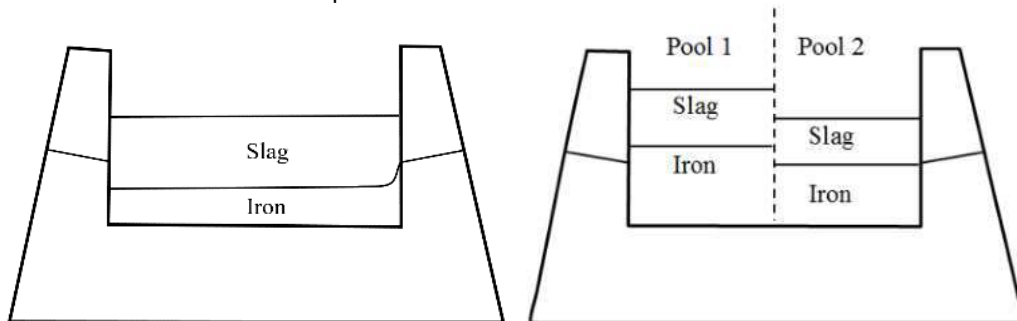


Figure 324: State close to the tap end in furnace hearth with (at least) two tapholes. right: two-pool model of the hearth.

In a nutshell, the model is based on the following main assumptions:

- The hearth is divided into two pools, with individual levels of iron and slag.
- The pools communicate with liquid flows proportional to the pressure difference in the pools (Eqs. (70)-(71)), controlled by two communication factors (φ_{ir} and φ_{si}).
- The inflow rates of iron and slag to the hearth (i.e., production rates) are given.
- The outflow rates show a fast-initial increase, followed by a gradual increase (Figure 325).
- The tap ends when the slag level in the draining pool bends to reach the taphole.

The mass flow $\dot{m}_i^{(jk)}$ of iron (subscript ir) and slag (subscript sl) from pool j to pool k was taken to be proportional to the pressure prevailing in the bottom of the pools, so

$$\dot{m}_i^{(jk)} = \varphi_i \Delta p_i^{(jk)}; \quad i = \text{sl, ir}, \quad j, k = 1 \dots 4, \quad j \neq k \quad (62)$$

with

$$\Delta p_{\text{sl}}^{(jk)} = \rho_{\text{sl}} (z_{\text{sl}}^{(k)} - z_{\text{sl}}^{(j)}); \quad \Delta p_{\text{ir}}^{(jk)} = \rho_{\text{sl}} (z_{\text{sl}}^{(k)} - z_{\text{sl}}^{(j)}) + \rho_{\text{ir}} (z_{\text{ir}}^{(k)} - z_{\text{ir}}^{(j)}) \quad (63)$$

Assumption 4 above is based on observations of the outflow rates in BF7 TSE, as discussed in section 3.2.3.7, with some further examples shown in Figure 326, where the initial "ramp up" of the tapping rate, followed by a period with slower increase can be seen. The former is expected to be due to two effects: 1) initially colder, and therefore more viscous liquids from the region close to the taphole flow out and are replaced by hotter liquids from the central parts of the hearth, 2) paths for the liquids in the coke bed in front of the taphole are gradually established along with the solution of carbon from coke into the hot metal [96]. The latter increase, in turn, depends on the erosion of the taphole that occurs as liquids flow through it.

In order to parameterize these trends, the outflow rates were approximated by two linear segments

$$\dot{m}_{i,\text{out}}(t) = \begin{cases} \gamma_i \dot{m}_{i,\text{in}} & \text{if } t_{i,\text{start}} \leq t \leq t_{i,\text{start}} + \Delta t_i \\ \gamma_i \dot{m}_{i,\text{in}} + \beta_i (t - \Delta t_{i,\text{start}}) & \text{if } t > t_{i,\text{start}} + \Delta t_i \end{cases} \quad i = \text{ir, sl} \quad (64)$$

where $t_{i,\text{start}}$ is the time when tapping of phase i starts and $\beta_i = \sin \theta_i$. The initial increase in the outflow rate thus occurs within a time period Δt_i and reaches a share, γ_i , of the production rate. The increase in outflow rate that occurs after this point makes the outflow rate exceed the inflow rate, which is a prerequisite for a drainage of the hearth.

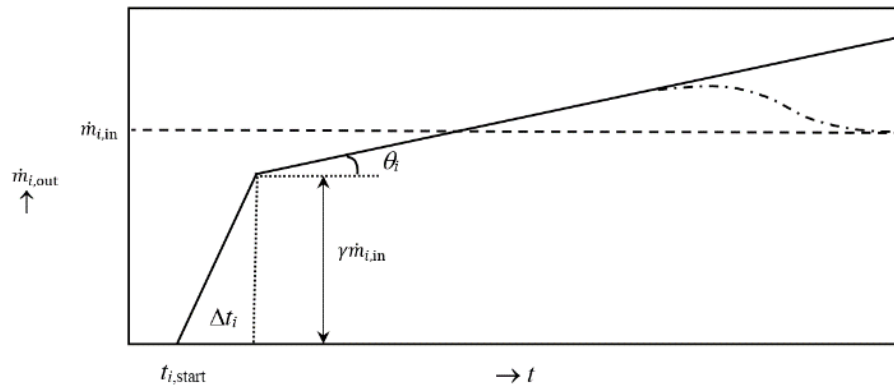


Figure 325: Schematic how the outflow rates are parameterized in the liquid level model.

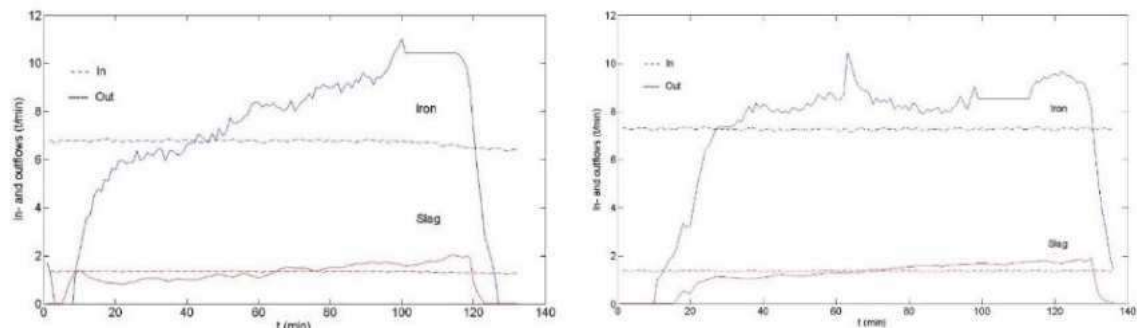


Figure 326: Outflow (solid lines) and inflow (dashed lines) rates of iron (blue) and slag (red) for two taps at TSE BF7.

Finally, a condition is needed for determining the point when a tap ends. It is generally believed that the bending of the slag surface against the taphole, which makes gas exit the taphole, is the primary reason. To estimate when this happens, several authors have studied the system in laboratory scale and proposed correlations, e.g., for the flow-out coefficient [97],[98] and [99]. For the case of simplicity, a reduced model was used here as a first attempt, still qualitatively considering the main trends captured by the flow-out-coefficient approach. Here, we simply take the final level of the slag-gas interface to be given by

$$\frac{z_{sl,end}}{m} = a \left(\frac{\dot{m}_{sl,out}}{t/min} \right)^b \quad (65)$$

where a and b are model parameters.

Simulations with the above model demonstrated its general feasibility, but the model was found to be very sensitive to cases where the iron-slag interface was close to the taphole level as the taphole was opened: In these cases, small differences in the initial condition could have considerable impact on the simulated drainage. To address this problem of excessive sensitivity, the inner end of the taphole was considered as indicated in Figure 327 with a shaded “fuzzy region” around the nominal inner level of the taphole, where three possible iron-slag interface levels at the start of the tapping have been indicated. For case a, the iron-slag interface is well above the taphole and the tap starts by draining iron, and not until the interface has descended into the shaded region slag starts flowing out. Conversely, for case c, where the interface is well below the taphole, the tapping starts with slag, and iron does not flow out until the interface has ascended into the shaded region. Finally, if the interface is within the shaded region, case b, the tapping is assumed to start with simultaneous outflows of iron and slag, which continue independent of the where the interface moves. This treatment of the tap start was found to give rise to a drainage in much better agreement with practical observations from the plant. However, two more a much revisions of the model were needed, which were both related to period of simultaneous draining of iron and slag, as it was found necessary to consider the effect on the outflow of the vertical location of the iron-slag interface. As the iron-slag interface descends below the taphole, it is likely that the iron outflow rate decreases at some point as the pressure difference needed to lift the heavier phase from lower levels in the hearth increases. Iida et al. (2009) considered the share of iron in the outflow to vary linearly with the iron-slag interface at levels below the taphole. Here, we instead impose the constraint that the outflow rate should asymptotically approach the production (i.e., inflow) rate, which means that the iron-slag interface would eventually stabilize if the tapping progresses long enough. This was realized by revising the original outflow Eq.(64) by

$$\dot{m}_{i,out}^{rev} = \dot{m}_{i,in} + \frac{\dot{m}_{i,out} - \dot{m}_{i,in}}{1 + \exp(-\alpha((z_{th} - z_{ir}) - \Delta z))} \quad (66)$$

which implements a sigmoidal transition from the straight line (with slope β) to the inflow rate, as indicated in the right part of Figure 325 by the dashed-dotted curve. In Eq.(66), the parameter α controls the steepness of the transition while Δz expresses the distance below the taphole around which the transition occurs. Thus, for large α the outflow rate decays suddenly, while a large Δz means that the transition point is well below the taphole. As for the case where the tapping starts with the interface close to the taphole (b in Figure 327) but ascends above the shaded region, it is natural to assume the slag outflow to decrease as the interface has to bend to allow for a simultaneous draining of both phases. This was considered in the model by a similar expression as Eq. (66), but with a slag outflow that approaches zero if the level of the interface rises excessively.

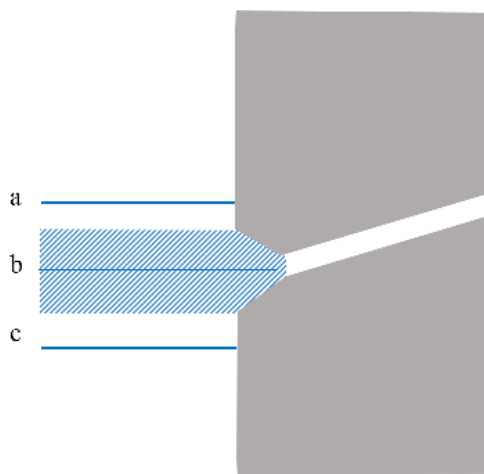


Figure 327: Schematic of the treatment of the taphole region with respect to the iron-slag interface (horizontal lines) at the moment the taphole is opened. The shaded area indicates the region where both iron and slag appear simultaneously in the runner.

In-order to illustrate the simulation model, a set of examples will be presented where a blast furnace with a production rate of 480 t_{hm}/h of pig iron, a slag ratio of 250 kg/t_{hm}, a hearth diameter of 14 m and a dead man voidage of 0.3 was simulated. The model ran enough cycles, so a quasi-

stationary state was reached. Important variables to be reported are the slag delay, defined as the time elapsed between the start of iron and slag draining, as well as the duration of the tap. The hearth was divided into two pools of equal size, so the inflow to each pool represents half of the production rate, and the hearth was drained by alternating the tapholes. Because of the quite large number of parameters in the model, a full evaluation of the effect of all parameter values will not be possible here.

The following parameter values were used initially: The two pools were quite well connected ($\varphi_{ir} = 2$, $\varphi_{sl} = 2$), the tapholes were assumed to be on identical levels, using $\Delta t_{ir} = 10$ min, $\Delta t_{sl} = 5$ min, $\gamma_{ir} = 0.8$ and $\gamma_{sl} = 0.5$ for the ramp-up phases of the outflows, $\beta_{ir} = 0.05$ t/min² and $\beta_{sl} = 0.015$ t/min² for the increase in the outflow rates due to taphole erosion, and $a = 10$ and $\Delta z = 0.3$ m in Eq. (66). The "fuzzy region" (Figure 327) around the taphole was taken to be ± 0.1 m and both tapholes were kept plugged 2 min between the taps. As for the tap end, the parameters of Eq. (65) we set to $a = 0.1$ and $b = 2$; it should be noted that these two parameters merely determine the absolute level of slag-gas interface, but do not influence the results qualitatively.

A simulation using the base-case settings (Example 1) resulted in no slag delay and a tap duration of 142 min (

Table 63, first row) and the liquid levels depicted in Figure 328a, where colours (green and red) have been used for the levels in the two pools and the dashed line indicates the taphole level. A stronger coupling of the iron pools ($\varphi_{ir} = 4$) does not change the tap duration but the slag delay decreases to -6 min, since the non-draining pool has a lower level at the end of the tap (Example 2, Figure 328b). Conversely, a decrease in the iron pool communication ($\varphi_{ir} = 1$) increases the tap duration by about 30 min and the slag delay becomes positive, 13 min (Example 3, Figure 328c). The effect of slag-pool communication is illustrated by Example 4, where the communication factor was considerably decreased to $\varphi_{sl} = 0.5$. Quite interestingly, the slag delay now becomes clearly negative. The reason is that the higher slag level in the non-draining pool presses more iron to the draining pool, thus lowering the iron-slag interface in it as seen in Figure 328d. This phenomenon has been discussed by Iida et al. [96].

The effect of the ramp-up phase of the outflow was next studied, where the factor γ for iron was increased to $\gamma_{ir} = 1.0$ (Example 5). The tap duration and slag delay remain unchanged, but the time evolution of the iron level becomes more linear (Figure 328e).

An increase in the slag factor to $\gamma_{sl} = 0.7$ has a very similar effect (not shown). Thus, the model does not seem to be particularly sensitive to these model parameters. Finally, the effect of the transition point where the iron outflow decreases towards the production rate was analyzed by increasing the value to $\Delta z = 0.5$ m (Example 6). As expected, the change makes the slag delay more negative as the iron levels descend more below the taphole (Figure 328f).

A more interesting aspect is the level of the taphole, which may change if the path taken by the drill varies, or if the taphole length changes. Assuming a constant drill angle (say, 10°), a 0.5 m change of taphole length yields a change of about 9 cm in the vertical level of the inner end of the taphole. Examples 7 and 8 illustrate the system where Taphole 2 (TH2) is 0.1 m or 0.2 m lower than TH1. As is seen from the results in

Table 63, the level has a quite remarkable effect on the slag delay, and for larger changes also on the tap duration: a lower taphole level yields a (more) positive slag delay when the taphole in question is operated, while for the other taphole the opposite trend is observed. The resulting liquid levels are illustrated in Figure 329.

Table 63: Tap duration, slag delay and figure number illustrating the liquid levels for the examples studied.

Example	Tap duration (min)	Slag delay (min)	Figure	Comment
1. Base case	142	0	Figure 328a	Reference case
2. $\varphi_{ir} = 4$	142	-6	Figure 328b	Better iron pool communication
3. $\varphi_{ir} = 1$	175	+13	Figure 328c	Worse iron pool communication
4. $\varphi_{sl} = 0.5$	144	-11	Figure 328d	Higher slag level improves iron communication
5. $\gamma_{ir} = 1.0$	142	0	Figure 328e	Increased iron outflow changes iron level evolution
6. $\Delta z = 0.5$ m	142	-9	Figure 328f	Deeper transition point increases slag delay

7. $z_{th,2} = z_{th,1} - 0.1 \text{ m}$	141/142	-5/0	Figure 329a	Lower TH2 level increases slag delay for tapping 1
8. $z_{th,2} = z_{th,1} - 0.2 \text{ m}$	163/217	-14/+3 9	Figure 329a	Lower TH2 level increases slag delay for tapping 1

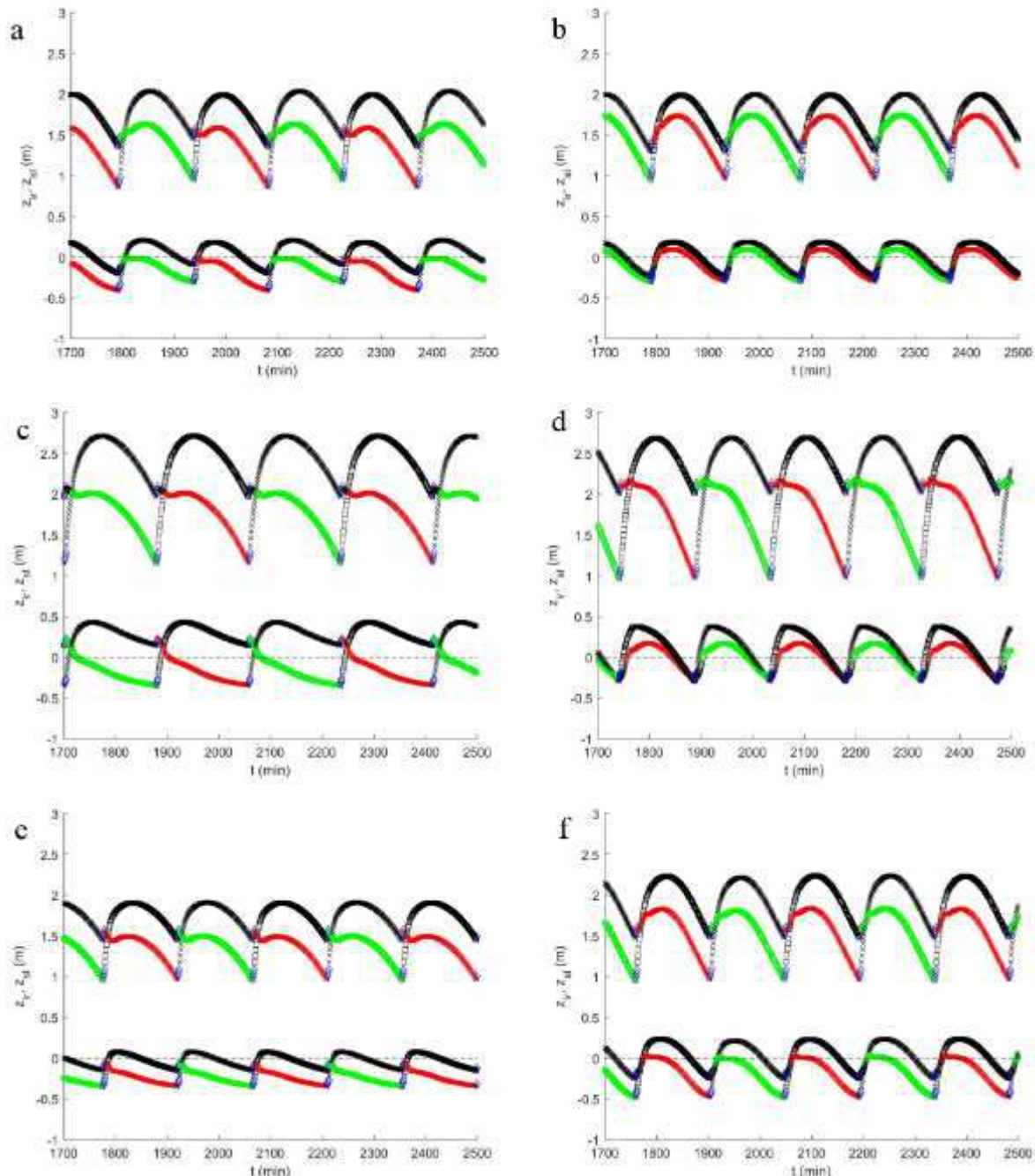


Figure 328: Simulated liquid levels for the first six examples of Table 63. a) Base case, b) better iron-pool communication, c) worse iron-pool communication, d) worse slag-pool communication, e) steeper ramp-up of iron outflow, and f) deeper transition point for iron outflow decrease.

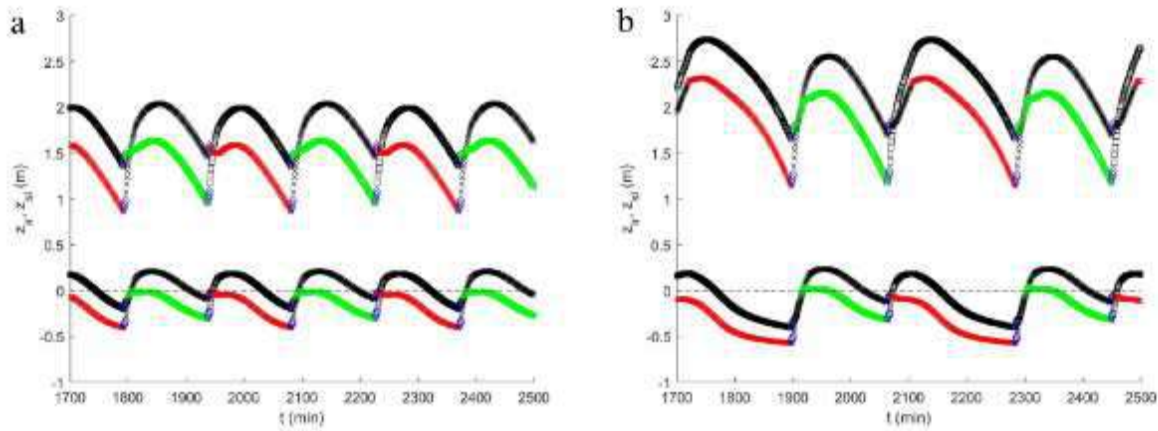


Figure 329: Simulated liquid levels for the last two examples of Table 63, where the level of taphole 2 is lower than taphole 1 by a) 0.1 m, and b) 0.2 m.

In analyzing tapping data from TSE BF7 from the present campaign, some interesting findings were made. Figure 330 depicts the in- and outflow rates for eight consecutive taps in January 2016. The left set of panels depict the taps from the south taphole while the right panels show the taps from the west taphole. By analyzing these results, it is seen that slag (red lines) consistently appears first in the south taphole (showing a negative slag delay of a few minutes) while iron (blue lines) appears first on the west side. Furthermore, the increase of the iron outflow is slower on the south side, which is natural as slag occupies part of the taphole, while the initial increase in the iron outflow is more rapid on the west side, but sometimes levels out locally at the moment when slag enters. Figure 331 shows ten consecutive taps from a period a week later, now with alternating tappings from the south and north side. Again, the tappings from south show a negative slag delay while those from the north a positive one and poor slag drainage. Based on these findings and the above analysis of the off-line model it may be suspected that the south taphole extends less deep into the hearth, as indicated schematically by the dashed and dotted curves in Figure 332.

In forthcoming work, the findings of the on-line liquid level model, and the correction factors needed to yield quasi-stationary liquid levels, will be combined with the results of the simple off-line draining model to yield a better view of the prevailing conditions in the hearth of BF7 of TSE. Furthermore, inspired by the trends in the observed out flowrates (Figure 330 and Figure 331), the possibility of expressing the ramp-up parameters (Eq.64) Figure 325) as a function of the conditions will be explored. For instance, it would be natural to apply different parameters depending on whether iron or slag is the first phase to be tapped, as indicated in the analysis of the outflows of Figure 330. A possibility is also to incorporate a more detailed model of the liquid flow in the taphole as outlined in [91], but this requires considerably more computational time as the solution becomes iterative. Another interesting matter to study is the share of slag and iron of the tapped liquids. In the off-line model the share decreases according to Eq. (66) (cf. dashed-dotted line in Figure 325) as the iron level descends deeper below the taphole. This is seen in the outflow rates of iron and slag in example 1 (Table 63), that have been depicted in Figure 333. For longer taps, it is obvious that the share of slag in the tapped liquids would increase. This is supported by observations of the tapped liquids in BF7 of TSE: Figure 334 illustrates the observed relation between the mass of tapped slag and the slag mass ratio of the tapped liquids for a period of three months: The quantity of tapped slag increases hand by hand with the slag ratio. It should be stressed that no such relation was found between the tapped quantity of iron and the mass share of slag.

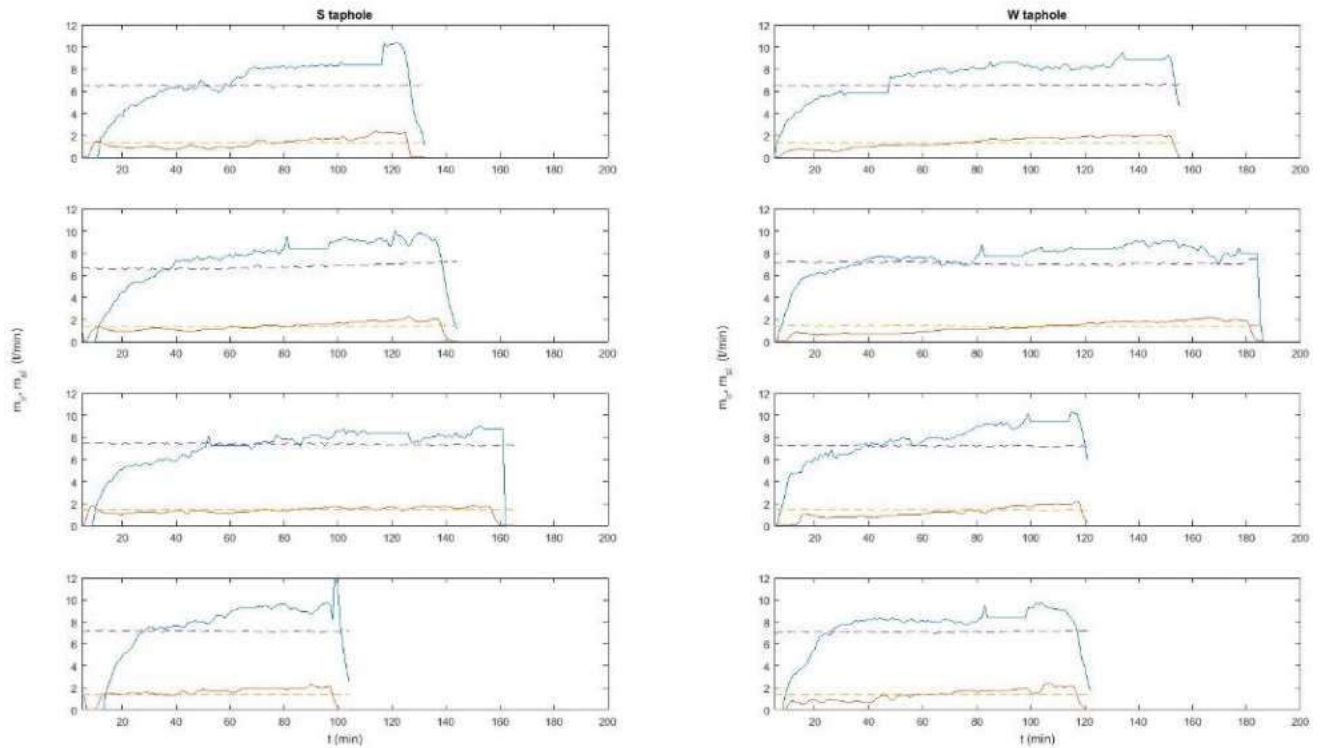


Figure 330: Observed inflows (dashed lines) and outflows (solid lines) of iron (blue) and slag (red) for eight consecutive taps alternating between the south and west tapholes of TSE BF7 in January 2016.

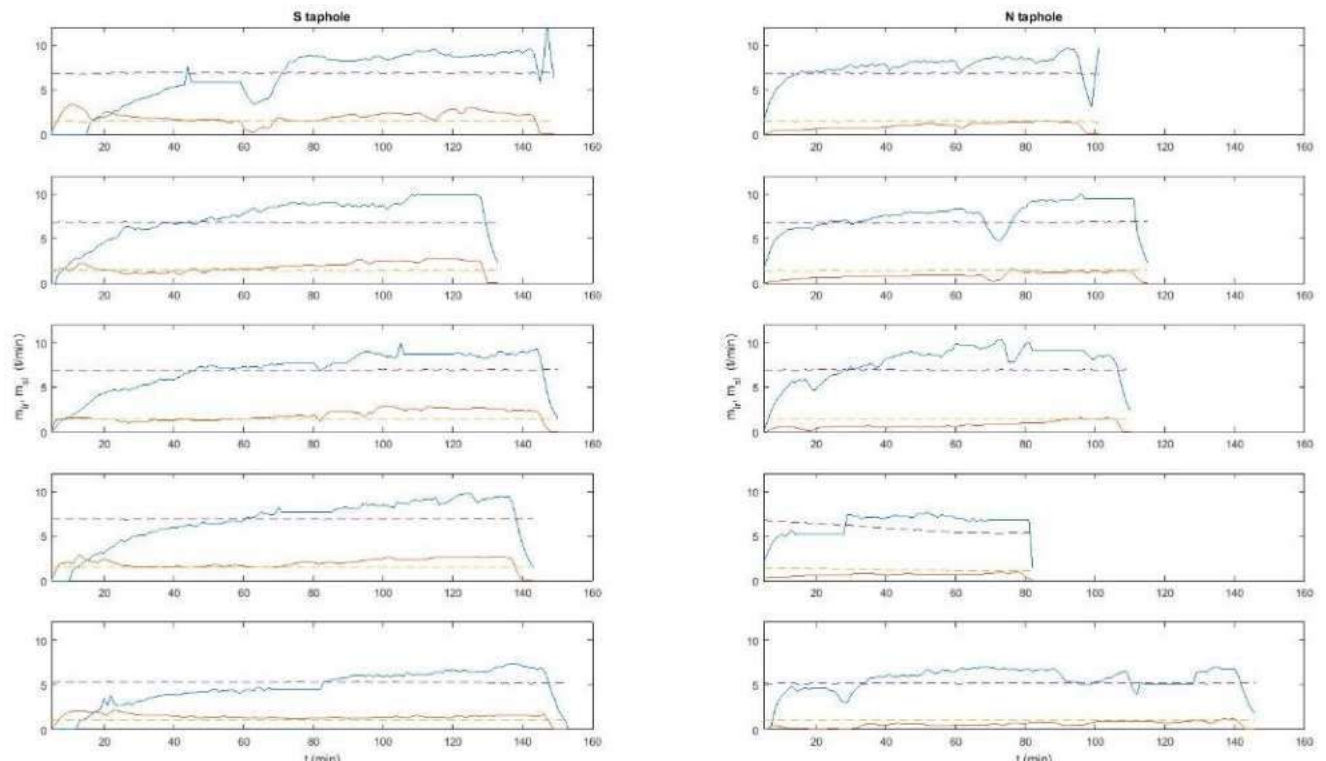


Figure 331: Observed inflows (dashed lines) and outflows (solid lines) of iron (blue) and slag (red) for ten consecutive taps alternating between the south and north tapholes of TSE BF7 in January 2016.

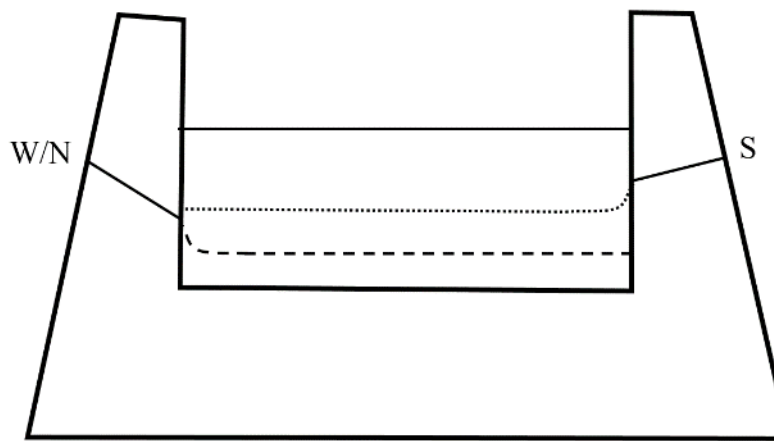


Figure 332: BF state where south taphole extends less deep into the hearth than the other (west or north) taphole, also indicating the final levels of the iron-slag interface by dotted and dashed lines, respectively.

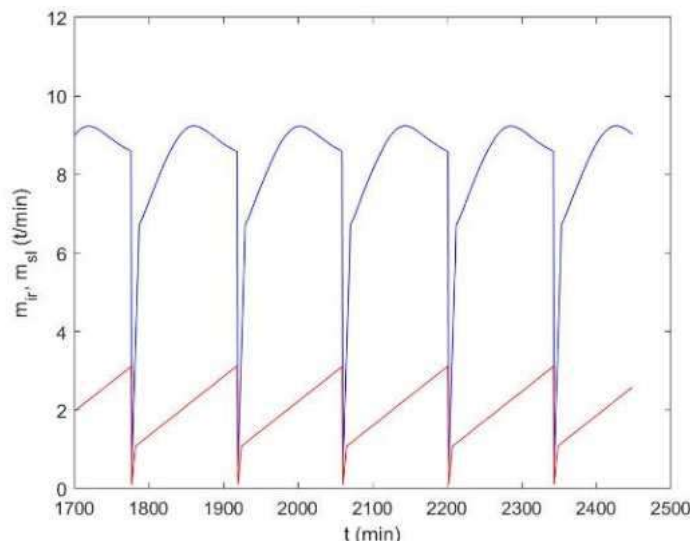


Figure 333: Outflow rates of iron (blue) and slag (red) in example 1 (Table 63).

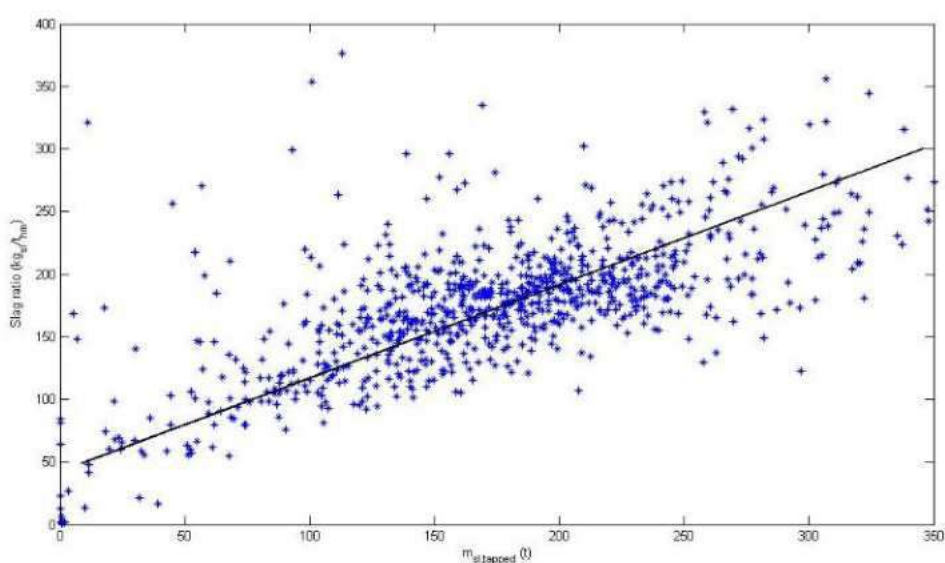


Figure 334: Relation between mass of tapped slag and slag ratio for BF7 of TSE for a period of three months.

Concluding remarks: The off-line simulation tool of the blast furnace hearth with two alternating tapholes has been demonstrated to shed light on the complex tapping in multi-taphole furnaces, and the simulation results have helped understand certain observations in the plant in conjunction

with the tappings. The tool can be used to test hypotheses concerning the operation of the hearth, and by applying it a better view of the internal conditions of the blast furnace can be obtained. A more detailed explanation of the model, and further examples on its use, are found in [100].

2.2.4.3 Verification and fitting of the on-line CFD model with a monitoring of liquid level indicators

2.2.4.3.1 Liquid level model using strain gauges

An advanced method was developed by CRM to measure real-time iron and slag levels in the hearth of a blast furnace. This model is based on the analysis of circumferential strain measurements of the outer shell along a vertical line near the taphole using strain gauges [55].

The CRM liquids levels model was initiated in 2004 within the framework of a program at CRM and continued from 2005 to 2008 in the RFCS project DEMPOLIFE [102]. At the beginning, several strain gauges were welded on three blast furnaces hearth shells in order to study if it was possible to measure strain variations accurately during operations. Figure 335 shows the strong correlation observed between the static pressure at the taphole and the strain gauge measurement performed at the same level.

Several campaigns of measurements were conducted during this earlier project. It could be concluded that the relation between pressure and strain has a relatively constant slope, but that the intercept varies with time. Temperature variations might cause these effects.

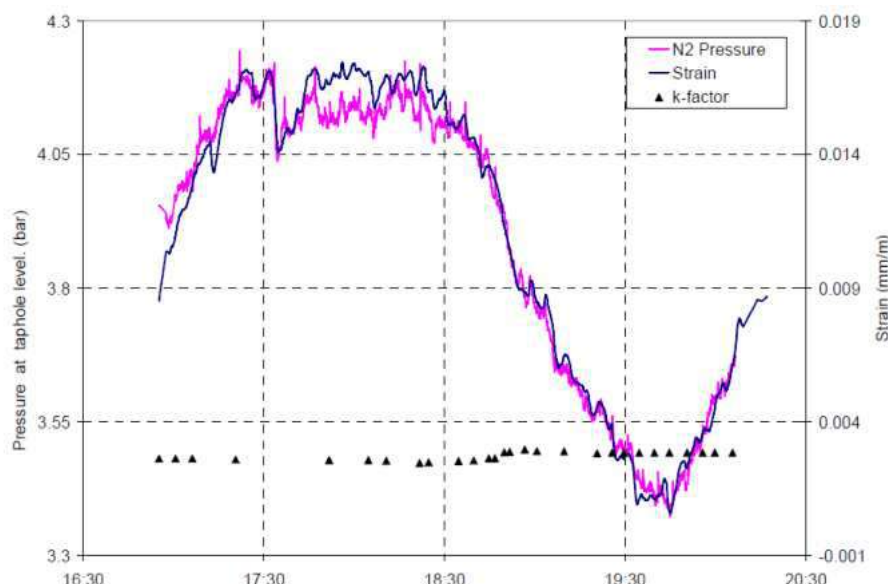


Figure 335: Comparison between pressure at the taphole and strain measured at taphole level (first campaign).

A complementary FEM simulation was conducted to understand the parameters that influence the strain measurements. The model gave as a result the stress and strain of the blast furnace wall, taking into account the temperature gradient, which caused a non-negligible strain. The following assumptions were made in the model:

- The geometry of the blast furnace is axisymmetric
- The material properties are constant and temperature independent
- The iron-slag and slag-gas interfaces are horizontal.

Three different cases were tested for calibration: with no charge and isothermal, with charge and isothermal and with charge and non-isothermal.

The calibration without charge and isothermal conditions was done for a period of time where the blast furnace was restarted after a stop. The transversal strain and the gas pressure were continuously measured for this period of time. The objective was to adjust the geometry of the refractory wall, the elastic boundary at the tuyeres and the Young moduli of the refractories to match the measurements.

The calibration with charge and isothermal conditions was used to determine the initial liquid levels, disregarding temperature variations.

Optimizing Blast Furnace Hearth Inner State (OPTIBLAFINS)

The last calibration was decomposed in two steps, using a heat transfer modulus and an FEM modulus. Several temperature probes located on both side of the shell give an estimation of the temperature differences in the shell. Measured strains using the last calibration model were compared with the measured strains according to their relative position in the wall, yielding the results presented in Figure 336.

There was a strong correlation between measurements and the FEM model except for the base of the hearth. However, there was still a strong influence of the shell temperature on strain measurements which need to be considered.

As a global conclusion of the DEMPOLIFE project [102], it was found that strain measurements on the outer shell could provide an estimation of what happens in the hearth and could be correlated to liquids levels. There were also strong dependencies of several parameters that could influence the measurements, as summarized in Figure 337.

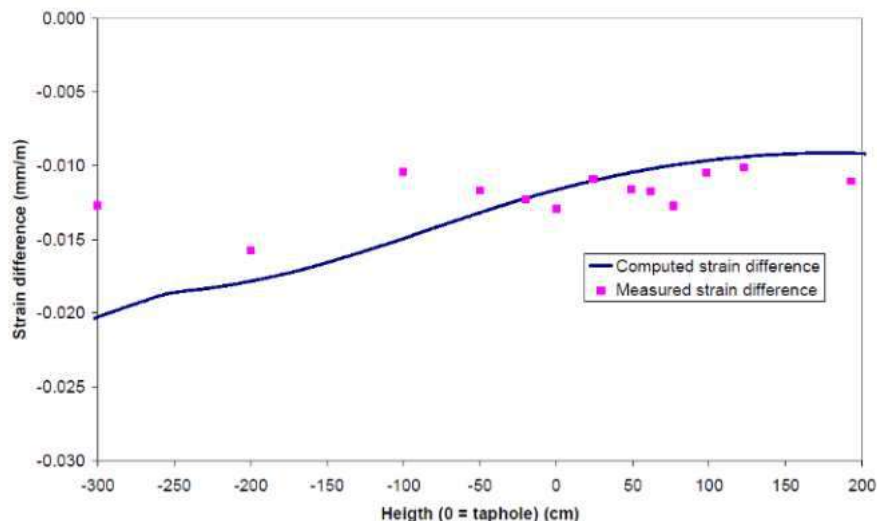


Figure 336: Calculated vs. measured strain differences at cooling water temperature.

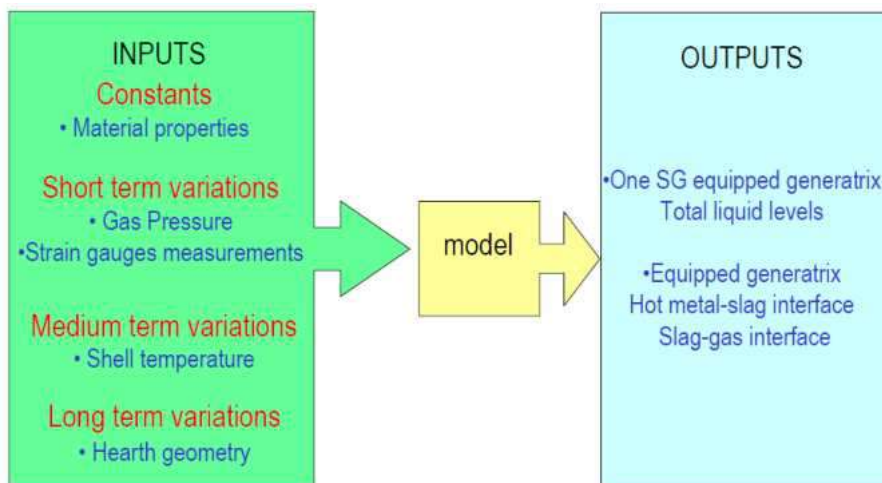


Figure 337: Scheme of parameters influencing the measurements and outputs of the model.

The RFCS SUSTAINTAP project [55] aimed to improve the blast furnace tapping practice, and CRM was involved, amongst other tasks, to develop and improve the liquid levels model.

The calculation procedure was as follows:

- The strain caused by the thermal expansion of the shell was compensated using the temperatures measured by the Pt100 installed on the steel shell.
- The strain measurements were treated with a high pass filter in order to compensate the long-term changes and to isolate only the strain changes originated by the pressure- and liquid-levels changes.
- The liquids levels were calculated using the Roark's formulas [103].

2.2.4.3.1.1 Theory behind the liquid level model

Liquids level model using strain gauges measurements is based on Roark's formulas, generally used to determine the bending profile of complex geometries [103]. The theoretical geometry setup used in this model is shown in Figure 338.

The profile of pressure inside the blast furnace hearth, schematically depicted in Figure 339, can be divided into three main different profiles which correspond to the impact of each liquid and gas on the shell:

- The hot blast pressure is applied on the total length of the shell and described with a uniform pressure (green);
- The hot metal (blue) is described with a uniformly increasing pressure from the bottom to the hot metal level;
- The slag (red) is described using both a uniformly increased pressure from the hot metal level to the slag level, and a uniform pressure from the bottom to the hot metal level.

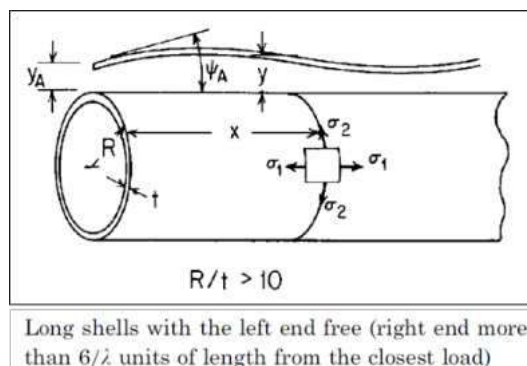


Figure 338: Geometry setup used to model the BF hearth.

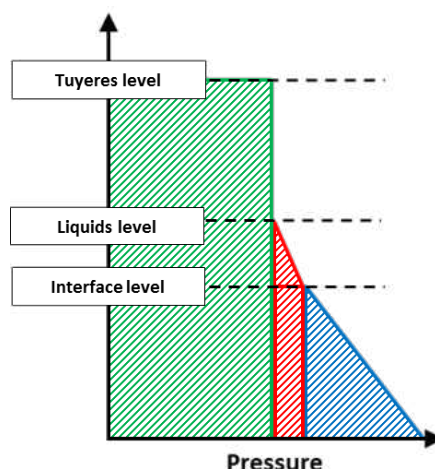


Figure 339: Pressure profiles of the gas (red), the slag level (green) and the hot metal level (blue) on the BF hearth shell.

Consequently, the pressure profile is directly related to the two parameters which are the interface level – between the hot metal and the slag – and the total liquid level. Roark's formulas are used in order to determine the bending profile of the hearth assuming that the blast furnace hearth is axisymmetric, loads and boundary conditions are axisymmetric, and liquid surfaces are horizontal.

An example of this bending profile with fixed values of liquid levels and blast pressure is shown in Figure 340.

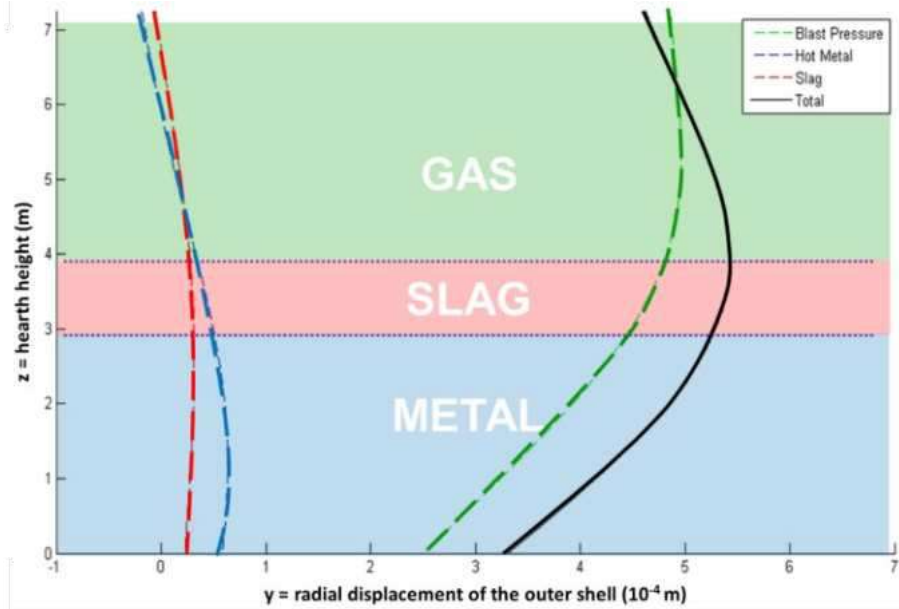


Figure 340: Bending profile of the BF hearth according to pressure profile induced by liquids and gas.

The link between the bending profile, which corresponds to the radial displacement of the shell, and its circumferential strains is a function of the mean radius of the shell

$$\varepsilon_\theta(z) = \frac{y(z)}{R(z)} \quad (67)$$

where z is the height considered, $R(z)$ is the mean radius of the shell, $y(z)$ is the radial displacement of the shell, and $\varepsilon_\theta(z)$ is the circumferential strain inside the shell.

2.2.4.3.1.2 Model architecture

The current version of the liquid levels model is a MATLAB script which is composed of several modules.

Figure 341 shows the general architecture of the script, which can be summarized by the following steps:

First step is dedicated to the strain gauges reading and corrections applied to convert signals in in-order to obtain the mechanical strain variations. Additional filtering is advised to eliminate long-term signal variation such as refractories erosion;

Next step consists in applying an offset to each strain gauge system which corresponds to the initial state when strain gauges have been welded on the shell;

A solver (calculation modulus) is used to determine the couple of solutions (hot metal and slag levels) that best fit the experimental measurements;

Outputs can be chosen amongst several types of parameters from the model. For a standard use, it has been chosen to display the time dependency of liquid levels and the absolute error calculated by the mismatch between the theory and the measurements.

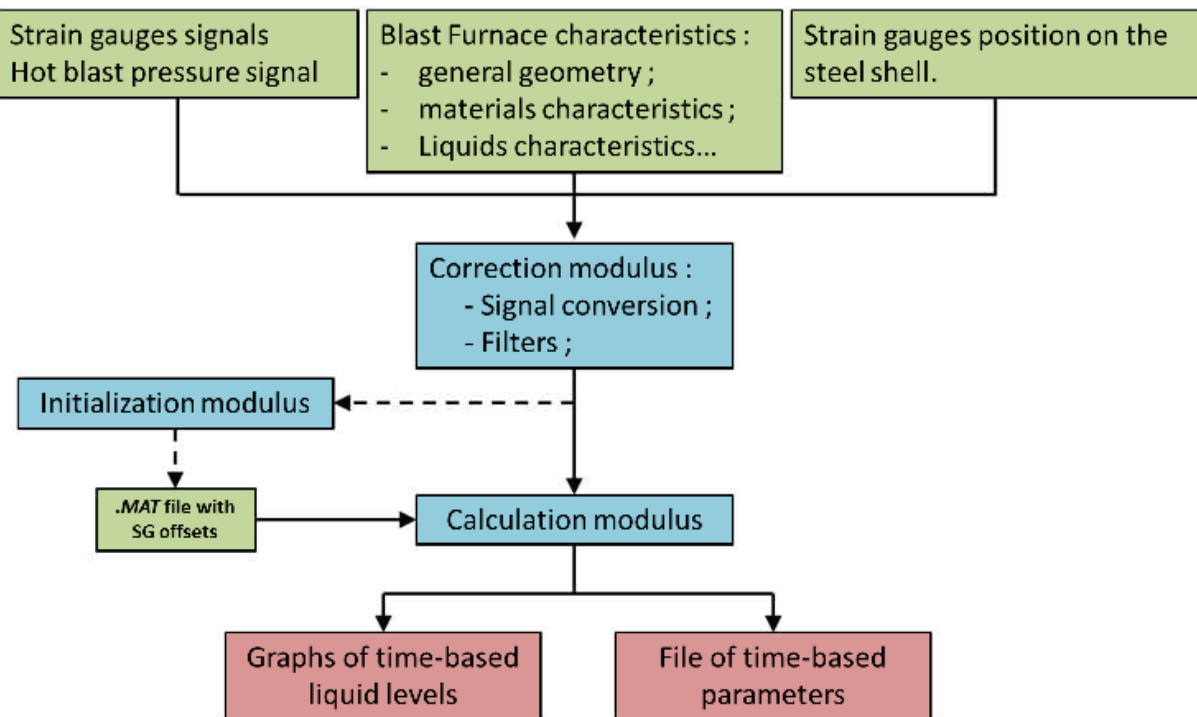


Figure 341: General architecture of the script of the liquid levels model.

As stated before, the initialization modulus is not mandatory if a previous estimation of the internal strain state of the blast furnace hearth has already been performed.

The calculation modulus is a two-step loop which calculates alternatively the slag level then the hot metal level:

- A uniform repartition of slag and hot metal mixed in a global unique phase is initially assumed in-order to estimate the average density of liquids and to determine the total liquid levels (slag level) by a linear expression.
- Considering the slag level (i.e. the total liquid level obtained in step i), the hot metal level is calculated in a two-fluid configuration with different densities.
- The new repartition of levels makes it possible to estimate a new value for the average density based on the relative volume of each fluid.

The loop ends when the difference between densities calculated in two consecutive loops is sufficiently small.

This solver is extremely reliable, due to the fact that every calculation is linear. The frequency of calculation for a simple vertical line is a bit lower than 1 Hz in offline mode, which is clearly sufficient considering the dynamics in the blast furnace hearth. Typically, a tap lasts between 45 min and 1 h 30 min. It is possible to calculate and display average values over time on a pre-defined time range, initially set at 60 s in the case of the AM Fos plant.

2.2.4.3.1.3 Strain gauge measurements

In the SUSTAINTAP project [55], the temperature compensation was handled by measuring the temperature of the outer shell using Pt100 probes and then processed in the code to remove the effect of thermal strain. Several adjustments to the method have then been considered. Strains are now measured along a vertical line with 6 or 7 systems using half-Wheatstone bridges (i.e., 2 out of 4 gauges per bridge designed to measure the mechanical strains). The temperature compensation is handled with 2 welded and 2 non-welded gauges, as depicted in Figure 342. The latter only measure the thermal strain which is subtracted from the total strain measured by the welded gauges.

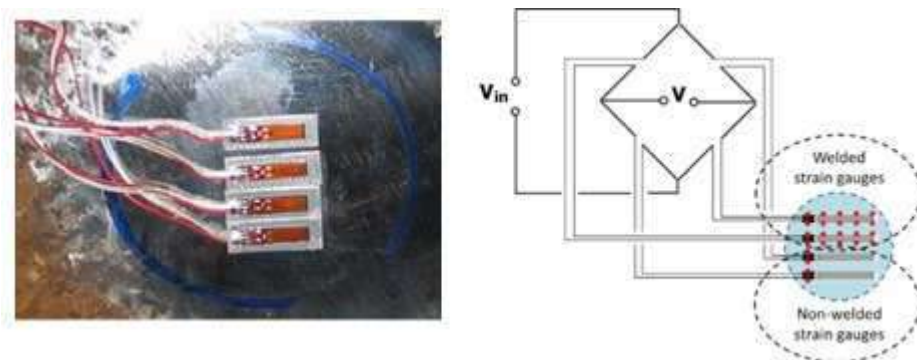


Figure 342: Strain gauges system using a half-Wheatstone bridge with temperature compensation.

Strain gauges can give a reliable measurement the variations in the total strains, but this is not what is needed for comparison with the theoretical model. In fact, the full mechanical strain must be measured, which corresponds to the measurements without the thermal strains and with the internal strain state of the shell when gauges are applied (Figure 343).

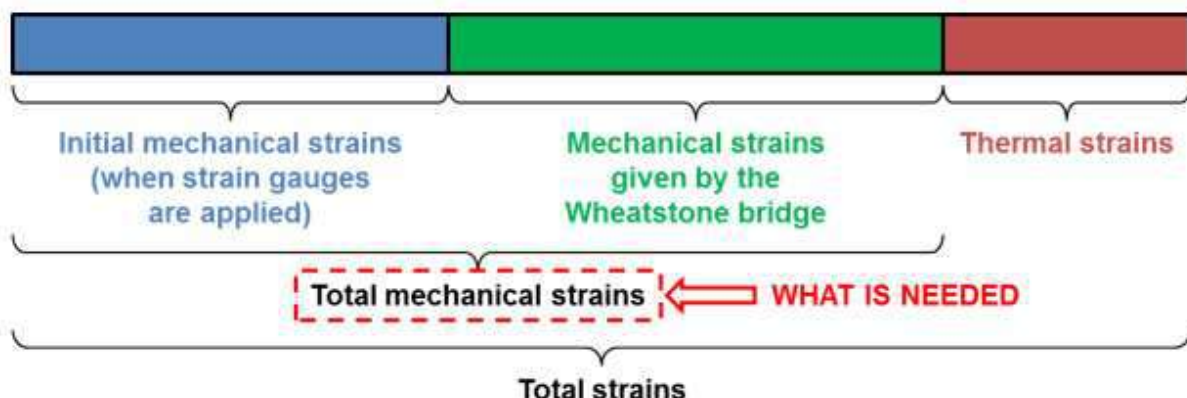


Figure 343: Scheme representing strains measured and strains needed for the model.

Experimentally measured strains mainly depend on:

- material characteristics of the shell.
- material characteristics of the refractories.
- geometry of the hearth and especially refractories.
- shell temperature.
- gas pressure.
- hot metal and slag levels.
- internal stress state.

Gauges were applied during a scheduled stop of the blast furnaces, so gas pressure and liquid levels were low. This is the simplest way to obtain the total mechanical strains because initial mechanical strains were considered null. However, because of the larger impact of gas pressure on the strains (Figure 340), a small variation of blast pressure can cause large change on strain measurements, which leads to incorrect liquid level estimates.

Some other solutions have been considered:

- Use another well-known state of liquid levels while blast is still on. For instance, an EMF signal could allow this estimation and the initial state could be determined while solving the theoretical model.
- Use strain gauges while the BF is operating and consequently reduce the impact of blast pressure variations compared to liquid level effects.

The former option was chosen because an initialization modulus, presented in Figure 341, was developed. It is based on the minimization of the mismatch between the theoretical and the measured strains. This script needs to be run once as a calibration tool and gives the internal strain state of the BF.

The calculation modulus is used in order to calculate the liquid levels on the one hand and the error on each strain gauge of the generatrix on the other hand. In this case, the input signals have been

averaged in several operating time portions to reduce computing time. The liquid levels were used only for validation, while errors are used to find the global offsets.

Differences between strain-gauge measurements after filtering and strains predicted by the theoretical model are here called “errors” in the liquid levels model. Because the liquid levels tend to find the best couple of liquid levels which minimize those errors, so applying those errors to signals into a new iteration will then tend to minimize the next errors. This sequence converges nicely, as shown in Figure 345. A convergence criterion has been defined to stop the calculation when the error is lower than a fixed threshold.

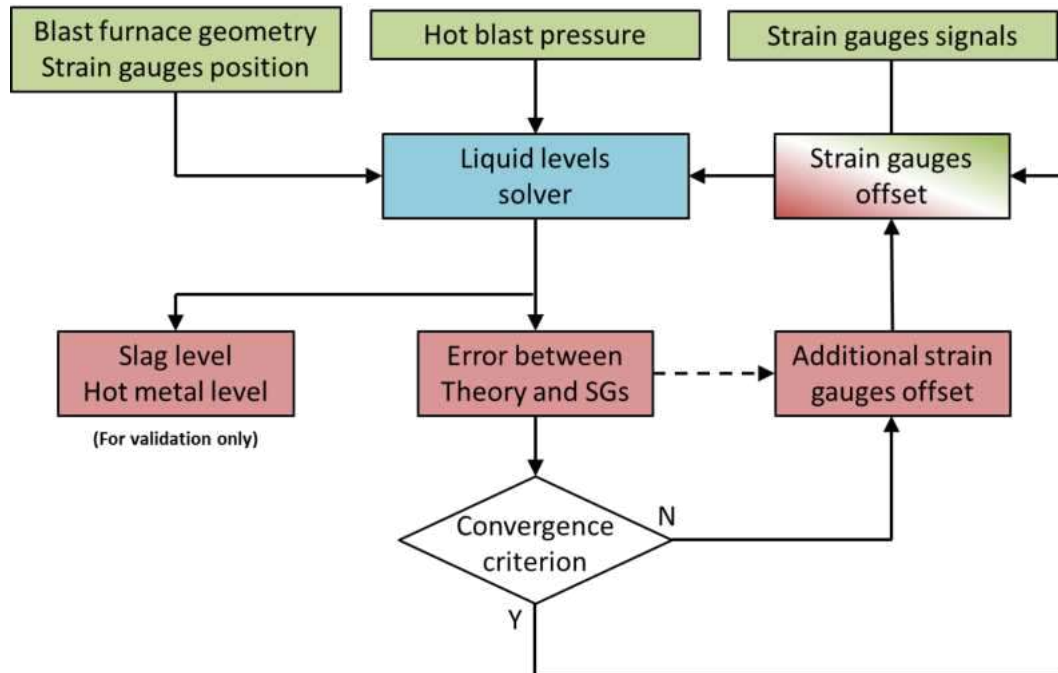


Figure 344: Architecture of the initialization module.

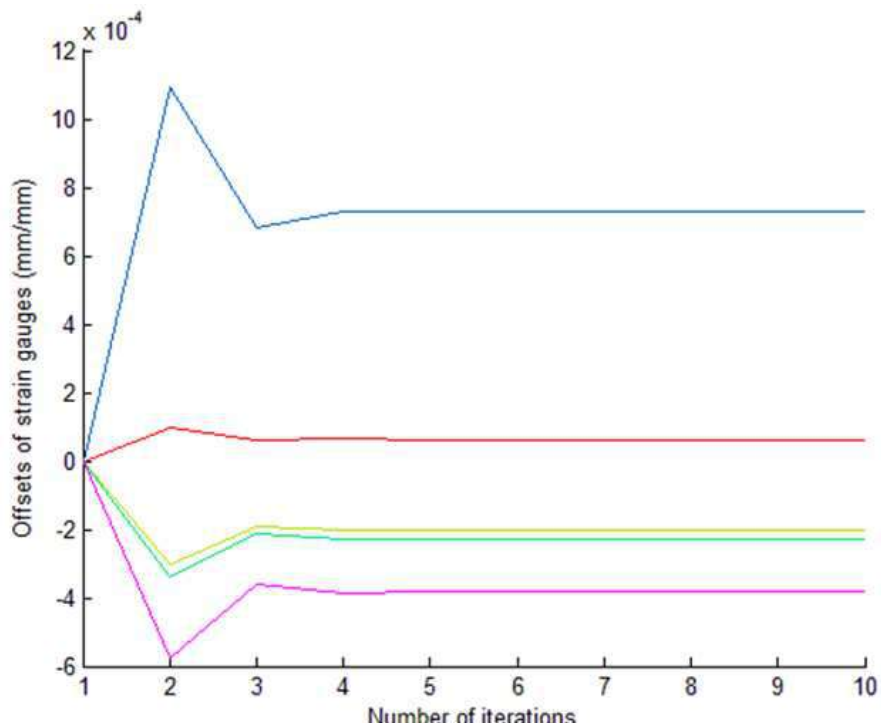


Figure 345: Convergence of the strain gauges offsets using the initialization module based on a dataset from Rogesa blast furnace at Dillinger Hütte.

General results and remarks:

The version of the model developed during the SUSTAINTAP project [55] was a FORTRAN script which calculated the total liquid level (i.e., the slag level) using only one gauge at the taphole level. Then the hot metal level was determined using Roark's formulas with a fixed number of iterations. An example of the liquid levels estimated by thus procedure for a full day at AM Fos is shown in Figure 346.

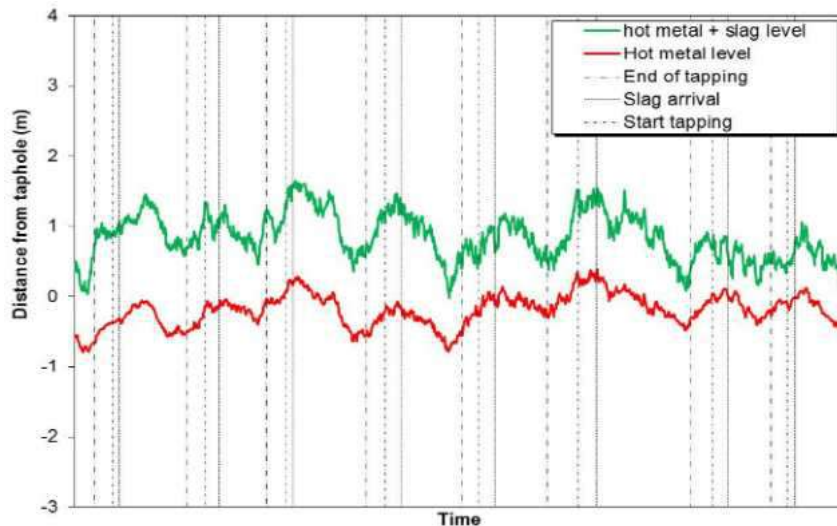


Figure 346: Hot metal and slag level variation during one day at AM Fos [55].

According to plant engineers, the liquid levels obtained by this method quite reliably reflected the hearth dynamics. However, both liquid level estimations seem biased mainly because they are highly dependent on the only gauge used for the estimation of the total liquid level. Moreover, phenomena of slag retention were sometimes observed which may lead to incorrect level estimations.

In the beginning of the OPTIBLAFINS project, an effort was made to improve the reliability, the reproducibility and the CPU-cost of the liquid level model. The model has also been converted from FORTRAN to MATLAB for better readability and easier debugging. The results of new model applied to the same day as in Figure 346 is depicted in Figure 347.

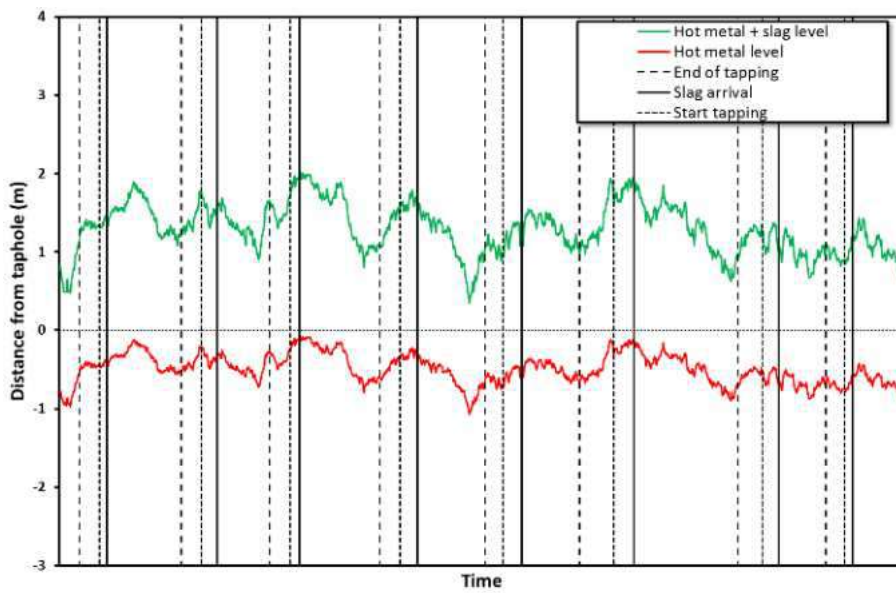


Figure 347: Hot metal and slag level variation during one day at AM Fos [55] using the new version of the liquid level model.

The first main difference between the results is seen in the slag level: the former model estimates a slag level varying between 0 m and +1.5 m while the new model estimates it to vary between +0.75 m and 2.25 m, i.e., to be on a 0.75 m higher level. More careful study of the tapping events reveals that the new version of the model still gives reliable results. The liquid levels

- tend to stabilize between the tap start and the time of slag arrival,
- continuously decrease after the slag arrival until the end of the tap, and

- increase after the end of the tapping and the beginning of the following.

According to plant engineers, the results of the new version are more realistic, e.g., because the previous under-estimation of the slag level is addressed. The script will be rewritten in C by AM Fos engineers to be used in on-line mode.

2.2.4.3.2 Tilting during tapping

A main objective for the strain gauges model development within the OPTIBLAFINS project is liquid surface tilting measurement. Based on previous results from the liquids level model, CRM argued that it may be possible to determine bending of the liquid surfaces inside the BF hearth during tapping after making some assumptions.

Initially, the project proposal claimed that a horizontal generatrix should be enough to determine the tilting angle. As it was stated before, it is a valid claim only if we can have a reliable measurement of each strain gauge, especially considering the initial strain state of the BF hearth. Unlike in a vertical generatrix, where each additional gauge reduces the global error, the measurements error in a horizontal generatrix are cumulative. Therefore, it was decided to use several vertical generatrixes in order to determine the liquid levels at different angles around the blast furnace, at least during the development of the technique.

The methodology to determine the tilting angle during tapping implies new sets of strain gauges, located along the circumference of the hearth to observe pressure variations on the wall. The generatrix located in the south part of the blast furnace has been revamped, adding several generatrixes h at -45° , -22.5° , $+22.5^\circ$ and $+45^\circ$ from the southern one, as illustrated in Figure 348. Unfortunately, it was impossible to go beyond the limit of $\pm 45^\circ$ for safety reasons because the gauges were installed while the BF was operated. At the moment, every strain gauge from the 30 initially planned one have been successfully installed and connected to the electrical box close to the BF (Figure 349).

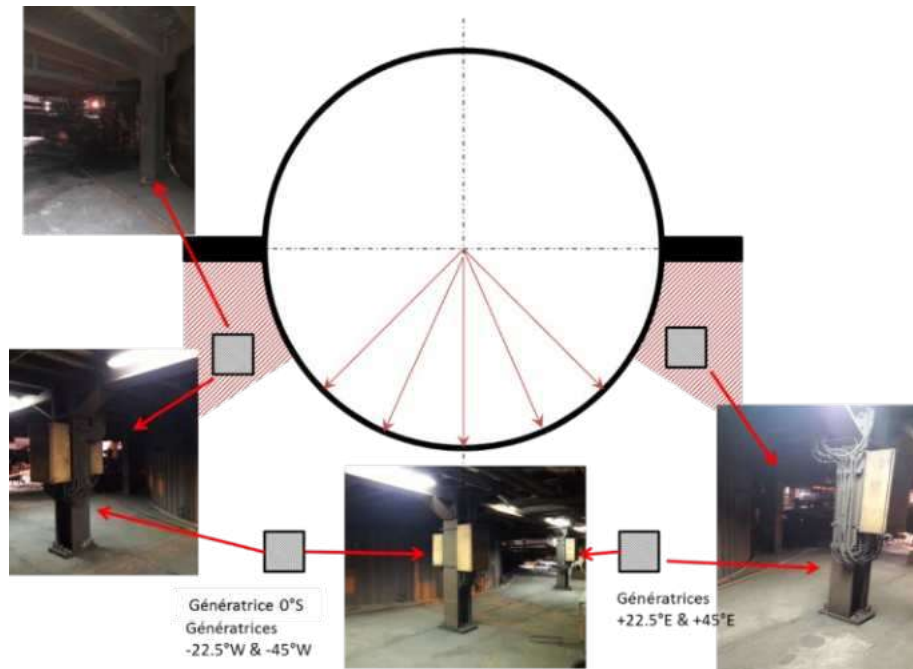


Figure 348: Drawing of the additional generatrixes for AM Fos HF1.

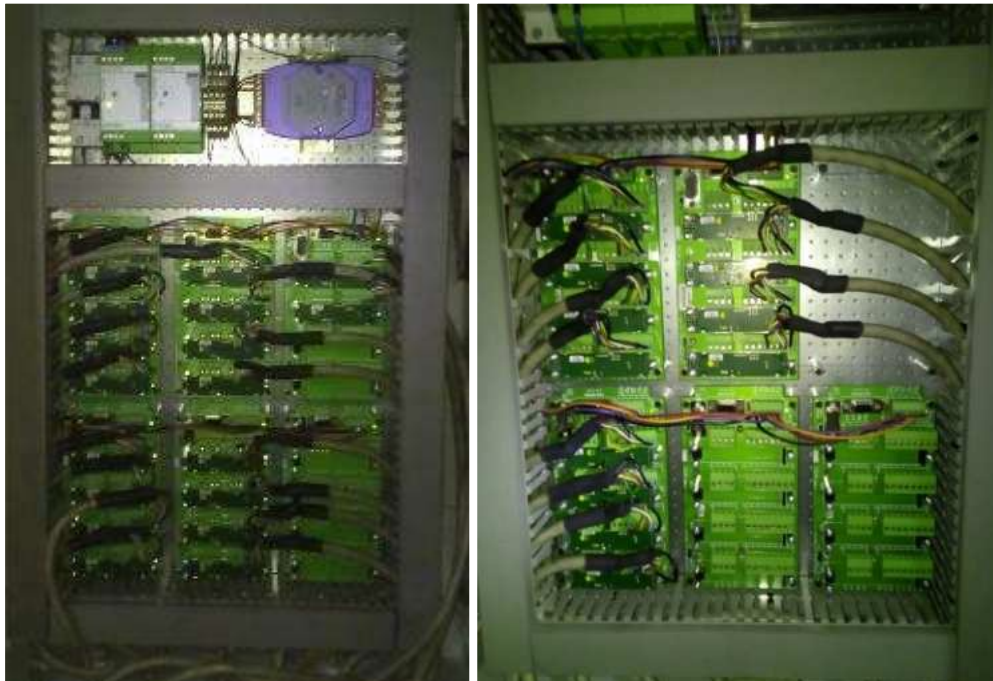


Figure 349: Electrical boxes containing 18 (left) and 12 (right) strain gauges acquisition cards used to measure strains at the AM Fos BF1.

The project is currently at a step that has to be handled by AM Fos: the electrical boxes have to be connected to the automation system of the blast furnace to gain remote access to the measurements. CRM will then be able to analyze the signals from the five generatrixes.

2.2.4.3.3 Conclusions

The liquid level model developed by CRM has been greatly improved since the launch of the DEMPOLIFE project [102]. Initially, gauges were used to clarify if a correlation existed between liquids level, especially before and after tapping, and strains in the steel shell. In the SUSTAINTAP project [55] the strain-gauge measurements were converted into liquid levels using Roark's formulas. Even if results were found fairly accurate with respect to frequency, the model could not reliably estimate both liquid levels simultaneously.

The developments within OPTIBLAFINS resulted in a huge step forward in terms of the calculating process, and now the model can give a fast and reliable estimation of both liquid levels. However, some limitations still exist:

- Long-term drift due to erosion of the hearth refractories. However, an estimate of the erosion from a wear model could be considered, modifying the geometry input. Alternatively, physical measurements during scheduled stops of blast furnaces could be utilized to estimate the present erosion profile.
- Strong dependency on blast pressure spikes and troughs are still challenges even with the modification of the gauges installed.
- Strong dependence on a good calibration of the strain gauges. A numerical estimation scheme has been proposed and seems to give decent solutions compared to the experimental ones, with no apparent downsides. The scheme can now be used as a calibration tool which may be performed regularly during the furnace campaign.

Observations for an industrial application of the technology:

- The installation of strain gauges is cheap and fast for one generatrix in order to estimate the liquids levels. A short period (two or three days) on site should be enough to access signals for offline analysis of the liquid levels.
- At the moment, every calculation has been made on a time basis of one point per minute, which is more than enough, considering the global duration of the tap events. However, the model allows a higher frequency, at least in offline mode.
- The model is currently coded in MATLAB. A global rewriting task must be performed to implement it in on-line mode.

The tilt estimation during tapping through strain-gauge measurements has not yet been studied and cannot be done until the plant gives access to the signals.

2.2.5 Work Package 5: Management and Reporting

The work package focussed on coordination, cooperation and reporting. Project meetings were held on a regular basis; The following meetings took place during the entire duration of the OPTIBLAFINS project:

- Kick-off meeting: 8th September 2015
- Progress meeting: 11th May 2016
- Progress meeting: 11th January 2017
- Progress meeting: 24th October 2017
- Final meeting: 9th October 2018

Minutes were made for all these meetings and distributed among the partners.

In addition, there were two CFD-DEM workshops (18th November 2015 and 23rd May 2017) organized. These workshops focussed on the expertise of the different universities and how to transfer their CFD-DEM knowledge into the business.

The first workshop started with an in-depth overview of the different university knowledge regarding the CFD-DEM approach in the project. There was a clear understanding of the use of the CFD-DEM in the different work packages. The challenge was to align the knowledge to be used in straight forward and clear activities. The second workshop was used to update the partners on the progress in the CFD-DEM field, discuss difficulties in using this new approach and come up with ideas how to valorise the fundamental results.

The following reports were issued:

- Technical report 1: Annual report (period 1st July 2015 – 31st December 2015)
- Technical report 2: Mid Term report (period 1st July 2015 – 31st December 2016)
- Technical report 3: Annual report (period 1st January 2017 – 31st December 2017)

2.3 Conclusions / Recommendations

The OPTIBLAFINS project aims to improve the blast furnace hearth life by the following objectives:

- Modelling of BF hearth processes
 - Implementation of a coupled CFD-DEM tool
 - Enhancement of BF Hearth models
- BF hearth monitoring
 - Implementation of on-line erosion/wear tool
 - Visualisation of refractory wear and flow behaviour
- Controlling the Dead Man
 - DM characterisation and modelling
- Operational data interpretation
 - Establish data-driven correlation tools

An in-depth analysis of dead man characteristics, based on real BF hearth samples, on-line BF monitoring techniques and combined with theoretical CFD-DEM / wear models led to a stable and more efficient blast furnace hearth process.

Recommended improvements (on-line) monitoring practices:

- It is recommended to use the multiphysics hearth monitoring model, that gives the operator on-line information regarding skull/gap/brittle layers/stress in the BF hearth refractory. Operators could identify (on-line) critical sections in the hearth and when using interpolated temperature plots, they could easily use that information for pro-active activities;
- It is recommended to install multipoint thermocouples, which could measure the hearth lining temperatures at different depths. Brittle layers could be detected;
- It is recommended to use an on-line 2D hearth wear model, that could support operators to prognose the wear in the BF hearth lining and to estimate the remaining campaign life.

Recommended instrumentation and modelling:

- It is recommended to install Fibre Bragg Grating sensors in the BF hearth wall and/or the multipoint thermocouples. It allows the operator to check the lining status more accurate compared to the actual situation with standard (single) thermocouples;
- It is recommended to perform the Hearth Echo Excellence technique on a regular time basis to monitor the wear of the BF refractory lining;
- Installation of an on-line DMD model is recommended to visualize the dead man state;

Optimizing Blast Furnace Hearth Inner State (OPTIBLAFINS)

- Water model setups (laboratory and full scale) are recommended to use to understand the liquid flow along the BF wall as well as for tapping practises;
- It is recommended to focus more and more on CFD-DEM analysis for the total BF. That means not only the BF hearth, but also the shaft should be taken into account to be more precise in boundary conditions;
- It is recommended to use the on-line multiphysics thermal stress model to visualize results and warn operators about process incidents in the BF hearth lining.

Overview of utilised modelling techniques:

An overview of the investigated models can be found in the following table. Note that some technologies need further development, several of which are being pursued further in the RFCS project "RIHANNE".

Table 64: Overview of utilised modelling techniques

	Subject	Model	Status
1	Thermal stress	On-line 3D finite element model	Implemented at BF
2	Enhanced Dead Man Dynamics	On-line analytical model for dead man state (permeability and shape)	Implemented at BF
3	Liquid flow	CFD-DEM BF hearth models	Principle proven. Further development in RIHANNE
4	Refractory wear	Inverse transient model	Further development needed
		Hearth Echo Excellence active acoustic inversion model	Further development in RIHANNE
		On-line multiphysics model	Implemented at BF
		On-line 2D static hearth model	Implemented at BF
		Asymptotic CFD wear model	Further development needed.
		Visualisation model of wall temperatures	Further development needed
5	Tapping	CFD MOHDRAIN 2.0 model	Implemented at BF
		CFD EBF model	Further development in RIHANNE
		1D tapping model	Implemented at BF
6	Liquid level	Balance-based pool model	Further development needed
		Strain gauge	Implemented at BF

Overview of utilised measurement techniques:

An overview of the investigated measurement techniques can be found in the table below:

Table 65: Overview of investigated measurement techniques.

	Subject	Technique	Status
1	Refractory wear	Active Hearth Echo Excellence	Implemented at BF
		Optical fibres (FBG)	Implemented at BF
		Multi-thermocouples	Implemented at BF
2	Liquid flow	Water model setups	Principle proven. Further development in RIHANNE
3	Liquid level	Strain gauge	Implemented at BF

The applications (tools and models) contribute to a stable, reliable and more efficient blast furnace process. This enables the ability of an improvement of a longer life blast furnace hearth. All partners in the consortium contribute to the success of the project.

2.4 Exploitation and impact of the research results

In this project, mathematical models have been developed and applied to gain understanding about the state and behaviour of the hearth region of the blast furnace. To support the interpretation, some existing measurement techniques have been further developed and some new ones have been tested and assessed. The methods developed shed light on phenomena such as refractory wear, liquid levels, hot metal flow paths, dead-man state and tapping behaviour. Even though some of the measurement techniques have not yet been developed to their maximum potential, several of them already provide interesting and useful results, e.g., Fibre Bragg Grating, Hearth Echo Excellence and multi-couple thermocouple measurements.

The potential of finite element method (FEM)-based analysis combined with thermography measurements in detecting regions with potential gaps between lining blocks has been demonstrated, and the findings are useful for designing strategies at BF stoppages without detrimental effects on the lining. The FEM analysis has also yielded deeper knowledge about the role of thermal conditions on strains measured at the furnace shells, which can be used in forthcoming work where strain gauges are used to sense liquid levels in the hearth. The occurrence of gaps between the refractory blocks in the hearth sidewall lining has also been confirmed by studying short-term fluctuations of thermocouple readings in the lining. This technology will be further developed for troubleshooting purposes in forthcoming work.

An enhanced Dead Man Dynamics model, describing the state of the dead man, has been successfully implemented online in the BF.

New hearth wear models have been implemented, giving on-line interpretations of the lining state, including wear and buildup formation, throughout the BF campaign. The tools will be used in the operation of the BF to provide on-line information that can be correlated with other variables to take proper actions in controlling the hearth state.

Novel CFD-DEM models have been demonstrated to be feasible for gaining understanding about the solid and liquid flow in the BF hearth. Despite limitations in computational capacity, the approach is promising and the models developed have revealed fundamental aspects of the hearth operation that cannot be gained by continuum models. The technique will be further developed in a forthcoming RFCS project ("RIHANNE").

Water models, both small and full scale, have been developed to visualize the tapping behaviour and the hot metal flow in more detail. The results of the models support findings gained by CFD analysis and can be used for verifying the computational results. Further developments of the water models will be carried out in the RIHANNE project.

CFD models further developed in the project, and partly validated by sampling in the LKAB Experimental Blast Furnace in Luleå, have provided deeper knowledge about the relation between dead-man state and iron flow paths in the hearth.

Simplified models of liquid levels and tappings have provided interesting explanations of observed drainage patterns in multi-taphole furnaces, which can be used to detect asymmetry and impermeable regions in the hearth. The on-line model of liquid levels will be further developed for automatic level estimation by combination with indirect (emf, strain-gauge) signals from the BF hearth.

In summary, the models and methods developed within the project have resulted in new and more detailed tools that can be used for a more accurate assessment of the BF hearth state, which can be applied to make appropriate decisions about the BF operation during the campaign to prolong the blast furnace hearth life.

The project results have already been disseminated in the following publications/presentations:

"Unresolved CFD-DEM modeling of multiphase flow in densely packed particle beds", M. Vångö, S. Pirker and T. Lichtenegger. Applied Mathematical Modelling 56 (2018) 501-516.

"Data-assisted CFD modelling of transient blast furnace tapping with a dynamic dead man", M. Vångö, C. Feilmayr, S. Pirker and T. Lichtenegger. Applied Mathematical Modelling 73 (2019) 210-227.

"Estimation of the hot face temperatures of the blast furnace hearth by an inverse method", M. Roche, M. Helle and H. Saxén, ECOS 2017, July 2017, San Diego, USA

Optimizing Blast Furnace Hearth Inner State (OPTIBLAFINS)

"COMSOL application to estimate 3D blast furnace hearth wear using thermocouple measurements", Y. Kaymak, T. Hauck, J. Mernitz, R. Lin and H. Rausch.
COMSOL conference in Lausanne, 22-24 October 2018.

"Transient DEM-CFD simulation of solid and fluid flow in a three-dimensional blast furnace model", F. Bambauer, S. Wirtz, V. Scherer and H. Bartusch. Powder Technology 334 (2018) 53-64.

"Off-line model of blast furnace liquid levels", M. Roche, M. Helle, J. vd Stel, G. Louwerse, L. Shao and H. Saxén. ISIJ International 58 (2018) 2236-2245.

"On-line estimation of liquid levels in the blast furnace hearth", M. Roche, M. Helle, J. vd Stel, G. Louwerse, L. Shao and H. Saxén. Steel Research International 90 (2019) 1800420.

"Multiphysics hearth lining state model", Y. Kaymak, H. Bartusch, T. Hauck, J. Mernitz, H. Rausch, R. Lin, to be published at METEC, Düsseldorf, June 2019.

"Estimation of liquid levels in the BF hearth", M. Helle, H. Saxén, M. Roche, G. Louwerse, J. vd Stel. 8th International Congress on Science and Technology of Ironmaking (ICSTI 2018), Vienna, September 2018, ASMET.

2.5 Appendix

2.5.1 CFD-DEM modelling approach (part 1)

The VOF method is used for solving systems consisting of two or more fluids in an Eulerian reference frame. It is suitable for free-surface flows where a continuous interface is present. An indicator function (volume fraction), ranging from 0 to 1, is used to distinguish between the fluids. If the discrete particle phase is considered, as well as introducing a compression term to sharpen the interface (as done by Rusche [24]), a set of transport equations for the volume fractions α_i can be written as:

$$\frac{\partial \epsilon \alpha_i}{\partial t} + \nabla \cdot (\epsilon \alpha_i \mathbf{u}_f) - \nabla \cdot (\mathbf{u}_c \alpha_i (1 - \alpha_i)) = 0 \quad (68)$$

where ϵ is the local void fraction and \mathbf{u}_c the artificial compression velocity. The local fluid properties are determined by taking the volume weighted average of all the physical values as shown in equation (69) and (70) for n phases.

$$\rho_f = \sum_{i=1}^n \alpha_i \rho_i \quad (69)$$

$$\mu_f = \sum_{i=1}^n \alpha_i \mu_i \quad (70)$$

The flow is described by the Navier-Stokes equations in the form of Anderson and Jackson [25]. In VOF methodology only one momentum equation is solved, using the mixture fluid properties, in contrast to a two-fluid model. The continuity and momentum equations are given by equations (71) and (72):

$$\frac{\partial \epsilon}{\partial t} + \nabla \cdot (\epsilon \mathbf{u}_f) = 0 \quad (71)$$

$$\frac{\partial \epsilon \rho_f \mathbf{u}_f}{\partial t} + \nabla \cdot (\epsilon \rho_f \mathbf{u}_f \mathbf{u}_f) = \epsilon (-\nabla p^* + \nabla \cdot \boldsymbol{\tau} - \mathbf{g} \cdot \mathbf{x} \nabla \rho_f) + \mathbf{F}^\sigma + \mathbf{F}^{pf} \quad (72)$$

$\boldsymbol{\tau}$ denotes the viscous stress tensor, usually expanded as $\boldsymbol{\tau} = \mu_f (\nabla \mathbf{u}_f + \nabla \mathbf{u}_f^T)$, \mathbf{F}^σ is the surface tension force modeled with the continuum surface force (CSF) model by Brackbill [26] as $\mathbf{F}^\sigma = \sigma \kappa \nabla \alpha$, where σ denotes the surface tension and κ the interface curvature. \mathbf{F}^{pf} is a source term describing the momentum exchange between the fluids and particles, which is further described in the next paragraph.

The DEM method is a common and established numerical method for granular flows and is based on the theory of Cundall and Strack [27], where at contact, the particle forces are determined, and the trajectories are calculated by Newton's laws of motion [27],[28]. When the acting forces and moments are known, the particle accelerations are calculated as in equation (73) and (74):

$$m_i \frac{d\mathbf{u}_{p,i}}{dt} = \mathbf{F}_i^{pp} + \mathbf{F}_i^{pf} + m_i \mathbf{g} \quad (73)$$

$$I_i \frac{d\boldsymbol{\omega}_{p,i}}{dt} = \mathbf{M}_i^{pp} + \mathbf{M}_i^{pf} \quad (74)$$

\mathbf{F}_i^{pp} denotes the inter-particle force and \mathbf{F}_i^{pf} the particle-fluid interaction term which was modeled by the expectedly dominant drag-, pressure gradient- and viscous forces [29]. Equation (73) can then be rewritten as,

$$m_i \frac{d\mathbf{u}_{p,i}}{dt} = \sum_{i=1}^n \mathbf{F}_i^{cont.} + \mathbf{F}_{drag,i} + \mathbf{F}_{Vp,i} + \mathbf{F}_{\tau,i} + m_i \mathbf{g} \quad (75)$$

where $\mathbf{F}_{Vp,i} = -V_{p,i} \nabla p$, $\mathbf{F}_{\tau,i} = V_{p,i} \nabla \cdot \boldsymbol{\tau}$. The Koch and Hill drag model [30] and [31] was used throughout all the simulations.

2.5.2 Dynamic void fraction model (part 2)

In part 1, the CFD-DEM model was applied to a small-scale BF hearth and identified the necessity to account for the dynamic dead man behaviour for an active dead man. Despite the CFD-DEM

model's several advantages, difficulties regarding simulation scale-up to industrial BF size were highlighted. The main issue is that the DEM becomes extremely computationally demanding as the particle number rapidly increases.

In this part 2, a model will be introduced to bridge the gap between the computationally cheap, fast Eulerian simulations with the expensive, accurate CFD-DEM ones. The CFD-DEM model was utilized to generate detailed porosity distributions based on local particle sizes. The porosity fields are related to the liquid levels in the BF, which has been subsequently used in a simplified Eulerian model for the dead man movement.

Furthermore, for a more realistic model, a set of boundary conditions has been proposed to account for the varying taphole properties.

Similar as for the CFD-DEM model, the fluid motion is governed by equation (68) and equations (71)-(72). However, the intention is to simulate longer time scales with this model, and therefore mass source terms have been added to incorporate the effect of hot metal production, described by a constant iron production rate \dot{m}_{iron} and slag ratio γ . The mass sources were divided among the cells involving the respective fluid to keep the fluids separated and thus retain sharp interfaces. The DEM part is not included in the dynamic void fraction model and thus ϵ and F^{pf} must be treated differently. Instead of calculating the void fraction from the particle positions, it is calculated from a pre-generated dead man database by linear interpolation with regards to the liquid levels in the system. Obviously, enough dead man states must be stored to avoid excessive interpolation effects.

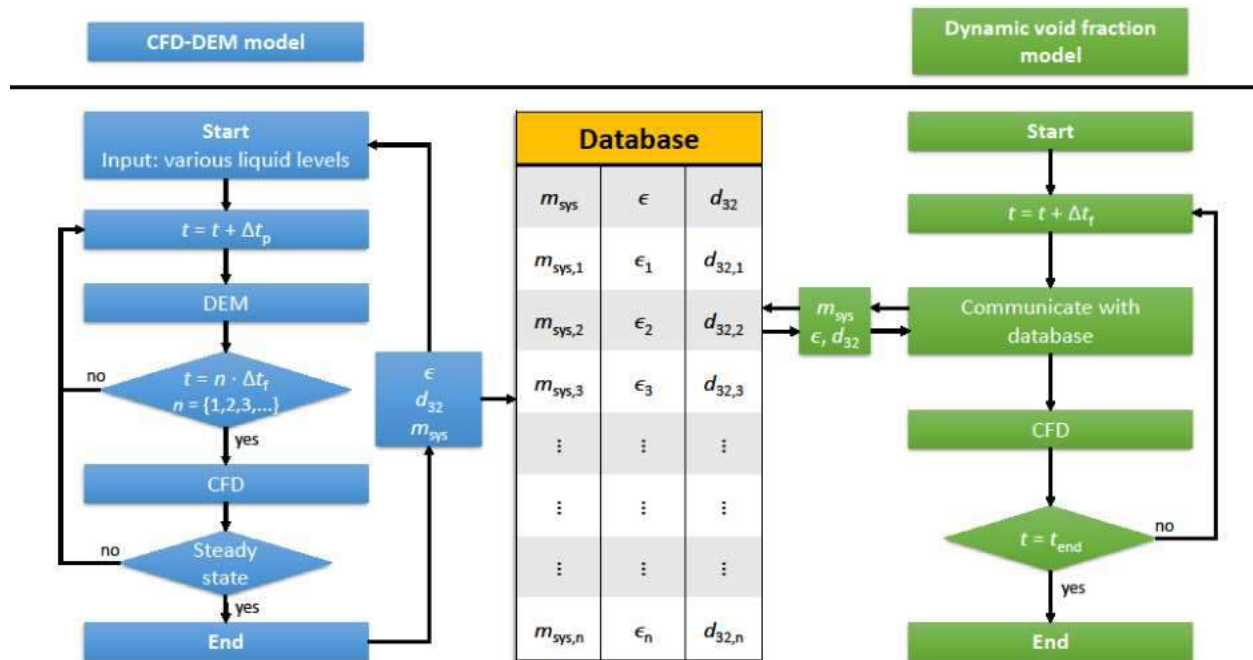


Figure 350: Illustration of the CFD-DEM model and dynamic void fraction model's interaction, figure from [2].

2.5.3 Optical Microscope analysis and SEM-EDS analysis

2.5.3.1 Optical microscope analysis



Figure 351: Optical Microscope Analysis of sample MS2.



Figure 352: Optical Microscope Analysis of sample MS4.

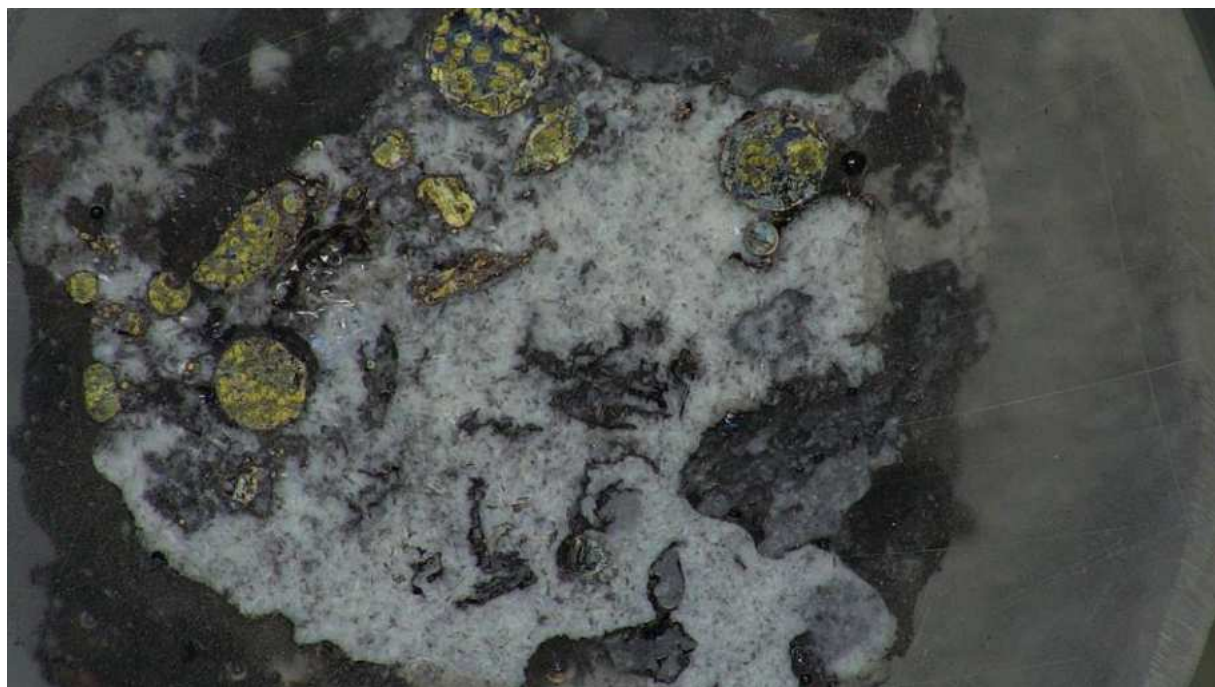


Figure 353: Optical Microscope Analysis of sample MS5.

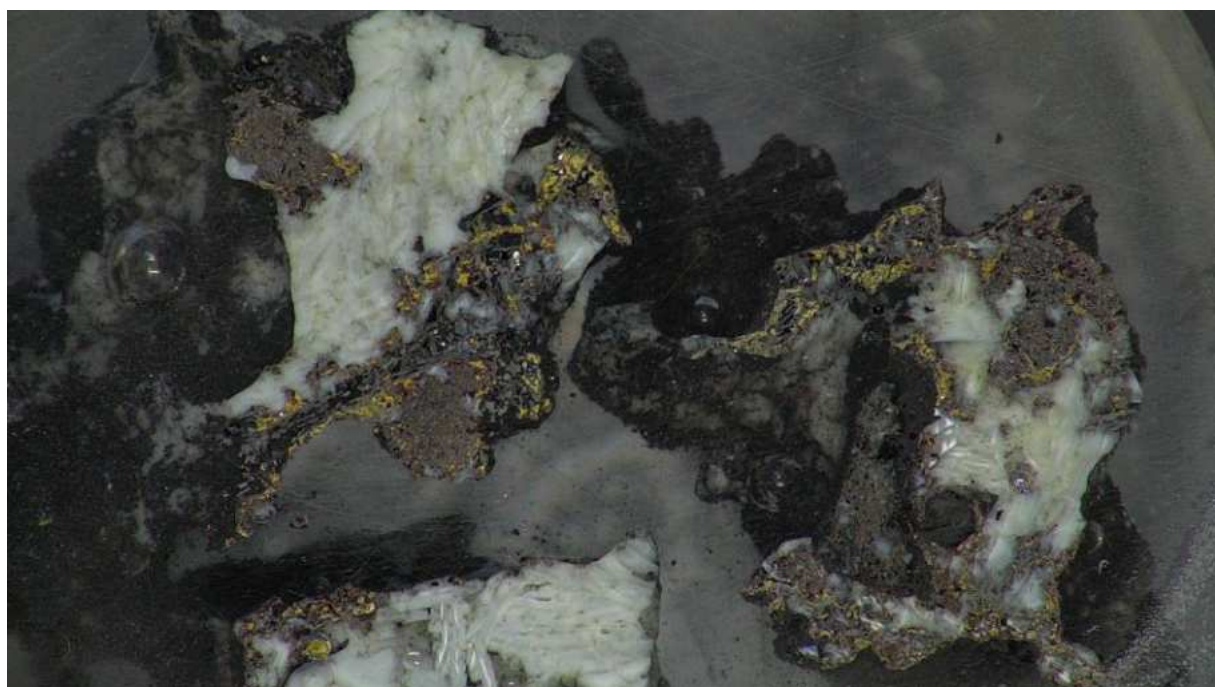


Figure 354: Optical Microscope Analysis of sample MS6.

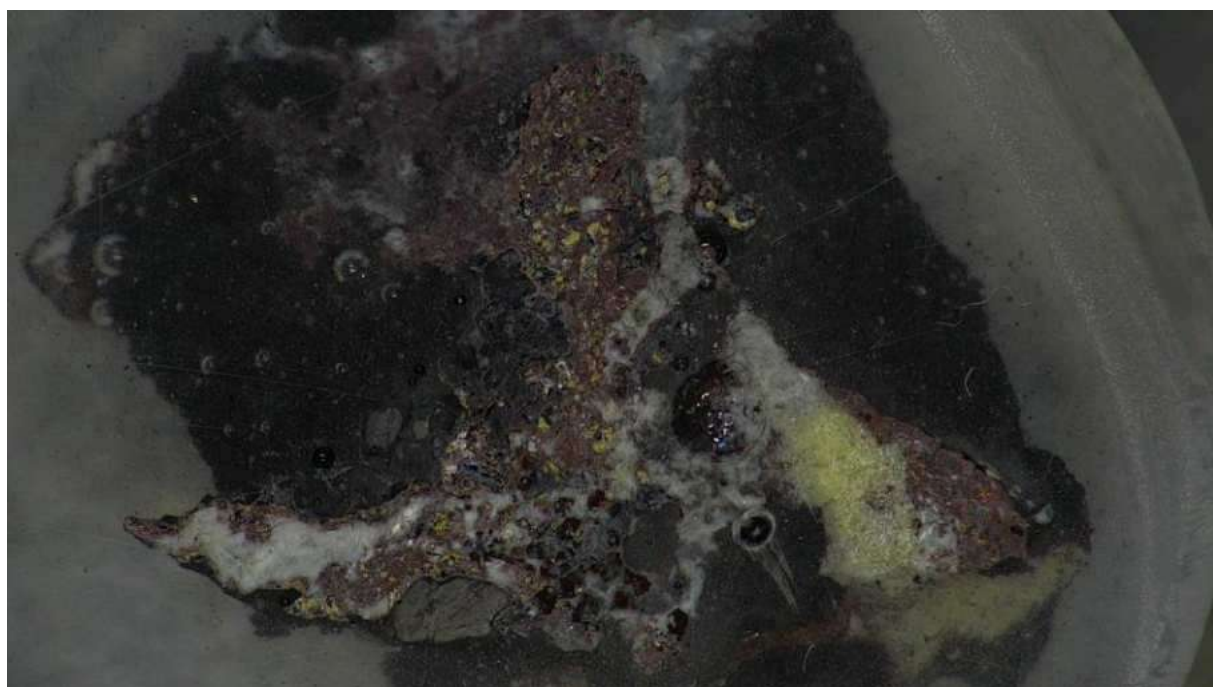
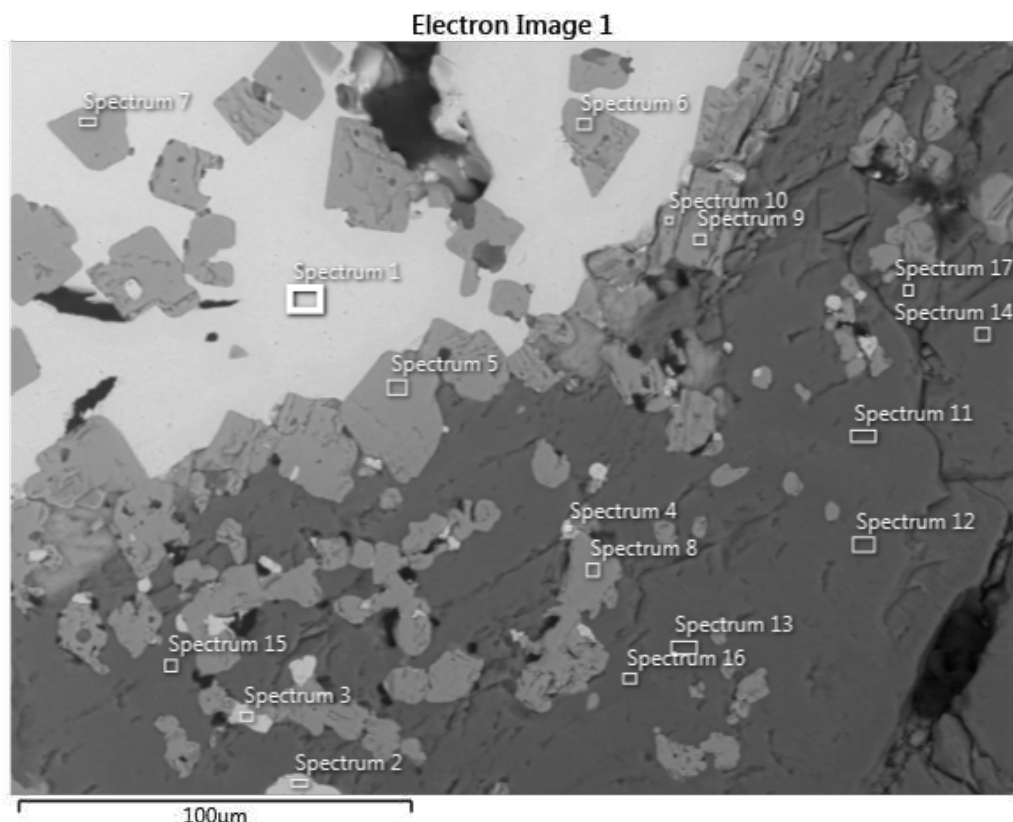


Figure 355: Optical Microscope Analysis of sample MS7.

2.5.3.2 SEM-EDS analysis

Certain trace element analyses were deemed insignificant and excluded from the tables below

Sample M2, Site 1:



Element (mol%)	1	2	3	4	5	6	7	8	9	10
C	38.51	36.4	35.18	47.02	23.57	23.13	26.51	22.76	22.44	26.44
N					22.06	23.92	23.31	17.78	21.53	21.76
O	8.99	15.93	17.23	16.02	19.96	17.73	13.79	26.7	23.17	19.83

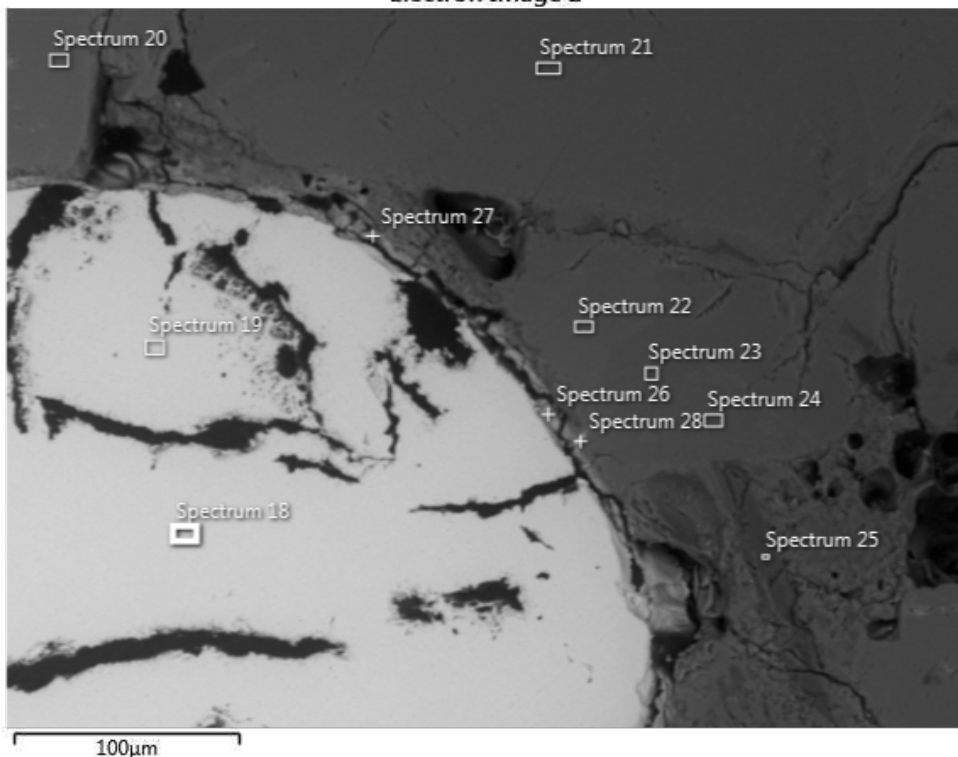
Optimizing Blast Furnace Hearth Inner State (OPTIBLAFINS)

Mg	1.72	3	2.72	2.23	1.19	1.08	0.72	1.66	1.37	1.17
Al	1.43	2.49	2.42	2.04	1.09	0.99	0.63	1.58	1.3	1.06
Si	2.36	4.55	4.15	3.5	1.79	1.66	1.06	2.8	2.14	1.84
S	0.42	0.47	0.46	0.44	0.33	0.35	0.21	0.32	0.4	0.35
K	0.05	0.07	0.05	0.05	0.04	0.06	0.04	0.06	0.06	0.04
Ca	1.33	2.55	2.42	2.13	1.23	1.12	0.68	1.93	1.49	1.27
Ti	3.53	3.47	5.74	4.86	20	19.22	19.3	18.48	18.54	17.97
V	0.26	0.2	0.35	0.26	0.93	1.03	0.92	0.82	0.92	0.86
Fe	41.33	30.81	29.27	21.47	7.81	9.71	12.84	5.1	6.64	7.40

Element (mol%)	11	12	13	14	15	16	17
C	19.03	18.90	19.02	18.37	23.62	19.14	19.14
N							
O	43.85	43.56	44.15	44.05	40.66	43.99	43.99
Mg	5.70	5.16	5.22	6.08	4.76	5.70	5.70
Al	5.07	6.09	5.41	4.56	4.96	4.75	4.75
Si	11.33	10.89	10.77	11.75	9.58	11.59	11.59
S	0.52	0.86	0.88	0.60	0.42	0.42	0.42
K							
Ca	6.55	6.95	6.69	6.51	5.69	6.41	6.41
Ti	2.37	2.23	2.69	2.26	3.65	2.79	2.79
V	0.17	0.16	0.16	0.16	0.20	0.18	0.18
Fe	5.40	5.19	5.01	5.66	6.45	4.98	4.98

Sample MS2, Site 2:

Electron Image 2

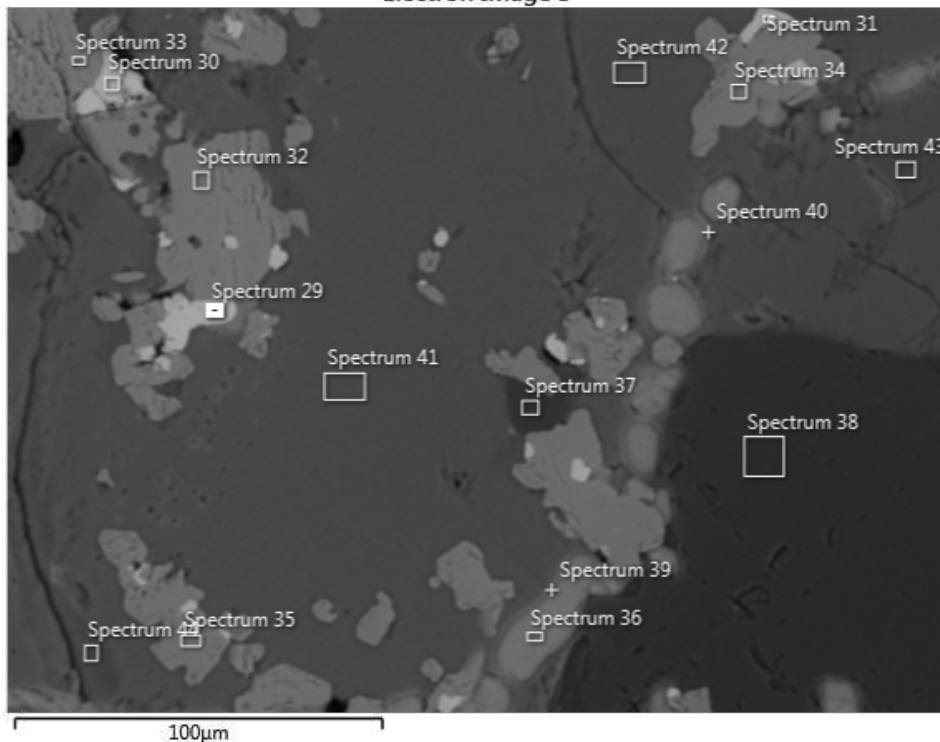


Optimizing Blast Furnace Hearth Inner State (OPTIBLAFINS)

Element (mol%)	18	19	20	21	22	23	24	25	26	27	28
C	42.61	41.30	24.12	17.97	21.74	20.52	22.63	22.12	47.02	51.46	35.97
O	6.75	7.98	39.67	46.17	42.68	44.38	43.10	44.15	19.46	18.18	29.05
Na			0.30				0.12	0.23	0.08	0.08	
Mg	1.85	2.24	5.36	5.54	5.61	5.60	5.44	15.53	1.65	1.46	3.52
Al	1.43	1.63	2.72	6.61	5.69	5.88	5.52	2.42	1.34	1.43	2.63
Si	2.88	3.35	11.41	11.72	11.38	11.68	11.07	9.27	2.56	2.40	5.94
S	0.26	0.35	0.34	0.68	0.85	0.37	0.87	0.36	11.10	9.60	5.75
K	0.07	0.12	0.14				0.16	0.50	0.10	0.31	0.11
Ca	1.77	2.12	10.96	7.94	7.48	7.34	7.42	2.41	10.88	9.31	8.19
Ti	0.18	0.22	0.21	0.59	0.54	0.61	0.49	0.25	0.18	0.18	0.29
V	0.13	0.10						0.05			0.06
Mn									0.33	0.43	0.30
Fe	42.07	40.58	4.76	2.79	4.04	3.62	3.18	2.70	5.31	5.16	8.18

Sample MS2, Site 3:

Electron Image 3



Element (mol%)	29	30	31	32	33	34	35	36	37
C	29.57	30.29	29.46	17.88	20.29	14.01	17.23	25.18	15.20
N				20.88	19.62	19.50	19.01		
O	20.34	20.96	22.38	30.61	29.80	34.49	33.09	32.42	50.81
Na	0.16			0.10	0.10	0.10	0.10		
Mg	4.13	3.89	4.24	2.03	1.90	2.41	2.30	2.88	8.99
Al	2.80	2.45	2.74	1.44	1.29	1.65	1.71	2.70	13.74
Si	6.28	6.05	6.59	3.39	3.32	3.80	3.69	3.22	4.03
S	0.75	0.46	0.53	0.27	0.28	0.38	0.40	14.94	0.47
K	0.05		0.06	0.04	0.05		0.04		

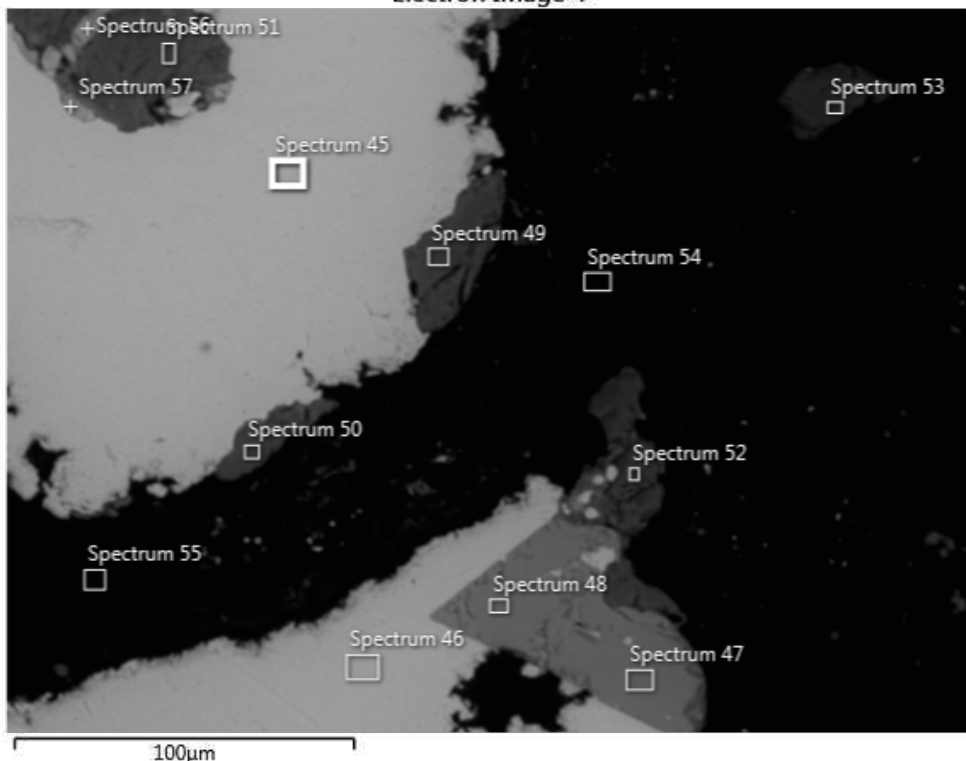
Optimizing Blast Furnace Hearth Inner State (OPTIBLAFINS)

Ca	5.38	4.83	5.37	3.07	3.02	3.55	3.73	15.76	3.43
Ti	3.61	4.19	4.33	17.84	17.39	17.97	16.38	1.39	1.92
V	0.19	0.24	0.24	0.71	0.74	0.79	0.66		0.10
Fe	26.73	26.63	24.06	1.73	2.20	1.35	1.65	1.52	1.31

Element (mol%)	38	39	40	41	42	43	44
C	15.18	27.26	20.66	16.11	15.73	16.43	19.26
N							
O	50.34	33.97	44.59	47.21	47.82	48.80	43.90
Na		0.09	0.27	0.28	0.22	0.13	0.22
Mg	9.73	3.02	5.14	5.60	5.45	5.62	4.88
Al	15.87	2.90	2.98	3.43	3.29	5.29	3.36
Si	3.41	3.50	10.06	11.67	11.59	11.68	10.44
S	0.49	11.41	2.23	0.42	0.45	0.60	0.84
K							
Ca	2.79	14.60	11.20	11.87	11.77	8.57	13.01
Ti	0.99	1.66	1.36	1.52	1.89	1.52	1.47
V			0.10		0.16	0.09	
Fe	1.13	1.59	1.27	1.79	1.56	1.21	2.39

Sample MS2, Site 4:

Electron Image 4



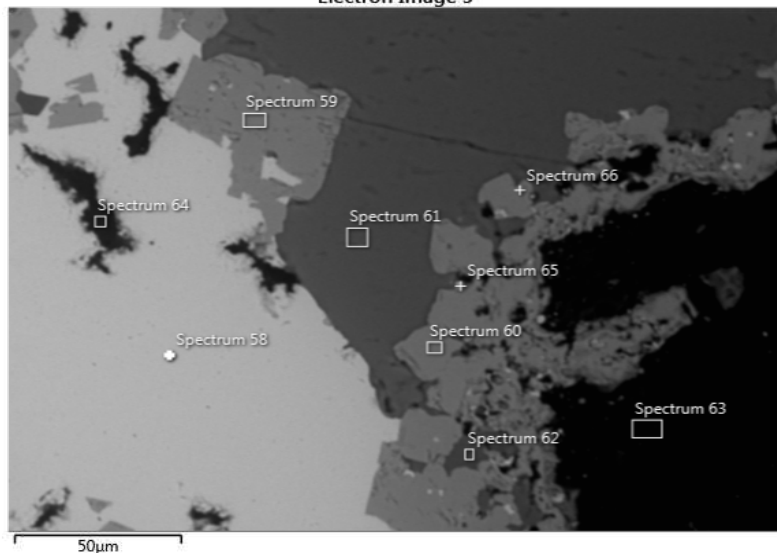
Element (mol%)	45	46	47	48	49	50	51	52	53	54	55	56	57
C	77.96	79.49	73.27	51.58	66.23	67.44	63.13	64.39	70.49	91.60	91.43	77.32	78.02
N				31.53									
O				0.21	19.70	18.77	20.59	22.09	18.91	5.13	4.82	5.12	3.94
Mg	0.35	0.31		0.16	2.13	1.97	2.32	2.13	1.74	0.16	0.16	0.55	0.45

Optimizing Blast Furnace Hearth Inner State (OPTIBLAFINS)

Al	0.26	0.22	0.28	0.33	1.53	1.48	1.62	1.52	1.41	0.15	0.15	0.33	0.24
Si	0.55	0.43	0.53		4.13	3.99	4.69	4.17	3.22	0.32	0.29	0.80	0.57
S	0.12	0.09		0.02	0.11	0.17	0.24	0.14	0.09	0.14	0.16	6.22	6.30
K	0.04	0.03		0.24	0.19	0.35	0.34		0.03	0.05	0.04	0.07	0.05
Ca	0.34	0.29	0.39	11.45	2.34	1.98	2.65	2.58	2.13	0.30	0.30	0.90	0.77
Ti	0.11	0.26	18.74	0.73	0.22	0.22	0.20	0.45	0.19	0.10	0.09	0.06	0.06
V	0.06	0.08	1.17	3.67	0.03		0.06	0.04		0.02	0.02	0.31	0.19
Mn							0.06					3.10	3.40
Fe	20.16	18.78	5.51		3.39	3.51	4.05	2.49	1.79	2.02	2.54	4.88	5.62

Sample MS2, Site 5:

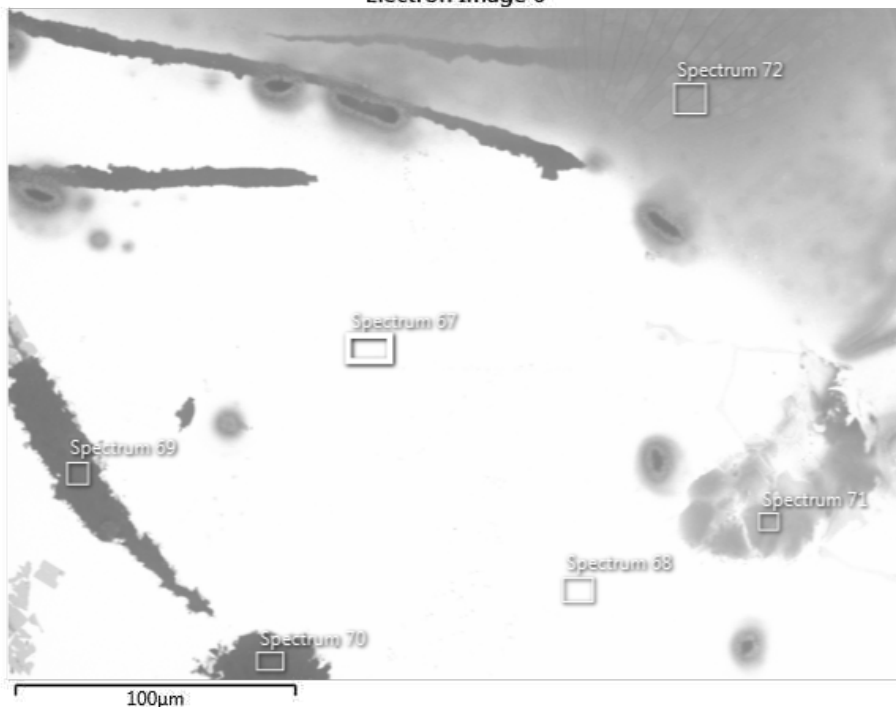
Electron Image 5



Element (mol%)	58	59	60	61	62	63	64	65	66
C	60.38	40.42	41.47	46.88	50.85	88.49	88.06	70.35	54.57
N			25.40						
O	6.14	29.09	11.99	29.36	29.46	7.38	5.43	11.10	20.24
Mg	0.90	1.08	0.64	3.47	2.68	0.35	0.27	0.70	1.23
Al	0.46	0.47	0.33	0.84	2.37	0.31	0.16	0.31	0.47
Si	1.30	1.75	1.08	6.98	5.32	0.55	0.46	1.16	2.02
S	0.11	0.10	0.07	0.09	0.07	0.09	0.05	0.08	0.09
Ca	0.93	1.47	1.04	6.68	3.23	0.52	0.46	1.01	1.87
Ti	1.59	19.45	14.09	1.82	3.01	0.92	0.83	4.87	11.68
V	0.14	0.97	0.72	0.13	0.17	0.03	0.05	0.27	0.48
Fe	28.05	5.21	3.15	3.58	2.83	1.31	4.22	10.12	7.35

Sample MS4, Site 1:

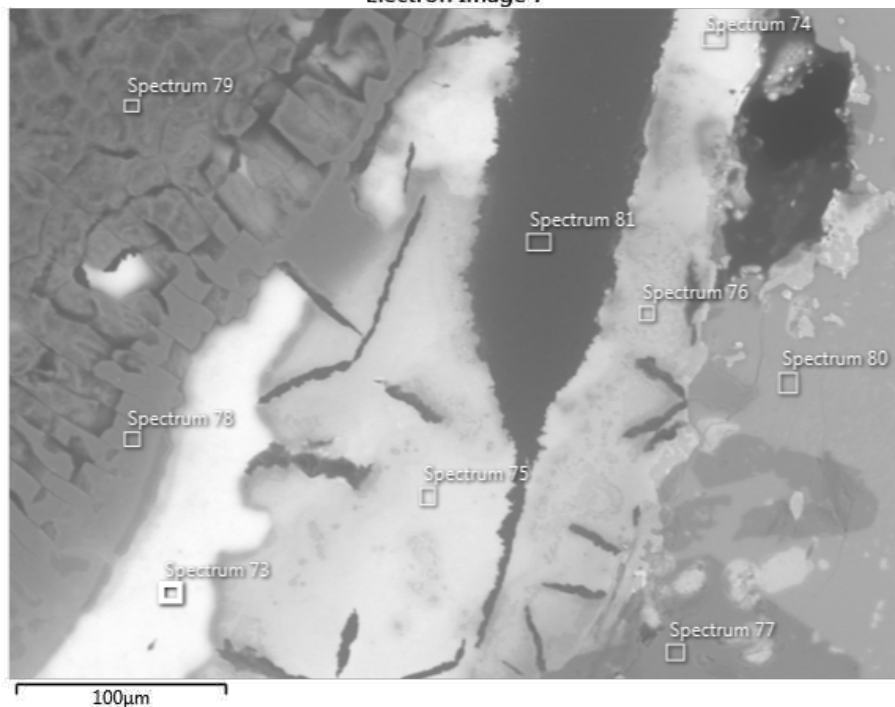
Electron Image 6



Element (mol%)	67	68	69	70	71	72
C	69.49	70.18	86.18	86.91	54.10	56.95
O	7.36	6.69	8.51	8.25	28.55	25.52
Na			0.06			
Mg			0.08	0.07		
Al			0.06	0.03		
Si	2.32	2.03	0.87	0.70	6.73	9.06
S	0.05	0.05	0.04	0.03		
Cl			0.03	0.03		0.04
Ca	0.10	0.10	0.09	0.07	0.11	0.15
Ti	0.13	0.09	0.21	0.13	0.07	0.08
V	0.13	0.09	0.03	0.03	2.63	0.04
Fe	20.43	20.77	3.83	3.76	7.76	8.07

Sample MS4, Site 2:

Electron Image 7



Element (mol%)	73	74	75	76	77	78	79	80	81
C	69.18	61.56	53.86	64.93	56.96	53.69	68.51	44.63	80.58
O	12.22	16.88	21.77	17.65	25.99	27.59	18.98	30.77	14.02
Mg	0.83	1.27	1.23	1.01	4.66	0.67	0.50	3.22	0.59
Al	0.57	0.85	0.91	0.71	7.33	0.49	0.32	3.14	0.42
Si	3.08	4.44	6.27	4.88	2.12	11.05	8.46	7.51	1.62
P					0.03				0.02
S	0.12	0.18	0.17	0.19	0.37	0.16	0.13	0.70	0.11
Cl	0.02			0.02		0.04	0.06		0.02
Ca	0.74	1.49	1.06	1.19	1.33	0.82	0.73	8.39	0.85
Ti	0.07	0.17	0.10	0.19	0.17	0.07	0.07	0.29	0.10
V	0.04	0.05	0.06	0.03	0.02				
Fe	13.04	13.12	14.47	9.14	0.99	5.34	2.24	1.23	1.66

Sample MS4, Site 3:

This is an analysis of the epoxy used to hold the samples

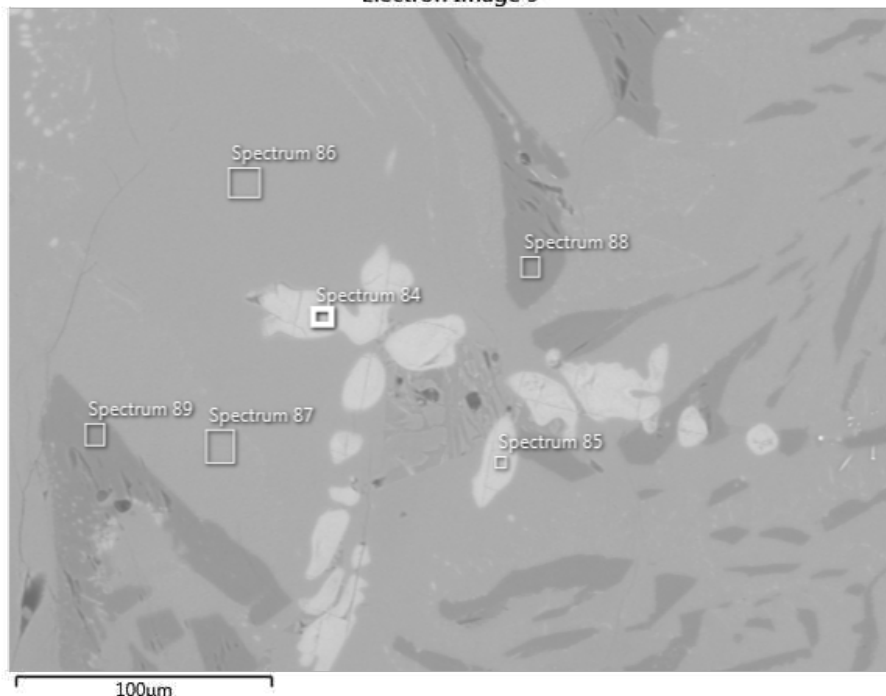
Electron Image 8



Element (mol%)	82	83
C	97.91	96.74
Mg	0.05	0.07
Al	0.05	0.05
Si	0.73	0.49
S	0.07	0.06
Cl	0.15	0.09
Ca	0.06	0.06
Ti	0.02	0.03
Fe	0.97	2.42

Sample MS4, Site 4:

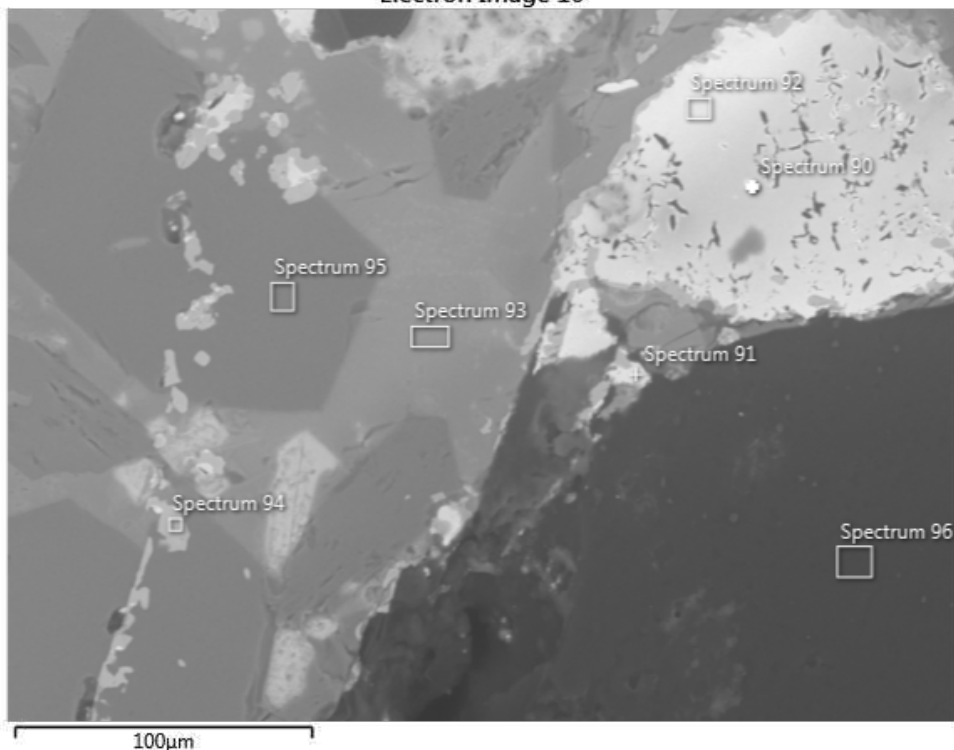
Electron Image 9



Element (mol%)	84	85	86	87	88	89
C	40.14	45.08	31.72	32.91	27.98	54.88
O	23.07	21.68	38.16	36.82	41.72	24.97
Mg	2.35	2.43	4.34	4.56	13.93	8.68
Al		1.43	4.14	3.72	1.86	1.23
Si	3.57	3.26	9.54	9.33	9.10	6.16
S	13.73	11.78	0.50	1.11	0.66	0.42
Ca	15.73	13.78	11.50	11.39	4.75	3.61

Sample MS4, Site 5:

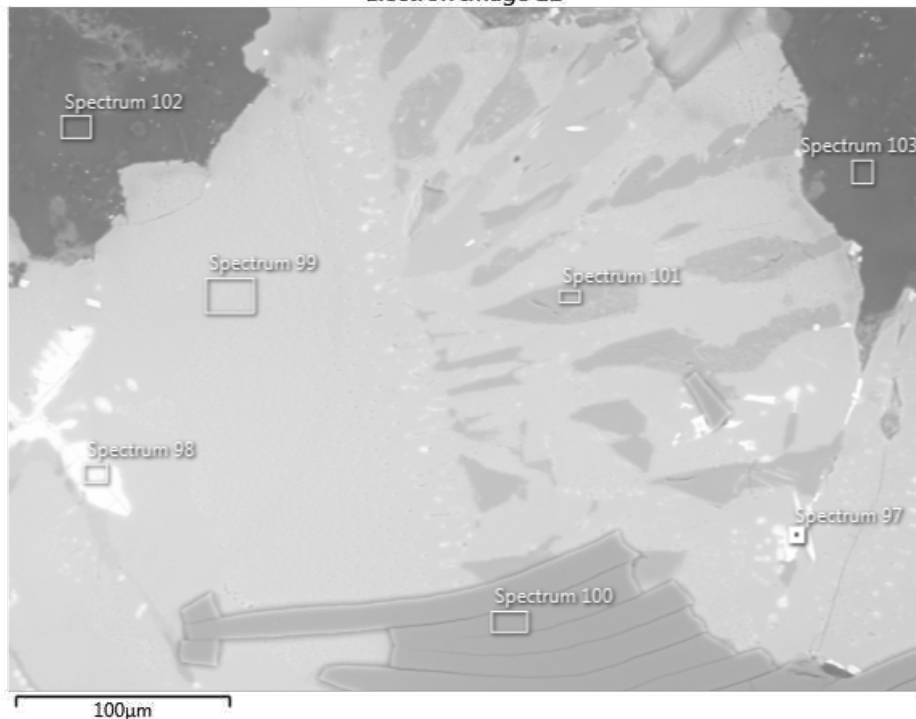
Electron Image 10



Element (mol%)	90	91	92	93	94	95	96
C	67.63	68.19	50.52	42.15	36.14	33.78	79.88
O	15.67	16.71	23.99	36.95	39.86	42.26	17.24
Na				0.16			
Mg	1.28	1.15	2.07	3.31	3.26	7.45	0.59
Al	1.15	1.02	1.91	2.75	3.34	12.10	0.55
Si	2.59	2.59	5.10	7.38	2.19	2.18	0.71
S	0.10	0.22	0.18	0.21	0.41	0.22	0.07
Cl	0.03	0.03	0.03				0.11
Ca	0.67	0.92	1.09	6.24	1.35	1.20	0.48
Ti	0.16	0.38	0.31	0.27	12.49	0.33	0.08
V	0.04	0.03	0.10		0.67		
Fe	10.68	8.75	14.70	0.54	0.28	0.44	0.28

Sample MS4, Site 6:

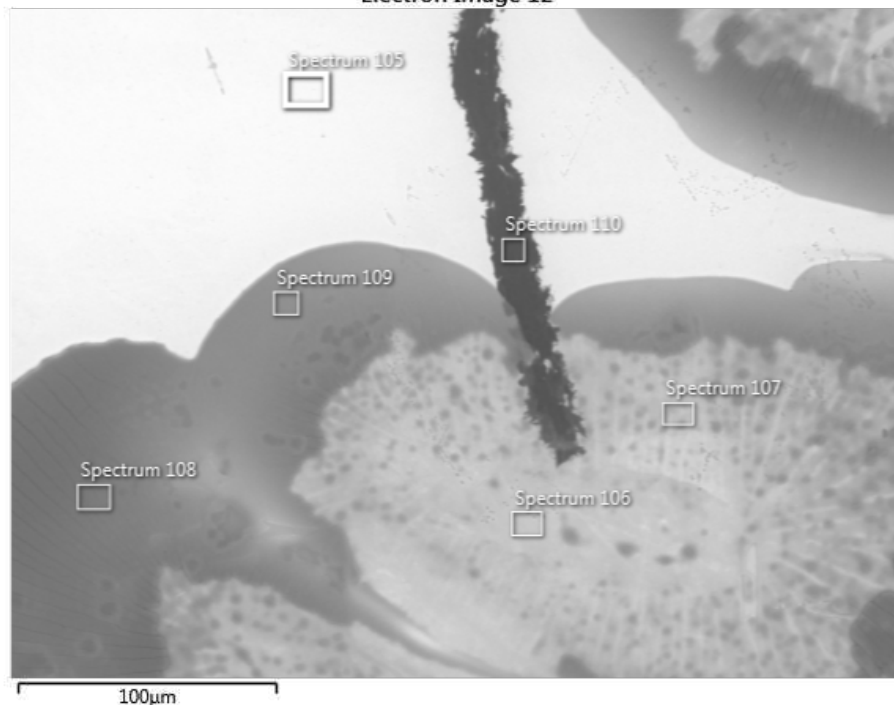
Electron Image 11



Element (mol%)	97	98	99	100	101	102	103
C	47.91	43.94	37.48	40.52	37.44	78.68	78.48
O	32.58	21.42	36.80	40.62	39.25	17.02	18.04
Mg	1.51	1.30	2.36	0.94	11.27	0.51	0.54
Al	2.12	1.35	4.61	0.84		0.56	0.38
Si	4.83	2.94	7.94	14.77	7.68	1.59	1.39
S	0.32	12.94	0.55	2.09	0.25	0.12	0.07
Cl						0.09	0.09
Ca	4.08	14.90	10.10		3.00	1.37	0.94
Ti	3.25						0.03
Fe						0.03	0.03
Zr	2.89						

Sample MS5, Site 1:

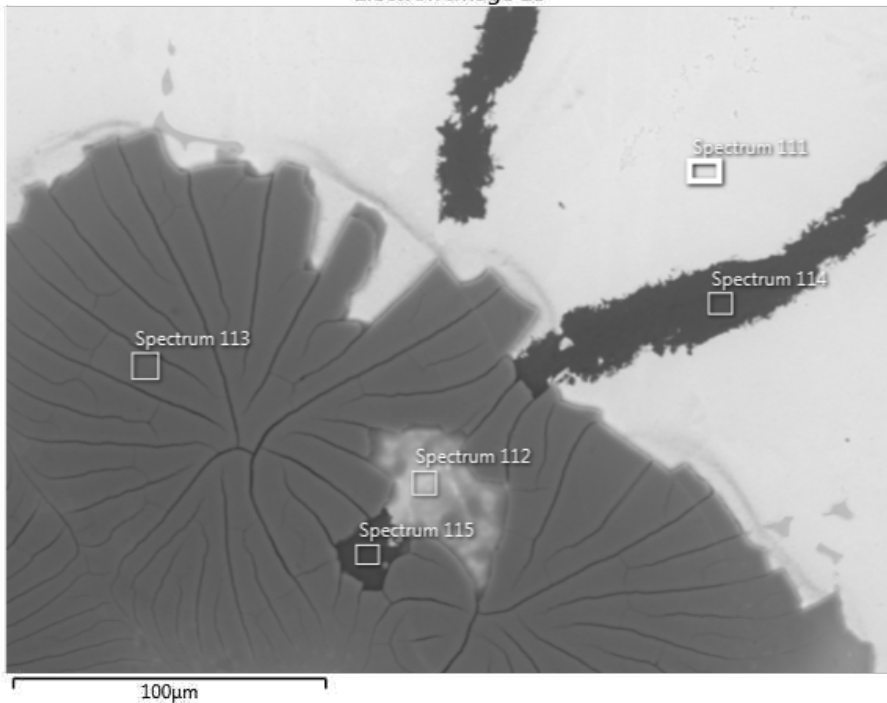
Electron Image 12



Element (mol%)	105	106	107	108	109	110
C	50.00	47.73	45.36	41.16	41.41	84.40
O	8.30	21.53	24.85	30.29	28.75	9.15
Mg						0.06
Al		0.11				0.04
Si	4.77	6.89	8.00	13.47	11.63	1.25
P						0.03
S	0.05	0.12			0.17	0.03
Cl						0.01
Ca	0.14	0.14	0.15	0.16	0.14	0.06
V	0.14	0.10	0.09	0.13	0.09	0.02
Fe	36.60	23.14	21.16	14.48	17.49	4.93

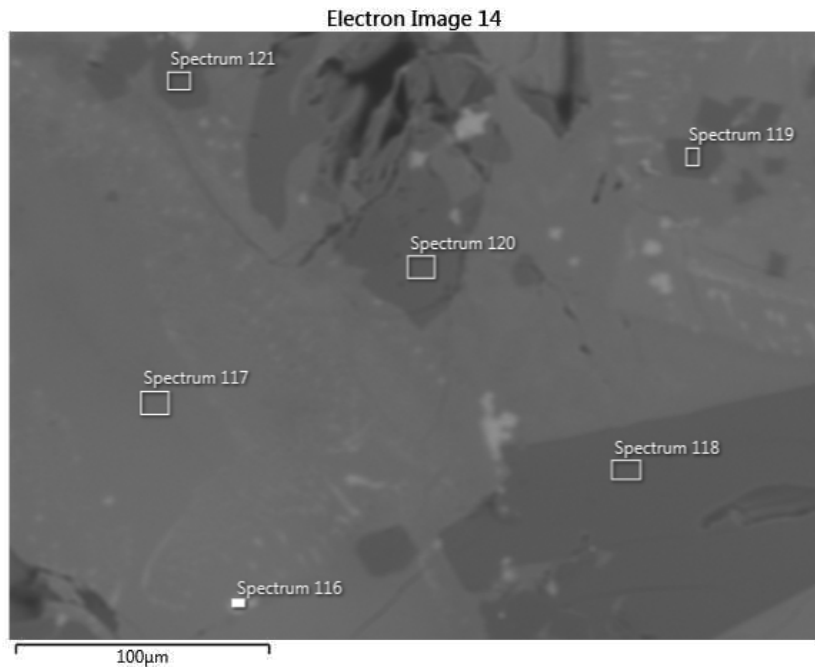
Sample MS5, Site 2:

Electron Image 13



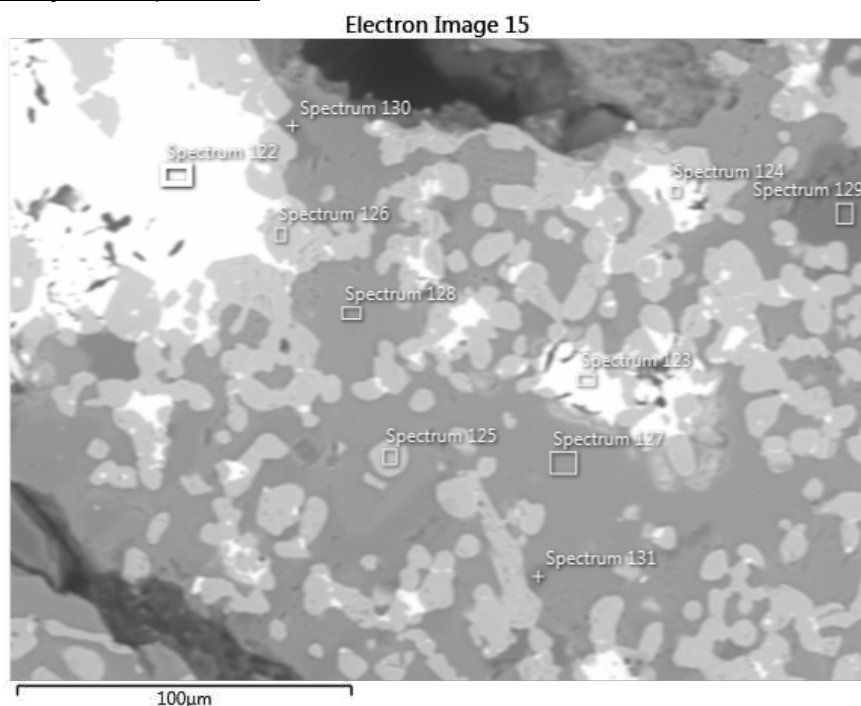
Element (mol%)	111	112	113	114	115
C	46.51	40.63	35.70	83.25	76.75
O	9.79	24.18	37.08	9.79	15.65
Mg	0.35	0.24		0.08	0.10
Al		0.15		0.05	0.05
Si	6.12	9.95	19.33	1.60	3.07
P				0.05	0.07
S		0.10		0.02	0.04
Cl				0.01	
Ca	0.22	0.24		0.09	0.12
V	0.13	0.11	0.07	0.03	0.03
Mn			0.10		
Fe	36.88	24.08	7.49	5.02	4.12

Sample MS5, Site 3:



Element (mol%)	116	117	118	119	120	121
C	45.67	30.12	24.06		26.51	31.26
O	24.53	42.87	46.19	55.78	43.62	40.98
Mg	2.04	3.72	15.04	11.98	14.70	7.77
Al	1.15	2.69		18.02		11.44
Si	3.89	11.10	9.99	8.31	10.11	4.75
S	10.16	0.39	0.33	0.65	0.39	0.40
Ca	12.36	9.00	2.88	5.24	3.37	3.28

Sample MS6, Site 1:

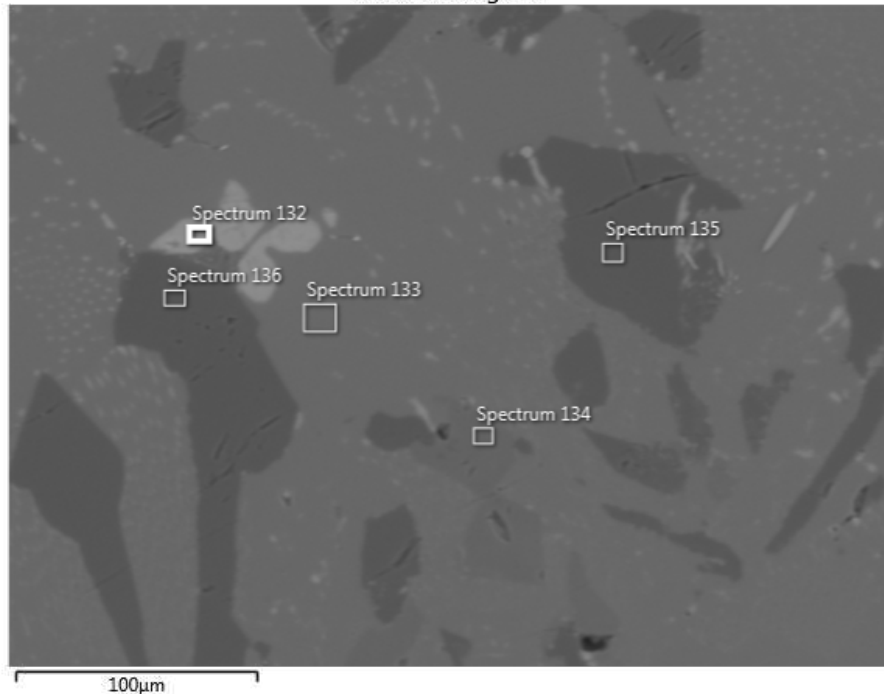


Optimizing Blast Furnace Hearth Inner State (OPTIBLAFINS)

Element (mol%)	122	123	124	125	126	127	128	129	130	131
C	31.14	28.29	29.22	21.56	24.60	18.26	18.20	16.17	21.72	19.90
N				9.97						
O	18.47	18.87	20.44	34.38	39.19	46.39	46.45	51.74	45.46	47.39
Mg	3.42	3.75	3.79	2.31	2.36	4.46	4.29	8.76	13.49	13.09
Al	2.04	2.18	2.22	1.40	1.34	3.64	4.04	13.23	1.37	1.67
Si	4.90	5.60	5.23	3.15	2.74	9.58	9.17	2.59	7.85	8.34
S	0.24	0.45	0.29	0.22	0.19	0.37	0.22		0.19	0.23
Ca	2.56	3.76	3.39	3.17	2.32	10.46	10.14	2.11	3.37	3.84
Ti	4.88	6.29	6.66	19.88	20.30	4.27	4.78	3.88	3.94	3.86
V	0.81	0.98	1.08	2.64	3.71	0.73	0.82	0.58	0.70	0.69
Fe	31.55	29.84	27.69	1.26	3.11	1.54	1.64	0.94	1.92	0.99

Sample MS6, Site 2:

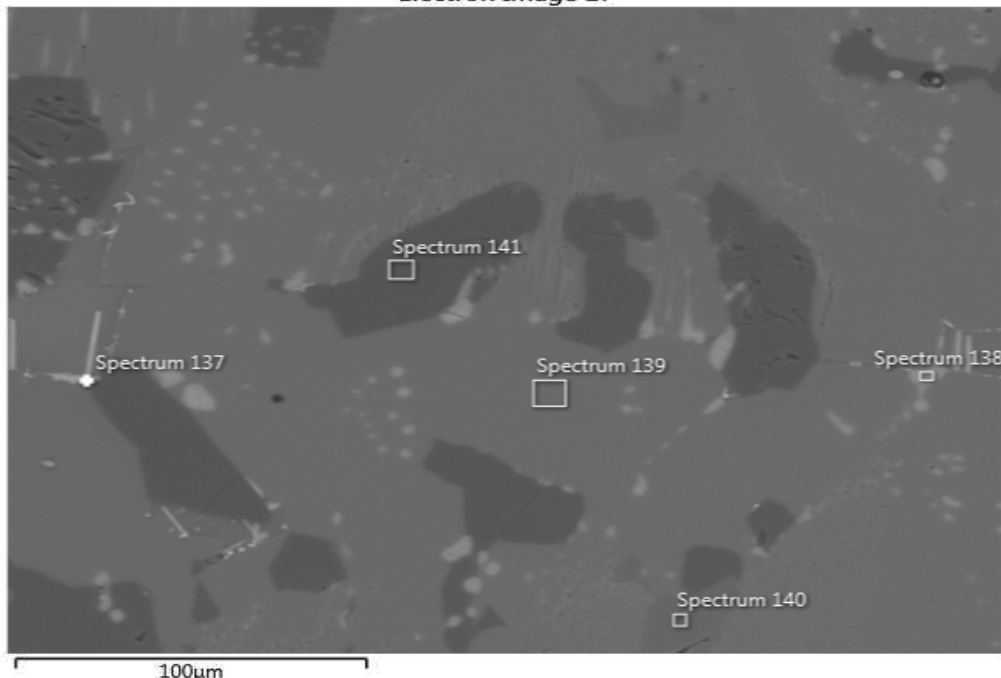
Electron Image 16



Element (mol%)	132	133	134	135	136
C	8.68	4.32			
O	36.53	53.65	55.73	56.06	57.75
Mg	4.53	5.88	12.59	19.56	18.75
Al	2.65	6.87			
Si	5.26	12.63	14.37	14.04	13.32
S	18.83	0.84	0.67	0.66	0.96
Ca	21.91	15.35	13.81	6.57	6.11
Te	1.07				
As		0.23	0.69	1.04	1.19
Br			1.95	1.83	1.88

Sample MS6, Site 3:

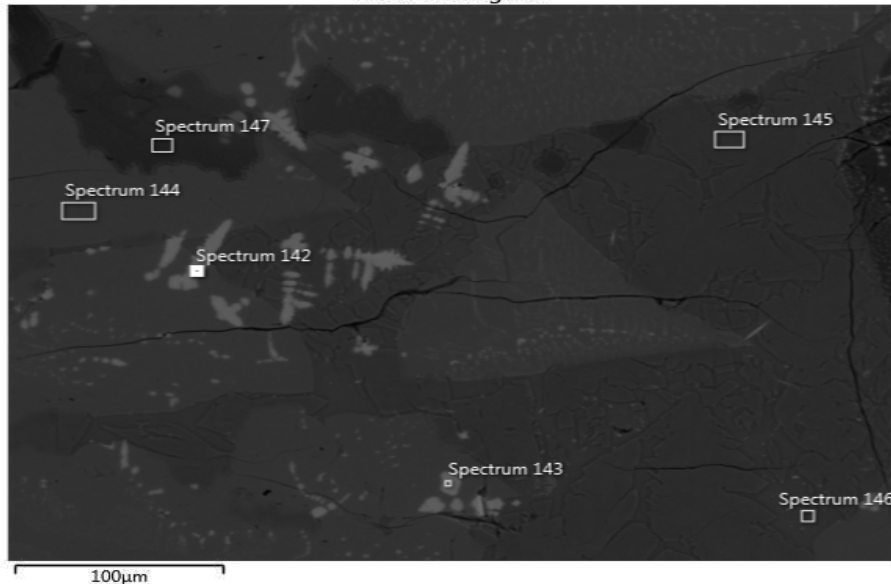
Electron Image 17



Element (mol%)	137	138	139	140	141
C			18.25	16.43	18.87
O	61.74		46.75	47.60	47.42
Mg	5.86		4.87	10.13	15.19
Al		5.49	5.30		
Si	15.35	11.34	10.82	11.63	10.54
S	0.67	34.14	0.43	0.44	0.42
Ca	6.91	45.24	13.10	11.44	5.10
Te		2.57			
Pb		1.22			
Br	5.99			1.46	1.37
Ba	2.60				

Sample MS7, Site 1:

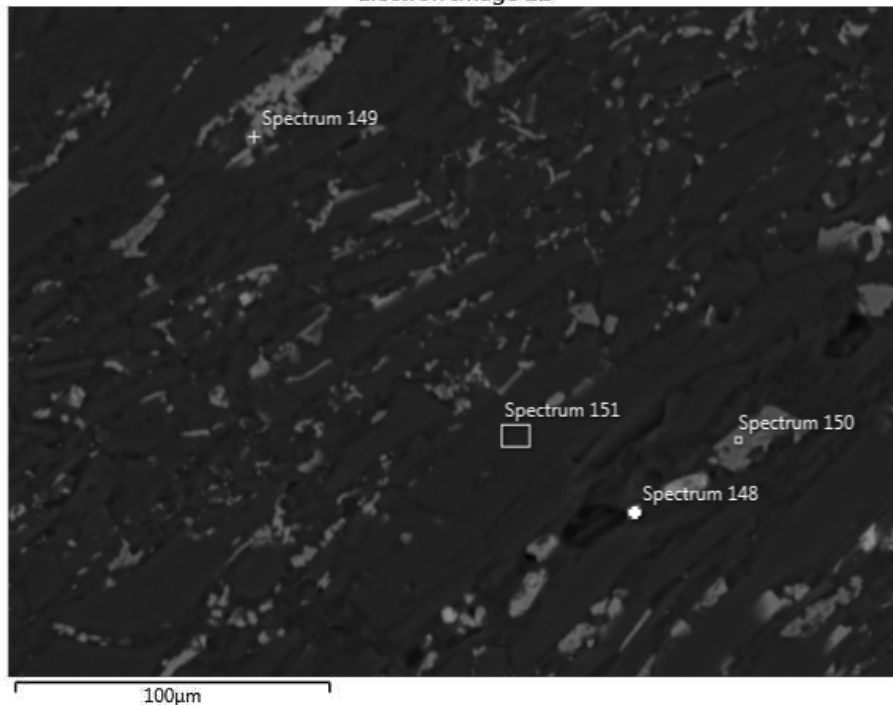
Electron Image 20



Element (mol%)	142	143	144	145	146	147
C	25.51	22.60	15.05	13.61	14.37	17.31
O	32.25	32.87	49.49	50.57	50.03	53.06
Na	0.19	0.16	0.31		0.66	0.27
Mg	2.18	2.23	4.76	5.08	2.81	2.99
Al	2.24	2.41	4.31	7.31	8.38	3.29
Si	5.06	4.92	12.45	12.54	12.89	13.45
S	15.02	16.25	0.45	0.70	0.79	0.45
K	0.25	0.34			3.97	
Ca	17.31	18.20	12.70	9.00	5.46	8.70
Ti			0.28	0.56	0.42	0.23
Fe				0.22	0.23	

Sample MS7, Site 2:

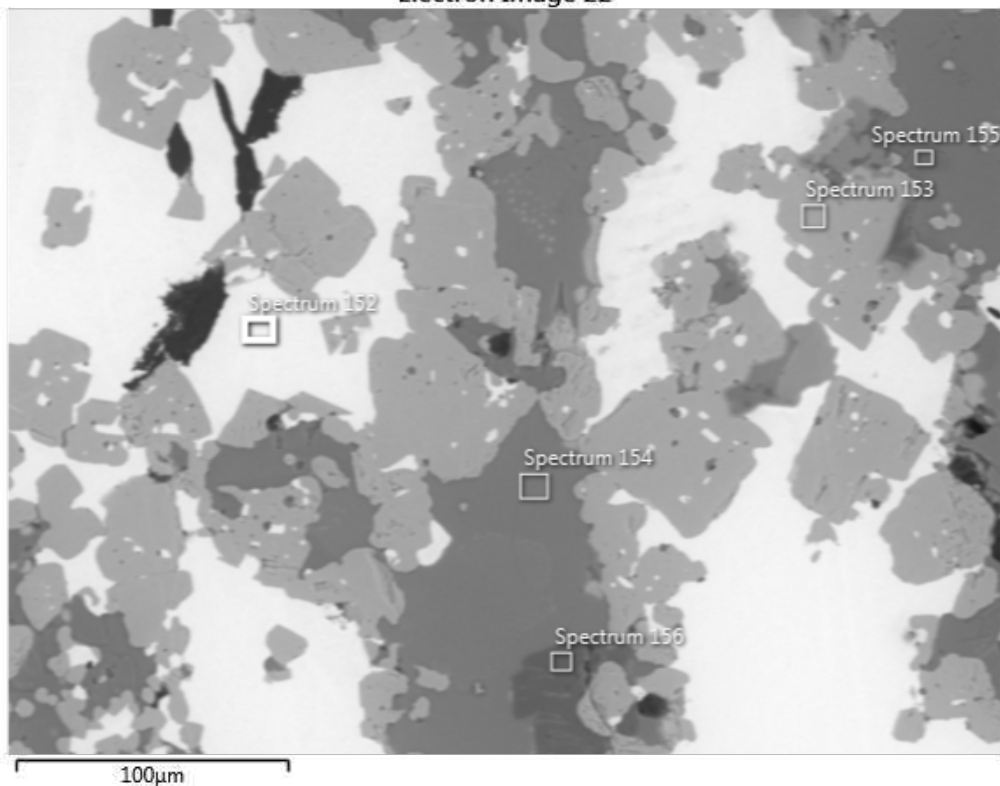
Electron Image 21



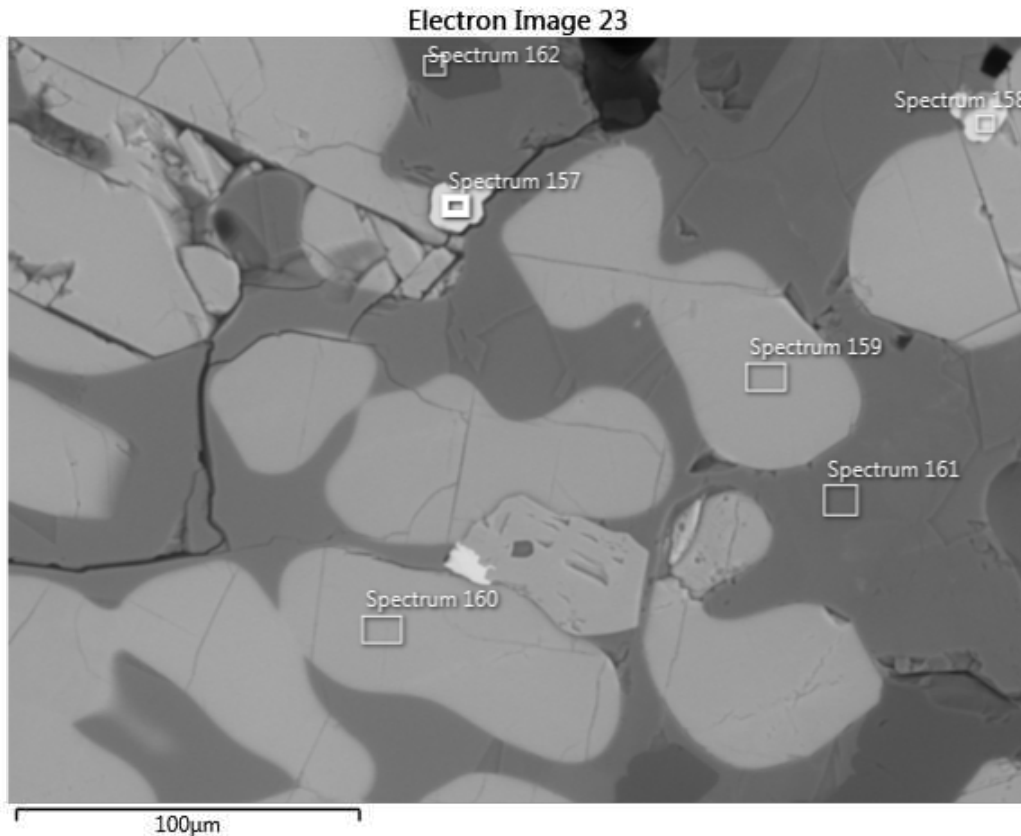
Element (mol%)	148	149	150	151
C	84.97	75.12	66.11	89.38
O	5.96	16.31	25.19	9.52
Mg	0.16	1.18	3.13	0.16
Al		1.01	5.03	0.16
Si	0.22	2.70	0.30	0.27
S	4.36	0.14		0.03
Ca	4.24	3.06	0.12	0.19
Fe		0.05	0.04	0.04

Sample MS7, Site 3:

Electron Image 22



Element (mol%)	152	153	154	155	156
C	37.46	20.16	15.84	14.22	13.65
N		19.12			
O	11.61	25.77	45.11	49.37	48.74
Mg	1.31	0.92	4.80	3.74	17.39
Al	0.98	0.65	2.72	6.39	0.96
Si	2.82	2.30	10.52	10.22	8.79
S	0.18	0.17	0.26	0.29	0.28
Ca	1.33	1.15	9.79	6.38	1.86
Ti	6.46	23.63	5.84	5.11	4.23
V	0.37	0.93	0.34	0.31	0.24
Fe	37.43	5.16	4.40	3.75	3.77

Sample MS7, Site 4:

Element (mol%)	157	158	159	160	161	162
C	21.50	25.72	16.74	17.29	11.65	12.27
O	19.82	18.74	26.37	24.54	49.17	50.47
Mg	4.06	4.02	2.25	2.15	4.75	15.54
Al	2.85	2.42	1.59	1.35	6.25	1.42
Si	5.02	4.31	2.70	2.34	10.17	8.54
S	8.48	8.69	25.29	26.16	5.48	5.11
Ca	8.87	8.97	25.06	26.17	10.98	5.81
Ti	0.53	1.39			1.09	0.39
Fe	28.87	25.46			0.15	0.16

2.5.4 SIMCA analysis**2.5.4.1 SIMCA**

SIMCA is a computer software used to analyze the statistical data and it is optimal to use when analyzing big datasets with multiple variables.

2.5.4.2 Terms used in the analysis

To have a better understanding of the SIMCA analysis, different terms will be used. These terms are explained in the following subsections.

2.5.4.2.1 Principal Component (PC)

To process large datasets for statistical analysis the computer program SIMCA was used. SIMCA is a multivariate tool that's capable to perform Principal Component Analysis (PCA), which is a procedure that uses orthogonal transformations to convert observations into linearly uncorrelated variables called principal components (PC).

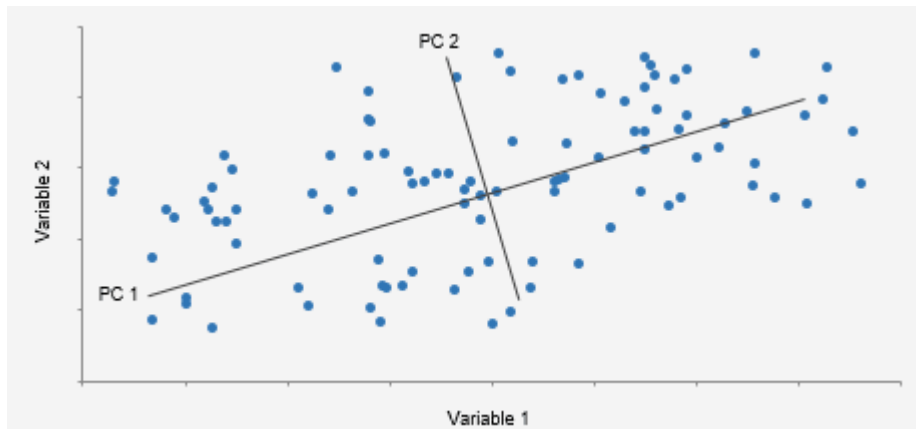


Figure 356: An example of how the orthogonal PC can be oriented in a dataset.

The dataset in the example Figure 356 has two directions which can be described with two PC, the more observations the easier it's to see the tendencies to directions in the dataset. With help of principal components insignificant variables can be excluded, since the dataset will have small tendencies in the variable direction that are insignificant.

2.5.4.2.2 Projection to Latent Structures (PLS)

The dataset has Y and X -variables therefore a Projection to Latent Structures (PLS) model will be used, since the X-variables is directly connected to the values of the Y-variable. With multiple X-variables a dataset can be difficult to interpret but with help of SIMCA this process can be distilled down to reading and observing graphs.

2.5.4.2.3 Variable Importance Projection (VIP)

The variables that are important for the model can be determined by using Variable Importance Projection (VIP). If a variable scores more than 1 then it's said to be important enough and should not be neglected. The variables can be efficiently excluded from the model until the model is left with the important variables.

2.5.4.3 Variable list used in the SIMCA analysis

The dataset used in the SIMCA analysis include 18 observations as shown in Table 66. The observations 27581, M103, M203, M204, M205, #7, #12 and #16 could not be used since these observations had missing Y-values. Observation M202 was excluded since this sample was taken from a position near to the taphole and it contained too much taphole clay. The variables used in the SIMCA analysis are listed in Table 67.

Table 66: The observations used in the statistical analysis, the crossed observations were not used.

<u>Observation</u>			
<u>Sample</u>	<u>Note</u>	<u>Sample</u>	<u>Note</u>
FS1	Original Coke used as coke substrate	M101	Slag/Coke couple from the hearth of the EBF
FS2		M102	
FS3		M103	
FS4		M104	
FS5		M105	
FS6		M106	
FS7		M107	
#1		M201	
#7		M202	
#12		M203	
#14		M204	
#15		M205	

#16		M206	
		M207	

Table 67: The variables used in the statistical analysis, the compositions of slag and coke were from the XRF and LECO analysis. The bold variables ended up as the most important ones.

Y-variables		
<i>Contact Angle (at temperature 1528 °C)</i>		
X-variables		
Slag (XRF/LECO)	Coke (XRF/LECO)	Calculated variables
<i>Fe (XRF_Slag)</i>	CaO (XRF_Coke)	<i>B2 (Slag)</i>
<i>CaO (XRF_Slag)</i>	Al2O3 (XRF_Coke)	<i>B3 (Slag)</i>
<i>SiO2 (XRF_Slag)</i>	MgO (XRF_Coke)	<i>B4 (Slag)</i>
<i>MnO (XRF_Slag)</i>	sum ash (XRF_Coke)	<i>Bells ratio (Slag)</i>
<i>Al2O3 (XRF_Slag)</i>	<i>SiO2 (XRF_Coke)</i>	<i>Viscosity (Slag)</i>
<i>MgO (XRF_Slag)</i>	<i>MnO (XRF_Coke)</i>	<i>viscosity 1500 [Pa*s]</i>
<i>Na2O + K2O (XRF_Slag)</i>	<i>Na2O + K2O (XRF_Coke)</i>	<i>0% melt temp (Slag)</i>
<i>S_Leco (Slag)</i>	<i>S_Leco (Coke)</i>	<i>50% melt temp (Slag)</i>
	<i>Fe (XRF_Coke)</i>	<i>75% melt temp (Slag)</i>
	<i>SiO2/Al2O3 (Coke)</i>	<i>95% melt temp (Slag)</i>
Slag (XRD)	Coke (XRD)	
<i>Akermanite (XRD_Slag)</i>	<i>Graphite (XRD_Coke)</i>	
<i>Quartz/SiO2 (XRD_Slag)</i>	<i>Carbon (XRD_Coke)</i>	
<i>FeO (XRD_Slag)</i>	<i>Fe/FeSi (XRD_Coke)</i>	
<i>Fe (XRD_Slag)</i>	<i>Gehlenite/Akermanite (XRD_Coke)</i>	
	<i>MgAl2O4 (XRD_Coke)</i>	
	<i>CristobaliteSiO2 (XRD_Coke)</i>	

2.5.4.4 Models

Four models, with four different groups of variables taken into account, are used in the SIMCA analysis and the descriptions of the models are shown as follows.

2.5.4.4.1 Model 1 (M1)

The first model had two principal components, the x-variables seem to tend to arrange in two directions.

Model	PC	Obs	nr of X-var	R2X	R2Y	Q2
M1	2	18	38	0.507	0.858	0.665

The first model had a R2X value of 0.507, a R2Y value of 0.858 and a Q2 value of 0.665. The model is a good fit to the Y-values, but since it still has 38 X-variables and is therefore using too many variables to be a practical model to predict the contact angle.

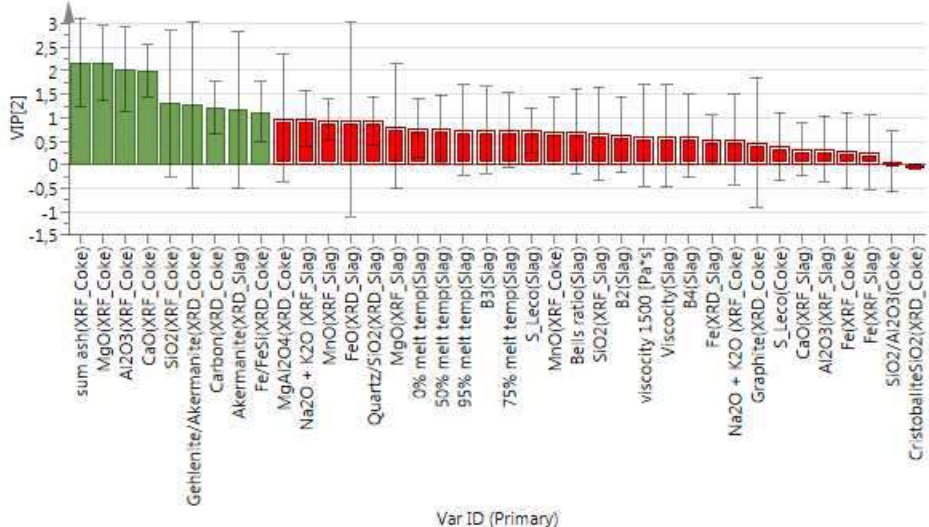


Figure 357: The VIP-plot for the first model, the variables excluded in the next model is marked red.

The model is further investigated with a VIP-plot, 29 of the variables have a VIP-score of less than 1 (marked red in Figure 357), therefore these variables are excluded from next model. To make sure no significant variables are excluded it's important to keep variables with a VIP-score over 1. The theoretical viscosity based on the composition of slag didn't have a VIP-score over 1 and was excluded from next model.

2.5.4.4.2 Model 2 (M2)

With the important variables still included will result in the second model, which only has one principal component (PC). The variables kept will have one direction. The variables based on the XRF slag composition, and calculated variables was excluded, this leaves XRF composition of coke and XRD left.

Model	PC	Obs	nr of X-var	R2X	R2Y	Q2
M2	1	18	9	0.735	0.781	0.758

The second model was better than M1 with a R2X-value of 0.735, a R2Y-value of 0.781 and a Q2-value of 0.758. With a better R2X-value can it be said that the variables are more grouped than with the 29 excluded variables. The R2Y value is less than M1 but still good, this is good since the first model was overfitted using more variables than necessary. To ensure that more unnecessary variables are excluded was the model further investigated using the VIP-plot.

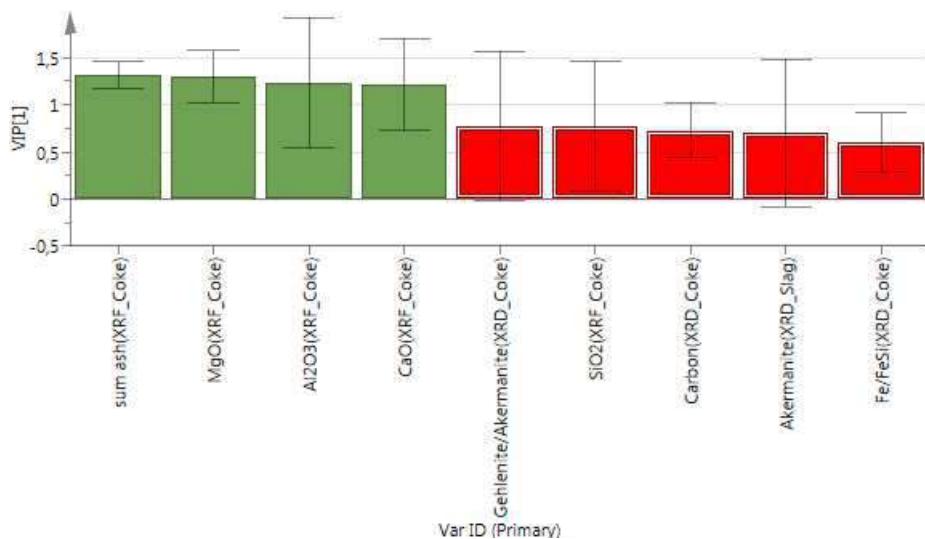


Figure 358: The VIP-plot for the second model, the variables excluded in the next model is marked red.

In the VIP-plot (as shown in Figure 358) it can be observed that the five most right variables have less than 1 in VIP-score which leaves only four important variables left for the next model. By now

the XRD variables was excluded and it leaves only the composition of the coke to determine the contact angle.

2.5.4.4.3 Model 3 (M3)

The third model had one principal component, the variables left has one direction. The last four variables were from the XRF composition of coke; Al_2O_3 , MgO , CaO and *sum ash* with the compositions is in wt% and where *sum ash* is the total of the compositions.

model	PC	Obs	nr of X-var	R2X	R2Y	Q2
M3	1	18	4	0.925	0.784	0.75

The third model is a significantly better model than the previous models. The third model did have a R2X-value of 0.925, a R2Y-value of 0.784 and a Q2-value of 0.75. R2X-value close to 1 means that the variables are grouped, which tend to be the case when the model starts to be good. The R2Y-value is lower than M1 but higher than M2; this means that the third model is a better fit than M2 but not M1. This makes the third model better than M1 since the first model is using 34 more X-variables. The first model is overfitted and will therefore have a better fit to the Y-values.

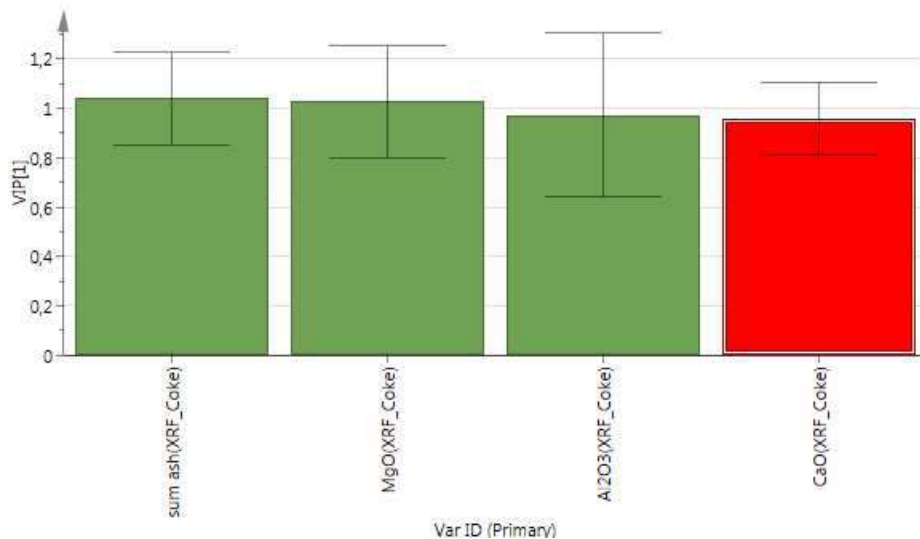


Figure 359: The VIP-plot for the third model, the variables excluded in the next model is marked red.

The variable $CaO(XRF_Coke)$ have a VIP-score under 1 and was excluded in M4. The variables in model 3 was from the composition of coke, the contact angle is therefore determined by the coke composition. The four variables have a good VIP-score (as shown in Figure 359) and are good enough to be kept, the model was further investigated using a prediction plot and correlation plot, as shown in Figure 360 and Figure 361.

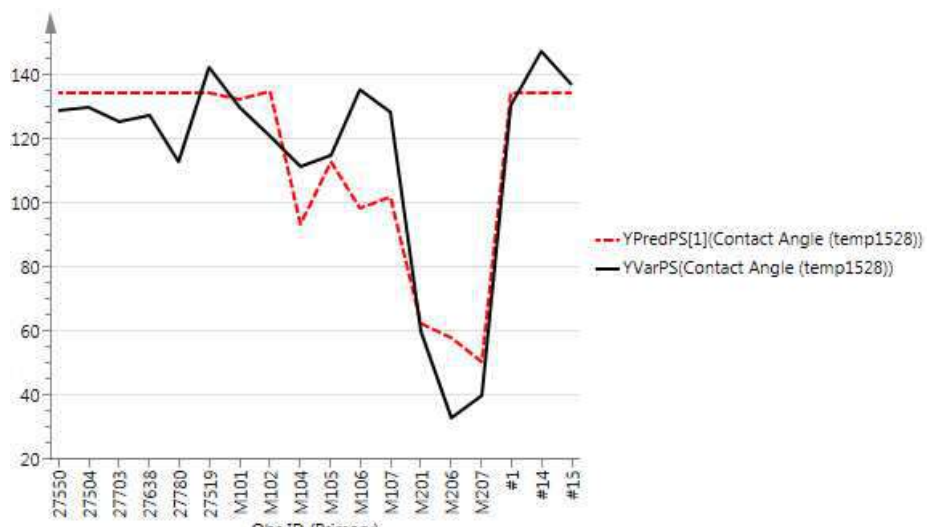


Figure 360: The prediction plot of M3 together with the observations.

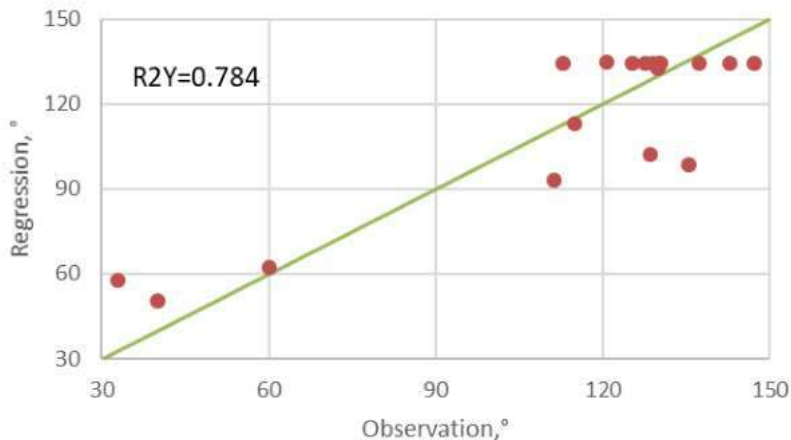


Figure 361: The correlation plot of M3.

In Figure 360 it can be seen, that the prediction set (red) from the third model resembles the original dataset (black). The model follows the observations with small deviation. The contact angle is predicted with good accuracy and the model was then exported in terms of coefficients which resulted in model 3 below:

$$M3(a, b, c, d) = 171.95 - 8.109 \cdot a - 3.531 \cdot b - 0.989 \cdot c - 2.123 \cdot d$$

a is wt% of Al_2O_3 in the coke,
 b is wt% of MgO in the coke,
 c is wt% of sum ash in the coke,
 d is wt% of CaO in the coke

The regression function has boundaries that it's recommended to keep within, values outside the boundaries might deviate from the regression.

CaO(Wt.%): (0.09 - 9.11),
 Al_2O_3 (Wt.%): (2.49 - 5.71),
 MgO(Wt.%): (0.09 - 6.55),
 sum ash(Wt.%): (8.74 - 34.72) and
 Contact Angle(degree, °): (33.00 - 147.24).

The contact angle was written as a function of the four variables, it was observed that the contact angle is determined by the coke compositions. The variables are obtained by doing an XRF-analysis of the coke, which becomes a simple way to predict the contact angle.

2.5.4.4.4 Model 4 (M4)

The fourth model had one principal component, but the three most important variables are left. The variables left to determine the fourth model were MgO , Al_2O_3 and *sum ash* from the XRF analysis of the coke.

Model	PC	Obs	nr of X-var	R2X	R2Y	Q2
M4	1	18	3	0.935	0.796	0.77

Model 4 is a significantly better model than M1 and M2. The model 4 did have a R2X-value of 0.935, a R2Y-value of 0.796 and a Q2-value of 0.77. The R2Y-value was better than M3 which makes it a reliable model although a variable has been excluded, the Q2-value was higher than M3. Since M4 only have three variables and still have a Q2-value of 0.77 and this means that the model isn't overfitted. The R2X-value shows that the variables are grouped together in one direction.

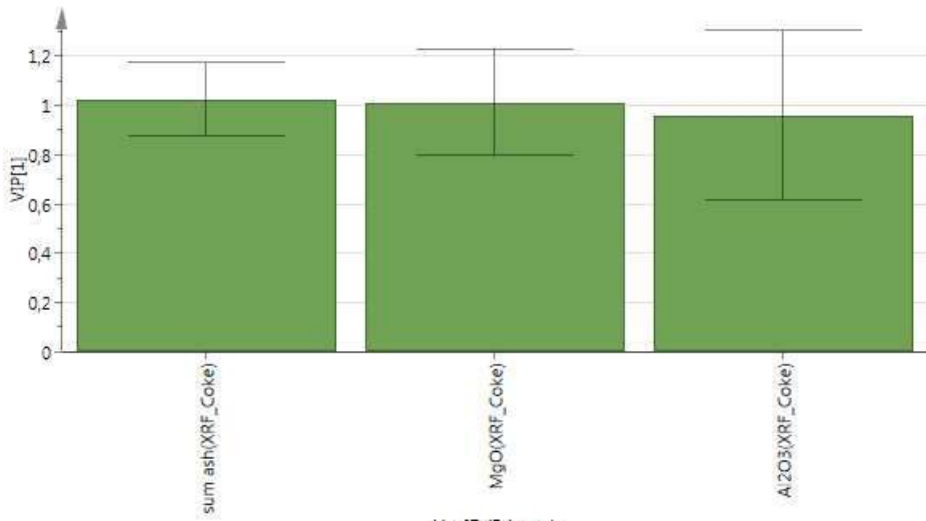


Figure 362: The VIP-plot for the final model.

The important variables left in the fourth model can be seen in Figure 362, *Sum ash*, Al_2O_3 and MgO . These are the variables that will affect the contact angle most. It can be seen that Al_2O_3 might have a VIP-score under 1 but it was chosen to be kept due to the error bar. The model can be written as a model using the coefficient of each variable.

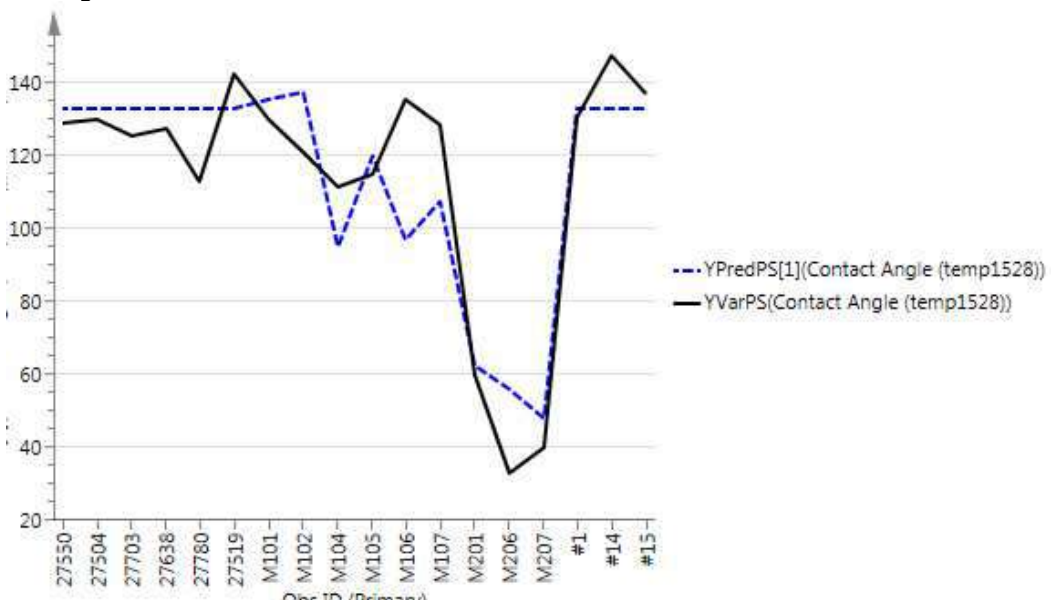


Figure 363: The prediction plot of the final model together with the observations.

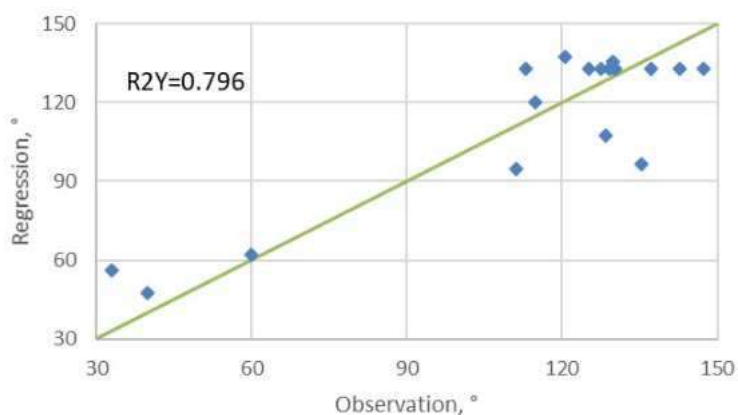


Figure 364: The correlation plot of M4.

As shown in Figure 363 and Figure 364, the prediction set follows the observation with a small deviation and the correlation plot from the model 4 resembles the original dataset. Therefore, the

Optimizing Blast Furnace Hearth Inner State (OPTIBLAFINS)

model is believed to be good since Q2 value is over 0.7. It's seen that the prediction is in general following the observations, since the model was good enough and the model function can be written using the coefficients of M4.

$$M4(a, b, c) = 182.193 - 10.694 \cdot a - 4.657 \cdot b - 1.304 \cdot c$$

a is wt% of Al₂O₃ in the coke,
b is wt% of MgO in the coke,
c is wt% of sum ash in the coke.

The regression function has boundaries that it's recommended to keep. Values outside the boundaries might deviate from the regression.

Al₂O₃(Wt. %): (2.49 - 5.71),
MgO(Wt. %): (0.09 - 6.55),
sum ash(Wt. %): (8.74 - 34.72) and
Contact Angle(degree, °): (33.00 - 147.24).

The final model of contact angle was determined by the coke compositions.

3 List of symbols, Indices, Acronyms and Abbreviations

<u>Symbols</u>	<u>Unit</u>	
A	[m ²]	cross-sectional area
C_D	[-]	drag coefficient
c_i	[J/(kg.K)]	specific heat capacity of layer i
d	[m]	diameter
\vec{F}	[N]	force vector
$\vec{F}^{\nabla p}$	[N]	pressure gradient force
\vec{F}^b	[N]	buoyancy force
\vec{F}^d	[N]	drag force
\vec{F}^{pf}	[N]	particle-fluid interaction force
\vec{f}_{int}	[N/m ³]	volumetric particle/fluid interaction momentum source
g	[m/s ²]	gravitational acceleration
i	[-]	general index
j	[-]	general index
J	[kg/m ²]	inertia tensor
K	[-]	number of discrete time steps in period in the inverse model
K_i	[W/(m.k)]	thermal conductivity of layer i
m	[kg]	mass
M	[Nm]	torque
n	[-]	number of particles
r	[m]	radius
\vec{R}	[m]	lever vector
\vec{r}	[m]	position vector
Re	[-]	Reynolds-number
t	[s,min]	time
T	[°C]	temperature
V	[m ³]	volume

Optimizing Blast Furnace Hearth Inner State (OPTIBLAFINS)

\vec{v}	[m/s]	particle velocity
\vec{u}	[m/s]	fluid velocity
U	[m/s]	velocity
x	[m]	spatial coordinate in the inverse model

Greek Unit

α	[-]	volume fraction
β	[kg/s]	particle/fluid friction coefficient
$\bar{\beta}$	[kg/m ³ ·s]	fluid cell average particle/fluid friction coefficient
ϵ , or ϵ	[-]	hearth voidage, or strain
ε_F	[-]	porosity
δ		Kronecker delta
σ	[MPa]	stress
ω		factor in slag surface declivity expression
	[rad/s ²]	angular acceleration
μ	[kg/m·s]	dynamic viscosity
ρ	[kg/m ³]	density
τ	[N/m ²]	stress tensor
ν	[kg/m·s]	kinematic viscosity
$\vec{\varphi}$	[rad/s]	angular velocity
φ		correction factor for outflow rates of last tap
χ	[-]	correction factor

Subscript

coke		
dm	dead man	
fluid		
free	Coke-free (volume)	
in	inflow	

Optimizing Blast Furnace Hearth Inner State (OPTIBLAFINS)

L	cold face	
lin	lining	
out	outflow	
p	pressure	
rel	relative	
sk	skull	
SI	slag	
start	tap start	
th	taphole	
TC1 / TC2	inner / outer thermocouple in transient inverse model	

Superscript

buoyancy	
drag	
init	initial state
particle	
pf	particle fluid
rev	revised value

A dot above a symbol denotes a flow rate

Acronyms

AGDH	AG der Dillinger Hüttenwerke
AMEH	ArcelorMittal Eisenhüttenstadt
BF	Blast Furnace
BFG	Blast Furnace Gas
BFHM	Blast Furnace Hearth Erosion Model
BFI	VDEH Betriebsforschungsinstitut
BL	Brittle Layer
CFD	Computational Fluid Dynamics

Optimizing Blast Furnace Hearth Inner State (OPTIBLAFINS)

COR	Coefficient Of Restitution
CSR	Coke Strength after Reaction
daf	dry-ash-free
DEM	Discrete Element Method
DM	Dead Man
DMD	Dead Man Dynamics
DMT	Deutsche Montan Technologie
EBF	Experimental Blast Furnace
FE	Finite Element
FEM	Finite Element Method
GUI	Graphical user interface
HM	Hot Metal
IT	Information Technology
LDA	Laser Doppler Anemometry
MP	Measurement Point
NSC	Nippon Steel Corporation
PIV	Particle Image Velocimetry
PC	Personal Computer
RTD	Residence Time Distribution
RUB-LEAT	Department of Energy Plant Technology of Ruhr University of Bochum (Lehrstuhl für Energie Anlagen und EnergieprozessTechnik)
TC	ThermoCouple
TH	TapHole
TRZ	Thermal Reserve Zone
TSE	Tata Steel Europe
SL	Slag
SQL	Standardized Query Language
VOF	Volume Of Fluid
VPN	Virtual-Private-Network
WLF	Thermal conductivity

Optimizing Blast Furnace Hearth Inner State (OPTIBLAFINS)

WM	Water Model
WP	Work Package
XRMT	X-Ray Micro Tomography

4 References

- [1] Vångö, M., Pirker, S., and Lichtenegger, T. "Unresolved CFD-DEM modeling of multiphase flow in densely packed particle beds." *Applied Mathematical Modelling* 56 (2018): 501–516.
- [2] Vångö, M., Feilmayr, C., Pirker, S., and Lichtenegger, T. "Data-assisted CFD modeling of transient blast furnace tapping with a dynamic dead man.", Preprint submitted to Applied Mathematical Modelling.
- [3] Nnanna, AG Agwu, et al. "Water model of a blast furnace hearth for flow pattern investigation.", AISTech 2004: Iron and Steel Conference Proceedings; 2004.
- [4] Tanzil, W. B. U., et al. "Experimental model study of the physical mechanisms governing blast furnace hearth drainage." *Transactions of the Iron and Steel Institute of Japan* 24.3 (1984): 197-205
- [5] Ariyama, Tatsuro, et al. "Recent progress on advanced blast furnace mathematical models based on discrete method.", *ISIJ international* 54.7 (2014): 1457-1471.
- [6] Tsuji, Yutaka, Toshihiro Kawaguchi, and Toshitsugu Tanaka. "Discrete particle simulation of two-dimensional fluidized bed.", *Powder technology* 77.1 (1993): 79-87.
- [7] Huang, D. Frank, et al. "Numerical Investigation of transient hot metal flows in a blast furnace hearth.", AISTech 2005 Volumes I & II and ICS 2005 Conference Proceedings; Volume I. 2005.
- [8] Guo, Bao-Yu, et al. "CFD modelling of liquid metal flow and heat transfer in blast furnace hearth.", *ISIJ international* 48.12 (2008): 1676-1685.
- [9] Huang, D. Frank, et al. "Simulation of the hearth draining process and thermal stress of a BF hearth.", AIST Proceedings: AISTech 2007. 2007.
- [10] Nishioka, Koki, Takayuki Maeda, and Masakata Shimizu. "A three-dimensional mathematical modelling of drainage behavior in blast furnace hearth.", *ISIJ international* 45.5 (2005): 669-676.
- [11] Nishioka, Koki, Takayuki Maeda, and Masakata Shimizu. "Effect of various in-furnace conditions on blast furnace hearth drainage.", *ISIJ international* 45.10 (2005).
- [12] Ashrafiyan, Alireza, and Stein Tore Johansen. "Tapping of stratified liquids from a packed bed.", International Conference on CFD in the Process Industries, Melbourne, Australia. 2006.
- [13] Gupta, G. S., et al. "Model studies of liquid flow in the blast furnace lower zone.", *ISIJ international* 36.1 (1996): 32-39.
- [14] Shao, Lei, and Henrik Saxén. "A simulation study of two-liquid flow in the taphole of the blast furnace". *ISIJ international* 53.6 (2013): 988-994.
- [15] Shao, Lei. "Model-based estimation of liquid flows in the blast furnace hearth and taphole.", (2013).
- [16] Natsui, Shungo, et al. "Simultaneous three-dimensional analysis of gas-solid flow in blast furnace by combining discrete element method and computational fluid dynamics.", *ISIJ international* 51.1 (2011): 41-50.
- [17] Adema, A. T. "DEM-CFD Modelling of the ironmaking blast furnace.", Diss. TU Delft, Delft University of Technology, 2014.
- [18] Zhou, Zongyan, et al. "Discrete particle simulation of solid flow in a model blast furnace." *ISIJ international* 45.12 (2005): 1828-1837.
- [19] Zhou, Z. Y., et al. "Discrete particle simulation of gas-solid flow in a blast furnace.", *Computers & Chemical Engineering* 32.8 (2008): 1760-1772.
- [20] Zhou, Zongyan, et al. "Numerical investigation of the transient multiphase flow in an ironmaking blast furnace.", *ISIJ international* 50.4 (2010): 515-523.
- [21] Sun, Xiaosong, and Mikio Sakai. "Three-dimensional simulation of gas-solid-liquid flows using the DEM-VOF method.", *Chemical Engineering Science* 134 (2015): 531-548.
- [22] Li, Yong, Jianping Zhang, and Liang-Shih Fan. "Numerical simulation of gas-liquid-solid fluidization systems using a combined CFD-VOF-DPM method: bubble wake behaviour.", *Chemical Engineering Science* 54.21 (1999): 5101-5107.
- [23] Li, Y., et al. "Numerical studies of bubble formation dynamics in gas-liquid-solid fluidization at high pressures.", *Powder Technology* 116.2 (2001): 246-260.
- [24] Rusche, Henrik. "Computational fluid dynamics of dispersed two-phase flows at high phase fractions.", Diss. Imperial College London (University of London), 2003.
- [25] Anderson, T. Bo, and Roy Jackson. "Fluid mechanical description of fluidized beds. Equations of motion.", *Industrial & Engineering Chemistry Fundamentals* 6.4 (1967): 527-539.
- [26] Brackbill, J. U., Kothe, D. B., and Zemach, C. "A continuum method for modeling surface tension.", *Journal of Computational Physics* 100.2 (1992): 335-354.
- [27] Cundall, Peter A., and Otto DL Strack. "A discrete numerical model for granular assemblies.", *geotechnique* 29.1 (1979): 47-65.

- [28] Martin, C. L., D. Bouvard, and S. Shima. "Study of particle rearrangement during powder compaction by the discrete element method.", *Journal of the Mechanics and Physics of Solids* 51.4 (2003): 667-693.
- [29] Zhou, Z. Y., et al. "Discrete particle simulation of particle-fluid flow: model formulations and their applicability.", *Journal of Fluid Mechanics* 661 (2010): 482-510.
- [30] Hill, Reghan J., Donald L. Koch, and Anthony JC Ladd. "The first effects of fluid inertia on flows in ordered and random arrays of spheres." *Journal of Fluid Mechanics* 448 (2001): 213-241.
- [31] Van Buijtenen, Maureen S., et al. "Numerical and experimental study on multiple-spout fluidized beds.", *Chemical engineering science* 66.11 (2011): 2368-2376.
- [32] Peng, Zhengbiao, et al. "Influence of void fraction calculation on fidelity of CFD-DEM simulation of gas-solid bubbling fluidized beds.", *AIChE Journal* 60.6 (2014): 2000-2018.
- [33] Pirker, S., D. Kahrimanovic, and C. Goniva. "Improving the applicability of discrete phase simulations by smoothening their exchange fields." *Applied Mathematical Modelling* 35.5 (2011): 2479-2488.
- [34] Radl, Stefan, et al. "State of the art in mapping schemes for dilute and dense Euler-Lagrange simulations.", *Progress in Applied CFD* 103 (2015): 112.
- [35] Capecelatro, Jesse, and Olivier Desjardins. "An Euler-Lagrange strategy for simulating particle-laden flows.", *Journal of Computational Physics* 238 (2013): 1-31.
- [36] Brännbacka, J., and Saxén, H. "Model analysis of the operation of the blast furnace hearth with a sitting and floating dead man.", *ISIJ International* 43.10 (2003): 1519-1527.
- [37] Jeong, In-Hyeon, Hyun-Soo Kim, and Yasushi Sasaki. "Trickle flow behaviors of liquid iron and molten slag in the lower part of blast furnace.", *ISIJ international* 53.12 (2013): 2090-2098.
- [38] Bierwisch, C., Kraft, T., Riedel, H., and Moseler, M. "Three-dimensional discrete element models for the granular statics and dynamics of powders in cavity filling.", *Journal of the Mechanics and Physics of Solids* 57.1 (2009): 10-31.
- [39] Sakai, M., and Koshizuka, S. "Large-scale discrete element modeling in pneumatic conveying." *Chemical Engineering Science* 64.3 (2009): 533-539.
- [40] Radl, S., Radeke, C., Khinast, J. G., and Sundaresan, S. "Parcel-based approach for the simulation of gas-particle flows.", 8th International Conference on CFD in Oil & Gas, Metallurgical and Process Industries, Trondheim (2011), 1-10.
- [41] Queteschner, D., Lichtenegger, T., Schneiderbauer, S., and Pirker, S. "Coupling resolved and coarse-grain DEM models.", *Particulate Science and Technology* 36.4 (2018): 517-522.
- [42] Brown, G. O. "The history of the Darcy-Weisbach equation for pipe flow resistance." *environmental and water resources history* (2003): 34-43.
- [43] Colebrook, C. F., and White, C. M. "Experiments with fluid friction in roughened pipe.", *Proceedings of the Royal Society of London. Series a-mathematical and physical sciences* 161.906 (1937): 367-381.
- [44] Haaland, S. E. "Simple and explicit formulas for the friction factor in turbulent pipe flow.", *Journal of Fluids Engineering* 105.1 (1983): 89-90.
- [45] Kloss, Christoph, et al. "Models, algorithms and validation for opensource DEM and CFD-DEM.", *Progress in Computational Fluid Dynamics, an International Journal* 12.2-3 (2012): 140-152.
- [46] Jing, L., et al. "Extended CFD-DEM for free-surface flow with multi-size granules.", *International Journal for Numerical and Analytical Methods in Geomechanics* 40.1 (2016): 62-79.
- [47] Link, J. M., et al. "Flow regimes in a spout-fluid bed: A combined experimental and simulation study." *Chemical Engineering Science* 60.13 (2005): 3425-3442.
- [48] Post, J., Peeters, T., Yang, Y., and Reuter, M. "Hot metal flow in the blast furnace hearth: thermal and carbon dissolution effects on buoyancy, flow and refractory wear.", 3rd International Conference on CFD in the Minerals and Process Industries, Melbourne (2003): 433-440.
- [49] Bejan, A., and Kraus, A. D. "Heat transfer handbook (1st ed.).", John Wiley & Sons, Inc. (2003).
- [50] Vadasz, P. "Fluid flow and heat transfer in rotating porous media.", Springer International Publishing (2016).
- [51] Syamlal, M., and Gidaspow, D. "Hydrodynamics of fluidization: prediction of wall to bed heat transfer coefficients.", *AIChE Journal* 31.1 (1985): 127-135.
- [52] Zehner, P., and Schlünder, E. U. "Wärmeleitfähigkeit von Schüttungen bei mäßigen Temperaturen." *Chemie Ingenieur Technik* 42.14 (1970): 933-941.
- [53] Gunn, D. J. "Transfer of heat or mass to particles in fixed and fluidised beds.", *International Journal of Heat and Mass Transfer* 21.4 (1978): 467-476.
- [54] "Improvement of hearth drainage efficiency and refractory life for high BF productivity and a well adjusted reductant injection rate at varying coke quality.", RFSR-CT-2007-00001, project finished in 2010.
- [55] "Blast furnace sustained tapping practice", SUSTAINTAP, RFSR-CT-2012-00001, (2015).

- [56] Brännbacka, J., Saxen, H., & Pomeroy, D. (2007). "Detection and quantification of the dead man floating state in the blast furnace". *Metallurgical and Materials Transactions B*, 38, 443–450.
- [57] Nightingale, R. J., & Tanzil, F. W. B. U. (1997). "A novel approach in the estimation of blast furnace hearth voidage.", *Iron & Steelmaker*, (February), 35–37.
- [58] Kaymak, Y., Hauck, T., Lin, R., Rausch, H. (2015), "Analysis of thermal stresses in the blast furnace hearth considering the contact of refractory blocks.", *METEC 2015*.
- [59] Kaymak, Y. (2011), "A simplified approach to the contact in thermo-mechanical analysis of refractory linings", *Comsol Conference in Stuttgart*.
- [60] Silva, S. N., Vernilli, F., Justus, S. M., Marques, O. R., Mazine, A., Baldo, J. B., Varela, J. A. (2005). "Wear mechanism for blast furnace hearth refractory lining." *Ironmaking & Steelmaking*, 32(6), 459–467.
- [61] Nitta, M. (2006). "Investigation of used carbon blocks for blast furnace hearth and development of carbon blocks with high thermal conductivity and high corrosion resistance."
- [62] S. Rickelt, F. Sudbrock, S. Wirtz, V. Scherer, "Coupled DEM / CFD simulation of heat transfer in a generic grate system agitated by bars.", *Powder Technol.* 249 (2013) 360–372.
- [63] S. Ueda, T. Kon, H. Kurosawa, S. Natsui, T. Ariyama, H. Nogami, "Influence of shape of cohesive zone on gas flow and permeability in the blast furnace analyzed by DEM-CFD model." *ISIJ Int.* 55 (2015) 1232–1236.
- [64] P.W. Cleary, J.E. Hilton, M.D. Sinnott, "Modelling of industrial particle and multiphase flows.", *Powder Technol.* 314 (2017) 232–252.
- [65] F. Bambauer, S. Wirtz, V. Scherer, H. Bartusch, "Transient DEM-CFD simulation of solid and fluid flow in a three dimensional blast furnace model.", *Powder Technol.* 334 (2018) 53–64.
- [66] R. Di Felice, "The voidage function for fluid-particle interaction systems.", *Int. J. Multiph. Flow.* 20 (1994) 153–159.
- [67] Z. Zhou, H. Zhu, A. Yu, P. Zulli, "Numerical Investigation of the transient multiphase flow in an Ironmaking blast furnace.", *ISIJ Int.* 50 (2010) 515–523.
- [68] Adema, DEM-CFD Modelling of the ironmaking blast furnace, Delft University of Technology, 2014.
- [69] W.J. Yang, Z.Y. Zhou, A.B. Yu, Discrete particle simulation of solid flow in a three-dimensional blast furnace sector model, *Chem. Eng. J.* 278 (2015) 339–352.
- [70] W. Yang, Z. Zhou, D. Pinson, A. Yu, "Periodic boundary conditions for discrete element method simulation of particle flow in cylindrical vessels.", *Ind. Eng. Chem. Res.* 53 (2014).
- [71] H. Rausch, S. Böhnisch, D. Sert, "Extended blast furnace permeability monitoring.", 2004.
- [72] D. Sert, G. Danloy, O. Havelange, J. Saiz de Ayala, "New approach for the determination of the blast furnace cohesive zone.", Final Report, Off. Off. Publ. Eur. Communities. (2004) Contract No. 7210-PR/122.
- [73] Roheisengesellschaft Saar mbH (ROGESA);
<http://www.rogesa.de/rogesa/home/index.shtml.de>, (2019).
- [74] G. Dombrowski, R. Jeschar, W. Pötke, "Ermitteln des örtlichen Lückengrades in der Schüttung des mit Stickstoff abgekühlten Hochofens der Mannesmann-Röhrenwerke AG", 1998.
- [75] M. Snir, S. Otto, S. Huss-Lederman, D.W. Walker, J. Dongarra, MPI : The Complete Reference, (1996) 332.
- [76] Z.Y. Zhou, H.P. Zhu, B. Wright, A.B. Yu, P. Zulli, "Gas-solid flow in an ironmaking blast furnace-II, discrete particle simulation.", *Powder Technol.* 208 (2011) 72–85.
- [77] T. Ariyama, S. Natsui, T. Kon, S. Ueda, S. Kikuchi, H. Nogami, "Recent progress on advanced blast furnace mathematical Models B".
- [78] J. Brännbacka and H. Saxén, "Model for fast computation of blast furnace hearth erosion and build-up profiles.", *Industrial & Engineering Chemistry Research* 47 (2008) 7793-7801.
- [79] M. Roche, M. Helle and H. Saxén, "Estimation of the hot face temperatures of the blast furnace hearth by an inverse method.", ECOS 2017 - the 30th International Conference on Efficiency, Cost, Optimization, Simulation and Environmental Impact of Energy Systems, July 2017, San Diego, USA.
- [80] V. Panjkovic, J. S. Truelove and P. Zulli, "Numerical modelling of iron flow and heat transfer in blast furnace hearth.", *Ironmaking & Steelmaking* 29 (2003).
- [81] K. Takatani, T. Inada and K. Takata, "Mathematical model for transient erosion process of blast furnace hearth", *ISIJ International* 41 (2001) 1139–1145.
- [82] J. Torrkulla and H. Saxén, "Model of the state of the blast furnace hearth.", *ISIJ International* 40 (2000) 438-447.
- [83] M. Zagaria, V. Dimastromatteo and V. Colla, "Monitoring erosion and skull profile in blast furnace hearth.", *Ironmaking & Steelmaking* 37 (2010), 229-234.
- [84] Y. Zhang, R. Deshpande, D. Huang, P. Chaubal and C. Q. Zhou, "Numerical analysis of blast furnace hearth inner profile by using CFD and heat transfer model for different time periods.", *International Journal of Heat and Mass Transfer* 51 (2008).

- [85] <http://www.openfoam.org/features/standard-solvers>.
- [86] <https://cfd.direct/openfoam/about>.
- [87] Pinczewski, W.V, Tanzil, W.B.U. (1980). "Mathematical and physical simulation of non-uniform liquid drainage in packed beds.", Australia: Department of Chemical Engineering and Industrial Chemistry, University of New South Wales, Sydney (4)
- [88] J. Brännbacka and H. Saxén, "Novel model for estimation of liquid levels in the blast furnace hearth," *Chem. Eng. Sci.*, vol. 59, no. 16, pp. 3423–3432, Aug. 2004.
- [89] L. Shao and H. Saxén, "Model of blast furnace hearth drainage.", *Steel Res. Int.*, vol. 83, no. 2, pp. 197–204, Feb. 2012.
- [90] A. Ullmann, M. Zamir, Z. Ludmer, and N. Brauner, "Stratified laminar countercurrent flow of two liquid phases in inclined tubes.", *Int. J. Multiph. Flow*, vol. 29, no. 10, pp. 1583–1604, Oct. 2003.
- [91] L. Shao and H. Saxén, "A simulation study of blast furnace hearth drainage using a two-phase flow model of the taphole.", *ISIJ Int.*, vol. 51, no. 2, pp. 228–235, 2011.
- [92] Nouchi, Taihei, Michitaka Sato, Kanji Takeda, et Tatsuro Ariyama. "Effects of operation condition and casting strategy on drainage efficiency of the blast furnace hearth.", *ISIJ International* 45, n° 10 (2005): 1515-1520.
- [93] Brännbacka, J., Torrkulla, J. & Saxén, H. (2005), "Simple simulation model of the blast furnace hearth.", *Ironmaking and Steelmaking*, 32, 479-486.
- [94] Tsuchiya, N., Fukutake, T., Yamaguchi, Y. & Matsumoto, T. (1998). "In-furnace conditions as prerequisites for proper use and design of mud to control blast furnace taphole length". *ISIJ International*, 38(2), 116-125.
- [95] Saxén, H. (2015). "Drainage model of a blast furnace hearth with a low-permeability zone.". *Metallurgical and Materials Transactions B*, 46B, 421-431.
- [96] Iida M., Ogura, K. & Hakone, T. (2009). "Numerical study on metal/slag drainage rate deviation during blast furnace tapping", *ISIJ International*, 49, (2009) 1123-1132.
- [97] Fukutake, T. & Okabe, K. (1976). "Experimental studies of slag flow in the blast furnace hearth during tapping operation", *Trans. ISIJ*, 16, 309–316.
- [98] Fukutake, T. & Okabe, K. (1976). "Influences of slag tapping conditions on the amount of residual slag in blast furnace hearth.", *Trans. ISIJ*, 16, 317–323.
- [99] Zulli, P. (1991). "Blast furnace hearth drainage with and without coke-free Layer", Ph.D Thesis, University of New South Wales, Sydney, Australia.
- [100] Roche, M., Helle, M., van der Stel, J., Louwerse, G., Shao, L. & Saxén, H. (2018). "Off-line model of blast furnace liquid levels.", *ISIJ International*, 58, 2236-2245.
- [101] Roche, M., Helle, M., van der Stel, J., Louwerse, G., Shao L. & Saxén, H. (2019). "On-line estimation of liquid levels in the blast furnace hearth.", to appear in *Steel research international*, 90.
- [102] "Determination of factors influencing dead man position and evaluation of its impact on blast furnace life time", RFSR-CT-2005-00002, project finished in 2008.
- [103] Young, W. C., Roark, R. J. & Budynas, R. G. (2002). "Roark's formulas for stress and strain", 7th ed., McGraw-Hill, New York.
- [104] Danloy, G., Desneux, P., Fischbach, J.P., Noville, J.F., Steyls, D., Lectard, E., "New characterization tests of the coke behavior at high temperature.", Tech.rep CRM, AMMR, Corus and TKS.
- [105] G. Danloy, P. Desneux, J. P. Fischbach, J. F. Noville, D. Steyls, E. Lectard, H. Pierret, J. Delinchant, B. van der Velden, J. Stuurwold, U. Janhsen and A. Y. G.Unbati, "New Characterisation Tests of the Coke Behaviour at High Temperature.,," 2007.

5 Table of Figures

Figure 1: Design of AMEH BF5A before the relining 2016.....	13
Figure 2: Design of AGDH BF4 before the relining 2016.....	13
Figure 3: Total displacement at steel shell of AMEH BF5A.....	15
Figure 4: Vertical stress at steel shell of AMEH BF5A.....	15
Figure 5: Vertical stress through a cut line ($z=7$ m under tuyere 7) for AMEH BF5A.	16
Figure 6: Hoop stress through a cut line ($z=7$ m under tuyere 7) for AMEH BF5A.	16
Figure 7: Gap formation between the carbon blocks at AMEH BF5A hearth wall.	17
Figure 8: AMEH BF5A hearth cooling shut-down during a stoppage – model vs thermography measurements. Note that drying of the hearth shell is empirically modelled by time-varying heat transfer coefficient.	17
Figure 9: Computed stress at hearth shell and gaps at cold side of carbon blocks at AMEH BF5A hearth when the cooling shut-down during a stoppage.	18
Figure 10: Liquid level, temperature and total strain comparison at steel shell of AMEH BF5A.	18
Figure 11: Liquid level, temperature and strain-difference comparison at steel shell of AMEH BF5A.	19
Figure 12: Thermocouple placements at Dillinger BF4 hearth at a typical vertical section and hearth bottom. The computed and measured temperatures differ systematically at the bottom corner (Table 3).	19
Figure 13: AGDH BF4 stoppage simulation – thermocouple reading (deepest of MTC at section 6) vs transient model computation. Note that the model uses a time varying uniform hot metal temperature on hot face of the hearth wall.	21
Figure 14: AGDH BF4 stoppage simulation – wall thermocouple readings at section 2 vs transient model computation.	21
Figure 15: AGDH BF4 stoppage simulation –bottom center thermocouple reading vs transient model computation (DT: temperature drop during the stoppage).	21
Figure 16: Stages of Model development.	23
Figure 17: Simulation setup with the main boundary conditions and the static temperature profile of the gas phase.	25
Figure 18: DMD Value for the considered time interval chosen for the calibration scenario (upper figure: overview, lower figure: 24h detail).	27
Figure 19: Results of the calibration case to three different times in (1) the beginning, (2) the middle, (3) the end of the intercast period.	29
Figure 20: Results of the $DMD < 0$ case at three different times in (1) the beginning, (2) the middle, (3) the end of the intercast period.	30
Figure 21: Results of the $DMD > 0$ case at three different times in (1) the beginning, (2) the middle, (3) the end of the intercast period.	30
Figure 22: Detail of the hearth in the end of the intercast period for $DMD > 0$	31
Figure 23: Particle arrangement in dependency of the hot blast volume.	31
Figure 24: Snapshot of the particle normal pressure for the DM (left), averaged particle pressure at tuyere (upper right) and Normal wall pressure for different hot blast volumes.	32
Figure 25: Parallelisation by domain decomposition.	34
Figure 26: Treatment of particles at periodic boundaries [8]	34
Figure 27: Periodic Boundary Conditions for 90° model.	35
Figure 28: Comparison between 10 times accelerated systems with the original simulation.	36
Figure 29: comparison between averaged particle velocities at shaft and hearth position for the initial and the scaled system.	36
Figure 30: Schematic overview of Particle Image Velocimetry (PIV) set-up.	37
Figure 31: CFD set-up of the water model with the different domains.	38
Figure 32:Total vector velocity field (left), enlarged image (right) indicating the size of the interrogation areas compared to the flow structure.....	39
Figure 33: Velocities in the mid plane for no particles and 9mm particles (1= air, 2= warm water and 3= cold water).....	39
Figure 34: Pictures illustrating three stages of the PIV image processing. The left picture shows the original images, the middle picture shows the average of all 100 recorded images of a single measurement and the right image shows the result after subtracting the average image from the original image.....	40
Figure 35: Average velocity as function of distance from wall for different ball sizes.	40
Figure 36: Calculated average velocities as function of distance from wall with different ball sizes.	41
Figure 37: Tapping sequences for the EBF process (Excel model), the SUSTAINTAP multiphase CFD model, water model (WM) in atmospheric pressure with constant taphole diameter (68 mm) and variating taphole diameter over time to obtain equal flow rate for the water model as the EBF process.	44
Figure 38: Measured contact angles of the metal beads on coke substrates at 1427°C : (a) coke and the metal beads collected from the center of the EBF hearth: 2 nd core-drilling layer, 10-20 cm	

sub-sample; (b) coke and the metal beads collected from the center of the EBF hearth: 2 nd core-drilling layer, 30-40 cm sub-sample.....	45
Figure 39: Measured contact angles of the water beads on asphalt substrates at room temperature: (a) the first test; (b) the second test.	45
Figure 40: EBF water model (left), inflow to dripping box (upper right) and inflow to the model hearth (lower right) from the dripping box. The white box is the pump speed control unit and the grey pipe is the rotameter (left image), the pipes guide the tracer to each injection point (lower right).	46
Figure 41: Drilling pattern (small crosses) and tracer injection positions (large crosses) for the dripping plate, seen from above. Taphole location is marked in the lower part of the drawing.	
Tracer injection positions serves as well as the vertical conductivity sensor positions on the bottom plate of the hearth.	47
Figure 42: Coke coating methodology (left) and drying procedure (right).	48
Figure 43: EBF water model hearth before coke bed installation (left) and during fill up (right). The embedding of the sensors in the coke bed is illustrated (right).	48
Figure 44: EBF water model hearth including embedded conductivity sensors placed on the square rods, coke bed and acid-proof baskets for zone separation. The obtained porosity is presented and compared to the requested values for each zone (values in brackets).	49
Figure 45: Finalized EBF water model (left) and injection of tracer at the start of one trial (right). 49	
Figure 46: Electrical conductivity at the taphole (K22) for each injection point for mean EBF tapping rate (upper) and fast EBF tapping rate (lower) for uniform inflow.	51
Figure 47: Residence time (either defined by conductivity peak or the start of conductivity increase) for each injection point (#1-#9, #15) for mean and fast EBF tapping rate (uniform inflow). Dashed lines indicate extrapolated values.	52
Figure 48: Electrical conductivity over time for mean tapping rate, injection point #9 (left). Sensor response at a certain time (black dashed line) is illustrated by blue circles (top view and side view), together with an estimated path-line (red dashed line).	53
Figure 49: Interpreted flow field for mean EBF tapping rate (uniform inflow). Red dashed lines indicate path-lines located in the centre of the hearth.	53
Figure 50: Interpreted path-lines from copper injection trials (solid lines) and related interpreted path-lines from water model trials (dashed lines).	54
Figure 51: Residence time (either defined by conductivity peak or the start of conductivity increase) for each injection point (#1-#9, #15) for mean EBF tapping rate with uniform and non-uniform inflow. Dashed lines indicate extrapolated values.	54
Figure 52: Electrical conductivity over time for EBF mean tapping rate, injection point #9, solid line – uniform inflow, dashed line – non-uniform inflow.	55
Figure 53: Electrical conductivity over time for EBF mean tapping rate, injection point #8, solid line – uniform inflow, dashed line – non-uniform inflow.	55
Figure 54: CAD model of the EBF hearth including taphole, taphole mushroom, lining materials and shell.	57
Figure 55: The EBF hearth mesh.	57
Figure 56: CFD region in BF hearth (a) and ignored region in the CFD EBF model (b).	58
Figure 57: Particles injected from point #5 leaving the domain after 75 sec (a) and from #6 leaving the domain after 90 sec (b).	59
Figure 58: Particles exit time.	59
Figure 59: Tracer timing and path-line.	60
Figure 60: Marked positions on bottom (lower right) and wall (upper right) indicates locations for shell temperature measurements.	61
Figure 61: EBF outer shell measurement vs. CFD calculation.	61
Figure 62: Outer shell temperature profile.	62
Figure 63: Symmetry plane temperature.	62
Figure 64: Phase distribution.	63
Figure 65: Fluid zone initial temperature.	63
Figure 66: Hot metal interface height: Maximum, average and minimum (red, black, green).	63
Figure 67: Volume of material in the taphole: hot metal, slag, gas (red, black, green).	63
Figure 68: Phase distribution in the symmetric plane.	64
Figure 69: Hot metal and slag interface.	64
Figure 70: Hot metal temperature profile.	64
Figure 71: Hot metal interface height: Maximum, average and minimum (red, black, green).	65
Figure 72: Volume of material in the taphole: hot metal, slag, gas (red, black, green).	65
Figure 73: Phase distribution in the symmetric plane.	65
Figure 74: Hot metal and slag interface.	65
Figure 75: Hot metal temperature profile.	66
Figure 76: Hot metal interface height: Maximum, average and minimum (red, black, green).	66
Figure 77: Volume of material in the taphole: hot metal, slag, gas (red, black, green).	66
Figure 78: Phase distribution in the symmetric plane.	67
Figure 79: Hot metal and slag interface.	67

Figure 80: Hot metal temperature profile.	67
Figure 81: Left: Updating principle of the hot face location in the asymptotic wear model. Right: Flowchart of the iterative calculations.	69
Figure 82: Dimensions of the hearth and pertinent material properties.	70
Figure 83: Boundary (referred to by ①–④) conditions applied in the model.	70
Figure 84: Left: Calculated final hearth profile and temperature distribution for case 1. Right: Comparison of the final hearth profiles for cases 1-3 (Table 11).	71
Figure 85: Top: Evolution of thermocouples in the hearth sidewall close to the taphole level. Bottom: Evolution of thermocouples in the hearth sidewall clearly below the taphole level.....	72
Figure 86: Model definitions: a) direct problem, b) inverse problem.....	73
Figure 87: Hot-face temperature (top curve) reconstructed by linear interpolation of $M = 6$ discrete temperatures (dots connected by dotted lines), thermocouple temperatures (solid lines) and temperature at TC1 simulated by the model (dashed line).....	74
Figure 88: Schematic of the reconstruction of the hot-face temperature history based on a sequence of solutions of the inverse problem for a time window.....	75
Figure 89: Left: Vertical and horizontal cross-sections of the hearth lining showing the location of the points equipped with thermocouples. Right: Snapshot of surface relief of reconstructed temperatures along the hot face.	76
Figure 90: Snapshots of hot-face temperature evolution at different times of the 8-day period studied. The locations of the three tapholes (TH1-3) along the periphery have been indicated above the uppermost panels.	77
Figure 91: Top panel: Signals for the thermocouple pair on level L1, located 1.7 m below taphole TH3. Middle and bottom panels: more detailed view of the hot-face temperature (blue lines) and TC1 (black lines) for the framed regions in the top panel. Vertical lines indicate opening (green) and closing (red) of TH3.....	78
Figure 92: Inner (red) and outer (blue) thermocouple temperatures for a vertical position close to the taphole and a peripheral position slightly east of the north taphole (see small insert). Top: long-term behavior, with bars illustrating the quantities of hot metal tapped from the north taphole. Bottom: short-term behavior, with grey regions illustrating the time when the north taphole was open.	79
Figure 93: Inner (red) and outer (blue) thermocouple temperatures for a vertical position between the taphole and hearth bottom level and a peripheral position slightly south of the west taphole (see insert), with grey regions illustrating the time the west taphole was open.	80
Figure 94: Possible explanation for opposite response shown by thermocouple pairs after a nearby taphole is closed. At lower forces from the hearth liquids, the thermal contact between the blocks is poor and the thermocouples show a larger temperature difference (red lines and dots in right subpanel). As the hearth liquid levels increase, the force acting on the lining increases, causing an improved thermal contact between the blocks and a smaller temperature difference (blue lines and dots).	81
Figure 95: Top: Composite wall setup for testing the hypothesis about a gap between the carbon blocks. Bottom: Gap implemented as a thin layer, the thermal conductivity of which is ramp-wise changed from a low value (k_{gap}) to a high value ($k_{layer,1}$) and back.	82
Figure 96: Simulated thermocouple temperatures in the system depicted in the top panel of Figure 95 after repeating the periodic changes in the "gap" conductivity depicted in its lower panel.	82
Figure 97: Schematic illustration of the experimental setup, figure from [1].	84
Figure 98: Normalized pressure at probe location 1 (left) and 2 (right) with various smoothing models, figure from [1].	84
Figure 99:: Total mass tapped over time for the experiments and corresponding simulations, figure from [1]....	85
Figure 100: Particle bed structure during drainage for experiment (left) and simulation (right) at $t = 7$ s, figure from [1].	85
Figure 101:: Burden weight boundary condition, figure from [1].	86
Figure 102: Scatter plot of the particle pressures at the cut-off location, compared with data supplied by RUB.	86
Figure 103: The resulting dead man equilibrium position of the hearth simulation only.	87
Figure 104: Snapshots of the blast furnace hearth at three different times. The columns represent from left to right $t = 0$ s, $t = 5$ s and $t = 20$ s. The first row shows the dead man and stress-controlled walls while the two lower ones represent the velocity fields at a normal and horizontal plane respectively. The white lines indicate the slag (upper) and iron(lower) interfaces, figure from [1].	87
Figure 105: Comparison of the time evolution of the tapped mass for a dynamic dead man and a fixed floating one, figure from [1].....	88
Figure 106: Illustration of the CFD-DEM model and dynamic void fraction model's interaction, figure from [2].....	Error! Bookmark not defined.
Figure 107: Drained mass over time for the CFD-DEM model and dynamic void fraction model compared with the experiments, where the simulations are visualized by lines and the experiments by symbols, figure from [2].	89

Figure 108: Hot metal velocities for a fixed sitting and floating dead man (upper left and right respectively), as well as with the dynamic void fraction model early and late (lower left and right respectively) during the simulation, figure from [2]. ..	91
Figure 109: Comparison of volumetric flow rates for a dynamic and a fixed floating dead man, figure from [2].....	91
Figure 110: Flow fields on a horizontal plane at taphole level for a uniform and a dense core dead man (left and right respectively). The less permeable center give rise to a peripheral flow pattern, figure from [2].....	92
Figure 111: Simulated mass flow rate compared with measured ones from voestalpine's HO5. The two figures represent two different tapping periods. In the right figure, we find an overall good agreement while in the left one, the slag delay is poorly captured. However remarkably, we managed to seemingly accurately predict the two drainage rate plateaus of pure iron and iron-slag mixed flows.	93
Figure 112: Fluid temperature distribution at a cross-section normal to the outlet (located on the left side) early during the simulation (left) and towards the end (right). The white lines indicate the air-slag (upper) and iron-slag (lower) interfaces. It is seen, that the iron close to the lower wall cooled down rapidly at the coke free zone, which propagated well in the iron with a high thermal conductivity.	94
Figure 113: Velocity fields at a cross-section normal to the outlet (located on the left side) early during the simulation (left) and towards the end (right). It is seen, that initially the flow field looks very similar to the non-isothermal one (Figure 108), whereas towards the end of the tap, due to the vertical temperature variation, the flow field changed significantly.	95
Figure 114: 2D mesh of validation case (a), 3D mesh of the industrial cases (b), and mesh details (c).....	98
Figure 115: Structure of MOHDRAIN 2.0.	98
Figure 116: List of the code handling dilation/contraction of phases in MOHDRAIN 2.0.	99
Figure 117: Validation of solver.....	100
Figure 118: Distribution of coke and tuyere reduction agents (12/2012 until 12/2016).	101
Figure 119: (a) Drainage rate vs tapping duration colored by taphole, (b) tapped slag mass vs. iron mass.	102
Figure 120: (a) Example of a coke size distribution and its cumulative curve, (b) fitted coke size distributions based on Weibull function.	103
Figure 121: Daily values for D_{10} , D_{50} and D_{90} values of the fitted coke size distributions.	103
Figure 122: (a) Correlation of $d90$ and $d10$, (b) Correlation of $I10$ and CSR.	103
Figure 123: Iron mass flow rate (t/h) over the tapping history (tapping nr.). The blue curve is the original data, the yellow curve is the training data for the neural network, and the red curve is the test data.	104
Figure 124: Melting rate and specific slag during the BF-5 campaign from 2010-2015.....	106
Figure 125: (a) Hot blast velocity and (b) tuyere area during the BF-5 campaign. To minimize the raceway effects on the eroded hearth geometry, the penetration depth was increased.	106
Figure 126: (a) Correlation of the standard deviation of Si %m with the standard deviation of hot metal temperature, (b) standard deviation of carbon content.....	107
Figure 127: Hot metal temperature over the entire campaign.	107
Figure 128: Mass percent of Si (blue) and standard deviation of Si content (orange). No change of the standard deviation if noticeable during the campaign.	108
Figure 129: (a) intermediate time before tapping, (b) slag delay.....	108
Figure 130: (a) taphole diameter, (b) tap duration.	109
Figure 131: Taphole length (orange) and amount of clay (blue).	109
Figure 132: Hot metal analysis for the three selected periods. (a) Average values, (b) standard deviation.....	111
Figure 133: (a) Tapping parameters (values in minutes) and (b) tap hole parameters (values in cm and liters).	112
Figure 134: Interlink of operator decisions and process parameters.....	112
Figure 135: Outline of 1D tapping model via simple state machine.	113
Figure 136: Layer model with interface deformation [88].	113
Figure 137: (a) Radial pressure distribution according to eq. (51) for $a = pdc$. (b) Relative radial buoyancy of dead man for $pdc = 150\text{kPa}$ according to eq. (52).	114
Figure 138: Buoyancy of dead man in BF center for different iron and pressure levels.	114
Figure 139: Results of a testcase for the drainage model; calculated liquid levels for a period of 135 hours.	115
Figure 140: Results of a testcase for the drainage model; calculated drainage rates and the production level of BF-A for a period of 135 hours.	115
Figure 141: Calculation flow of MOHDRAIN 2.0.	116
Figure 142: Results of simulations: influence of taphole erosion rate.	118
Figure 143: Results of simulations: Influence of taphole erosion rate and gas pressure.	118
Figure 144: Results of simulations; influence of slag viscosity and dead man porosity.	119

Figure 145: Schema of the “water model” including the process tank (on the left), two preparation tanks (on top) and a decantation bund (on the bottom)	120
Figure 146: Evolution of oil (blue) and slurry (red) viscosities and viscosity ratio (green) with temperature.	120
Figure 147: Observations of the water level and water jet at the taphole during tapping of the water model.	121
Figure 148: Evolution of the tapped volume of water and the waterjet length during preliminary tapping trial on the water model.	122
Figure 149: Evolution of the jet length as a function of the distance of the water level from the taphole.	122
Figure 150: Analytical estimations of water velocity at taphole using a kinematic analysis and Bernoulli’s equations, and the estimation of the pressure drop inside the taphole.	123
Figure 151: Hearth Echo Excellence, general working principle.....	125
Figure 152: Blast furnace wall in detail.....	126
Figure 153: Sensor set up for measurement 1 and 2.	127
Figure 154: Set up of 7 sensors at tuyere 9, hearth level +3150 TSE BF6.	127
Figure 155: Refractory wear TSE BF6, hearth level +3150, calculation based on temperature measurements.....	128
Figure 156: Frequency spectra for type 1 (above) and type 2 (below) measurements at TSE BF6, tuyere 9.	130
Figure 157: Optical Fibre build-up.	131
Figure 158: Fibre Bragg Grating (FBG) principle.	131
Figure 159: Temperature measurement with FBGs.	132
Figure 160: FBG temperature profile +3800 level BF6.....	132
Figure 161: Comparison temperatures of FBG versus standard thermocouples BF6.....	133
Figure 162: Stepped drillings at AMEH BF5A.	134
Figure 163: Thermography camera measurements at AMEH BF5A (below tuyere #7 and #19)...134	134
Figure 164: Evolution of hearth shell temperature at AMEH BF5A (below tuyere #7 and #19)...135	135
Figure 165: Wall thickness measurement under tuyere 19 during AMEH BF5A relining.	135
Figure 166: Results of the wall thickness measurement during relining: a) the residual wall thickness contours, b) wear at the upper bottom layer.....	136
Figure 167: Wall thickness measurement at section 8 during AGDH BF4 relining.	136
Figure 168: Results of the wall thickness measurement during relining for sections 2, 4, 6 and 10.	137
Figure 169: Results of the wall thickness measurements compared with the wear model estimations for the AGDH BF4 (black numbers are measured wall thickness in mm, deviation from model estimation is red numbers in mm). Purple rectangles: sampled carbon blocks. Red dots: TC positions.	138
Figure 170: Brittle layer related results of the chemical analysis of the samples from AMEH BF5A.	139
Figure 171: Photo showing some of the AMEH samples for the chemical analysis.	140
Figure 172: Brittle layer related results of the chemical analysis of the samples from AGDH BF4.141	141
Figure 173: Photo showing some of the AMEH samples for the chemical analysis.	142
Figure 174: Brittle layers in carbon blocks at AMEH BF5A and the crack in AGDH BF4.	142
Figure 175: Photo showing some of the AGDH samples for the heat conductivity analysis.	143
Figure 176: Thermal conductivity, chemical composition and some physical properties of the worn carbon block samples from AMEH BF5A.	143
Figure 177: Summary of the cold crush tests of the refractory samples from AGDH BF4.....	144
Figure 178: Summary of the cold crush tests of the refractory samples from AMEH BF5A.	144
Figure 179: Thermal softening test for AMEH BF5A material 7RD-N.	145
Figure 180: Creep test for AGDH BF4 material BC 8SR.	145
Figure 181: Kenneth modelling response for typical BF geometry.	146
Figure 182: Iterative inversion process based on frequency spectra.....	146
Figure 183: BF setup for modelling analysis using two geometry 1 (left) and geometry 2 (right).147	147
Figure 184: Frequency spectra based on geometry 1 (left) and geometry 2 (right).....	147
Figure 185: The isotherms in the refractory will be affected by a crack with the same temperature as the hot metal in the blast furnace hearth.	148
Figure 186: The FEM computer model domain and boundary conditions. The simulated crack is shown orange in the lower left corner.	148
Figure 187: The temperature distribution in the refractory with no crack (left) and 200 mm crack (right).....	149
Figure 188: Temperature difference between simulation of 100 mm crack and no crack (left) resp. 200 mm crack and no crack (right).....	150
Figure 189: Positions of the selected coke/slag and coke/metal samples from the LKAB EBF hearth, campaign 31 (in the bottom of the hearth beneath Tuyere 3, there was no coke piece, therefore the sub-sample above was used instead).	151
Figure 190: Procurement of the solid samples by core drilling into the bed of the EBF's hearth...151	151

Figure 191: Illustration of the sampling positions (with respect to the 3 tuyeres and taphole) of the core-drilling samples as well as their reference numbers.	152
Figure 192: Illustration of the sampling positions (with respect to the depth in the hearth) of the core-drilling samples as well as the manual samples (MS 1-8).	152
Figure 193: Procedure of the sub-samples from the core drilling tube.	153
Figure 194: Appearance of the materials in the core drilling tubes.	154
Figure 195: Particle size distribution of (a) first layer drilling cores and (b) second layer drilling cores into the hearth of the EBF as well as the bulk densities of the materials in each drilling cores.	155
Figure 196: Particle size distribution of the second layer drilling cores procured from (a) the centre of the EBF hearth and (b) from the circumference of the EBF hearth.	156
Figure 197: Distribution of the coarse fractions (> 5 mm) of coke, the magnetic, slag and aggregate in each sub-sample beneath the three tuyeres ((a) first layer drilling cores; (b) second layer drilling cores).	157
Figure 198: Sampling positions of the coke/slag from the core drilling tubes in the EBF hearth for the heating microscope study (Figure 192 can be referred to for the sampling depth into the EBF hearth).	158
Figure 199: Overview of the core boring machines used at ArcelorMittal Fos-sur-Mer.	158
Figure 200: Results of the core borings at ArcelorMittal Fos-sur-Mer; lengths of zones.	160
Figure 201: Results of the core borings at ArcelorMittal Fos-sur-Mer: particle size distribution. ..	161
Figure 202: Copper injection device (left) and device mounted onto the coal injection pipe (right).	162
Figure 203: Cu concentration in tapped hot metal.	163
Figure 204: Cu contents (given in ppm) in the metallic samples procured from the EBF hearth.	165
Figure 205: Positions of manual samples selected for SEM analysis.	165
Figure 206: Optical microscope image of sample MS5.	165
Figure 207: Magnified optical microscope image of sample MS6.	166
Figure 208: SEM image of sample MS5, Site 2.	166
Figure 209: SEM image of sample MS6, Site 2.	166
Figure 210: SEM image of sample MS7, Site 3.	167
Figure 211: Copper content in each sub-sample illustrated by differentiated spheres (left). Images from the EBF hearth excavation (right) for the first layer (upper right) and the second layer (lower right). The location of the taphole is marked by the red arrow.	168
Figure 212: Interpreted 2d-path-lines (top view – left, side view – right) based on the copper content in each sub-sample.	168
Figure 213 Estimated 3d-path-lines based on the copper content in each sub-sample (left) and the interpreted flow field (right).	169
Figure 214: Variations of the slag chemical composition with the charged ferrous MPBO pellets.	170
Figure 215: Variations of the hot metal chemical composition with the charged ferrous MPBO pellets.	170
Figure 216: DM voidage calculated by force- and mass-balance sub-models.	172
Figure 217: Correlation between force- and mass-balance sub-model results.	172
Figure 218: Results of the on-line implementation of DMD at AMEH (left) and Dillinger (right). ..	173
Figure 219: GUI of the MATLAB based model (left) and browser GUI (right).	173
Figure 220: Long time similarities between DMD and weekly averaged hot blast data.	174
Figure 221: General view (a) and inside (b), without the SiC drum, of the electric furnace and of the mini-Micum drum (c).	175
Figure 222: First Cokarac trial (standard).	176
Figure 223: Influence of the gasification degree on the size change in the CRM Cokarac test [104].	176
Figure 224: Influence of temperature and gasification degree on the change in size during the CRM Cokarac test [104].	177
Figure 225: Design of the apparatus used for the dissolution trials.	177
Figure 226: Coke samples used for the second dissolution trial.	178
Figure 227: Observation of the coke sample dived into both liquids during the second dissolution trial.	178
Figure 228: XRD diffraction spectra of slag samples procured from various positions of the EBF hearth, campaign 31.	180
Figure 229: Alkali contents in the slag samples procured from the hearth of the EBF, campaign 32: (a) side view; (b) top view.	182
Figure 230: Fe and TiO ₂ contents in the slag samples procured from second core drilling layer of the EBF hearth, campaign 32.	182
Figure 231: XRD analysis of the selected slag samples procured from first core drilling layer of the EBF hearth, campaign 32.	183
Figure 232: XRD analysis of the selected slag samples procured from second core drilling layer of the EBF hearth, campaign 32.	183
Figure 233: Rheometer used at CRM for viscosity measurements on BF slags.	187

Figure 234: Foams (left) and garlands (right) produced during the early tests of the viscometer using molybdenum crucibles.....	187
Figure 235: Evolution of viscosity and temperature during 2 nd and 3 rd viscosity trials.....	188
Figure 236: Cross section of the voestalpine slag sample after cooling.....	188
Figure 237: Evolution of viscosity as a function of shear rate at 1600 (top), 1550 (mid) and 1500 (bottom) °C.....	189
Figure 238: Evolution of viscosity (green) and temperature (red) of the voestalpine BF slag sample under a 20s ⁻¹ shear rate.....	190
Figure 239: Evolution of viscosity of industrial slags with temperature.....	190
Figure 240: Evolution of viscosity of industrial slags with temperature in the melted zone.....	191
Figure 241: Measured viscosities of the selected slag samples plotted together with the FactSage calculated viscosities in the temperature range 1250-1600 °C, ((a) Slag #2; (b) Slag #5; (c) Slag #9; (d) Slag #12; (e) Tata6 slag; (f) Tata7 slag and (g) voestalpine slag).....	192
Figure 242 Correlations of the measured viscosities with the calculated viscosities by FactSage and empirical equation at 1500 °C.....	193
Figure 243: Comparison of experimental viscosities with literature models (Riboud and Urbain) on four SWERIM samples.....	193
Figure 244: Comparison of viscosity between industrial and slag sample (SWERIM 12) with impact of TiO ₂	194
Figure 245: Comparison of viscosity between industrial and slag sample (SWERIM 5).....	194
Figure 246: Heating microscope furnace setup [56].....	195
Figure 247: Principle of the sessile drop test.....	195
Figure 248: Definition of the contact angle α	196
Figure 249: Visual observations of the slag briquettes under heating microscope.....	197
Figure 250: Comparison of the temperatures from the FactSage calculations (50% melt) and from the heating microscope observations (sphere temperature).....	198
Figure 251: Heating microscope images of the final tapped EBF slag (campaign 31) on the original EBF coke substrate at two different temperatures (1500 and 1528 °C).....	199
Figure 252: Heating microscope images of the final tapped EBF slag (campaign 32) and industrial BF slag on the original EBF coke substrate at two different temperatures (1500 and 1528 °C)....	199
Figure 253: Correlation of the contact angle to the main components (basicity, Al ₂ O ₃ , FeO and MgO) in the slag.....	200
Figure 254: Heating microscope images of the EBF hearth slag (campaign 31) on their coupled hearth coke substrates at around 1400 °C).....	200
Figure 255: Heating microscope images of the EBF hearth slag (campaign 32) on their coupled hearth coke substrates at two different temperatures (1500 and 1528 °C).	201
Figure 256: The predicted wetting angles (from Model 3 and Model 4 described in Appendix B) and the measured wetting angles for various slag samples on coke.	202
Figure 257: The predicted wetting angles (from Model 3(red) and Model 4(blue) described in Appendix B) and the measured wetting angles for various slag samples on coke.	203
Figure 258: XRD diffraction spectra of the coke beneath tuyere 3 of the EBF, campaign 31.	204
Figure 259: XRD diffraction spectra of the coke in the centre of EBF hearth, campaign 31.....	204
Figure 260: XRD diffraction spectra of the coke close to the taphole.	205
Figure 261: Alkali contents in the coke samples procured from the hearth of the EBF, campaign 32: (a) side view; (b) top view.	206
Figure 262: XRD analysis of the EBF original coke.	207
Figure 263: XRD analysis of the selected coke samples procured from first core drilling layer of the EBF hearth, campaign 32.	207
Figure 264: XRD analysis of the selected coke samples procured from second core drilling layer of the EBF hearth, campaign 32.....	208
Figure 265: Cross sectional view of the core drilling sample M101 (first layer, center). The top of the sample is indicated by 0 and the lowest part by 50 (cm). The material between the red dashed lines illustrates the sub-sample 2 (10-20 cm).	208
Figure 266: Coke bed porosity distribution for the first layer (left) and the second layer (right)..	210
Figure 267: Selected process parameters 36 hours before the end of the EBF campaign 31 (K31) and campaign 32 (K32): (a) PCI rate; (b) hot blast pressure; (c) pressure at the top of EBF and (d) cooling effect at the tuyeres.	211
Figure 268: Variations of the selected elements/components in the slag 36 hours before the end of the EBF campaign 31 (K31) and campaign 32 (K32): (a) alkali in the slag; (b) MgO in the slag; (c) TiO ₂ in the slag and (d) temperature of the tapped slag/hot metal.	211
Figure 269: Variations of the selected elements/components in the hot metal 36 hours before the end of the EBF campaign 31 (K31) and campaign 32 (K32): (a) C in the hot metal and (b) V in the hot metal.	212
Figure 270: Illustration of the positions of the thermocouples into the refractory of the EBF hearth.	212
Figure 271: Variations of the measured temperatures into the refractory of the EBF hearth 36 hours before the end of the EBF campaign 31 (K31) and campaign 32 (K32).	213

Figure 272: Procurement of core drilling samples into the hearth of the EBF, campaign 31 (T1-T3: tuyeres 1-3)	214
Figure 273: Schematic illustration of the iron levels in a four-pool liquid level model (left) with the three tapholes in the reference furnace indicated (right).	215
Figure 274: Principles of corrections in the model, with vertical lines denoting important times for the corrections and horizontal lines denoting the bands around the taphole and the estimated slag-end level. The insert in the right part of the figure indicates the idea behind the band of uncertainty around the inner end of the taphole.....	216
Figure 275: Iron outflow rate in BF7 reported in the data base of TSE (blue lines) and the revised signal after removing spikes at torpedo changes (red lines) for a period of two shifts (the two signals overlap most of the time).	217
Figure 276: Estimated outflow (solid lines) and inflow (dashed lines) rates of iron (blue) and slag (red) for a tap at TSE BF7. At the end of the period, a decrease in production rate is seen. The periods with constant iron outflow are the result of the correction algorithm.	217
Figure 277: Estimated liquid levels (a and d), location of bands around the (inner end of) the taphole and the nominal slag-end level (b and e) and correction of the mass of produced iron and tapped slag (c and f) for a period where pools 1 (TH1) and 3 (TH2) were operated (left panels, a-c), and for a period where pools 1 (TH1) and 4 (TH3) were operated (right panels, e-f). Pool 1: blue solid line, Pool 2: black dash-dotted line, Pool 3: red dashed line, and Pool 4: magenta dash-dotted line.....	219
Figure 278: Corrections of the mass of produced iron (black) and tapped slag (red) for four different periods. Top panel set: Slag-end level parameter $\omega(j) = 20$ min; $j = 1, \dots, 4$. Bottom panel set: $\omega(1) = \omega(4) = 20$ min and $\omega(3) = 5$ min in Eq. (69).	220
Figure 279: Schematic of the expected end state of liquid levels for the case where the coke-bed permeability in front of one taphole (here TH2) is higher than in front of the others (TH1 and TH3), yielding smaller bending of the iron and slag surfaces.....	221
Figure 280: Vertical cross-sections along three radial lines going through the tapholes (top: TH1, middle: TH2, bottom: TH3) for TSE BF7 for a day in March 2016 reconstructed by BFHEM.	221
Figure 281: Improved GUI for the time evolution of wear and residual wall thickness.	222
Figure 282: Several examples of time evolution visualizations.	223
Figure 283: Visualization-GUI for a selected date.	223
Figure 284: Cut-line visualizations for a selected date.....	224
Figure 285: 3D Visualizations for a selected date.....	224
Figure 286: Unrolled 2D visualizations for a selected date.	224
Figure 287: Explanation of visualizations of measured temperatures and plausibilities.	225
Figure 288: Visualizations of measured temperature differences and average plausibilities at hearth wall.	225
Figure 289: Visualizations of measured temperatures and plausibilities at hearth wall.....	225
Figure 290: Visualizations of measured temperatures and plausibilities at hearth bottom.	226
Figure 291: Left: General locations of the TSE BF7 hearth lining thermocouples in the sidewall and (the outer parts of) the bottom. Right: Location of thermocouples in the bottom layer at the height (+1650) indicated by the turquoise diamond in the left part of the figure.....	226
Figure 292: Top: interface of wear model material setup tool. Middle: calculation lines.	227
Figure 293: Wear profile and isotherms reconstructed by the model for a specific day. Thermocouple readings (expressed in °C) for the day at two radii have been inserted as labelled blue bullets.....	228
Figure 294: Hearth bottom temperatures on the +1650 mm level (dashed lines) and +900 mm level (solid lines), at two radial points, $r = 2.9$ m (red) and $r = 5.8$ m (blue).	228
Figure 295: Top: horizontal (left) and vertical (right) cross section of the hearth of TSE BF7 at campaign start. Bottom: evolution of the estimated hearth volume inside the (red) skull (blue curve) and inside the (yellow) intact lining (green curve) to the end of 2016.	229
Figure 296: Estimated hearth lining state 1.5 months after blown in (top panel) and one year later (middle and bottom panels) for two different cross sections (cf. dashed lines in top left subgraphs).	230
Figure 297: Estimated hearth lining state for two different cross sections 21 months into the campaign.	231
Figure 298: Estimated hearth lining state for two different cross sections 2.5 years into the campaign.	232
Figure 299: Estimated hearth lining state for two cross sections 7 years after blow in.	233
Figure 300: Estimated hearth lining state for two different cross sections at the end of 2016, ten years after blow in.....	234
Figure 301: Estimated hearth lining state for two different cross sections at the end of 2018, twelve years after blow in.....	234
Figure 302: Terms considered in the simplified force balance of the blast furnace for estimating the dead man floating level in TSE BF7.....	235
Figure 303: Daily mean values of the ore-to-coke ratio and the gas pressure drop in TSE BF7 for days 1000-3500 of the campaign.	235

Figure 304: Estimated coke-free volume for TSE BF7 for days 1000-3500 of the campaign for an average cohesive zone level 9 m (top panel), 12 m (middle panel) and 15 m (bottom panel) above the taphole.....	236
Figure 305: Lower dead man profile on a specific day in late 2010 estimated by the force balance with a cohesive zone level 9 m (blue curve), 12 m (red curve) and 15 m (orange curve) above the taphole. The abscissa expresses the normalized radius of the hearth.....	236
Figure 306: Installation of Multipoint Thermocouples (MPTC) at AGDH BF4.....	237
Figure 307: Positions of 6 MPTCs at AGDH BF4.....	237
Figure 308: Yearly average T at MP TC 2a.....	238
Figure 309: Yearly average T at MP TC 4a.....	238
Figure 310: Yearly average T at MP TC 6a.....	238
Figure 311: Yearly average T at MP TC 8a.....	238
Figure 312: Yearly average T at MP TC 10a.....	239
Figure 313: Yearly average T at MP TC 12a.....	239
Figure 314: Selected time series of hearth wall thermocouple readings at AGDH BF4.....	240
Figure 315: Flat projection of temperatures measured at the hearth wall of AGDH BF 4 in 2011 and 2013.....	241
Figure 316: Filtering of effect from stoppages on hearth wall temperatures (left: all campaign, right: zoom to end of 2012).....	241
Figure 317: Removal of implausible data (left: by ΔT criterion, right: by correlation criterion)....	242
Figure 318: Standardization of thermocouple data (left: before, right: after).....	243
Figure 319: Grid used for interpolation for flat projection of AGDH BF4 hearth wall thermocouple data obtained from Delaunay Triangulation.....	243
Figure 320: Movement of regions with high correlations.....	244
Figure 321: Example for local correlation of hearth wall thermocouple data (upper: flat projection of correlation coefficient r, lower left: temperatures at section 9 – vertical cut, lower right: temperatures at layer 4 – horizontal cut).....	245
Figure 322: Tapping regime at 07.06.2010.....	245
Figure 323: Long term correlation patterns of hearth wall thermocouple data.....	246
Figure 324: Correlation of hearth wall temperatures with BF operational and data and model results (left: thermocouples at layer 3 – sump level, right: thermocouples at layer 7, ~1m below tap hole).	246
Figure 325: State close to the tap end in furnace hearth with (at least) two tapholes. right: two-pool model of the hearth.....	247
Figure 326: Schematic how the outflow rates are parameterized in the liquid level model.	248
Figure 327: Outflow (solid lines) and inflow (dashed lines) rates of iron (blue) and slag (red) for two taps at TSE BF7.....	248
Figure 328: Schematic of the treatment of the taphole region with respect to the iron-slag interface (horizontal lines) at the moment the taphole is opened. The shaded area indicates the region where both iron and slag appear simultaneously in the runner.	249
Figure 329: Simulated liquid levels for the first six examples of.....	251
Figure 330: Simulated liquid levels for the last two examples of.....	252
Figure 331: Observed inflows (dashed lines) and outflows (solid lines) of iron (blue) and slag (red) for eight consecutive taps alternating between the south and west tapholes of TSE BF7 in January 2016.....	253
Figure 332: Observed inflows (dashed lines) and outflows (solid lines) of iron (blue) and slag (red) for ten consecutive taps alternating between the south and north tapholes of TSE BF7 in January 2016.....	253
Figure 333: BF state where south taphole extends less deep into the hearth than the other (west or north) taphole, also indicating the final levels of the iron-slag interface by dotted and dashed lines, respectively.....	254
Figure 334: Outflow rates of iron (blue) and slag (red) in example 1 (Table 63).	254
Figure 335: Relation between mass of tapped slag and slag ratio for BF7 of	254
Figure 336: Comparison between pressure at the taphole and strain measured at taphole level (first campaign).	255
Figure 337: Calculated vs. measured strain differences at cooling water temperature.	256
Figure 338: Scheme of parameters influencing the measurements and outputs of the model.	256
Figure 339: Geometry setup used to model the BF hearth.	257
Figure 340: Pressure profiles of the gas (red), the slag level (green) and the hot metal level (blue) on the BF hearth shell.	257
Figure 341: Bending profile of the BF hearth according to pressure profile induced by liquids and gas.	258
Figure 342: General architecture of the script of the liquid levels model.	259
Figure 343: Strain gauges system using a half-Wheatstone bridge with temperature compensation.	260
Figure 344: Scheme representing strains measured and strains needed for the model.	260
Figure 345: Architecture of the initialization module.	261

Optimizing Blast Furnace Hearth Inner State (OPTIBLAFINS)

Figure 346: Convergence of the strain gauges offsets using the initialization module based on a dataset from Rogesa blast furnace at Dillinger Hütte.....	261
Figure 347: Hot metal and slag level variation during one day at AM Fos [55].....	262
Figure 348: Hot metal and slag level variation during one day at AM Fos [55] using the new version of the liquid level model.	262
Figure 349: Drawing of the additional generatrixes for AM Fos HF1.....	263
Figure 350: Electrical boxes containing 18 (left) and 12 (right) strain gauges acquisition cards used to measure strains at the AM Fos BF1.	264

6 Table of Tables

Table 1: Material properties of hearth lining at AMEH BF5A (supplier data sheets).....	14
Table 2: Material Properties of hearth lining at AGDH BF4 (used in [55]).....	14
Table 3: The computed and measured temperatures at Dillinger BF4 hearth differ systematically at the bottom corner (marked in red).....	20
Table 4: General Boundary Conditions (BC).....	26
Table 5: Specific boundary conditions for $DMD < 0$ and $DMD > 0$	28
Table 6: Material properties in water model.....	38
Table 7: EBF water model operational conditions.....	50
Table 8: Mean temperature in °C for each position on the EBF shell.....	61
Table 9: Reference case (volume fraction).....	62
Table 10: Case two; volume fraction of the bed	64
Table 11: Key parameters in the model, where the temperature, T , is expressed in °C	70
Table 12: Physical fluid properties used in the demonstration case.	87
Table 13: List of simulation parameters for the fluids.....	90
Table 14: List of simulation parameters for the particles.....	90
Table 15: List of thermophysical properties used.....	94
Table 16: Properties of phases in validation case.....	99
Table 17: Data coverage and BF-A properties.	101
Table 18: Main properties of tapping data (averages and standard deviations).....	101
Table 19: Properties of tapping data sorted by tap hole.....	102
Table 20: Multiple linear regression result for melt performance.....	104
Table 21: BF-A in the period right before and after the 2018 relining.	105
Table 22: Comparison of BF-5 data for the three selected periods, operational data.	110
Table 23: Comparison of BF-5 data for the three selected periods, chemical properties.	110
Table 24: Comparison of BF-5 data for the three selected periods, tapping data.....	111
Table 25: Industrial AM Fos BF1 cast data.	117
Table 26: Details of cases run in the sensitivity study.	117
Table 27: Results of the sensitivity study.	119
Table 28: Dimensions per layer and corresponding dominant frequencies for tuyere 9.	129
Table 29: Re-calculated dominant frequencies (kHz) per sensor, measurement type 1.....	129
Table 30: Re-calculated dominant frequencies (kHz) per sensor, measurement type 2.....	129
Table 31: General data of AMEH BF5A.....	133
Table 32: General data of AGDH BF4.	133
Table 33: Chemical analysis of the carbon block samples from AMEH BF5A.....	138
Table 34: Chemical analysis of the carbon block samples from AGDH BF4.	141
Table 35: Thermal conductivity, chemical composition and some physical properties of the worn carbon block samples from AGDH BF4.	143
Table 36: Core borings performed at ArcelorMittal Fos-sur-Mer BF's 1 and 2.....	159
Table 37: Time response from Cu injection in tuyere 3.....	162
Table 38: Chemical compositions of the metal samples taken from the drilling cores (balanced amount for other elements).....	163
Table 39: Example SEM-EDS point analysis (wt.%) results.	167
Table 40: Comparison of force- and mass-balance sub-model principles and assumption.....	171
Table 41: Initial experimental plan of the coke gasification trials.	175
Table 42: Measured maximum length of each sample before and after dissolution trial in hot metal.	177
Table 43: Chemical compositions of the slag samples procured from the hearth of EBF, campaign 31	179
Table 44: Chemical compositions of the final tapped slag samples from EBF, campaign 31.	180
Table 45: Chemical compositions of the slag samples procured from the hearth of EBF, campaign 32	181
Table 46: Chemical compositions of the selected final tapped slag samples from EBF campaign 32 as well as selected industrial slag samples.....	184
Table 47: Calculated melting temperatures of slag samples from the EBF hearth (campaign 31) assuming either FeO or Fe ₂ O ₃ in parenthesis.	184
Table 48: Calculated viscosities of the slag samples procured from the hearth of EBF (campaign 31) in the temperature range 1250-1600 °C with FactSage.	185
Table 49: Calculated melting temperatures of final tapped slag samples from the EBF (campaign 31) assuming FeO in the slag.....	185
Table 50: Calculated viscosities of the slag samples taken from the final tapped slag of EBF (campaign 31) in the temperature range 1250-1600 °C with FactSage.	185
Table 51: Calculated melting temperatures of the slag samples from EBF (campaign 32) and of the industrial slag samples assuming FeO in the slag.	185
Table 52: Calculated viscosities of the slag samples from EBF hearth (campaign 32) and of the industrial slag samples in the temperature range 1300-1600 °C with FactSage.	186

Table 53: Calculated viscosities of the slag samples from EBF final tapped slag (campaign 32) and of the industrial slag samples in the temperature range 1250-1600 °C with FactSage.	186
Table 54: Normalized chemical composition (wt%) of synthetic slag samples and their blast furnace reference samples.	194
Table 55: Wetting properties for a liquid according to its contact angle.	196
Table 56: Temperatures for softening and sphere of the slag samples from EBF hearth and the final tapped slag (campaign 32) by heating microscope observations.	197
Table 57: Temperatures for softening and sphere of the slag samples from EBF hearth and the final tapped slag (campaign 32) as well as the industrial slag samples by heating microscope observations.	197
Table 58: Chemical compositions of coke ashes for the coke samples taken from EBF hearth, campaign 31 (in wt.%).	204
Table 59: Chemical compositions of the ash components in the coke samples procured from the hearth of EBF hearth, campaign 32.	205
Table 60: Chemical compositions of the ash components in the EBF original coke.	206
Table 61: Categorization of sub-sample 2 (10-20 cm) from core drilling sample M101.	209
Table 62: Categorization of sub-sample 5 (40-50 cm) from core drilling sample M101.	209
Table 63: Tap duration, slag delay and figure number illustrating the liquid levels for the examples studied.	250
Table 64: Overview of utilised modelling techniques	266
Table 65: Overview of investigated measurement techniques.	266

Getting in touch with the EU

In person

All over the European Union there are hundreds of Europe Direct information centres. You can find the address of the centre nearest you at:

https://europa.eu/european-union/contact_en

On the phone or by email

Europe Direct is a service that answers your questions about the European Union. You can contact this service:

- by freephone: 00 800 6 7 8 9 10 11 (certain operators may charge for these calls),
- at the following standard number: +32 22999696 or
- by email via: https://europa.eu/european-union/contact_en

Finding information about the EU

Online

Information about the European Union in all the official languages of the EU is available on the Europa website at: https://europa.eu/european-union/index_en

EU publications

You can download or order free and priced EU publications at: <https://publications.europa.eu/en/publications>. Multiple copies of free publications may be obtained by contacting Europe Direct or your local information centre (see https://europa.eu/european-union/contact_en).

EU law and related documents

For access to legal information from the EU, including all EU law since 1952 in all the official language versions, go to EUR-Lex at: <https://eur-lex.europa.eu>

Open data from the EU

The EU Open Data Portal (<https://data.europa.eu/euodp/en/home>) provides access to datasets from the EU. Data can be downloaded and reused for free, for both commercial and non-commercial purposes.

A better understanding of the blast furnace inner state (dead man characteristics, refractory wear and hot metal flow) contributes to a stable and more reliable blast furnace process. Fundamental knowledge of the blast furnace hearth inner state will result in an improved efficiency with less stoppages.

In the field of hearth wear monitoring, active Hearth Echo Excellence measurements were found to be able to determine the residual refractory thickness and to detect cracks / gaps in the lining. Accurate temperature information was provided by optical fibres with high-temperature Bragg gratings (so called Fibre Bragg Grating sensors). Multipoint thermocouples were installed successfully to observe brittle layer formation.

A new coupled CFD-DEM-model was developed to provide details of the spatial porosity distribution within the dead man, the velocity fields and the fluid flows within the hearth.

A detailed analysis of the hearth erosion (build-up / melting of hearth lining) was performed for a certain BF hearth, using a 2D hearth wear model.

Hot metal liquid flow was clearly visualized using small-as well as full-scale (EBF) water models. The small-scale experiments showed a boundary layer with high velocity close the hearth wall, while the full-scale model focussed on real porosity values using two tapping rates. A three phase CFD EBF model accomplished these experiments.

A study of coke degradation showed that the gasification degree is the main parameter of its degradation, while the gasification is a direct function of heating time.

Coke bed porosity was determined (between 0.12 and 0.49) and used as input for the CFD models.

